

BULLETIN OF MAGNETIC RESONANCE

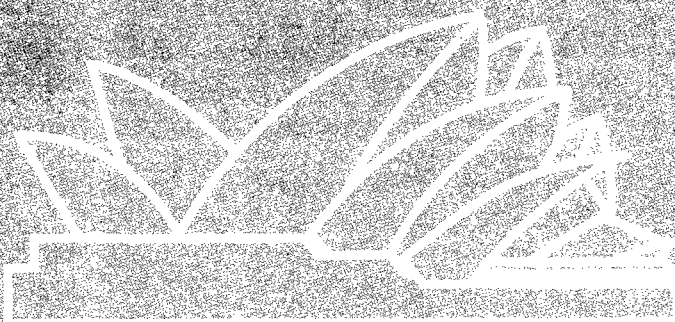
*The Quarterly Review Journal of the
International Society of Magnetic Resonance*

VOLUME 17

December 1995

NUMBER 1-4

Proceedings of the International Society of Magnetic Resonance XIIIth Meeting Part I



16th - 21st JULY 1995 • SYDNEY • AUSTRALIA

ISMAR

95

... the next 50 years

TWELFTH CONFERENCE OF THE INTERNATIONAL SOCIETY OF MAGNETIC RESONANCE

BULLETIN OF MAGNETIC RESONANCE

*The Quarterly Review Journal of the
International Society of Magnetic Resonance*

Editor:

DAVID G. GORENSTEIN

*Sealy Center for Structural Biology
The University of Texas Medical Branch
Galveston, Texas 77555-1157 U.S.A.
Phone: 409-747-6800
Fax: 409-747-6850
INTERNET: david@nmr.utmb.edu*

Editorial Board:

E.R. ANDREW
*University of Florida
Gainesville, Florida, U.S.A.*

LAWRENCE BERLINER
*Ohio State University
Columbus, Ohio, U.S.A.*

ROBERT BLINC
*University of Ljubljana
Ljubljana, Slovenia*

H. CHIHARA
*Osaka University
Toyonaka, Japan*

GARETH R. EATON
*University of Denver
Denver, Colorado, U.S.A.*

DANIEL FIAT
*University of Illinois at Chicago
Chicago, Illinois, U.S.A.*

SHIZUO FUJIWARA
*University of Tokyo
Bunkyo-Ku, Tokyo, Japan*

DAVID GRANT
*University of Utah
Salt Lake City, Utah, U.S.A.*

ALEXANDER PINES
*University of California
Berkeley, California, U.S.A.*

M. MIK PINTAR
*University of Waterloo
Waterloo, Ontario, Canada*

CHARLES P. POOLE, JR.
*University of South Carolina
Columbia, South Carolina, U.S.A.*

BRIAN SYKES
*University of Alberta
Edmonton, Alberta, Canada*

The *Bulletin of Magnetic Resonance* is a quarterly review journal by the International Society of Magnetic Resonance. Reviews cover all parts of the broad field of magnetic resonance, viz. the theory and practice of nuclear magnetic resonance, electron paramagnetic resonance, and nuclear quadrupole resonance spectroscopy including applications in physics, chemistry, biology and medicine. The *BULLETIN* also acts as a house journal for the International Society of Magnetic Resonance.

CODEN: BUMRDT

ISSN: 0163-559X

Bulletin of Magnetic Resonance, The Quarterly Journal of International Society of Magnetic Resonance. 1995 copyright by the International Society of Magnetic Resonance. Rates: Libraries and non-ISMAR members \$80.00, members of ISMAR, \$25.00. All subscriptions are for a volume year. All rights reserved. No part of this journal may be reproduced in any form for any purpose or by any means, abstracted, or entered into any data base, electronic or otherwise, without specific permission in writing from the publisher.

Council of the International Society of Magnetic Resonance

President: A. PINES, U.S.A.
Vice-President: M. GOLDMAN, France
Founding Chairman: D. FIAT, U.S.A.
Secretary-General: P. SERVOZ-GAVIN, France
Treasurer: R.R. VOLD, U.S.A.
Past President: R. FREEMAN, England

J. ANGLISTER <i>Israel</i>	E. BECKER <i>U.S.A.</i>	R. BENDALL <i>Australia</i>
G. BODENHAUSEN <i>Switzerland</i>	P.T. CALLAGHAN <i>New Zealand</i>	S. CLOUGH <i>England</i>
R. DESLAURIERS <i>Canada</i>	D. FIAT <i>U.S.A.</i>	S. FORSÉN <i>Sweden</i>
C. FYFE <i>Canada</i>	E. HAHN <i>U.S.A.</i>	R. HARRIS <i>England</i>
M.J.R. HOCH <i>South Africa</i>	H.-J. JAKOBSEN <i>Denmark</i>	R. KAPTEIN <i>The Netherlands</i>
D. KELLY <i>Australia</i>	C.L. KHETRAPAL <i>India</i>	B. MARAVIGLIA <i>Italy</i>
M. MEHRING <i>Germany</i>	H.C. PANEPUCCI <i>Brazil</i>	V. PETROSIAN <i>C.I.S.</i>
M.M. PINTAR <i>Canada</i>	M. PUNKINEN <i>Finland</i>	J. REISSE <i>Belgium</i>
G.C.K. ROBERTS <i>England</i>	V. SKLENÁR <i>Czechoslovakia</i>	C.P. SLICHTER <i>U.S.A.</i>
P. SOHÁR <i>Hungary</i>	H.W. SPIESS <i>Germany</i>	H. STERK <i>Austria</i>
T. TERAŌ <i>Japan</i>	J.S. WAUGH <i>U.S.A.</i>	A.B. WIECKOWSKI <i>Poland</i>
X.-W. WU <i>China</i>	K. WÜTHRICH <i>Switzerland</i>	N. YANNONI <i>U.S.A.</i>

The aims of the International Society of Magnetic Resonance are to advance and diffuse knowledge of magnetic resonance and its applications in physics, chemistry, biology, and medicine, and to encourage and develop international contacts between scientists.

The Society sponsors international meetings and schools in magnetic resonance and its applications and publishes the quarterly review journal. The *Bulletin of Magnetic Resonance*, the house journal of ISMAR.

The annual fee for ISMAR membership is \$20 plus \$25 for a member subscription to the *Bulletin of Magnetic Resonance*.

Send subscription to: International Society of Magnetic Resonance
Professor Regitze R. Vold, Treasurer
Department of Chemistry & Biochemistry
University of California, San Diego
9500 Gilman Drive
La Jolla, CA 92093-0359
(619) 534-0200; FAX (619) 534-6174
e-mail: rrvoid@ucsd.edu

**ORGANIZING COMMITTEE
for
ISMAR 95**

L.D. FIELD, CHAIRMAN

*Department of Organic Chemistry
University of Sydney
Sydney, NSW 2006
Australia*

M. BATLEY

*School of Chemistry
Macquarie University
North Ryde, NSW 2109
Australia*

W.A. BUBB

*Department of Biochemistry
University of Sydney
Sydney, NSW 2006
Australia*

E.J. DELIKATNY

*Department of Cancer Medicine D06
University of Sydney
Sydney, NSW 2006
Australia*

G.L. MENDZ

*School of Biochemistry
& Molecular Genetics
UNSW
Sydney, NSW 2052
Australia*

B.A. MESSERIE

*Department of Organic Chemistry
University of Sydney
Sydney, NSW 2006
Australia*

J.M. POPE

*School of Physics
Queensland University of Technology
GPO Box 2434
Brisbane, QLD 4001
Australia*

F. SEPAROVIC

*Division of Food Science & Technology
CSIRO
PO Box 52
North Ryde, NSW 2113
Australia*

G. TOWN

*Department of Electrical
Engineering (J03)
University of Sydney
Sydney, NSW 2006
Australia*

CO-EDITORS OF THE PROCEEDINGS

D.G. GORENSTEIN

*Department of HBC&G
Sealy Center for Structural Biology
University of Texas Medical Branch
Galveston, TX 77555-1157*

L.D. FIELD

*Department of Organic Chemistry
University of Sydney
Sydney, NSW 2006
Australia*

ACKNOWLEDGMENTS

On behalf of everyone attending the Conference, the Organizing Committee thanks all those who have provided us with financial or material support. We are extremely grateful to the following organizations for their generous assistance.

US Department of Energy/Lawrence Berkeley Laboratory

Bruker Australia Pty. Ltd.

Siemens, Medical Applications Pty. Ltd.

Varian Australia Pty. Ltd.

Society of Magnetic Resonance

Australian Tourist Commission

General Electric Medical Systems

NMR Magnex Scientific Inc.

Australian Institute of Physics

Australian Society for Biochemistry and Molecular Biology

Royal Australian Chemical Institute (Polymer Division)

NSW Travel Centre

Air New Zealand

Adrich Chemical Co.

National Australian Bank

ISMAR-95, Sydney, Australia, July 16-21, 1995

Following a delightful reception at the Sydney Opera House on Sunday evening, Alexander Pines, President of the Society, opened the meeting with a brief address:

"Fellow resonators, founders of magnetic resonance, members of the organizing committee, councilors and members of the International Society of Magnetic Resonance, eminent guests, ladies and gentlemen-

We have come to this magnificent place to celebrate magnetic resonance, to acclaim the marvel of spin, the ultimate spy (in the words of our eminent friend, Richard Ernst). Who else but spins could, with so little nourishment - a diet of low energy electromagnetic waves - reveal so much, open for us so incisive an atomic window on structure and dynamics of molecules, materials and organisms.

The International Society of Magnetic Resonance - ISMAR - has as its objectives the advancement and dissemination of the principles, developments and applications of magnetic resonance in physics, chemistry, biology, medicine, and other disciplines, and is dedicated to the fostering of scientific interactions among magnetic resonance spectroscopists throughout the world. The vitality of ISMAR is a tribute to the legacy of our founding chairman, Daniel Fiat, and the recent presidents of our society, Raymond Andrew, Charles Slichter, and Ray Freeman, to the council of ISMAR, to the executive committees whose current members include the secretary-general Pierre Servoz-Gavin and the treasurer, Regitze R. Vold, and to you, ladies and gentlemen, the constituents, the members of ISMAR. This year the Presidency of ISMAR passes to our distinguished colleague, Maurice Goldman.

I was born in 1945, the same year as NMR, so I had no choice but to go into magnetic resonance, under the illusion of free will. When Isaac Bashevis Singer was once asked if he believed in free will, he answered, Of Course - do I have a choice? From the foundations laid by the pioneers of a magnetic resonance, we have been privileged to witness the

evolution of EPR, NMR and NQR through many exciting developments, among them Fourier and multi-dimensional spectroscopy, multiple-pulse and high-resolution solid-state spectroscopy, and magnetic resonance imaging. At this 12th ISMAR conference we shall hear about some of the recent developments in our field, and on Thursday the ISMAR prize will be awarded to one of the giants of magnetic resonance.

This evening is a special pleasure, a celebration of fifty years - four of our founding fathers, Robert Pound, Martin Packard, Erwin Hahn, and Raymond Andrew, will tell us about the early days of NMR, of their participation and their interactions with the groups of Bloch and Purcell. It is illuminating and refreshing on occasion to hear about the authentic original. The translation is not always better - James Thurber was once approached by a fan at a social gathering, Mr. Thurber, I love your work, I read it in French, its even better in French. To which Thurber replied dryly, Yes, it tends to lose something in the original.

Before I ask John S. Waugh, the Vice-President Elect of ISMAR, to moderate the historical session, I would like to thank Les Field and his organizing committee - they represent the vibrant Australian magnetic resonance community - Les, you and your colleagues have gone to considerable effort in bringing us together for what will surely be an inspiring week of excitation and relaxation, of history and Australian hospitality in beautiful Sydney, a fitting prelude to the next fifty years. Thank you."

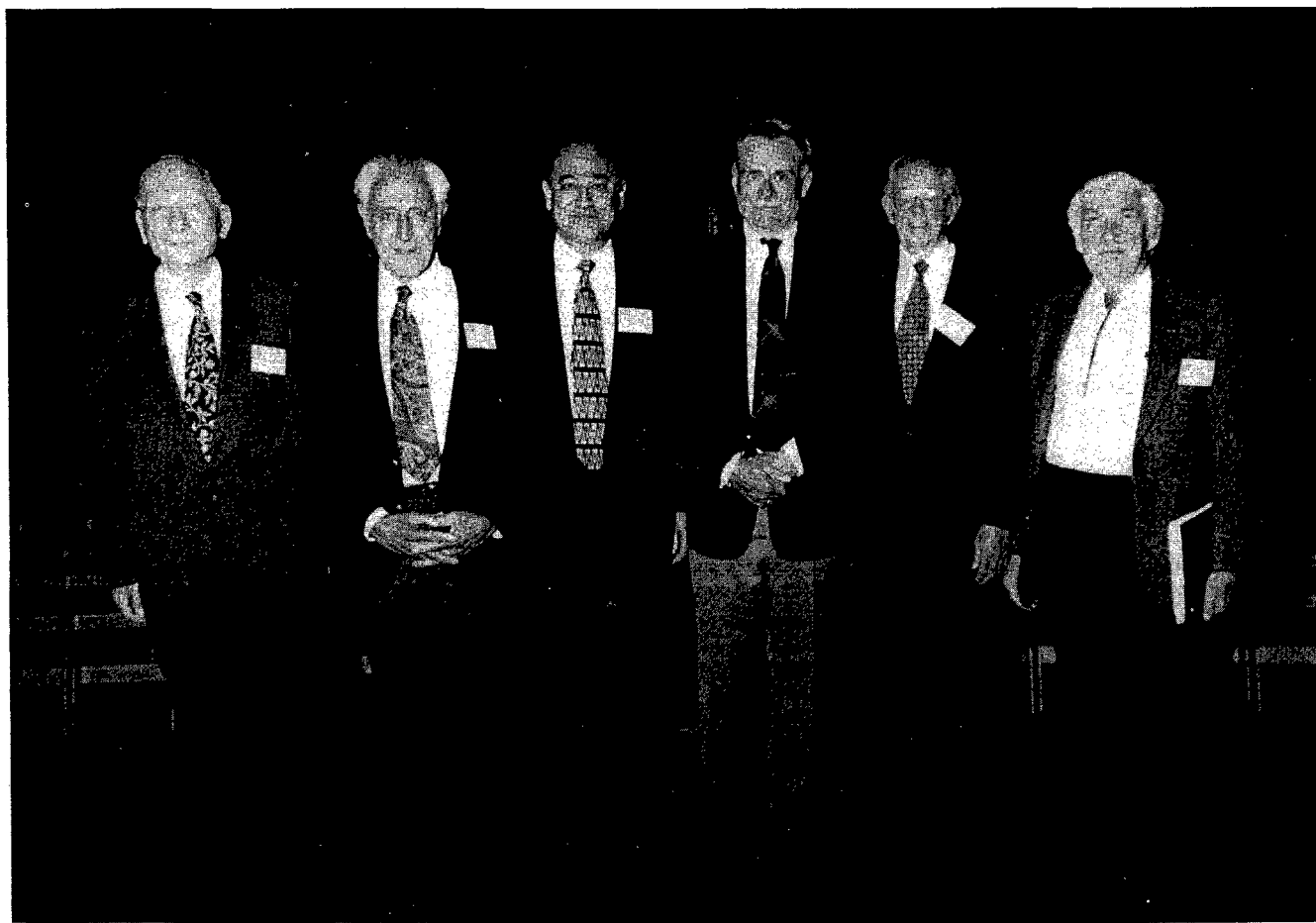
The chair was turned over to Waugh who introduced the four speakers for the historical session - Pound, Packard, Hahn, and Andrew, for a rousing, informative collection of anecdotes, recollections, and marvelous descriptions of the pioneering discoveries of NMR. On Thursday, the ISMAR Prize was awarded to Alfred G. Redfield for his pioneering contributions to magnetic resonance, in particular for the theory of relaxation and spin-temperature in the rotating frame.

On Friday, President Pines closed the very successful conference. He thanked the Australian organizing committee for their extraordinary preparation of both the scientific and social interactions. The conference hosted more than 500 delegates from

30 countries. As well as being a meeting of ISMAR, this also marked the formation of ANZMAG (the Australia and New Zealand Society for Magnetic Resonance) which will be the coordinating organization for magnetic resonance "downunder".

The meeting was a celebration of 50 years of magnetic resonance that all of us will long remember.

David Gorenstein
Les Field
Co-Editors of the Proceedings of ISMAR-95



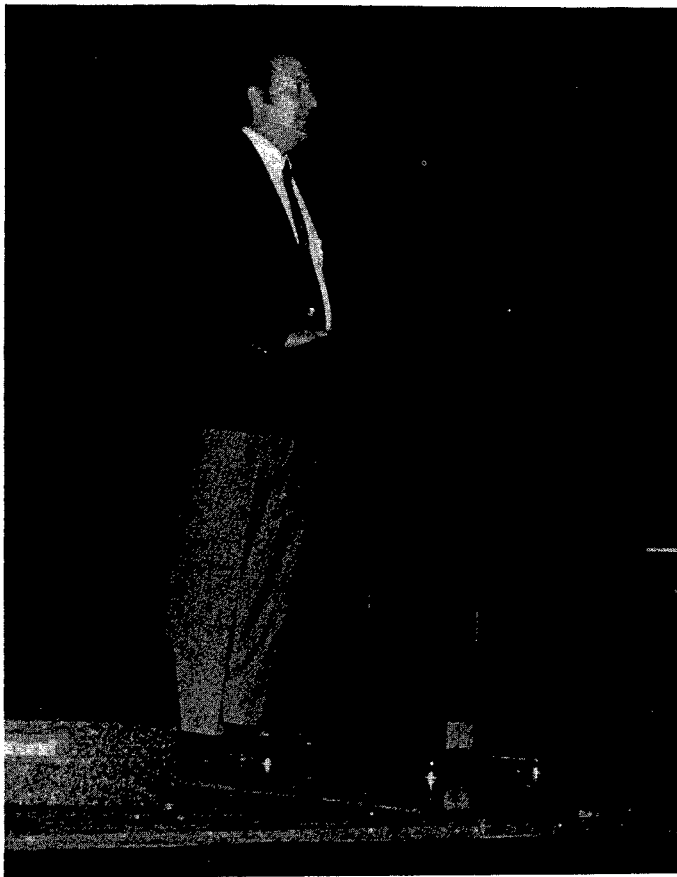
From left to right, Raymond Andrew, Erwin Hahn, Alex Pines (President, ISMAR), John Waugh (Vice President Elect, ISMAR), Martin Packard and Robert Pound



Al Redfield receiving the ISMAR prize from John Waugh, Vice President of ISMAR



Al Redfield giving his ISMAR Award address to the conferees



Les Field, Chairman, XIIth ISMAR Meeting



Conferees attending the Sydney Opera House festivities



Conferees attending the Sydney Opera House festivities

**Proceedings of the XIIth Meeting of the
International Society of Magnetic Resonance**

July 16 - 21, 1995

Sydney, Australia

Contents

Introduction, ISMAR 95, D.G. Gorenstein and L. Field.....	5
A History of NMR from a Lifetime's Work, E.R. Andrew.....	16
Advances in Diffusion Ordered NMR Spectroscopy, D. Wu, A. Chen and C.S. Johnson, Jr..	21
Resolution Without Solution: Retrieving Anisotropic Information in Solid-State NMR, M.J. Duer and C. Stourton.....	27
High-Resolution Fluorine-19 Solid-State NMR of Materials Containing Both Fluorine & Hydrogen, R.K. Harris, S.A. Carss, R.D. Chambers, P. Holstein, A.P. Minoja and U. Scheler.....	37
The Effect of Bulk Magnetic Susceptibility in NMR, I. Palyka, W. Huang and C.S. Springer, Jr.....	46
Noise in EPR Bridges with Multiple Time-Locked Microwave Frequencies, J.S. Hyde, R.A. Strangeway, J. Luglio, H.S. Mchaourab and W. Froncisz.....	54
A Hybrid-Hybrid Matrix Method for 3D NOE-NOE Data Analysis, D.G. Donne, E.K. Gozansky, F.Q. Zhu, Q. Zhang, B.A. Luxon and D.G. Gorenstein.....	61
The Observed Steric Isotope Effects in Cyclooctanone Isotopomer, M. Jung.....	67
Transversal Relaxation Rate Distribution Analysis in Porous Media, M. Martin-Landrove, R. Martin and A. Benavides.....	73
Magnetic Resonance in the Development of Better Strategies for Protecting the Brain during Surgery, R. Deslauriers, C.L. Filgueiras, J. Ye, M. Ede, R. Summers, T.A. Salerno, L. Ryner, P. Kozlowski, B. Winsborrow, J.K. Sun and J.K. Saunders.....	79
Applications of Intermolecular Multiple-Quantum Coherences in Solution NMR, W.S. Warren.....	87
Droplet Size Evolution in Disperse Systems by NMR, I. Scheurmann, M. Martin-Landrove and J. Espidel.....	93
High-Sensitivity NMR Spectroscopy Probe Using Superconductive Coils, W.A. Anderson, W.W. Brey, A.L. Brooke, B. Cole, K.A. Delin, L.F. Fuks, H.D.W. Hill, M.E. Johanson, V.Y. Kotsubo, R. Nast, R.S. Withers and W.H. Wong.....	98
EPR & Molecular Orbital Investigation of the Superoxide Scavenger Complex Bis(Piroxicam) Copper (II), R. Cini, R. Pogni and R. Basosi.....	103
NMR Study of Ligand Exchange in Hexacoordinate Silicon Chelates, D. Kost and I. Kalikhman.....	108

- The ^{13}C NMR Studies on a Snake Venom Protein (Cardiotoxin III) from the Taiwan Cobra (*Naja naja atra*),** C.-S. Lee and C. Yu 113
- Study of Intra-Erythrocytic pH & Metabolites in Renal Failure Patients by ^{31}P NMR,** W. Jinsart, S. Eiam-ong, P. Tosukhowong, S. Chinayon and V. Sitprija 118
- Unified Theory of NMR Spectra in Condensed Media,** G.E. Karnaukh, T.P. Kulagina and B.N. Provotorov 122
- Fatty Acid Binding to the Mitochondrial Uncoupling Protein,** P. Jezek, M. Bauer, P.D. Vogel, K.D. Garlid and W.E. Trommer 126
- Novel Models & Designs for Small Bore RF Resonators,** S. Crozier, L.K. Forbes, W. Roffman, K. Luescher and D.M. Doddrell 130
- New Semi-Empirical Approach for the Calculation of ^{13}C Chemical Shift Tensors,** U. Sternberg and W. Priess 134
- Elucidation of Metabolic Pathways Employing One- & Two-Dimensional NMR Spectroscopy,** G.L. Mendz 138
- 2D and 3D ^{15}N NMR Studies of Long [Arg₃]-IGFB-I,** E.R. Lebreton, J.A. Carver, G.L. Francis, G. Shooter, J.C. Wallace, B.N. Gray and M.A. Keniry 142
- $^3\text{J}(^{113}\text{Cd}, ^1\text{H})$ Couplings in Cd(S-Cys) and Cd- μ_2 (S-Cys)-Cd Moieties Follow a Karplus-Like Dependence with the $\text{H}^\beta\text{-C}^\beta\text{-S}\gamma\text{-Cd}$ Torsion Angle: Application to Protein Structure,** D.L. Pountney, O. Zerbe, W. von Philipsborn, J.B. Egan and M. Vasak 146
- FMR Studies of Cobalt Substituted Magnetite Prepared by Novel Mechanochemical Method,** W.A. Kaczmarek and S.J. Campbell 148
- NMR, CD & Molecular Modeling Studies on the Solution Conformation of a Modified Fragment of the First Extra-Cellular Loop of the Angiotensin II AT₁ Receptor,** A. Spisni, L. Franzoni, G. Sartor, C.R. Nakaie, R.S.H. Carvalho, A.C.M. Paiva, R.K. Salinas, T.A. Pertinhez and S. Schreier 151
- Measurement and Compensation of Susceptibility Induced Inhomogeneities in B_0 ,** F.O. Zelaya, S. Crozier, S. Dodd, R. McKenna and D.M. Doddrell 154
- High Resolution Solid State ^1H NMR of Organic Nanoparticles by Brownian Motion (UFP-NMR Method),** K. Kimura, A. Naito, H. Saito and N. Satoh 157
- ^{71}Ga NMR Investigations for Gallium Microparticles in a Pore Glass,** E. Shabanova, K. Schaumburg, E.V. Charnaya, Y.A. Kumzerov 160
- MRI Observations of Hippocampal Lesions in the Thiamin Deficient Rat Brain Under Glucose Load,** T. Wholohan, F. Zelaya, P. Nixon, S. Rose, A. Bower and D. Doddrell 163
- NMR Structure of Parathyroid Hormone-Related Protein (1-34),** J.A. Barden and B.E. Kemp 167
- Structure of the Pseudosubstrate Domain of Chicken Smooth Muscle Myosin Light Chain Kinase,** J.A. Barden and B.E. Kemp 169

Developments in STRAFI for the Quantitative Relaxation Analysis of Solvent Imbibition into Polymers, T.B. Benson and P.J. McDonald	172
^2H NMR Spectroscopy of D_2O in Silicate Sol-Gel Glasses, S. Wonorahardjo, J. Hook and G. Moran	174
Bulk & Surface Relaxation in Spheres during NMR Diffusion Measurements: Analytical Expressions using Neuman's Approach, P.W. Kuchel, A.J. Lennon and C. Durrant	176
Multinuclear (^1H, ^{13}C, ^{15}N, ^{59}Co) NMR Studies of Dithiocarbamic Acid Derivative Complexes of Cobalt(III) in Solution, U. Himmelreich, F. Tschwatschal and R. Borsdorf	178
Fraction of H_2^{17}O Bound to Macromolecules Measured by Triple Quantum NMR, E. Baguet, B.E. Chapman and P.W. Kuchel	180
Urea Exchange Across the Erythrocyte Membrane Measured Using Pulsed Field Gradient NMR Spectroscopy, B.E. Chapman, A.R. Waldeck and P.W. Kuchel	182
Solid State NMR Study of a New Combined Type Liquid Crystalline Polymer & Related Materials, O.H. Han, J.-I. Jin, J.-S. Kim, Y.-K. Yoon and S.-M. Huh	184
Solid-State MAS ^{207}Pb NMR of Lead Compounds, M. Logan, A. El-Dewik, R. Howe, N. Singh, L.C.M. van Gorkom and J.M. Hook	186
MRI/S of the Middle Cerebral Artery Occlusion Model of Stroke in the Mouse, P.D. Hockings, D.A. Middleton, S.J. Bailey, D.G. Reid and D.M. Doddrell	188
MR Assessment of Oxidative Stress Processes in Rat Liver & Kidneys, R.A. Tower, J.P. Williams, Z.H. Endre, M. Kadkhodae, S. Wilson, I.M. Brereton, G. Hanson and D.M. Doddrell ...	190
Bioactive Peptides: Solution Structure Determination by NMR Methods of Cyclo-decapeptides Inhibiting the Cholate Uptake in Hepatocytes, T. Tancredi, G. Saviano, P. Fucile and G. Zanotti	192
Study of Relaxation via EPR Linewidth of Gd^{3+} in Diluted Van Vleck Paramagnets $\text{Tm}_x\text{Lu}_{1-x}\text{PO}_4$ and $\text{Ho}_x\text{Y}_{1-x}\text{VO}_4$, S.K. Misra and S.I. Andronenko	194
GROESY and Related Selective 1D Analogs of Gradient-Enhanced nD Sequences, P. Adell, P. Parella, F. Sánchez-Ferrando and A. Virgili	196
NMR of ^7Li and EPR of Cr^{3+} in Ferroelectric LiTaO_3 Single Crystals, S.H. Choh, T.H. Yeom and S.W. Ahn	198
Nuclear Magnetic Resonance of ^7Li in $\text{Li}_2\text{B}_4\text{O}_7$ and LiB_3O_5 Single Crystals, I.G. Kim, N.K. Sung, S.H. Choh and J.N. Kim	200
Novel Designs for High Purity, Shielded Z^n Coils, S. Crozier, S. Dodd and D.M. Doddrell .	202
EPR Studies of Fe^{3+} Ion in Mg-Doped LiNbO_3 Single Crystal, T.H. Yeom, S.H. Choh and S.H. Lee	204
^{15}N NMR Spectroscopy in Phosphazene Compounds, F. López-Ortiz and E. Peláez-Arango .	206

- Stereochemistry of Some Anaesthetic Steroids by ^{13}C NMR**, L Fielding, N. Hamilton, R. McGuire, M. Maidment and A.C. Campbell.....208
- Trimethylammonium Group as a Relay to Control the Lipid Headgroup Dynamics by the Reorientation of Water Dipoles**, W.-G. Wu and C.-H. Hsieh210
- Bioactive Conformation of Stromelysin Inhibitors Determined by Transferred Nuclear Overhauser Effects**, N.C. Gonnella, R. Bohacek, X. Zhang, I. Kolossváry, C.G. Paris, R. Melton, C. Winter, S.-I. Hu and V. Ganu212
- Development of a Solenoidal Nanoliter-Volume RF Coil for NMR**, A.G. Webb, D.L. Olson, T.L. Peck, J.V. Sweedler and R.L. Magin.....214
- Fluorine-Based MRI Agents for in-vitro Temperature Mapping**, A.G. Webb.....216
- Use of ^{15}N NMR Peak Heights to Measure Rate & Equilibrium Constants for Reaction of Platinum(II) Amine Complexes**, T.G. Appleton and K.J. Barnham.....218
- Chemical Shift Selective Flow Imaging: Applications in Membrane Filtration of Oil-Water Emulsions**, S. Yao, J.M. Pope and A.G. Fane220
- High Resolution Proton Magnetic Resonance Imaging in Experimental Acute Renal Failure**, I.A. Leditschke, G. Cowin, S. Crozier and Z.H. Endre.....222
- T_2 Effects in PFG NMR Analysis of Ligand Binding to Macromolecules**, A.J. Lennon, B.E. Chapman and P.W. Kuchel.....224
- Mercury-Polymer Interactions Characterized by ^{199}Hg -NMR**, N. Onyewuenyi, J. Hook and G. Moran226
- Spin Echo Measurements with Pulsed NMRON**, W.D. Hutchison, N. Yazidjoglou and D.H. Chaplin.....228
- Oscillatory Free Induction Decay in NMRON: The Extension of the Theorem on Coherent Transients for Higher Rank Statistical Tensors**, D.H. Chaplin, L.N. Shakhmuratova, W.D. Hutchison and D.J. Isbister.....230
- ^7Li and ^{19}F NMR Study of LiCF_3SO_3 Containing Polymer Electrolytes: The Effect of Plasticizers**, M.C. Garcia, M.E. Smith and J.H. Strange.....232
- Paramagnetic Ion Relaxation in Rare-Earth Doped Phosphate Glasses via ^{31}P NMR**, I.P. Goudemond, J.M. Keartland, M.J.R. Hoch.....234
- Non-Exponential Nuclear Magnetization Recovery in Magnetic Glasses**, I.P. Goudemond, J.M. Keartland and M.J.R. Hoch.....236
- Conformational Mapping of a Fusion Peptide by Electrospray MS/MS, Isotope-Enhanced FTIR Spectroscopy and EST Spin-Labeling**, A.J. Waring, K. Faull, C.C. Curtain and L.M. Gordon.....238
- ^{31}P NMR Visibility of ATP and Phosphocreatine *In vivo***, J.P. Williams and J.P. Headrick...240

Advantages of Long-Range-INEPT Measurements for Structure Determination of Catechin Esters , A. De Groot, R. Dommissse and G. Lemièrre, J. Lepoivre.....	242
Unusually Stable Hydrates of N-Substituted 3-Hydroxy-2-(phenylselenenyl) methylpiperidine Derivatives. Where is the Water? - An NMR Study , M.A. Cooper, S.M. Pyke and A.D. Ward.....	244
The Application of Nuclear Magnetic Resonance Spectroscopy to the Analysis of Archaeological Materials , L.T. Byrne, E.L. Ghisalberti and I.M. Godfrey.....	246
The Mixed Alkali Effect of Li/Na Disilicate Glasses , F.A. Ali, A.V. Chadwick, G.N. Greaves, M.C. Jermy and M.E. Smith.....	248
Solid State Satellite Transition MAS NMR Spectroscopy of Quadruple Nuclei , T.J. Bastow, C. Jaeger, G. Kunath-Fandrei and M.E. Smith.....	250
Nuclear Magnetic Resonance of X in XMnCl₃(X=Na, Cs) Single Crystals , A.R. Lim, S.H. Choh and S.Y. Jeong.....	252
¹H Nuclear Magnetic Resonance of Liquid Crystalline Polymer Blends , J.-H. Chang and K.-S. Hong.....	254
In-Vivo and In-Vitro Analysis of CNS Cancers by ¹H-NMR Spectroscopy , S. Dodd, B.P. Shehan, O. Hennessy and D.J. Craik.....	256
Spectral Editing in ¹³C CP/MAS Experiment at High Magnetic Field , J.Z. Hu, X. Wu, N. Yang, L. Li and C. Ye.....	258
PFG-Inadequate for Detection of Two and Three Bond ¹³C-¹³C Couplings , H. Koshino and J. Uzawa.....	260
¹H-NMR Spectroscopic Studies on the Interaction between Local Anesthetic Dibucaine & a Na⁺-Channel Inactivation Gate Peptide , Y. Kuroda, M. Ogawa, N. Fujii and T. Nakagawa..	262
Cerebral Metabolic Compartmentation as Revealed by ¹³C NMR, ¹³C-¹³C and ¹³C-¹⁵N Isotopomer Analyses , A. Lapidot.....	264
Biodynamics and NMR , R. Lenk.....	266
Cellulose-Cellulase Interaction , M.-L. Mattinen, M. Kontteli, J. Kerovuo, M. Linder, A. Amila, G. Lindeberg, J. Stahlberg and T. Drakenberg.....	268
The 2,3-Bisphosphoglycerate Shunt of Human Erythrocytes: Multinuclear NMR & Computer Simulation , P.J. Mulquinev, W.A. Bubb and P.W. Kuchel.....	270
Secondary Solution Structure of Calf Thymus Histone H1 Globular Region , C. Nicolini, G. Nicastro and C. de Chiara.....	272
Studies of Human Calcitonin Fibrillation by Proton Nuclear Magnetic Resonance Spectroscopy: Characterization of the Lyophilized Fibril , K. Kanaori and A.Y. Nosaka....	274
The Effect of the Fourth-Order Zero-Field Splitting on EPR for S = 5/2 Ions at the Three-Fold Symmetry , I.-W. Park and S.H. Choh.....	276

Comparing a Neural Network Based Image Enhancement Technique with Keyhole Magnetic Resonance Imaging , Y. Hui and M.R. Smith.....	280
Solution Structure Studies of the Low-Density Lipoprotein Receptor Ligand-Binding Domain , N.L. Daly, M.J. Scanlon, J.T. Djordjevic, P.A. Kroon and R. Smith	280
Pulsed NQR in Antimony Metal at High Pressures: Changes in the Electric Field Gradient and the Electronic Structure , G.J. Hill, J.M. Keartland and M.J.R. Hoch.....	282
A Water Proton Spin-Lattice Relaxation Study of the Adsorption of Paramagnetic Ions in Aqueous Colloidal Silica Suspensions , P. Roose, J. Van Craen, G. Andriessens, H. Eisendrath.....	284
Quick Spinning Sideband Suppression in MAS-NMR Experiments , T.J. Bonagamba, H. Panepucci, E.A. Vidoto and E.L.G. Vidoto.....	286
<i>In vivo</i> ³¹P NMR and Histological Investigation of Muscle Recovery after Induced Injury , T.J. Bonagamba, T.F. Salvini, H. Panepucci, E.L.G. Vidoto, A. Tannús, A.C.M. Zerri and C.C. Morini	288
Demagnetization Fields in NMR Experiments which Employ Magnetic Field Gradients , G.J. Bowden and T. Heseltine	290
NMR Structural Studies of Amphipatic Helices , G.K. Pierens, G.W. Buchko, G. Wang, W.D. Treleaven, A. Rozek and R.J. Cushley.....	292
Relaxation Changes in Persimmon Fruit Stored at Low Temperature and Modified Atmosphere , C.J. Clark and J.S. MacFall.....	294
ENDOR Spectra of an X-Irradiated Single Crystal of the R₃P=CH-C(O)CH₃ Wittig Reagent , T. Berclaz, M. Geoffroy, G. Rao and Z. Tancic	296
Use of the Pseudocontact Shift as a Structural Constraint for Macromolecules in Solution , M. Gochin and H. Roder.....	298
Nuclear Spin-Lattice Relaxations Caused by Paramagnetic Impurities in Layered Silicates: Effect of Magic Angle Spinning , S. Hayashi.....	300
A Comparison of Frequency and Time Domain Fitting of ¹H MRS Metabolic Data , A. Freise, E. Spencer, I. Marshall and J. Higinbotham	302
Electronic & Molecular Structure of Room-Temperature Stable Triplet Carbene as Studied by ESR Spectroscopy & X-Ray Crystal Analysis of the Diazo Precursor , K. Furukawa, T. Takui, K. Itoh, I. Miyahara, K. Hirotsu, T. Watanabe, K. Hirai and H. Tomioka..	304
Water Structure and Dynamics in Membranes Studied with Two-Dimensional Magic-Angle-Spinning-NMR , F. Volke, A. Pampel, R. Scott and A. Bick.....	306
Calendar of Forthcoming Conferences	307
Instructions for Authors	308

A History of NMR from a Lifetime's Work

E.R. Andrew

*Departments of Physics and Radiology, University of Florida,
P.O. Box 118440, Gainesville, Florida 32611, USA*

Abstract

A history of NMR is sketched from the author's 48 years of NMR experience from 1947 to the present (1995). This includes terms as President of ISMAR and of the Groupement AMPERE, as Editor-in-Chief of *Magnetic Resonance in Medicine*, and as author of the first book on NMR. He mentions interactions with other MR scientists in the early days including Abragam, Bloch, Bloembergen, Ernst, Gorter, Gutowsky, Kastler, Pound, Purcell, Ramsey, Richards, Slichter and Van Vleck, and his experiences while working in Harvard, St. Andrews, Wales, Nottingham, Cambridge and Florida. The author mentions some of his contributions, especially to molecular structure, dynamics and relaxation, discovery of magic angle spinning, spin multiplets in solids, conformational motion and order in solids, magnetic resonance imaging and current work on NMR microscopy.

The first two papers presented at the Sydney ISMAR conference were those by Professor Robert Pound and Dr. Martin Packard, two of the original discoverers of NMR back in 1945 (1,2). By contrast I am an example of the many who followed in this wonderfully fruitful field of research which they opened up. My practical interest in NMR began in 1947, and has continued throughout my life, and I believe I am now the longest serving NMR practitioner still working in the field.

When the first papers on NMR were published (1,2) in 1946, I was a graduate student in Cambridge, England, working with Professor David Shoenberg on problems in superconductivity. Whenever something of interest caught David's eye in the literature he would depute one of us to read it up and present a talk at the weekly seminar, and in this way I learnt about NMR. Then soon afterwards we had a visit from Gorter (who had made unsuccessful attempts to find NMR (3,4) in 1936 and 1942) and then visits from Felix Bloch, Nicolaas Bloembergen and Robert Pound.

It was clear that NMR was an exciting new subject, so in 1948 with a Commonwealth Fund Fellowship, I was very fortunate to spend a year working in the NMR laboratory of Professor Edward Purcell at Harvard.

Besides Pound and Bloembergen, other famous scientists there included Van Vleck, Bridgman and Ramsey.

I had a laboratory on the basement floor of the Lyman laboratory and worked with a CW NMR spectrometer previously used by Herbert Gutowsky and George Pake. It consisted of a permanent magnet, a General Radio signal generator, an rf bridge, pre-amplifier, a Halli-krafters receiver and an oscilloscope. There was a large rectangular hole in the side wall about 1 m wide and 0.3 m high and in the next lab was one of Ed Purcell's graduate students, Charlie Slichter, now a Professor at the University of Illinois. Charlie and I got to know each other well through that hole in the wall and I'm very happy that our paths have crossed frequently over the years. At the 9th ISMAR Conference in Rio de Janeiro, Brazil, in 1986, I was President of ISMAR and Charlie Slichter was Vice-President. Three years later in Morzine, France, at the 10th ISMAR conference he was President and I was Past-President. My first published NMR result (5) from Harvard, shown in Fig. 1, shows the narrowing of the proton NMR line from solid benzene due to reorientation of the molecules about their six-fold axes.

After this splendid year in America, during which I visited Henry Torrey at Rutgers University and Felix Bloch at Stanford University, I returned to Britain as a lecturer in Physics at St. Andrews University, the oldest university in Scotland. There Alwyn Rushworth and I designed a 2-ton 0.6 Tesla permanent magnet for NMR in solids, the largest permanent magnet in Britain at the time. We studied molecular dynamics including molecular diffusion in the solid state (6,7). We also used NMR to solve structural problems in solids, for example that of urea (8).

St. Andrews was somewhat remote in the north of Britain but we were very pleased to welcome Ed Purcell, Bob Pound and Herb Gutowsky in the early 50's. Another welcome visitor was a young Japanese theorist Kazuhisa Tomita, who was then working on the famous relaxation paper by Kubo and Tomita (9); we met from time to time over the years until his death in 1991.

By 1954, many physicists and chemists were taking an interest in NMR and there was need for a book on the

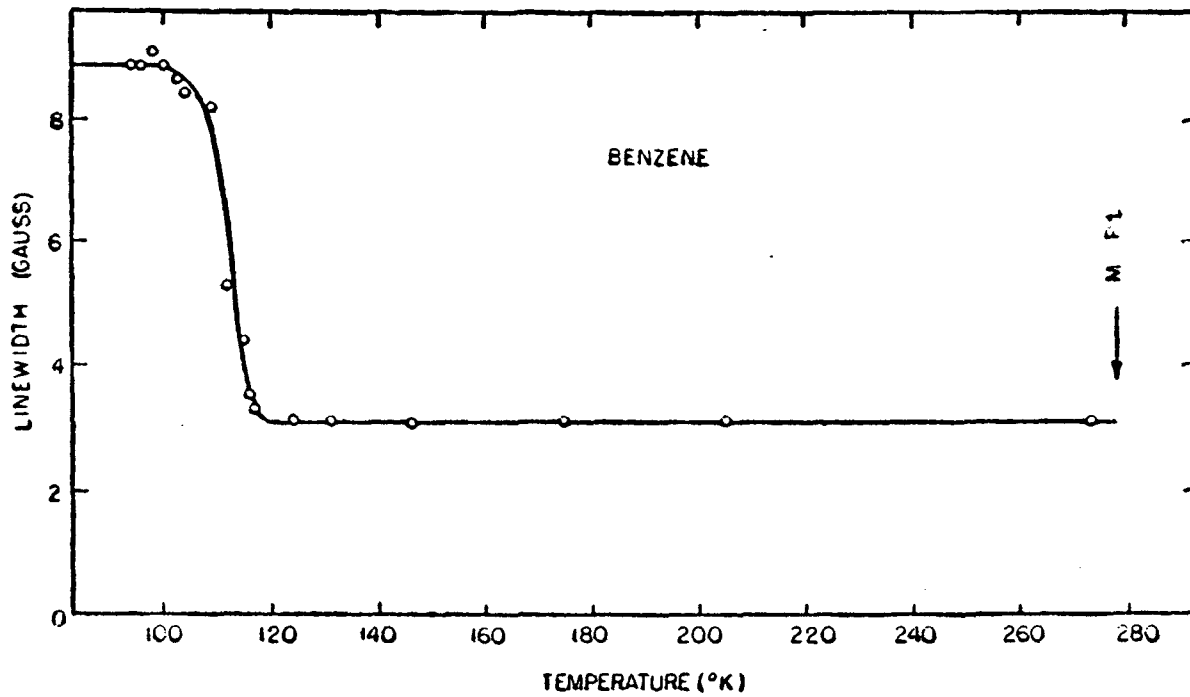


Fig. 1 The author's first published NMR result (5) which shows the narrowing of the proton NMR linewidth in solid benzene, arising from reorientation of the benzene molecules about their hexad axes.

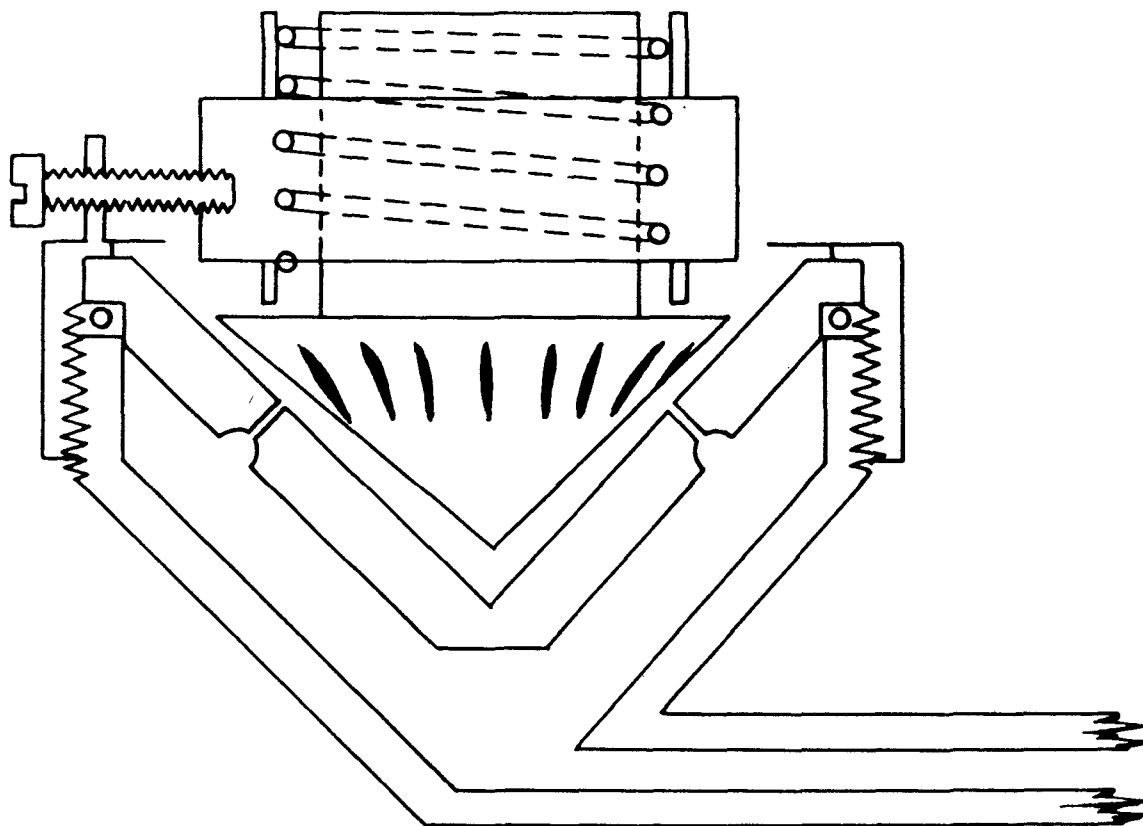


Fig. 2 An early turbine assembly for magic angle spinning (11,12).

subject. So while in St. Andrews I wrote my book *Nuclear Magnetic Resonance* in 1953-54 and it was published by Cambridge University Press the following year (10). When my first royalty cheque for £50 arrived I remember calculating this represented a return of about sixpence (5 Australian cents) per hour spent on the project!

My stay in Scotland, the land of my grandfathers, was five years and in 1954 I moved to the University of Wales as Professor of Physics and Head of Department and we continued our work on NMR in the solid state. Although it was a quiet cathedral and university town, we had some distinguished visitors to our NMR lab including Prince Philip, Duke of Edinburgh; from the USA came Erwin Hahn, Walter Knight, George Pake and Philip Anderson, and from France came Abragam and Kastler. Professor Jacek Hennel came for a year from Krakow, Poland, the first of many mutual visits. NMR was a good subject for research in a small department with limited resources but good students.

On my visit to Australia for this ISMAR conference I shall go on to Melbourne for a reunion with my first postdoctoral fellow in Wales in 1956, Geoffrey West, from CSIRO at Monash, who returned to be one of the pioneers of NMR in Australia and has worked in the field of NMR in Australia longer than anyone else. Also in Melbourne I shall meet again Geoffrey Jenks, my first Australian NMR graduate student.

In 1963 I moved my NMR operations to Nottingham University, where I had been appointed Head of the Physics Department. We had started our work on Magic Angle Spinning (MAS) in Bangor in 1958, and we continued this in Nottingham. A diagram of one of our spinners (11,12) which could rotate solid specimens up to 14 kHz is shown in Fig. 2. Nowadays David Doty can spin somewhat smaller rotors twice as fast as this. Using this MAS technique we resolved the first spin multiplet in a solid (12,13), Fig. 3. It was the ^{19}F quartet from polycrystalline KAsF_6 arising from coupling to the ^{75}As nucleus (spin $\frac{3}{2}$).

Our studies of molecular dynamics in solids by NMR led us to an awareness of conformational motion in solids (14). In some materials this leads to conformational order-disorder phenomena and a specific heat anomaly. The conformational disorder can be propagated in a manner analogous to spin waves in magnetism and the quasi-particle characterizing elementary excitation of conformational waves we called a conformon (15).

In 1974 a new chapter in our NMR work opened up when we began work on NMR imaging. Our early image of a transverse section of a lemon appeared on the front

cover of Nature (16) and we published the first image of a live human wrist (17,18), that of my Australian graduate student Paul Bottomley, now a Professor at Johns Hopkins University. In April 1976 we organized the first international conference on NMR imaging in Nottingham (19). Most of the activists in the world of magnetic resonance imaging (MRI), about 25 in all, were there. These included Lauterbur, Mansfield, Ernst, Moore, Hinshaw and Hutchison (19). We soon moved up to whole body sizes in 1979 and a first clinical assessment of pathology was obtained by Bill Moore, Brian Worthington and colleagues (20).

Scientists are great travellers and international conference goers and NMR has provided wonderful opportunities. Over the years I have visited over seventy countries. There have been opportunities to meet notable people including Pope John Paul II and Queen Elizabeth of Britain.

The years were passing and I began to notice without enthusiasm that the age of my compulsory retirement (65) at Nottingham University was approaching. So I was very delighted to receive an invitation to come to the University of Florida in 1983 as a Research Professor without a specified date of retirement. Here in Florida I have joint appointments in the Physics Department where I can do solid state NMR and in the College of Medicine where I do MRI. Here I could start a new journal, *Magnetic Resonance in Medicine* (21), write another book with several colleagues, *Clinical Magnetic Resonance* (22), take sabbatical leave back to Cambridge University in England in 1989, and continue participating in conferences including Kazan, Russia, last year, 1994, for the AMPERE congress which celebrated the 50th anniversary of the discovery of ESR by Zavoisky (1907-1976). In Kazan we saw Zavoisky's original magnet and his other early equipment and I had the pleasure of meeting his daughter and granddaughter. In Florida I have been able to participate in the founding of the United States National High Magnetic Field Laboratory where NMR has now been observed in a field of 30 Tesla (23) in seven nuclear species.

My current interests include NMR microscopy and the design of gradient coils for microimaging. In Fig. 1 I showed my first published result in NMR, so here in Fig. 4 is our latest NMR result, a microimage of a cross-section of human spinal cord in vitro, with a resolution of $40\ \mu$ (24).

Finally it should be mentioned that those of us, like the author of this article, who have Scottish ancestry, know very well that 1995 is not only the 50th anniversary of NMR, but also the 250th anniversary of the famous '45. In 1745 Prince Charles Edward Stuart (Bonnie

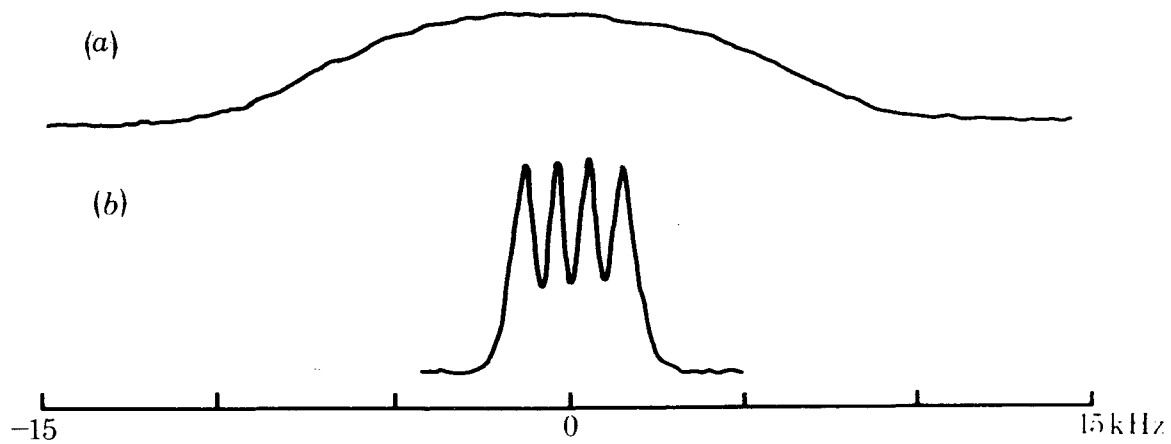


Fig. 3 The first spin multiplet resolved in the solid state (12,13). ^{19}F NMR spectra of polycrystalline KAsF_6 . (a) Static specimen, (b) specimen spinning at 5.5 kHz, displaying quartet structure due to J coupling between ^{19}F and ^{75}As nuclei.

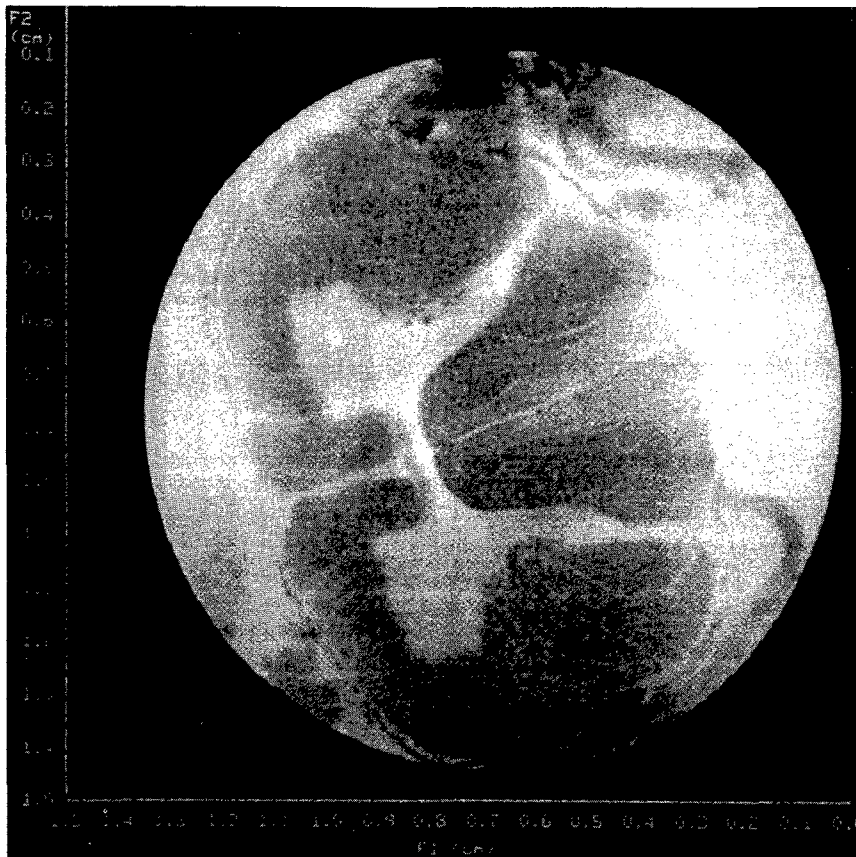


Fig.4 The author's most recent NMR work which uses a novel transverse gradient assembly to obtain this transverse section proton NMR microimage of human spinal cord in vitro at 300 MHz with resolution $40\mu\text{m}$ (24).

Prince Charlie) raised the Scottish standard and rallied the clans at Glenfinnan on the shores of Loch Shiel. His rebellion reached Derby before he was stopped. Meantime he had produced the recipe for the famous Scottish liqueur Drambuie, surely a discovery comparable with NMR, and we may all drink a toast to the next 50 years of NMR with a dram of this perfect liquid!

References

1. E.M. Purcell, H.C. Torrey and R.V. Pound. *Phys. Rev.* **69**, 37 (1946).
2. F. Bloch, W.W. Hansen and M.E. Packard. *Phys. Rev.* **69**, 127 (1946).
3. C.J. Gorter. *Physica* **3**, 995 (1936).
4. C.J. Gorter and L.F.J. Broer. *Physica* **9**, 591 (1942).
5. E.R. Andrew. *J. Chem. Phys.* **18**, 607 (1950).
6. E.R. Andrew and R.G. Eades. *Proc. Roy. Soc.* **A216**, 398 (1953).
7. E.R. Andrew and R.G. Eades. *Proc. Roy. Soc.* **A218**, 537 (1953).
8. E.R. Andrew and D. Hyndman. *Disc. Faraday Soc.* **19**, 195 (1955).
9. R. Kubo and K. Tomita. *J. Phys. Soc. Japan* **9**, 888 (1954).
10. E.R. Andrew. *Nuclear Magnetic Resonance*. Cambridge University Press (1955).
11. E.R. Andrew, L.F. Farnell, M. Firth, T.D. Gledhill and I. Roberts. *J. Mag. Res.* **1**, 27 (1969).
12. E.R. Andrew. *Phil. Trans. Roy. Soc.* **A299**, 505 (1981).
13. E.R. Andrew, L.F. Farnell and T.D. Gledhill. *Phys. Rev. Lett.* **19**, 6 (1967).
14. E.R. Andrew and J.R. Brookeman. *J. Mag. Res.* **2**, 259 (1970).
15. E.R. Andrew. *Phys. Letters* **34A**, 30 (1971).
16. E.R. Andrew, P.A. Bottomley, W.S. Hinshaw, G.N. Holland and W.S. Moore. *Nature* **270**, #5638 (1971).
17. W.S. Hinshaw, E.R. Andrew, P.A. Bottomley, G.N. Holland, W.S. Moore and B.S. Worthington. *Neuroradiology* **16**, 607 (1978).
18. E.R. Andrew. *Phil. Trans. Roy. Soc.* **B289**, 471 (1980).
19. E.R. Andrew. *Proc. Roy. Soc.* **B255**, 399 (1985).
20. R.C. Hawkes, G.N. Holland, W.S. Moore and B.S. Worthington. *J. Computer Assisted Tomography* **4**, 577 (1980).
21. *Magnetic Resonance in Medicine*. Ed. E.R. Andrew, Academic Press (1984 onwards).
22. E.R. Andrew, G. Bydder, J. Griffiths, R. Iles and P. Styles. *Clinical Magnetic Resonance: Imaging and Spectroscopy*. Wiley: Chichester (1990).
23. P.L. Kuhns, A. Kleinhammes, W.G. Moulton and N.S. Sullivan. *J. Mag. Res.* (accepted for publication 1995).
24. E.R. Andrew, B.A. Inglis, M. Kempka, T.H. Mareci and E. Szczesniak. (in course of publication 1995).

Acknowledgements

The author gratefully acknowledges support from NIH grant P41 RR 02278.

Advances in Diffusion Ordered NMR Spectroscopy

Donghui Wu, Aidi Chen, and Charles S. Johnson, Jr.

*Department of Chemistry
The University of North Carolina
Chapel Hill, North Carolina 27599-3290, USA*

I. Introduction

Modern NMR diffusion measurements are all based on the Stejskal-Tanner (S-T) pulsed field gradient spin echo experiment in which a gradient pulse is used to encode the spatial positions of nuclear spins and a second matched gradient pulse decodes positions. Translation diffusion in the interval between the gradient pulses results in attenuation of the spin echo, and a Fourier transformation (FT) of the half echo permits diffusion rates to be associated with individual lines in the NMR spectrum. The echo attenuation is described by the well-known S-T factor $\exp[-Dq^2(\Delta - \delta/3)]$ (1).

Pulsed field gradient NMR (PFG-NMR) has become a standard method for the measurement of diffusion rates. In particular the FT version has been exploited by Stilbs and others for the study of mixtures (2). Unfortunately, this powerful method has not yet found widespread use because the necessary hardware is not generally available and the data analysis software is not part of standard NMR packages. The Diffusion Ordered Spectroscopy (DOSY) method described here seeks to remedy this situation by providing an automated experiment with data analysis and display that provide "at a glance" recognition of components in complex mixtures (3).

II. Principles of Diffusion Ordered 2D NMR Spectroscopy (DOSY)

The essence of DOSY is the display of a "diffusion spectrum" at each chemical shift. This requires the acquisition of an undistorted data set containing complete information about the diffusion rates of all molecular components, and data inversion procedures to convert S-T attenuation curves into diffusion peaks. The desired data set has the form:

$$f(q, \nu) = \sum_{j=1}^{N_\lambda} A_j \exp[-D_j (\Delta - \delta/3) q^2] \quad [1]$$

where the area of a gradient pulse is $q = \gamma g \delta$, γ is the magnetogyric ratio, and g and δ are the gradient pulse amplitude and duration, respectively. $A_j(\nu)$ is the one-dimensional NMR spectrum of the j^{th} diffusing species when $q = 0$ (taking into account nuclear spin relaxation), D_j is the

associated tracer diffusion coefficient, and N_λ is the number of components required to describe the data set at frequency ν . The time interval Δ between the leading edges of the gradient pulses is typically much greater than the pulse duration δ .

In order to obtain an undistorted set of NMR spectra, each with a different value of q , it is necessary that the gradient pulse areas be matched to within 10 ppm and that the data (FID's) be acquired in the absence of pulse induced eddy currents (4). Eddy current effects have been minimized by active shielding of gradient coils (5) and by shifting the data acquisition period away from the gradient pulse through the design of pulse sequences (6). Eddy currents can also be reduced through the use of shaped gradient pulses and even more effectively with bipolar pairs of (self-compensating) pulses as discussed in Section III.

The generation of diffusion spectra from data sets described by Eq. [1] or with the summation replaced by an integral for continuous distributions of diffusion coefficients is the heart of DOSY (7). Unfortunately, the data inversion is inherently ill-conditioned and in many cases intractable. It must be accepted that the amount of information in the diffusion dimension is limited, and the possibility of resolving components in the presence of noise may be lost. DOSY depends on approximate methods for determining the most likely sets of diffusion coefficients. Thus far, the data inversion program SPLMOD (8), supplemented with prior knowledge and acceptability criteria, has been the most successful for resolving "discrete" sums, *i.e.* when N_λ is a small number. An example of the resolution of a mixture of amino acids by means of DOSY with SPLMOD processing is shown in Fig. 1 (9).

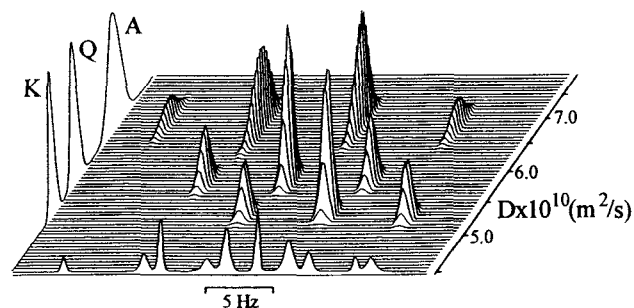


Figure 1: DOSY 2D display for protons on alpha carbons in a mixture containing alanine (A), glutamine (Q), and lysine (K) in D_2O .

Our experience with discrete mixtures is that a single exponential component can be analyzed with high precision to yield a diffusion coefficient with an error of less than 3%. Two overlapping exponential components can be resolved if they have diffusion coefficients that differ by at least a factor of two, have comparable intensities, and have high signal-to-noise (S/N) ratios. However, three components can rarely be resolved to obtain accurate diffusion coefficients and often show artifacts related to the simultaneous analysis of multiple data sets with SPLMOD (10).

The analysis of PFG-NMR data sets for polydisperse samples is possible by means of a number of computer algorithms. Most DOSY analyses thus far have been performed with the constrained regularization program CONTIN (11,12). This program has the advantage of being widely distributed and thoroughly tested. It makes use of prior knowledge, *e.g.* non-negative amplitudes and diffusion coefficients, and the principle of parsimony. An improvement of CONTIN is discussed in Section V.

It is certain that better schemes will be developed for the analysis of PFG-NMR data sets. One obvious idea is to take into account the complete NMR spectrum of each species in the CONTIN or SPLMOD analyses. Such advances are expected to improve the accuracy and convenience of DOSY, but not to avoid the fundamental problem of limited information content of PFG-NMR data sets in the presence of noise.

III. Improved Pulse Sequences for Pulsed Field Gradient NMR

The original S-T diffusion measurements were based on the spin echo sequence $90^\circ\text{-}\tau\text{-}180^\circ\text{-}\tau\text{-echo}$ with gradient pulses inserted on both sides of the 180° rf pulse. There are four major disadvantages with this sequence: (i) the magnetization is transverse throughout so that spin relaxation depends on T_2 , (ii) J-modulation effects may appear in the spectrum when spin coupling is present, (iii) eddy currents induced by the first gradient pulse cause the effects of the two pulses to be unequal, and (iv) eddy currents induced by the second gradient pulse may interfere with data collection. The stimulated echo (STE) sequence (13,14) shown in Fig. 2a alleviates problems (i) and (ii) when $\tau \ll \Delta$, but eddy currents remain and, in fact, problem (iv) is worse for small values of τ . The longitudinal eddy-current delay (LED) sequence (6) shown in Fig. 2b introduces a train of three gradient prepulses to equalize the effects of the two gradient pulses in the STE sequence; and, furthermore, stores the STE in the z or longitudinal direction by means of a fourth 90° rf pulse. After a suitable settling

period (T_e) for eddy currents, a fifth rf pulse returns nuclear magnetization to the xy plane so that the FID can be recorded.

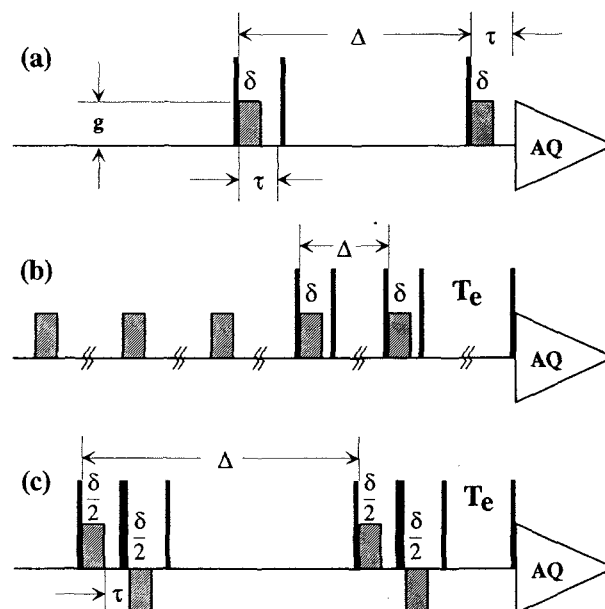


Figure 2: The pulse sequences: (a) STE, (b) LED, and (c) BPP-LED.

The LED sequence has been used successfully in a number of laboratories but its advantages come at a cost. In particular, the prepulses add to resistive heating of the sample and the delay time T_e required for complete avoidance of eddy current effects may be unacceptably long. Fortunately, both of these problems can be considerably diminished by replacing each gradient pulse with a pair of accurately matched pulses having different polarities and separated by a 180° rf pulse. Bipolar pulse pairs (BPP) of this type have been used to minimize the effects of background gradients (15), and the self compensating effects of BPP's were recently demonstrated by Wider, *et al.* (16).

We find that BPP's with short pulse separations (~ 1 ms) cancel more than 95% of the eddy currents. This simultaneously removes the need for the gradient prepulses in the LED sequence and greatly reduces the settling times (T_e). The resulting BPP-LED sequence is illustrated in Fig. 2c (9). This sequence gives less signal distortion with $T_e = 5$ ms than the LED sequence gives with $T_e = 100$ ms. The effectiveness of the BPP in reducing frequency excursions of the deuterium lock is dramatically illustrated in Fig. 3.

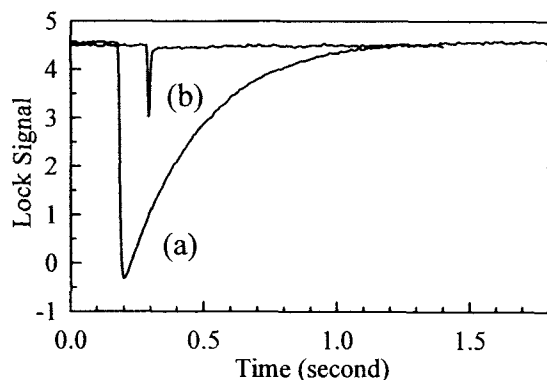


Figure 3: Response of NMR (deuterium) lock signal to: (a) a monopolar gradient pulse ($0.89 \text{ Tm}^{-1} \times 2 \text{ ms}$), (b) bipolar pulse pair ($g = \pm 0.89 \text{ Tm}^{-1}$, $\delta/2 = 1 \text{ ms}$, $\tau = 1.5 \text{ ms}$)

IV. DOSY in the Supercon Fringe Field

There remains the problem of how to obtain very large magnetic field gradients ($> 30 \text{ Tm}^{-1}$) without unacceptably large heating effects and pulse induced eddy currents. Kimmich, *et al.*, overcame these problems by using the gradient provided by the fringe field of a superconducting magnet (17). The two major drawbacks of this ingenious method result from the presence of the gradient during both the rf pulses and data collection. The former diminishes sensitivity by selecting only a thin slice of sample for excitation while the latter obliterates resolution.

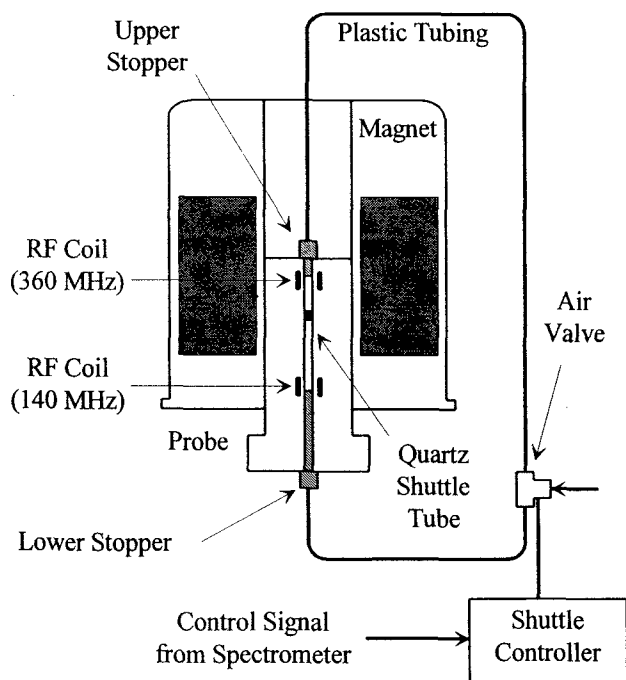


Figure 4: Block diagram of the shuttle system.

In special cases useful information about diffusion can be obtained in the absence of chemical shift resolution, and it is even possible that species can be resolved through the use of the diffusion spectrum. However, it is important to recover resolution so that 2D DOSY and other experiments requiring selectivity can be performed. For this purpose we have developed experiments in which diffusion information is encoded in the fringe field and then detected in the homogeneous high field to obtain high-resolution spectra (18). This of course requires rapid transport of the sample, and we have developed a shuttle system similar to that employed in zero-field NMR experiments.

Figure 4 illustrates the magnet, probe, and shuttle system. A Bruker MSL-360 spectrometer with a widebore magnet was used with a homebuilt shuttle probe and shuttle controller. The shuttle probe contained two rf coils, one resonant at 360 MHz (homogeneous field) and one resonant at 140 MHz (fringe field 0.3 m below the homogeneous field), and a pneumatic system was used to shuttle the sample in a precision bore quartz tube. The direction of compressed air was determined by a computer controlled DC air valve.

A cylindrical Kel-F sample cell with an internal volume of $36 \mu\text{L}$ was used in the initial experiments, and Viton O-rings absorbed vibrations on impact. With this arrangement and with specially programmed air pulses, the total time required to transfer the sample and damp out vibrations was 100 - 150 ms. The pulse sequence designed for the shuttle experiment and the location of the sample as a function of time (dotted line) are shown in Fig. 5. A stimulated echo is created by the first three 90° rf pulses, the fourth 90° pulse stores the echo for the shuttling period T_s , and the fifth 90° pulse recalls the magnetization for detection.

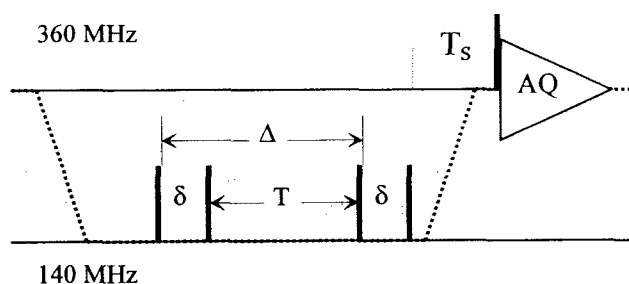


Figure 5: Pulse sequence and sample position for shuttle based DOSY.

In the fringe field at the 140 MHz position, the gradient $g = 53 \text{ Tm}^{-1}$. Since the 90° rf pulse width at 140 MHz was $1.4 \mu\text{s}$, only a slice about 0.3 mm thick could be excited. In the homogeneous field all of the protons were excited and a special phase cycle was required to separate out those spins encoded with diffusion information. An illustration of fringe

field DOSY for a mixture containing sodium dodecyl sulfate (SDS), glycerol, and H₂O (1 : 2 : 4 by weight) is shown in Fig. 6. The data set was processed with the SPLMOD, and the resulting three components are well resolved in both the chemical shift and diffusion dimensions. The single OH peak in both the NMR and diffusion dimensions results from fast exchange of protons between water and the OH group of glycerol.

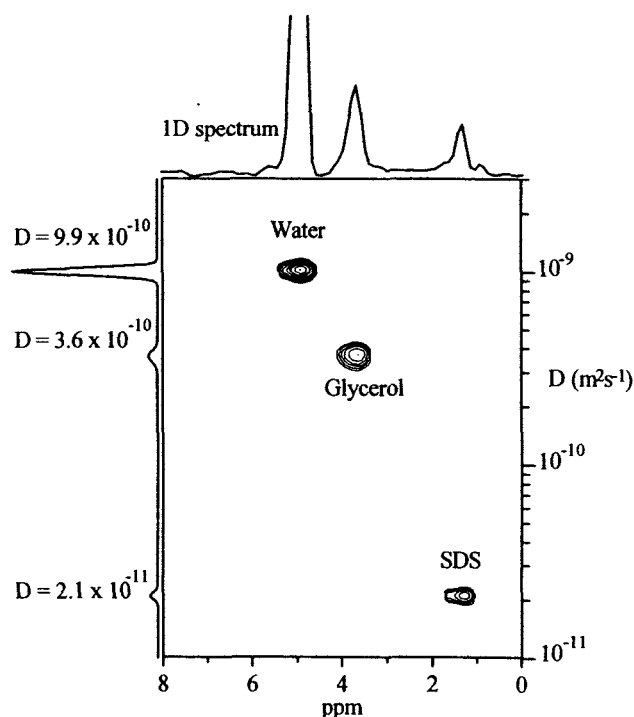


Figure 6: The 2D DOSY display for a mixture containing SDS, glycerol, and H₂O with $T = 5$ ms, $T_s = 150$ ms, and δ incremented from 10 to 300 μ s in 18 steps.

The NMR linewidths result from bulk susceptibility effects related to the geometry of the sample cell. This problem can be remedied, but the transfer time and sensitivity remain limitations. However, shuttle/fringe field experiments offer distinct advantages for samples with very low diffusion coefficients and in cases where short diffusion times must be investigated. These advantages are obtained without the need for expensive gradient drivers and coil sets.

V. CONTIN Analysis and Molecular Weight Distributions for Polymers

Molecular weight distributions (MWD's) are essential features in the characterization of polymers. In those cases where the scaling law relating diffusion coefficients to

molecular weights is known, the mass weighted MWD, $W(M)$, can be computed from the mass weighted distribution $G(D)$ of diffusion coefficients. In the application of DOSY to the determination of MWD's the crucial step is the estimation of $G(D)$. The overall procedure is outlined in Fig. 7.

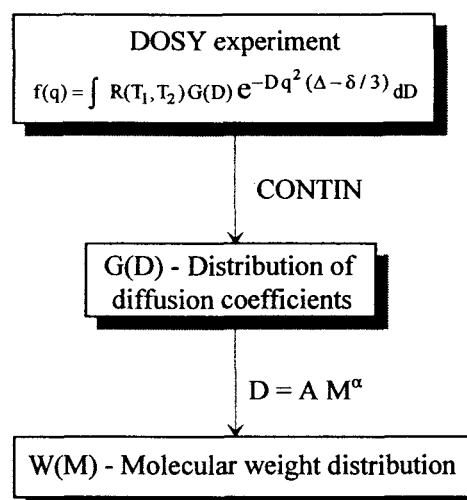


Figure 7: Steps in the determination of the MWD.

Proton NMR of polymers automatically returns mass weighted signals, and the DOSY analysis with CONTIN in principle yields $G(D)$. Unfortunately, DOSY only provides an estimate of $G(D)$ constrained by prior knowledge and parsimony (11). Here parsimony implies that distributions are selected on the basis of smoothness and the minimum number of peaks consistent with the PFG-NMR data. This selection is implemented by rejecting solutions with large integrated squared second derivatives. It turns out that the standard application of CONTIN seriously undersmooths $G(D)$ for large values of D in broad distributions (19). In the presence of noise one sometimes finds an oscillation or "noise peak" on the high D side of the distribution. The problem is that CONTIN penalizes solutions on a logarithmic D axis where the appropriate distribution is $G(D)D$ rather than $G(D)$. This switch to $G(D)D$ is easily made by setting the control parameter $IQUAD = 1$ in CONTIN to select the weighting factor $c_m = 1$ in the quadrature formula. The result is that the "noise peak" disappears and the main peak gives more accurate values of $\langle D \rangle$ and smaller standard deviations.

The idea of improved weighting factors was extended by proposing that c_m be replaced with a function that depends explicitly on D (20). The functional form can be chosen to emphasize regions of low amplitude. In particular we replaced c_m with $(D_m / D_{max})^{x_m}$ where x_m was incremented from +2 to -2 as $\log(D)$ ranged from -12 to -9. Near the center of the distribution where $D = D_{max}$, $c_m = 1$; and at $x_m = \pm 1$ the

amplitude of $G(D)D$ is about 10% of its maximum value. Of course, c_m is carefully fitted to the distribution of interest after a trial run with $c_m = 1$.

The effect of various choices of c_m on the $G(D)D$ distributions obtained with CONTIN was investigated by means of simulated MWDs. The simulations were all based on the log normal distribution defined in Eq. [2] with Gaussian noise.

$$W(M) = \frac{1}{M(\ln \sigma)\sqrt{2\pi}} \exp\left[-\frac{(\ln M - \ln M_0)^2}{2(\ln \sigma)^2}\right] \quad [2]$$

A simulated distribution $G(D)D$ obtained from Eq.[2] and the assumed scaling relation $D = A M^\alpha$ is shown in Fig. 8 along with the effect of computed c_m values.

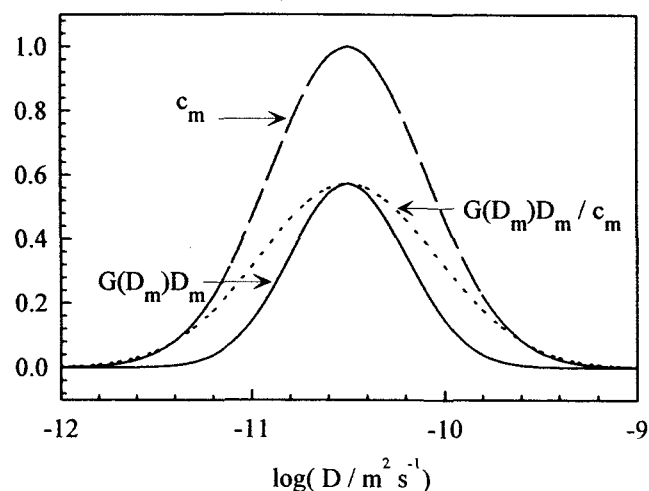


Figure 8: Simulations obtained with $M_0 = 10^5$, $A = 10^{-7.5}$, $\sigma = 3.2$, and $\alpha = -0.6$.

Analyses were performed with standard CONTIN, CONTIN with $c_m = 1$, and with computed c_m values for simulated PFG-NMR data sets based on having different values of σ and various signal-to-noise ratios. The resulting distributions were used to compute $\langle D \rangle$, number average molecular weights \bar{M}_n , weight average molecular weights \bar{M}_w , polydispersity (\bar{M}_w/\bar{M}_n), and the ratio (standard deviation)/ $\langle D \rangle$ as functions of the width σ for comparison with the simulated distribution. The plots of $\langle D \rangle$ versus σ shown in Fig. 9 are typical of our results. In general standard CONTIN shows the largest errors, the analysis with $c_m = 1$ is better, and the computed c_m results are almost perfect. These conclusions are based on simulations with S/N of $10^3:1$. Accurate results were also obtained with S/N down to 500:1

In practical applications it is important to note that intermolecular interactions between solute molecules lead to a "microaveraging effect" in which the effective diffusion coefficient of a molecule depends on the molecular weights of neighboring molecules (21). It is therefore necessary to establish that the concentration is sufficiently low that solute molecules behave independently. In a study of poly(ethylene oxide) (PEO) we found that at a total concentration of 1 g/L a mixture of monodisperse samples with equal weights of $M_w = 5000$ and $M_w = 100,000$ material gave the same diffusion coefficients as measured for samples containing the solutes separately.

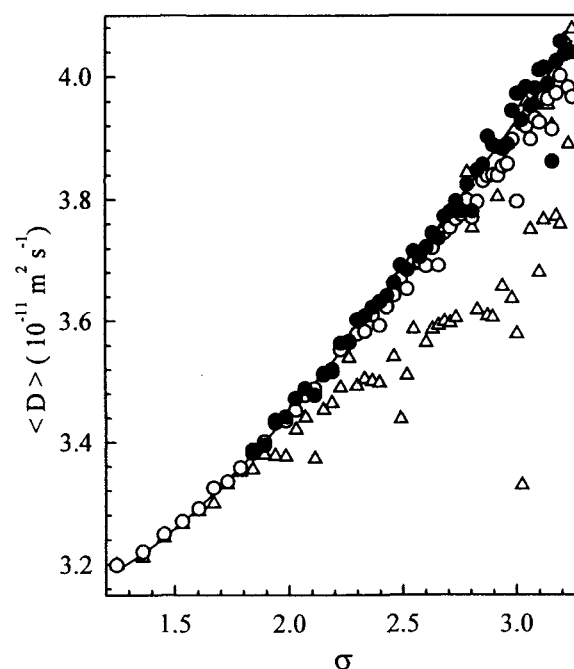


Figure 9: $\langle D \rangle$ versus σ for the simulation (solid line), standard CONTIN analysis (Δ), CONTIN with $c_m = 1$ (\circ), and CONTIN with computed c_m values (\bullet).

PEO was used to test the NMR method with computed c_m values. First a set of monodisperse samples was used to verify the scaling relation and to determine the parameters ($A = 10^{-7.62}$, $\alpha = -0.62$). Then two polydisperse samples previously characterized by American Polymer Standards Corporation (APSC) were analyzed by PFG-NMR with CONTIN. The data set for the methylene signals was processed with standard CONTIN so that the derived values of $G(D)$, $\langle D \rangle$, and S.D. could be used to compute a set of c_m values. A CONTIN analysis with the computed c_m values then produced improved estimates of $G(D)$. After converting to the MWD, the molecular weights \bar{M}_n and \bar{M}_w were computed for comparison with values provided by the manufacturer (Table 1) (20).

Table 1. Molecular weights of polydisperse PEO

sample type	\bar{M}_n kg/mol (APSC)	\bar{M}_w kg/mol (APSC)	\bar{M}_n kg/mol (DOSY)	\bar{M}_w kg/mol (DOSY)
PEO200K	47.0	204	46	180
PEO120K	36.5	123	35	110

Under certain conditions the DOSY/CONTIN method provides accurate MWD's for polymers and may be the method of choice. Compared with dynamic light scattering, DOSY offers the following advantages: (a) sample preparation is easy, (b) dust and impurities do not interfere, and (c) mixtures can be analyzed if the chemical shifts of components are different.

VI. Conclusions

DOSY was developed to provide useful displays of PFG-NMR data sets that incorporate all reliable information about the system under study obtained from PFG-NMR data and prior knowledge. The implementation of DOSY required enhancements to PFG-NMR hardware and pulse sequences as well improvements in data analysis methods. A state-of-the-art DOSY system now makes use of a high performance gradient driver, shielded gradient coils, pulse sequences with bipolar gradient pulse pairs, automated data collection at programmed values of q , and non-subjective data analysis. Furthermore, DOSY has been extended to take advantage of high gradients found in the fringe field. DOSY is now a powerful tool for the analysis of polydisperse samples and complex mixtures. The development of DOSY methods for less receptive nuclei, currently underway through polarization transfer and inverse detection, promises to extend the resolution of this method to even more complex mixtures.

Acknowledgments

This work was supported in part under National Science Foundation Grants CHE 9222590 and CHE-9318655.

References

1. E. O. Stejskal and J. E. Tanner, *J. Chem. Phys.* **42**, 288 (1965).
2. P. Stilbs, *Prog. NMR Spectros.* **19**, 1 (1986).
3. K. F. Morris and C. S. Johnson, Jr. *J. Am. Chem. Soc.* **114**, 3139 (1992).
4. R. M. Boerner and W. S. Woodward, *J. Magn. Reson. A* **106**, 195 (1994).
5. P. Mansfield and B. Chapman, *J. Magn. Reson.* **66**, 573 (1986).
6. S. J. Gibbs and C. S. Johnson, Jr. *J. Magn. Reson.* **93**, 395 (1991).
7. K. F. Morris, P. Stilbs, and C. S. Johnson, Jr. *Anal. Chem.* **66**, 211 (1994).
8. S. W. Provencher and R. H. Vogel, in *Numerical Treatment of Inverse Problems in Differential and Integral Equations*, P. Deuffhard and E. Hairer, Eds. (Birkhauser, Boston, 1983), p. 304.
9. D. Wu, A. Chen, and C. S. Johnson, Jr. *J. Magn. Reson. A* **115**, 260 (1995).
10. K. F. Morris and C. S. Johnson, Jr. *J. Am. Chem. Soc.* **115**, 4291 (1993).
11. S. W. Provencher, *Comput. Phys. Commun.* **27**, 213 (1982).
12. S. W. Provencher, *Comput. Phys. Commun.* **27**, 229 (1982).
13. E. L. Hahn, *Phys. Rev.* **80**, 580 (1950).
14. J. E. Tanner, *J. Chem. Phys.* **52**, 2523 (1970).
15. R. F. Karlicek, I. J. Lowe, *J. Magn. Reson.* **37**, 75 (1980).
16. G. Wider, V. Dotsch, K. Wüthrich, *J. Magn. Reson. A* **108**, 255 (1994).
17. R. Kimmich, W. Unrath, G. Schnur, and E. Rommel, *J. Magn. Reson.* **91**, 136 (1991).
18. D. Wu and C. S. Johnson, Jr. *J. Magn. Reson. A* **116**, 270 (1995).
19. J. Jakes, *Czech. J. Phys.* **B38**, 1305 (1988).
20. A. Chen, D. Wu, and C. S. Johnson, Jr. *J. Am. Chem. Soc.* **117**, 7965 (1995).
21. P. T. Callaghan, D. N. Pinder, *Macromolecules* **18**, 373 (1985).

Resolution without solution: retrieving anisotropic information in solid-state NMR

Melinda J. Duer and Clare Stourton

Department of Chemistry, University of Cambridge, Lensfield Road, Cambridge, CB2 1EW, United Kingdom

It is the anisotropic nuclear interactions existing in the solid-state which make solid-state NMR so interesting, and often, challenging experimentally. Various nuclear interactions have been used by chemists in recent years to provide information about chemical structures and molecular mobility in the solid-state, to name but two important applications.

In the determination of structures in the solid-state, connectivities between atoms may be established using well-known "solution" NMR techniques like COSY and INADEQUATE [1,2], which rely on scalar couplings between nuclei. In solids, the dipole-dipole interaction is also at the experimenter's disposal. The internuclear distance dependence of this interaction renders it ideal for determining molecular structures, providing that we can measure the strength of this interaction. This proviso governs much of solid-state NMR: the anisotropic nuclear interactions contain much useful information of interest to a chemist. The problem is usually extracting this information, because of course, the other feature of anisotropic nuclear interactions is the large degree of line broadening and consequent loss of resolution that they cause in NMR spectra.

In response to this, many ingenious techniques have arisen for measuring dipolar coupling constants, such as TEDOR, REDOR, rotational resonance etc. [3-8]. These have been applied with excellent results to many chemical systems, particularly highly crystalline systems, where the lack of large single crystals precludes the use of diffraction techniques [9-12]. Indeed, it is interesting to note that even in these days of automated X-ray diffractometers, and relatively easy access to neutron diffractometers, techniques such as solid-state NMR still have an important role to play in structure determination. As well as those crystalline systems which do not grow crystals large enough for diffraction techniques, there are also many important materials which are amorphous, and others, such as polymers, which show varying degrees of heterogeneity. Neither

category is particularly suited to analysis by diffraction techniques.

Studies of molecular motion in solids are becoming increasingly important, as it is realised that molecular motion plays a large part in the physical properties of a solid. It may influence phase transitions, as motion in the solid state contributes to the entropy of a solid. In turn, the entropy change upon phase transition determines the temperature of a phase transition, and whether the transition is to an isotropic liquid phase or an ordered liquid-crystalline phase. NMR is an excellent tool for studying molecular motion in solids [13, 14]. Nuclear interactions which depend on molecular orientation are partially averaged by molecular motions which change the molecular orientation. Such averaging is reflected in the NMR spectra. As with the study of solid-state structures, the difficulty is often resolving the lines in the spectra due to different chemical sites, whilst retaining the effects of the anisotropic interactions.

This paper deals first with some NMR techniques which utilise the chemical shift interaction in the study of molecular motion. In particular, it deals with ways of studying very slow molecular motions. Such motions are frequently important in polymers for instance, but studying them with NMR is difficult because the timescale of the motion is so much smaller than the normal NMR timescale. The second part of this paper deals with a method for separating quadrupolar-broadened lines, by making use of multiple-quantum coherences. This work is still in early stages, and preliminary results are given.

Studying molecular motion using chemical shift anisotropies.

Molecular motion partially averages orientation-dependent nuclear interactions, such as the chemical shift. An NMR spectrum which monitors the nuclear interaction thus contains information about the motional process [13, 14]. We simply have to arrange that the signals due to

different chemical sites in the sample are resolved.

One method of resolving signals due to different chemical sites and yet retaining the effects of chemical shift anisotropy is simply to use magic-angle spinning [15, 16]. This time-honoured technique provides one of the best methods for studying molecular motion in complex chemical systems. Slow magic-angle spinning (slower than the chemical shift anisotropy) produces spinning sidebands [15, 16] which retain information about the chemical shift anisotropy and thus about motional processes. This information can be extracted by comparing simulations of the complete sideband pattern for different possible models of the molecular motion with the experimental one until reasonable agreement is obtained. The result is thus a list of motional processes which could be occurring in the sample.

The simulations themselves can be lengthy for complicated motional models, but follow simple principles as outlined below [17-19].

The motional process is assumed to involve molecular hops between N different sites, where each site represents a different orientation of the molecule. The time-dependence of the (complex) transverse magnetization under such circumstances follows the stochastic Liouville equation (1):

$$\frac{d\mathbf{M}^+(t)}{dt} = \{i\mathbf{\Omega}(t) + \mathbf{W}\} \mathbf{M}^+(t) \quad (1)$$

$\mathbf{M}^+(t)$ is an N -dimensional vector, the i th element of which is the complex transverse magnetization of the i th molecular site. The matrix $\mathbf{\Omega}(t)$ is a diagonal matrix whose elements are the resonance frequencies of each of the N sites: each site resonates at a different frequency in general due to their different orientations. The frequencies are time-dependent due to the magic-angle spinning. The matrix \mathbf{W} is the so-called kinetic matrix: an element W_{ij} is the rate of hopping between sites i and j . The time dependence of $\mathbf{\Omega}$ and the presence of \mathbf{W} means that the superoperator $\{i\mathbf{\Omega}(t) + \mathbf{W}\}$ does not commute with itself at different times, t . Thus equation (1) cannot be integrated directly, but must be integrated numerically. In practise, the integration is performed over one rotor cycle, the

solutions for subsequent times being easily derived from this initial calculation [19].

An example the utility of this technique is the study [20] of the motional degrees of freedom available to the hydrogen-bonded carboxylic acid-pyridyl complex shown in Figure 1. The motion of the aromatic regions of this complex have been studied with magic-angle spinning: the experimental ^{13}C NMR spectra of the aromatic region for two different spinning speeds at 373 K are also shown in Figure 1.

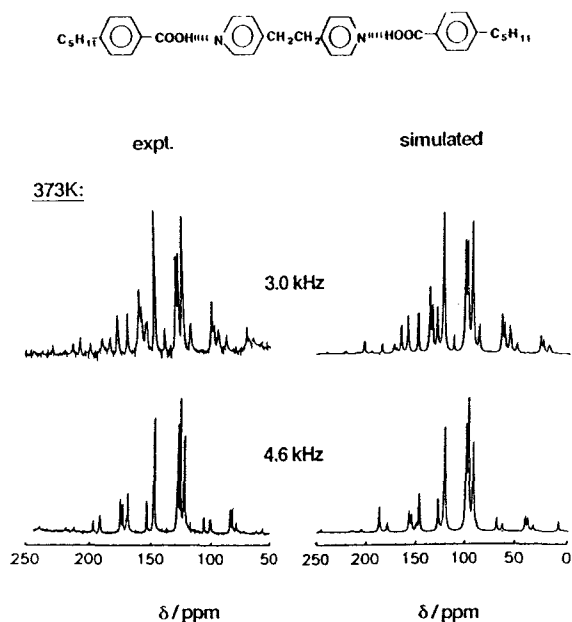


Figure 1: Top, the hydrogen bonded carboxylic acid-pyridyl complex under study. Below, left: experimental ^{13}C MAS NMR spectra of the aromatic region of this complex at the spinning speeds indicated at 373 K and right, simulated spectra assuming the pyridyl and phenylene rings of the complex undergo 180° flips. See text and Figure 2 for details.

In fact the complete study involved three or four different spinning speeds at each temperature of interest (250 - 400 K). Alongside the experimental spectra are simulated spectra for a motional model in which the pyridyl and phenylene rings are all performing 180° flips about their approximate two-fold axes as illustrated in Figure 2, at a rate of 10^5 Hz.

Overall the study showed that up to 363 K, the phenylene and pyridyl rings only undergo small angle ($< 20^\circ$) librations about their approximate two-fold axes. However, there is an abrupt transition at this temperature, and above 363 K the rings perform rapid ($\geq 10^5$ Hz) 180° flips

about these axes. This behaviour has since been related to the phase transition properties of this material, and has shed light on its formation of liquid-crystalline phases [20, 21].

Below 363 K:



Above 363 K:

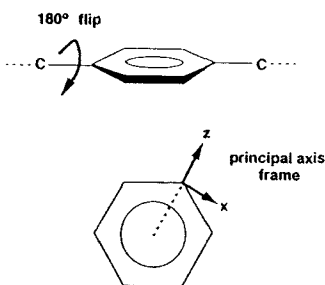


Figure 2: the motional model used to calculate the simulated spectra in Figure 1. The principal axis frame assumed for the chemical shift tensor is shown.

Sensitivity of NMR spectra to hopping rate.

Chemical shift powder patterns in NMR spectra of static (i.e. non-spinning) samples are sensitive to motions with hopping rates which are similar in magnitude to the chemical shift anisotropy [13, 14]. For hopping rates which are significantly lower than the chemical shift anisotropy, the powder patterns are essentially unchanged from those expected for static nuclei.

As the hopping rate is increased above the chemical shift anisotropy, the powder pattern changes with hopping speed until the hopping rate is significantly larger (by a factor of ~ 10) than the chemical shift anisotropy, when it reaches a limiting shape. As the hopping rate is increased above this, there are no further changes to the spectral lineshape, and so no higher hopping rates can be monitored.

In magic-angle spinning spectra, the situation is less clear. The spectra are sensitive to motions which have hopping rates similar in magnitude to the chemical shift anisotropy or which are similar in magnitude to the spinning rate [22]. This is illustrated in Figure 3, where the simulated spectra for a two-site motion with various hopping rates are shown. In this motion, the

unique principal axis of the (axial) chemical shift tensor moves through 109° on each hop between the two sites.

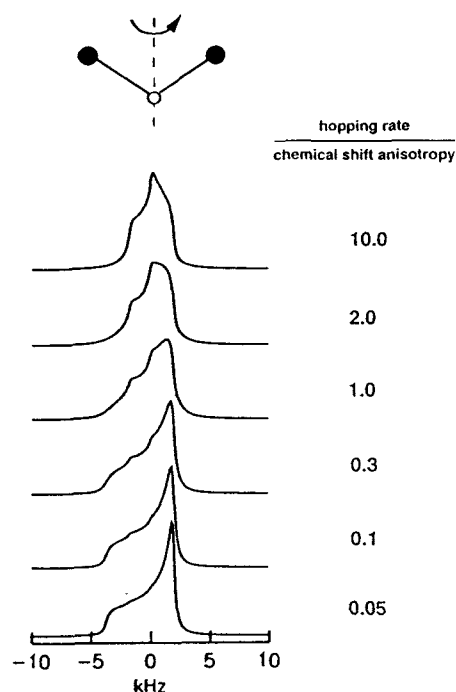


Figure 3: Calculated spectra for static samples arising from chemical shift anisotropy for a two-site motional process. The chemical shift tensor is axial and its unique axis hops through 108° between the two sites involved in the motion. The spectra are calculated for various hopping rates as shown.

As is evidenced by Figure 4, the spectra are most sensitive to motion when [22]

$$\frac{w^2}{\Delta\sigma \nu_r} \sim 1 \quad (2)$$

where ν_r is the rotor spinning frequency, $\Delta\sigma$ is the chemical shift anisotropy, and w is the hopping rate of the motion. As with the spectra of static samples, the MAS lineshapes are not sensitive to motions significantly smaller or greater than the chemical shift anisotropy.

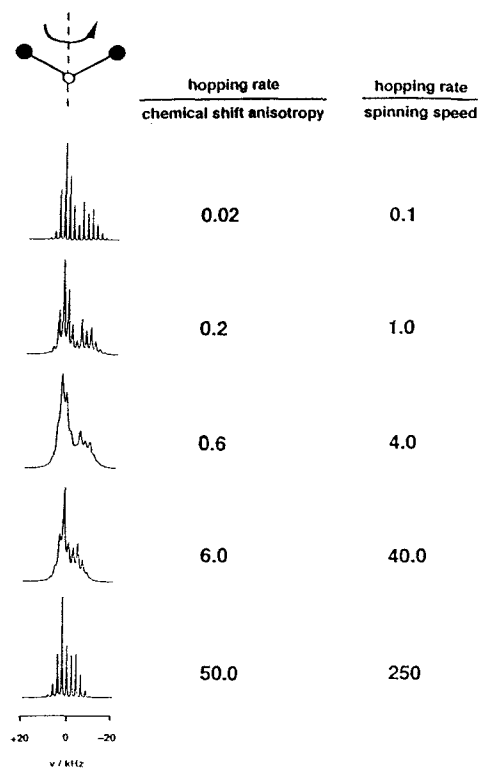


Figure 4: Calculated magic-angle spinning spectra arising from chemical shift anisotropy, for a two-site motional process. The chemical shift tensor is axial and its unique axis hops through 109° between the two sites involved in the motion. The spectra are calculated for various hopping rates.

Studying slow molecular motion with chemical shift anisotropy

Many motional processes of importance in solids are relatively slow, of the order of a few hundreds or a few thousands of hertz. This is the case for instance in polymeric materials where rotations of the polymer backbone may be very slow, but yet important in determining the physical properties of the polymer solid. The rates of these motions are frequently much lower than the chemical shift anisotropies associated with the nuclei available to monitor the motion, and hence these motions cannot be studied by the conventional lineshape analysis techniques referred to above.

Various two-dimensional exchange experiments [13, 14] have been used to study molecular motion which falls into this regime. However, the difficulty with these experiments is that in order to resolve the signals from different sites one must record a three-dimensional spectrum [13], which is of course very time consuming. We require practicable NMR experiments which

can measure slow motions and resolve the signals from different chemical sites.

A brief inspection of Figure 3 shows that we need to arrange that the effective chemical shift in the experiment similar in magnitude to the hopping rate of the motion to be studied. Thus, if we wish to monitor very slow motions, we need an experiment which scales chemical shift anisotropies to smaller than their true values.

Probably the simplest way to scale the effective chemical shift anisotropy is to spin the sample rapidly about an axis inclined at an angle θ to the applied magnetic field. This scales the effective chemical shift anisotropy observed in the spectrum by a factor of $\frac{1}{2}(3 \cos^2\theta - 1)$ [15, 16].

Figure 5 shows calculated spectra for rapid sample spinning at different angles θ . The same molecular motion as used for Figures 3 and 4 is assumed, with an axial chemical shift tensor. The ratio of hopping rate to true chemical shift anisotropy is 0.2. Hence, for spinning at 0° (scaling of effective chemical shift anisotropy = 1), there is little influence of the motion upon the observed lineshape. However, as the angle θ is increased towards the magic-angle (54.75°), and the scaling of the chemical shift anisotropy decreases from one, features appear in the powder lineshape which are due to the partial averaging of the interaction by the molecular motion.

Clearly, variable-angle spinning in this manner could be used as a simple method to monitor slow motions: the particular angle used in the experiment can be changed according to the expected rate of the motion under study, so as to achieve maximum sensitivity in each case.

The advantage of this experiment is its simplicity. However, it will not necessarily achieve resolution between different chemical sites, since we are still inevitably dealing with chemical shift anisotropy-broadened lines. If we narrow the lines further by spinning closer to the magic-angle, so we lose the spectral resolution in each powder pattern required for sensible analysis of the lineshape.

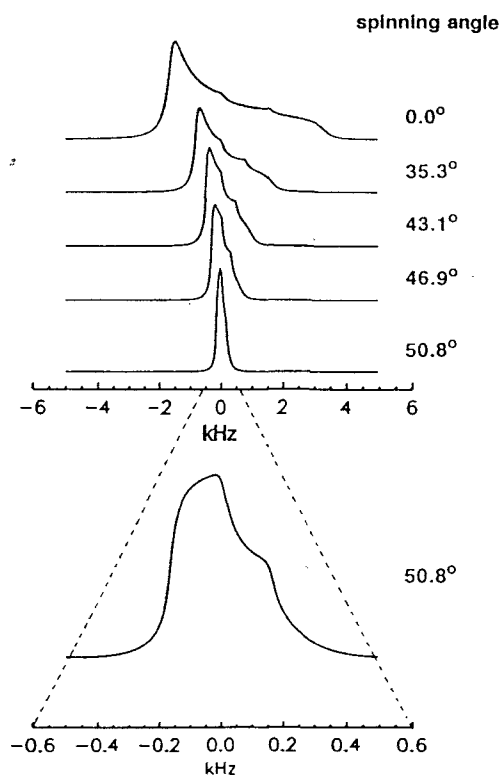


Figure 5: Calculated spinning spectra for different spinning angles θ arising from chemical shift anisotropy for a two-site motional process. The chemical shift tensor is axial and its unique axis hops through 108° between the two sites involved in the motion. The spectra are calculated for a hopping rate: true chemical shift anisotropy rate of 0.2.

An alternative approach which deals with the scaling of the chemical shift anisotropy, and the problem of resolution is a two-dimensional experiment which resolves chemical shift powder patterns in one dimension (f_1) according to the isotropic chemical shift for each pattern in the second dimension (f_2). There have been several pulse sequences developed which achieve this separation [23]. We use that due to Tycko et al. [30] which is illustrated in Figure 6 and is henceforth labelled 2DCSA.

The entire experiment takes place under magic-angle spinning. The six π pulses per rotor period in t_1 counter the averaging effect of the magic-angle spinning upon the chemical shift anisotropy during this period. The π pulses are placed symmetrically within each rotor period. A concomitant effect of the π pulses is that they scale the effective chemical shift anisotropy during t_1 . The scaling factor depends upon the

exact location of the π pulses within the rotor periods. Scaling factors of 0.3 downwards can be achieved by different spacing of these pulses.

Theoretical analysis of this pulse sequence [30] demonstrates that in the presence of molecular motion [35] the resulting chemical shift anisotropy powder patterns in f_1 are identical to those that would arise from a normal one-dimensional NMR experiment on a static sample, but with the effective chemical shift anisotropy scaled by a factor which depends only on the spacing of the six π pulses in t_1 . Thus, the scaling factor can be chosen by the experimenter to be appropriate to the rate of the molecular motion in the system under study.

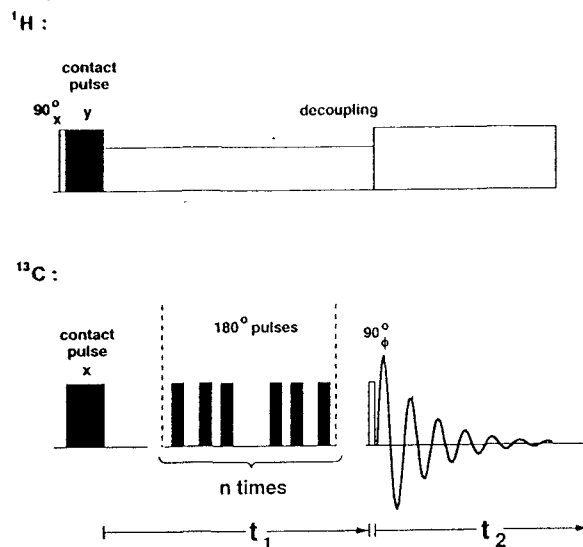


Figure 6: the 2DCSA pulse sequence [30] which separates chemical shift anisotropy powder patterns in f_1 according to their isotropic chemical shifts in f_2 . The whole experiment is conducted under magic-angle spinning. ^{13}C transverse magnetization is created by an initial cross-polarisation step from ^1H . Six π pulses are applied symmetrically within each rotor period during t_1 . t_1 itself is an integral number of rotor periods.

We performed initial experiments with this pulse sequence on dimethylsulphone (DMS). Figure 7 shows the two dimensional ^{13}C NMR spectrum which results at 300 K when the t_1 pulses are arranged to give a 0.1 scaling factor to the chemical shift anisotropy.

Figure 8 compares the f_1 slices from two 2DCSA experiments at 300 K employing chemical shift anisotropy scaling factors of 0.1 and 0.05 respectively with the one-dimensional static

spectrum recorded at the same temperature. Whilst the one-dimensional spectrum contains no features to support a lineshape analysis, both the 2DCSA experiments show the effects of partial averaging of the chemical shift anisotropy by the slow molecular motion which occurs at this temperature. The simulated spectra employ a true chemical shift anisotropy of 56 ppm, asymmetry of zero and assume a motional model in which the unique axis of the ^{13}C chemical shift tensor jumps between two orientations 108° apart at a rate of 500 Hz. This models reorientations of the DMS molecule about its two-fold axis in 180° jumps. It is worth noting that with a scaling factor of 0.05, the ^{13}C powder lineshape in this experiment is approaching the fast hopping, limiting lineshape.

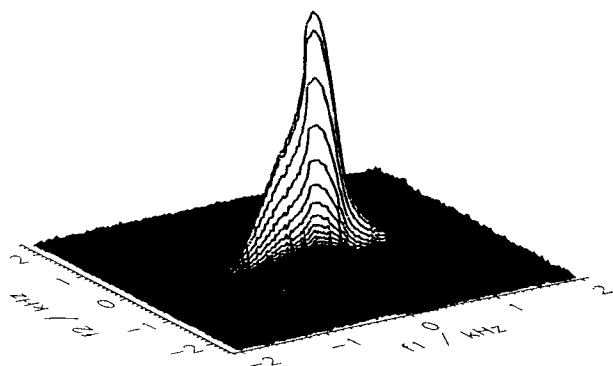


Figure 7: an experimental 2DCSA ^{13}C NMR spectrum for DMS at 300 K. The effective chemical shift anisotropy is scaled by 0.1 from the true chemical shift anisotropy. The f2 dimension contains the normal ^{13}C MAS spectrum, whilst f1 contains the chemical shift anisotropy powder pattern.

This experiment affords resolution of signals from different chemical sites quite naturally. It can be used with success even on complex chemical systems. Figure 9 shows the resulting 2DCSA spectrum for just such a chemical system. The molecular motion in the alkyl regions of the hydrogen-bonded complex shown in Figure 9 have been studied using the 2DCSA experiment [36]. The results of the study indicate that the C_5 alkyl chains in the complex undergo relatively rapid rotational diffusive motions (rotations via small angle hops) above room temperature, whilst the cyclohexane ring is essentially static at all temperatures of measurement up to 400 K.

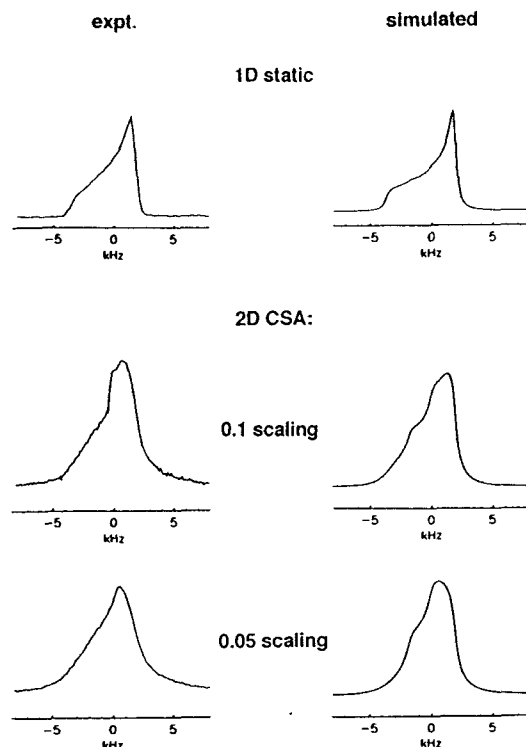


Figure 8: comparison of the results of the 2DCSA experiment and a normal static 1D experiment for DMS (top). The results of two 2DCSA experiments, employing chemical shift anisotropy scalings of 0.1 and 0.05 respectively, are shown. Simulated spectra are shown alongside. See text for details.

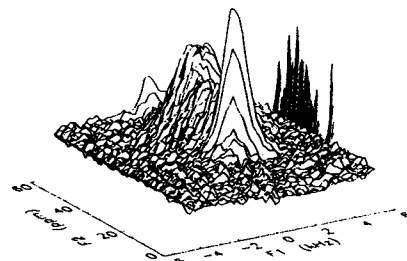


Figure 9: the ^{13}C 2DCSA spectrum of the hydrogen-bonded complex shown at the top of this figure at 373 K. Only the alkyl region of the spectrum is shown.

Multiple quantum spectroscopy of quadrupolar nuclei

If the quadrupole coupling is small compared with the Zeeman splitting, its perturbative effect on the spin levels need only be considered to first

order. This has the effect of adding a term $E_m^{(1)}$ to the energy levels E_m of a spin I , where $E_m^{(1)}$ is given by [37]

$$E_m^{(1)} = \frac{1}{4} \chi (m^2 - I(I+1)) (3 \cos^2 \theta - 1) \quad (3)$$

for an axial quadrupole tensor, where m is the magnetic quantum number of the spin level, θ is the angle between the unique axis of the quadrupole tensor, and χ is the quadrupole coupling constant, given by

$$\chi = \frac{3 e^2 q Q}{2I(2I-1)} \quad (4)$$

The dependence of the quadrupolar correction term on θ , which in turn depends upon molecular orientation, means that the quadrupole interaction broadens all single-quantum lines in an NMR spectrum of a powder sample, except for the $\frac{1}{2} \rightarrow \frac{1}{2}$ transition for half-integer spins. It is worth noting at this point that the maximum multiple quantum transition for a spin I , the $2I$ quantum transition is *not* broadened by the quadrupole coupling to first order.

If the quadrupole coupling has a significant magnitude compared with the Zeeman splitting, then the corrections to the spin level energies must be taken to second order. This gives rise to a correction term $E_m^{(2)}$ [37]:

$$E_m^{(2)} = -\frac{\chi^2}{12\nu_0} m \left[\frac{3}{2} \cos^2 \theta (1 - \cos^2 \theta) \times (8m^2 - 4I(I+1) + 1) + \frac{3}{8} (1 - \cos^2 \theta)^2 (-2m^2 + 2I(I+1) - 1) \right] \quad (5)$$

where ν_0 is the Larmor frequency. This broadens all transitions for a quadrupolar nucleus, including all multiple quantum ones.

The single quantum transition frequencies, $\Delta\nu_{SQ}$, are easily derived from equations (3) and (5) and may be written in the following convenient form [38]:

$$\Delta\nu_{SQ} = \Delta\nu_0 + \sum_{l=2}^{+1} \sum_{4m=-1}^{+1} A_{lm} Y_{lm}(\theta, \phi) \quad (6)$$

where the coefficients A_{lm} are determined by the quadrupole tensor, and the $Y_{lm}(\theta, \phi)$ are spherical harmonics. $\Delta\nu_0$ is the isotropic shift, including second-order quadrupolar shift. Equation (6) holds for non-axially symmetric quadrupole tensors: for axial symmetry only A_{10} terms in equation (6) are non zero. As already pointed out, all transitions are broadened by the quadrupole coupling. Lines arising from first-order interactions such as chemical shift anisotropy, can be narrowed by spinning the sample about a single axis. However, the dependence of the quadrupolar transition frequencies on spherical harmonics of both rank 2 and rank 4 means that the lines arising from second-order quadrupole broadening cannot be narrowed in this way: second and fourth rank spherical harmonics are averaged to their isotropic values by spinning about different angles. This feature has led to two ingenious experiments for the removal of quadrupolar effects in solid-state NMR spectra: double-angle rotation (DOR) [38] and dynamic-angle spinning (DAS) [39-41]. Both experiments allow the quadrupole parameters for each signal resolved to be determined, in the first case by analysis of spinning sidebands, and in the second case by analysis of powder patterns appearing in one dimension of the resulting two-dimensional spectrum. In addition both experiments require rather specialist probes which are only now beginning to become available commercially. Therefore, we have begun to investigate the possibility of separating quadrupolar lineshapes according to multiple quantum transition frequencies, for this would separate signals by $n\Delta\nu_0$, where n is number of quanta involved in the transition rather than $\Delta\nu_0$ as in the single-quantum spectrum. The multiple quantum lineshapes are still broadened to second-order by the quadrupole coupling, but the hope is that this will not matter if the signals are more widely separated. The multiple-quantum powder patterns could then be analysed to determine the quadrupole parameters.

Triple quantum spectroscopy of spin-3/2 nuclei.

In this preliminary work, we concentrated on observing triple-quantum coherences in spin-3/2 nuclei. As explained above, this is expected to lead to triple quantum resonances with offsets of $3\Delta\nu_0$ where $\Delta\nu_0$ is the offset in the single quantum spectrum. Figure 10 compares the single-quantum and triple-quantum spectra expected for spin-3/2 in a sample with two distinct chemical sites, with quadrupole coupling constants of 8 MHz and 4 MHz respectively and asymmetry of zero.

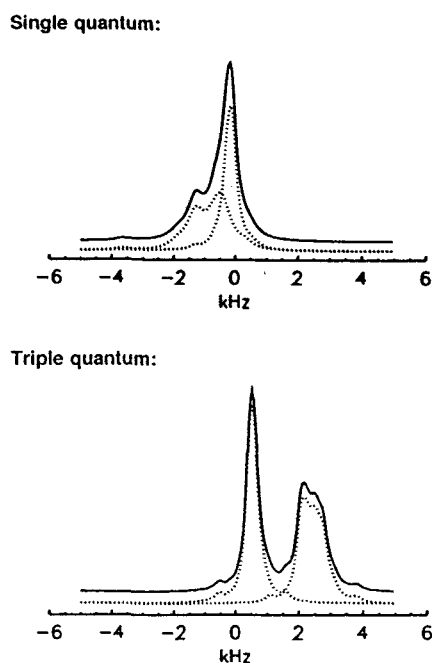


Figure 10: simulated single and triple-quantum spectra for a spin-3/2 nucleus in two distinct chemical sites. The isotropic shifts of the two sites differ by 250 Hz. Both sites have axially symmetric quadrupole tensors with quadrupole coupling constants of 8 MHz and 4 MHz respectively. The simulations assume the sample is spun at the magic-angle (54.75°) with respect to the applied field at a rate of 10 kHz.

Using equations (3) and (5), one can show that the triple quantum (TQ) coherence for a spin-3/2 evolves at frequency $\Delta\nu_{TQ}$:

$$\Delta\nu_{TQ} = 3\Delta\nu_0 + \sum_{m=-4}^{+4} A_{4m} Y_{4m}(\theta, \phi) \quad (7)$$

In this special case, the "transition" frequency depends only on fourth rank spherical harmonics. Thus the anisotropic TQ lineshape may be spun out by spinning at a single angle, 30.56° or 70.12° [42]. This is illustrated in Figure 11.

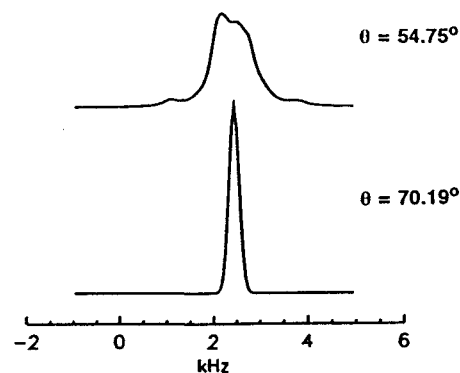


Figure 11: simulations of the triple-quantum lineshape for a spin-3/2 nucleus with a quadrupole coupling constant of 8 MHz; asymmetry, zero; isotropic chemical shift, zero, spinning at (θ) the magic-angle (54.75°) and 70.19° with respect to the applied field at a rate of 10 kHz. At $\theta = 70.19^\circ$, the second-order broadening of the triple-quantum line is averaged to its isotropic value resulting in a high resolution line.

We thus have the possibility of obtaining high resolution quadrupolar lines. The quadrupole parameters could still be determined from an experiment producing high-resolution TQ lines, as the TQ coherence cannot be observed directly of course, and so must be observed in the indirectly detected dimension of a two-dimensional NMR experiment. Such an experiment must yield single quantum lines in the second spectral dimension, and these lines will inevitably be broadened by the quadrupole interaction. The quadrupole parameters may be determined from these lines, which should now be properly resolved.

Generating TQ coherences

Vega [43] has shown that TQ coherence may be efficiently generated for spin-3/2 by a single pulse, providing that the strength of the rf field is much less than the quadrupole coupling constant and the length of the pulse, τ is:

$$\tau = \frac{1}{6} \frac{\nu_Q^2}{\nu_{rf}^3} \quad (8)$$

where v_{rf} is the amplitude of the radio-frequency (rf) pulse and v_Q is given by

$$v_Q = \frac{1}{12} e^2 q Q \left(\frac{1}{2} (3 \cos^2 \theta - 1) + \eta \sin^2 \theta \cos 2\phi \right) \quad (9)$$

Clearly, this method will be most suitable when the quadrupole coupling is large. Unfortunately, as Vega pointed out, this method of excitation is of no use for powder samples, as the length of the excitation pulse depends on the molecular orientation as defined by (θ, ϕ) . The result of using a single pulse to generate TQ coherence in a powder sample is very uneven excitation across the different orientations in the sample. This is a problem if we are hoping to determine quadrupole parameters from a powder lineshape. Even if we were not interested in the quadrupole parameters, this method of excitation would only generate significant TQ coherence for a small fraction of the total spins in the sample, and thus the signal-to-noise ratio is likely to be very poor.

We have therefore investigated different methods of exciting TQ coherence.

One method which seems promising is to use the single pulse method combined with rapid spinning of the sample. The excitation pulse length τ is optimised for molecules oriented such that θ is equal to the angle between the applied field and the sample spinning axis. For molecules oriented so that their θ is not equal to the spinning angle, the effect of the spinning is to change θ . The TQ coherence which results at the end of the pulse is thus the average TQ coherence from all the orientations visited during the course of the sample rotation. This results in a much more even generation of TQ coherence for a powder sample.

Generating single-quantum coherence from triple-quantum coherence

In order to detect TQ coherence, we must convert it to observable single-quantum (SQ) coherence.. This is readily achieved, with little orientation dependence by applying a short ($< \pi/10$ flip), powerful pulse.

Experimental results

We used a single pulse with length optimised as discussed above to generate TQ coherence in t_1 and SQ coherence (central transition only) in t_2 . Phase cycling was employed to ensure that only TQ coherences are detected in t_1 .

This pulse sequence was applied to the ^{23}Na spins in a sample of sodium zirconate (Na_2ZrO_3) [44]. There are known to be three different ^{23}Na sites in this solid. Deconvolution of the one-dimensional SQ spectrum [44] of the central transitions for these sites has given the isotropic shifts of these sites as 15, 19.5 and 27 ppm relative to NaCl solution. The single-quantum spectrum is shown in Figure 12. Quite clearly, the three signals may only be resolved by deconvolution methods.

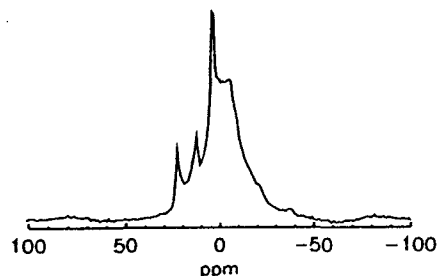


Figure 12: central transitions of the ^{23}Na NMR spectrum of sodium zirconate, recorded at 105.78 MHz with a $\pi/15$ pulse and magic-angle spinning at 10 kHz.

Figure 13 shows the TQ spectrum for this sample spinning at 10 kHz at an angle of 70.19° . The lines are broad, due to residual homonuclear dipole-dipole coupling which is not averaged to zero by spinning at this angle, but nevertheless, three signals are resolved.

Future work will include application of multiple pulse sequences during t_1 to remove the effects of homonuclear dipole-dipole coupling and further investigation into methods of exciting TQ coherence.

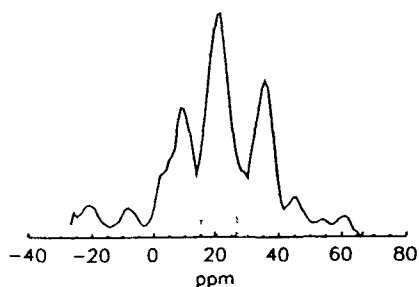


Figure 13: the F1 dimension of the 2D ^{23}Na NMR spectrum recorded at 105.78 MHz as discussed in the text and spinning at 10 kHz at an angle of 70.19° to the applied field. This dimension represents the triple-quantum spectrum.

References

- [1] R. Benn, H. Grondey, C. Brevard, A. Pagelot, *J. Chem. Soc. Chem. Comm.*, (1988), 102.
- [2] C.A. Fyfe, H. Gies, Y. Feng, *J. Chem. Soc. Chem. Comm.*, (1989), 1240.
- [3] A.W. Hing, S. Vega, J. Schaefer, *J. Magn. Reson.*, (A) **103**, (1993), 151.
- [4] A.W. Hing, S. Vega, J. Schaefer, *J. Magn. Reson.*, **96**, (1992), 205.
- [5] M.J. Lizak, T. Guillon, M.S. Conradi, *J. Magn. Reson.*, **91**, (1991), 254.
- [6] T. Guillon, J. Schaefer, *J. Magn. Reson.*, **81**, (1989), 196.
- [7] D.P. Raleigh, M.H. Levitt, R.G. Griffin, *Chem. Phys. Lett.*, **146**, (1988), 71.
- [8] D.P. Raleigh, F. Creuzet, S.K. Das Gupta, M.H. Levitt, R.G. Griffin, *J. Am. Chem. Soc.*, **111**, (1989), 4502.
- [9] E.R.H. van Eck, R. Janssen, W.E.J.R. Maas, W.S. Veeman, *Chem. Phys. Lett.*, **174**, (1990), 428.
- [10] V. Bork, T. Guillon, A. Hing, J. Schaefer, *J. Magn. Reson.*, **88**, (1990), 523.
- [11] Y. Pan, T. Guillon, J. Schaefer, *J. Magn. Reson.*, **90**, (1990), 330.
- [12] F. Creuzet, A. McDermott, R. Gebhard, K. van der Hoef, M.B. Spijker-Assink, J. Herzfeld, J. Lugtenburg, M.H. Levitt, R.G. Griffin, *Science*, **251**, (1991), 783.
- [13] H.W. Spiess, *Chem. Rev.*, **91**, (1991), 1321 and references therein.
- [14] A.K. Roy, P.T. Inglefield, *Progr. NMR Spectr.*, **22**, (1990), 569 and references therein.
- [15] M.M. Maricq, J.S. Waugh, *J. Chem. Phys.*, **70**, (1979), 3300.
- [16] J. Herzfeld, A.E. Berger, *J. Chem. Phys.*, **73**, (1980), 6021.
- [17] A. Schmidt, S.O. Smith, D.P. Raleigh, J.E. Roberts, R.G. Griffin, S. Vega, *J. Chem. Phys.*, **85**, (1986), 4248.
- [18] A. Schmidt, S. Vega, *J. Chem. Phys.*, **87**, (1987), 6895.
- [19] M.J. Duer, M.H. Levitt, *Solid-State NMR*, **1**, (1992), 211.
- [20] M.J. Duer, L.F. Gladden, A.C. Griffin, C.P. Jariwala, E.C. Stourton, submitted to *J. Chem. Soc. Faraday Trans.*
- [21] M.J. Duer, L.F. Gladden, A.C. Griffin, C.P. Jariwala, E.C. Stourton, submitted to *J. Chem. Soc. Chem. Comm.*
- [22] S. Vega, private communication.
- [23] M.A. Alla, E.I. Kundla and E.T. Lippmaa, *JETP Lett.*, **27**, (1978), 194.
- [24] Y. Yarim-Agaev, P.N. Tutunjian and J.S. Waugh, *J. Magn. Reson.*, **47**, (1982), 51.
- [25] A. Bax, N.M. Szeverenyi and G.E. Maciel, *J. Magn. Reson.*, **51**, (1983), 400.
- [26] A. Bax, N.M. Szeverenyi and G.E. Maciel, *J. Magn. Reson.*, **52**, (1983), 147.
- [27] A. Bax, N.M. Szeverenyi and G.E. Maciel, *J. Magn. Reson.*, **55**, (1983), 494.
- [28] T. Terao, T. Fujii, T. Onodera and A. Saika, *Chem. Phys. Lett.*, **107**, (1984), 145.
- [29] R.C. Zeigler, R.A. Wind and G.E. Maciel, *J. Magn. Reson.*, **79**, (1988), 299.
- [30] R. Tycko, G. Dabbagh and P.A. Mirau, *J. Magn. Reson.*, **85**, (1989), 265.
- [31] Z. Gan, *J. Am. Chem. Soc.*, **114**, (1992), 8307.
- [32] C.D. Hughes, M.H. Sherwood, D.W. Alderman, and D.M. Grant, *J. Magn. Reson. (A)*, **102**, (1993), 58.
- [33] J. Hu, A.M. Orendt, D.W. Alderman, C. Ye, R.J. Pugmire, D.M. Grant, *Solid-State NMR*, **2**, (1993), 235.
- [34] M. Hong, K. Schmidt-Rohr, Y.K. Lee, C. Husted, A. Pines, Poster at ENC April 1994, Pacific Grove, California, USA.
- [35] M.J. Duer, submitted to *J. Magn. Reson.*
- [36] J. Clauss, M.J. Duer, L.F. Gladden, A.C. Griffin, C.P. Jariwala, E.C. Stourton, submitted to *J. Chem. Soc. Faraday Trans.*
- [37] A. Abragam, "Principles of Nuclear Magnetism", Clarendon Press, Oxford (1961).
- [38] A. Samoson, E. Lippmaa, A. Pines, *Molec. Phys.*, **65**, (1988), 1013.
- [39] A. Bax, N.M. Szeverenyi, G.E. Maciel, *J. Magn. Reson.*, **52**, (1983), 147.
- [40] T. Terao, H. Miura, A. Saika, *J. Chem. Phys.*, **85**, (1986), 3816.
- [41] B.F. Chmelka, K.T. Mueller, A. Pines, J. Stebbins, Y. Wu, J.W. Zwanziger, *Nature*, **339**, (1989), 42.
- [42] K.T. Mueller, B.Q. Sun, G.C. Chingas, J.W. Zwanziger, T. Terao, A. Pines, *J. Magn. Reson.*, **86**, (1990), 470.
- [43] S. Vega and Y. Naor, *J. Chem. Phys.*, **75**, (1981), 75.
- [44] T.J. Bastow, M.E. Hobday, M.E. Smith, H.J. Whitfield, *Solid-State NMR*, **3**, (1994), 49.

HIGH-RESOLUTION FLUORINE-19 SOLID-STATE NMR OF MATERIALS CONTAINING BOTH FLUORINE AND HYDROGEN

Robin K. Harris*, Steven A. Carss, Richard D. Chambers, Peter Holstein†, Anna P. Minoja†† and Ulrich Scheler

Department of Chemistry, University of Durham, South Road, Durham DH1 3LE, England

Contents

- I. Abstract
- II. Introduction
- III. Experimental
- IV. Results and Discussion
- V. Acknowledgements
- VI. References

I. Abstract

We demonstrate herein the feasibility and use of high-resolution fluorine-19 magic-angle spinning NMR for organic and organometallic fluorine-containing solids which require high-power proton decoupling. Examples are given for fluoropolymers, fluorinated steroids, an organotin compound and an adamantane derivative fluorinated in side-chains. The influences of decoupler power and cross-polarization are discussed. Fluorine-fluorine spin exchange for a trifluorosteroid is illustrated. Spinning sidebands of tin satellites for tri-isobutyltin fluoride indicate an interplay between dipolar coupling, indirect coupling and shielding tensors. Spin-lattice relaxation in the rotating frame is explored for PVDF and the fluorinated adamantane, and triple-resonance $^{13}\text{C}\{-^1\text{H}, ^{19}\text{F}\}$ spectra are shown for the latter.

* To whom correspondence should be addressed.

† Permanent address: Fakultät für Physik und Geowissenschaften, Universität Leipzig, Linnéstrasse 5, D-04103 Leipzig, Germany.

†† Permanent address: Bruker Spectrospin, Via Pascoli 70/3, I-20133, Milano, Italy

II. Introduction

Although ^{19}F is arguably second only to the proton as an ideal nucleus for NMR (because of its high magnetic moment, spin- $\frac{1}{2}$ and 100% natural abundance), and has been extensively used for solution-state studies, it has been neglected in comparison with other nuclei such as ^{13}C , ^{29}Si , ^{27}Al and ^{31}P for high-resolution work on solids. There are two reasons for this. The first is that its favourable properties imply strong ($^{19}\text{F}, ^{19}\text{F}$) dipolar interactions when it is chemically-abundant in the sample of interest. This requires either very high speed magic-angle spinning (1) or use of combined rotation and multiple pulse spectroscopy (2), both of which are technically demanding. In spite of this, a number of studies have been carried out (3) for perfluorinated compounds. The second problem is that when protons are also present in the sample in substantial concentration, strong ($^{19}\text{F}, ^1\text{H}$) dipolar interactions form a principal cause of line-broadening in the ^{19}F spectrum, which is further complicated by the indirect effects of $^1\text{H}, ^1\text{H}$ dipolar coupling. The obvious answer to this difficulty lies in high-power proton decoupling, either by continuous-wave (or

suitably gated) irradiation or multiple-pulse homonuclear proton decoupling. The latter would not eliminate isotropic indirect ("scalar") (F,H) coupling effects. However, there have been very few attempts at these decoupling modes, primarily because of the fear that the proximity of ^1H and ^{19}F resonance frequencies (which are within 6% of each other) would make for difficulties. A suitable probe was reported some time ago by Kendrick and Yannoni (4), but these authors gave few applications. Veeman and his colleagues have made some extensive studies (5) of fluorinated synthetic polymers containing protons, but these systems have substantial mobility at the molecular level so that proton decoupling has a relatively small impact. In the last 18 months we have turned our attention to this matter (6-8), since in our view ^{19}F NMR of solids has considerable potential. Simultaneously, Hagaman and co-workers have also entered the area (9,10). The present paper incorporates a number of our results for several different chemical systems.

III. Experimental

The ^{19}F solid-state spectra, including those obtained with high-power proton decoupling, were recorded using a Chemagnetics CMX 200H spectrometer, operating at 200.13, 188.29 and 50.32 MHz for ^1H , ^{19}F and ^{13}C respectively. Direct observation of ^{19}F (and of ^1H) was carried out using a specially-built (8) Chemagnetics H-F Double Resonance APEX MAS probe in conjunction with 4 mm o.d. zirconia pencil rotors fitted with Vespel drive-tips and end-caps, together with PTFE or Vespel spacers (chosen to avoid unwanted signals in ^1H and ^{19}F resonance respectively). These rotors are capable of MAS at rates up to 18 kHz. Both single-pulse (SP) and cross-polarisation (CP) experiments have been implemented, using 90° pulse durations of ca. $1.8 \mu\text{s}$ at minimum, corresponding to B_1 powers equivalent to 140 kHz at maximum. Some ^{13}C -observe CPMAS experiments were carried out with a Chemagnetics H-F-X triple-resonance MAS probe accepting 7.5 mm o.d. zirconia rotors, with a maximum spin rate of 7 kHz. In this case the spacers are boron nitride and the drive tips

and end-caps are made of either Vespel or Kel-F (for $^{19}\text{F} \rightarrow ^{13}\text{C}$ and $^1\text{H} \rightarrow ^{13}\text{C}$ CP respectively). Typically 90° pulse durations were 4-5 μs (corresponding to 50-60 kHz).

IV. Results and Discussion

The H-F probe contains some fluorinated components so that SP spectra reveal a broad background signal (8). This is generally not a problem with fluorine-rich samples, but can cause difficulties for low-concentration species, such as are present for adsorbed systems. Cross-polarization from ^1H to ^{19}F readily removes this difficulty (8), which presumably is caused by PTFE (see Figure 1). High-power

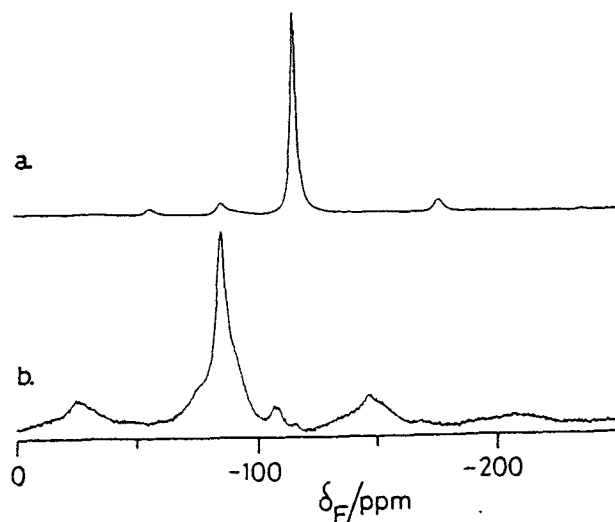


Figure 1: Fluorine-19 MAS spectra of a physical mixture of Teflon and PVDF (5%). (a) single pulse. (b) ^1H - ^{19}F cross polarization, contact time 1 ms. Both spectra involve proton decoupling during the acquisition. Both are from 32 transients, with $\pi/2$ pulse duration $1.75 \mu\text{s}$, spectral width 50 kHz, and spinning speed 14.5 kHz. The peak at -117 ppm is from Teflon, whereas that at -85 ppm arises from PVDF.

decoupling proceeds smoothly, and interference between the ^{19}F and ^1H channels is efficiently prevented by the rf network and external filters. As mentioned above, polymers such as

poly(vinyl difluoride), $(\text{CH}_2\text{CF}_2)_n$, do not exhibit the full advantages of the decoupling (Figure 2), although even in such a case, the

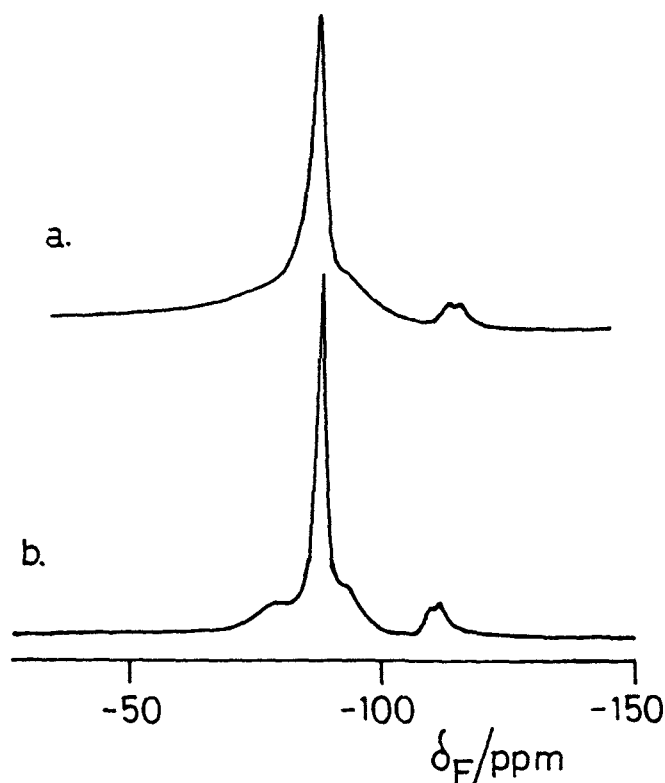


Figure 2: Effect of proton decoupling on ^{19}F MAS spectra of PVDF. (a) single pulse without decoupling. (b) single pulse with decoupling (decoupling field strength 140 kHz). MAS rate 16.7 kHz. Other parameters as in Figure 1. The scale refers to (b); that for (a) is not identical.

improvement in resolution is actually significant in revealing details of the polymorphism (11) - see below. The sample consists of crystalline and amorphous domains, the latter giving the most prominent signal. The small pair of peaks at low frequency arises from head-to-head and tail-to-tail monomer links. A more typical case of a relatively rigid organofluorine system is shown in Figures 3 and 4. The sample for Fig. 3 is of the monofluorinated steroid I. Proton decoupling reveals a typical shielding anisotropy powder pattern, from which the

tensor components have been obtained (7). The importance of decoupling is very clear. Figure 4

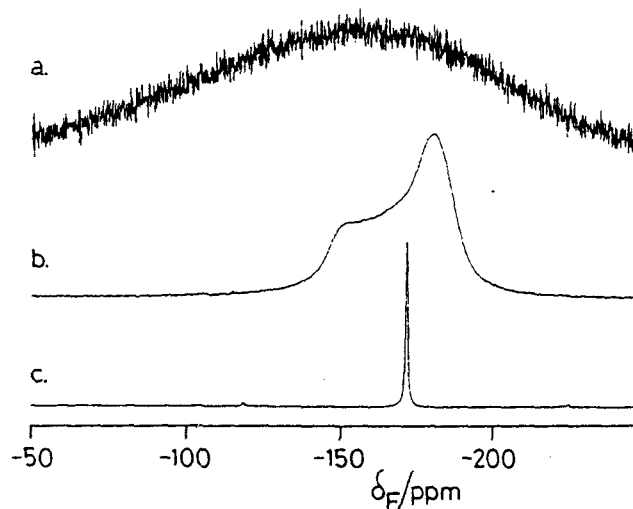


Figure 3: Fluorine-19 spectra of the monofluorinated steroid I. (a) static single pulse. (b) static single pulse with proton decoupling. (c) MAS with decoupling, spinning speed ca. 10 kHz.

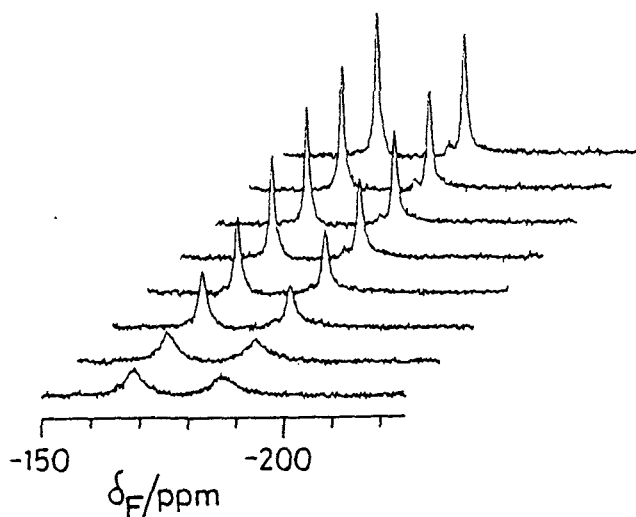
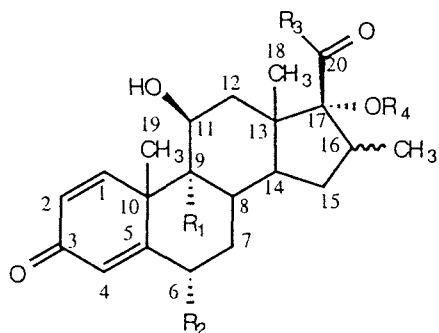


Figure 4: Fluorine-19 MAS spectra of the difluorinated steroid II. The proton decoupling field strength increases (bottom to top) from 10 kHz to 50 kHz. Spinning speed 13 kHz; other parameters as in Figure 1.

shows that, for the difluorinated, steroid II, optimum line narrowing is achieved (8) by a decoupling field strength equivalent to at least 40 kHz. Discriminating techniques such as are commonly used for ^{13}C MAS NMR are equally applicable to ^{19}F . For instance, the dipolar dephasing experiment distinguishes fluorines remote from protons or unusually mobile (7).



I $R_1 = \text{F}$, $R_2 = \text{H}$, $R_3 = \text{CH}_2\text{OH}$, $R_4 = \text{CO}^n\text{C}_4\text{H}_9$

II $R_1 = R_2 = \text{F}$, $R_3 = \text{SH}$, $R_4 = \text{H}$

III $R_1 = R_2 = \text{F}$, $R_3 = \text{SCH}_2\text{F}$, $R_4 = \text{COC}_2\text{H}_5$

Relaxation times like $T_{1\rho}$ give insight into molecular dynamics in the system under study. Prominent examples are proton relaxation measurements. However, the chemical shift resolution in proton spectra of solids is usually poor. Therefore only an average value of the relaxation time for the entire sample can be obtained. One way of attributing different proton relaxation times to different domains in a sample (or to different functional groups in the molecule) is to combine the proton relaxation measurement with the chemical shift resolution of another nucleus like ^{13}C . However, carbon-13 in natural abundance suffers from poor sensitivity. In this paper the focus is on ^{19}F which exhibits both high sensitivity and good resolution. The experiment consists of two parts. The first is the encoding of the relaxation information. After proton excitation there is a spin-lock pulse whose duration is a variable in the experiment. The second step is the transfer of the remaining proton magnetization into the fluorine nuclei in the vicinity via cross polarization. In order to avoid distortions of the results arising from spin diffusion the contact time has to be reasonably short. (A more elegant method for the magnetization transfer would involve isotropic

mixing.) The ^{19}F magnetization which can now be detected is modulated by the time evolution of the protons under the spin lock. The resulting series of one-dimensional ^{19}F spectra contains the information about $T_{1\rho}$ for the protons in the vicinity of each distinguishable type of fluorine. Moreover, a carefully-chosen value for the spin-lock time can be used to discriminate between different domains of a heterogeneous sample (as has been common for ^{13}C studies of solid polymers) - the "delayed contact" experiment. Figures 5 and 6 give an example (11) for poly(vinylidene difluoride), PVDF. Thus, Figure 5a shows the proton-decoupled CP spectrum of a biaxially-stretched PVDF sample, which contains amorphous and crystalline regions (the latter involving both α and β forms). The minor peaks at ca. -113 ppm are assigned to imperfections in the polymer chain arising from head-to-head or tail-to-tail linkages between

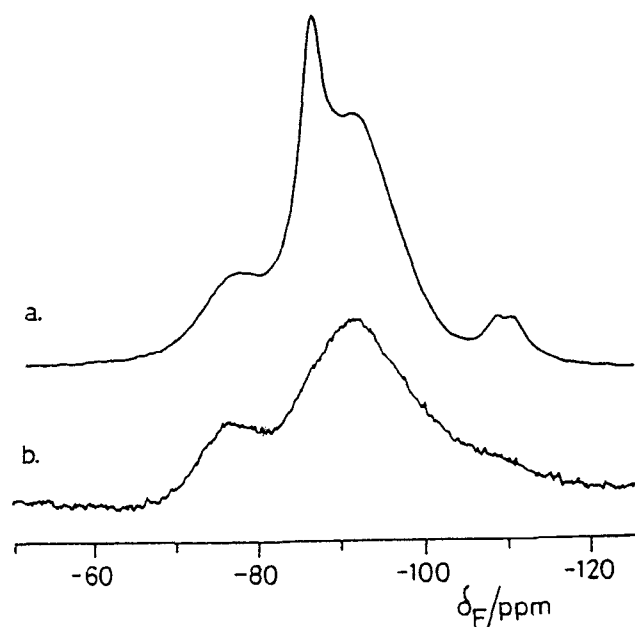


Figure 5: Fluorine-19 MAS spectra of a biaxially stretched film of PVDF. (a) $^1\text{H} \rightarrow ^{19}\text{F}$ cross polarization, contact time 1 ms. (b) $^1\text{H} \rightarrow ^{19}\text{F}$ cross polarization, contact time 1 ms after 40 ms ^1H spin lock. The signal of the amorphous region is suppressed due to the shorter $T_{1\rho}$ (^1H).

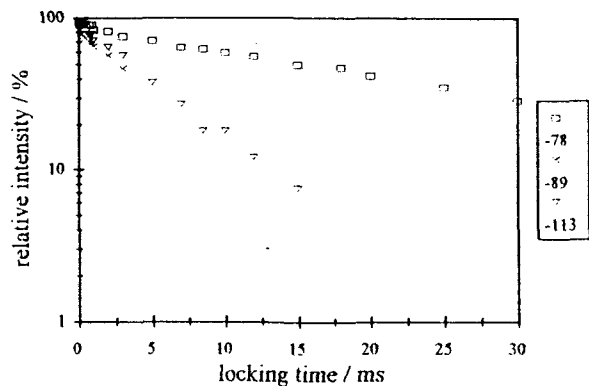


Figure 6: Determination of $T_{1\rho}(^1\text{H})$ for PVDF via ^{19}F detection (see the text). Experimental conditions: contact time $50\ \mu\text{s}$, recycle delay 3 s, number of transients 16, number of values of the spin-lock time 23, decoupler strength 80 kHz.

monomer units. Proton $T_{1\rho}$ data, monitored via ^{19}F resonances, are given in Figure 6, and it can be clearly seen that these minor peaks have relatively short $T_{1\rho}$ values, which are shared by the most significant signal at ca. -89 ppm. We attribute all these signals to amorphous domains of the polymer - it is reasonable that the imperfections cause difficulties for crystallisation. The delayed-contact spectrum of Figure 5b is therefore of the crystalline domains. The values obtained for $T_{1\rho}(^1\text{H})$ are ca. 25 ms (crystalline regions) and 5 ms (amorphous regions). These domains must be sufficiently large (more than a few hundred Å) so that spin-diffusion between them is minimal during the spin-lock and contact times. It should be noted that for the experiments illustrated in Figs. 5 and 6 (and for those described later in relation to Figs. 10 and 12) the sampling of the signals is done at integral rotor periods to avoid modulations arising from the MAS.

Slow-spinning experiments can be used to derive shielding tensor components via analysis of spinning sidebands. When a third type of magnetic nucleus is present, such analysis can reveal (12) the interplay of dipolar coupling, indirect coupling and shielding tensors. Figure 7 shows the case of tri(isobutyl)tin fluoride which, in the solid state,

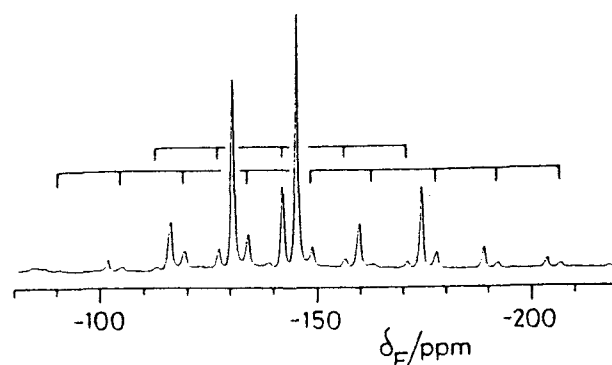


Figure 7: Fluorine-19 MAS spectrum of triisobutyltin fluoride. $\pi/2$ pulse duration $3.95\ \mu\text{s}$, spinning speed 2.7 kHz, 128 transients, 5 s recycle delay. The spinning sideband manifolds of the two "tin satellite" resonances are indicated separately.

has trigonal bipyramidal coordination around tin. The isotropic chemical shift is $\delta_{\text{F}} = -145$ ppm. Indirect isotropic coupling to ^{119}Sn causes splittings which have spinning sideband manifolds with different effective shielding anisotropies, giving detailed information on dipolar coupling. It can be seen that the high-frequency tin satellite resonance has a substantially smaller effective anisotropy than the low-frequency satellite. Analysis of the spinning sideband manifold of the central resonance yields the true shielding tensor components, showing that the anisotropy (defined as $\sigma_{33} - \sigma_{\text{iso}}$) is 38 ppm and the asymmetry parameter is, within experimental error, zero. The latter is consistent with a trigonal bipyramidal coordination at tin in the solid state, with the fluorines in axial positions linking two tin atoms (in agreement with ^{119}Sn results (12)). The isotropic indirect coupling constant, $|J_{\text{iso}}|$ is measured as ca. 1300 Hz.

Figure 8 shows the results of a two-dimensional spin-exchange experiment on the trifluorinated compound III. The pulse sequence of Jeener et al. (13) was used, with a cross-polarization preparation and proton decoupling during both evolution and detection times (but not during the mixing time). The

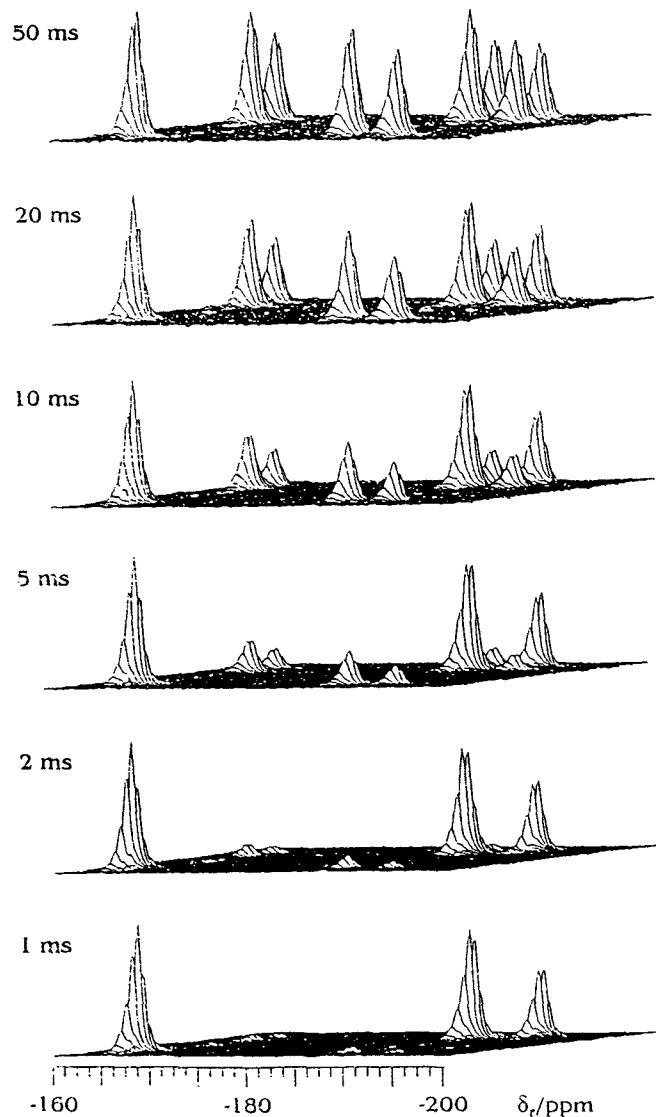


Figure 8: Stack of stacked plots for 2-D spin-exchange MAS spectra of the trifluorinated steroid III. Mixing times from the bottom to the top: 1 ms, 2 ms, 5 ms, 10 ms, 20 ms, 50 ms. The height of the most intense peak has been kept constant for the plots, so the apparent noise level increases with mixing time. $^1\text{H} \rightarrow ^{19}\text{F}$ cross polarization, contact time 2 ms, spectral width in both dimensions 20 kHz, ^1H $\pi/2$ pulse duration 2.6 μs , ^{19}F $\pi/2$ pulse duration 2.9 μs . Other experimental parameters as in Figure 1.

diagonal peaks at $\delta_{\text{F}} = -166, -188$ and -192 ppm are assigned to CF, CHF and CH_2F fluorine nuclei respectively. The effect of spin diffusion between all three fluorine nuclei can be seen in the increasing relative intensity of the off-diagonal peaks as the mixing time increases. Quantitative analysis is currently being carried out. Intramolecular F,F distances are estimated to be 4.0, 7.5 and 8.0 Å for F6/F9, F9/F21 and F6/F21 respectively, resulting in dipolar coupling constants of 1663, 252 and 208 Hz respectively. Mobility of the CH_2F group about the relevant C-C bond is believed to be a factor influencing the results.

Figure 9 illustrates a study of the fluorinated adamantane, IV. The three types of fluorine give clearly-resolved signals, revealing the chemical structure. The peak at -75 ppm corresponds to the CF_3 fluorine nuclei, the peaks at -122 ppm and -130 ppm correspond to the CF_2 (the two fluorines are non-equivalent but splittings arising from isotropic coupling

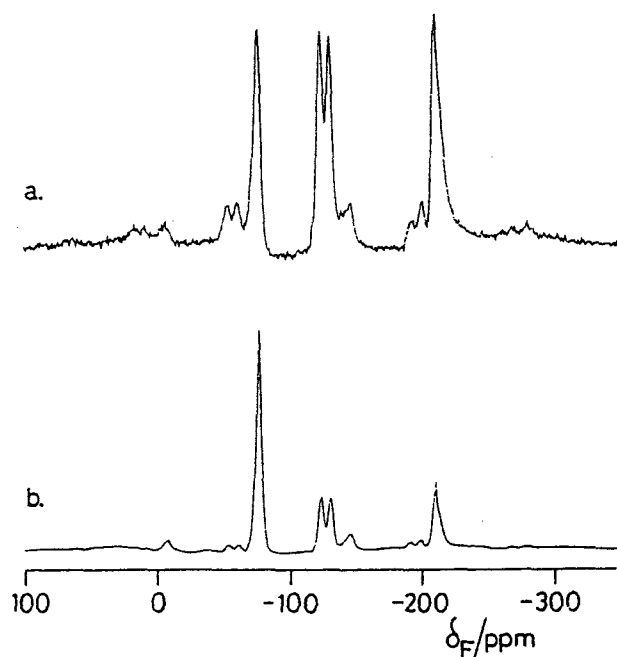


Figure 9: Fluorine-19 MAS spectra of the fluorinated adamantane IV. (a) $^1\text{H} \rightarrow ^{19}\text{F}$ cross polarization (contact time 1 ms); (b) single pulse with proton decoupling. Spinning speed 12.8 kHz; other parameters as in Figure 1.

between them are unresolved) and the peak at -209 ppm corresponds to the CFH group. The cross-polarisation dynamics can be explored (Figure 10) both for $^{19}\text{F} \rightarrow ^1\text{H}$ and $^1\text{H} \rightarrow ^{19}\text{F}$ cases. For the former experiment (Fig. 10a) the data do not fit well to the usual model equation (probably because of effects from proton spin diffusion), but the averaged $T_{1\rho}(^{19}\text{F})$ is ca. 28 ms and the cross-polarisation time, T_{CP} , is ca. 0.8 ms. In the case of $^1\text{H} \rightarrow ^{19}\text{F}$ CP (Figure 10b), the CF_3 and CF_2 signals fit reasonably well to the simple model, with $T_{\text{CP}} = 0.8$ ms and $T_{1\rho}(^1\text{H}) = 38$ ms for the former and $T_{\text{CP}} =$ ca.

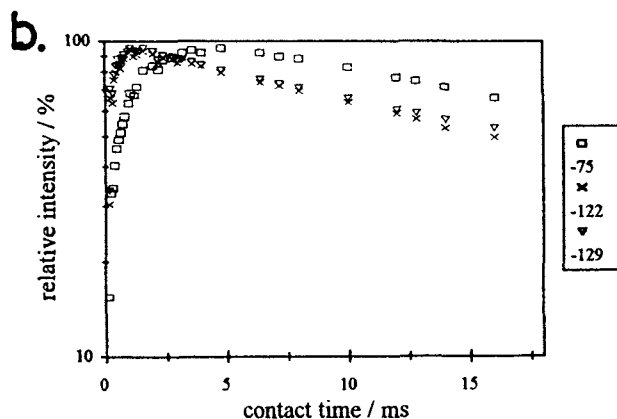
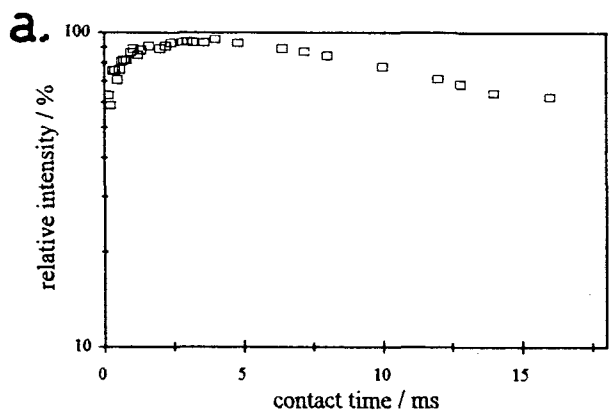
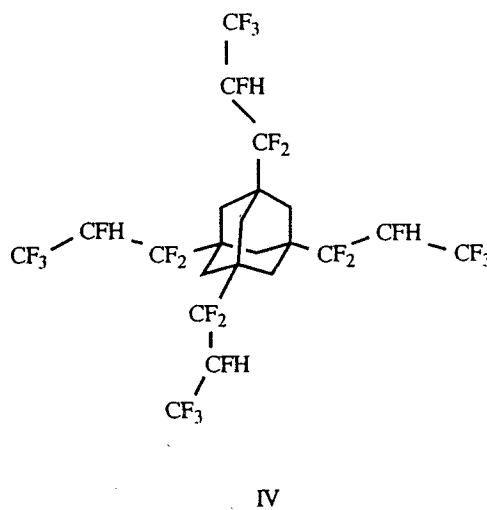


Figure 10: Variable-contact cross-polarization experiments on the fluorinated adamantane IV. (a) $^{19}\text{F} \rightarrow ^1\text{H}$ cross polarization; (b) $^1\text{H} \rightarrow ^{19}\text{F}$ cross polarization. The spin rate is 12.5 kHz and the $\pi/2$ pulse duration (on both channels) is 3 μs .

0.2 ms and $T_{1\rho}(^1\text{H}) = 24$ ms for the latter. The $\text{CF}_3\text{CFHCF}_2$ sidechains are probably relatively mobile and the CF_3 fluorines are more remote from the rigidly-held protons of the adamantane skeleton than the CF_2 fluorines, which explains the relatively long value of T_{CP} for the former. The behaviour of the CFH fluorines (not illustrated in Fig. 10b) is more complex.



Once the principle of $^1\text{H}/^{19}\text{F}$ double resonance is accepted as feasible experimentally, it became of interest to us to extend the experiments to $^{13}\text{C}\{-^1\text{H}, ^{19}\text{F}\}$ triple resonance, and Figure 9 shows such spectra for compound IV, using either $^1\text{H} \rightarrow ^{13}\text{C}$ or $^{19}\text{F} \rightarrow ^{13}\text{C}$ cross polarization. Obviously, in order to optimise the resolution, and hence the value in structure-determination, simultaneous decoupling of ^{19}F and ^1H is essential. In contrast to the case of PVDF, discussed above, $T_{1\rho}(^1\text{H})$ measurements for IV, monitored via the ^{19}F spectrum, give only a unique result within experimental error (14 ms) independent of the ^{19}F signal observed (Fig. 12a), indicating rapid spin diffusion between all the protons (no domain structure is expected). Of course, $T_{1\rho}(^1\text{H})$ can be monitored also via ^{13}C spectra, though the sensitivity is much lower than for ^{19}F observation. Figure 12b shows such results (using simultaneous decoupling of ^1H and ^{19}F) for IV - again, all signals show the same dependence on spin-lock time, giving $T_{1\rho}(^1\text{H}) = 10$ ms, in reasonable agreement with the value derived from ^{19}F observation.

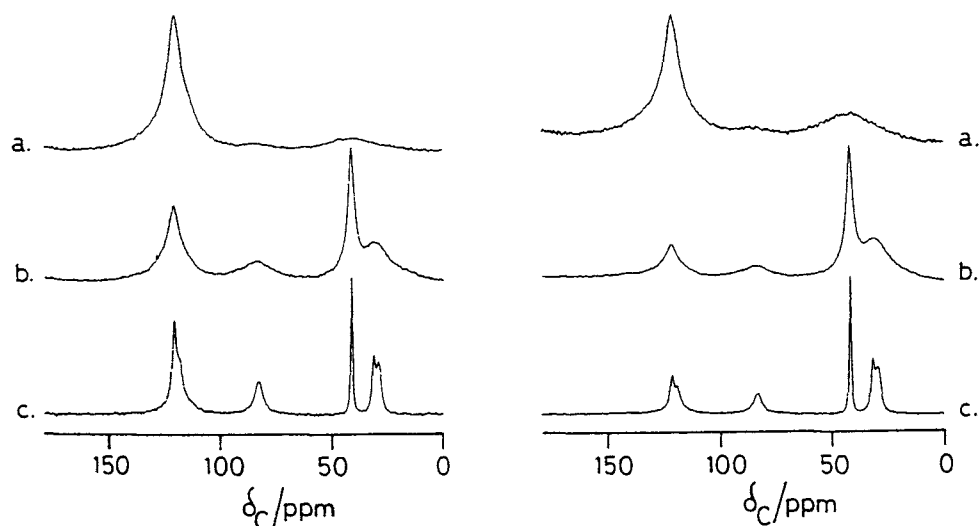


Figure 11: Carbon-13 MAS spectra of the fluorinated adamantane IV. Left column: $^{19}\text{F} \rightarrow ^{13}\text{C}$ cross polarization, contact time 4 ms. Right column: $^1\text{H} \rightarrow ^{13}\text{C}$ cross polarization, contact time 1 ms. The spectra are: (a) ^{19}F decoupling; (b) ^1H decoupling; (c) ^{19}F and ^1H decoupling. $\pi/2$ pulse duration 5 μs , spectral width 20 kHz, recycle delay 5 s. The peaks are 127 ppm CF_3 , 124 ppm CF_2 , 85 ppm CFH , 42 ppm quaternary and 29 and 32 ppm CH_2 .

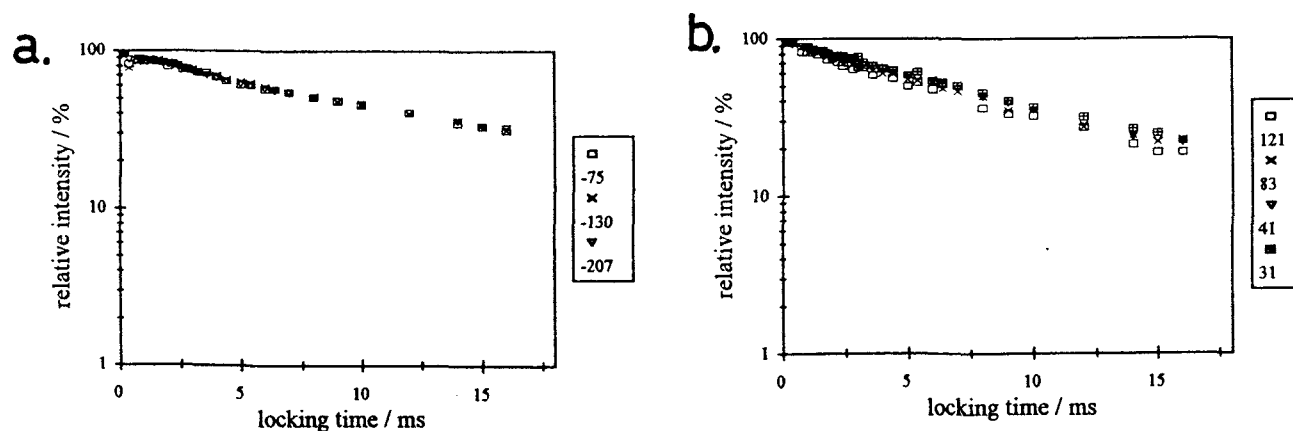


Figure 12: Determination of $T_{1\rho}(^1\text{H})$ for compound IV: (a) via ^{19}F detection; (b) via ^{13}C detection. Experimental conditions: (a) contact time 50 μs , number of transients 128, decoupler strength 62 kHz; (b) contact time 100 μs , number of transients 1024, decoupler strength 50 kHz (in both channels). In each case 30 values of the spin-lock time were used and the recycle delay was 10 s.

V. ACKNOWLEDGEMENTS

We thank Dr. R.A. Fletton for gifts of the three steroids, and the U.K. EPSRC for financial support under grant H/96096. S.A.C.

is grateful to the University of Durham for a research studentship, as is P.H. to the Deutsche Forschungsgemeinschaft for a research fellowship.

VI. REFERENCES

¹S.F. Dec, R.A. Wind, G.E. Maciel & F.E. Antonio, *J. Magn. Reson.* **70**, 355 (1986).

²R.K. Harris, P. Jackson & G.J. Nesbitt, *J. Magn. Reson.* **85**, 294 (1989).

³R.K. Harris & P. Jackson, *Chem. Rev.* **91**, 1427 (1991).

⁴R.D. Kendrick & C.S. Yannoni, *J. Magn. Reson.* **75**, 506 (1987).

⁵W.E.J.R. Maas, W.A.C. van der Heijden, W.S. Veeman, J.M.J. Vankan & G.H.W. Buning, *J. Chem. Phys.* **95**, 4698 (1991).

⁶S.A. Carss, R.K. Harris, P. Holstein, B.J. Say & R.A. Fletton, *J.C.S. Chem. Comm.* 2407 (1994).

⁷S.A. Carss, U. Scheler, R.K. Harris, P. Holstein & R.A. Fletton, *Magn. Reson. Chem.*, in press.

⁸U. Scheler, P. Holstein, S.A. Carss & R.K. Harris, *Chemagnetics Application Note* (May 1995).

⁹Hagaman & J.H. Burns, *Fuel* **72**, 1239 (1993).

¹⁰E.W. Hagaman, *J. Magn. Reson. A* **104**, 125 (1993).

¹¹R.K. Harris, P. Holstein & U. Scheler, to be published.

¹²H. Bai & R.K. Harris, *J. Magn. Reson.* **96**, 24 (1992).

¹³J. Jeener, B.H. Meier, P. Bachmann & R.R. Ernst, *J. Chem. Phys.* **71**, 4546 (1979).

THE EFFECTS OF BULK MAGNETIC SUSCEPTIBILITY IN NMR

Ildikó Pályka, Wei Huang, and Charles S. Springer, Jr.

Chemistry Department, Brookhaven National Laboratory, Upton, New York 11973
and Department of Chemistry, State University of New York,
Stony Brook, New York 11794-3400 / USA

INTRODUCTION

In this year of celebration of the 50th anniversary of the discovery of nuclear magnetic resonance, it is particularly fitting to also consider the large effects on this phenomenon that can be caused by the magnetism of unpaired electrons. This is so because the first reports of such effects (1,2) followed not long after the announcement of NMR. We have recently contributed a detailed review on the effects of molecules exhibiting more than simple diamagnetic behavior; i.e., paramagnetic, superparamagnetic, ferromagnetic, antiferromagnetic, etc. (We refer to these as *nondiamagnetic*.) (3). Here, we will provide a qualitative elaboration on the *bulk magnetic susceptibility* (BMS) aspects of these effects. For a quantitative treatment, the reader is referred to (3).

In general, nondiamagnetic molecules cause shifts in nuclear spin resonance frequencies, reductions in nuclear spin relaxation rate constants, or (usually) both. We have found it particularly useful to categorize the major mechanisms in terms of their contributions to the frequency shift (3). Thus, the two largest terms giving rise to such a shift are those representing the *hyperfine* and BMS interactions.

THE HYPERFINE INTERACTION

The hyperfine interaction is that which occurs with the nuclear spin of an atom in the same molecule, or (even transient) molecular complex, as the atom containing the unpaired electron density. Since these two atoms are usually not the same, this interaction is most often really a *superhyperfine* one (3). The hyperfine interaction has two

distinctive contributions: the scalar (contact), and the dipolar (pseudocontact). The scalar interaction involves the delocalization of some unpaired electron density into the s atomic orbitals of the nuclear spin observed (Fermi contact mechanism). The dipolar term represents the through-space interaction of the magnetic moments of the unpaired electron(s) and the nuclear spin (3). Over the years, the hyperfine interaction has played a very important role in the study of the electronic and molecular structures of paramagnetic metal coordination complexes and metalloproteins. More recently, this effect has been essential in the development of contrast agents for use in nuclear magnetic resonance imaging (MRI) (3).

THE BMS INTERACTION

The BMS effect embodies the sum of the dipolar interactions of the magnetic moments of distant (non-bonded) unpaired electronic and nuclear spins with that of the nuclear spin under observation (3). Thus, it is most important to realize that it can act across compartmental walls. Since the hyperfine effect requires (at least transient) chemical bonding, this aspect is an essential distinction between the two major mechanisms. The BMS interaction can itself be expressed as the sum of homogeneous and inhomogeneous contributions (3). The homogeneous term is that which is common to all of the nuclear spins (hetero- or homonuclear) within a compartment. It determines the *average* value of the resonance frequency of the spins relative to that of the same nuclear species in a vacuum. Thus, it is distinct from, and added to, any *chemical* shift that is extant. (A hyperfine shift is a

strong example of a chemical shift.) The inhomogeneous term depends on the spatial position of the nuclear spin in the compartment. Indeed, this is the sense in which *inhomogeneity* is meant. It is, however, independent of the nature of the nuclear isotope. The inhomogeneous contribution determines the *spread* of resonance frequencies for the compartmental spins (3). These considerations are perfectly general, and apply even if there are no unpaired electrons present in the sample. The BMS interaction is expressed in terms of the dimensionless, volume bulk magnetic susceptibility (χ) values of the media occupying the various sample compartments (3).

Dickinson first reported, and correctly identified, the homogeneous interaction, in 1951 (2). McConnell and co-workers first reported, and correctly identified, the inhomogeneous contribution, in 1955 (4). In 1957, Zimmerman and Foster first suggested, without comment, that the homogeneous and inhomogeneous interactions were additive (5). Thus, within the first decade of NMR, knowledge of the essentials of the BMS effect was in place. Some proceeded to use it for the determination of the magnetic moments of solute molecules (6). However, the general development of BMS theory was very haphazard, disorganized, and not known to most NMR practitioners.

The probable reason for the lack of theory development is that investigators learned very soon that the dissolution of an (inert) internal reference compound in the (physically) homogeneous solution in a single-compartmented sample tube eliminated any homogeneous BMS shift. Likewise, the small size and placement of the transceiver coil relative to the entire sample volume eliminated any inhomogeneous BMS contribution. However, with a growing interest in multicompartimented samples smaller than the coil (powdered solids, organisms *in vivo*, etc.), these experimental corrections were precluded. Now, BMS effects were unavoidable, and sometimes even useful.

For these reasons, we have reported our attempts to organize and systematize the theory of the BMS frequency shift, starting with our 1990

papers (6,7), and later with subsequent contributions (3,8-11), which we illustrated particularly with the issues arising in cell suspension and tissue samples. The principles of the effects of isotropic and anisotropic BMS tensors on spectra from solid samples were enunciated by Van der Hart, Earl, and Garroway in 1981 (12), Barbara in 1994 (13), and also nicely illustrated by Tang, Pines, and co-workers in 1992 (14).

In addition to experimentally demonstrating the additivity of the homogeneous and inhomogeneous contributions (6), we showed the profound effects on the homogeneous term caused by the local cancellation of the dipolar interactions in the immediate molecular environment of the observed spin; when it is present in a mobile phase (3,6). This is modeled by the so-called *Sphere of Lorentz* – an imaginary vacuum bubble (or insulating cavity) that surrounds each spin and remains with it during all of its diffusional excursions. For example, this effect gives rise to certain **magic situations** – when the homogeneous term for the spins in a compartment is independent of the value of χ for the medium in that compartment. These are: (a.) the **magic shapes** of: (1.) the *sphere*, and (2.) the right circular *cylinder* or *disk* with the *magic aspect ratio* (a height/diameter ratio of 0.9), and (b.) the **magic angles** of $54^{\circ}44'$ or $125^{\circ}16'$ between the axis of a cylindrical compartment, or the normal of a disk-shaped compartment, and the static magnetic field (\mathbf{B}_0) direction (3). A magic situation obviates the need for an internal reference compound.

In general, however, we found that the homogeneous term depends on the *difference* ($\Delta\chi$) between the BMS value of the medium in the compartment containing the spin (χ_i), and that of the medium surrounding the compartment (χ_e) ($\Delta\chi = \chi_i - \chi_e$), the value of χ_e itself, the shape of the compartment, and the orientation of the compartment in \mathbf{B}_0 (3). The inhomogeneous interaction depends also on $\Delta\chi$, the shape, and the orientation of the compartment, but, importantly, on the size of the compartment and the spatial position of the nuclear spin as well (3). These

terms can be expressed analytically for highly symmetrical compartments, present individually in an otherwise homogenous surrounding medium of infinite extent. For example, we have presented the expressions for special cases of the universal ellipsoid of revolution (3), and these have led to the generalizations just listed. For the vast majority of real situations, however, these interactions must be computed numerically.

MRI ASPECTS

In the study of MRI, the BMS interaction was considered initially as only a problem. The manifestation of a BMS effect in a sample as a resonance frequency shift can cause a distortion in the NMR image of that sample. Since the essence of MRI is the use of an imposed magnetic field gradient to encode spatial information in the resonance frequency in an analytical manner, the presence of an unimposed BMS frequency shift will be encoded as an incorrect spatial shift during the image construction (7). In addition, the presence of large $\Delta\chi$ values usually causes large magnetic field inhomogeneities near the compartmental boundaries. These, in turn, cause a large reduction in the apparent T_2 value, T_2^* , for the magnetization of spins present near these boundaries, or diffusing into these regions. This can cause a loss of detected signal intensity and a darkening of the resulting image. The vast majority of MR images are constructed from the very strong signal due to the magnetization of the ubiquitous, and diffusing, $^1\text{H}_2\text{O}$ spins. Since the value of χ for most tissue is *ca.* -9 ppm (in rationalized MKS units (3)), and that for air is 0.4 ppm (slightly above the vacuum value of zero because of the presence of paramagnetic O_2 (3)), the image intensity of spins near tissue/air interfaces (and tissue/bone interfaces) can be particularly distorted and/or darkened. This represents a very large value for $\Delta\chi$. Also, since these interfaces are macroscopic in size, the image artifacts are present over large areas of space. Considerable effort has been put into calculating, and compensating for, these effects (15).

THE BALD MECHANISM

Starting in 1986, however, the Brady bunch (16), and later others, began reporting considerations of BMS differences between the lumens of brain blood vessels and the surrounding parenchyma. Since the most important blood vessels, the capillaries, are very small ($< 10 \mu\text{m}$ in diameter), and the values of $\Delta\chi$ were small (3), the BMS inhomogeneities in question were microscopic in dimension; limited to the immediate vicinity of the capillary vessel. These interesting experiments ultimately led to the use of contrast agent-based susceptibility contrast imaging to map cerebral blood volume (17), and actual brain function (18).

Rosen and his co-workers demonstrated unambiguously that the transient image intensity darkening they observed during the first pass through the brain after a bolus injection of contrast agent was due to BMS effects. They did this by using a series of lanthanide chelate contrast agents that featured essentially isomorphic substitution with different paramagnetic lanthanide ions possessing different magnetic moments (16,19,20). (We have tabulated these for the entire lanthanide series in reference (3).) They showed that the size of the intensity decrease was proportional to the square of the magnetic moment; a certain signature of the BMS interaction (3).

We have referred to this effect as the BALD (Blood Agent Level Dependent), or Rosen, mechanism (3,10). Its evocation requires that a bolus iv injection be made of a solution with a χ value significantly greater than that of tissue, *ca.* -9 ppm. During the first pass of the agent bolus through the brain, there is a transient but noticeable mismatch of the BMS in the vessel lumen and that of the surrounding parenchyma. The value of $\Delta\chi$ is transiently positive. Thus, the T_2^* values of the signals of $^1\text{H}_2\text{O}$ spins just outside the capillary vessels are transiently shortened (3). If a series of rapid images is acquired during this passage, a transient darkening is observed. Plots of the time course of image intensity can be made for image regions of interest (ROIs) or even individual

pixels. The area subtended by the peaked function is proportional to the blood volume in the tissue volume represented by the ROI or pixel. The curve resulting from a passage occurring during cerebral activity is different from that arising from the same ROI or pixel during rest (18). The difference is a measure of the extent of activity. The changes observed using this approach are very sizable and easily measurable. Unfortunately, the BALD approach requires the rapid injection of a clinical dose of contrast agent for each instance of mental activation to be studied. Since one usually wants to study the responses to repeated stimulations, this is really quite impractical.

THE BOLD MECHANISM

Fortunately, during this same time period, an important series of reports of studies by Ogawa and co-workers began to appear. They showed that changes in the value of χ_{blood} itself, consequent to manipulations of brain tissue blood oxygenation, were sufficient to cause detectable contrast changes in T_2 -weighted images (21-25). Turner and co-workers also reported similar results (26). Ogawa and his colleagues reasoned that these changes were due to the changes in the electronic spin state of the hemoglobin iron atoms known to occur upon deoxygenation. Pauling and Coryell had reported in 1936 that oxyhemoglobin is diamagnetic, while deoxyhemoglobin is paramagnetic (27). When coordinated to dioxygen, the heme iron is diamagnetic. However, when deoxygenated, each iron atom has four unpaired electrons. Ogawa and co-workers coined the phrase BOLD (Blood Oxygenation Level Dependent) mechanism to describe this phenomenon. We have also referred to it as the Ogawa mechanism (3,10).

FUNCTIONAL MRI

It was not long until the first appearance of reports that one could directly obtain images showing cerebral activity in a totally noninvasive manner (28-30). This approach has rapidly become extremely popular and is usually referred to as *functional* MRI (fMRI; though some have also

called it "spot-o-mania"). Understandably, investigators immediately ascribed a BOLD mechanism to the fMRI phenomenon. The fact that the response was much stronger at higher B_0 values (31) supported the BMS nature of the mechanism.

Curiously, the fMRI intensity has always been reported to be *greater* (i.e., brightening) during a neural response. This means that the T_2 values of the magnetization of extravascular $^1\text{H}_2\text{O}$ spins became transiently longer. This is the opposite response from the BALD mechanism.

Assuringly, this seemed to be compatible with earlier positron emission tomography (PET) studies of brain activation. These had shown that there were focal increases in the metabolic utilization of glucose (32). Though a considerable part of this increase is due to anaerobic metabolism (32), this process is rather invisible to the standard fMRI protocol, and to MRI in general. It can be detected by functional MR spectroscopy (33,34), albeit with much poorer spatial and temporal resolution than MRI. The PET studies, however, also demonstrated lesser, but still increased, focal rates of oxygen consumption (32). Now, an aerobic component of glucose metabolism might be expected to cause an image *darkening*, because the metabolic product is the *paramagnetic* deoxyhemoglobin – a BALD-like effect. However, a third aspect of the PET findings was the observation of fractional increases in local cerebral blood flow that were greater than the fractional increases in O_2 consumption (32). This could be expected to result in a transient *hyperoxygenation* of the blood, and cause it to become briefly more diamagnetic.

Thus, the fMRI result was explained in the following way (3). It could be considered that, in the resting state, the blood is very slightly less diamagnetic than the surrounding parenchyma, because of the low level of deoxygenated heme iron present even in the arterial input to the capillary bed. This would represent a very small value of $\Delta\chi$ – probably no more than 0.2 ppm (3) – and a T_2 -weighted image would be slightly darker than it

might otherwise be. If the blood were transiently more diamagnetic, the value of $\Delta\chi$ would become transiently smaller, perhaps even zero, and the image would become transiently brighter. We have shown (10) that this explanation would predict that, in addition to being of the opposite sign, the fMRI response caused by such a BOLD mechanism would be smaller than that for a perfectly analogous BALD experiment by roughly a factor of thirty. Frank, Moonen, and co-workers have recently reported BALD and BOLD experiments on the same subjects (35). Accounting for the differences in their experimental BALD protocol and our calculated simulation of it, one finds reasonable quantitative agreement with our prediction (10).

However, there are some problematic aspects to the explanation of the fMRI result given above. Our theoretical calculations of the χ value for blood show that it is determined mostly by the concentration of deoxygenated heme iron (3,9). Since oxygenated hemoglobin is diamagnetic, as is the rest of the blood medium, its concentration has almost no effect on the blood BMS. Recent optical reflectance studies at a wavelength specific for deoxyhemoglobin (really, deoxygenated heme iron) show focal increases in its blood level during stimulation (36,37). The preliminary report of a mathematical model of aerobic cerebral activity at the capillary level suggests that the blood concentration of deoxyhemoglobin rises, even though the blood flow through the capillary also increases (38). Taken together, these observations would predict that the fMRI experiment should detect at least some regions with *negative* BOLD effects; i.e., image darkening.

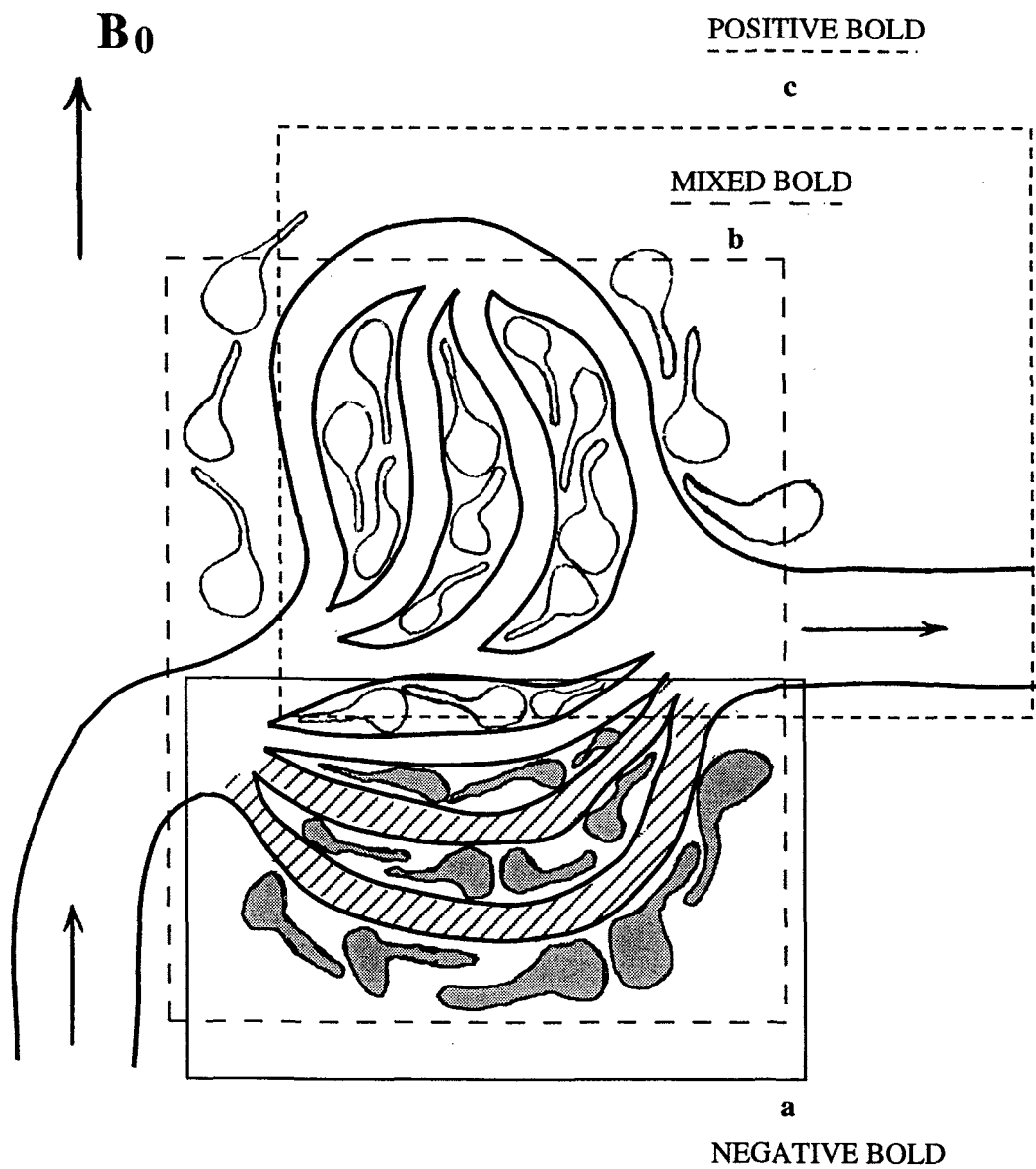
Very recently, Ugurbil and co-workers have reported high field (4 Tesla) fMRI studies of visual stimulation in humans, in which certain pixels first *decrease* in intensity before becoming brighter later in the stimulation (39). Other pixels show the common positive-only intensity changes. We have recently carried out very high field (9.4 Tesla) fMRI studies of visual stimulations of mice (40,41). In these, we observe some pixels that show only darkening during stimulation, while others exhibit intensity increases. We suspect that the negative

fMRI changes represent the actual response of the visual cortex to stimulation (40). The very high field allows us to make fMRI maps with very high spatial resolution (nominal pixel dimensions: $230\ \mu\text{m} \times 470\ \mu\text{m}$ (40)).

We have offered a model that could explain these varied fMRI results (40). It is illustrated in the cartoon seen in the Figure. This depicts two extremely stylized capillary beds, their supplying arteriole and draining venule, and neuronal cells that they service. The actual geometries of real capillary beds are considerably more complicated (3). The Figure indicates three ROIs. ROI **a** circumscribes the capillary bed servicing mostly neurons that are activated (shown in gray) by a stimulus. ROI **b** (that is larger in size than ROI **a**) contains this capillary bed as well as the other, which services nonactivated neurons. ROI **c** (that is the same in size but different in orientation than ROI **b**) encompasses the "nonactivated" capillary bed but is dominated by the draining venule. In our paper, we cite the growing literature evidence that brain capillary volume remains unchanged and that flow through the capillary vessels is controlled by appropriate dilation and contraction of the supplying arterial and draining venous vessels (40). Thus, imagine that activation of the neurons indicated causes at least some aerobic glycolysis and also signalling for the dilation of the arteriole, which in turn increases the flow through the capillary beds. The χ values of the blood in the capillaries (indicated by cross-hatching) servicing the active neurons could rise above the parenchymal value and produce a negative BOLD effect in ROI **a**, which is dominated by them. There would also be increased flow through the upper capillary bed since it is supplied by the same arteriole. However, this bed services neurons whose activity is not increased by stimulation. Thus, the blood in these capillary lumens would certainly become hyperoxygenated in the transient high-flow steady state condition (38). In larger animals, there is a delay between the activation and the flow increase (40). Thus for an ROI such as **b**, which contains both capillary beds but is controlled by inactive neurons, there would be an initial

negative BOLD effect followed by a subsequent increase in signal intensity later in the stimulation. The fMRI response in ROI c will be dominated by the draining venous vessel. Since most venous vessels likely drain more inactive than active neural tissue, their blood would also be hyperoxygenated and an ROI such as c would exhibit a positive-only

BOLD effect. Since the venous vessels have diameters larger than those of the capillaries, their BMS effects should be more extensive. It is considered likely that most fMRI results, which are obtained on low field instruments, are dominated by the larger effects of the draining vessels (39).



Figure

A stylized version of a pair of capillary beds fed by one arteriole and drained by one venule.

ACKNOWLEDGEMENTS

We thank the National Institutes of Health (Grant GM 32125) and the Laboratory Directed Research and Development Program of Brookhaven National Laboratory (grant to Joanna S. Fowler and CSS) for support of these studies. Part of this work was carried out at Brookhaven National Laboratory under contract DE-AC02-76CH00016 with the U.S. Department of Energy and supported by its Office of Health and Environmental Research.

REFERENCES

1. W. D. Knight *Phys. Rev.* **76** 1259 (1949).
2. W. C. Dickinson *Phys. Rev.* **81** 717 (1951).
3. C. S. Springer, in *NMR Physiology and Biomedicine*, Ed. by R. J. Gillies, Academic Press, New York, p. 75 (1994).
4. C. A. Reilly, H. M. McConnell, and R. G. Meisenheimer *Phys. Rev.* **98** 264 (1955).
5. J. R. Zimmerman, and M. R. Foster *J. Chem. Phys.* **61** 282 (1957).
6. S. C-K. Chu, Y. Xu, J. A. Balschi, and C. S. Springer *Magn. Reson. Med.* **13** 239 (1990).
7. Y. Xu, J. A. Balschi, and C. S. Springer *Magn. Reson. Med.* **16** 80 (1990).
8. C. S. Springer and Y. Xu, in *New Developments in Contrast Agent Research*, Ed. by P. A. Rinck and R. N. Muller, Europ. Magn. Reson. Forum, Blonay Switzerland, p. 13 (1991).
9. M. S. Albert, W. Huang, J-H. Lee, J. A. Balschi, and C. S. Springer *NMR Biomed.* **6** 7 (1993).
10. M. S. Albert, W. Huang, J-H. Lee, C. S. Patlak, and C. S. Springer *Magn. Reson. Med.* **29** 700 (1993).
11. C. S. Springer *NMR Biomed.* **7** 198 (1994).
12. D. L. Van der Hart, W. L. Earl, and A. N. Garroway *J. Magn. Reson.* **44** 361 (1981).
13. T. M. Barbara *J. Magn. Reson. A* **109** 265 (1994).
14. D. Raftery, H. Long, L. Reven, P. Tang, and A. Pines *Chem. Phys. Lett.* **191** 385 (1992).
15. M. B. Smith *MR* **2** (No 2) 47 (1992).
16. A. Villringer, B. R. Rosen, R. B. Lauffer, J. L. Ackerman, V. J. Wedeen, R. B. Buxton, and T. J. Brady *Proc. Soc. Magn. Reson. Med.* **5** 2 1 (1986).
17. B. R. Rosen, J. W. Belliveau, H. J. Aronen, D. Kennedy, B. R. Buchbinder, A. Fischman, M. Gruber, M. Glas, R. M. Weisskoff, M. S. Cohen, F. H. Hochberg, and T. J. Brady *Magn. Reson. Med.* **22** 293 (1991).
18. J. W. Belliveau, D. N. Kennedy, R. C. Mckinstry, B. R. Buchbinder, R. M. Weisskoff, M. S. Cohen, J. M. Vevea, T. J. Brady, and B. R. Rosen *Science* **254** 716 (1991).
19. A. Villringer, B. R. Rosen, J. W. Belliveau, J. L. Ackerman, R. B. Lauffer, R. B. Buxton, Y.S. Chao, V. J. Wedeen, and T. J. Brady *Magn. Reson. Med.* **6** 164 (1988).
20. B. R. Rosen, J. W. Belliveau, and D. Chien *Magn. Reson. Quart.* **5** 263 (1989).
21. S. Ogawa, T-M. Lee, A. S. Nayak, and P. Glynn *Magn. Reson. Med.* **14** 68 (1990).
22. S. Ogawa, T-M. Lee, A. R. Kay, and D. W.

- Tank *Proc. Natl. Acad. Sci. USA* **87** 9868 (1990).
23. S. Ogawa and T-M. Lee *Magn. Reson. Med.* **16** 9 (1990).
24. S. Ogawa, T-M. Lee, and B. Barrere *Magn. Reson. Med.* **29** 205 (1993).
25. S. Ogawa, R. S. Menon, D. W. Tank, S-G. Kim, H. Merkle, J. M. Ellerman, and K. Ugurbil *Biophys. J.* **64** 803 (1993).
26. R. Turner, D. LeBihan, C. T. W. Moonen, D. Despres, and J. Frank *Magn. Reson. Med.* **22** 159 (1991).
27. L. Pauling and C. D. Coryell *Proc. Natl. Acad. Sci. USA* **22** 210 (1936).
28. P. A. Bandettini, E. C. Wong, R. S. Hinks, R. S. Tikofsky, and J. S. Hyde *Magn. Reson. Med.* **25** 390 (1992).
29. K. K. Kwong, J. W. Belliveau, D. A. Chesler, I. E. Goldberg, R. M. Weisskoff, B. P. Poncelet, D. N. Kennedy, B. E. Hoppel, M. S. Cohen, R. Turner, H-M. Cheng, T. J. Brady, and B. R. Rosen *Proc. Natl. Acad. Sci. USA* **89** 5675 (1992).
30. S. Ogawa, D. W. Tank, R. Menon, J. M. Ellerman, S-G. Kim, H. Merkle, and K. Ugurbil *Proc. Natl. Acad. Sci. USA* **89** 5951 (1992).
31. R. Turner, P. Jezzard, H. Wen, K. K. Kwong, D. LeBihan, T. Zeffiro, and R. S. Balaban *Magn. Reson. Med.* **29** 277 (1993).
32. P. T. Fox, M. E. Raichle, M. A. Mintun, and C. Dence *Science* **241** 462 (1988).
33. J. Pritchard, D. Rothman, E. Novotny, O. Petroff, T. Kuwabara, M. Avison, A. Howseman, C. Hanstock, and R. Shulman *Proc. Natl. Acad. Sci. USA* **88** 5829 (1991).
34. D. Sappey-Mariniere, G. Calabrese, G. Fein, J. W. Hugg, C. Biggins, and M. W. Weiner *J. Cereb. Blood Flow Metab.* **12** 584 (1992).
35. V. S. Mattay, D. R. Weinberger, F. A. Barrios, G. S. Sobering, K. J. Kotrla, P. van Gelderen, J. H. Duyn, R. H. Sexton, C. T. W. Moonen, and J. A. Frank *Radiology* **194** 687 (1995).
36. R. Turner and A. Grinvald *Proc. Soc. Magn. Reson.* **2** 430 (1994).
37. A. Grinvald, R. D. Frostig, R. M. Siegel, and E. Bartfield *Proc. Natl. Acad. Sci. USA* **88** 11559 (1991).
38. R. B. Buxton and L. R. Frank *Proc. Soc. Magn. Reson. Med.* **12** 4 (1993).
39. R. S. Menon, S. Ogawa, X. Hu, J. P. Strupp, P. Andersen, and K. Ugurbil *Magn. Reson. Med.* **33** 453 (1995).
40. W. Huang, I. Palyka, H-F. Li, E. M. Eisenstein, N. D. Volkow, and C. S. Springer, submitted for publication.
41. I. Palyka, W. Huang, H-F. Li, E. M. Eisenstein, N. D. Volkow, and C. S. Springer, submitted for publication.

Noise in EPR Bridges with Multiple Time-Locked Microwave Frequencies

James S. Hyde, Robert A. Strangeway, J. Luglio,
Hassane S. Mchaourab and W. Froncisz

Biophysics Research Institute, Medical College of Wisconsin
Milwaukee, Wisconsin 53226

I. INTRODUCTION

The overall receiver noise figure of X-band CW EPR spectrometers of 1970's vintage using 100 kHz field modulation was about 10 dB. With rectangular TE₁₀₂ cavities of unloaded Q about 7000 and high quality external cavity reflex klystrons, noise from the source and noise from the receiver were approximately equal at an incident power on the cavity of about 100 mW with the bridge adjusted to observe absorption spectra. When a cylindrical TE₀₁₁ cavity of unloaded Q about 20,000 was used, source and detector noise were about equal for an incident power of about 10 mW. The quadratic dependence on cavity Q is consistent with the hypothesis that phase noise of the source rather than amplitude noise dominated when tuned to the absorption mode.

Introduction of low noise microwave amplifiers reduced the overall receiver noise figure to about 1.5 dB, and phase noise from the source became much more apparent. Two separate approaches were undertaken at the National Biomedical ESR Center to reduce contributions of phase noise. In the first approach, a Gunn diode was carefully coupled to a high Q cylindrical TE₀₁₁ tank circuit. Robbins (1) gives the following expression for the ratio of phase noise density N_{OP} to carrier power ratio P .

$$\left(\frac{N_{OP}}{P}\right)_{f_m} = \frac{FkT}{P} \frac{1}{8Q^2} \left(\frac{f_0}{f_m}\right)^2. \quad [1]$$

Here f_m is the offset from the carrier frequency f_0 . Although the device-specific noise figure term F in this equation is not so favorable for Gunn diodes, this disadvantage was overcome by the high Q of the tank circuit as well as optimized coupling to the diode. This scheme was initially developed at Q band (2,3) and subsequently at X-band (4).

Table 1 lists phase noise data for these microwave sources in a 1 Hz bandwidth at

100 kHz offset from the carrier. The first phase noise entry is the specification for a Varian VA-313 klystron. Our phase noise measurement of an older unit gave -103 dBc/Hz (2,3). The phase noise of the Q-band Gunn diode oscillator was measured with the same technique and apparatus. The X-band reflex klystron phase noise is a Varian VA-297 specification. The X-band Gunn diode oscillator entry is a measured result. Three separate units were built and measured several times, all with consistent results. The -140 dBc/Hz entry is 5 dB higher than that reported in Ref. 4. However, the entry in Table 1 is for a unit with higher power output (over 200 mW) and a larger mechanical tuning range (800 MHz) than those reported earlier. The X-band and rf synthe-

Table 1. Typical phase noise data of some microwave sources.

Microwave Source	Phase Noise 100 kHz offset, dBc/Hz
Q-band reflex klystron	-107
Q-band Gunn diode oscillator	-129
X-band reflex klystron	-121
X-band Gunn diode oscillator	-140
X-band synthesizer	-100
300 MHz synthesizer	-127

sizer phase noise specifications refer to high performance, commercially available units.

In this paper we are primarily interested in phase noise in the range of 1 to 100 kHz

offset. Equation 1 predicts a dependence of phase noise power on offset frequency of 20 dB per decade. We are generally confident that the microwave fundamental oscillator entries of Table 1 can be scaled to offset frequencies as low as 1 kHz at 20 dB per decade although detailed experimental data are lacking. Data for the synthesizers, last two entries in the table, are available and show a weaker dependence. Synthesizer noise will be discussed in the next section.

The second approach was introduction of the loop-gap resonator (LGR) (see Ref. 5 for a review). These lumped-circuit devices are characterized by low Q and high resonator efficiency parameter Λ :

$$\Lambda(x,y,z) = \frac{H_1(x,y,z)}{P_0^{1/2}} \quad [2]$$

Here $H_1(x,y,z)$ is the spatial variation of the component of the microwave field in the resonator that is perpendicular to H_0 . There are two relevant aspects. a) For a given value of H_1 at the sample, P_0 is lower when using an LGR than when using a cavity, which reduces the demodulation of phase noise. b) Because the Q is lower, demodulation is further reduced.

These developments essentially eliminated phase noise from consideration when tuned to the absorption mode. In addition, it was almost eliminated when tuned to the dispersion. The low noise microwave amplifier establishes the noise floor, permitting simultaneous detection of both absorption and dispersion. Application of a Hilbert transform to the dispersion converts it to absorption, which can be added to the de-

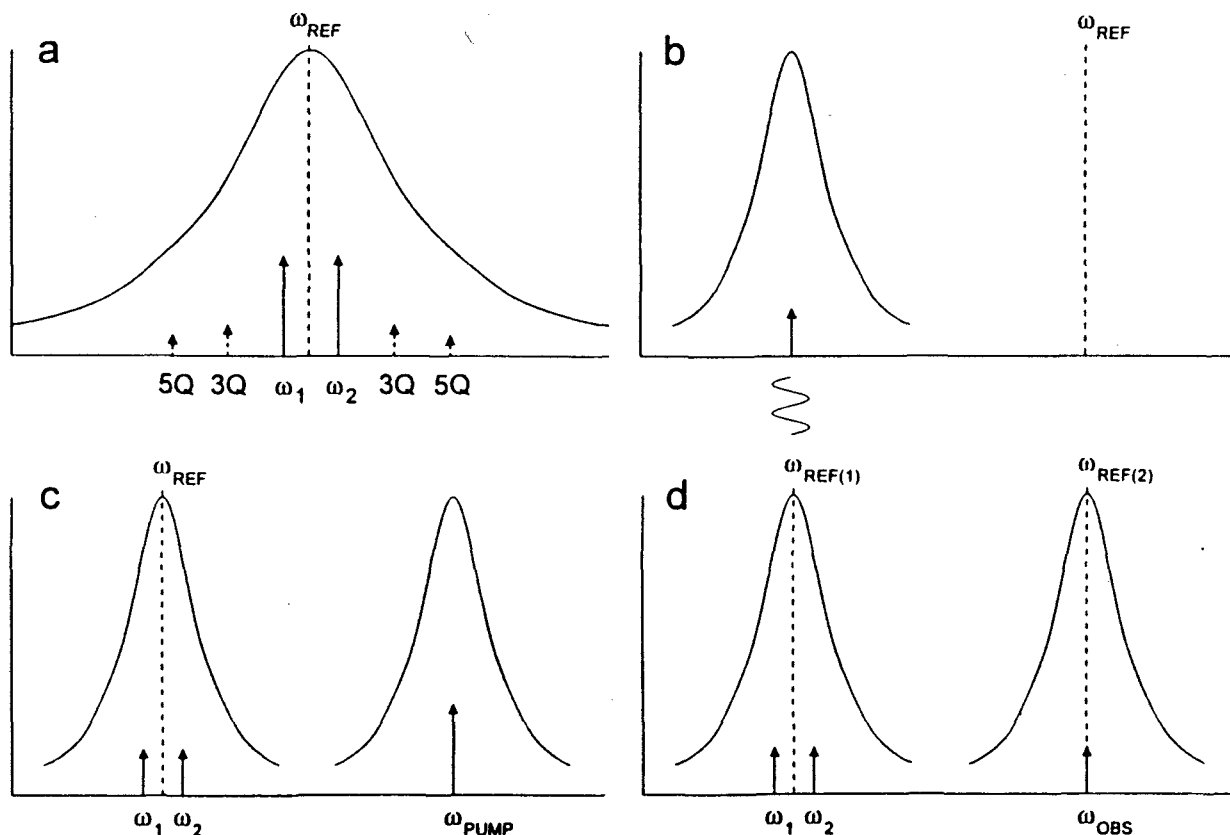


Figure 1. Selected experiments using multiple time-locked microwave frequencies. a) MQ-EPR. There are three frequencies, the incident pair at ω_1 and ω_2 and the reference at the mean value of ω_1 and ω_2 . Three and five quantum spin system generated sidebands are illustrated. b) Superheterodyne detection—two frequencies, c) MQ-ELDOR, but with pump and observe frequencies reversed compared with the method of Ref. 9, d) simultaneous MQ-EPR and MQ-ELDOR.

tected absorption. The system performance is improved by an additional 3 dB.

In a separate line of research, the techniques of multiquantum (MQ) EPR were developed at the National Biomedical ESR Center (6,7). Figure 1a illustrates the central idea: two microwave frequencies, called the incident pair, which are time-locked (or coherent) with a nominal separation of 10 kHz, are incident on a homogeneous line. The spin system generates intermodulation sidebands that are symmetrical about the irradiation pattern. A time-locked microwave reference at the mean value of the two frequencies serves as an effective local oscillator, which superimposes upper and lower intermodulation sidebands at the output of the microwave bridge. They can be detected with a lock-in amplifier with a suitably synthesized reference. It is believed that MQ-EPR can become a general purpose EPR methodology, replacing field modulation in many experiments.

A low phase-noise microwave oscillator is used in MQ-EPR. The process of generating the three time-locked frequencies of Fig. 1a (ω_1 , ω_2 , ω_{REF}) necessarily introduces additional noise. An LGR is routinely employed in all multiquantum experiments, which reduces demodulation of phase noise generated during the mixing processes employed to produce these time-locked frequencies. Nevertheless, noise was a problem in our first MQ-EPR spectrometer. It became apparent that a careful analysis of source noise generated by the mixing process was required. Based on this analysis, a new MQ-EPR spectrometer was designed and constructed (8).

In addition to MQ-EPR, a number of other time-locked irradiation schemes can readily be envisaged. Figure 1b shows one of the simplest: superheterodyne detection. Figure 1c shows an electron-electron double resonance multiquantum pattern: two frequencies incident on one line and one on another (9). Figure 1d shows an elaboration of Fig. 1c with four time-locked sources that could, in principle, be used to detect not only the ELDOR response, but also, simultaneously, the intermodulation sidebands produced by the pumped microwave transition. Numerous other experiments involving a

multiplicity of time-locked microwave frequencies can be envisaged. This is an attractive area for future development of EPR instrumentation. However, it is appropriate that noise in spectrometers that employ time-locked microwave sources is understood first. This is the subject of the present paper.

II. BACKGROUND

In MQ-EPR, the spin system generates new microwave frequencies that are to be detected. A central requirement is that there be negligible instrumentally generated intermodulation sidebands that coincide with spin-system generated intermodulation sidebands. The incident pair as well as any instrumentally generated frequencies will have source noise that will tend to exhibit a $1/f$ dependence, according to Eq. [1], and the dependence can be higher very close to the carrier (1). If an instrumental sideband coincides with a spin system sideband, f is near zero, and noise will be high. The analysis of Ref. 8 arrived at a design specification that all instrumental sidebands that are incident on the LGR should be -70 dBc, where the carrier power reference is the intensity of one member of the incident pair.

The noise of each frequency in the incident pair exhibits a $1/f$ dependence at offsets on the order of the incident pair separation $\Delta\omega$. The separation of the first sideband from one member of the incident pair in the scheme of Fig. 1a is nominally 10 kHz, and MQ experiments can be carried out at sideband separations as low as 1 kHz or even less. This results in significant overlap of the spin-system intermodulation sidebands and the phase noise skirts of the incident pair, as illustrated in Fig. 2. Thus, one must be fundamentally concerned with $1/f$ source noise even when using LGRs.

Finally, the discrete spurious frequencies and noise floor produced in the generation of the incident pair must be considered, especially if any spurious products overlap a spin-system intermodulation sideband frequency. The same -70 dBc specification as before is desired for discrete spurious frequencies. These factors will be examined in detail for a specific MQ-EPR bridge configuration in the Noise Discussion section.

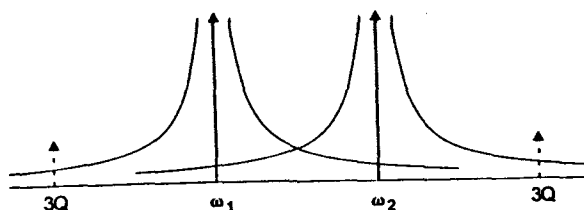


Figure 2. Cartoon illustrating overlap of $1/f$ noise skirts of the incident pair with three-quantum spin-system generated sidebands. These noise skirts arise from the microwave source as well as from the rf synthesizer. The question of coherence of noise in the four skirts illustrated here remains open.

In modern CW reference arm bridges using 100 kHz field modulation and a low noise microwave amplifier, techniques have been developed that effectively eliminate contributions of source noise to the performance of the instrument, as discussed in the introduction. In MQ-EPR, not only is noise introduced during generation of the incident pair, but also the offset frequency is generally lower, with 10 kHz typical. Thus, source noise can be expected to be a serious consideration even when using the techniques developed for CW bridges. The goal of the work reported here is, by careful attention to engineering detail, to eliminate source noise as a limitation of MQ-EPR system performance much as has already been done in conventional spectrometers.

Schemes of three general types can be envisaged for producing an array of time-locked microwave sources: a) direct microwave synthesis using a number of separate synthesizers with a common time base, b) use of multiple microwave oscillators plus audio frequency synthesizers that correspond to *differences* of frequency, for example $\omega_1 - \omega_2$ or $\omega_1 - \omega_{REF}$ in Fig. 1a, and c) schemes that employ a fundamental microwave source plus a number of intermediate frequency synthesizers, ca 300 MHz, that have a common time base and are offset from each other by the desired microwave frequency separations. Each of these three schemes employs a synthesizer and, therefore, one must be concerned with discrete spurious frequencies generated during the synthesis process as well as with the noise contributed by the synthesizer.

Thus far, scheme a) has been impossible to evaluate experimentally because of cost. However, a representative phase noise specification for high quality X-band synthesizers is shown in Table 1. The value is significantly higher than that of a high quality fundamental microwave oscillator. Several variations of scheme b) were discussed in Ref. 8. One of the most interesting was the offset phase lock loop. The outputs of two microwave oscillators were mixed and the difference frequency was locked to a high quality audio synthesizer. All of these schemes were finally abandoned because the -70 dBc specification could not be satisfied over the range of desired separation frequencies of the incident pair.

Scheme c), which was called *DSB/FF* (*double sideband/fixed filter*) in Ref. 8, has finally been adopted. The central building block of this scheme, one of the microwave bridge arms, is illustrated in Fig. 3. Key

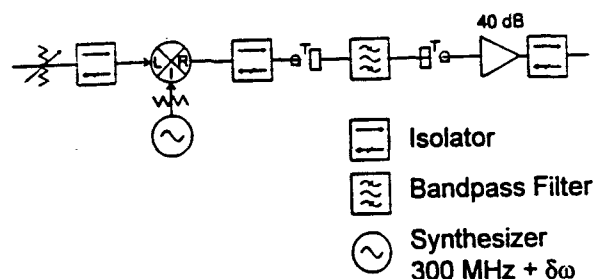


Figure 3. Representative building block for one time-locked frequency. Three such blocks are used in the MQ-EPR bridge of Ref 8. Each block has a separate power amplifier to avoid intermodulation products.

components of this scheme are a) a microwave bandpass filters with very sharp skirts, and b) a separate microwave power amplifier for each arm. Sidebands produced by the mixing process are separated by 300 MHz intervals, and the sideband of interest readily selected by the bandpass filter. The microwave oscillator, which feeds the local oscillator port of each mixer, can be tuned over more than 200 MHz without the necessity of any change in the center frequency of the bandpass filters. Higher frequency rf synthesizers could be utilized to produce an even larger frequency tuning

range. Third-order intercepts are sufficiently unfavorable that it was finally decided to use a separate amplifier for each arm and then combine, rather than combine and then use a single amplifier. The MQ-EPR spectrometer described in Ref. 8 satisfies the -70 dBc specification.

member of the incident pair, and c) the noise floor associated with the incident pair as well as discrete spurious products.

Overlap of instrumental and spin-system generated sidebands arose from two causes in our first MQ spectrometer. a) Because the various microwave frequencies had a

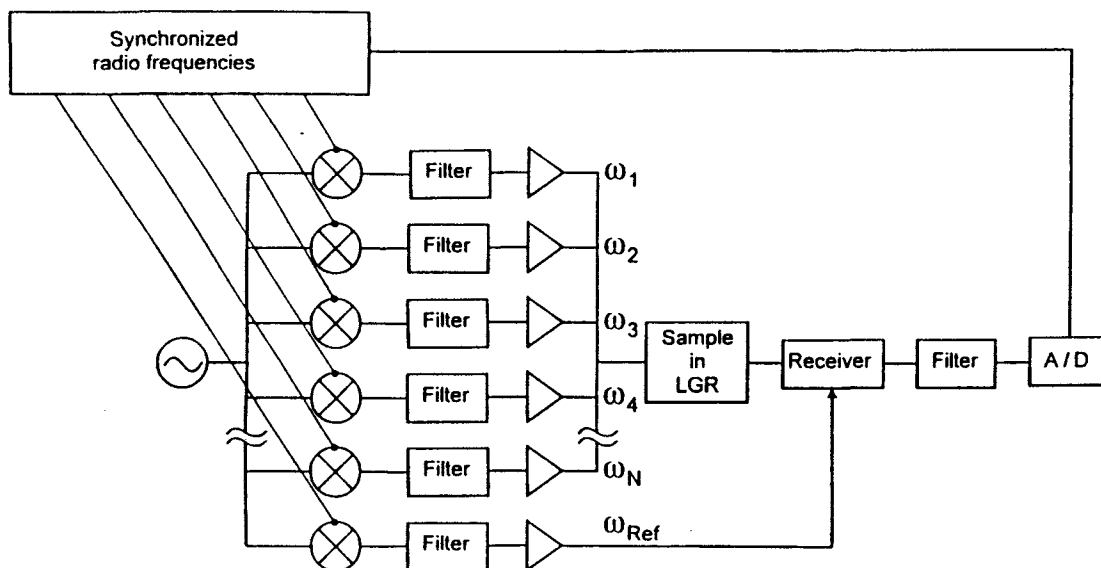


Figure 4. Generalization of the MQ-EPR bridge of Ref 8. There can be as many time-locked microwave frequencies as desired. Bandpass filters for each block are important. A Nyquist filter before the A/D is shown. Locking the A/D to the rf synthesizer as shown here is routine in MRI scanners, but not in NMR or EPR spectrometers.

A generalized time-locked microwave bridge is illustrated in Fig. 4. The MQ-EPR bridge of Ref. 8 employed three blocks of the type shown in Fig. 3. The number is increased indefinitely in Fig. 4.

All MQ-EPR experiments performed to date have used conventional lock-in amplifiers (also called phase-sensitive detectors). A more modern approach using A/Ds that are time-locked to microwave frequency differences is suggested in Fig. 4. We believe that digital analogues of lock-in amplifiers will be used in future spectrometers.

III. NOISE DISCUSSION

Three categories of source noise occur in time-locked schemes: a) noise very close to the carrier because of instrumental and spin-system intermodulation sideband overlap, b) $1/f$ noise that is $(n\Delta\omega)$ from a

common microwave power amplifier, overlapping intermodulation products were generated during production of the incident pair. This problem was completely eliminated by the use of separate power amplifiers in each arm as discussed in Ref. 8 and illustrated in Figs. 3 and 4. b) Overlapping intermodulation products can be formed in the receiver portion of the bridge in the low noise microwave power amplifier and the microwave mixer. The level of these products depends on the level of the incident pair at the input to the low noise amplifier. For an ideal circulator and perfect match of the resonator, this level is zero. In practical circumstances, this can be a problem, although Ref. 8 established that the problem was manageable.

Phase noise on the incident pair overlaps the frequencies where the spin-system sidebands are generated, and becomes more significant at smaller separation frequencies

$\Delta\omega$ as shown in Fig. 2. For a $1/f$ noise dependence, the phase noise increases 20 dB per decade reduction in f , as is apparent from Eq. [1]. The microwave oscillator exhibits this dependence, but the rf synthesizer does not. In our X-band MQ-EPR spectrometer, the phase noise contributions of the microwave oscillator and synthesizer are essentially equal for a 10 kHz separation frequency. At 100 kHz separation frequency, the rf synthesizer dominates the carrier phase noise by approximately 13 dB (see Table 1), and vice-versa by at least 15 dB for a 1 kHz separation.

A preliminary analysis of our X-band MQ-EPR spectrometer indicates that at -120 dBc/Hz source phase noise at a 10 kHz offset, the phase noise in a 1 Hz bandwidth is 120 dB down relative to the incident pair. The spin-system intermodulation sidebands immediately adjacent to the incident pair are typically -80 dBc relative to the incident pair (6); hence, the phase noise sideband power in a 1 Hz bandwidth, as set by the integrating time constant in the phase sensitive detector, is insignificant relative to the spin-system sideband magnitude. However, at smaller incident pair separations, this favorable ratio will not be maintained because the microwave oscillator phase noise will increase at least 20 dB/decade and even faster at lower offsets. At higher offsets, MQ-EPR system performance will improve, but may be somewhat less than expected due to the noise contributions of the rf synthesizers.

The noise floor generated along with the incident pair is the remaining consideration. In our MQ-EPR spectrometer, the -135 dBc/Hz noise floor of the synthesizers dominates because the microwave oscillator, already with AM noise significantly lower than phase noise, feeds the local oscillator port of the translation mixers. These are balanced mixers, and the AM noise on the local oscillator signal is suppressed typically by 20 dB. After tracing the synthesizer noise floor through the losses and gains in the circuit, a -132 dBc/Hz noise floor is incident on the LGR (both carriers on). This noise floor is 12 dB below that of the phase noise for this bridge.

An important figure of merit is the power level of the incident pair at which noise at the output of the bridge increases by 3 dB. In the MQ-EPR bridge discussed here and in Ref. 8, this power level is about 8 dBm for a separation of the incident pair of 10 kHz. This 8 dBm level is dependent on the degree of match of the LGR. For investigators who are familiar with conventional TE_{102} rectangular cavities, 8 dBm in an LGR corresponds with 70 mW incident power in the cavity for the same microwave field at the sample. Careful consideration of the selection of synthesizers in MQ-EPR bridges is essential.

Spurious peaks generated by the mixer in each arm have been eliminated by the bandpass filter. However, discrete spurious signals from the rf synthesizer which are close to the rf frequency will also mix onto the microwave signal and will pass through the bandpass filter. These cannot be conveniently filtered and should be reduced by specification of sufficiently low discrete spurious output from the rf synthesizer. The spurious output specification of the 300 MHz units utilized in (8) was -70 dBc typical and -65 dBc guaranteed. No evidence of synthesizer spurious products has been observed in our X-band MQ-EPR utilized to date.

IV. CONCLUSIONS

This paper has examined the evolution of the noise reduction in EPR spectrometers from the beginning of low phase noise oscillators, low noise microwave amplifiers, and LGRs to the noise effects in MQ-EPR bridges. It has been determined that the primary contributor to noise and spurious frequencies in a MQ-EPR spectrometer is the synthesizers, although at very small carrier frequency separations, the phase noise of the microwave oscillator will dominate. It has been shown in Ref. 8 that the instrumentally generated intermodulation sidebands can be made insignificant relative to the spin-system generated sidebands. One then needs to be concerned with the phase noise skirts and noise floor of the synthesizers and the phase noise skirts of the microwave source for small carrier separ-

ations. In addition, one must utilize a low discrete spurious product synthesizer.

If we consider phase noise at some off-set frequency in a conventional EPR spectrometer, sidebands are present on either side of the carrier. When the microwave reference is at the carrier frequency with phase set to detect absorption, these sidebands cancel. When tuned to absorption, phase noise enters only in quadrature, which is a higher order process. All phase noise skirts illustrated in Fig. 2 arise from the phase noise of the source and of the synthesizer, and there ought to be coherence among the four skirts illustrated. With the reference set at the mean of the incident pair, it seems possible that cancellation of phase noise sidebands can also occur. However, this hypothesis has not yet been tested. It would require systematic variation of the relative phases of the carrier pair as well as of the reference as a function of separation of the incident pair.

The scheme of Fig. 4, which exploits modern digital electronics, seems clearly to be the wave of the future. However, in order to realize the full potential of this approach, continued efforts to reduce phase noise of both the fundamental microwave source and the rf synthesizers are appropriate. The loop gap resonator, because of its high efficiency parameter (Eq. 2), gives an immediate 10 dB benefit and would appear to be central to this strategy.

REFERENCES

- ¹ W. P. Robbins, *Phase Noise in Signal Sources* (London, Peter Peregrinus, Ltd., 1982).
- ² R. A. Strangeway, T. K. Ishii, and J. S. Hyde. *IEEE Trans. Microwave Theory Tech.* **36**, 792-794 (1988).
- ³ R. A. Strangeway, T. K. Ishii, and J. S. Hyde. *Microwave J.* **July**, 107-111 (1988).
- ⁴ T. Oles, R. A. Strangeway, J. Luglio, W. Froncisz, and J. S. Hyde. *Rev. Sci. Instrum.* **63**, 4010-4011 (1992).
- ⁵ J. S. Hyde and W. Froncisz, in: *Advanced EPR: Applications in Biology and Biochemistry*, A. J. Hoff, ed. (Amsterdam, Elsevier, 1989) pp.277-306.

⁶ P. B. Sczaniecki, J. S. Hyde, and W. Froncisz. *J. Chem. Phys.* **94**, 5907-5916 (1991).

⁷ H. S. Mchaourab and J. S. Hyde. *J. Chem. Phys.* **98**, 1786-1796 (1993).

⁸ R. A. Strangeway, H. S. Mchaourab, J. R. Luglio, W. Froncisz, and J. S. Hyde. *Rev. Sci. Instrum.* (in press).

⁹ H. S. Mchaourab, T. C. Christidis, W. Froncisz, P. B. Sczaniecki, and J. S. Hyde. *J. Magn. Reson.* **92**, 429-433 (1991).

A Hybrid-Hybrid Matrix Method for 3D NOE-NOE Data Analysis

David G. Donne, Elliott K. Gozansky, Frank Q. Zhu, Qun Zhang,
Bruce A. Luxon, and David G. Gorenstein*

Sealy Center for Structural Biology
and Department of Human Biological Chemistry and Genetics
University of Texas Medical Branch
Galveston, Texas 77555-1157

I. Introduction

In the application of NMR to the structure determination of biomolecules of increasing size, three-dimensional NMR techniques have been developed to overcome problems of peak overlap (1) and increase the structural information that can be obtained. While heteronuclear 3D NMR spectroscopy has been used more often to make the sequential assignment and obtain distance estimates, 3D homonuclear NOE-NOE methods have been found to contain more information for quantitatively determining the structure once the assignments have been made (1-5).

The main advantage of a 3D NOE-NOE spectrum over a 2D NOESY spectrum is the added spectral resolution provided by the third frequency dimension. For molecules >10,000 Daltons, spectral overlap often prevents adequate measurement of enough NOEs from the 2D spectrum. This severely limits the precision and accuracy of any refined structure. This problem has been a major impetus in the continued development of new 3D and 4D techniques. So far, most quantitative 3D NOE-NOE studies are based upon the two-spin approximation (1-5). However, as we have recently demonstrated (6), at realistic mixing times that allow reasonably accurate measurement of 3D NOE NOE volumes, both the two-spin and the Taylor series expansion approximation methods can lead to considerable systematic errors.

Both 2D and 3D NOE spectra are a function of the 2D relaxation matrix, which depends on the distances between pairs of spins. 3D NOE-NOE spec-

tra can be described by,

$$A_{ijk} = [\exp(-\tau_{m1}\mathbf{R})]_{ij}[\exp(-\tau_{m2}\mathbf{R})]_{jk}M_0 \quad (1)$$

where \mathbf{R} is the relaxation rate matrix, τ_{m1} and τ_{m2} are the two mixing times and M_0 is the equilibrium magnetization. In terms of 2D and 3D volumes,

$$A_{ijk}^{3D} \propto A_{ij}^{(1)} A_{jk}^{(2)} \quad (2)$$

where A_{ijk}^{3D} is a single 3D volume and $A_{ij}^{(1)}$ and $A_{jk}^{(2)}$ are the 2D volumes during the two mixing times (8).

We have recently introduced a new algorithm that allows us to deconvolute the 3D volume matrix into a hybrid-hybrid NOE volume matrix (9). Theoretically, a 2D NOE matrix can be obtained from any single plane in the 3D matrix; however, each plane in the 3D matrix is invariably incomplete due to numerical truncation. Our algorithm allows us to calculate the 2D volumes, A_{ij} , from the 3D volumes, A_{ijk}^{3D} :

$$A_{ij} = \frac{A_{ijk}^{3D}}{A_{jk}} \quad (3)$$

In principle, of course, we gain little. If there is enough spectral resolution in the 3D spectrum, A_{jk} values can be obtained from the cross-diagonal volumes A_{jjk} , A_{jkk} or A_{jkj} or 2D volumes independently measured from a well-resolved 2D NOESY spectrum. Unfortunately, this will be uncommon for larger biomolecules. Our recently developed hybrid-hybrid matrix solution to this problem, implemented in a 3D version of our complete relaxation matrix program, MORASS, is shown in Figure 1. An initial model structure and the measured r_{ij} values are used to calculate the rate matrix. We

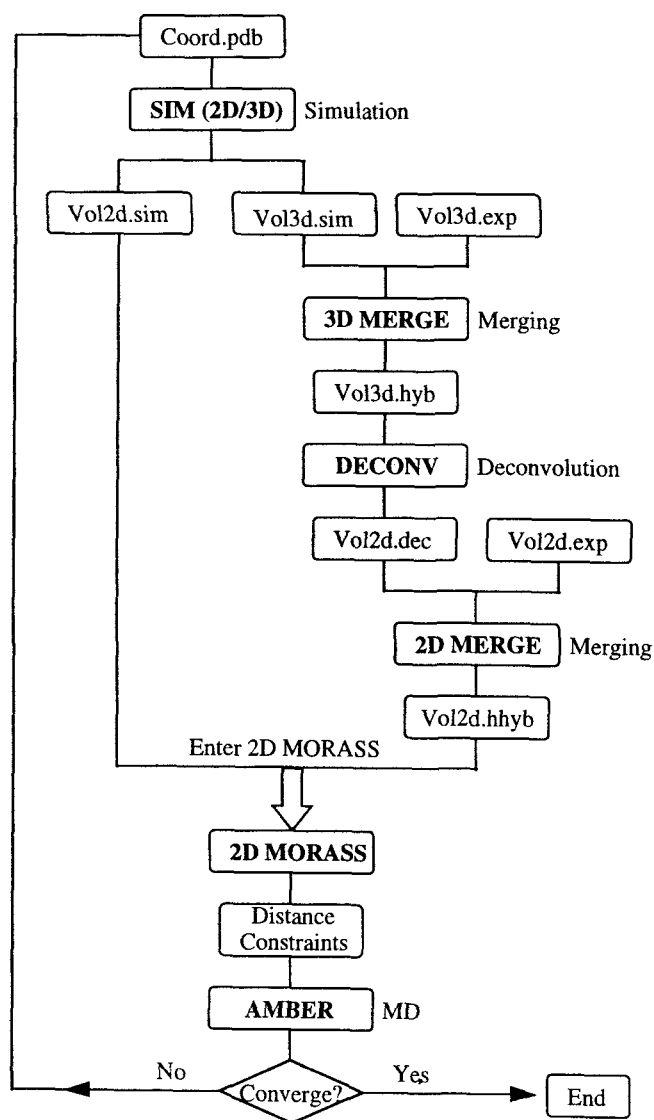


Figure 1. Schematic description of our hybrid-hybrid matrix method for 3D NOE-NOE structural refinement.

then simulate 2D NOESY and 3D NOE-NOE spectra. The experimental and simulated 3D NOE-NOE data are scaled and then merged to create a hybrid 3D data set, vol3d.hyb.

The 3D hybrid data are then deconvoluted into a 2D matrix, vol2d.dec, with elements

$$\langle A_{ij} \rangle = \frac{1}{n} \sum_{k=1}^n \frac{A_{ijk}^{\text{exp}}}{A_{jk}^*} \quad (4)$$

where non-zero A_{jk}^* values may be obtained from $*$ = exp (experimental) or $*$ = simul (simulated) 3D spectra. Additional experimental or simulated 2D NOESY volumes can then be merged into the

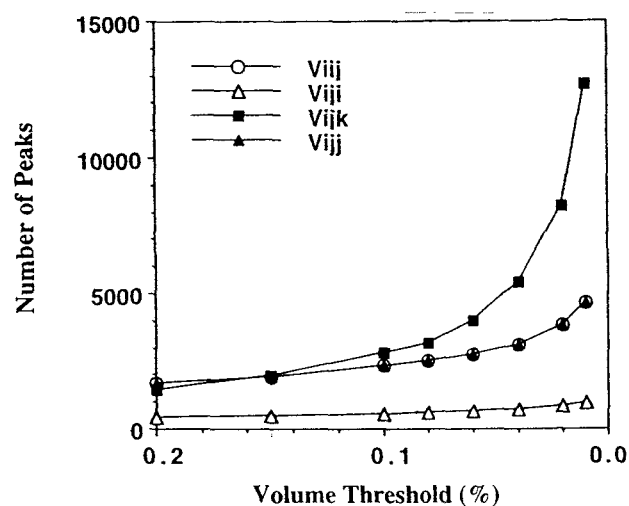


Figure 2. Number of integratable 3D volumes as a function of the percentage intensity relative to the largest diagonal peak in a 3D NOE-NOE spectrum for $d(\text{CGCGAATTCGCG})_2$ with $\tau_c = 3.2$ ns and $\tau_{m1} = \tau_{m2} = 100$ ms.

vol2d.dec matrix to give a complete 2D hybrid-hybrid volume matrix, vol2d.hhyb. Importantly 2D NOEs from 3D HMQC-NOESY can also be merged into the hybrid-hybrid volume matrix. The rate matrix can then be calculated from the hybrid-hybrid volume matrix, using our MORASS (or other) relaxation matrix approach. The resulting distances are taken from the cross-relaxation rates and then utilized in a distance geometry or restrained molecular dynamics refinement of the structure. The entire process is repeated until a satisfactory agreement between the calculated and observed 3D crosspeak volumes is obtained.

While it is true that many good quality structures have been obtained from NMR (10), especially with the development of heteronuclear 3D and 4D NMR (11-14), it is obvious that using more and tighter constraints will achieve greater precision (and hopefully accuracy) in the refined structures (15-17). Indeed as shown in Figure 2, the number of 3D volumes that can be integrated increases dramatically as the threshold level of cutoff of peak volume decreases. At high field and larger sample volumes, it may well be possible to intergrate thousands of 3D volumes.

Thus, 3D NOE-NOE holds the promise of providing more accurate structures, given the vastly increased number of resolvable 3D NOE-NOE volumes. Calculations based upon the complete relaxation matrix are well within current computational

resources, even for larger macromolecules (<600 spins).

II. Simulation Studies, Approximate vs. Exact Methods

Most quantitative methods in 3D NOE-NOE simulation and structure refinement studies are based upon the two-spin approximation methods. The approximation most often used is to expand the exponential matrix $\exp(-\tau_m \mathbf{R})$ into a Taylor series:

$$\begin{aligned} \exp(-\tau_m \mathbf{R}) = & 1 - \tau_m \mathbf{R} + \frac{1}{2!} (\tau_m \mathbf{R})^2 + \dots \\ & + \frac{1}{n!} (-\tau_m \mathbf{R})^n + \dots \end{aligned} \quad (5)$$

and then keep one or two terms in the above expansion in the simulation and refinement. The initial rate or two-spin approximation method is based upon the linear term in this equation. In the 3D version, this method gives a very simple expression of intensities (1-4,8,18). However, this approach suffers from the fact that a Taylor series converges relatively slowly, and therefore the method is limited to cases with very short mixing times, τ_m . In addition, it cannot answer such crucial questions as how long a mixing time is too long a mixing time for the simulation method used.

To better understand the limitations of the approximation method and appreciate the advantages of using the exact eigenvalue method, we have performed comparative studies on the Dickerson dodecamer oligonucleotide, $d(\text{CGCGAATTCGCG})_2$ as described previously (19,20). NOE-NOE intensities are simulated using the exact method and various approximations. All field strengths are taken to be 500 MHz. For the motional model, isotropic tumbling correlation times for the dodecamer were assumed and methyl protons were treated similarly to the 2D method (19,20). In the comparison, RMS errors were used as a criterion for the statistical analysis of the deviation between the simulated NOE-NOE volumes using the "exact" method (v_{ijk}^{exact}) and the approximate method (v_{ijk}^{approx}). The RMS is defined as:

$$\%RMS = \sqrt{\frac{1}{N} \sum_{ijk} \left[\frac{v_{ijk}^{exact} - v_{ijk}^{approx}}{v_{ijk}^{exact}} \right]^2} \times 100 \quad (6)$$

Since 3D NOE-NOE experiments at mixing times of 140 ms (2,3), 160 ms (1), and 200 ms (8,18) have been used for quantitative studies, comparison between the two methods has been done using mixing times from 20 ms to 200 ms.

In Figure 3 (A) and (B), the RMS errors for one-term and two-term approximations for the whole data set have been plotted against mixing times. If an RMS error of 50% is acceptable, then the first-order approximation fails at very short mixing times (> 60 ms). For short mixing times, say, 50 ms, adding a second-order term to the partial sum substantially reduces the RMS errors of the approximation. However, the second-order approximation does not improve the approximation method significantly for longer mixing times.

Mathematically, for a series expansion approximation to be successful, the series has to converge uniformly and fast. Although the Taylor series converges uniformly, it doesn't converge as fast as required for NOE volume approximations (21). In the context of NOE simulation, usually the series does not converge after two terms as shown in Figure 4. Therefore it is inadequate to take one or two terms in the Taylor series to simulate NOE-NOE volumes or interpret spin diffusions. In situations like this, the exact eigenvalue method should be the method of choice, especially for 3D NOE-NOE experiments.

In 3D NOE-NOE structure determination, an exact simulation method is required because to get reasonable signal-to-noise ratios one has to use as long a mixing time as possible. The two-spin approximations are invalid at long mixing times. As for 3D gradient refinement methods, one potential advantage is the vastly increased number of 3D NOE-NOE volumes resolvable (thousands rather than hundreds for a medium-sized biomolecule). This makes a model-free refinement possible for 3D NOE-NOE experiments. It must be emphasized however, that NOE gradient refinements must utilize relaxation matrix methods for calculating 3D volumes in order to achieve the highest accuracy for the refined structure. Alternatively, the 3D hybrid-hybrid method for structure refinement can

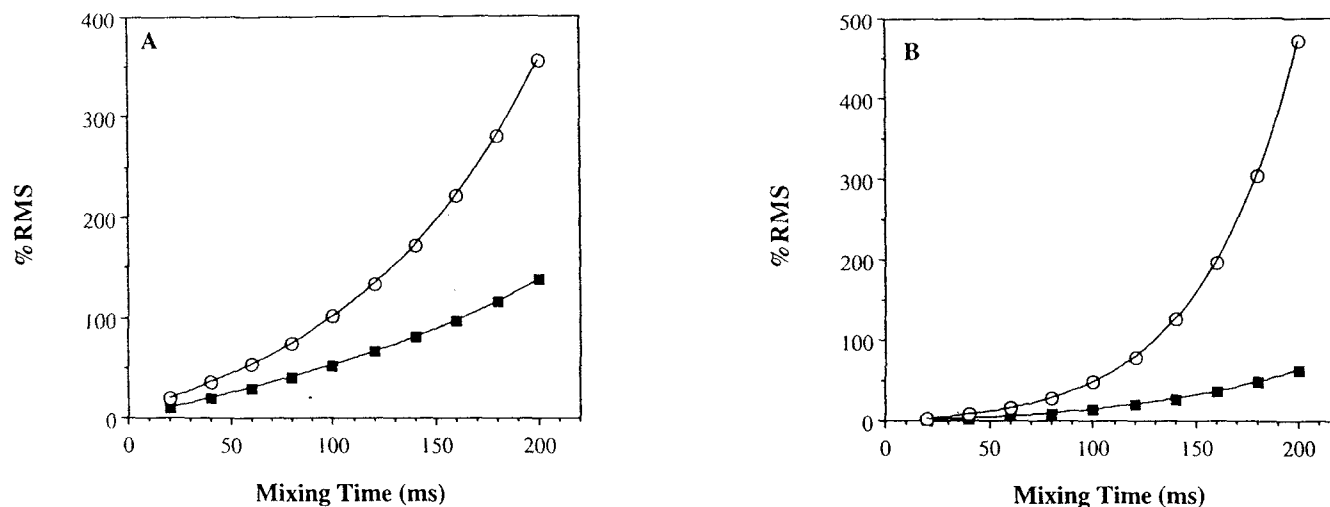


Figure 3. The %RMS error of 3D volumes for two approximations is plotted as a function of τ_m (A,B). Correlation times are 1.6 ns (■) and 3.2 ns (○) respectively. The oligonucleotide is $d(\text{CGCGAATTCGCG})_2$. RMS errors from one-term approximation (A) and two-term approximation (B) are plotted.

be used to retrieve the structural information in the 3D NOE-NOE spectra, as will be described in the next section.

III. Simulation Study of Hybrid-Hybrid Matrix Methods in 3D NOE-NOE Refinement

In this simulation study, the target structure is taken from the x-ray structure of Dickerson's dodecamer duplex DNA $d(\text{CGCGAATTCGCG})_2$. Three different NOE data set were simulated using this target model. Two 3D NOE-NOE data sets were simulated where 20% and 50% integration noise, with a Gaussian distribution was added (using Eqn. 1). A 2D NOE data set was simulated with 20% integration noise (2D20). 0.2% random thermal noise was added to all three data sets. All nonzero 3D crosspeaks above a 0.2% cutoff were saved in a linear table as the "experimental" data. A three-dimensional matrix was not used since over 99% of the 3D NOE-NOE peaks were zero. A total of 1667 "true" 3D crosspeaks ($i \neq j \neq k$) were picked for deconvolution which generated 481 2D NOE data. The volume %RMS of the simulated 3D data was checked as well as the 2D volume %RMS recovery. For the 2D NOE, 359 crosspeaks were selected with a baseline cutoff of 2.50%. This cutoff was used to limit the number of chosen peaks to a realistic level. For a 12-mer duplex DNA, 359 2D NOE crosspeaks can be considered a reasonable experimental upper

limit range. 100 ms was used for each mixing time in the 3D NOE-NOE simulations.

The hybrid-hybrid matrix refinement calculations were performed using the scheme in Figure 1. In each iteration, a new 3D NOE-NOE and a 2D data sets were simulated from the model being refined. The 2D data was used to deconvolute the 3D "experimental" data. The simulated 3D data was used to scale the 3D "experimental" data before carrying out the deconvolution. The deconvolution would generate a new 2D NOE data ("experimental"). A 2D standard MORASS/AMBER refinement procedure was followed to generate a new set of distances for the restrained molecular dynamics simulation with a flatwell potential. Such iterations were continued until convergence was reached. The final force constants were 8.0 - 10.0 kcal/(mol·Å) for all refinements. The final distance errors allowed were 12 % for 3D data sets and 9% for the 2D data set. This choice was due to the consideration that 2D data should be more accurate in general than 3D data. A single structure after the final iteration was considered the refined structure. Normally an extended restrained MD is used to generate an averaged final structure. However, we considered it sufficient here to use the single structure for the test of the method as normally there is no significant difference between such single structure and that from the MD averaging. The quality of the final structure was judged by several indicators. The most important one in this case was the Cartesian RMS difference with the target model. Others were

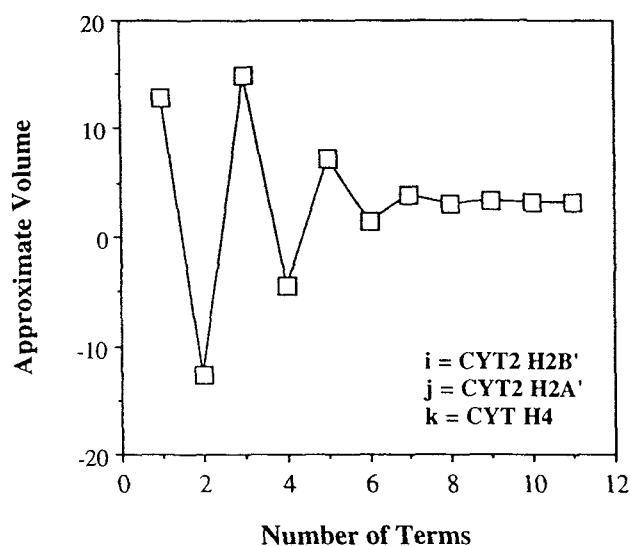


Figure 4. Approximate calculated 3D NOE-NOE volume utilizing variable number of terms in the Taylor series approximation. The simulation was done for $d(\text{CGCGAATTCGCG})_2$ with $\tau_c = 3.2$ ns and $\tau_{m1} = \tau_{m2} = 200$ ms. The initial magnetization before cross-relaxation was taken to be 1000.

Table I. Cartesian RMSD (Å) to the Target Duplex.

	Refinement		
	3D20	3D50	2D20
A-DNA (3.7) ^a	1.44 ^b	1.37	1.23
B-DNA (2.7)	1.54	1.51	1.10

^aCartesian RMSD to the target structure.

^bFinal RMSD to the target.

%RMS(volume) as well as the R-factor.

The result from the simulated refinement demonstrated that the proposed method is quite powerful and efficient. The quality of the refinement can be seen directly from the Cartesian rms difference values between each final structure and the target model. All are below 1.54 Å (Table I). The structures from the simulated 2D NOE data set were better than those from 3D NOE-NOE data sets.

The quality of the final structures utilizing various 3D and 2D data sets was also measured by the %RMS and the R-factor (Table II). The %RMS is more sensitive to the weak crosspeaks which corre-

Table II. Quality of Refinements.

Data Set	3D20	3D50	2D20
Number of RIJ	481	477	359
A-DNA Results			
%rms (vol)	72 (41) ^a	133 (32)	32
R-Factor	0.31 (0.36)	0.47 (0.18)	0.22
Force	8	10	8
Error %	12	12	9
Total Energy	-935	-921	-913
Constraint energy	5	25	25
Number of iter	5	8	5
B-DNA Results			
%rms (vol)	54 (24)	138 (33)	31
R-Factor	0.26 (0.16)	0.46 (0.16)	0.22
Force	8	10	8
Error %	12	13	9
Total Energy	-954	-947	-959
Constraint energy	5	8	20
Number of iter	6	8	3

^aValues in parentheses for 2D deconvoluted volumes.

spond to longer range, interresidue distances. Usually a value less than 50% has proven to be acceptable. For a 2D NOE data, an %RMS value of 50% roughly corresponds to a distance error of about 8 - 9% (by propagation of error treatment, a 1/6th factor). However, a 3D NOE-NOE crosspeak is a product of two 2D NOE volumes, therefore a simple direct relationship between %RMS and distance error is not obvious. It seems that the 2D refinement yields slightly better structures and fit to the spectra than the 3D refinement. This may well be related to the slightly larger error bar placed on the distances obtained from the 3D refinement.

IV. Conclusions

3D NOE-NOE spectra hold the promise of giving more accurate structures given the vastly increased number of resolvable 3D NOE-NOE volumes (1). However, approximation methods may not yield accurate distances for the mixing times required to achieve adequate magnetization transfer and signal-to-noise (6). Competing with the hybrid-hybrid matrix method described here, are various direct gradient NOE refinement methods (1). Even with approximations to the gradient calculations, these scale as n^3 whereas the hybrid-hybrid matrix method is still basically an n^2 problem (diagonaliza-

tion of the $n \times n$ volume matrix). It must be emphasized that NOE gradient refinements should utilize relaxation matrix methods for calculating 3D volumes in order to achieve the highest accuracy for the refined structure (6).

An additional advantage of this methodology is that software written for 2D NOESY data analysis does not need to be significantly modified since the 2D deconvoluted matrix replaces the experimental 2D NOESY volume matrix. The analysis techniques described here are also general enough that they can be expanded to include even higher dimensional experiments (such as a 4D NOE-NOE-NOE spectrum).

V. References

1. A.M.J.J. Bonvin, R. Boelens and R. Kaptein, *J. Magn. Reson.*, **95**, 626-631 (1991).
2. J. Habazettl, A. Ross, H. Oschkinat and T.A. Holak, *J. Magn. Reson.*, **97**, 511-521 (1992).
3. J. Habazettl, M. Schleicher, J. Otlewski and T.A. Holak, *J. Mol. Biol.*, **228**, 156-169 (1992).
4. T.A. Holak, J. Habazettl, H. Oschkinat and J. Otlewski, *J. Am. Chem. Soc.*, **113**, 3196-3198 (1991).
5. R. Berstein, A. Ross, C. Cieslar and T.A. Holak, *J. Magn. Reson.*, **B101**, 185-188 (1993).
6. D.G. Donne, E.K. Gozansky and D.G. Gorenstein, *J. Magn. Reson.*, **B106**, 156-163 (1995).
7. H. Kessler, S. Seip and J. Saulitis, *J. Biomol. NMR*, **1**, 83-92 (1991).
8. R. Boelens, G. Vuister, T. Koning and R. Kaptein, *J. Am. Chem. Soc.*, **111**, 8525-8526 (1989).
9. Q. Zhang, J. Chen, E.K. Gozansky, F. Zhu, P.L. Jackson and D.G. Gorenstein, *J. Magn. Reson.*, **B106**, 164-169 (1995).
10. K. Wüthrich, *Science*, **243**, 45-50 (1989).
11. S. Grzesiek, H. Dobeli, R. Gentz, G. Garotta, A.M. Labhardt and A. Bax, *Biochemistry*, **31**, 8180-8190 (1992).
12. L.E. Kay, G.M. Clore, A. Bax and A.M. Gronenborn, *Science*, **249**, 411-414 (1990).
13. E.R.P. Zuiderweg, A.M. Petros, S.W. Fesik and E.T. Olejniczak, *J Am Chem Soc*, **113**, 370-372 (1991).
14. G.M. Clore, P.T. Wingfield and A.M. Gronenborn, *Biochemistry*, **30**, 2315-2323 (1991).
15. A. Pardi, D.R. Hare and C. Wang, *Proc. Natl. Acad. Sci. USA*, **85**, 8785-8789 (1988).
16. K. Kaluarachchi, R.P. Meadows and D.G. Gorenstein, *Biochemistry*, **30**, 8785-8797 (1991).
17. A.T. Brunger, G.M. Clore, A.M. Gronenborn, R. Saffrich and M. Nilges, *Science*, **261**, 328-331 (1993).
18. R. Boelens, T.M.G. Koning, G.A. van der Marel, J.H. van Boom and R. Kaptein, *J. Magn. Reson.*, **82**, 290-308 (1989).
19. C.B. Post, R.P. Meadows and D.G. Gorenstein, *J. Am. Chem. Soc.*, **112**, 6796-6803 (1990).
20. E.P. Nikonowicz and D.G. Gorenstein, *J. Am. Chem. Soc.*, **114**, 7494-7503 (1992).
21. B.A. Borgias, M. Gochin, D.J. Kerwood and T.L. James, *Prog. Nucl. Magn. Reson. Spectrosc.*, **22**, 83-100 (1990).

The Observed Steric Isotope Effects in Cyclooctanone isotopomer

Miewon Jung

*Department of Chemistry, SungShin Women's
University, Seoul 136-742, Korea*

Conformational equilibrium isotope effects (CEIEs) are found in deuterated cyclooctanone-3,3-D₂ by observing equilibrium NMR isotope shifts in ¹³C spectra. Isotope effects are analyzed in relation to the preferred boat-chair conformation of cyclooctanone. Equilibrium constants and the changes in the free energies, enthalpies and entropies, which are derived from the temperature dependence of the isotope shifts, are also reported for this cyclooctanone isotopomer.

I. Introduction

The ¹³C shielding changes associated with deuterium substitution in organic molecules arise from either intrinsic or a combination of intrinsic and equilibrium isotope effects.^{1,2,3} A conformational equilibrium isotope effect (CEIE) was especially used by Robinson and Baldry in their research involving N,N-dimethyl piperidinium ions and 1,3-dioxanes, using ¹³C NMR spectroscopy.⁴ They suggested that the steric isotope effect was the cause of CEIEs in the compounds. Forsyth and Suzanne have recently reported how NMR-invisible conformational processes in amines can be revealed through NMR isotope shifts.⁵

Deuterated cyclooctanone-3,3-D₂ isotopomer was investigated for intrinsic and equilibrium NMR isotope shifts in this paper. These intrinsic and equilibrium isotope effects are discussed in relation to the preferred boat-chair conformation of cyclooctanone.⁶ The temperature dependence of the isotope shifts were also studied in order to better understand the origin of the isotope effects. Equilibrium constants for the perturbed equilibria between boat-chair conformers were calculated, and changes in the free energies, enthalpies and entropies were derived from the temperature dependence of the equilibrium isotope effects.

II. Experimental

¹³C NMR spectra were recorded on a Varian XL-300 NMR spectrometer equipped with a broad band probe at 75.4 MHz NMR spectra measured with narrow spectral width to afford good digital resolution (ca. 0.001 ppm/point). Temperature was controlled during acquisition of spectra for the purpose of determining isotope shifts: spectra recorded while temperature varied by more than ± 1°C were discarded. All chemical shifts reported were referenced to Me₄Si (0.00ppm) either directly for ¹H NMR spectra or indirectly for ¹³C NMR spectra by using solvent signals for reference: CDCl₃ (77.00 ppm) as a triplet, CF₂Cl₂ (126.30 ppm) as a triplet, CFC₃ (115.670ppm) as a doublet. ¹³C NMR spectra of unlabeled and labeled cyclooctanone samples were measured with a width of 20000 Hz and 65000 data points.

Synthesis of cyclooctanone-3,3-D₂. The cyclooctanone-2,2,7,7-D₄ was prepared and was refluxed with H₂O during which time the mixture was monitored by ¹³C NMR spectroscopy. After work up on the usual manner, cyclooctanone-3,3-D₂ (95%) was obtained. ¹³C NMR(CDCl₃) : 218.08(s, C-1), 41.83 (s, C-2 or C-8), 27.18(s, C-4 or C-6), 25.96(s, C-7), 25.19ppm(s, C-5).

Cyclooctanone-2,2,7,7-D₄. This isotopomer was obtained by a method modified from the one used by Nicolaou et al.⁷ It was efficiently synthesized by a two-step sequence. Deuterated cycloheptanone was ring-expanded via an intermediate dibromo alcohol which was prepared by addition of LDA to a cold

solution of cycloheptanone in THF in the presence of dibromomethane. Treatment of the dibromoalcohol with *n*-butyllithium gave a β -oxido carbonate, which decomposed smoothly to the enolate via β -oxido carbene and resulted in final product, i.e., cyclooctanone, in high yield after acidic workup.⁸

Cycloheptanone-2,2,7,7-D₄. This was prepared by the deuterium exchange Method.⁹ Distillation gave cycloheptanone-2,2,7,7-D₄. ¹³C NMR(CDCl₃): 214.2(s), 42.5(p, J_{CD}=20Hz, C-2, C-7) 29.8(s), 23.6ppm(s).

1-(Dibromomethyl)-1-Cycloheptanol-2,2,7,7-D₄. ¹³C NMR(CDCl₃): 77.31(s, C-1), 60.51(s, -CHBr₂), 36.12(p, J_{CD} =20Hz, C-2, C-8), 28.71, 22.36ppm. ¹H NMR(CDCl₃): 5.68(s, 1H), 2.51(br s, 1H), 1.80-1.40ppm (m, 8H). Cyclooctanone-2,2,7,7-D₄. ¹³C NMR(CDCl₃): 217.45(s, C-1), 41.60(s, C-8), 41.19(p, J_{CD} =19.39Hz, C-2), 26.78 (s, C-4 or C-6), 25.40(s, C-3), 24.35ppm (s, C-5). ¹H NMR(CDCl₃): 2.42(br s, 2H), 1.21-1.83ppm(m, 8H).

III. Results and Discussion

Intrinsic and equilibrium NMR isotope shifts were obtained from ¹³C NMR spectra of cyclooctanone-3,3-D₂ and 2:1 mixture of labeled and unlabeled cyclooctanone at several temperatures (from room temperature to -148.5 °C) in CFC1₃ as solvent. The peaks of the methylene carbons of unlabeled cyclooctanone are easily distinguished by comparison of Figures 1(a) and 1(b). When unlabeled cyclooctanone was added to the labeled cyclooctanone mixture, some of the peaks increased. One peak increased in each of four groups of peaks in the alkyl portion of the spectrum. The chemical shifts of the four groups correspond to the chemical shifts of C-5 and the averaged resonances for C-2 and C-8, C-3 and C-7, and C-4 and C-6. The increased peaks could be assigned to the averaged methylene carbons of unlabeled cyclooctanone and are indicated by an asterisk in Figures 1(a) and 1(b). These peaks will serve as reference peaks for the determination of isotope shifts. The remaining ma-

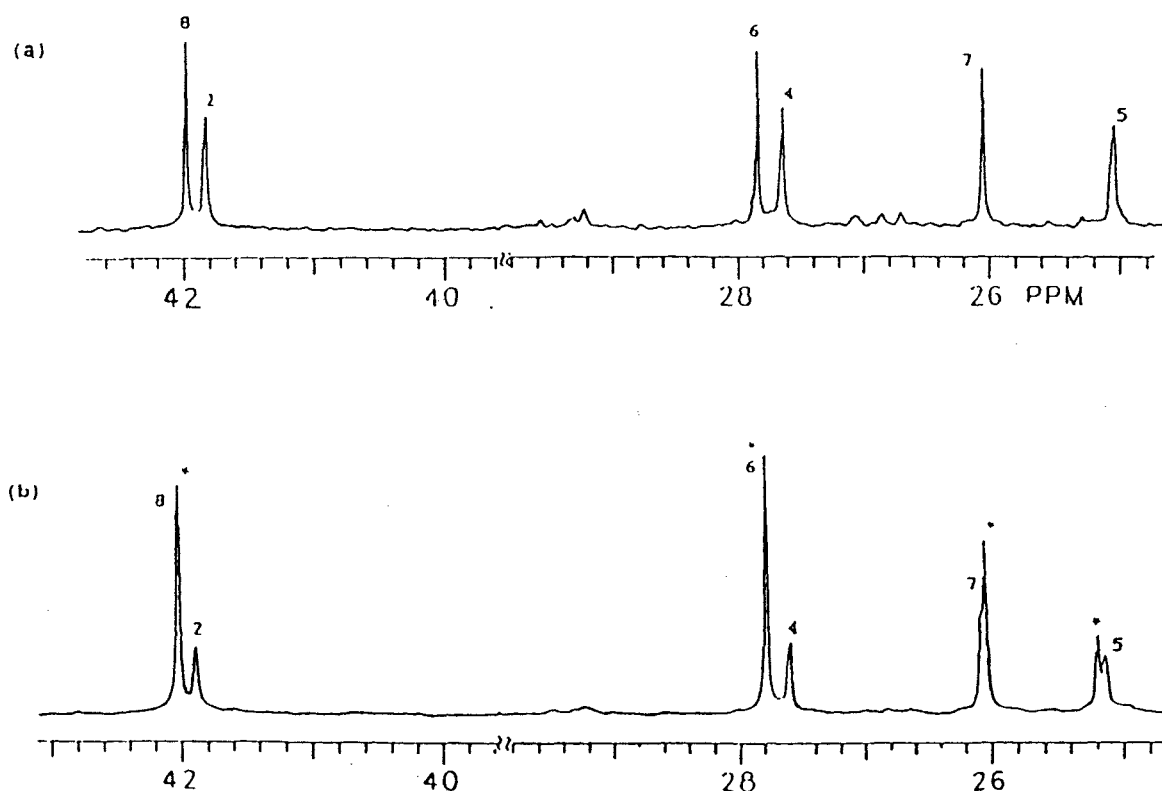


Figure 1. (a) ¹³C NMR Spectrum of Cyclooctanone-3,3-D₂ at 20.2 °C (b) ¹³C NMR Spectrum of 2:1 Mixture of Cyclooctanone-3,3-D₂ and Cyclooctanone 20.2 °C: (Asterisks indicate peaks of unlabeled cyclooctanone).

major peaks in Figure 1(a) arise from the methylene carbons of cyclooctanone-3,3-D₂. Some peaks appear upfield and some appear downfield of the reference peaks. The signals are shifted from the reference positions by a combination of equilibrium and intrinsic isotope effects. However, the "splitting" will be symmetrical only if the intrinsic isotope shifts are equivalent at both carbons in the pair. If deuteriums are substituted for hydrogens at C-3, only two carbon environments can be distinguished and the apparent equilibrium will be between only two different conformers, i.e., [A] ⇌ [B]. (Figure 2) Each particular carbon has chemical environment in both A and B, e.g., C-3 is in the β environment in A and C-3 is in the β' environment in B. The equilibrium isotope shifts in ¹³C spectra can be used to detect the proportion of time C-3 is in each environment, β and β'.

When equilibrium constants were derived from equilibrium isotope shifts using Saunders' equation,¹⁰ the direction of the isotope effects were not indicated. The equilibrium constants were always expressed as values greater than unity, K > 1. The direction of the isotope effect can be determined by noting whether individual carbons are moved upfield or downfield by the equilibrium isotope shift. It was reported that α, β', and γ carbons appear upfield of the corresponding α', β, and γ' carbons.⁶ Thus, for example, if C-3 is moved downfield and C-7 upfield by the isotope effect, it is clear that C-3 resides more of the time in the β environment, C-7 is correspondingly more in the β' environment, and the [A] ⇌ [B] equilibrium favors [A].

Each carbon signal could be shifted relative to the reference by an additional intrinsic isotope effect which is unlikely to be the same for both carbons in an exchanging pair. Carbons at two or three bonds distance from the deuterium may also exhibit coupling, although the coupling is much smaller and may not be detected unless the linewidths are quite narrow. Carbons close enough to the site of deuteriation to show coupling will also experience an isotope shift. In the α and γ peaks region, downfield C-8 and C-6 carbon peaks of cyclooctanone-3,3-D₂ remained in the same position as peaks of unlabeled cyclooctanone, while the corresponding C-2 and C-4 carbon peaks are moved upfield from unlabeled cyclooctanone peaks by intrinsic isotope effects because these carbons are affected by two deuteriums at C-3. Only for C-3 and C-7 carbon peaks are both equilibrium and intrinsic isotope shifts observed. However, the multiplet peak of C-3 carbon is absent because of di-deuteriation of C-3. (Figure 2) The C-7 carbon peak is shifted toward the downfield direction from the reference peak by involvement of an equilibrium isotope shift. The shift difference of the C-3 peak from the reference cyclooctanone peak is half of the equilibrium isotope shift.

The equilibration process is slowed down as temperature is lowered, thus the equilibrium isotope shift of C-3 and C-7 positions at -90 °C can not be observed due to line broadening of the peak. Hence, equilibrium constant and free energy difference could not be calculated at this temperature. Chemical and equilibrium isotope shift at various temperatures are listed in Tables 1 and 2. The

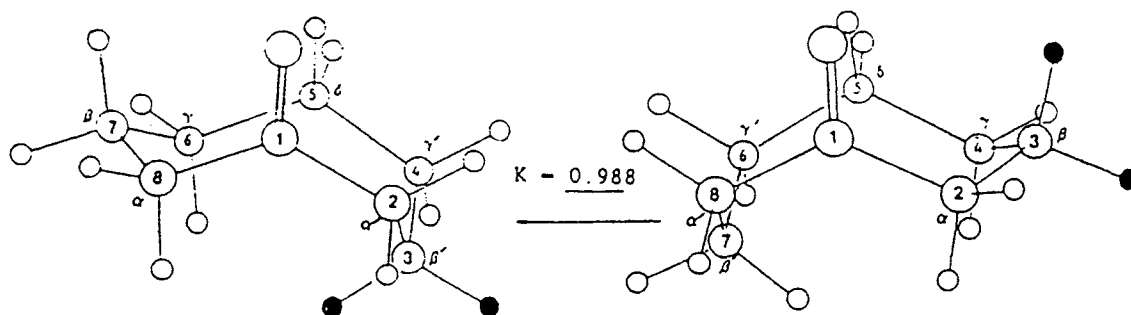


Figure 2. Isotopically Perturbed Equilibria for 3,3-D₂ isotopomer.

Table 1. The Chemical Shifts of 2:1 Mixture of Cyclooctanone-3,3-D₂ and Cyclooctanone

Temp. (°C)	C-2,8 ^a	C-3,7	C-4,6	C-5	C=O
	*42.01	26.18	*27.78	*25.19	214.91
20.2	41.88	*26.15	27.59	25.16	*214.88
	*41.96	25.94	*27.65	*24.96	215.37
-19.0	41.83	*25.99	27.47	24.91	*215.34
	*41.84	25.78	*27.42	*24.68	215.89
-58.3	41.72	*25.85	27.24	24.64	*215.85
	*41.76	25.70	*27.28	*24.50	216.58
-90.3	41.68	br.	27.10	24.42	*216.55

*Averaged methylene peak for unlabeled cyclooctanone.

^aUpfield peak is C-2 carbon, and downfield peak is C-8 carbon

br.: Peak is broadened at -90.3 °C .

equilibrium constants and the free energy differences, at 20.2, -19.0, and -58.3 °C were calculated. The enthalpy (-17cal/mol) and entropy differences(-0.033 cal/K) for the perturbed equilibrium of this isotopomer are found by employing regression analysis.

An MM2 calculation¹¹ was carried out on the boat-chair conformation of cyclooctanone to assist in the interpretation of the NMR isotope shift results. Geometrical optimization starting with a boat-chair conformation (BC-1) of cyclooctanone resulted in a BC-1 boat-chair conformation as the optimized structure. The results of the MM2 calculation are summarized in Table 3. Axial hydrogens at the α , β' , and γ carbons have strong mutual steric interactions due to their close proximity in the boat-chair conformation. One indication of this steric effect in the MM2 calculations is the van der Waals interaction energies. Van der Waals repulsive interactions are seen for hydrogen atom pairs located on adjacent carbons in gauche alignment.¹² In addition, there are mutual transannular interactions of H(20) with H(10) and H(14) on the α , γ and β' car-

Table 2. The Equilibrium and Intrinsic Isotope Shifts as well as Equilibrium Constants and Free Energy Differences in Cyclooctanone-3,3-D₂

Temp. (°C)	Equilibrium Isotope Shifts (ppm)	Equilibrium Constants (K)	Free Energy Differences (cal/mol)
	C-3,7	C-3,7	ΔG°
20.2	0.064	1.012	-7.00
-19.0	0.084	1.015	-7.05
-58.3	0.112	1.017	-7.12

Temp. (°C)	Intrinsic Isotope Shifts (ppm)		
	C-2	C-4	C-5
20.2	0.130	0.188	0.032
-19.0	0.129	0.182	0.032
-58.3	0.122	0.186	0.041
-90.3	0.123	0.184	0.043

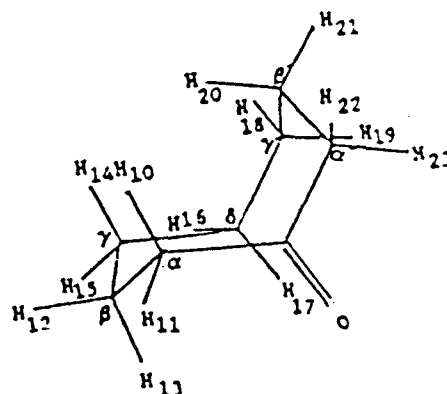
bons. There is a near eclipsing interaction between H(15) and H(16) on the γ and δ carbons. The sum of the van der Waals energies for the important steric interactions is given in the Table 3 for each hydrogen atom. The important feature is the change in steric interactions as hydrogen atoms exchange environments during the equilibration process between conformers. For example, hydrogens at the α carbon (H-10 + H-11) exchange into the α' position (H22 + H23). The calculations show that the α hydrogens would become less sterically crowded in becoming α' hydrogens, with the van der Waals energy decreasing by -0.43 kcal/mol. Hydrogens at the β carbon become more crowded in exchanging into the β' position(+0.72kcal/mol); this is the result of the uncrowded H(13) at β and the crowded H(20) at β' . Hydrogens at the γ carbon become less crowded in exchanging into the γ' position(0.48 kcal/mol).

Consideration of the change in steric environment is relevant to equilibrium isotope effects because in a process where protons and deuterons are allowed to equilibrate

Table 3. Key Features of MM2 Geometry for Boat-Chair Conformation of Cyclooctanone

Carbon Atom Pair ^a	Interatomic Distance (Å)	Van der Waals Interaction Energy ^b (kcal/mol)	Total Van der Waals Energy
α	H(10),H(12)	2.4237	0.1803
	H(10),H(20)	2.3151	0.3808
	H(10),C-8	2.6480	0.2458
α	H(11),H(12)	2.3647	0.2760
	H(11),H(13)	2.4140	0.1942
	H(11),O	2.5722	0.2515
β	H(12),H(11)	2.3647	0.2760
	H(12),H(10)	2.4237	0.1803
	H(12),H(14)	2.4211	0.1840
	H(12),H(15)	2.3313	0.3436
β	H(13),H(15)	2.3901	0.2314
	H(13),C-1	2.7422	0.2217
γ	H(14),H(12)	2.4211	0.1840
	H(14),H(20)	2.3949	0.2235
	H(14), γ'	2.6317	0.2717
γ	H(15),H(12)	2.3313	0.3436
	H(15),H(13)	2.3901	0.2314
	H(15),H(16)	2.2031	0.7315
γ'	H(18),H(20)	2.3739	0.2501
	H(18),H(16)	2.2986	0.4216
	H(18),H(21)	2.3626	0.2799
γ'	H(19),H(16)	2.4064	0.2055
	H(19),H(17)	2.3541	0.2964
	H(19),H(21)	2.3667	0.2722
β'	H(20),H(10)	2.3151	0.3808
	H(20),H(14)	2.3949	0.2235
	H(20),H(18)	2.3739	0.2591
	H(20),H(22)	2.4171	0.1896
	H(20),C-1	2.8326	0.1185
β'	H(21),H(18)	2.3626	0.2799
	H(21),H(19)	2.3667	0.2722
	H(21),H(22)	2.3315	0.2458
	H(21),H(23)	2.3872	0.2362
α'	H(22),H(20)	2.4171	0.1896
	H(22),H(21)	2.3815	0.2458
α'	H(23),H(21)	2.3872	0.2362
	H(23),O	2.4853	0.4278

Dihedral Atom	Dihedral Angle (°)	Cos ² θ
H ₂₂ - α' -C ₁ -P _{orbital}	16.51	0.919
H ₂₃ - α' -C ₁ -P _{orbital}	82.00	0.019
H ₁₁ - α -C ₁ -P _{orbital}	42.00	0.552
H ₁₀ - α -C ₁ -P _{orbital}	73.00	0.085



^aNumbering system for hydrogen atoms is shown below.

^bOnly interactions greater than 0.1 kcal/mol are indicated.

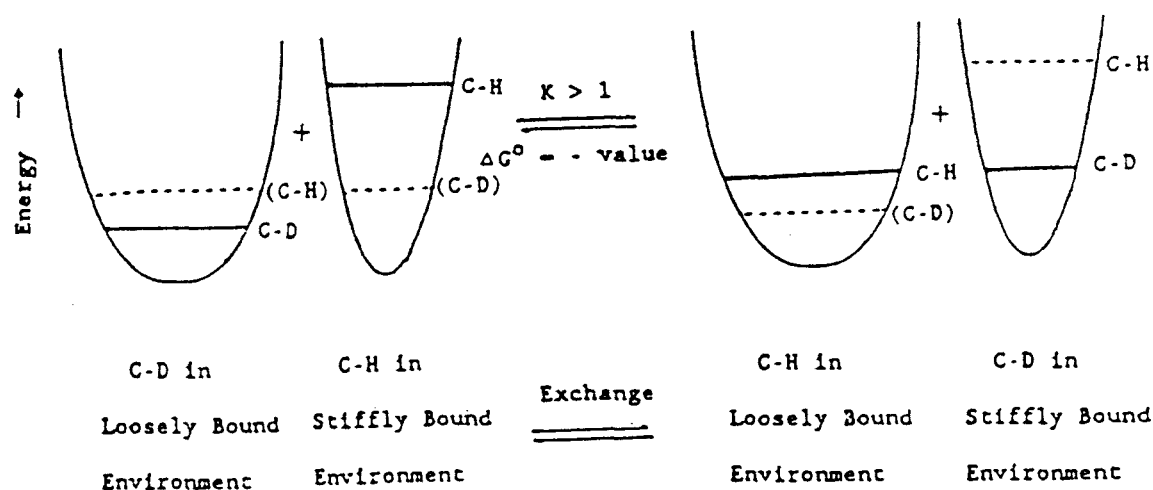


Figure 3. Origin of Isotope Effect on Equilibria for Exchange between Stiffly and Loosely Bound Positions.

among two or more sites, the deuterons will be found preferentially at the more stiffly bound positions. A steeper and narrower potential well is associated with greater force constants and results in a more closely confined vibrational motion. The restraining forces may originate from the bond holding the proton or deuteron, but also from non-bonding steric repulsive interactions. The difference between zero-point energy levels for C-H and C-D bonds is greater in a narrower potential well. This leads to the preference of the deuteron for the more stiffly bound position, as shown in Figure 3.

Introduction of deuterium would be expected to cause isotopic perturbation of the boat-chair equilibria by the steric isotope effect. Deuterium is expected to prefer the α position over α' , β' over β , and γ over γ' . The observed isotope effects for the boat-chair conformation would lead to the conclusion that labeled methylene groups indeed prefer the sterically crowded positions. The cyclooctanone-3,3-D₂ equilibrium favors the conformer with deuterium at the β' position. The free energy difference for the equilibria of 3,3-D₂ isotopomer was +7 cal/mol at room temperature. The equilibrium isotope shifts proved good evidence of the origin of CEIEs in cyclooctanone, in which isotope labeling perturbs conformational equilibria by the steric isotope effects. Molecular mechanics (MM2) calculations of steric interactions and molecular geometry strongly support the steric origin of the observed isotope shift results.

IV. References

- 1D. A. Forsyth, *Isot. Org. Chem.*, 6, 1 (1984).
- 2L. Melander and W. H. Saunders, "Reaction Rates of Isotopic Molecules", Wiley, New York, 6 (1980).
- 3H. J. Scheider, W. Freitag and V. Hopper, *Org. Magn. Reson.*, 13, 266 (1980).
- 4K. W. Baldry and M. J. Robinson *J. Chem. Res(s)*, 86, 1001 (1977).
- 5D. A. Forsyth and M. J. Suzanne *J. Am. Chem. Soc.*, 116, 11481 (1994).
- 6M. W. Jung, *Bull. Korean. Chem. Soc.*, 12, 224 (1991).
- 7K. C. Nicolaou, R. L. Magolda and D. A. Claremon, *J. Am. Chem. Soc.*, 102, 1404 (1980).
- 8H. Taguhi, H. Yamamoto and H. Nozaki, *J. Am. Chem. Soc.*, 96, 6510 (1974).
- 9F. C. Brown and G. J. Boxter, *Aus. J. Chem.*, 31, 327 (1978).
- 10M. Saunders, M. M. Jaffe and P. Vogel, *J. Am. Chem. Soc.*, 93, 2588 (1971).
- 11N. L. Allinger and H. L. Flanagan, *J. Comput. Chem.*, 4, 399 (1983).
- 12F. L. Anet, A. K. Cheng, M. St. Jacques, L. Wong and J. Krane, *Tetrahedron*, 30, 1629 (1974).

TRANSVERSAL RELAXATION RATE DISTRIBUTION ANALYSIS IN POROUS MEDIA.

M. Martín-Landrove, R. Martín and A. Benavides

Centro de Resonancia Magnética, Facultad de Ciencias, Universidad Central de Venezuela,
Apartado Postal 47586, Caracas 1041A, Venezuela.

Introduction.

Exchange of magnetic nuclei between two chemically shifted sites leads to a broadening and coalescence of the lines when the exchange rate is of the same order of magnitude as the difference in resonance frequencies at the two sites, i.e., the relaxation rate is increased [1].

This phenomenon induces a dispersion in the transversal relaxation rate when a Carr-Purcell-Meiboom-Gill (CPMG) experiment is performed in heterogeneous systems such as protein solutions [2,3,4] and sedimentary rocks [5], and it is dependent on the delay time between r.f. pulses used during the experiment. The effect becomes particularly strong when the delay time is comparable to the characteristic time of the exchange process.

Sedimentary rocks usually exhibit a non exponential behavior characterized by a stretched exponential function [6,7], but sometimes a three exponential function can equally fit the experimental data. To overcome this problem, it is necessary to obtain the actual relaxation rate distribution function, which can be done by Inverse Laplace Transform (ILT) algorithms. It has been also observed that stretched exponential parameters or the relaxation rate distribution function [5] depends on the r.f. pulsation rate in CPMG experiments.

In the present work, two types of CPMG experiments were performed on sedimentary rock samples at 90 MHz. For the first type of CPMG experiment, the complete decay of the signal was registered at different delay times between r.f. π pulses and the experimental data was analyzed by means of a specially designed program to perform

the ILT to obtain the relaxation rate distribution function. In the second type of CPMG experiments, at different r.f. delay times a careful measurement of the spin-echo signal was performed, to obtain possible variations in the magnetic local field in the sample.

Materials and Methods.

Samples of sedimentary rocks were cut from original rock nuclei, cleaned with toluene in a Soxhlet extractor and dried at 180 °C for 2 hours. The samples were cylindrical, 8 mm in diameter and 1 cm in height and were completely saturated with distilled water and measured at room temperature.

Two different sedimentary rocks were used in this study, as a control two Berea sandstone samples, with different permeability of 100 and 500 mDarcy respectively, were used. The other samples correspond to local oil reservoirs.

The measurements were carried out in a BRUKER CXP100 spectrometer operating at 90 MHz for protons. To register the complete decay of the transversal magnetization, the spectrometer was operated in the external address advance mode. For the second type of experiment, the maximum of the echo signal was carefully registered at a fixed echo time of 4 ms for all the samples. In both types of experiment, the delay time between r.f. π pulses was maintained fixed. The experiments covered a range of r.f. delay times between 200 μ s - 2 ms.

The experimental data were analyzed by Non Linear Regression Analysis (NLRA) and Inverse Laplace Transform (ILT). NLRA and ILT were used together to determine stretched-exponential or multiexponential behavior in the decay data. The stretched exponential parameters were determined

by NLRA. To determine the second derivative of the spin-echo signal, i.e., the second moment, NLRA was performed using an appropriate set of functions.

Let us discuss further the Inverse Laplace Transform algorithm used in this work. Since the signal is known in a finite number of points on the real axis, the numerical solution of the problem corresponds to a very ill-posed first kind Fredholm integral equation of the form:

$$M(t) = \int_0^{\infty} d\lambda e^{-\lambda t} P(\lambda)$$

where λ is the relaxation rate. The relaxation rate distribution $P(\lambda)$ can be represented by a histogram or collection of bars of variable width, which is given by

$$P(\lambda) = \sum_{k=1}^N P_k(\lambda)$$

where N is the number of components and $P_k(\lambda)$ is the k -th elemental component given by

$$P_k(\lambda) = P_k \Theta(\lambda - \lambda_k) \Theta(\lambda_k + \Delta\lambda_k - \lambda)$$

This representation can be used for the description of discrete and continuous distributions as well. In the particular case of a discrete one, a set of very localized functions with a small width can be obtained and it is indistinguishable from a very narrow and continuous distribution. This width is a function of relevant physical effects, noise and loss of information due to the use of a number of finite points. In practice it is very difficult to separate each contribution although in the case of noise, previous filtering procedures can be considered.

The problem to be solved can be stated as an optimization procedure where a set of distribution components, which provides the best fit for the $M(t)$ function, has to be found. For that purpose Simulated Annealing and Metropolis algorithms [8-11] are used. The configuration to be tested in each Metropolis algorithm cycle is given by a finite number of elementary components which are

sampled in the relaxation rate position λ_k and width $\delta\lambda_k$ for the k -th element. At the same time, the total number of components N for the configuration is also changed, which is a new feature in an optimization procedure of this kind. This sampling in the total number of components is performed by considering two options with the same probability within the Metropolis algorithm cycle:

(a) The total number of components N is unchanged and in this case one component is taken with equal probability from the current configuration set to change the numerical value of the relaxation rate position and its width. This change is achieved by adding an increment with uniform probability within the interval $[-\epsilon, +\epsilon]$ and by taking the absolute value of the result for the energy position first, and then the same process is repeated for the corresponding width. The value $\epsilon=1$ was taken arbitrarily. The time scale is set by taking the maximum measurement time equals to one.

(b) A new component is created and added to the existing configuration. The creation of this component implies the generation of a relaxation rate position and its corresponding width through the following steps: (i) A choice with equal probability is made in order to decide whether the new relaxation rate is going to be within the existing set or, on the contrary, happens to be the maximum of the new configuration set. (ii) In the former case the new relaxation rate is placed with equal probability in between two other relaxation rates of the old configuration, while in the latter case, the new relaxation rate is chosen with a non-uniform probability distribution. This probability distribution provides a practical boundary for the domain to be sampled and it should vanish for large relaxation rates. The simplest choice corresponds to an exponential distribution, but other distributions can be considered as well and it is an open problem.

The cost function was chosen on results of robust statistics to noise filtering and it is known in the literature as Least Absolute Deviation (LAD) optimization [12]. For n_P points it is given by

$$\Delta = \frac{1}{n_p} \sum_{i=1}^{n_p} \frac{|M_{\text{exp}}(t_i) - M_{\text{op}}(t_i)|}{|M_{\text{exp}}(t_i)|}$$

and it can be seen as an average relative error. In the presence of information loss the absolute value provides a better noise filtering than the usual quadratic value since the median is much less sensitive than the mean to the presence of fluctuations of any size. The quantity $M_{\text{exp}}(t)$ corresponds to the measured signal and $M_{\text{op}}(t)$ is the optimized signal given by

$$M_{\text{op}}(t) = \sum_k \int_0^{\infty} d\lambda e^{-\lambda t} P_k(\lambda)$$

In this work a fast simulated annealing approach is used (Cauchy machine) [13] and then it means that the temperature parameter is proportional to the inverse of the Monte Carlo iteration number.

The amplitudes are calculated through a simple least squares procedure, which means that a pure LAD optimization is not done in full extent. The main reason for this modification is to avoid in a simple way the classical instabilities frequently found in such procedures [12]. The standard description for this kind of problem is to use conjugate gradient methods [12]. The main disadvantage of these methods is related to the strong dependence of the results on the initial conditions. In the simulated annealing algorithm the results are in principle independent of the initial conditions. However there is a well known problem of the Metropolis algorithm related to the appearance of metastable states [8-11] which correspond to local minima and where the calculation in its evolution is going to remain for a very long time in the same region of the domain before the global minimum can be reached. This phenomenon clearly depends on the initial conditions and this inconvenience can be circumvented by performing several parallel simulations with different initial conditions to test the minima under consideration.

The immediate inclusion of extra conditions, that operate as constraints, is another clear

advantage of simulated annealing procedures over the currently used conjugate gradient methods. The amplitudes for the relaxation rate distribution should be positive or zero and this condition is implemented in a very simple fashion by discarding the components with negative amplitudes in a particular Metropolis algorithm cycle and in this way, a natural mechanism for a reduction in the number of components is provided.

The ill-posed nature of the least squares procedure does not allow to obtain more than a small number of components to build the corresponding histogram. This is due to an increase in the condition number for the matrix used in the least squares procedure when the number of components is also increased. The solution to this problem is to take an average for a set of histograms obtained from different initial conditions and cost functions Δ of nearly equal size, which means that they are equal within a given number of significant figures. The set of histograms should be generated anyway to look for a global minimum candidate. The resultant averaged histogram provides the final relaxation rate distribution and its cost function is smaller than the original ones.

Experimental Results and Discussion.

The results obtained for Berea sandstone samples are shown in Figure 1, where it can be appreciated a common behavior for the second moment almost independent of the permeability of the sample. In Figure 2a, the results for three different samples of local oil reservoirs are shown and in Figure 2b, the average is presented. The samples covered a range of porosity between 12.90 to 16.20 and permeability between 23 to 581 mDarcys. Within the same geological group the samples behave similarly as the r.f. delay time is increased, with few variations depending on permeability and paramagnetic impurities concentration. In the case of Berea samples, the curves depicted in Figure 1 have a common trend or regime, while for the local oil reservoir samples, three zones with different regimes are clearly distinct.

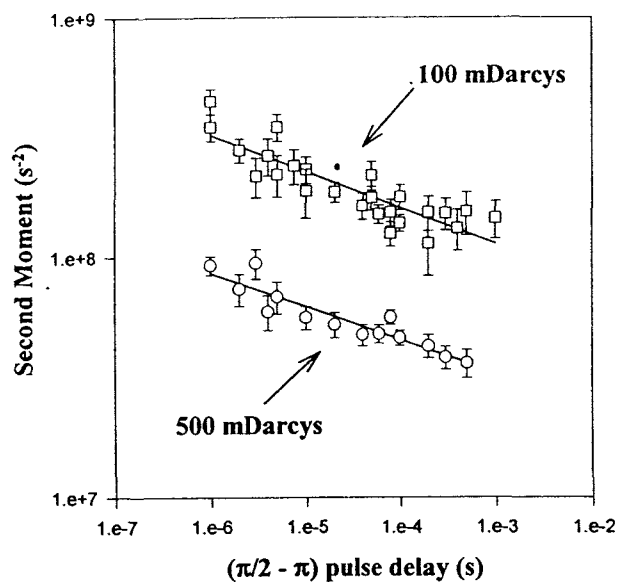


Figure 1. Berea sandstone second moment measurement as a function of r.f delay time in CPMG experiments.

In Table 1, some characteristic parameters of the local rock samples are summarized together with the stretched exponential parameters for longitudinal relaxation. It is worthwhile to note the high degree of homogeneity of these parameters within the same oil reservoir even while the porosity and permeability cover a wide range of values.

Table 1. Properties of rock samples from local oil reservoirs. The symbols indicate the oil reservoir.

Sample	Porosity ϕ (%)	Permeability k (mD)	$T_{1\alpha}$ (ms)	α
(1) *	12.9	116	386.4	0.75
(2) *	13.1	182	384.4	0.89
(3) *	8	0.71	104.5	0.61
(4) *	11.9	8.65	230.8	0.8
(5) *	14.3	281	303.7	0.82
(6) *	16.2	581	382.1	0.81
(7) *	12.9	23	138.6	0.79
(8) +	7.43	0.57	86.4	0.62
(9) +	14.1	180.14	309.4	0.54

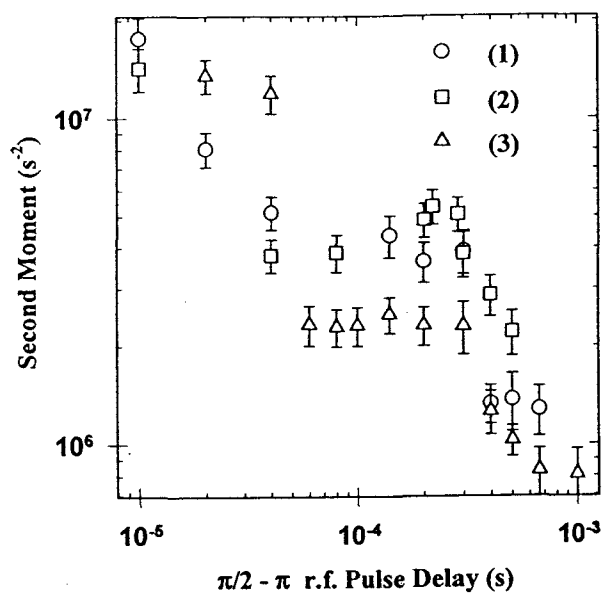


Figure 2a. Second moment measurements for three different rock samples taken from the same oil reservoir. Data correspond to sample (5), (6) and (7) of Table 1.

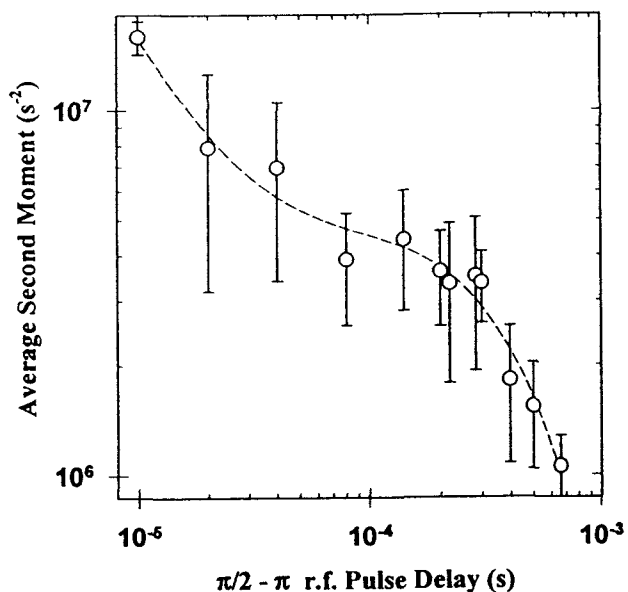


Figure 2b. Average second moment for rock samples shown in Figure 2a.

The results obtained for these samples by means of ILT are shown in Figure 3. It is important to note that the transversal relaxation distribution function is obtained at different r.f. delay times, so the evolution with this parameter can be traced easily. From Figure 3 it can be observed a complex structure for each distribution, composed of at least three peaks with variable widths and with a relaxation rate span of some decades on a logarithmic scale. This type of relaxation rate distribution is typical of natural porous media and it is directly connected to the stretched exponential character of the relaxation decay. The dependence

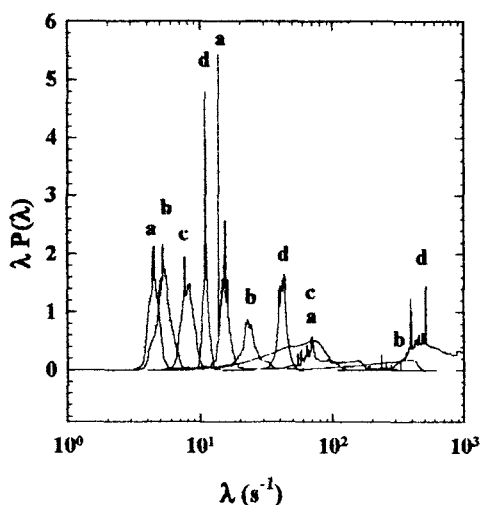


Figure 3. Relaxation rate distributions for sample (5) in Table 1. The letters indicate components for the same distribution. The r.f. delay times are as follows: (a) 100 μ s, (b) 600 μ s, (c) 1 ms and (d) 2 ms.

on the r.f. delay time is also complex, some of the components are displaced to lower relaxation rates while others are displaced to higher relaxation rates, with additional changes in the shape of each component of the relaxation rate distribution function. In Table 2, this complex situation is summarized in the dependence of the average relaxation rate and the average relaxation rate distribution width on the r.f. delay time.

To understand the effect of diffusion on the second moment and the relaxation rate distributions, the following qualitative model can be used. In a

porous material there is a distribution of magnetic local fields depending on the pore size distribution, Throat size distribution, physical and chemical properties of the inner pore and throat surface, surface roughness, etc.. For r.f. times smaller than the time required for a water molecule to get out of a pore, the local magnetic field averages to a value

Table 2. Relaxation rate distribution parameters.

r.f. delay time	$\langle \lambda \rangle$ (s^{-1})	$\langle \delta \lambda \rangle$ (s^{-1})
100 μ s	52.04	97.47
500 μ s	44.82	127.35
600 μ s	34.18	51.03
800 μ s	184.11	180.72
1 ms	34.43	30.14
1.5 ms	83.32	108.07
2 ms	268.76	294.79

which is typical of that pore, so the distribution of average local fields should be related to the distribution of pore sizes. It is generally expected that the average local magnetic field distribution is peaked at high values of the local magnetic field, since there are a majority of small pores in the rock. As the r.f. delay is increased, water molecules can reach other pores and so the average local magnetic field distribution is then lowered. The exact way by which the local magnetic field distribution is changed depends on the geometry and physicochemical properties on the pore surface, so it will be necessary to use a simulation to obtain further information about these materials.

Nevertheless, the methodology described in this work can be easily implemented in commercial spectrometers and can be standardized to characterize sedimentary rocks in oil reservoirs.

Acknowledgments.

This work was partially supported by INTEVEP, S.A. and the Centro de Resonancia Magnética, Facultad de Ciencias, Universidad Central de Venezuela.

References.

- [1] Harris R.K., Nuclear Magnetic Resonance Spectroscopy, A Physicochemical View; Pitman: London, 1983.
- [2] Hills B.P., Takacs S.F. and Belton P.S., Molecular Physics, 67, 903 (1989).
- [3] Hills B.P., Takacs S.F. and Belton P.S., Molecular Physics, 67, 919 (1989).
- [4] Hills B.P., Molecular Physics, 76, 509 (1992).
- [5] Kleinberg R.L., Straley C., Kenyon W.E., Akkurt R. and Farooqui S.A., SPE 26470, 553 (1993).
- [6] Kenyon W.E., Day P.I., Straley C. and Willemsen J.F., SPEFE, Sept., 622 (1988).
- [7] Attard J.J., Dorand S.J., Herrod N.J., Carpenter T.A. and Hall L.D., J. Magn. Reson., 96, 514 (1992).
- [8] Bhanot G., Rep. Prog. Phys., 51, 429 (1988).
- [9] Kirkpatrick S., Gelat C.D. and Vecchi M.P., Science, 220, 671 (1983).
- [10] Kirkpatrick S., J. Stat. Phys., 34, 975 (1984).
- [11] Bonomi E. and Lutton J.L., SIAM Rev., 26, 551 (1984).
- [12] Scales A. and Gersztenkorn A., Inverse Problems, 4, 1071 (1988).
- [13] Szu H. and Hartley R., Phys. Lett. A, 122, 157 (1987).

Magnetic Resonance in the Development of Better Strategies for Protecting the Brain during Surgery

R. Deslauriers, C.L. Filgueiras, J. Ye, L. Yang, M. Ede, R. Summers, T.A. Salerno*,
L. Ryner, P. Kozlowski, B. Winsborrow, J.K. Sun and J.K. Saunders

Institute for Biodiagnostics, National Research Council of Canada, Winnipeg, MB, R3B 1Y6, Canada

* Buffalo General Hospital, Buffalo, NY 14203, USA

Introduction

Deep hypothermic circulatory arrest has become a useful technique in complex cardiovascular surgery. However, neurological injury remains a serious consequence despite the protective effect of hypothermia. Some degree of cerebral cortical damage occurs regardless of the ischemic time, although the generally accepted "safe" duration of circulatory arrest ranges from 45-60 minutes. Various techniques have been devised to overcome the disadvantages of circulatory arrest, including selective perfusion of the cerebral vessels during the arrest period.

To assess the efficacy of selective brain perfusion techniques, we developed an experimental protocol for the localized *in vivo* ^{31}P NMR spectroscopic study of brain energetics and intracellular pH in a porcine model [1].

Our results show that selective antegrade perfusion of the brain at 15° [2,3] or 28° C [4] during circulatory arrest preserves normal levels of high energy metabolites and intracellular pH. Retrograde brain perfusion provides better metabolic protection at 15° C than does circulatory arrest, however the method is not as effective as antegrade perfusion. Retrograde brain perfusion provides less protection at 28° C than at 15° C.

Materials and Methods

a) Experimental Groups and Surgical Procedures

Young farm pigs of either sex were used (25 to 30 kg, 89 to 103 days old). All animals received humane care in compliance with the guidelines of the Canadian Council on Animal Care.

Pre-anesthesia was induced with xylazine (2.2 mg/kg), ketamine (20 mg/kg) and atropine (0.03 mg/kg) intramuscularly. After endotracheal intubation, the animal was ventilated mechanically with 60% oxygen and 40% nitrogen. The ventilator rate and tidal volume were adjusted to maintain the arterial carbon dioxide tension at about 40 mmHg. Anesthesia was maintained with 1.0-2.0% isoflurane. A temperature probe was placed in the esophagus to monitor the core temperature. Catheters were placed in the right carotid artery and right external jugular vein for withdrawal of blood samples and measurement of blood pressure. Urine output was collected through a bladder catheter.

The chest was opened via a median sternotomy. Heparin at 300 IU/kg was given intravenously. The ascending aorta was cannulated, which was used for arterial blood return to the body during normal cardiopulmonary bypass and for collection of blood returning from the brain during retrograde perfusion of the brain. Venous cannulas were placed into both the superior and inferior vena cava. The superior vena cava cannula was used for collecting blood into the reservoir during normal bypass or for providing retrograde perfusion of the brain. A cannula was inserted into the innominate artery to provide antegrade perfusion of the brain. The left ventricle was vented via the left atrium. The lungs were not inflated during bypass or circulatory arrest.

The cardiopulmonary bypass circuit consisted of Cobe roller pumps (model C22.2), cardiotomy reservoir (Cobe), arterial filter (Cobe Sentry), water bath (Laud MGW type RMSG) and a membrane oxygenator (Cobe CML) with integral heat exchanger. The circuit was primed with 1.5 L lactated Ringer solution, 1 L homologous blood and 5,000 IU heparin. Sodium bicarbonate was given to maintain the pH around 7.40, when necessary. Arterial blood gases were monitored and measured at 37° C with a blood gas analyzer (Stat 7, NOVA Biomedical, U.S.A.). No correction was made for the temperature during hypothermia, and the alpha-stat approach was used. Blood electrolytes and osmolality were monitored and kept within the normal range. A 15 to 23% hematocrit was maintained. The bypass circuit was specially designed to be suitable for retrograde brain perfusion and normal bypass by simply switching clamps.

Cardiopulmonary bypass in the pigs was initiated and maintained for a period of approximately 30 min at 60 - 100 ml/kg/min flow with gradual cooling of the pig until the esophageal temperature was lowered to 15° C. The arterial pressure was maintained between 60-100 mmHg. When the core temperature reached 15° C, the pigs received 120 minutes of circulatory arrest or 120 minutes of circulatory arrest with retrograde perfusion at a venous pressure of 35-45 mmHg and a blood flow of 300-500 mL/min or antegrade cerebral perfusion at a perfusion pressure of 65-85 mmHg and a blood flow of 180-200 mL/min. A water circulation blanket was used to cover the pig to maintain the core temperature at 15° C during circulatory arrest. At the end of circulatory arrest, retrograde or antegrade perfusion, bypass was started again in

all groups with gradual rewarming to 37° C, and continued for 60 min.

For NMR studies of brain protection at 15° C the pigs were randomly assigned to one of five groups: anesthesia (control) (n=5), cardiopulmonary bypass (control) (n=5), circulatory arrest (n=5), circulatory arrest with retrograde cerebral perfusion (n=7), circulatory arrest with antegrade cerebral perfusion (n=5)

For studies at 28° C twenty-four pigs were divided into three groups: anesthesia alone (control) (n=8), antegrade brain perfusion during hypothermic circulatory arrest (n=8) and retrograde brain perfusion during hypothermic circulatory arrest (n=8). The two experimental groups received 40 min of cardiopulmonary bypass before 120 minutes of circulatory arrest and one hour of bypass for reperfusion at 37° C.

b) NMR Methods

³¹P NMR spectra were acquired during three stages of the surgical protocol: prearrest, circulatory arrest, and recovery bypass. The prearrest stage is defined as the first 40-50 minutes after completion of the surgery required to place the animal on sanguineous cardiopulmonary bypass during which the temperature is lowered from 37° C to 15° C. During this stage the animal was placed in the magnet where positioning and shimming were performed and one localized ³¹P NMR spectrum of the brain was obtained. For the second stage of the protocol, the bypass pump was stopped for 120 minutes and various brain protection methods were applied. Three methods were used: deep hypothermia alone (15° C) and deep hypothermia with deep hypothermic retrograde or antegrade cerebral perfusion. Finally, during the 60-minute recovery bypass stage, the bypass pump was restarted and the animal was warmed to 37° C. Localized ³¹P NMR spectra were acquired every 30 minutes during the last two stages of the surgical protocol.

The data were acquired with a Bruker Biospec spectrometer equipped with a Magnex 4.7T magnet (15° C data) or a Bruker MSLX system equipped with a Magnex 7 T/40 cm horizontal bore magnet and actively-shielded gradients with a clear bore of 30 cm (28° C data). The animal was placed in the supine position in a custom-built polyvinylchloride cradle shaped to fit the bore of the magnet; the head was fastened to an r.f. coil attached to the cradle. Positioning of the animal in the magnet and slice definition within the skull were performed with the standard Multi Slice Multi Echo imaging sequence (TE = 30 msec). B₀ field homogeneity in the selected slice was optimized by shimming on its ¹H₂O time domain signal; the line width at half-height was typically 20-30 Hz.

The r.f. coil was a semi-cylindrical surface coil specially designed to conform to the back of the pig skull (Morris Instruments, Gloucester, Ont., CAN). The cortex of the brain was reproducibly selected by identifying the eyes in a coronal image. The coil shape improved the B₁ homogeneity relative to a standard surface coil and allowed deeper uniform

r.f. penetration into the pig skull. This was necessitated because the brain is located about 2 cm below the surface of the pig head and under physiological conditions (scalp and skull intact) a standard surface coil could not adequately excite the brain cortex. The r.f. coil was inductively coupled and fixed to both ¹H (200.4 MHz) and ³¹P (81.1 MHz) frequencies. The sensitivity of a double-tuned coil relative to a single-tuned ³¹P coil is about 80%; the ¹H sensitivity is much poorer but the signal is sufficient for any imaging experiment. The ¹H signal was used to define the slice position. The principal advantage of the double-tuned coil is that the animal need not be removed from the magnet to change the experimental frequency from ¹H to ³¹P.

Two-dimensional Spectroscopic Imaging (SI) [5] was used to obtain the localized pig brain ³¹P NMR spectra, the localized volume was 8 cm³. This was accomplished with two phase encoding gradients applied in the two directions in-plane with the selected slice. The duration of the gradient pulses was 1 msec with a rise time of 0.5 msec. The actively-shielded gradients ensured that no distortions were observed in the spectra due to eddy currents. Localization in the third direction was achieved by using a 1 msec slice selective Gaussian r.f. pulse with 750 W r.f. power and a repetition time of 1.5 sec. Due to the weak in-vivo ³¹P signal, the pulse gain was set to maximize the S/N in a phantom experiment, therefore it is difficult to define the pulse angle used in the actual experiment. Data filtering during acquisition reduced the time required to obtain one spectroscopic image to 22 minutes and improved the voxel shape. Although the acquisition time was 22 minutes, experiments were performed every 30 minutes to coincide with the timing of the surgical protocol.

A gradient strength of 2 G/cm was used to produce a 2 cm slice thickness with a 1 msec Gaussian pulse. Under these conditions, the maximum difference in the slice position due to the spread in resonance frequencies across the spectrum is 5 mm. This difference was minimized by positioning the carrier frequency in the middle of the spectrum, between the phosphocreatine (PCr) and γ -ATP signals. Centering the carrier frequency also ensured uniform excitation across the spectrum.

The data were processed with 3D data processing software developed "in-house" [6]; 30 Hz line broadening was used in the spectral direction. Because no r.f. refocusing pulse was used, a large first order phase correction was needed to process the data; baseline correction was achieved by fitting a fourth order polynomial to the baseline. The pH was calculated from the chemical shift difference between the inorganic phosphate (Pi) and PCr signals and was corrected for different brain temperatures [7]. The spectral width was 12 kHz and 2048 data points were acquired in the spectral dimension; with a spectral resolution of 5.8 Hz/pt the accuracy was limited to 0.1 pH units.

The data obtained on the 7T/40 cm bore magnet at 28° C data were acquired with a similar experimental set-up to

that obtained on the 4.7T magnet. The main differences were the use of a single-tuned ^{31}P surface coil (10 cm diameter, 121.5 MHz), no data-filtering during acquisition, 10 kHz spectral width, and 50 Hz line-broadening along the spectral direction

Comparisons of intracellular brain pH (pHi) between the groups throughout the protocol were carried out using one-way ANOVA, the Kruskal-Wallis ANOVA, and the Tukey test. Statistical significance was said to exist with $p < 0.05$.

c) Histopathological Methods

At the end of the NMR experiments, which was 3 hours after the onset of circulatory arrest, retrograde or antegrade cerebral perfusion, the brains were perfused under anesthesia with heparinized saline through the carotid arteries to wash blood from the brain which was followed by perfusion with 10% buffered formaldehyde solution. The perfusion pressure was monitored and maintained between 80-120 mmHg. After perfusion fixation, the pig heads were immersed in 10% buffered formaldehyde solution and kept at 4° C for 24-72 hrs. The brains were then removed for further fixation by immersion in the same solution at 4° C. After one to two weeks of immersion fixation, the brains were separated into anatomical areas of interest. The tissue blocks were further cut into approximately 1x1x0.5 cm slabs (samples), which were transferred to a 30% sucrose solution and kept at 4° C overnight. The tissue slabs were placed into the 2-methylbutane solution (-40 to -50° C) for 30 to 60 s, and then were transferred to a Cryostat (-40° C) for 5 min. The samples were stored in the deep freezer (-70° C) for at least 24 hrs before sectioning.

The prepared samples were cut into 5, 10, 15, and 20 μm thick slices using a Cryostat (at a temperature of -25 to -28° C). The slices were mounted on uncoated slides and dried at room temperature. Haematoxylin and eosin (H and E) staining was performed on every tenth section. The severity of injury was based on the number of damaged neurons in eight different brain areas including the pons, mesencephalic gray area, Purkinje cells of the cerebellum, thalamus, putamen, cortex, caudate cortex, and pyramidal neurons of the hippocampus. During this early period after the onset of hypoxic ischemic brain injury, the minimum criteria for diagnosis of ischemic neuronal necrosis (ischemic cell change) included mild cytoplasmic eosinophilia, shrunken neurons with scalloping of the margins, and nuclear changes consisting of coarse nuclear chromatin or pyknosis. Injury was graded (0 to 5) based on the number of damaged neurons in 8 slices which contained the same areas. Neurons were counted using a rectangular ocular graticule at an ocular magnification of x 400. The grading scheme was as follows: 0: no necrotic cells; 1: less than 10% necrotic cells; 2: between 10 and 25% necrotic cells; 3: between 25 and 50% necrotic cells; 4: between 50 and 75% necrotic cells; 5: more than 75% necrotic cells.

All data are presented as mean \pm standard error of the mean (SEM). Comparisons between groups of results for total brain damage was carried out by ANOVA. The Tukey test was used for comparisons of pathological results between the different areas of the brain. $P < 0.05$ was considered to be significant.

Results

a) NMR Evaluation of Brain Protection at 15° C

The localized ^{31}P NMR spectra in Figure 1a) are representative of those obtained from the brains of animals in the anaesthetized and bypass control groups. These spectra are typical of normal pig brains where the PCr signal is the most intense and the Pi signal is very weak.

Figures 1b) and 1c) show series of localized in-vivo pig brain ^{31}P NMR spectra acquired during the experimental protocol when only deep hypothermia was used during circulatory arrest. Of the six animals used in this group the spectra presented in Figure 1b) were observed for two animals and those in Figure 1c) were observed for the remaining four animals. These figures both indicate a total loss of high energy phosphate metabolites after approximately 40 minutes of circulatory arrest. The largest differences between the two series of spectra are observable during the recovery stage: Figure 1b) shows no recovery of the high energy phosphate metabolites whereas Figure 1c) shows that although the Pi signal remains intense during the recovery bypass stage, there is a limited return of signals due to the high energy phosphate metabolites during the recovery period.

Figure 1d) shows spectra obtained during an experiment where deep hypothermic (15° C) retrograde perfusion was performed during circulatory arrest: there is significant loss of signals from the high energy phosphate metabolites after about 40 minutes of circulatory arrest and subsequent recovery of the signals during recovery bypass. After 50 minutes of recovery bypass the Pi signal intensity is low relative to the signals due to PCr and ATP. In addition, the S/N ratio in the recovery spectra is lower than that in the corresponding prearrest spectra.

Figure 1e) consists of spectra obtained during an experiment where deep hypothermic (15° C) antegrade perfusion was performed during circulatory arrest. There is no significant difference between any of the spectra during the entire experimental protocol. In fact, all the spectra are similar to those obtained from the control groups in Figure 1a).

Table 1 shows the intracellular pH of the brain with the different methods of brain protection. The large standard deviations of the pH measurements (greater than 0.2) in some of the data at the beginning of the circulatory arrest and recovery bypass stages are believed to result from different response times for the different animals. At the end of each stage of the study the standard deviation of the pH measurements was much lower.

The pH of the control bypass group was on average 0.2 pH units higher than that of the control anaesthetized

group. For the retrograde and antegrade cerebral perfusion groups the initial and final pH values were within 0.1 pH units, suggesting return to normal prearrest conditions before the end of the 60 minute recovery bypass stage. It is important, however, to assess the pH stability throughout the experimental protocol because highly acidic conditions have been linked to neurological damage following recovery. Only the control and antegrade perfusion groups had normal pH levels throughout the experiment. Although the final pH of the retrograde perfusion group was normal (7.1 ± 0.2), the pH was low (6.4 ± 0.1) at the end of circulatory arrest.

The circulatory arrest group demonstrated even less pH stability: the pH after circulatory arrest and the final pH were lower than the initial pH. Within this group the data followed two patterns. In subgroup A ($n=3$) shown in Table 1 there was little or no recovery of high energy phosphate metabolite signals observed in the localized ^{31}P NMR spectra, (Figure 1b), and the final pH was 6.2 ± 0.1 , 0.7 pH units lower than the initial pH. In subgroup B ($n=3$) of Table 1 the high energy phosphate metabolite signals recovered (Figure 1c), but the Pi signal remained fairly intense, and the final pH was 6.9 ± 0.1 , 0.4 pH units lower than the initial pH. One may suspect that a low initial pH for subgroup A could cause the final pH to be low, however the initial pH prior to circulatory arrest for subgroup B does not support this hypothesis because the final pH of subgroup B was also low.

The pH of the brain during circulatory arrest may be an indicator of its potential for recovery. Both subgroups A and B of Table 1 showed low pH values at the end of the circulatory arrest stage, 6.3 ± 0.1 and 6.2 ± 0.1 , respectively. The pH during circulatory arrest in the retrograde perfusion group was also low, 6.4 ± 0.1 . Moreover, although the high energy metabolite signals are present in the recovery ^{31}P NMR spectra, the S/N level was in many cases lower than that in the corresponding prearrest spectra. The tuning and matching of the NMR probe was carefully checked during the experiment and no changes which might have influenced the overall S/N ratio were observed. The coil loading before, during, and following circulatory arrest did not change. The T_1 relaxation time of phosphorus metabolites may vary in this type of experiment, however it is very unlikely that all resonances present in the spectrum would be affected in the exact same way. Therefore the lower S/N ratio can best be attributed to cell death during circulatory arrest with subsequent breakdown of the blood brain barrier. The result is a loss of high energy metabolites, washout of inorganic phosphate upon reperfusion with concomitant loss of NMR signal. These speculations are supported by a separate study (detailed below) using light microscopy performed brains that were perfusion fixed at the end of the NMR experiments. This suggests that the brain pH may be a sensitive indicator of the probable success of a brain protection method.

b) Histopathological Results.

Table 2 shows the level of cell damage measured in different areas of the pig brains [8]. Figure 2 shows the total grade of brain damage obtained by summing the grades of the ten areas of the brains [8] given in Table 2. These data show unequivocally that deep hypothermia alone does not protect the brain during 120 minutes of circulatory arrest. In addition, although retrograde perfusion offers a significant measure of protection relative to circulatory arrest alone, very significant damage was observed in all brains areas examined. Antegrade perfusion during hypothermic circulatory arrest provides a significant degree of protection relative to circulatory arrest alone as well as to retrograde perfusion during circulatory arrest.

c) NMR Studies of Brain Protection at 28° C

Although the protective properties of deep hypothermia (eg 15° C) relative to normothermic conditions during circulatory arrest are well documented, the method presents a number of disadvantages, such as increased time for cooling and rewarming the patient, coagulopathy, and an increased risk of infection. In addition, the hemoglobin dissociation curve is left-shifted and release of oxygen to the tissue is less under hypothermic than normothermic conditions. We used NMR to evaluate the level of metabolic protection provided by brain perfusion under moderate hypothermic conditions (28° C). We have compared the relative protection provided by antegrade and retrograde perfusion during circulatory arrest because antegrade perfusion methods are unsuitable in many surgical circumstances (such as in patients with severe atherosclerotic disease). The control groups received anesthesia alone.

The pHi in the anesthesia group was 7.1. In the group with circulatory arrest and antegrade brain perfusion, the cerebral metabolites remained normal during the entire course of the experiment and the lowest pHi was 7.1. There was no statistically significant difference in pHi for the anesthesia and antegrade groups throughout the protocol. However, beginning with circulatory arrest and thereafter the pHi values for the retrograde group were significantly different from the anesthesia and the antegrade perfusion groups. During circulatory arrest in the retrograde group, PCr and ATP decreased more rapidly at 28° C than at 15° C and never recovered during reperfusion. The loss of high energy phosphates is attributed to greater energy requirements for brain metabolism at 28° C than at 15° C which are not fully compensated by the better dissociation of oxygen from hemoglobin at 28° C due to poor distribution of flow through the retrograde route (R. Deslauriers, et al, unpublished).

Conclusion

These ^{31}P NMR studies provide experimental evidence that hypothermic circulatory arrest with antegrade perfusion of the brain provides good protection of brain metabolites and intracellular pH both at 15° C and 28° C. Retrograde brain perfusion does not fully protect brain

metabolites. When retrograde perfusion is necessary during circulatory arrest for surgery on the aortic arch, better protection is achieved at 15° C than at 28° C. In addition, the results obtained using NMR are in good agreement with histopathological studies performed on tissue at the end of the NMR experiments which show that only antegrade perfusion provides any real measure of cerebral protection during long duration (120 minutes) hypothermic circulatory arrest.

Currently, NMR imaging studies are underway to determine the pattern and adequacy of blood flow to the brain provided by antegrade and retrograde brain perfusion during circulatory arrest and reperfusion. The use of both spectroscopic and imaging techniques should allow optimization of retrograde brain perfusion conditions and help prolong the safe duration of circulatory arrest.

References

1. Winsborrow, BG, Kozlowski, P, Filgueiras, C et al, *Can J Appl Spectroscopy*, 1994; 39:135-42.
2. Filgueiras, CL, Winsborrow, B, Ye, J, et al, *Surg Forum*, 1994; 263-5.
3. Filgueiras, CL, Winsborrow, B, Ye, J, et al, *J Thorac Cardiovasc Surg*, 1995, in press.
4. Deslauriers, R, Filgueiras, CL, Ryner, CL, et al., *Proc. Third Annual Meeting SMR*, 1995, in press
5. Brown, TR, Kincaid, BM, Ugurbil, K et al, *Proc Natl Acad Sci USA*, 1982; 79:3523-6.
6. Somorjai, RL, Morrow, R and Deslauriers, R, *Proc Tenth Annual Meeting SMRM*, 1991, p. 4219
7. Kost, GJ, *Magn Reson Med*, 1990, 14: 496-506
8. Ye, J, Yang, L, DelBigio, MR, et al, unpublished results.

Acknowledgement: This work was supported in part by the Heart and Stroke Foundation of Ontario and the Heart and Stroke Foundation of Manitoba through grants to RD, JKS and TAS.

Table 1: pH Measured From Localized ^{31}P MR Spectra of Pig Brains During the Different Methods of Brain Protection¹

Stage (Time)	Experimental Groups					
	Anesthesia ² (Control)	Bypass ² (Control)	Circulatory Arrest (A) ³ (B)		Retrograde	Antegrade
Pre-arrest	7.1 ± 0.1	7.3 ± 0.1	7.0 ± 0.1	7.2 ± 0.0	7.1 ± 0.1	7.2 ± 0.1
Circulatory Arrest (10 min)	7.1 ± 0.1	7.3 ± 0.1	6.3 ± 0.2	6.6 ± 0.2	6.8 ± 0.3	7.2 ± 0.2
(50 min)	7.1 ± 0.1	7.3 ± 0.1	6.2 ± 0.1	6.3 ± 0.1	6.5 ± 0.1	7.2 ± 0.2
(110 min)	7.1 ± 0.1	7.3 ± 0.1	6.3 ± 0.1	6.2 ± 0.0	6.4 ± 0.1	7.2 ± 0.1
Recovery Bypass (10 min)	7.1 ± 0.1	7.3 ± 0.1	6.2 ± 0.1	6.5 ± 0.1	6.7 ± 0.4	7.2 ± 0.1
(50 min)	7.1 ± 0.0	7.3 ± 0.1	6.2 ± 0.1	6.9 ± 0.1	6.1 ± 0.2	7.1 ± 0.1

- ¹ Data were acquired over 22 minute intervals; the reported time is the mid point of the measurements. In groups undergoing circulatory arrest, the temperature was decreased to 15°C during prearrest and rewarmed to 37°C during recovery.
- ² These control groups did not undergo circulatory arrest or reperfusion. In the Anesthesia group, the temperature was 37°C. In the Bypass group, the animals were cooled to 15°C.
- ³ Circulatory arrest with low venous return during bypass prior to circulatory arrest.

Table 2: Histopathological Damage Grading in Different Brain Areas

	Anesthesia	Circulatory Arrest	Retrograde	Antegrade
Caudate nucleus	0.2±0.2	4.2±0.2 *+	3.9±0.3 *+	0.6±0.2
Putamen	0	3.0±0.4 *+	2.0±0.5*+	0
Cortex (cingulate)	0	3.4±0.7 *+	2.3±0.7	0.8±0.2
Cortex (temporal)	0	3.4±0.7 *+	2.7±0.6 *+	0.4±0.2
Thalamus	0	2.4±0.7 *	1.4±0.5	0.6±0.4
Hippocampus-CA1	0	2.0±0.8*	0.7±0.5	0.4±0.2
Hippocampus-CA4	0	5.0±0.0 *+	4.4±0.4 *+	0.6±0.2
Purkinje cells	0.4±0.25	2.4±0.5 *+	1.0±0.4	0.4±0.2
Pons	0.2±0.2	2.4±0.7 *	0.9±0.6	0.4±0.2
Mesencephalic gray	0.2±0.2	1.8±0.5 *+	0.4±0.3 #	0

Values shown as grade and mean±SEM

* P < 0.05 vs

Anesthesia

+ P < 0.05 vs

Antegrade

P < 0.05 vs

Circulatory Arrest

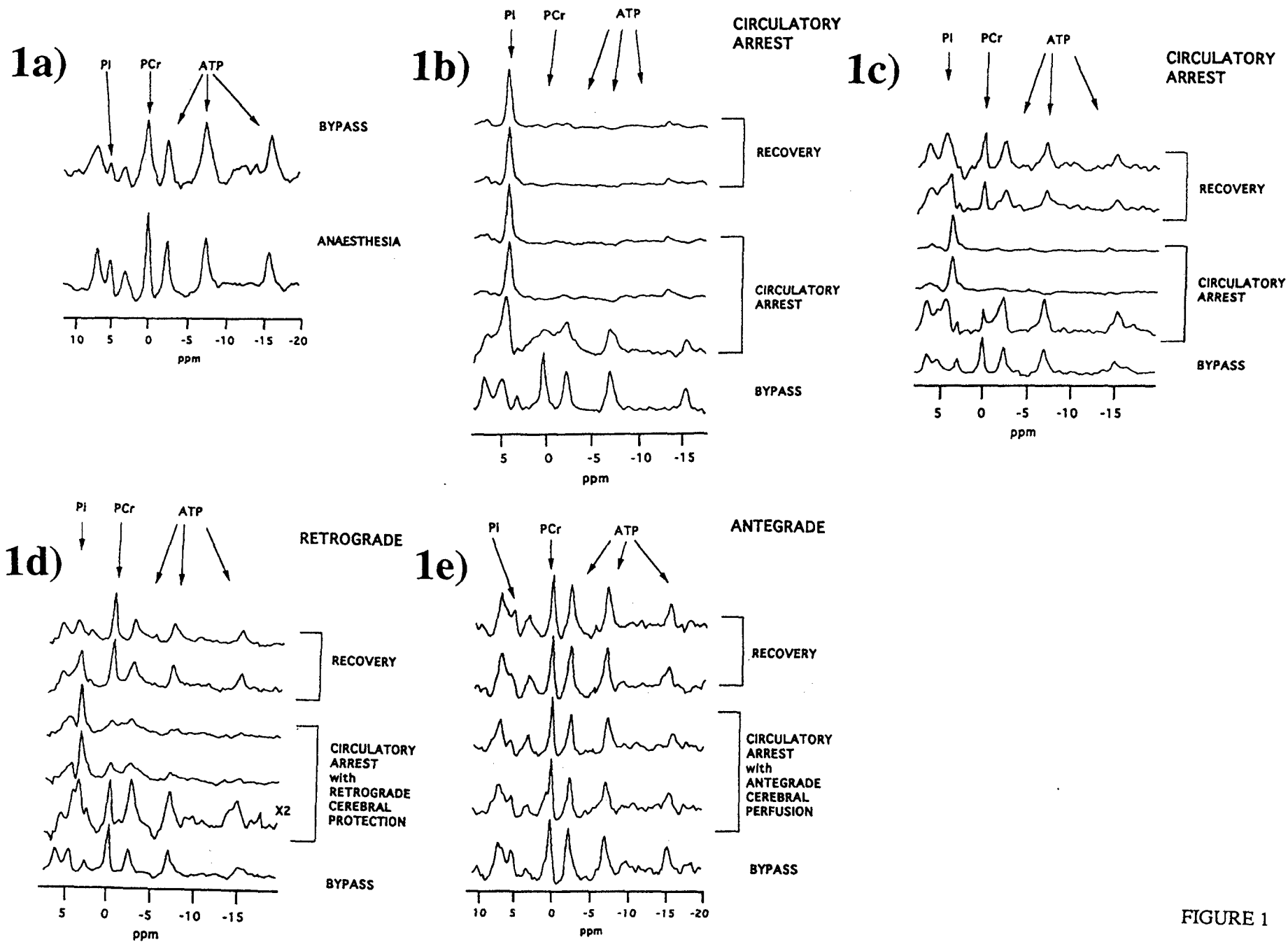


FIGURE 1

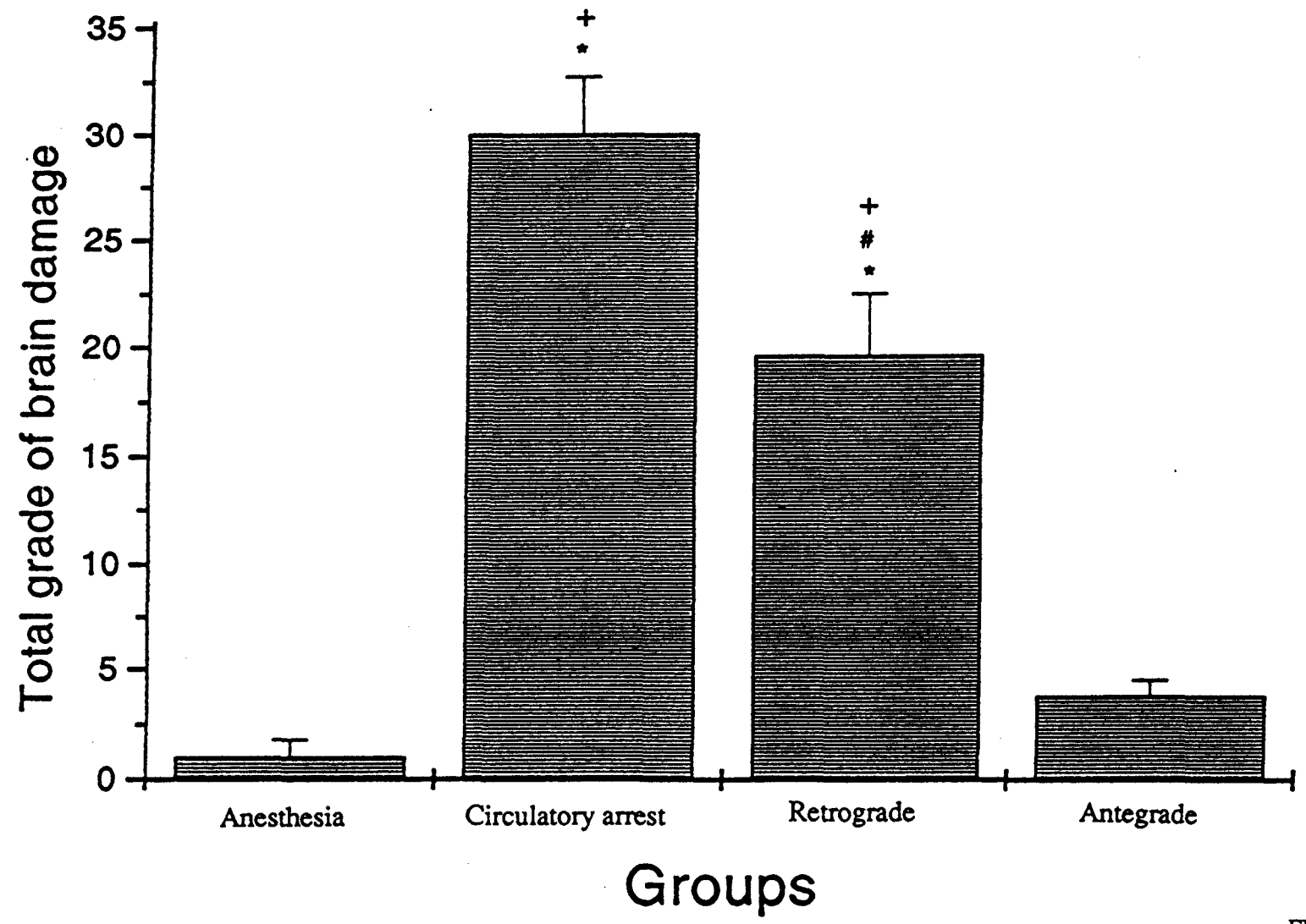


FIGURE 2

Applications of Intermolecular Multiple-Quantum Coherences in Solution NMR

Warren S. Warren, Department of Chemistry, Princeton University, Princeton, NJ 08544

In a wide variety of two-dimensional solution NMR experiments, samples with at least one concentrated component (such as proteins in water) show anomalous cross-peaks and additional resonances in the indirectly detected dimension.^{1,2,3,4,5,6,7} Perhaps the most striking example is the CRAZED sequence, which is a COSY sequence modified to include an N-quantum coherence transfer echo around the second radiofrequency pulse; it can be readily shown to give no signal in the conventional NMR framework⁸. Instead, if at least one sample component is concentrated, one observes strong peaks in the indirectly detected dimension which have *all* of the experimental properties of N-quantum coherences between independent molecules¹. Peaks appear at multiples of the resonance frequency of the concentrated component(s), and at combinations of the frequencies of concentrated and dilute component(s); these peaks behave exactly as multiple-quantum coherences would if pulses are phase shifted; they decay in exactly the expected manner due to diffusion in a gradient. These extra peaks can have >10% of the intensity of the diagonal peaks in a normal COSY experiment.

Such experiments have attracted recent theoretical attention, in those papers and in work from other groups.^{9,10,11} We have published two fundamentally different approaches (which we will call the classical and quantum models) to understanding the presence of these additional peaks. The classical model uses modified Bloch equations¹ including the dipolar demagnetizing field, which was originally introduced^{12,13} to explain the existence of multiple echoes in concentrated solutions—first in ³He and recently in more conventional samples such as pure water^{14,15,16}. References [10] and [11] use this same approach to describe sequences which do not contain gradient pulses, viewing these effects primarily as due to variations in the magnetic susceptibility as the direction of the

magnetization changes. Bowden's work⁹ uses *exactly* the same framework as reference [1], but expresses the results in terms of spatial frequencies rather than times. We have recently uncovered an omission in the original formulation of the demagnetizing field (for samples with both modulated and unmodulated magnetization), which leads to a "corrected classical" model¹⁷.

Unfortunately, the modified Bloch equations are nonlinear, hence they produce propagators which depend explicitly on the initial state of the spins. As a result, virtually none of the propagator-based tools commonly used to analyse NMR experiments are valid. These limitations led to development of a quantum (density matrix) model^{2,18} which reintroduces linear equations of motion and shows that the extra frequencies do indeed correspond to evolution of multiple-quantum coherences involving spins on separated molecules.

This paper summarizes our recent work about the corrected classical and quantum models of these effects, and addresses some of the questions we frequently get asked about them (including possible applications). We believe there are two important reasons for examining the theory carefully. For many existing experiments, these additional peaks are at best a nuisance, and at worst could be misinterpreted as intermolecular cross peaks; thus it is helpful to understand when they are expected to occur and how they can be eliminated. In addition, these intermolecular coherences permit several entirely new classes of experiments. We will discuss two applications which look particularly promising to us (imaging and removal of inhomogeneous broadening) at the end.

What is needed in the density matrix framework to describe these effects?

The density matrix framework, which has of course been very successful in describing modern NMR experiments, can also be used

to predict intermolecular multiple-quantum coherences in solution if two modifications are made^{2,18}. First, the assumption that all dipolar couplings between spins can be ignored must be modified. The dipole-dipole coupling between spins i and j is proportional to $(3 \cos^2 \theta_{ij} - 1)/r_{ij}^3$, where θ_{ij} is the angle between the internuclear vector and the applied magnetic field. For small values of r_{ij} , θ_{ij} takes all possible values owing to diffusion, and the dipolar coupling is averaged away. However, this averaging cannot occur for spins separated by more than the distance molecules diffuse on an NMR timescale ($\approx 10 \mu\text{m}$ for small molecules). Thus the full dipolar Hamiltonian has to be retained for distant pairs of spins. The retained individual dipolar couplings are very small, but the total number of coupled spins is very large, and if the spatial distribution of the magnetization is made nonuniform (by gradient pulses or even by edge effects) dipolar effects reappear. For fully modulated magnetization, the magnitude of the residual dipolar field is approximately $\gamma \mu_0 M_0$, which for water at room temperature in a 600 MHz spectrometer is approximately $14 \text{ rad}\cdot\text{s}^{-1}$.

The other needed modification is to remove the high temperature approximation to the equilibrium density matrix ρ_{eq} . Including only the Zeeman Hamiltonian, ρ_{eq} is:

$$\rho_{eq} = \frac{\exp(-\mathcal{H}/kT)}{\text{Tr}\{\exp(-\mathcal{H}/kT)\}} = \frac{\exp(-\hbar \sum_i \omega_0 I_{zi}/kT)}{\text{Tr}\{\exp(-\mathcal{H}/kT)\}}$$

$$= \frac{\prod_i \exp(-\hbar \omega_0 I_{zi}/kT)}{\text{Tr}\{\exp(-\mathcal{H}/kT)\}} \quad [1]$$

To evaluate the partition function $\text{Tr}\{\exp(-\mathcal{H}/kT)\}$ explicitly, note that, for an N spin system, the number of states with $M \equiv N_+ - N_- \ll N$ more spins up than down satisfies a binomial distribution, which for this large number of spins is almost exactly a Gaussian:

$$P(M) dM = \exp(-M^2/2N) dM / (\sqrt{2\pi N}) \quad [2]$$

The Zeeman energy of a state with M more spins up than down is $M\hbar\omega_0/2$; the number of states within a range dM is the total number (2^N) times $P(M) dM$. The partition function is then

$$\text{Tr}\{\exp(-\mathcal{H}/kT)\}$$

$$= 2^N (2\pi N)^{-1/2} \int_{-N}^N e^{-M\hbar\omega_0/2kT} e^{-M^2/2N} dM$$

$$= 2^N \exp(N(\hbar\omega_0/kT)^2/8) \quad [3]$$

$$\text{hence } \rho_{eq} = 2^{-N} \frac{\exp(-\hbar \sum_i \omega_0 I_{zi}/kT)}{\exp(N(\hbar\omega_0/kT)^2/8)} \quad [4]$$

The high temperature approximation expands the sum in eq. [1] as a Taylor series. Truncating after the term proportional to $\hbar\omega_0/kT$ and normalizing so that $\text{Tr}\{\rho_{eq}^{HT}\} = 1$ gives:

$$\rho_{eq}^{HT} = 2^{-N} \left(1 - \frac{\hbar\omega_0}{kT} \sum_i I_{zi} \right) \quad [5]$$

since the operators I_{zi} are traceless. If the expansion neglected only small terms, the normalization constants would be the same; instead, for a macroscopic sample the ratio ($\exp(N(\hbar\omega_0/kT)^2/8)$) is enormous (on the order of $\exp(10^{13})$).

In ρ_{eq}^{HT} , each of the spin eigenstates with nearly the equilibrium magnetization $M = -N\hbar\omega_0/2kT \approx -2 \times 10^{18}$ (for 4×10^{22} spins) has 10^{14} more population than does each state with $M=0$; however, from equation (2), there are about $\exp(5 \times 10^{13})$ more states with $M=0$ than with $M = -N\hbar\omega_0/2kT$. Thus states within a few standard deviations $\sigma = \sqrt{N}$ of $M=0$ (which have little bulk magnetization) overwhelmingly dominate the population distribution.

In the *correct* equilibrium density matrix ρ_{eq} , each of the spin eigenstates with nearly the equilibrium magnetization has $\exp(10^{14})$ more population than does each

state with $M \approx 0$. The ratio of states with $M \approx 0$ to states with equilibrium magnetization is of course the same, so now there is $\exp(5 \times 10^{13})$ more population with equilibrium magnetization than with no magnetization, and states within a few standard deviations $\sigma = \sqrt{N}$ of the equilibrium magnetization dominate the distribution.

In summary, the high temperature approximation to the density matrix for N coupled spins saves only a nearly infinitesimal part of the full equilibrium density matrix. Fortunately, in the absence of a very large number ($\approx 10^4$) of comparably sized couplings to other spins, the higher order terms cannot be translated into observable magnetization, which is why this approximation has worked so well until our work^{1,2} (although others have questioned its validity as well, see for example Appendix E of Slichter's book).

It turns out to be useful to decompose ρ_{eq} in a somewhat different manner than the Taylor series, explicitly separating the different N -spin operators. We do this by constructing basis functions as direct products of the eigenfunctions of individual spins. It is then straightforward to show that

$$\exp\left(-\frac{\hbar\omega_0}{kT} I_{zi}\right) = \cosh\left(\frac{\hbar\omega_0}{2kT}\right) \mathbf{1} - 2 \sinh\left(\frac{\hbar\omega_0}{2kT}\right) I_{zi};$$

$$\text{Tr} \left\{ \prod_i \exp\left(-\frac{\hbar\omega_0}{kT} I_{zi}\right) \right\} = 2^N \cosh^N\left(\frac{\hbar\omega_0}{2kT}\right).$$

[5]

Thus the equilibrium density matrix can be written as

$$\rho_{eq} = 2^{-N} \prod_i (1 - \mathfrak{S} I_{zi}), \text{ where } \mathfrak{S} = 2 \tanh\left(\frac{\hbar\omega_0}{2kT}\right).$$

[6]

We have recently used equation [6] to generate exact expressions for the signal from a CRAZED sequence¹⁸, and from a variety of other simple pulse sequences.

Incidentally, even the high temperature version of the density matrix includes

multispin terms if more than the Zeeman Hamiltonian \mathcal{H}_Z is included; in very low fields, this leads to effects such as quadrupolar order.¹⁹ However, that is not the origin of the effects we see. Retaining only the J couplings (and ignoring the dipolar interactions we consider) predicts signals with about 10^{-8} of the total magnetization²⁰ with the high temperature approximation, or about 10^{-4} of the magnetization without the high temperature approximation.²¹

In a 600 MHz NMR spectrometer the dipolar Hamiltonian \mathcal{H}_d , even in a solid, generates splittings between spin states which are typically only 10^{-4} of the Zeeman Hamiltonian; in solution, the residual dipolar effects after diffusional averaging generate splittings which are reduced by a further four orders of magnitude. Keeping the high temperature approximation but adding the secular part of \mathcal{H}_d to the equilibrium density matrix is thus expected to produce potentially observable signals which are on the order of 10^{-8} of the normal magnetization; Jeener and coworkers²² have recently verified this expectation with a more detailed calculation.

Our experimental observations^{1,2} give signals which are far larger—on the order of 15% of the normal magnetization. As a result, the dipolar couplings are unimportant in evaluation of the equilibrium density matrix (although not in the time evolution- J couplings of similar magnitude profoundly alter two-dimensional spectra). As we showed in reference [2], retaining the long-range dipolar couplings and removing the high temperature approximation does predict signals this large for short values of t_2 , and the extensions in reference [18] give essentially quantitative agreement with experiment. If either of these changes to the standard picture is omitted, the predicted signal falls by orders of magnitude.

Is it possible to understand these effects using only modified Bloch equations?

Reference [12] analysed multiple echoes in ^3He by introducing the "dipolar

demagnetizing field" \mathbf{B}_d , which is just the local field seen by each spin due to its dipolar coupling with all of the other spins in the sample. In general \mathbf{B}_d is inhomogeneous and shape-dependent. However, if the magnetization $\mathbf{M}(\mathbf{r})$ varies only in a single direction s (as can happen if gradient pulses are only applied in a single direction), Fourier transformation back into the spatial domain creates a local relation involving the single tensor component \underline{C}_k , and $\mathbf{B}_d(\mathbf{r})$ will depend only on $\mathbf{r} \cdot \hat{s} \equiv s$:

$$\mathbf{B}_d(s) = \mu_0(\Delta M_z(s) \hat{z} - \frac{1}{3} \Delta \mathbf{M}(s));$$

$$\Delta = [3(\hat{s} \cdot \hat{z})^2 - 1]/2 \quad [7]$$

This field is then added into the normal Bloch equations, giving an additional contribution $\gamma(\mathbf{M} \times \mathbf{B}_d)$ to $d\mathbf{M}/dt$. We showed in reference [2] that this approach gives qualitative agreement with the simplest experiments, at the expense of introducing nonlinearity into the equations of motion. With these equations, the concept of a propagator which describes the effect of a pulse sequence and which is independent of the initial condition is lost; the rotation generated by any pulse sequence depends explicitly on the initial condition. A simple equation of motion can easily hide complicated dynamics (in fact, the dipolar demagnetizing field Bloch equations can actually predict chaotic dynamics).

We show in reference [17] that the expression for \mathbf{B}_d in equation [7] is not correct in the case where the magnetization is not fully modulated. For a spherical sample, a corrected version would be

$$\mathbf{B}_d(s) \approx \mu_0 \Delta \{ (M_z(s) - \langle M_z \rangle) \hat{z} - \frac{1}{3} [(\mathbf{M}(s)) - \langle \mathbf{M} \rangle] \}$$

[8]

These additional corrections can dramatically alter the dynamics, particularly for complex sequences.

What is the relation between the classical and quantum pictures?

The *corrected* classical picture (with the modified version of the demagnetizing field, equation [8]) and the quantum picture are equivalent under the following assumptions¹⁸:

- A. Diffusional effects cause spins to move sufficiently that sums over dipolar coupled spins can be replaced by an integral;
- B. Diffusion is isotropic over short distances in the sample, so the *lower* limit (but not necessarily the upper limit) of the integral reflecting the interaction of any one spin with all other spins is spherically symmetric;
- C. When we explicitly calculate the evolution of M-spin operators in a sample with N spins, we assume $M \ll N$.
- D. For each retained dipolar coupling D_{ij} , and for any time t of interest in calculating the time evolution, $D_{ij} t \ll 1$.

The most important of these assumptions is that $D_{ij} t \ll 1$, which is clearly not satisfied for a solid, but is satisfied very well for the dipolar couplings which survive diffusional averaging in an isotropic liquid. If we assume a relaxation time of 1 s as an approximate upper limit for T , then (since $|D_{ij}| \approx 1 \text{ rad} \cdot \text{s}^{-1}$ when $r = 10 \text{ nm}$) we merely need to have molecules diffuse much more than 10 nm in 1 s, which is satisfied even for large macromolecules. In an anisotropic liquid, such as a liquid crystal, the assumption of isotropic diffusion can also be violated.

The equivalence of the corrected classical and quantum pictures described above is very useful for understanding the experimental consequences of the dipolar demagnetizing field, because the two approaches have different strengths. The corrected classical picture can readily incorporate effects such as radiation damping and diffusion, which are quite painful to include in a full quantum treatment. Radiation damping is particularly important if the magnetization is not fully modulated, since for a normal sized sample the characteristic radiation damping time $\tau_r =$

$((\eta Q/2)\gamma\mu_0 M_0)^{-1}$ is far shorter than $\tau_d = (\gamma\mu_0 M_0)^{-1}$. In fact, CRAZED sequences create a large enough signal that radiation damping has significant effects, even if the magnetization is initially fully modulated.¹⁷

On the other hand, the corrected classical picture gives essentially no intuition for pulse sequence design when the magnetization is modulated, because the nonlinearities in the Bloch equations remove the concept of a propagator as noted earlier. The quantum picture is much more intuitive, particularly in the limit where only the first few terms of the equilibrium density matrix are needed. The quantum picture explains why the unexpected peaks have all of the properties associated with multiple-quantum coherences (for example, the expected behavior due to phase shifts or diffusion). They *are* multiple-quantum coherences by the conventional definition (they are off-diagonal matrix elements between eigenstates of the spin Hamiltonian), which in this case originate from higher order terms in the initial density matrix. The quantum picture also explains a large number of experimental observations, some of which are essentially at the "folklore level" among biological NMR spectroscopists.

What are the applications of these effects?

Elimination of these peaks, in order to remove the possibility of misassignment of cross-peaks to intramolecular NOEs (for example) is readily done with magic angle gradients^{2,6,14,23,24}. In addition, the density matrix picture reveals a range of new applications.

1. We have shown that the intensity of the CRAZED intermolecular double-quantum coherence is a sensitive probe of the two-body correlation function over a distance determined by the strength and length of the gradient pulses. The gradients wind magnetization into a helix; most of the signal comes from spins separated by about one-half of the helix repeat length (typically 10-1000

μm). For example, we generated or suppressed cross-peaks between molecules in separated tubes by adjusting the strength of the gradient. This could lead to an imaging method which complements existing techniques.

2. As another example, consider the zero-quantum CRAZED experiment $((\pi/2)_x - t_1 - \text{gradient} - (\pi/2)_x - t_2)$. It is found both theoretically and experimentally that this sequence produces only very weak zero-quantum peaks between equivalent spins. The quantum treatment also predicts this, but immediately shows the reason why this is so and the solution to the problem. Starting from the \mathfrak{S}^2 term in the equilibrium density matrix, the only zero-quantum term in t_1 which survives spatial averaging has the form $|x_i| |x_j| + |y_i| |y_j|$; and the second $\pi/2$ pulse does not project this onto one-quantum operators. Replacing the second pulse with a $\pi/4$ pulse makes these coherences observable¹. We have recently used modified versions of this sequence to produce spectra which retain full chemical shift and J coupling information, while suppressing inhomogeneous broadening²⁵.

This work is supported by the NIH under grant GM35253.

References

- ¹Q. He, W. Richter, S. Vathyam and W. S. Warren, *J. Chem. Phys.* **98**, 6779(1993)
- ²W. S. Warren, W. Richter, A. H. Andreotti and S. Farmer, *Science* **262**, 2005(1993)
- ³Wolfgang Richter, Sanghyuk Lee, Warren S. Warren, and Qihong He, *Science* **267**, 654(1995)
- ⁴M. McCoy and W.S. Warren, *J. Chem. Phys.* **96**, 858 (1990).
- ⁵W. S. Warren, Qihong He, M. McCoy, F. C. Spano, *J. Chem. Phys.* **96**, 1659(1992).
- ⁶Debra L. Mattiello, Gaetano T. Montelione, Luciano Mueller, Warren S. Warren and Bennett T. Farmer II, presented at the Experimental NMR Conference, Boston, March 1995; D. L. Mattiello, W. S. Warren, L. Mueller and B. T. Farmer II, *J. Am. Chem. Soc.* (submitted)

- ⁷K. Zilm, presented at the March 1994 American Physical Society meeting, Pittsburg, PA; M. Augustine and K. Zilm, *J. Mag. Reson.* (in press)
- ⁸See, for example, R. R. Ernst, G. Bodenhausen and A. Wokaun, Principles of Nuclear Magnetic Resonance in One and Two Dimensions (Clarendon Press, Oxford, 1987)
- ⁹C. J. Bowden, T. Heseltine and M. J. Prandolini, *Chem. Phys. Lett.* 233, 639(1995)
- ¹⁰J. Jeener, A. Vlassenbroek and P. Broekaert, *J. Chem. Phys.* (submitted)
- ¹¹M. Levitt, *Concepts in Magnetic Resonance* (in press)
- ¹²G. Deville, M. Bernier and J. M. Delrieux, *Phys. Rev. B* 19, 5666(1979).
- ¹³D. Einzel, G. Eska, Y. Hirayoshi, T. Kopp and P. Wölfle, *Phys. Rev. Lett.* 53, 2312 (1984).
- ¹⁴R. Bowtell, R. M. Bowley and P. Glover, *J. Mag. Res.* 88, 643 (1990).
- ¹⁵H. Körber, E. Dormann and G. Eska, *J. Mag. Res.* 93, 589 (1991).
- ¹⁶A. S. Bedford, R. Bowtell and R. M. Bowley, *J. Mag. Res.* 88, 517 (1991).
- ¹⁷W. S. Warren, S. Lee, W. Richter and S. Vathyam, *Chem. Phys. Lett.* (in press)
- ¹⁸S. Lee, W. Richter, S. Vathyam and W. S. Warren, *J. Chem. Phys.* (submitted)
- ¹⁹A. Abragam, The Principles of Nuclear Magnetism (Clarendon Press, Oxford, 1961); A. Abragam and M. Goldman, Nuclear magnetism: Order and Disorder (Clarendon Press, Oxford, 1982)
- ²⁰M. Ravikumar and A. Sheth, *Chem. Phys. Lett.* 126, 352 (1986); M. Ravikumar, *Chem. Phys. Lett.* 144, 521 (1988)
- ²¹J. Courtieu, N. T. Lai and L. Werbelow, *Chem. Phys. Lett.* 140, 565 (1987)
- ²²J. Jeener, private communication; J. Jeener, A. Vlassenbroek and P. Broekaert, *J. Chem. Phys.* (in press)
- ²³W. S. Warren and W. Richter, "Concentrated Solution Effects", *Encyclopedia of Magnetic Resonance* (in press)
- ²⁴P. C. M. van Zijl, M. O. Johnson, S. Morri and R. E. Hurd, *J. Magn. Reson.* A113, 265 (1995)
- ²⁵S. Vathyam, S. Lee and W. S. Warren, *Science* (submitted)

DROPLET SIZE EVOLUTION IN DISPERSE SYSTEMS BY NMR.

I. Scheurmann,

Departamento de Ingeniería General, INTEVEP, S.A.,
Apartado Postal 76343, Caracas 1070A, Venezuela

M. Martín-Landrove

Centro de Resonancia Magnética, Facultad de Ciencias, Universidad Central de Venezuela,
Apartado Postal 47586, Caracas 1041A, Venezuela.

and

J. Espidel

Departamento de Análisis y Evaluación, INTEVEP, S.A.,
Caracas, Venezuela.

Introduction.

Exchange of magnetic nuclei between two chemically shifted sites leads to a broadening and coalescence of the lines when the exchange rate is of the same order of magnitude as the difference in resonance frequencies at the two sites, i.e., the relaxation rate is increased [1].

This phenomenon induces a dispersion in the transversal relaxation rate when a Carr-Purcell-Meiboom-Gill (CPMG) experiment is performed in heterogeneous systems such as protein solutions [2,3,4] and sedimentary rocks [5], and it is dependent on the delay time between r.f. pulses used during the experiment. The effect becomes particularly strong when the delay time is comparable to the characteristic time of the exchange process.

In the present work, CPMG experiments were performed on xylene/water emulsions at 90, 270, 300 and 400 MHz for different droplet sizes. A strong dispersion of the transversal relaxation rate was obtained, particularly at 300 MHz. The results suggest that some exchange between the interior and exterior of xylene droplets or with the surfactant molecules is taking place. It was also observed that

the relaxation rate dispersion was dependent on the droplet size distribution, an effect that could be used to study coalescence and flocculation processes.

Materials and Methods.

Xylene/water emulsions were prepared with a composition of approximately 70 % xylene, 30 % water and less than 0.5 % surfactant. The initial droplet size was about 10 μm and evolved slowly up to a mean value of about 80 μm . The preparation was stored in a bottle under appropriate temperature conditions to assure the stability and equilibrium of the resulting phases. Due to the slow evolution of the droplet size, nmr measurements were performed at least 6 months after emulsion preparation.

Three characteristic zones were observed in the preparation bottle:

Zone 1: On the top of the bottle, about 2/3 of the preparation volume with a white color and rich in xylene droplets of small size usually denoted as creamy phase.

Zone 2: A very narrow band located in the middle of the bottle with a bright white color and a droplet size smaller than in Zone 1.

Zone 3: In the bottom of the bottle, about 1/3 of the preparation volume with turbid appearance. This zone is rich in water and the droplet size is the biggest in the preparation bottle.

The droplet size distributions for each zone were measured with a Malvern instrument and were determined each time the nmr samples were taken. High resolution ^1H nmr spectra were obtained for each sample at 270 MHz using a JEOL spectrometer and at 400 MHz using a BRUKER ACP400 spectrometer. The CPMG experiments were performed in a BRUKER CXP100 spectrometer at 90 MHz and a BRUKER MSL300 at 300 MHz, both of them operating in the External Address Advance Mode to obtain the echo envelope directly and covering a r.f. pulsation frequency range of 10^2 - 2.10^3 Hz and 10 - 3.10^3 Hz respectively. For this type of experiments, three samples were taken:

Mixed sample: Obtained by mixing slowly the three zones in the preparation bottle and measured at 300 MHz.

Creamy Phase sample: Taken from Zone 1 and measured at 90 MHz.

Turbid Phase sample: Obtained from Zone 3 and measured at 90 MHz.

The relaxation data were analyzed by to different methods: Non Linear Regression Analysis (NLRA) and Inverse Laplace Transform (ILT) [6]. This methodology was carried out since the relaxation data showed a clear non exponential behavior in correspondence to the expectation of different relaxation environments due to the heterogeneity of droplet sizes. Among these two methods, ILT was the most reliable since no particular assumptions were carried out about the functional dependence of the relaxation decay.

Experimental Results and Discussion.

The droplet sizes covered a range among 37-98 μm as shown in Table 1, which summarizes the results of the Malvern measurements. According to Table 1, there are two well defined droplet sizes in Zone 1, nearly resolved as two peaks in the extremely broad droplet size distribution, with a mean size of 91.35 μm , in Zone 2 the distribution

has a mean size value of 29.73 μm and for Zone 3, the mean size value is 66.80 μm . For the mixed sample, the droplet size distribution is more symmetric and has mean size value of 45.83 μm . High resolution ^1H nmr experiments showed a certain dependence of the spectra on the droplet size distributions, even for the water and xylene proton resonances. Table 2 shows some of the relevant information of the ^1H nmr spectra according to the mean and width of the droplet size distributions.

Table 1. Malvern measurements data

Sample	Size D (μm)	D (90%) (μm)	D (10%) (μm)
Zone 1 Creamy Phase	91.35	171.57	30.36
Zone 2	29.73	65.52	11.71
Zone 3 Turbid Phase	66.80	106.41	36.95
Mixed	45.83	109.91	20.93

Table 2. High resolution ^1H nmr data at 400 MHz

Sample	Size (μm)	Width (μm)	Water (ppm)	Xilene (ppm)
Zone 1 Creamy Phase	91.35	141.21	5.69	1.58-2.91 7.28-7.46
Zone 2	29.73	53.81	5.38	2.30-3.00 6.65-7.20
Zone 3 Turbid Phase	66.80	69.46	5.30	3.40-4.45 5.81-6.14
Mixed	45.83	88.98	5.34	1.50-2.51 7.20-7.34

The relaxation data obtained from CPMG experiments showed a non exponential behavior, particularly for the 300 MHz data for which up to 5 components have to be added to fit by NLRA the decay curve. In Figure 1, the mean transversal relaxation rate obtained by NLRA, is represented for the mixed sample. As can be seen from the Figure, the relaxation rate dispersion is relatively high and abrupt, with a step of about 2 s^{-1} for a delay time of 1 ms. For delay times longer than 50 ms, there is a

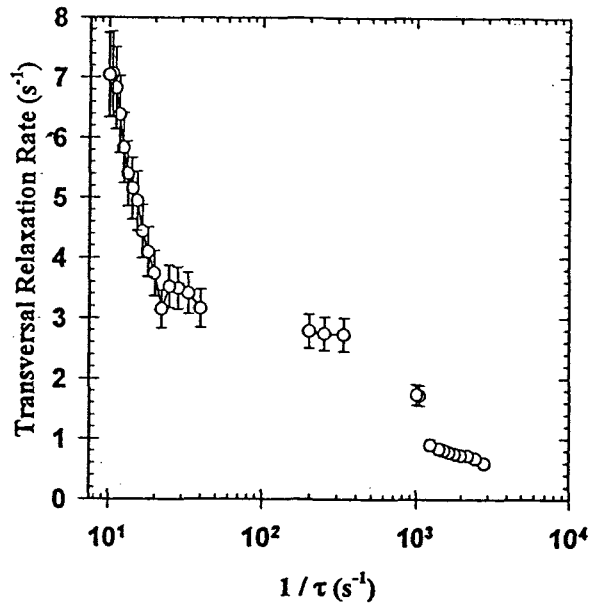


Figure 1. Mean transversal relaxation rate as a function of r.f. pulsation rate for the mixed sample, measured at 300 MHz.

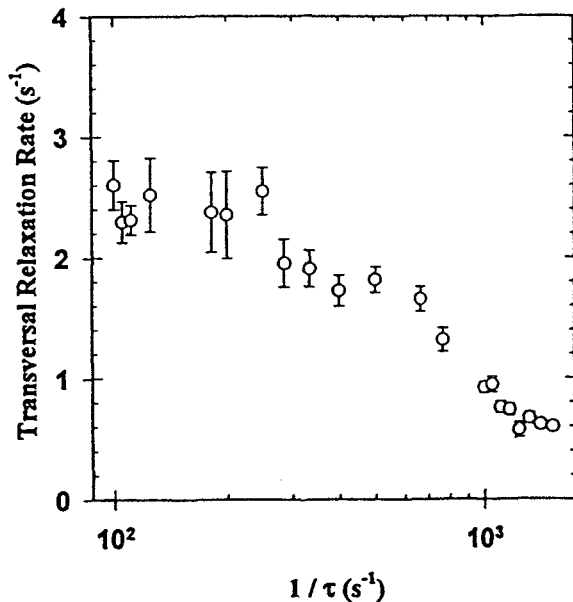


Figure 2a. Mean transversal relaxation rate as a function of the r.f. pulsation rate for the creamy phase sample, measured at 90 MHz.

continuous increase in the relaxation rate. In Figure 2a, the mean relaxation rate at 90 MHz for the creamy phase sample is shown, which also exhibits a

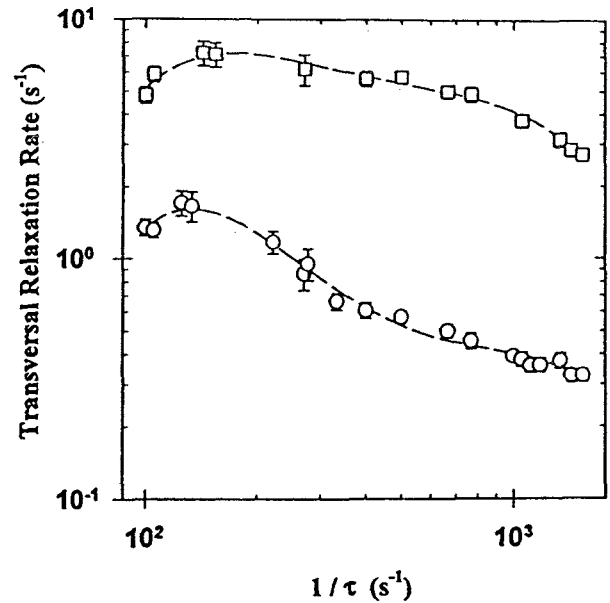


Figure 2b. Non linear regression analysis decomposition of transversal relaxation rate shown in Figure 2a.

dispersion characterized by a step nearly at 1 ms, but for this case, the step is smaller and less abrupt, it occurs within a delay time range of 700 μ s - 1.5 ms and a step size of 0.8 s^{-1} . Since for this type of sample there are two clearly distinct droplet sizes covering a wide range of sizes in the emulsion, it is reasonable to suppose that the relaxation decay can be decomposed into two exponentials, corresponding each one to a different droplet size. The decomposition was obtained by NLRA and it is shown in Figure 2b. Also, ILT was performed upon the relaxation decay data and the result is shown in Figure 3. Both results, Figure 2b and Figure 3, support the assumption that different relaxation rates could be assigned to different droplet sizes. Also from Figure 3, some additional information can be extracted concerning the behavior of the individual relaxation rate distributions as the delay time in a CPMG sequence is varied, for example the width of each distribution increases as the r.f. pulse delay time is reduced, a result which is consistent with the fact that some relaxation channels are not mixed by the exchange process during the delay time and so different relaxation rates are present; when the delay time is long enough, a common relaxation rate, and consequently a narrow distribution width could be

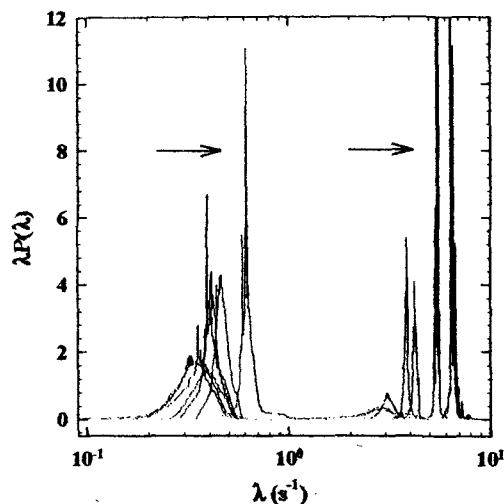


Figure 3. Relaxation rate distributions for the creamy phase sample, measured at 90 MHz. The r.f. delay time covers a range from 650 μ s to 1.5 ms. The arrows indicate the progression of the data.

observed. The transition from slow to fast exchange rates for different molecular processes can also be traced similarly. It can be concluded that ILT gives all the information that is important to describe the system. Nevertheless, there are always some drawbacks, since to apply ILT properly, the

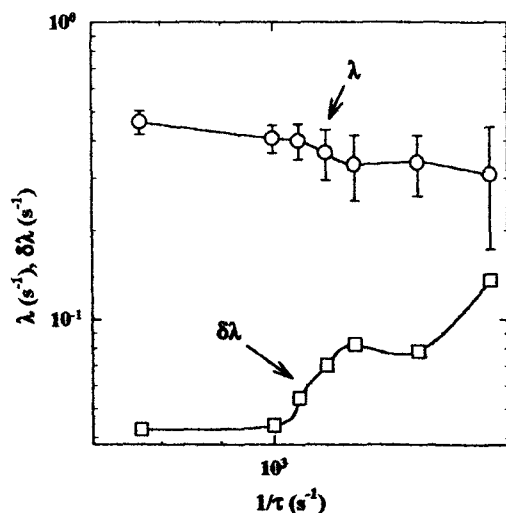


Figure 4. Mean relaxation rate and relaxation rate distribution width for the low relaxation rate component of Figure 3.

magnetization decay has to be sampled completely, with enough points and with a high signal to noise ratio. In the case of a short delay time this requirement implies the application of a high number or r.f. π pulses, which in many cases causes serious damage in the transmitter and for long delay times, not so many points are obtained so the ILT is highly deformed. In general this method could be applied within a certain range of pulsation rates, depending of the kind of equipment available. In the present work, the observation range was between 650 μ s up to 10 ms. In Figure 4, the calculated mean relaxation rate and the distribution width for the low relaxation rate component are shown. The curves represent the progression of the data and not a fitting of the calculated points. The evolution of the mean relaxation rate or the relaxation rate distribution width with the r.f. delay time suggests the possibility of using them to characterize the exchange of protons for a particular droplet size. For the present system two different models can be proposed to describe the exchange process: Exchange between hydration water protons and surfactant protons and exchange of water molecules across the surfactant film of the xylene droplet and this type of measurement could complement the information that is obtained by high resolution ^1H nmr experiments [7].

The results obtained in this work open the possibility of using a relatively simple experimental methodology such as Carr-Purcell-Meiboom-Gill to study proton exchange processes in disperse systems. Nevertheless, theoretical models to describe the experimental evidence related to those exchange processes are needed, a task that we are going to accomplish in a near future.

Acknowledgments.

This work was partially supported by INTEVEP, S.A. and the Centro de Resonancia Magnética, Facultad de Ciencias, Universidad Central de Venezuela.

References.

[1] Harris R.K., Nuclear Magnetic Resonance Spectroscopy, A Physicochemical View; Pitman: London, 1983.

[2] Hills B.P., Takacs S.F. and Belton P.S., Molecular Physics, 67, 903 (1989).

[3] Hills B.P., Takacs S.F. and Belton P.S., Molecular Physics, 67, 919 (1989).

[4] Hills B.P., Molecular Physics, 76, 509 (1992).

[5] Kleinberg R.L., Straley C., Kenyon W.E., Akkurt R. and Farooqui S.A., SPE 26470, 553 (1993).

[6] Martin R., in preparation.

[7] Hey M.J. and Al-Sagheer F., Langmuir, 10, 1370 (1994).

High-sensitivity NMR spectroscopy probe using superconductive coils

W.A.Anderson¹, W.W.Brey², A.L.Brooke¹, B.Cole², K.A.Delin², L.F.Fuks²,
H.D.W.Hill¹, M.E.Johanson², V.Y.Kotsubo², R.Nast², R.S.Withers² and W.H.Wong².

¹ Varian NMR Instruments, 3120 Hansen Way, Palo Alto, CA 94304, USA

² Conductus Inc, 969 West Maude Avenue, Sunnyvale, CA 94086, USA

I. Introduction

Sensitivity has always been a limitation with NMR detection and much of the development in NMR instrumentation has been directed towards its improvement. A major advantage of the move to ever higher magnetic field strengths is the increased sensitivity brought about by the greater induced signal. An alternative approach to improving sensitivity is to reduce the noise associated with the detection. Reducing this noise is the motivation for considering a superconductor as a very low resistance coil material.

Thermal noise from the detection coil is often the dominant noise source in an NMR spectrometer. The idea of using a superconducting detection coil was first proposed by Rollwitz (1) but was not reduced to practice. A ¹³C probe using a cooled coil of a normal metal was constructed by Styles *et al* (2) and demonstrated a sensitivity gain of about three compared with a conventional probe. The development of high temperature superconducting (HTS) materials provides the impetus for new attempts to build practical probe systems with improved sensitivity. Black *et al* (3) have described an NMR imaging probe using these materials. This paper describes the application of HTS materials to a high resolution NMR probe.

A simple calculation shows that the potential

sensitivity gain can be large. For a given sample volume, the sensitivity of a coil is proportional to $\eta(Q/T)^{1/2}$, where η is the filling factor, Q is the quality factor and T is the temperature of the coil. A superconducting coil may have a Q of 20000 compared with 250 for a room temperature coil and operate at 25K rather than 300K. With the geometry appropriate for a 5mm sample tube and allowing for the loss of filling factor required for thermal isolation, the potential sensitivity gain can still approach a factor of ten.

II. Coil design

In addition to low resistance and low operating temperature, a cooled coil should possess other desirable characteristics. The temperature coefficient of the resonant frequency and the Q should be sufficiently small that stable operation can be obtained by normal temperature control techniques. For use in high resolution probes, the perturbation of the magnetic field due to the magnetic properties and geometry of the coil structures must be small. Finally, for use as a transmit coil in a pulsed spectrometer, the coil must be capable of carrying several amps of rf current. Some of these requirements may be more easily met with normal metals, but the benefits in terms of lower resistance of superconducting materials make the effort to use them worthwhile.

For this work, coils have been fabricated from the HTS material $\text{YBa}_2\text{Cu}_3\text{O}_{7,\delta}$ (YBCO) deposited as an epitaxial film between 300 and 650nm in thickness on a planar substrate. Substrates which have been used include lanthanum aluminate, sapphire and magnesium oxide. In the absence of a magnetic field, these films have a superconducting transition temperature of about 87K and have critical current densities of approximately $10^6\text{A}/\text{cm}^2$ at 77K. The films are patterned to form a resonant coil by standard lithographic techniques. A typical coil is shown in Fig.1. The dimensions have been chosen to provide an rf field volume similar to that of existing probe coils. The coil has an inductance of approximately 45nH and the interdigital capacitor on one of the sides provides a self resonant frequency of approximately 400MHz. Its unloaded Q as a function of temperature both in zero magnetic field and in a field of 11T (with the field parallel to the plane of the coil) is shown in Fig.2. This indicates that, for satisfactory use as a high Q coil, the operating temperature should be

considerably less than 77K.

Magnetic field perturbations are kept to a minimum by using as thin a film of superconductor as possible and by placing the coil as far from the sample as possible. This, of course, is in conflict with the desire to achieve a large filling factor, so some compromise is necessary. The geometry of surrounding structures are also chosen to minimize field perturbations.

The current carrying capability of the coils is measured in a transmission mode using an input coupling loop matched to the coil and an output loop very loosely coupled to the coil. At low power, the current in the coil is determined from the calculated inductance, the measured Q, and the measured input power. As the input power is increased, the coil exhibits significant non-linear effects until a limiting current is reached. For the coil of Fig.1, this corresponded to about 4A of rf current.

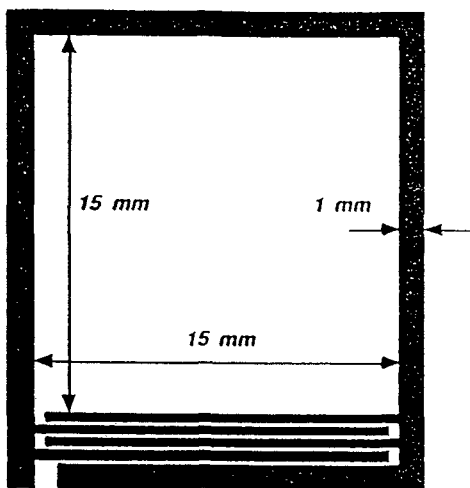


Figure 1. A typical coil pattern for a self resonant coil at approximately 400MHz.

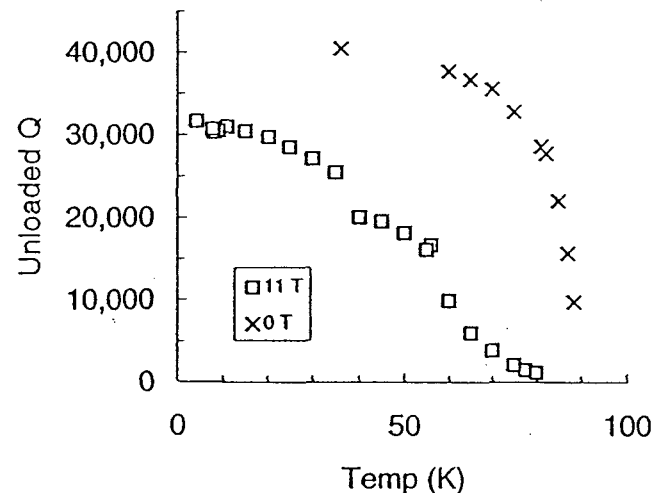


Figure 2. The unloaded Q as a function of temperature, for the coil shown in Figure 1, both in zero magnetic field and in a magnetic field of 11T.

III. A prototype 400MHz probe

A prototype high resolution NMR probe designed to observe proton resonances at 400MHz has been constructed using a pair of resonant coils placed symmetrically about the sample as shown schematically in Fig.3. The pair of coils form a magnetically coupled system. The coils are initially tuned by laser trimming of the interdigital capacitor fingers and finely tuned in the probe by adjustment of a conductive "paddle" close to one of the coils. Energy is coupled into and out of the system through a coupling loop adjacent to the other coil. Matching is adjusted by moving this coupling loop.

A second set of coils, orthogonal to the first, resonant at approximately 61MHz and tuned and matched by its own paddle and coupling loop, is used to provide a deuterium lock signal.

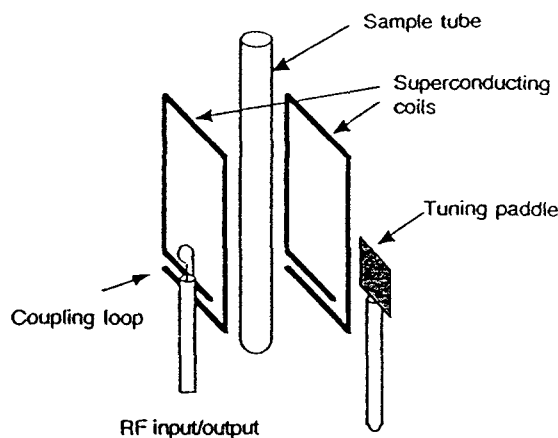


Figure 3. The schematic arrangement of superconducting coils, matching loop and tuning paddle in relation to the NMR sample.

The coils are cooled by flowing helium with the temperature regulated by a heater, thermometer and conventional feedback controller. The sample is isolated from the cold coils by a vacuum jacket and its temperature is controlled around room temperature by the standard variable temperature system of the NMR spectrometer. The probe interfaces to the normal bore equipment of a high resolution spectrometer so that sample insertion, spinning and ejection is the same as with a conventional probe.

The source of helium for cooling can either be from a pressurized liquid helium storage vessel in an open cycle configuration or by recirculating helium cooled by a closed cycle refrigerator. Either system provides stable operation at any temperature down to below 20K. Most of the work reported here was recorded with a coil temperature of 25K.

With greatly reduced noise from the probe, the preamplifier may become the dominant noise source in the system unless it, too, is improved. This is accomplished by using a GaAs FET preamplifier cooled in liquid nitrogen (4) to achieve a noise temperature of approximately 15K.

IV. Probe performance

To gauge the potential of the superconductive probe, its performance has been compared with the best that can be achieved by an optimized probe using conventional technology. In terms of sensitivity, the superconductive probe shows a gain of close to a factor of five. Fig.4 shows a spectrum from a single 90° pulse excitation of a spinning 5mm sample of 0.1% ethylbenzene in CDCl₃. The normal 1Hz line-broadening is used and the measured signal-to-noise ratio is more than 2250, compared with about 500 from an optimized normal probe at the same frequency.

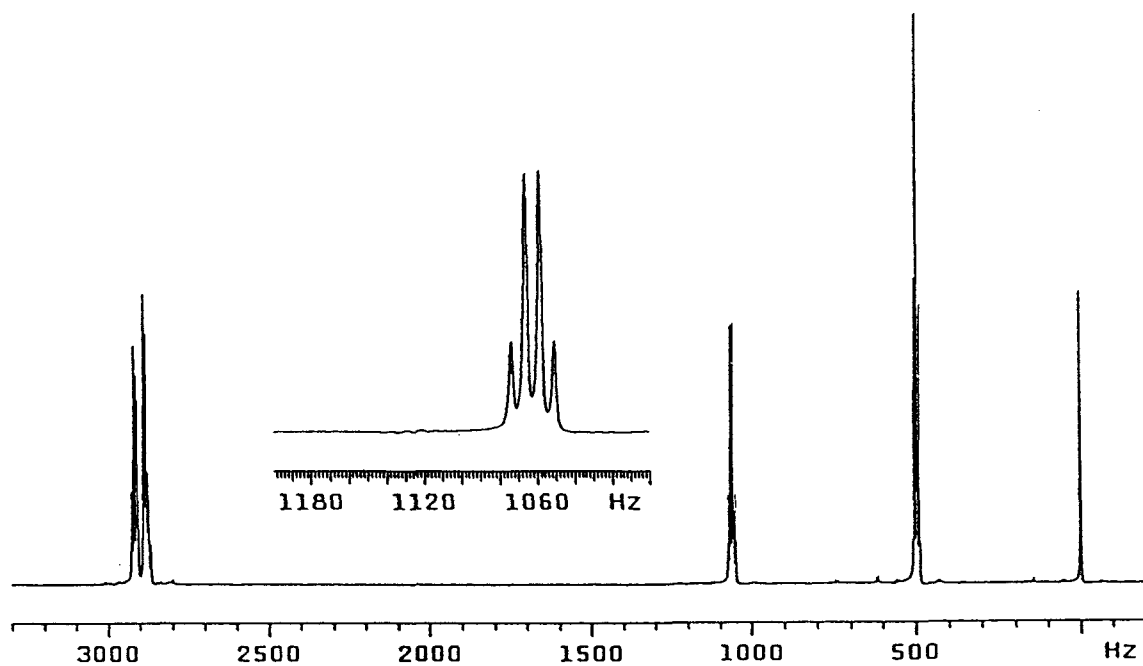


Figure 4. A 400MHz spectrum from a single 90° pulse excitation of 0.1%ethylbenzene in CDCl_3 . A line broadening of 1Hz was used and the measured signal-to-noise ratio is >2250 .

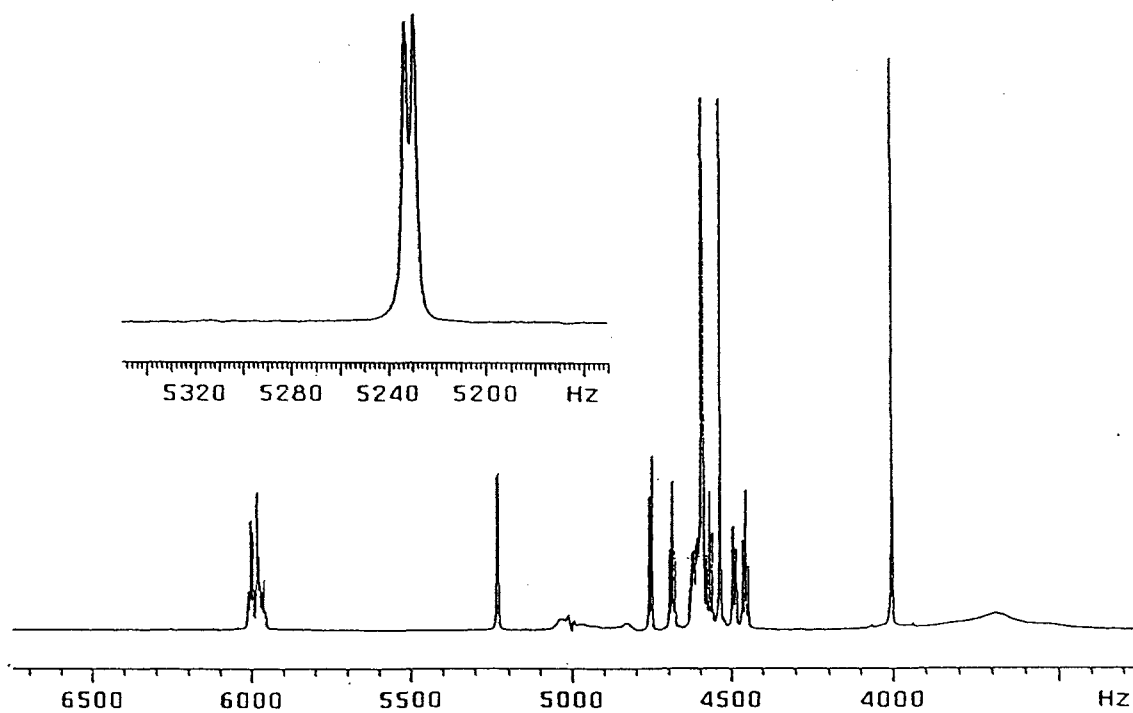


Figure 5. A spectrum from a non-spinning sample of $300\mu\text{g}$ sucrose in $600\mu\text{l}$ D_2O . Four acquisitions were accumulated and the HOD resonance was suppressed by a weak presaturation pulse. Line broadening of 1Hz was used.

This measured sensitivity of the 400MHz superconductive probe is significantly greater than that reported at 750MHz for a 5mm sample of ethylbenzene. The sensitivity for more dilute samples scales as expected. Resolution and lineshape are not quite as good as a conventional probe but are still acceptable. Measured linewidths with a non-spinning sample of 1% chloroform in deuterio-acetone are 0.5Hz, 6.6Hz and 12.8Hz at 50%, 0.55% and 0.11% signal amplitude, respectively. Typical 90° pulse times are 20µsec with about 1 watt of input power.

One disadvantage of operating with such a high Q is that radiation damping effects (5,6) are more severe than with a conventional probe. For lineshape measurements with 1% chloroform, it is necessary to de-tune the probe to avoid such effects. Nevertheless solvent suppression techniques do work as shown by the spectrum from a non-spinning sample of sucrose in D₂O in which the residual HDO was suppressed by pre-saturation (Fig.5). The sensitivity observed in this spectrum shows the same gain over a conventional probe and is about a factor of two greater than the sensitivity achieved with a normal probe at 600MHz.

The bandwidth of the probe is approximately 40kHz and the transient rise-time is about 4µsec. These values are not of great concern for proton spectroscopy but may cause some difficulties for observation of other nuclei (*e.g.* ¹³C) which have a wider range of chemical shifts.

The sensitivity gain from using superconductive coils will decrease if the sample itself is lossy. In this case the sample loss represents a resistive loading of the coils and is at the temperature of the sample, so it contributes a high noise voltage. Measured performance with the probe described here shows that with a 250mM saline solution the sensitivity gain over a normal probe is almost negated.

V. Conclusion

A high resolution proton NMR probe using superconductive coils has been shown to give an improvement in sensitivity of more than a factor of four over the best that can be achieved with an optimized conventional probe when using non-lossy samples. Other aspects of the probe performance, such as lineshape and pulse width, approach the performance of a normal probe. Additional advances in the technology can be anticipated to improve the performance of the superconductive coils further and to allow their application to more complex probe types, *e.g.* indirect detection, and probes for low frequency observation with proton decoupling.

VI. References

- ¹ W.L.Rollwitz, U.S. Patent 3,764,892
- ² P.Styles, N.F.Soffe, C.A.Scott, D.A.Cragg, F.Row, D.J.White and P.C.J.White, *J. Magn. Reson.* **60**, 397 (1984)
- ³ R.D.Black, T.A.Early and G.A.Johnson, *J. Magn. Reson. Series A*, **113**, 74 (1995)
- ⁴ D.I.Hoult and R.E.Richards, *Electron. Lett.* **11**, 596 (1975)
- ⁵ N.Bloembergen and R.V.Pound, *Phys. Rev.* **95**, 8 (1954)
- ⁶ X.Mao and C.Ye, *J. Chem. Phys.* **99**, 7455 (1993)

EPR and Molecular Orbital Investigation of the Superoxide Scavenger Complex Bis(Piroxicam) copper (II)

R. Cini, R. Pogni and R. Basosi

Department of Chemistry, University of Siena, Pian dei Mantellini 44, I-53100 Siena, Italy

1 Introduction

Reactive oxygen species such as superoxide anion, hydroxyl radical, hydrogen peroxide, and singlet oxygen have been postulated as playing an important role in a wide variety of physiological and pathological processes [1]. It is well known that $\text{Cu}_2\text{Zn}_2\text{SOD}$ (SOD, superoxide dismutase) is one of the metallo-proteins which catalyzes the proton dependent dismutation of superoxide anions into dioxygen and hydrogen peroxide[2]. In this reaction the copper(II) active site undergoes a reduction to copper (I) followed by a reoxidation to copper (II). It is also known that the coordination geometry of copper (II) is tetrahedrally distorted [3]. This peculiar geometry facilitates the reduction to copper (I) [4].

In this perspective, a copper (II) complex which can be considered to possess SOD-like activity must fulfill some requirements. In particular, it must possess: a) a flexible arrangement of the ligands around copper(II) ions, b) enough stability to avoid dissociation in the acid region, c) an accessible site in order to easily add the O_2^- radical, hence, giving a quick reduction to copper(I), d) an equatorial field of medium strength because the strong fields would not favour the attack of O_2^- on the accessible apical sites [5].

Piroxicam (feldene, Pfizer) is a powerful anti-inflammatory agent. It has been shown that copper complexes of anti-inflammatory anti-arthritic drugs are more active than the parent compounds[6]. Recently, a copper (II) piroxicam complex has been prepared and its scavenger activity thoroughly investigated [7,8].

The aim of the present research is to characterize the complex, determining the arrangement around copper $[\text{Cu}(\text{II})(\text{Pir})_2(\text{DMF})_2]$ (DMF, N,N-dimethylformamide), using EPR and Extended-Hückel techniques to correlate structure and SOD-like activity.

2 Materials and Method

The materials and procedure used for the synthesis of $[\text{Cu}(\text{II})(\text{Pir})_2(\text{DMF})_2]$ are reported in Ref. 7.

EPR Simulations

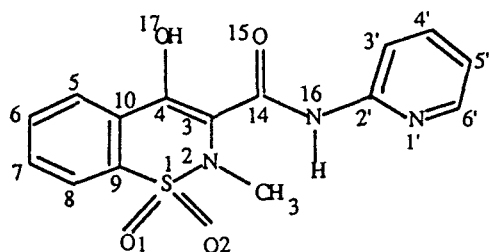
For the simulation of EPR spectra two different computer programs have been used: the first one, CUSIMNE, is devoted to simulation of rigid limit EPR spectra [9,10] whereas the second, COSMOS, is able to simulate copper complexes EPR spectra in liquid phase for a wide range of motional conditions (11).

Extended-Hückel Calculations

The molecular orbital calculations were carried out by using

the ICONC & INPUTC [12] program implemented on a VAX 6600 computer and interfaced with the MacroModel (MMOD) V3.0 package [13]. The graphic output was obtained through an Evans & Sutherland PS390 machine. The parameters used were those contained in ICONC & INPUTC [see also Ref. 8]. The distance-dependent weighted Wolfsberg-Helmholz formula [14] was employed. A self-consistent iteration calculation on the Cu atom was performed on the complex molecule.

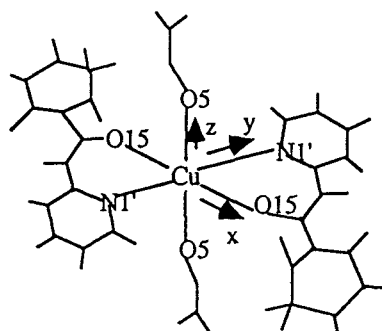
The ligand moieties (HPir, Scheme 1) of the complex molecule were treated with the MMOD package, in order to reduce the number of the atoms.



Scheme 1, HPir

Dimethylformamide was replaced by formamide.

The C5:C8 and H5:H8 atoms of the Pir⁻ anion were deleted and one hydrogen atom was attached to C9 and one to C10 (C-H bond distance, 1.05 Å). The modified Pir⁻ anion is hereafter denoted as RPIr⁻. The geometry for the starting structure of [Cu(II)(Pir)₂(DMF)₂] was that obtained through the molecular mechanics analysis reported by Cini et al. [8], and the reference system chosen is depicted in the Scheme 2.



Scheme 2

3 Results and discussion

The powder spectrum of [Cu(Pir)₂(DMF)₂] paired with the simulation which gave the best fit is shown in Fig. 1.

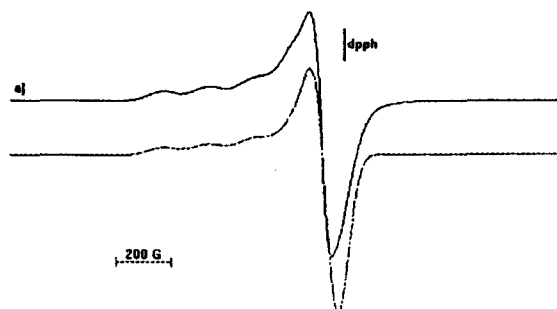


Fig.1

Fig. 2 shows the frozen EPR spectrum of the complex in DMF:

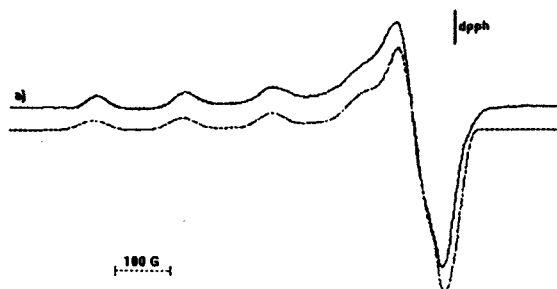


Fig. 2

The complex was synthesised using copper in natural form. The contemporaneous presence of $^{63}\text{Cu}/^{65}\text{Cu}$ results in different nuclear g factors of the two isotopes which, for the large A_{\parallel} values of copper brings about sizeable shifts. However, the computer simulation programs used take into account this difference as well as the ratio of isotopic weights both in liquid and frozen solutions. The broad lines in the parallel region of the spectrum in Fig. 1 and Fig.2 are direct evidence of N-ligation, because of the unresolved shf structure. Furthermore, local inhomogeneities ("strain") leading to distribution in the g and hyperfine tensors may contribute to line broadening [15,16].

In the experimental and simulated EPR spectrum of Fig.1 values of $g_z > g_{x,y} > 2.040$, suggest a $d_{x^2-y^2}$ or d_{xy} ground state, peculiar of square planar, square-base-pyramidal, or octahedral stereochemistries [17,18]. The spin Hamiltonian parameters determined from powder and frozen EPR spectra are in substantial agreement. They are: $g_{\parallel} = 2.290$; $g_{\perp} = 2.060$; $A_{\parallel}^{\text{Cu}} = 500.0$ MHz; $A_{\perp}^{\text{Cu}} = 29$ MHz; $A_{\parallel}^{\text{N}} = 45$ MHz; $A_{\perp}^{\text{N}} = 37$ MHz.

The introduction of an axial spin Hamiltonian was sufficient to fit satisfactory the experimental spectrum. In the case of $[\text{Cu}(\text{Pir})_2(\text{DMF})_2]$ the two DMF molecules are located in axial positions. This contributes to maintain the system in a tetragonally elongated pseudo-octahedral arrangement.

Assuming the EPR parameters reported previously and using the theoretical approach of Maki and McGarvey [19] for copper (II) complexes, it is possible to apply a semiempirical LCAO-MO scheme and

express anisotropic g values and hyperfine constants as a function of molecular-orbital coefficients and certain atomic constants. Chemical considerations suggest that it is reasonable to confine the study to the case of a tetragonally distorted octahedral effective D_{4h} symmetry.

The magnetic parameters can then be used to measure the extent of ionic bonding (α^2) and the extent of the contact term (k) from the equations of Maki and McGarvey [19], we obtain $\alpha^2 = 0.9141$ and $k = 0.3115$. These are typical values for copper complexes.

Furthermore, Peisach-Blumberg diagrams can be used to deduce the ligation scheme because the number of ^{14}N ligands is related to a decrease in the g_{\parallel} value and an increase in the A_{\parallel} value with respect to Cu^{2+} bound to oxygen only. The values of g_{\parallel} and A_{\parallel} for the complex reported in Fig. 1 and Fig. 2 are in agreement with a coordination of two nitrogens and two oxygens.

If we consider the ratio $R = A_{\parallel}^{\text{N}}/A_{\perp}^{\text{N}}$ in order to distinguish imidazole coordination from that of other nitrogens [20], our values are in agreement with a coordination from aromatic aza nitrogens like pyridine, and on the basis of a previous study [21], are coherent with a trans- N_2O_2 coordination.

Room temperature EPR spectra paired with their simulations for $[\text{Cu}(\text{Pir})_2(\text{DMF})_2]$ in DMF (Fig.3a), in DMSO (Fig.3b) and in DMSO + 1,2,3-propantriol + excess of free piroxicam (Fig.3c) are reported. The spin hamiltonian parameters are in substantial agreement with those reported from powder and frozen spectra suggesting that there is no

change in coordination for the complex in the two physical states and with different solvents.

From top to the bottom in Fig. 3, an increase in the correlation time (τ_c) of the complex (3a, $\tau_c = 140$ ps, 3b, $\tau_c = 185$ ps, 3c, $\tau_c = 833$ ps) is apparent. The spectrum in Fig. 3c is typical of a quasi-immobilized motional condition. This is due to the increase in viscosity of the solutions from the top to the bottom spectrum of Fig. 3.

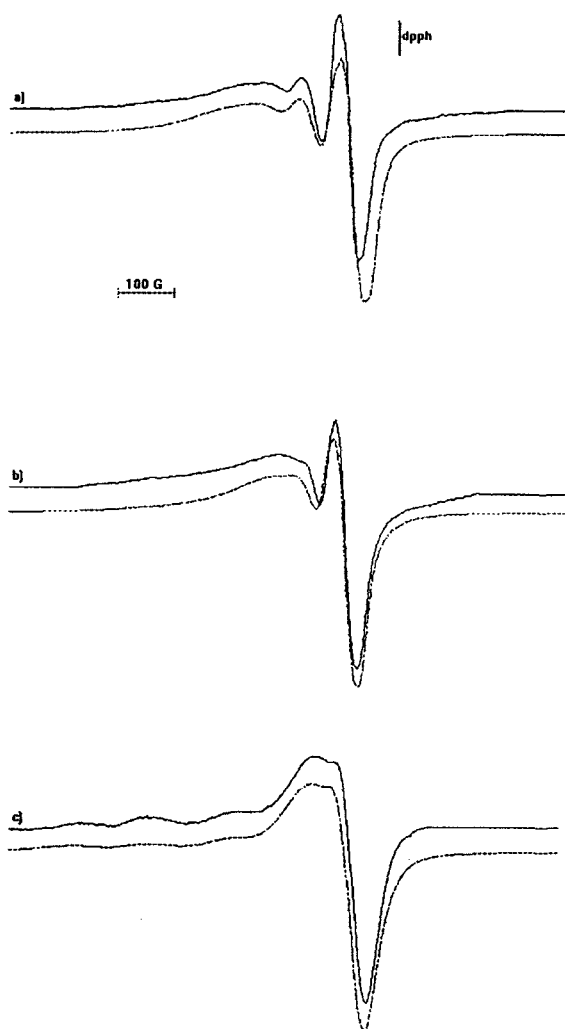


Fig. 3

The geometry of the coordination sphere of the $[\text{Cu}(\text{RPir})_2(\text{DMF})_2]$ molecule used for the extended Hückel calculations can be described as tetragonally elongated pseudo-octahedral. The two pyridyl nitrogen atoms and the two amide oxygen atoms of two Pir^- anion occupy the equatorial positions (the N atoms are trans, Scheme 2). The oxygen atoms of the two molecules of the solvent are weakly bound through the axial position (Cu-O5 (average), 2.445; Cu-O15, 1.920; Cu-N1', 2.127 Å for the gas phase energy minimized structure) [8]. As it is usually found for this type of hexa-coordinate copper (II) complex, the HOMO has a high character of $d_{x^2-y^2}$ (Cu) atomic orbital [8], whereas the $py(\text{O15})$ and $px(\text{N}')$ have also significant contributions. The total occupancy of the $d_{x^2-y^2}$ (Cu) orbital is 1.846 electrons. The values of the net atomic charges (see Table I) show also that the positive charge of the metal center is extensively spread over the donors and some other atoms of the ligand moieties.

These findings are in agreement with the hyperfine substructure of the "perpendicular" region of the EPR spectrum of $[\text{Cu}(\text{Pir})_2(\text{DMF})_2]$ as recorded from frozen solution (110 K, see Fig.2). This can be ascribed to the coupling of the unpaired electron and N1' nuclear spin.

The energy gap HOMO-LUMO is 2.15 eV (495.8 Kcal/mol) which corresponds to a wavelength of 576 nm and correlates well with the maximum absorption at 620 nm found for $[\text{Cu}(\text{Pir})_2(\text{DMF})_2]$ in the microcrystalline state [7].

Table I. Selected atomic charges (electron unit) for $[\text{Cu}(\text{Pir})_2(\text{DMF})_2]$ (those for Pir^- are added for comparison)

Atom	Complex	Pir^-
Cu	0.192	
S	2.816	2.800
O1	-1.191	-1.206
O2	-1.200	-1.206
O5	-0.698	
O15	-0.494	-0.822
O17	-0.695	-0.941
N1'	-0.459	-0.678
N2	-0.625	-0.650
N16	-0.204	-0.177
C3	-0.048	-0.013
C4	0.386	0.347
C9	-0.153	-0.118
C10	-0.049	0.016
C13	0.087	0.089
C14	0.561	0.583
C2'	0.530	0.524
C3'	-0.129	-0.167
C4'	0.046	0.035
C5'	-0.109	-0.163
C6'	0.258	0.272

4 References

- 1) P.A.Cerutti, *Science*, 227, 375, 1985
- 2) J.M.McCord and I.Fridovich, *J. Biol. Chem.*, 74, 6049, 1969
- 3) J. A. Tainer, E. D. Getzoff, J. S. Richardson, D. C. Richardson, *Nature* 306, 284, 1983
- 4) B.J.Hathaway, in *Comprehensive Coordination Chemistry*, G.Wilkinson, Ed., Pergamon Press, 1987, Vol.5,p.134
- 5) R.P.Bonomo, E.Conte, R.Marchelli, A.M.Santoro, G.Tabbi, *J. Inorg. Biochem.*, 53, 127, 1994
- 6) J.R.J.Sorenson, *Prog.Med.Chem.*, 26, 437, 1989
- 7) R.Cini, G.Giorgi, A.Cinquantini, C.Rossi, M.Sabat, *Inorg. Chem.*, 29, 5197, 1990
- 8) R.Cini, R.Pogni, R.Basosi, A.Donati, C.Rossi, L.Sabadini, L.Rollo, S.Lorenzini, R.Gelli, R.Marcolongo, *Metal Based Drugs*, 2, 43, 1995.
- 9) G.Rakhit, W.E.Antholine, W.Froncisz, J.S.Hyde, J.R.Pilbrow, G.R.Sinclair, B.Sarkar, *J. Inorg. Biochem.*, 25,217, 1985
- 10) R.Pogni, G.Della Lunga, R.Basosi, *J. Am. Chem. Soc.*, 115, 1546, 1993
- 11) G.Della Lunga, R.Pogni, R.Basosi, *J. Phys. Chem.*, 98(15), 3937, 1994
- 12) G. Calzaferri, M.Brändle, ICONC & INPUTC, University of Berne, QCPE programme QCMP116, 1992
- 13) W.C.Still, F.Mohammadi, N.G.J.Richards, W.C.Guida, M.Lipton, G.Chang, T.Hendrickson, F.DeGunst, W.Hasel, Macromodel V3.0, Department of Chemistry, Columbia University, New York, 1990.
- 14) a) G.Calzaferri, L.Forss, I.Kamber, *J.Phys.Chem.*, 93, 5366, 1993; b) G.Calzaferri, R.Hoffmann, *J. Chem. Soc., Dalton Trans.*, 917, 1991; c) ICONC & INPUTC documentation (see ref. 14)
- 15) W.Froncisz, J.S.Hyde, *J. Chem. Phys.*, 73(7), 3123, 1980
- 16) R.Basosi, W.E.Antholine, J.S.Hyde, in *EMR of Paramagnetic Molecules*, Berliner & Reuben eds. vol.13, 103, 1993
- 17) B.J.Hathaway, D.E.Billing, *Coord. Chem. Rev.*, 5, 143, 1970
- 18) B.J.Hathaway, A.A.G.Tomlinson, *Coord. Chem. Rev.*, 5, 1, 1970
- 19) A.H.Maki, B.R.McGarvey, *J. Chem. Phys.*, 29, 31, 35, 1958
- 20) H.Yokoi, *Biochem. Biophys. Res. Commun.*, 108, 1278, 1982
- 21) M.Iwaizumi, T.Kudo, S.Kita, *Inorg. Chem.*, 25, 1546, 1986

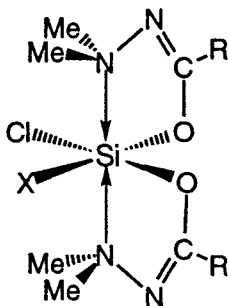
NMR STUDY OF LIGAND EXCHANGE IN HEXACOORDINATE SILICON CHELATES.

Daniel Kost and Inna Kalikhman

Department of Chemistry, Ben Gurion University of the Negev, Beer Sheva 84105, Israel

A series of novel hexacoordinate silicon complexes have been prepared, and their structures as well as complex stereodynamic behavior studied by utilizing ^1H , ^{13}C and ^{29}Si NMR spectroscopy.

The reaction of XSiCl_3 with O-trimethylsilylated N,N-dimethylhydrazides of various carboxylic acids afforded, in high yields, the hexacoordinate compounds 1 - 4.¹ Hexacoordinate silicon compounds generally adopt a nearly octahedral geometry.² However,



- | | |
|---------------------------------|------------------------------------|
| 1a, X = H; R = Me | 3a, X = Ph; R = Me |
| 1b, X = H; R = Ph | 3b, X = R = Ph |
| 1c, X = H; R = CF ₃ | 3c, X = Ph; R = CF ₃ |
| 2a, X = R = Me | 3d, X = Ph; R = CH ₂ Ph |
| 2b, X = Me; R = Ph | 4a, X = Cl; R = Me |
| 2c, X = Me; R = CF ₃ | 4b, X = Cl; R = Ph |
| | 4c, X = Cl; R = CF ₃ |

recently a series of silicon complexes have been reported with complexation patterns similar to the ones reported here (two bidentate and two monodentate ligands), whose geometries were described as "bicapped tetrahedral".³ In these compounds four of the ligands formed an essentially tetrahedral arrangement, with two loosely bound dative-ligands centered opposite two of the triangular faces of the tetrahedron.

It was thus first necessary to establish the geometry of the newly formed complexes. Evidence regarding the geometry is provided by the ^{29}Si chemical shift, which serves as a sensitive probe for silicon coordination

number.⁴ Table 1 lists ^{29}Si chemical shifts for tetra- and hexa-coordinate silicon compounds and, where appropriate, the ^{29}Si - ^1H one-bond coupling constants. It can be seen that increasing coordination is associated with a 70 - 80 ppm upfield shift. However, examination of ^{29}Si shifts for the bicapped tetrahedral complexes shows essentially no change in chemical shift as a result of changes in coordination number.³ It might be concluded that the present compounds 1 - 4 have octahedral geometries.

Table 1: ^{29}Si shifts for selected compounds

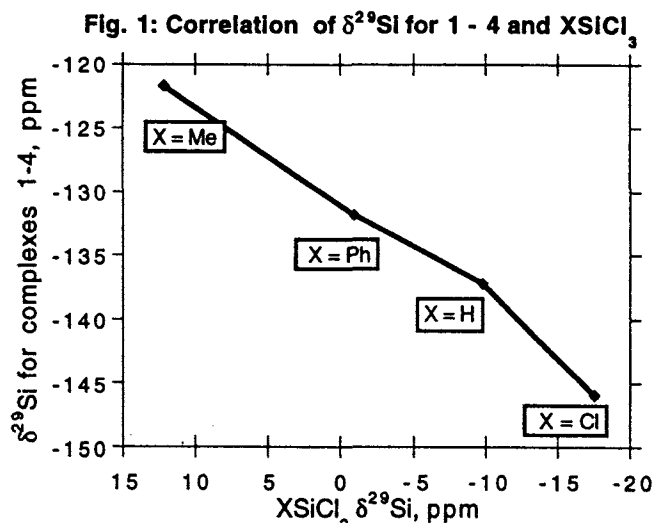
Compound	$\delta^{29}\text{Si}$ ppm ($1J^{29}\text{Si}-^1\text{H}$) Hz
<i>Hexacoordinate:</i>	
(Hydr) ₂ SiClH, 1b	-137.2 (341.8)
(Hydr) ₂ SiClMe, 2b	-121.7
(Hydr) ₂ SiClPh, 3b	-131.8
(Hydr) ₂ SiCl ₂ , 4b	-145.9
Ar ₂ SiMeH ^a	-26.8 (235.8)
<i>Tetra-coordinate:</i>	
(-O) ₂ SiClH ^b	-64.8 (381.0)
(Me ₃ SiO) ₂ SiClMe ^b	-46.2
NpPhSiMeH ^b	-19.8 (194.2)

a. Ar = 8-(dimethylamino)naphthyl; this is a bicapped tetrahedral complex.^{3a} b. Ref. 5.

Likewise examination of the one-bond coupling constant $J(^{29}\text{Si}-^1\text{H})$ shows a similar trend: a change from tetra- to hexacoordinate silicon, keeping the ligands similar, reduces $J(^{29}\text{Si}-^1\text{H})$ by *ca.* 40 Hz. However, in the bicapped tetrahedral complexes this trend is *reversed*: increasing coordination *increases* $J(^{29}\text{Si}-^1\text{H})$ by *ca.* 40 Hz.^{3a} This may be rationalized in terms of changes in the silicon hybridization, rather than coordination number: a geometry change from tetrahedral

to octahedral is associated with reduction of s-character at the silicon atom, and results in a decrease in $J(^{29}\text{Si}-^1\text{H})$; however, in the bicapped tetrahedral complexes the geometry at silicon remains essentially unchanged, and hence no change in hybridization takes place. In these compounds the increase in coordination from 4 to 6 results in electron donation from the nitrogen-ligands to silicon, and consequent higher electron density at the Si-H bond and greater coupling constant.

^{29}Si chemical shifts are strongly dependent upon the electronegativity of ligands.^{4b} Figure 1 shows that there is a linear correlation between $\delta^{29}\text{Si}$ of hexacoordinate complexes 1 - 4 and the corresponding shifts for similarly substituted XSiCl_3 compounds.



Octahedral complexes with this ligand arrangement (*i.e.*, with two bidentate and two monodentate ligands) can in principle assume six different diastereomeric geometries. The striking observation is that for all of the complexes 1 - 4 *only one* of these diastereomers can be detected in solution, the one depicted above.

Complexes 1 - 4 undergo several different ligand-site exchange processes, observable by NMR spectroscopy. At least two distinct rate processes at the NMR time scale are evident from the temperature dependence of the

spectra. A third exchange process takes place at slower rates, compatible with the laboratory time scale.

Table 2: Temperature dependence of 200-MHz ^1H -NMR spectra of 1 - 4 in toluene- d_8 .

Comp	temp K	$\delta(\text{N-Me})$, ppm	$\delta(\text{C-Me})$, ppm
1a	280	3.00 2.89 2.65 2.55	1.66 1.65
	298	2.75	1.67
2a	250	2.89 2.84 2.73 2.64	1.63 1.58
	298	2.75	1.61
3a	243	3.02 2.42 2.40 2.12	1.73 1.71
	340	2.50	1.75
3d	278	2.99 2.54 2.30 2.14	3.30 ^a 3.33 ^a
			3.06 ^a 3.30 ^a
	350	2.20	3.18
4a	298	3.15 2.98	1.87
	360	3.08	1.87

a. Entries represent chemical shifts of each CH_2 proton, four for two AB-quartets; $J_{\text{AB}} = 14$ Hz.

The ^1H and ^{13}C NMR spectra of 1 - 4 change dramatically with temperature. At the slow exchange limit temperatures (which vary among different compounds), four singlets are observed for the N-methyl groups (Table 2). In addition, the two R groups on the chelate cycles, and the pair of imidic carbons on both cycles were, respectively, diastereotopic and nonequivalent. Increase in temperature brings about coalescence of the four singlets in *two separate steps*, initially to two signals, followed by further coalescence to one singlet. In acetone- d_6 solution (Fig. 2) these rate processes were distinct and well separated; however, the barriers for interconversion were found to be solvent dependent. Indeed in toluene- d_8 solution these two coalescence processes were simultaneous. Distinction between the two coalescence phenomena in this solvent was observable by spectra simulation, which showed that good calculated fits to experimental spectra could only be obtained when two different rate constants were invoked (Fig. 3, Table 3).

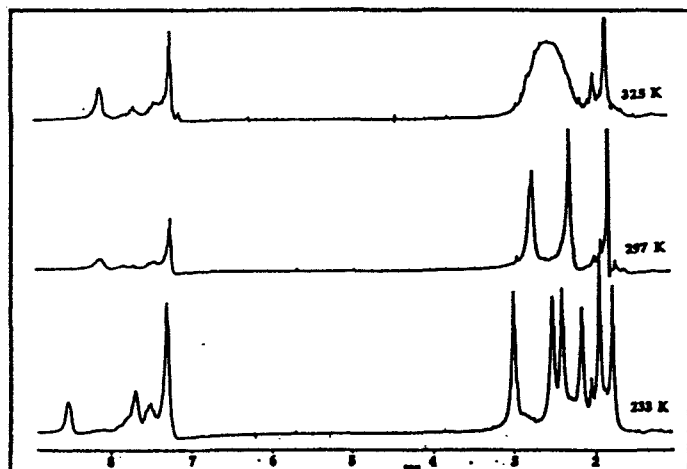


Fig. 2: ^1H DNMR spectra for the exchange processes of 3a in acetone- d_6 .

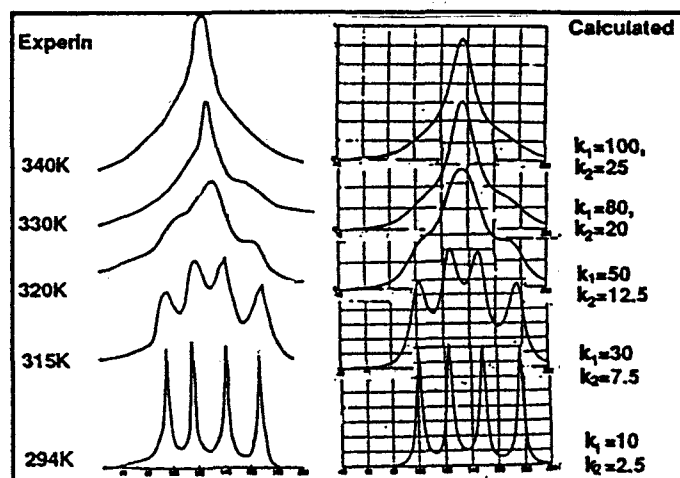


Fig. 3: Experimental (left) and simulated (right) spectra of the N-methyl region of 1a in toluene- d_3 solution.

The first question concerning the two rate-phenomena is whether geminal or distant N-methyl groups exchange first. The following NOE and saturation transfer experiment serves to answer this question (Fig. 4). Low power irradiation of one of the N-methyl singlets at the slow exchange limit temperature should effect both NOE and saturation transfer to neighboring N-methyl groups. At the given temperature (240K) in acetone- d_6 solution, only the faster of the two processes will generate significant saturation transfer, as a result of 5 s irradiation. If this process interconverts geminal N-methyls, only saturation transfer would be observed as negative signals (in the difference spectrum),

while the expected NOE between the same groups (positive signals) would be lost. Figure 4 shows clearly both positive Overhauser enhancements, as well as saturation transfer (negative signal). It follows that saturation is transferred to the distant methyl group residing on the second chelate cycle, while the geminal N-methyl signal, which is enhanced, does *not* exchange with the irradiated group.

Many different ligand exchange mechanisms can be envisioned and have been proposed for hexacoordinate silicon complexes.² These include inter-⁶ and intra-molecular⁷ ligand exchanges, brought about by pseudorotation or dissociation. The experimental evidence presented below leads to the conclusion that exchange in 1 - 4 takes place by two consecutive, nondissociative, intramolecular processes.

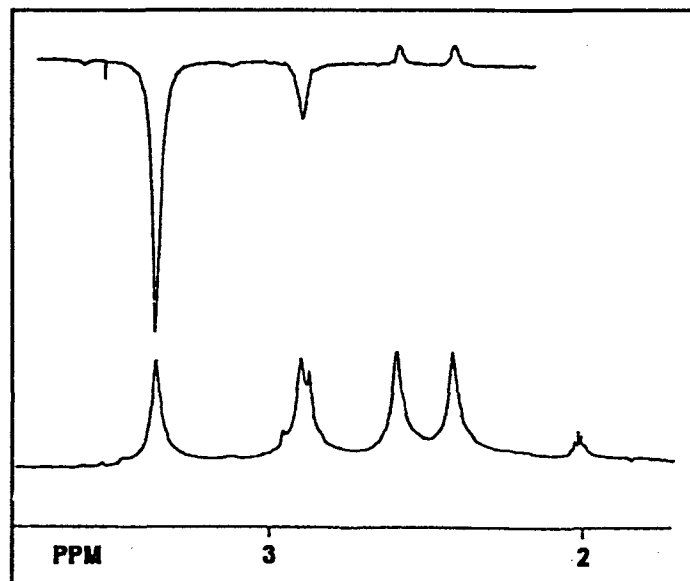


Fig 4: Difference NOE and saturation transfer spectrum (upper trace) of the N-methyl region of 3b at 240K in acetone- d_6 solution. Lower trace: reference spectrum.

The first result leading to this conclusion is the observed independence of exchange barriers upon concentration: dilution of the solutions up to eight-fold did not result in significant changes in coalescence temperatures or calculated free energy barriers. Thus bimolecular processes may be excluded.

Table 3: Calculated rate constants and activation free energies for exchange in 1 - 3 in toluene- d_8 , and for 4 in nitrobenzene- d_5 solutions.

Compd.	Temp, K ^a	ΔG_1^{*b} kcal/mol	ΔG_2^{*b} kcal/mol
1a	340	17.0	17.8
1b	345	17.5	18.5
1c	345	17.5	18.0
2a	280	13.8	14.8
2b	285	13.7	14.8
2c	283	13.7	14.6
3a	337	15.9	16.9
3b	337	15.8	16.4
3c	335	15.9	16.3
3d	335	15.9	16.9
4a ^c	346	17.9	
4b ^c	363	19.5	
4c ^c	393	20.7	

a. Temperatures near the coalescence at which the corresponding rate constants were obtained by spectra simulation. b. ΔG^* obtained from simulated rate constants using Eyring's equation, derived from the N-methyl signals, and are accurate within 0.2 kcal/mol. c. Measured at 90 MHz, in nitrobenzene- d_5 solution. Due to the higher symmetry only two N-methyl singlets and a single coalescence process are observed.

Possible exchange *via* dissociation-recombination reactions was also studied. The two most likely bonds which might be expected to cleave in a dissociation process during ligand exchange in 1 - 4 are the dative N-Si bond, and the Si-Cl bond. The DNMR spectra for the benzyl substituted 3d provide evidence against N-Si dissociation. The coalescence and respective exchange of the N-methyl singlets and the benzyl-methylene quartets (initially to one quartet and then to a singlet) occur *simultaneously*, with the same free energy barriers: first barrier, 11.2 - 11.3 kcal/mol; second barrier: 15.5 - 15.6 kcal/mol. If N-methyl coalescence were associated with Si-N bond dissociation, followed by rapid rotation about the N-N bond and recombination of the Si-N bond, one would

not observe simultaneous exchange of the methylene protons, as the dissociation-recombination does not effect this exchange. The fact that both exchanges take place at the same rate and the same process rules out dissociation and cleavage of the Si-N bond.

Ionic dissociation of the Si-Cl bond may be ruled out as a result of the ^{29}Si NMR spectra of 5, the analog of 3b in which fluorine replaces chlorine. The large one-bond ^{29}Si - ^{19}F coupling constant ($J = 272$ Hz) does not collapse or change significantly at temperatures well above the fast exchange limit temperature for exchange of N-methyl or other exchanging groups. The analogy of the NMR spectra and their temperature dependencies in compounds 1 - 4 and in 5 ensures that the same types of processes occur in all complexes, and hence the evidence against Si-F dissociation also proves that Si-Cl does not dissociate in 1 - 4.

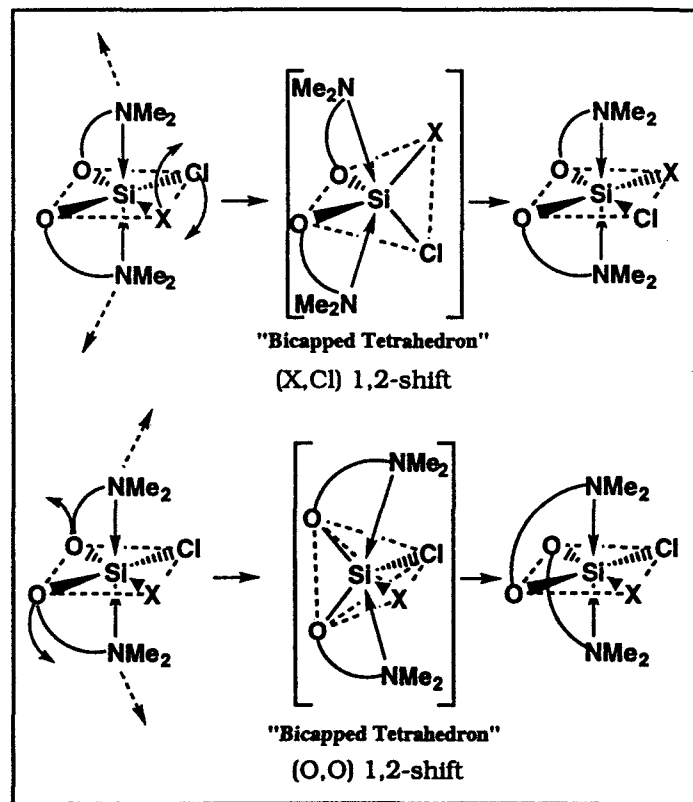
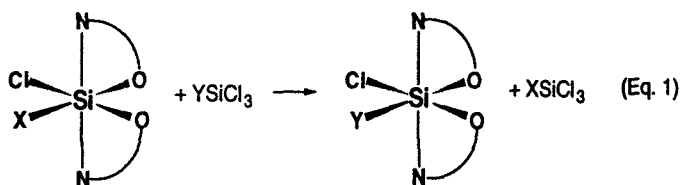


Fig 5: Topomerization *via* bicapped tetrahedron transition state or intermediate

The most simple exchange mechanism which accounts for all of the observations is a 1,2 shift of adjacent ligands, *i.e.* interchange

of the X and Cl groups, as well as interchange of the two oxygen ligands (Fig. 5). First, each of these exchanges comprises a topomerization, *i.e.* interchange of equivalent or enantiomeric structures, as is required by the observation in solution of only one diastereomer. Second, the interchange of adjacent ligands *via* a bicapped tetrahedral transition state or intermediate is a very likely low energy process, in view of the recent discovery of stable hexacoordinate complexes with this geometry.^{3b,8} Third, the two proposed 1,2-shift reactions interchanging X with Cl and O with O, respectively, are rather similar processes and can account for the observation of two relatively similar exchange barriers in these compounds.

Finally, a third type of ligand exchange reaction has been observed in 1 - 4. This is a slower process, compatible with the laboratory time scale. By reacting one of the complexes with XSiCl_3 at ambient temperature slow *intermolecular* ligand exchange is observed: the NMR spectra of the initially introduced 1 - 4 gradually change to those of a differently substituted complex (Equation 1).



However, this exchange is not a random equilibration. The ligand Y appears to replace only ligands X which are positioned to its right in the following ligand priority list: $\text{F} > \text{Cl} > \text{H} > \text{Ph} > \text{Me}$. The scope and exact mechanism of this reaction are still under investigation.

Acknowledgment. We thank the Israeli Ministry of Absorption and Ministry of Sciences and Arts for financial support.

References

1. For preliminary communications see: Kalikhman, I. D.; Gostevskii, B. A.; Bannikova, O. B.; Voronkov, M. G.; Pestunovich, V. A. *Metalloorg. Khim.* **1989**, *2*, 937; *CA* **1990**, *112*, 1188926r. Kalikhman, I.; Kost, D.; Raban, M. *J. Chem. Soc., Chem. Commun.* **1995**, 000.
2. (a) Tandura, St. N.; Alekseev, N. V.; Voronkov, M. G. *Top. Curr. Chem.* **1986**, *131*, 99. (b) Chuit, C.; Corriu, R. J. P.; Reye, C.; Young, J. C. *Chem. Rev.* **1993**, *93*, 1371.
3. (a) Breliere, C.; Corriu, R. J. P.; Royo, G.; Zwecker, J. *Organometallics*, **1989**, *8*, 1834. (b) Breliere, C.; Carré, F.; Corriu, R. J. P.; Poirier, M.; Royo, G.; Zwecker, J. *Organometallics* **1989**, *8*, 1831.
4. (a) Cella, J. A.; Cargioli, J. D.; Williams E. A. *J. Organomet. Chem.* **1980**, *186*, 13. (b) Marsmann, H. C. *NMR Basic Principles and Progress* **1981**, *17*, 65.
5. Horn, H. G.; Marsmann, H. C. *Makromol. Chem.* **1972**, *162*, 255.
6. Farnham, W. B.; Whitney, J. F. *J. Am. Chem. Soc.* **1984**, *106*, 3992.
7. Breliere, C.; Carré, F.; Corriu, R. J. P.; Douglas, W. E.; Poirier, M.; Royo, G.; Wong Chi Man, M. *Organometallics*, **1992**, *11*, 1586.
8. Boyer-Elma, K.; Carré, F. H.; Corriu, R. J. P.; Douglas, W. E. *J. Chem. Soc., Chem. Commun.* **1995**, 725.

The ^{13}C NMR Studies on a Snake Venom Protein (Cardiotoxin III) from the Taiwan Cobra (*Naja naja atra*)

Chang-Shin Lee and Chin Yu
 Department of Chemistry, National Tsing Hua University
 Hsinchu, Taiwan, R. O. C.

1. INTRODUCTION

^{13}C and ^{15}N NMR spectroscopy are powerful tools to understand the structure and dynamics properties of proteins (1). However, the low natural abundance and weak gyromagnetic ratio of these nuclei drastically limited the sensitivity of these spectra. This problem was overcome to a very large extent by the use of modern molecular biology techniques to obtain the enriched proteins (2). As yet, most papers published the backbone dynamics information and resonance assignment of ^{15}N nuclei based on isotope enriched samples. Investigation with ^{13}C nuclei is still limited especially when isotope enriched samples cannot be obtained due to expensive and difficult in enriched procedure. Introduction of 2D heteronuclear reverse spectroscopy at high fields has significantly helped to circumvent problems of sensitivity (3). Here we use two different experiments, heteronuclear single-quantum coherence spectroscopy (HSQC) (4) and heteronuclear multiple bond correlation spectroscopy (HMBC) (5), to assign ^{13}C chemical shifts.

Cardiotoxin analogue III (CTX III) isolated from Taiwan cobra (*Naja naja atra*) is a single chain (60 amino acids), membrane protein crosslinked by four disulfide bridges (6). The 3D structure in solution of CTX III has been elucidated by ^1H 2D NMR (7). The secondary structure of CTX III is in consisting of five β -strands protruding from the globule head and three main chain loops acting as linkers of these β -strands (Fig. 1). It is believed that knowledge of main-chain internal motion of CTX III could help in correlating the structure of the toxin with its biological function(s). In the final objective of understanding the dynamic behavior, we report the assignment of ^{13}C resonances of CTX III.

The correlation between the α -carbon chemical shifts and structure of CTX III is also discussed.

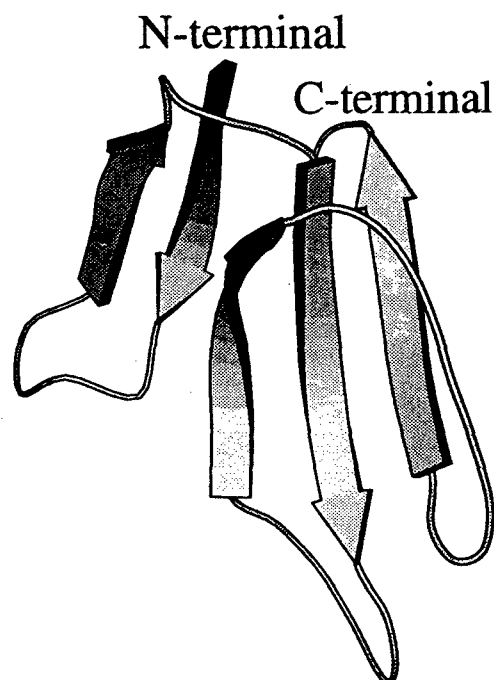


Figure 1. The molscript figure of CTX III. Ribbon arrows represent the regions of β -sheet conformation.

2. MATERIALS AND METHODS

CTX III was purified from the crude venom of *Naja naja atra* (Sigma) as described elsewhere (8). NMR experiments were made by dissolving lyophilized CTX III (60 mg) in a mixture (0.5 ml) of H_2O (90%) and D_2O (10%) at 25 °C. NMR experiments were acquired on Bruker DMX-600 spectrometer and processed on an INDIGO II workstation using UXNMR software. HSQC and HMBC spectra were acquired with 512 experiments (1024 data points) and 192, 72 scans each, respectively. Spectra were apodized using a 90-shifted q sine

function in both dimension. Water suppression was achieved by using pulse field gradient technique.

The α -carbon secondary chemical shift of individual amino acid residue in CTX III was calculated as per the procedure of Wishart and Sykes(9). The secondary chemical shift for C^α was computed as the difference between its observed C^α chemical shifts (δ_{obs}) and the C^α random coil shifts (δ_{rc}) of amino acid residues in H_2O as reported by Thanabal and others (10), using the relation,

$$\Delta\delta = \delta_{obs} - \delta_{rc}$$

The $\Delta\delta$ value of each amino acid residue was then plotted against the amino acid sequence.

3. RESULTS AND DISCUSSION

^{13}C chemical shifts were determined based on the published proton chemical shift assignments. Fig. 2 is an expansion of the aliphatic C^α - H^α region from the HSQC spectrum of CTX III. The signals from the C^β - H^β of Ser46, Ser45, Thr13, Thr29 and Thr56 are also exhibited in this region of the spectrum. Cross peaks from the two glycine doublets arising from Gly17 and Gly37 can also be seen on top of this spectrum.

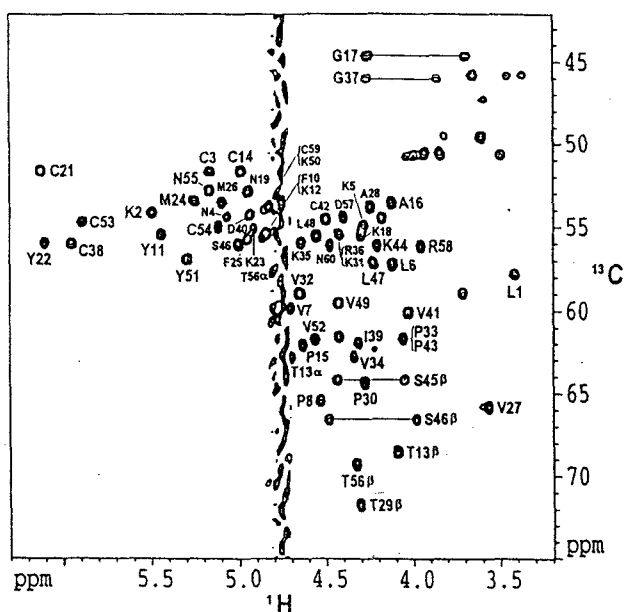


Figure 2. C^α - H^α region of the HSQC spectrum of CTX III. Cross peaks originate from C^β - H^β are specifically labeled.

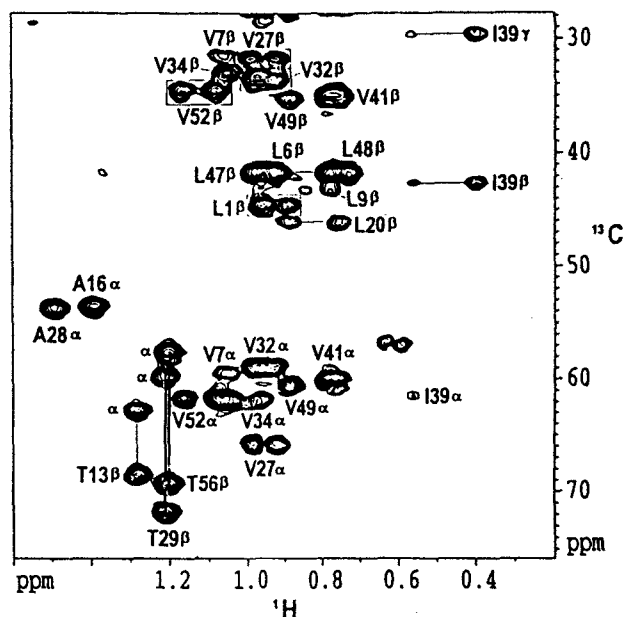


Figure 3. Region of the HMBC of CTX III, resonances of the methyl protons are shown.

Assignment of C^α resonances is straightforward in figure 2 due to the nice correlation of 1H and ^{13}C resonances. HMBC spectrum is useful for assigning the methyl groups of Ala, Val, Thr, Leu and Ile. Fig. 3 shows the use of HMBC experiment in the assignment procedure. Correlation through multiple bond is observed from methyl protons to β and (or) α carbons. There are five aromatic residues in CTX III (Phe10, Phe25, Tyr11, Tyr22 and Tyr51) and cause 20 different ^{13}C resonances to be assigned. The resonances of aromatic carbon are located between 115 and 160 ppm in ^{13}C dimension and between 6.2 and 7.6 ppm in the 1H dimension. All the chemical shifts of aromatic carbon were assigned (Figs. 4a and 4b). The quaternary carbons can be assigned using the HMBC spectrum. Table 1 lists the assigned ^{13}C chemical shifts of CTX III.

The conformation dependent chemical shifts of C^α has been applied to identify regular secondary structures and sketch the mobility of proteins. The structure of CTX III consists of a double-stranded β sheet with residue ranges 1-5 and 10-14 for strand 1 and 2 and a triple-stranded β sheet formed by the segment of residues 20-26, 34-39 and 50-55 for strands 3, 4 and 5, respectively. A secondary chemical shift plot smoothed with $n=1$ is shown in Fig. 5, together

Table 1. Assigned ^{13}C chemical shifts of CTX III from *Naja naja atra*

Residue	Chemical shifts (ppm)			Residue	Chemical shifts (ppm)		
	C^α	C^β	others		C^α	C^β	others
Leu1	57.58	44.45	C^δ 22.89	Met26	53.09		C^γ 31.83
			C^δ 23.58	Val27	65.63	31.44	C^γ 19.82
Lys2	53.70						C^γ 20.56
Cys3	51.27			Ala28	53.42	18.85	
Asn4	54.03	39.12		Thr29	59.45	71.65	C^γ 21.38
Lys5	54.49			Pro30	64.08		
Leu6	56.93	41.51	C^δ 22.84	Lys31	55.10		
			$\text{C}^{\delta\text{t}}$ 25.53	Val32	58.61	33.07	C^γ 19.87
Val7	59.50	31.00	C^γ 22.05	Pro33	61.46		
Pro8	65.2			Val34	62.59	32.73	C^γ 20.45
Leu9	3.12		C^δ 2 4.16				C^γ 20.88
Phe10	55.20	39.30	C_1 138.61	Lys35	55.51		
			$\text{C}_{2,6}$ 131.63	Arg36	55.10		
			$\text{C}_{3,5}$ 131.02	Gly37	45.61		
			C_4 129.59	Cys38	55.57	46.90	
Tyr11	55.06	39.30	C_1 128.37	Ile39	61.70	42.55	C^γ 29.50
			$\text{C}_{2,6}$ 133.00				C^γ 16.10
			$\text{C}_{3,5}$ 117.86	Asp40	53.89		C^δ 13.83
			C_4 157.27	Val41	59.83	34.67	C^γ 20.24
Lys12	55.20			Cys42	54.71	42.55	
Thr13	62.54	68.39	C^γ 21.45	Pro43	61.46		
Cys14	51.22	50.36		Lys44	55.76		
Pro15	61.79		C^δ 50.36	Ser45	63.94		
Ala16	53.19	17.40		Ser46	55.67	66.37	
Gly17	44.30			Leu47	56.88	41.51	C^δ 24.32
Lys18	55.15			Leu48	55.20	41.51	C^δ 21.62
Asn19	52.49	39.13					$\text{C}^{\delta\text{t}}$ 25.01
Leu20	45.95		C^δ 22.62	Val49	59.17	34.91	C^γ 19.82
			$\text{C}^{\delta\text{t}}$ 26.28	Lys50	53.37		
Cys21	51.25	41.89		Tyr51	56.55	41.33	C_1 131.09
Tyr22	55.64	43.97	C_1 128.70				$\text{C}_{2,6}$ 132.66
			$\text{C}_{2,6}$ 132.83	Val52	61.46	34.16	$\text{C}_{3,5}$ 118.06
			$\text{C}_{3,5}$ 117.11				C_4 157.19
			C_4 158.10	Cys53	54.26	49.14	
Lys23	54.78			Cys54	4.64	45.45	
Met24	53.05			Asn55	51.27	39.39	
Phe25	55.34	41.72	C_1 37.78	Thr56	57.20	69.13	C^γ 21.66
			$\text{C}_{2,6}$ 132.49	Asp57	56.03	38.08	
			$\text{C}_{3,5}$ 130.24	Arg58	55.85		
			C_4 129.25	Cys59	53.37	40.85	
				Asn60	55.76	45.40	

with the positions of secondary structure elements.

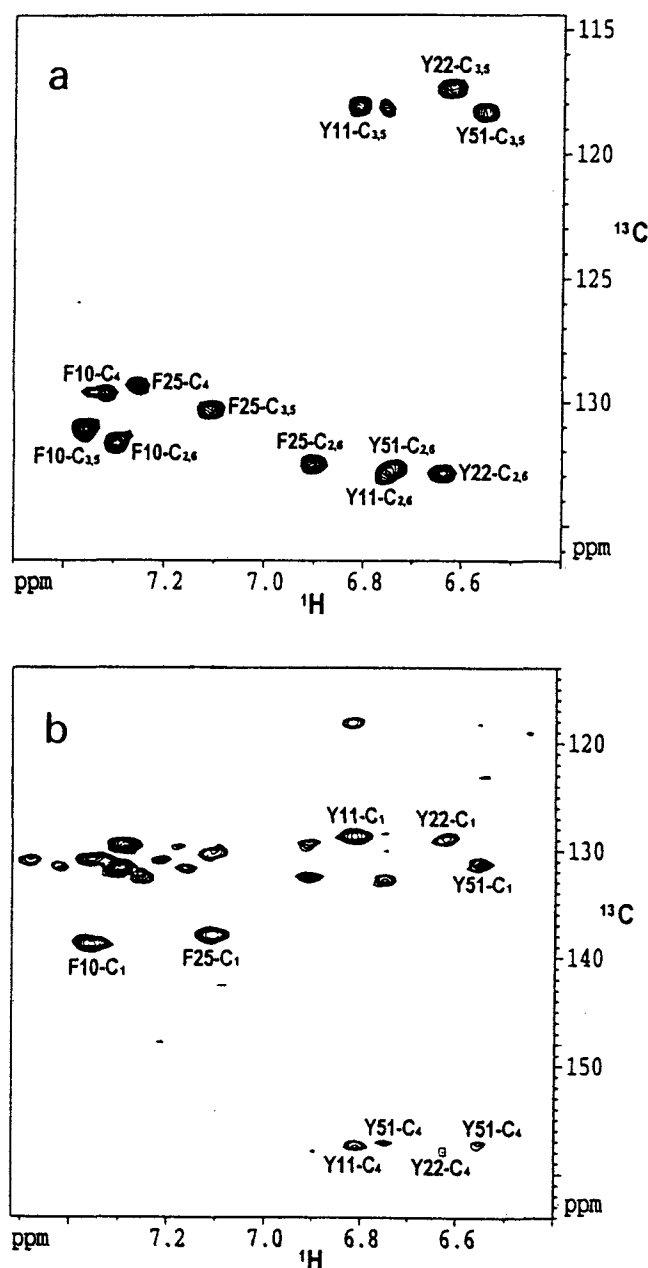


Figure 4. Aromatic carbon assignment of CTX III in (a) HSQC spectrum and (b) HMBC spectrum.

The negative secondary shifts of strands 1, 2, 3 and 5 are in agreement with the secondary structure of CTX III. The secondary chemical shifts of the segments 40-49 and 56-59 indicate flexible behavior that can attribute to the conformation of these two segments being not properly defined. Contrary to the expectation, the $\Delta\delta$ values of strand 4 are positive and closer to zero than the other strands. This might be due to the flexibility of strand 4. A similar trend (data

not shown) was found for cardiotoxin analogue II (CTX II) from Taiwan cobra (*Naja naja atra*). This phenomenon can be explained that Lys35 suggested acts as the probable cationic site for the binding of a phosphate ion. This active site is believed to be flexible. However, the theory behind the ^{13}C chemical shift of proteins is not yet completely understood. It is known that chemical shift deviations may arise from local electric fields (such as ring current effects of spatially close aromatic group or local fields from charged neighbours) (11, 12) or by the presence of proline residues in the segment (13). The segment between Val34 and Ile39 contains positively charged amino acids such as Lys35 and Arg36. The reasons mentioned above could have been cumulatively or individually responsible for the anomalous behaviour of 34 - 39 segment in the secondary chemical shift plot of CTX III.

Nevertheless, it is worthwhile to map the plot before going further in detail and on evidence about the mobility of proteins. The standard method (T_1 , T_2 and heteronuclear NOE measurements) must be done to get insight into the backbone dynamics of CTX III. This work is now in progress in our laboratory.

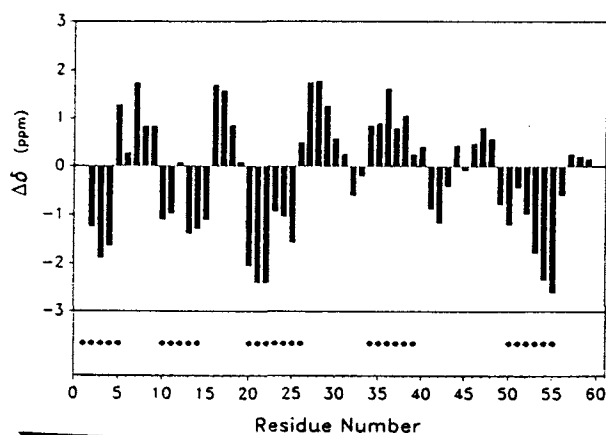


Figure 5. Secondary chemical shifts of α -carbons versus the amino acid sequence. Plot was smoothed with $n=1$ (averaging each point with its preceding and following residues). The amino acid residues in β -sheet region were labeled with full circles.

ACKNOWLEDGEMENTS

This work was supported by the Taiwan National Science Council grants (NSC84-2113-

M007-016 & NSC84-2811-M007-010). NMR experiments reported in this paper were carried out on the 600 MHz spectrometer at the regional Instrumentation Center at Hsinchu, Taiwan (R.O.C) supported by the National Science Council.

REFERENCES

1. Wuthrich, K., *NMR in Biological Research: Peptides and Proteins*, Elsevier, New York, NY, pp. 157-209 and 293-316 (1976).
2. Grassberger, B.I., Gronenborn, A.M. and Clore, G.M., *J. Mol. Biol.*, **230**, 364-372 (1993).
3. Bax, A., Griffey, R. H. and Hawkins, B. L., *J. Magn. Reson.*, **55**, 301-315 (1983).
4. Clore, G.M. and Gronenborn, A.M., *Annu. Rev. Biophys. Biophys. Chem.*, **20**, 29-45 (1991).
5. Bax, A. and Summers, M.F., *J. Am. Chem. Soc.*, **108**, 2093-2094 (1986).
6. Yu, C., Bhaskaran, R. and Yang, C.C., *J. Toxicol. Toxin. Rev.*, **13**, 291-315 (1994).
7. Bhaskaran, R., Haung, C.C., Chang, D.K. and Yu, C., *J. Mol. Biol.*, **235**, 1291-1301 (1994).
8. Hayashi, K., Takechi, M., Kaneda, N. and Sasaki, T., *FEBS Letters*, **66**, 210-214 (1976).
9. Wishart, D.S. and Sykes, B.D., *J. Biomol. NMR*, **4**, 171-180 (1994).
10. Thanabal, V., Omencinsky, D.O., Reily, D.O. and Cody, W.L., *J. Biomol. NMR*, **4**, 47-59 (1994).
11. de Dios, A.C., Pearson, J.G., Oldfield, E., *Science*, **260**, 1491-1496 (1993).
12. Laws, D.D., de Dios, A.C. and Oldfield, E., *J. Biomol. NMR*, **3**, 607-612 (1993).
13. Clore, G.M., Bax, A., Driscoll, P.C., Wingfield, P.T. and Gronenborn, A.M., *Biochemistry*, **29**, 8172-8184 (1990).

Study of Intra-Erythrocytic pH and Metabolites in Renal Failure Patients by ^{31}P - NMR

W. Jinsart^{1*}, S. Eiam-ong², P. Tosukhowong³, S. Chinayon⁴ and V. Sitprija²

^{1*}Department of General Science, Faculty of Science; ²Nephrology Unit, Faculty of Medicine;

³Department of Biochemistry, Faculty of Medicine; ⁴Department of Medical Technology, Faculty of Medicine
Chulalongkorn University, Bangkok 10330 Thailand

ABSTRACT

^{31}P NMR spectroscopy has been applied to identify metabolites in whole blood, packed red blood cells and hemolysates as well as to measure intracellular pH. In our study, phosphorus-containing metabolites and intra-erythrocytic pH in renal failure patients were monitored with a high resolution NMR spectrometer at an operating ^{31}P resonance frequency at 202.35 MHz. NMR spectra-derived parameters such as time, temperature and pH were investigated in order to achieve real time *in vivo* condition. ^{31}P resonance signals of ATP, 2,3-diphosphoglycerate and inorganic orthophosphate were recorded comparatively in hemolysates and intact red blood cells. Metabolic activity in the cells provided a probe through the variation in ATP concentrations. The intracellular pH is significantly decreased in the acute stage compared with the chronic renal failure and control packed erythrocytes.

Keywords: ^{31}P -NMR; renal failure; human erythrocytes

INTRODUCTION

Study of human red blood cells by using ^{31}P - NMR provides much information on intracellular phenomena (1,2). One can determine the concentrations of several components in intact erythrocytes, such as inorganic phosphorus (Pi), ATP and 2,3-diphosphoglycerate (DPG). ^{31}P -NMR spectroscopy can be applied to measure an intracellular pH (pHi) since the chemical shifts (δ) of phosphorus compounds are pH sensitive. The plots of chemical shift of intracellular phosphate vs pH provide a titration curve for determining pHi (3,4,5).

In this work, intracellular pH and level of ATP in intact human red blood cells were monitored directly by high magnetic field NMR

spectroscopy. We show the effect of intra-erythrocytic variable difference in the pathological stages of renal failure patients and healthy volunteers. The pilot experiments were set up to determine the appropriate *in vivo* condition. The information obtained from this work will be further applied in other metabolic disease research.

MATERIALS AND METHODS

Preparation of Erythrocytes

Freshly drawn venous heparinized blood samples were obtained from renal failure patients and healthy volunteers. The blood samples were centrifuged at 1500 x g, 4^o C, 10 min. The plasma and buffy coats were gently removed. The remaining red blood cells at a packed cell volume of 80-90 % were divided into two portions, one for an ATP assay, using enzymatic ATP determination SIGMA diagnostic kits, procedure No. 366-UV, another part for NMR measurements.

* Corresponding author. Tel: 66-2-2185181; Fax: 66-2-2185180; E-mail: fsciwijs@chulkn.car.chula.ac.th

Preparation of Hemolysate for pH Standard Titration Curves

Packed erythrocytes were lysed by two repeated freeze-thawings in sealed tubes. The pH of the lysates was adjusted to different values with 1 N HCl or 1 N NaOH and measured with a microelectrode pH meter (option in Automatic Blood Gas Analyzer System AVL 9957) immediately before NMR observations.

NMR Measurements

Blood sample (0.6 ml) was pipetted into a 5mm NMR tube fitted with sealed capillary tube containing D₂O, serving as an external lock for the adjustment of magnetic homogeneity. ³¹P-¹H- decoupled experiments (Bilevel Complete decoupling Mode) were performed at 27° C and 37° C, using a JEOL-JNM 500 spectrometer (11.7 T) operating at 202.35 MHz. Acquisition conditions were 45° (7-μs) RF pulses at 4- s intervals; the spectral width was 8000 Hz. Free-induction decays were collected as 16K data points and processed with 5 Hz exponential line broadening.

RESULTS

Several components in red blood cells were identified from ³¹P NMR spectra. Chemical shifts were assigned with respect to 85% H₃PO₄ as an external reference (0 ppm). In Fig. 1, the assignment of metabolites show resonances of the individual phosphate groupings of β,α, γ- ATP, inorganic phosphate (P_i) and 2,3-diphosphoglycerate (DPG), respectively.

P_i in fresh erythrocytes, Fig.1A is lower concentration than in the hemolysate sample Fig. 1B. The ATP level in hemolysate is undetectable, due to the hydrolysis of ATP to inorganic phosphate during the freeze-thaw process. We also followed the metabolic level change in intact red blood cells over one hour, every 10 min. as shown in Fig. 2. Under most circumstances, phosphorylated metabolites of erythrocytes can be detected in 10 min accumulation and they remain constant throughout two hours of experimental time.

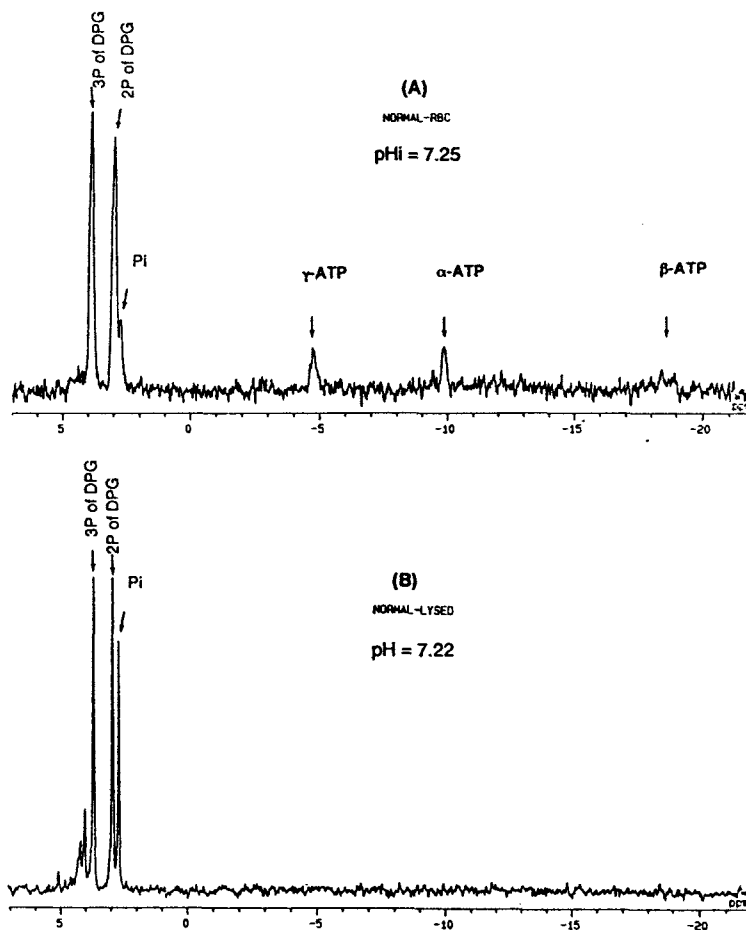


Fig.1 ³¹P- NMR spectra of human red blood cells (control) at 37° C :
(A) packed erythrocytes ; (B) hemolysate.

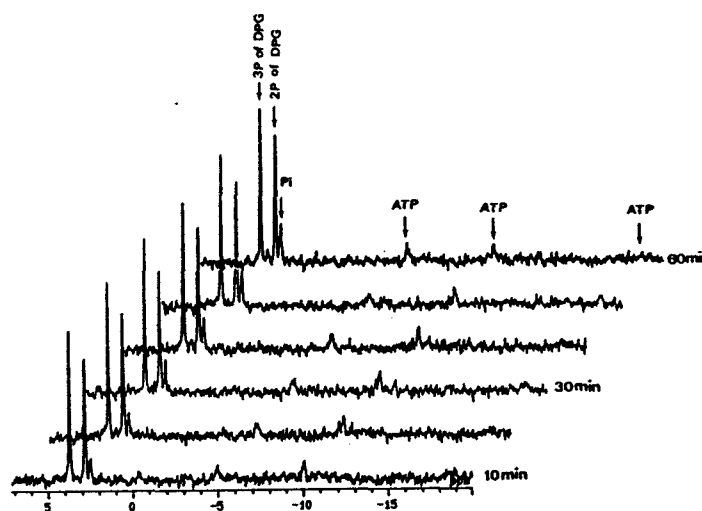


Fig. 2 ³¹P-NMR spectra of packed erythrocytes (control) (continuous 1 hour experiment with 10 min. loop-recycle time).

Figure 3 shows a standard titration curve of P_i vs pH. This curve was drawn from hemolysate venous blood sample of a healthy control. The different temperatures 27°C and 37°C slightly affect the titration curve. However, most of the NMR measurements are performed under physiological conditions, at 37°C .

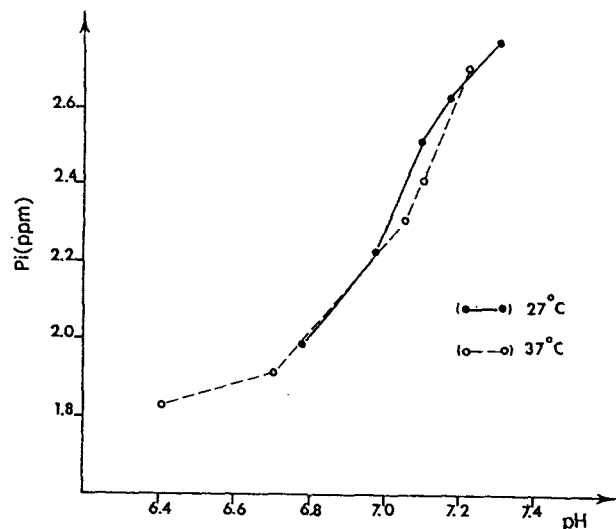


Fig. 3 Titration curve of inorganic Phosphate (P_i) resonance as a function of pH

Figure 4 shows the comparison of ^{31}P -NMR spectral data of intact erythrocytes from an acute renal failure patient (4A), a chronic stage patient (4B) and a healthy control (4C). From our observations, we found that, the intracellular pH in abnormal renal failure subjects is significantly lower than in controls. The NMR % integration of ATP phosphorus to the normalised total phosphorus in patients blood samples is higher than in controls. This also is supported by biochemical analysis of ATP. Although the enzymatic assays show change less effectively than NMR data, there is some relevant information. The results of intracellular pH and ATP concentration are summarized in Table 1 which reveal the levels of ATP_i and P_i to be markedly increased in abnormal samples relative to the control.

CONCLUSION

The results from this study indicate that the metabolic change in renal failure disease can be monitored by ^{31}P -NMR spectroscopy as a function of ATP concentration and intracellular pH. A challenge for future research is to look for phosphorus-containing metabolites in other systems with the aim of understanding the mechanism of metabolic diseases.

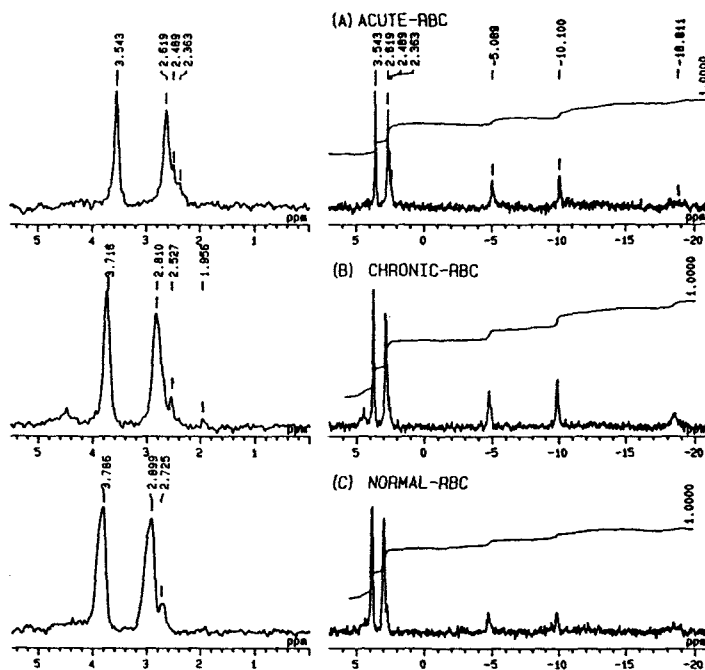


Fig. 4 Comparison of ^{31}P -NMR spectra of red blood cells from renal failure patients: (A) Acute, (B) Chronic and (C) healthy person

Table 1 Summary of pHi and ATP concentration in red blood cells from controls and renal failure patients

RBC	pHi	[ATP] nmol/mlRBC	[ATP] NMR%
Normal (n=10)	7.21 ± 0.03	967 ± 154	23.8 ± 2.2
Chronic (n=10)	7.13 ± 0.11	1254 ± 364	30.8 ± 1.9
Acute (n=3)	6.96 ± 0.13	1023 ± 132	28.3 ± 1.5

Acknowledgements:

We thank the Scientific & Technological Research Equipment Center, Chulalongkorn University for NMR spectrometer and technical assistance.

This work was supported by a grant from the National Research Council of Thailand. The travelling expense to attend ISMAR95 was funded by Chulalongkorn University.

References:

1. J.D. de Certaines, W. M. M. J. Bovee and F. Podo (1992) "Clinical and Experimental MRS" In: *Magnetic Resonance Spectroscopy in Biology and Medicine*, Pergamon Press, 280-350
2. K.M. Brindle (1988) "NMR method for measuring enzyme kinetics *in vivo*", *Progress in NMR Spectroscopy* 20, 253-293
3. S. Chinayon, W. Jinsart, S. Eiam-ong, S. Suvanpha and P. Pansin (1988) "*In vitro* study of ^{31}P nuclear magnetic resonance in human red blood cells" *Thai J. Hlth. Resch.* 2, 1-8
4. J.P. Monti, P. Gallice, M. Baas, A. Murisasco and A. Crevat (1987) "Modification of intra-erythrocytic homeostasis in uremic patients, as studied with ^{31}P Nuclear Magnetic Resonance" *CLIN. CHEM.* 33/1 76-80
5. J.D. Bell, I.J. Cox, J. Sargentoni, C.J. Peden, D.K. Menon, C.S. Foster, P. Watanapa, R.A. Iles and J. Urenjak (1993) "A ^{31}P and ^1H -NMR investigation *in vitro* of normal and abnormal human liver" *Biochimica et Biophysica Acta*, 1225, 71-77

Unified Theory of NMR Spectra in Condensed Media
Karnaukh G.E., Kulagina T.P., Provotorov B.N.
Institute of Chemical Physics, Russian Academy of Sciences,
Chernogolovka, Moscow Region, 142432 Russia

To date, nearly 40% information about molecular motion in dielectrics have been provided by NMR [1]. In order to obtain the characteristics of molecular motion from the spectra observed, a well-developed theory is urgently required. In this theory, the effects of thermal motion of the dipole-carrying molecule on local dipole fields and spectra must be taken into account over a wide temperature range.

Such a theory should be based on the kinetic equations for the dipole density derived from those for the matrix density. The relevant kinetic equations for magnetic and optical dipoles have been derived recently [2, 3].

In this work, the unified analytical theory of NMR spectra based on these kinetic equations is suggested for the first time. This theory is applicable to NMR studies of ordinary liquids and solids as well as of viscous liquids and polymers over a wide temperature range. The theory allows one to obtain the principal characteristics of molecular motion -- correlation time τ_c , relaxation time, and absorption band moments at a given temperature -- from the comparison of calculated and experimental spectra.

The kinetic equations for macroscopic variables $\sigma^\beta(h, t)$, $\beta = x, y, z$, which are components of the dipole densities in the longitudinal local field h at the moment t , prove to be the most convenient. Hereinafter, we will term them simply "layer polarization" and denote $\sigma^\beta(h, t) = \sigma^\beta$. These kinetic equations were obtained in [3] with regard to the dipole precession in local magnetic fields:

$$\frac{\partial \sigma^y}{\partial t} = -(\Delta + 3h/2)\sigma^y - (3/2 - \alpha)(-h\sigma^y + h\sigma_\delta^y + \sigma_1^y) + (\sigma_0^z - \sigma^y)/\tau_\perp - \sigma^x/T_\perp$$

$$\frac{\partial \sigma^x}{\partial t} = (\Delta + 3h/2)\sigma^x + (3/2 - \alpha)(-h\sigma^x + h\sigma_0^x + \sigma_1^x) + (\sigma_\delta^y - \sigma^y)\tau_\perp - \omega_1\sigma^x - 2\omega_1 h\sigma_1^z / \langle h^2 \rangle - \sigma^y/T_\perp$$

$$\frac{\partial \sigma^z}{\partial t} = \omega_1\sigma^z + 2\omega_1 h\sigma_1^y / \langle h^2 \rangle + (\sigma_0^z + \sigma_1^z h / \langle h^2 \rangle - \sigma^z) / \tau_\parallel + (\sigma_{eq}^z - \sigma^z) / T_{\parallel z} - \sigma_1^z h / \langle h^2 \rangle T_{\parallel D}$$

$$\sigma_0 = \int \sigma(h, t) g(h) dh,$$

$$\sigma_1 = \int \sigma(h, t) h g(h) dh, \quad (1)$$

where $g(h)$ is the distribution function for longitudinal local fields in dense spin systems, Δ is the frequency off-set, ω_1 is the amplitude of resonance alternative field, h is the longitudinal local dipole field, $1/\tau_\perp$ is the variation rate for the longitudinal local fields induced by spin exchange and thermal motion of atoms, $1/\tau_\parallel$ is the rate of equilibration in the spin system of a solid, $1/T_{\perp, \parallel}$ are the rates of transverse and longitudinal relaxation, respectively. The relaxations are coupled by thermal motion, which leads to the absorption of a quantum at a Larmore frequency ω_0 . $T_{\parallel z}, T_{\parallel D}$ are the times of longitudinal spin-lattice relaxation of the Zeeman and dipole--dipole reservoirs.

In deriving (1), the Hamiltonian of the dipole--dipole interaction (DDI) was written in the form:

$$H_d^z = \sum b_{ik} (3S_i^z S_k^z - S_i \cdot S_k) \equiv 3H_{zz} - H_{is},$$

where $H_{is} = H_{xx} + H_{yy} + H_{zz}$; b_{ik} are the known coefficients of DDI [1].

The contribution from $3H_{zz}$ is defined by terms $3h\sigma^y/2$ and $3h\sigma^x/2$ in (1). For the contribution proportional to $(3/2 - \alpha)$ (which is the isotropic component of DDI H_{is} between the spins), the variation rates of layer polarization are determined by five physical parameters of a given interaction: inasmuch as the contribution is associated with the dipole precession in the local field, it must be proportional 1) to the local field h , and 2) to the layer polarization components $\sigma^{x,y}$; 3) the H_{zz} component of isotropic interaction makes an exactly calculated contribution proportional to $h\sigma^{x,y}$ to the rate of variation of layer polarization. Since the interaction H_{is} describes the spinspin polarization exchange, its contribution goes to zero 4) at multiplying by the function $g(h)$ and at integrating over all the layers, and 5) in case of

equal polarization of the layers. The parameter α characterizes the isotropic component of DDI, which depends both on the orientation of a solid and on the structure of condensed media.

In (1), the terms proportional to $\omega_1 h / \langle h^2 \rangle$ are significant only in the case of solids because they describe the transfer of a fraction of the energy of relaxation field quantum $h\omega$ into the dipole-dipole reservoir.

It should be noted that system (1) is linear with respect to $\sigma^{\beta}(h,t)$ and h . This allows both analytical and numerical calculations.

By applying the steady-state treatment, we obtained the analytical solution for the case of Gaussian distribution of local fields $g(h)$ (see Appendix). The theoretical predictions are in agreement with the experimental data available. The obtained solution was used to elaborate the software which allows calculation of model spectra in seconds. Figure 1 shows the experimental (solid line) and calculated (dotted line) free induction decay (FID) in solid CaF_2 . Obviously, the oscillating portion of FID describes the collective coherent oscillation of dipoles. We elucidated also the influence of spectral diffusion on the oscillation amplitude and estimated the times of the spectral diffusion: $\tau_{\perp} = 4 \cdot 10^{-4}$ s, $\tau_{\parallel} = 10^{-5}$ s. In calculations, we used the following data: $M_2 = 8.08 \cdot 10^8 \text{ s}^{-2}$, $T_{\parallel D} = 20$ s, $T_{\parallel x} = 480$ s, $T_{\perp} = 2c$, $\omega_1 = 10^{-6} \text{ s}^{-1}$, $\alpha = 1.25$, orientation [111].

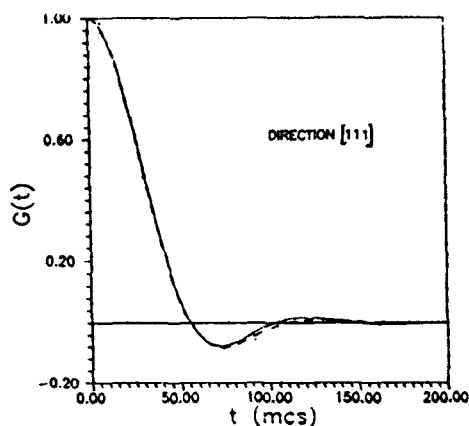


Fig. 1.

The suggested theory was also applied to the NMR studies under saturation conditions [4]. Figure 2 shows the calculated (solid line) and

experimental (asterisks) dependence of saturation time θ with the frequency off-set Δ . The calculations were carried out in terms of theory [2]:

$$[\theta(\Delta)]^{-1} = f(\Delta)(1 + \Delta^2/M_2),$$

where $f(\Delta)$ is the shape of the absorption line whose signal was derived, for the first time, from the steady-state solution to kinetic equations (1) using the data of Fig. 1. at $\omega_1 = 0.27$ G.

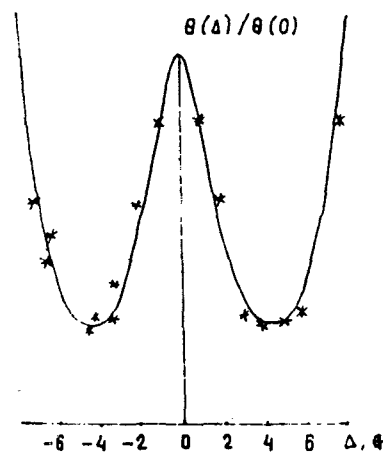


Fig. 2.

The same parameters were used when the absorption lines $P(\Delta)$ were compared with the experimental data [4] under saturation conditions either from the left or from the right side of the line:

$$P(\Delta) = f(\Delta) (\Delta_1(\Delta_1 - \Delta)) / (\Delta_1^2 + M_2),$$

where $\Delta_1 = -1.4$ G (Fig. 3a), $\Delta_1 = 1.1$ G (Fig. 3b), (solid line refer to calculated data).

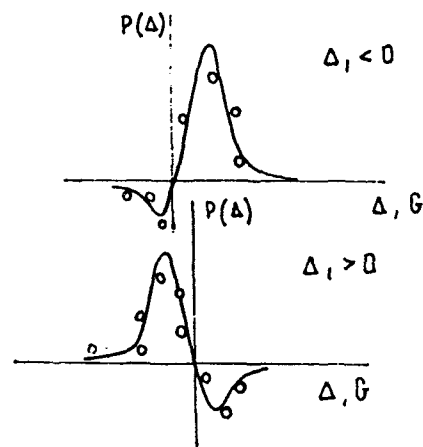


Fig.3a,b

These data agree with those reported in [5] and experimental results [4]. The suggested theory allows the description of NMR spectra of solids and determination of characteristic relaxation times τ_{\perp} , τ_{\parallel} , M_2 , α .

The theory is also applicable to liquids.

For fast thermal molecular motion, at $\omega_{loc} \tau_c \ll 1$, from (1) one can easily derive the Bloch kinetic equations:

$$\begin{aligned} \partial \sigma_0^x / \partial t &= -\Delta \sigma_0^y - \sigma_0^x / T'_{\perp} \\ \partial \sigma_0^y / \partial t &= \Delta \sigma_0^x - \omega_1 \sigma_0^z - \sigma_0^y / T'_{\perp} \quad (2) \end{aligned}$$

$$\partial \sigma_0^z / \partial t = \omega_1 \sigma_0^y + (\sigma_{eq}^z - \sigma_0^z) / T_{\parallel}$$

where $1/T'_{\perp} = 1/T_{\perp} + 9\tau_{\perp} \langle h^2 \rangle / 4$.

Figure 4 shows the calculated line shape for a solid (1) (parameters are the same as in Fig. 1) and for liquids (2) at a relaxation times of 10^{-6} s.

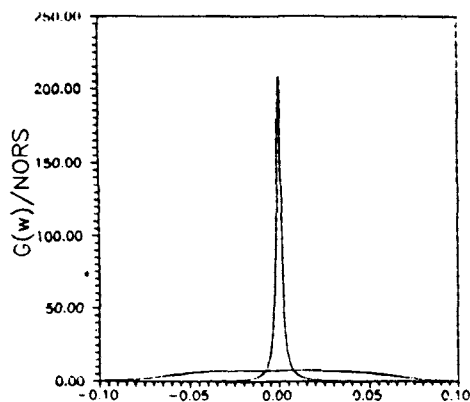


Fig. 4.

The broad Gaussian absorption band for solid is seen to transform to the narrow Lorentz band typical of liquids.

Eqs.(1) can be applied for the description of NMR spectra in partially crystallized polymers as well. In this case, the typically observed free induction decay can be represented as a combination of those for crystalline and amorphous portions of a polymer, $G_{cr}(t)$ and $G_a(t)$, respectively:

$$G(t) = (1 - p)G_a(t) + pG_{cr}(t) \quad (3)$$

$G_a(T)$ was reported in [6] at $T > T_g$, where T_g is the glass-transition temperature. Within the temperature range under study, it can be represented in terms of Bloembergen

correlation function within the Anderson--Weiss model and has either a Gaussian or exponential form.

For partially crystallized polymers, $G_{cr}(t)$ manifests itself in two different types of FID [7]. The most typical is poly(ethylene oxide) (PEO) and poly(vinylidene fluoride) (PVF). In PEO, the FID is similar to that in crystalline solids and is well described by the Abraham formula (proportionality to $\sin(bt)/bt$), whereas, in PVF, the oscillations are proportional to $\cos(bt)$. The reasons for different behavior of FID in these substances was not clear so far.

It can be easily shown that the $\cos(bt)$ oscillations appear at $\alpha = 3/2$ for intraspin coupling. Upon introducing the variables:

$$F(h,t) = \sigma^x(h,t) + i\sigma^y(h,t),$$

$$F_0(t) = \int g(h)F(h,t)dh,$$

and a new variable:

$$W(h,t) = \exp(-3ibt/2)F(h,t),$$

where b is the constant of interspin coupling, equation (1) has the form:

$$\begin{aligned} dW(h,t)/dt &= 3ihW(h,t)/2 + (W_0(h,t) - W(h,t))/\tau_{\perp} \\ &- W(h,t)/T_{\perp}. \end{aligned}$$

It follows that

$$G_{cr}(t) = (F_0(t) + W_0(t))/2 = \cos(3bt/2)W_0(t). \quad (6)$$

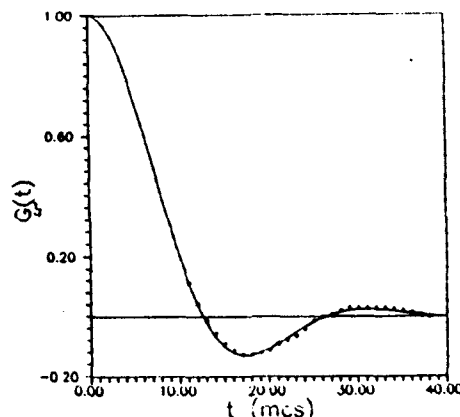


Fig. 5

Figure 5 demonstrates good agreement between the calculated and the experimental data available. Two forms of FID can be explained by the difference in the transfer of spin--spin polarization: for PEO, a structure similar to that

the difference in the transfer of spin-spin polarization: for PEO, a structure similar to that of CaF_2 forms in the polymer bulk. This structure is described by system (1). For PVF, the DDI of a separate CH_2 -group provides the main contribution into the spin-spin DDI. This process is described by (4).

The suggested theory is applicable to the NMR studies of solids, liquids and partially crystallized polymers.

The work is supported by the Russian Foundation for Fundamental Research.

REFERENCES

1. A. Abragam, M. Goldman, Nuclear Magnetism: order and disorder, Clarendon Press: Oxford (1982).
2. G.E. Karnaukh, A.A. Lundin, B.N. Provotorov, K.T. Summanen, Zh. Eksp. Teor. Fiz., 91, 2229 (1986).
3. A.V. Ivanova, B.N. Provotorov, Zh. Eksp. Teor. Fiz., 108, 1 (1995).
4. A. Mefed, M. Rodak, Zh. Eksp. Teor. Fiz., 59, 404 (1970).
5. B.N. Provotorov, Zh. Eksp. Teor. Fiz., 44, 1582 (1961).
6. T.P. Kulagina, XXV11 Congress AMPERE, Kazan, 620, (1994).
7. V.D. Fedotov, V.M. Chernov, Vysokomol. Soedin, Ser. A, 19, 1501 (1977).

APPENDIX

The stationary solution of the kinetic system (1) for the line shape $\sigma_\delta^y/\sigma_{eq}^z$, where σ_{eq}^z is the constant of equilibrium polarization, is a fraction with a numerator

$$\omega_I [- (1/\tau_L + 1/T_L)(1 + 4A/9)T_e R + ((1/\tau_L + 1/T_L)(1 + 4A/9) - 4\alpha^2/9T_L)(R^2 + I^2)],$$

where

$$A = \omega_I^2 T' / \langle h^2 \rangle T_L, \quad T' = 9(1/T_{||D} + 1/T_{||z})^{-1} - (1/\tau_{||} + 1/T_{||z})^{-1},$$

$$T_e^{-2} = (1/\tau_L + 1/T_L)(1/\tau_L + 1/T_L + \omega_I^2 (1/\tau_{||} + 1/T_{||z})^{-1}),$$

$$R + iI = \int (g(h)/(T_e^{-1} - i(\Delta + \alpha h)) dh, \quad \langle h^2 \rangle = \int h^2 g(h) dh,$$

$$\text{for calculations } g(h) = \exp(-h^2/\langle h^2 \rangle) / (2\pi\langle h^2 \rangle)^{1/2}, \quad \langle h^2 \rangle = 4M_2/9,$$

and a denominator is

$$\begin{aligned} & 9/4\alpha^2 + A/\alpha^2 - 2\Delta R(9/4 - \alpha^2 + A)/\alpha^2 + \\ & \{1/T_e^2 [\tau_L/(\tau_L + T_L) - 2(9/4 + A)/\alpha^2] + (1/\tau_L + 1/T_L) [4\Delta^2 AT_L/9 + (1/T_L + \omega_I^2 T_{||z}) (1 + 4A/9)]\} T_e R + (4/9\alpha^2) \{[\alpha^2/T_L - (1/\tau_L + 1/T_L)(9/4 + A)] [\alpha^2(1/T_L + \omega_I^2 T_{||z}) + \Delta^2 T_L A - 9(1/\tau_L + 1/T_L) / 4T_e^2 + \Delta^2(9/4 - \alpha^2 + A)(9/4 - \alpha^2 + (1/\tau_L + 1/T_L) AT')\} (R^2 + I^2). \end{aligned}$$

Next relations was used for the solution:

$\langle h \rangle = \int h g(h) dh = 0$, $g(h) = g(-h)$, this follows from the spin's nature.

Fatty Acid Binding to the Mitochondrial Uncoupling Protein

Petr Jezek¹, Michael Bauer², Pia D. Vogel², Keith D. Garlid³ and Wolfgang E. Trommer²

¹Institute of Physiology, Academy of Sciences of the Czech Republic, Prague

²Fachbereich Chemie der Universität Kaiserslautern, Kaiserslautern, Germany

³Oregon Graduate Institute of Science and Technology, Portland, OR, USA

I. Introduction

The mechanism of thermogenesis in brown adipose tissue (BAT) involves the regulated short-circuiting of the proton-motive force in BAT mitochondria due to the tissue-specific uncoupling protein (UcP). The net transport of protons from the intermembrane space into the mitochondrial matrix is regulated in several ways. Adenine nucleotides strongly inhibit transport, whereas fatty acids serve as activator [1-3].

Besides its function in H⁺ uniport, Nicholls et al. [4] could show that UcP also transports chloride ions electrophoretically. More recently, other ions including alkyl-sulfonates, alkylsulfates and phosphates were found to be substrates as well. Transport rates depended on the alkyl chain length with longer chains being more effective [5]. This finding has led to the suggestion that UcP in fact transports negatively charged fatty acid anions. Since protonated fatty acids diffuse freely within the bilayer membrane, this would lead to a net transport of protons mediated by UcP [6].

In order to establish such a mechanism, it has to be shown that the known monovalent amphiphilic substrates of UcP, such as alkylsulfonates compete with fatty acids for binding to the protein.

We have previously employed spin-labeled (SL) derivatives of ATP to study the interaction of nucleotides with UcP by ESR spectroscopy [7]. These studies confirmed the broad specificity of the enzyme for adenine derivatives. Attachment of the spin-label, 2,2,6,6-tetramethyl-piperidine-1-oxyl, to N⁶ or, via an additional amino group, to C8 of the adenine ring, allowed for tight and functional complex formation, whereas substitution at the ribose moiety strongly impaired binding. Detailed binding studies with C8-SL-ATP confirmed the known pH and Mg²⁺ dependence and showed a stoichiometry of one C8-SL-ATP bound per 66 kDa dimer.

Here we describe the interaction of UcP with a spin-labeled fatty acid, 5-Doxyl-stearate.

II. Materials and Methods

BAT mitochondria were isolated from Syrian hamsters by a standard method [8] in medium containing 5 mg bovine serum albumin per ml. Isolation of UcP was performed by the step-wise elution method using octylpentaoxyethylene extraction as described previously [9]. For the EPR measurements, several fractions were collected and pressure-concentrated up to 0.5 mg/ml. The detergent content was subsequently reduced by adsorption on Bio-Beads SM2 (Bio-Rad, D-80939 München, Germany; 40 mg beads/mg protein). Removal of excess detergent was essential for observing the 'bound' EPR signal with Doxyl-stearate. Final concentration of 2 mg/ml was reached using Centricon concentrators (cut-off M_R 10,000, Amicon GmbH, D-58454 Witten, Germany).

5-Doxyl-stearate was purchased from Sigma Chemie GmbH (D-80240 Deisenhofen, Germany) and alkyl-sulfonates were from Lancaster Synthesis (D-63155 Mühlheim/Main, Germany). N⁶-SL-ATP was synthesized as previously described [10].

EPR spectra were recorded in 50 µl flat cells with a Bruker ESP 300E spectrometer operating in the X-band mode. A microwave power of 6.3 mW and a peak-to-peak modulation amplitude of 0.8 Gauss at 100 kHz were routinely applied.

III. Results

Fig. 1 shows the ESR spectrum (top trace) of 5-Doxyl-stearate (124 µM) in the presence of UcP (30 µM) solubilized with octylpentaoxyethylene. The spectrum shows a clear separation of two components each in the low and high field region corresponding to a fairly mobile (denoted h_M) and a motionally more restricted fraction (denoted h_I) of the probe. With UcP that had been denatured by treatment with trichloroacetic acid prior to the ESR experiment or in samples without protein, the component with the larger 2A_{zz} value (47.8 Gauss) was

missing (bottom trace). Addition of excess palmitic acid (2 mM) led to a partial loss of the 'immobilized' component, and 27 mM hexanesulfonate caused a complete shift of the ESR lines to those observed in the absence of UcP (Fig. 1). The release of 'immobilized' 5-Doxyl-stearate at 2 mM palmitate was about 40% and about 20% at 1 mM palmitate (not shown).

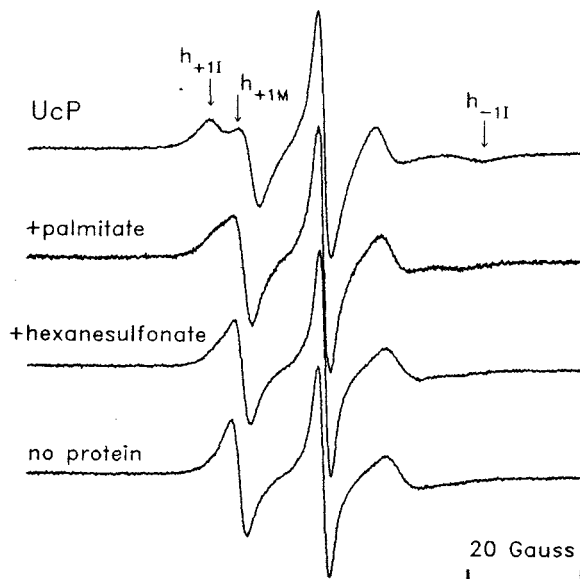


Fig. 1. ESR spectra of 124 μM 5-Doxyl-stearic acid in the presence of 30 μM UcP in 5 mM TEA-TES, 30 mM TEA_2SO_4 , 0.2 mM TEA-EDTA, pH 7.2, and their changes after addition of palmitic acid and hexanesulfonate. From the top: UcP, only; in the presence of 2 mM palmitic acid; in the presence of 27 mM hexanesulfonate; control. All solutions contained 2% octylpentaoxyethylene.

Prevention of 5-Doxyl-stearate binding to UcP was achieved as well with long chain alkylsulfonates as undecanesulfonate and octadecanesulfonate. They were more effective in replacing the spin-labeled fatty acid on UcP, which is in accordance with earlier findings that they are also better substrates of UcP [5]. Detailed ESR titrations as shown in Fig. 2 for octadecanesulfonate were plotted as dose-response curves (Fig. 3), using the ratio of h_{+1I}/h_{+1M} as a measure for binding. These yielded IC_{50} values of 2.2 mM for octadecanesulfonate, 7.7 mM for undecanesulfonate and 26 mM in case of hexanesulfonate.

Addition of ATP resulted in similar effects on the ESR spectra of 5-Doxyl-stearate with UcP as palmitate (Fig. 4A). Again, the 'immobilized', bound component was diminished in the presence of ATP with an IC_{50} of about 3 mM. Binding of ATP to UcP is pH-dependent and is considerably weaker at pH 8.5 as compared to neutral pH [1]. Raising the pH to 8.5 in the ESR experiment led to reappearance of the 'immobilized' component (h_i) in the spectra, *i.e.*, re-binding of 5-Doxyl-stearate to UcP (Fig. 4B).

The reciprocal effect, *i.e.*, displacement of bound ATP as monitored by potential changes in the ESR spectrum of

bound N^6 -SL-ATP, was not observed in the concentration range studied (up to 5 mM palmitic acid). The K_D for N^6 -SL-ATP binding to UcP was determined by Scatchard plot analysis [11] of the ESR titration data to be about 13 μM .

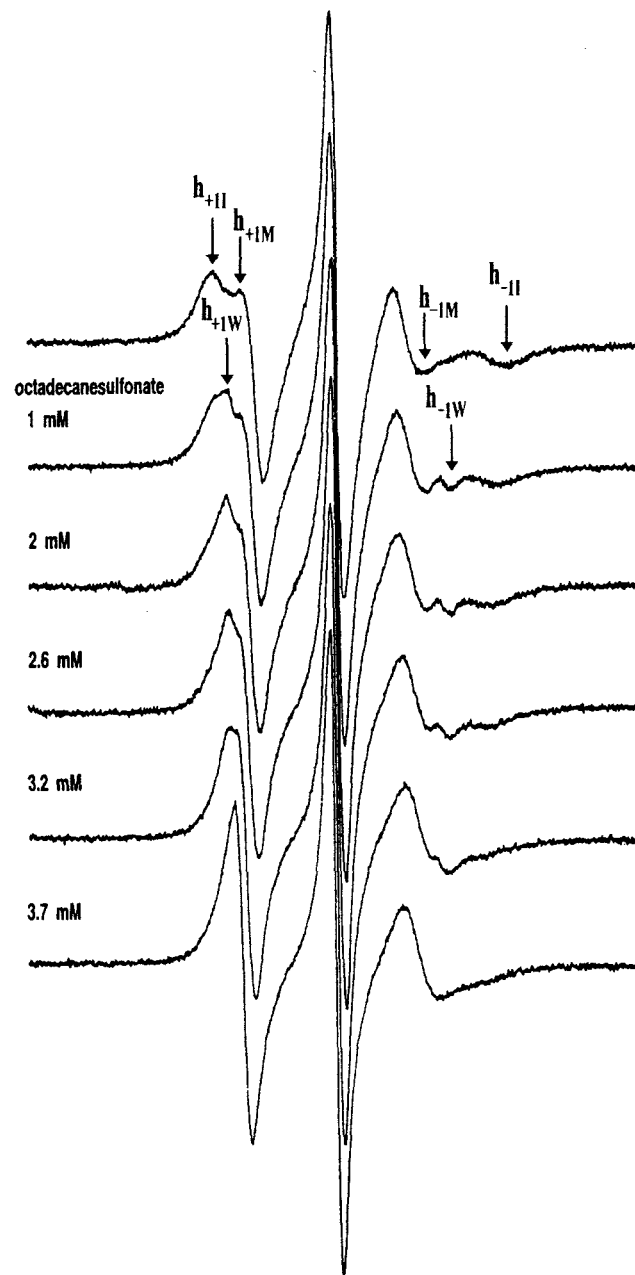


Fig. 2. Effect of octadecanesulfonate on the ESR spectra of 5-Doxyl-stearate bound to UcP. Experimental conditions as described in the legend to Fig. 1.

IV. Discussion

We have employed a spin-labeled fatty acid, 5-Doxyl-stearate, to investigate the interaction of UcP with fatty acids as part of its reaction mechanism. The ESR spectra clearly showed an 'immobilized' spectral component attributable to protein-bound 5-Doxyl-stearate. Both,

palmitic acid and alkylsulfonates, compete with the probe for binding to Ucp. This result supports a reaction mechanism for Ucp-mediated net transport of protons across the inner mitochondrial membrane according to which the function of Ucp is the translocation of negatively charged fatty acids [6,7].

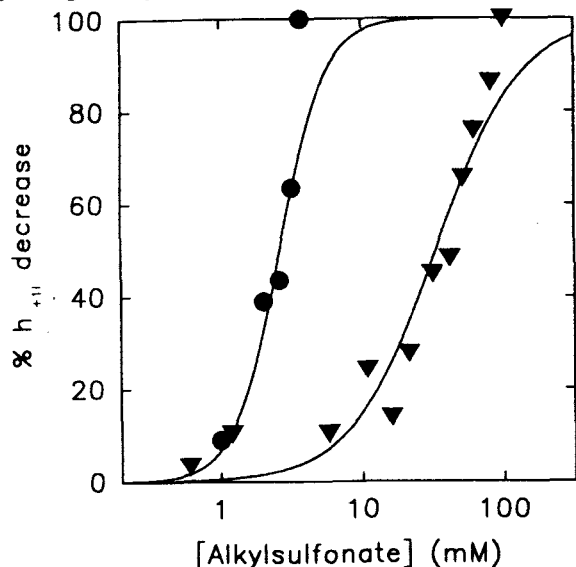


Fig. 3. Dose-response curves for displacement of bound 5-Doxyl-stearate from Ucp by octadecanesulfonate (circles) or undecanesulfonate (triangles) as studied by ESR spectroscopy. Experimental conditions as described in the legend to Fig. 1.

5-Doxyl-stearate spectra were also affected by the addition of ATP. The latter apparently reduces the affinity of Ucp for the fatty acid as indicated by a loss of binding. Under conditions when ATP binding is weak, *i.e.*, at alkaline pH, the spectral changes were reversed as 5-Doxyl-stearate was re-bound. Certain Doxyl-fatty acids embedded in short chain phospholipids and with the Doxyl group closer to the terminal methyl residue were reported to give similar spectral changes, *i.e.*, larger $2A_{zz}$ values at high pH [12]. The data were explained by a protonation of the carboxyl group, that allows for deeper insertion into the membrane, whereas deprotonation reverses this effect. In our system of a long chain detergent such an effect is not likely to occur as supported by experiments in the absence of proteins. Hence, we conclude that ATP causes partial displacement of bound 5-Doxyl-stearate from Ucp and the probe re-binds at alkaline pH which causes ATP to be released from the protein [1].

It has been reported previously that fatty acids have no effect on binding of ATP [3]. Our data are consistent with this finding as palmitic acid did not affect binding of N^6 -SL-ATP in the concentration range studied (up to 5 mM). Hence, the displacement of 5-Doxyl-stearate is likely to be allosteric as pictured in Fig. 6.

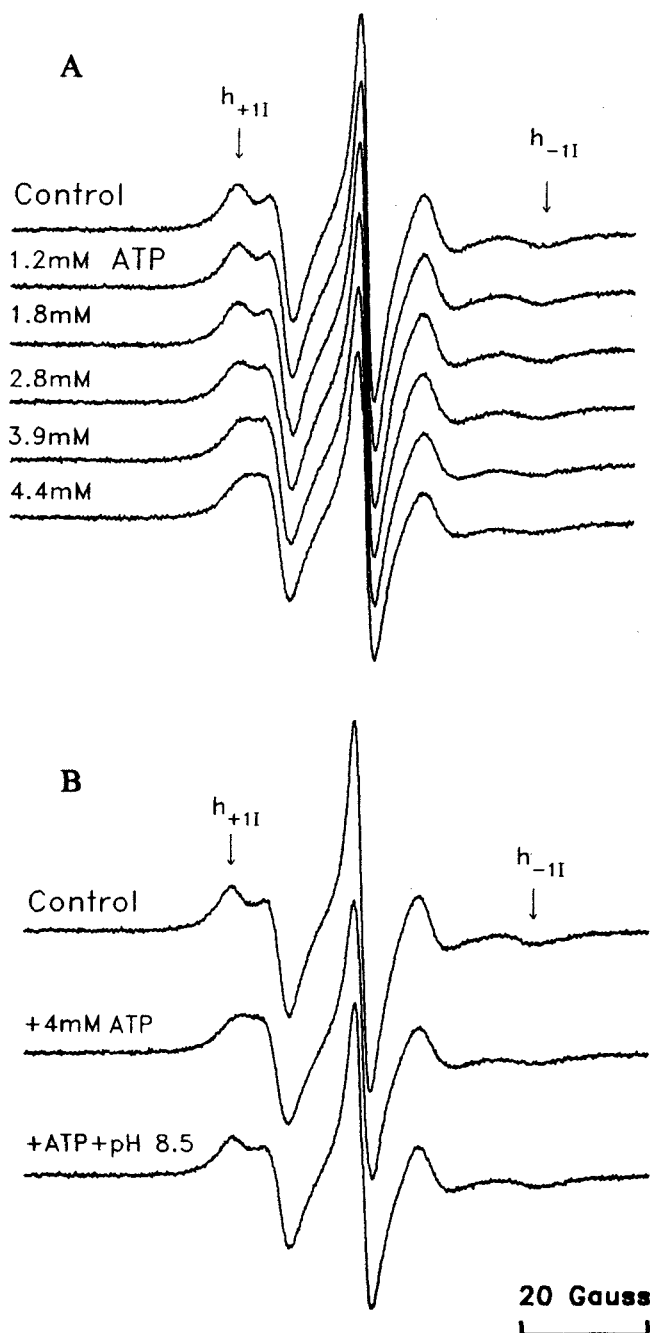


Fig. 4. ESR spectra of 5-Doxyl-stearate bound to Ucp in the absence or presence of ATP at pH 7.2 (A) or 8.5 (B). Experimental conditions as given in the legend to Fig. 1 and concentrations of ATP as shown in the figure.

Pyrimidine nucleotides bind to Ucp but do not inhibit transport [13]. Hence, in contrast to the effect exerted by ATP, binding of fatty acids and of 5-Doxyl-stearate to Ucp should not be reduced in the presence of CTP. Corresponding experiments are presently under way in our laboratory.

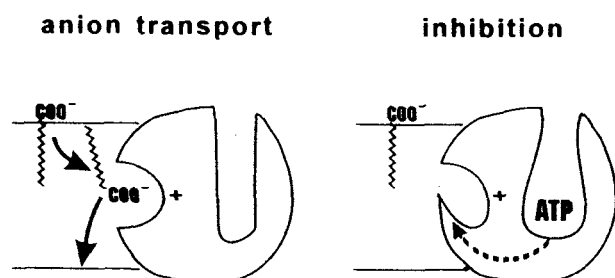


Fig. 5. Model for the molecular mechanism of gating by nucleotides in Ucp. The two states, when either transport or nucleotide inhibition takes place, are schematically shown. Under the functional, *i.e.*, the transporting state, the internal anion binding site in Ucp is exposed and is accessible also for fatty acid anions. Upon reaching the site, anionic fatty acids (or other anions) can move to the opposite side of the membrane. The internal binding site thus lowers the energy barrier imposed by the membrane. ATP inhibition is caused by conformational changes which render the anion binding site inaccessible for anions.

In further studies a photoaffinity-spin-labeled derivative of ATP, 2-azido- N^6 -SL-ATP (Fig. 6) [14], will be employed in order to gain information about the relative arrangement and the distance between 5-Doxyl-stearate and the nucleotide analog. Dipolar interactions between spin-labeled coenzymes and/or substrates bound to adjacent sites on a protein have allowed for precise distance measurements in case of glyceraldehyde-3-phosphate dehydrogenase [15,16], as well as distance estimates in case of 3-hydroxyacyl-CoA-dehydrogenase [17] and F_1 -ATPase [18]. For corresponding studies with Ucp one of the interacting species should be covalently attached in order to reduce the number of spectral components. Excess 2-azido- N^6 -SL-ATP can be removed by dialysis after covalent incorporation and hence, would not overlap with the ESR spectrum of 'free' 5-Doxyl-stearate [19].

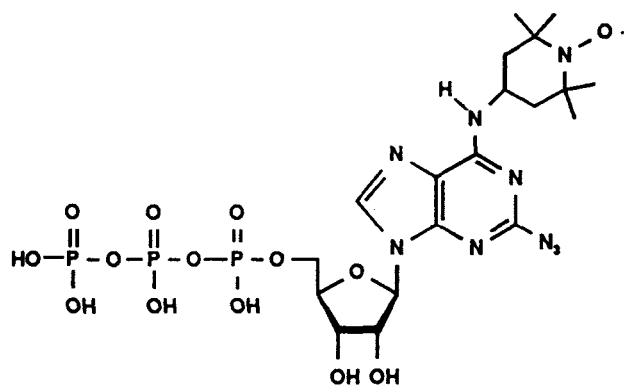


Fig. 6. Structural formula of 2-azido- N^6 -SL-ATP

V. References

- Klingenberg, M. (1988) *Biochemistry* 27, 781-791.
- Rial, E., Poustie, A., and Nicholls, D.G. (1983) *Eur. J. Biochem.* 137, 197-203.
- Cunningham, S.A., Weisinger, H., and Nicholls, D.G. (1986) *Eur. J. Biochem.* 157, 415-420.
- Nicholls, D.G., and Lindberg, O. (1973) *Eur. J. Biochem.* 37, 523-530.
- Garlid, K.D. (1990) *Biochim. Biophys. Acta* 1018, 151-154.
- Jezeek, P., Orosz, D.E., Modrianský, M., and Garlid, K.D. (1994) *J. Biol. Chem.* 269, 26184-26190.
- Jakobs, P., Braun, A., Jezeek, P., and Trommer, W.E. (1991) *FEBS Lett.* 284, 195-198.
- Cannon, B., and Lindberg, D. (1979) *Methods Enzymol.* 55, 65-78
- Jezeek, P., and Freisleben, H.-J. (1994) *FEBS Lett.* 343, 22-26.
- Glöggler, K.G., Fritzsche, T.M., Huth, H., and Trommer, W.E. (1981) *Hoppe Seyler's Z. Physiol. Chem.* 362, 1561-1565.
- Scatchard, G. (1949) *Ann. NY Acad. Sci.* 51, 600-673.
- Reboiras, M.D., and Marsh, D. (1991) *Biochim. Biophys. Acta* 1063, 259-264.
- Nicholls, D.G., Cannon, B., Grav, H.J., and Lindberg, O. (1974) in *Energy Dissipation in Nonshivering Thermogenesis. V. Dynamics of Energy Transducing Membranes*, vol. 13 (Ernster, L., Estabrook, R., and Slater, E.C., eds.) pp. 529-537, Elsevier, Amsterdam.
- Seiter, M.S., Bauer, M.P., Vogel, P.D. (1995) *Synthesis*, in press.
- Beth, A.H., Robinson, B.H., Cobb, C.E., Dalton, L.R., Trommer, W.E., Birktoft, J.J., and Park, J.H. (1984) *J. Biol. Chem.* 259, 9717-9728.
- Deparade, M.P., Glöggler, K., and Trommer, W.E. (1981) *Biochim. Biophys. Acta* 659, 422-433.
- Hartmann, D., Philipp, R., Schmadel, K., Birktoft, J.J., Banaszak, L.J., and Trommer, W.E. (1991) *Biochemistry* 30, 2782-2790.
- Vogel, P.D., Nett, J.H., Sauer, H.E., Schmadel, K., Cross, R.L., and Trommer, W.E. (1992) *J. Biol. Chem.* 267, 11982-11986.
- Jakobs, P., Sauer, H.E., McIntyre, J.O., Fleischer, S., and Trommer, W.E. (1989) *FEBS Lett.* 254, 8-12.

Acknowledgements:

This work was supported by grants from Deutsche Forschungsgemeinschaft and Fonds der Chemischen Industrie to W.E.T. and P.D.V., by the Academy of Sciences of the Czech Republic Grant 51151 to P.J., and N.I.H. Grant GM 31086 to K.D.G.

Novel Models and Designs for Small Bore RF Resonators

S. Crozier, L. K. Forbes, W. Roffmann, K. Luescher and D. M. Doddrell

Centre for Magnetic Resonance, Queensland University, St. Lucia. Qld. 4072, Australia

I. Introduction

In this work we introduce a new numerical technique for calculating the current densities in and resultant fields from RF resonators of the distributed conductor design. The numerical technique is based on iterative applications of the inverse Hilbert Transform. Shielded coils may also be analysed by this approach. By being able to calculate the current density for a given coil we are able to investigate a number of coil geometries.

We illustrate the technique for high-pass birdcage resonator (1) type structures where the conductors are "streamline", that is, they are of variable azimuthal width (see figure 1).

II. Numerical Calculations

When electric and magnetic fields are in these probes, apart from components in time and the axial direction, then the electric field may be taken to have the approximate form

$$E = E_T(x,y) \exp(k\omega[z\sqrt{\mu\epsilon} - t]) \quad (1)$$

in which x,y are the transverse coordinates and z points axially. The operating angular frequency of the probe is ω . The vector $E_T(x,y)$ has no axial component, and similar forms to equation (1) are assumed for the magnetic fields B and H . It has been shown by Carlson (2), for example, that the approximation in Eq. (1) permits the choice

and that, as a consequence of equation (2),

$$B_T = -\sqrt{\mu\epsilon}(\hat{z} \times E_T) \quad (2)$$

Maxwell's equations reduce to

$$\text{div } E_T = 0; \text{ curl } E_T = 0 \quad (3)$$

It is now possible from Eq. (3) to define a scalar potential Φ for the transverse component E_T of the electric field, by means of the relation $E_T = -\nabla\Phi$. The problem is now to solve Laplace's equation $\nabla^2\Phi = 0$ outside the conducting rungs of the probe, with Φ held constant at conducting boundaries. The current density (per unit length) J_T on the conductor is then found from

$$J_T = \sqrt{\frac{\epsilon}{\mu}} \left(\frac{\partial\Phi}{\partial n} \right) \hat{n} \quad (4)$$

in which n denotes the normal pointing out of the conductor. The total current I on each rung is

obtained from

$$I = 2 \int J_T \hat{n} dl \quad (5)$$

with the integral taken across the rung. The factor of 2 arises from the fact that current flows down both sides of the rung, which is assumed to be thin.

Suppose that N conducting rungs are arranged around the circumference of a circular cylinder of radius a , so that the n -th rung is located in the interval $\theta_{n1} < \theta < \theta_{n2}$. The conformal mapping

$$u + iv = \frac{ia(x + iy + a)}{(x + iy - a)} \quad (6)$$

is now used, to transform the circle $x^2 + y^2 = a^2$ in the physical $x - y$ plane to the line $v = 0$ in the mapped $u - v$ plane. The n -th rung is now located in the interval

$\gamma_{n1} < u < \gamma_{n2}$ on the u -axis, with

$$\gamma_{n1} = a \cot(\frac{1}{2}\theta_{n2}) ; \gamma_{n2} = a \cot(\frac{1}{2}\theta_{n1})$$

Since the scalar potential Φ also obeys Laplace's equation in the transformed $u - v$ plane, the solution is obtained at once in the form

$$\Phi(u, v) = \sum_{n=1}^N \int_{\gamma_{n2}}^{\gamma_{n1}} m_n(\bar{u}) \cdot \ln \left[\frac{(u - \bar{u})^2 + v^2}{a^2} \right]^{1/2} d\bar{u} \quad (7)$$

The moment functions $m_n(u)$ on each conducting rug $n = 1, 2, \dots, N$ are unknown, and must be found from the boundary condition that Φ is constant on each rung. Differentiating Eq. (7) with respect to u , in the limit $v \rightarrow 0$, therefore gives

$$0 = \sum_{n=1}^N \int_{\gamma_{n1}}^{\gamma_{n2}} \frac{m_n(\bar{u})}{u_k - \bar{u}} d\bar{u} \quad k=1, 2, \dots, N. \quad (8)$$

Equations (8) are a coupled system of N first-kind integral equations, to be solved for the moment function $m_n(u)$ on each rung, $n=1, 2, \dots, N$. These functions are singular at each edge of the rung, $u=\gamma_{n1}$ and $u=\gamma_{n2}$, and so must be written in the form

$$m_n(u) = \frac{K_n}{[(\gamma_{n2} - u)(u - \gamma_{n1})]^{1/2}} + M_n(u) \quad (9)$$

Substituting equations (9) and (8) then gives coupled integral equations

$$\int_{\gamma_{n1}}^{\gamma_{n2}} M_k(\bar{u}) \frac{d\bar{u}}{u_k - \bar{u}} = h_k(u_k) \quad k=1, 2, \dots, N \quad (10)$$

for the unknown functions $M_n(u)$. Here, the right-hand side function $h_k(u_k)$ may be shown to have the form

$$h_k(u_k) = - \sum_{n=1}^N \int_{\gamma_{n1}}^{\gamma_{n2}} M_n(\bar{u}) \frac{d\bar{u}}{u_k - \bar{u}} + \pi K_n \frac{\text{sgn}(u_k - \gamma_{n1})}{[(u_k - \gamma_{n1})(u_k - \gamma_{n2})]^{1/2}} \quad (11)$$

after evaluation of a certain integral.

If equation (10) were a single equation, rather than a coupled system, it could be solved at once by the inverse finite Hilbert transform

$$M_k(u_k) = - \frac{1}{\pi^2} \left[\frac{\gamma_{k2} - u_k}{u_k - \gamma_{k1}} \right]^{1/2} \int_{\gamma_{n1}}^{\gamma_{n2}} \left[\frac{\bar{u} - \gamma_{k1}}{\gamma_{k2} - \bar{u}} \right]^{1/2} \frac{h_k(\bar{u})}{u_k - \bar{u}} d\bar{u} \quad (12)$$

Because (10) is actually a coupled system, the inverse formula (12) is solved by fixed-point iteration to give the functions $M_k(u)$ on each rung, $k=1,2,\dots,N$.

After equation (12) has been solved, the moment functions $m_n(u)$, $n=1,2,\dots,N$ can be computed from Eq. (9). These are related to the current densities in each rung through equation (4) and the conformal mapping (6), and yield

$$J_T = \sqrt{\frac{\epsilon}{\mu}} \frac{\pi m_n(u) (u^2 + a^2)}{2a^2} \hat{z} \quad (13)$$

for each $n=1,2,\dots,N$. Notice that the arbitrary constant K_n in equations (9) and (11) is determined by specifying the total current I_n on the n -th rung. From equation (5) it follows that

$$K_n = \sqrt{\frac{\mu}{\epsilon}} \frac{I_n}{2\pi^2} - \frac{1}{\pi} \int_{\gamma_n} M_n(\bar{u}) d\bar{u} \quad (14)$$

and this fact must be incorporated into the iterative solution of equation (12). Further details are given in reference 3.

Unfortunately, in the shielded case the conformal mapping techniques cannot be used and a more general solution for the scalar potential is needed, full details will be given in reference 4. This more general solution can also be used for resonators with cross-sections other than circular, such as elliptical coils.

III. Results and Discussion

Figure 1 shows the current density from a narrow rung birdcage resonator (1). Having this flexible algorithm to calculate current densities means that a number of conductor arrangements

can be thoroughly investigated and optimized.

Conventional feeding arrangements for resonators of this type are to input the RF, via tuning and matching networks, directly onto a rung (conductor) of the resonator. As the current standing wave is set up around the periphery of the resonator, this means that two rungs carry zero net integrated current. An alternate arrangement is to feed equally onto two rungs (so-called inter-rung feeding) (4), this turns out to slightly improve homogeneity and makes the resonator less susceptible to shielding variations (5).

Figure 2 shows the currents on a shielded coil and the field it generates. In fig 2A the primary current density is represented by a solid line and the shield by a dashed line. The shield has a profound effect on the primary current density, particularly where the shield is close to the primary. The shield has the effect of reducing the central field strength of the coil assembly but, somewhat surprisingly, improves the homogeneity of the coil. It also has the desired effect of reducing radiation to surrounding conductors such as gradient and shim sets (5).

III. Conclusion

We have briefly outlined a novel numerical scheme for calculating current densities and therefore fields in RF resonators. This scheme can be applied to a plethora of conductor layouts. Experimental work supporting the model has been presented elsewhere (3-5).

IV. References

1. C.E. Hayes, W.A. Edelstein, J.F. Schenck, O.M. Mueller and M.A. Eash, *J. Magn. Reson.* **63**, 622 (1985).
2. J.W. Carlson, *Magn. Reson. Med.*, **3**, 778 (1986).
3. L.K. Forbes, S. Crozier and D.M. Doddrell, *Meas. Sci. Technol.* **6**, 284 (1995).
4. S. Crozier, K. Luescher, L.K. Forbes and D.M. Doddrell, *J. Magn. Reson.*, in press (1995).
5. L.K. Forbes, S. Crozier and D.M. Doddrell, *SIAM J. Appl. Math.*, submitted (1995).

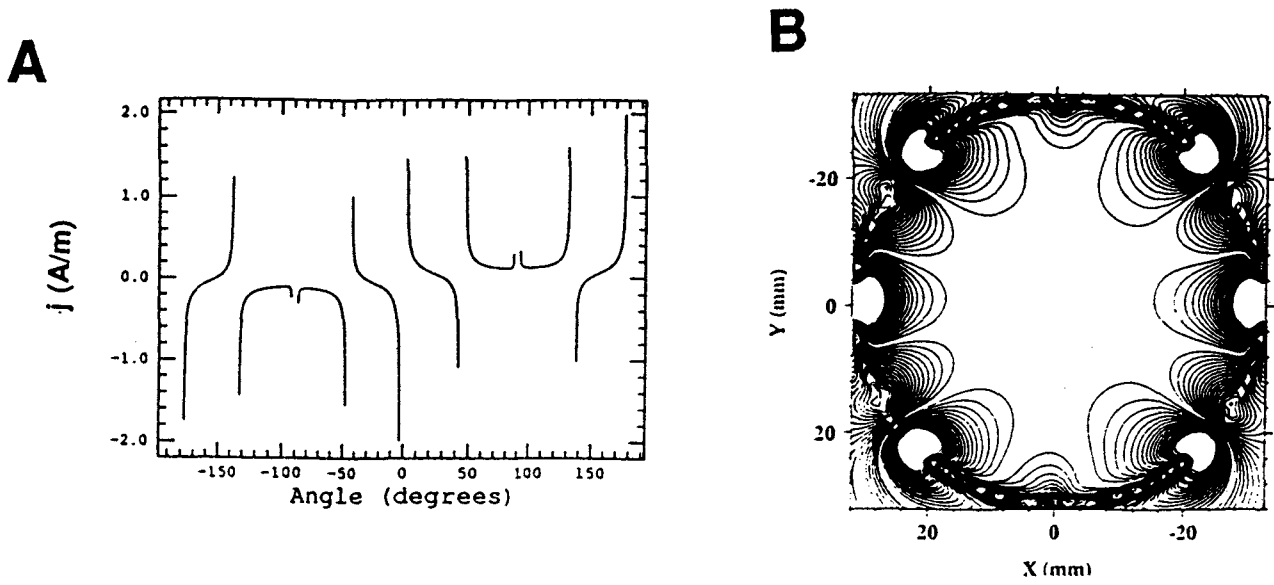


Figure 1 A The current density of an eight-strip wide rung resonator. B The resultant transverse magnetic field in 5% contours.

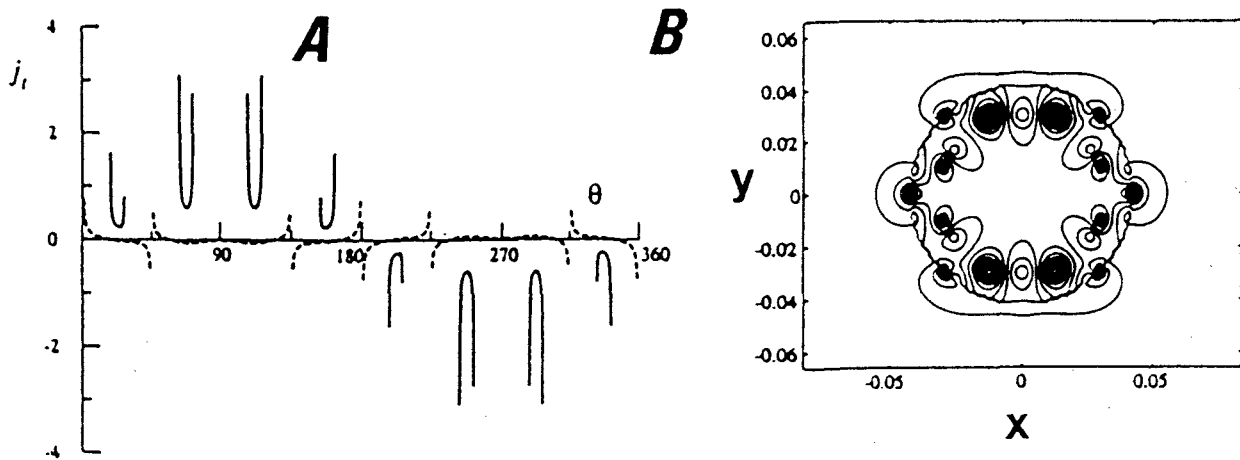


Figure 2 A The current densities of a shielded resonator. B The resultant transverse magnetic field in 5% contours.

New Semi-empirical Approach for the Calculation of ^{13}C Chemical Shift Tensors

U. Sternberg and W. Priess, Friedrich-Schiller-Universität Jena

Abstract

A novel semi-empirical method for the calculation of chemical shift tensors is presented and this method is well suited to calculate derivatives of the chemical shifts with respect to the coordinates of the nuclei. This feature is of great importance if chemical shifts shall be used as target functions in molecular mechanics calculations.

The three principal values of the ^{13}C chemical shift tensors can be determined in solid state ^{13}C NMR investigations of crystalline powders whereas for the determination orientation of the tensor with respect to the crystalline axis single crystal investigation have to be carried out. Using modern experimental techniques (Sherwood et al. (1)) the tensors can be measured very precisely even in the case of many overlapping lines. With the possibility to measure a large number of tensors for complicated substances one has to face two tightly interconnected problems: assignment and interpretation. The tensors have to be assigned to distinct carbon sites within the crystal. This set of six measured figures per carbon atom bids fair to contain detailed information about the spatial geometry and electronic environment of the surrounding of the carbon atom under study. The problem is that up to now there are no simple rules for the estimation of the tensors as in the case of the isotropic chemical shift. Isotropic chemical shifts can be estimated from empirical increments and correlations and these estimates are in most cases precise enough to reveal the topology or constitution of a molecule. Up to now ab initio quantum chemical calculations on the GIAO or IGLO (2) level have to be performed if chemical shift tensors shall be understood with respect to the structure of a molecule. This approach is limited to medium size molecules that do not interact too strongly with their neighbours within the crystal lattice as for instance naphthalene. If tensorial data are to be used in molecular mechanics calculation the computational effort of the ab initio methods inhibits its application.

The aim of this work is the introduction of a semi-empirical method for the calculation of chemical shift tensors. This method is based on the bond polarization theory (3-6). It was demonstrated that ^{13}C chemical shift tensors can be predicted with this method with deviations from experiment comparable to the errors of the ab initio methods. The calculations can be performed for molecules with hundreds of atoms even on a PC computer. In contrast to the ab initio method a set of empirical parameters is needed for the calculations. In the case of the bond polarization theory these parameters can be estimated directly from experimental chemical shifts solving a set of linear equations. The coefficients of this overdetermined set of equations are bond polarization energies that have to be calculated within the framework of this theory. In fig. 1 a correlation of calculated and observed tensors values is presented. This correlation contains all tensors of 5 Pyranosides, Sucrose, Naphthalene, Pyrene, Perylene, Acenaphthene, Glycine, L-Alanine, L-Serine Monohydrate, L-Threonine and L-Asparagine Monohydrate. These substance were selected because precise tensors and the solid state structures are available. For most of the 630 values the difference between experiment and calculation is within the limits of ± 10 ppm (see fig. 2). Larger deviations occur if ring strain has to be taken into account. The chemical shift tensors of Triphenylene were calculated with the parameters obtained from the correlation (see Table 1). This molecule did not belong to the set of calibration molecules. One has to keep in mind that this calculation took several seconds on a PC-computer.

Table 1: Experimental and calculated ^{13}C chemical shift tensor values of Triphenylene

	δ	Experiment (7)	LORG (4-31G) (7) ab initio calculation	Bond Polarisation Theory this work
C(1)	11	225	246	222
	22	137	149	143
	33	8.2	4	17
C(2)	11	215	239	220
	22	140	141	140
	33	2.8	7	17
C(3)	11	208	219	205
	22	171	175	202
	33	-1	8	4

References

- 1 M. H. Sherwood, D. W. Alderman, and D. M. Grant,
J. Magn. Res. **84**, 466 (1989)
- 2 K. Wollinski, J. F. Hinton, and P. Pulay,
J. Am. Chem. Soc. **112**, 8251 (1990)
- 3 U. Sternberg, Molecular Physics **63**, 249 (1988)
- 4 U. Sternberg, F. Pietrowski und W. Priess,
Z. f. phys. Chem. (Neue Folge) **168**, 115 (1990)
- 5 U. Sternberg and E. Brunner,
J. Magn. Res. **A108**, 142 (1994)
- 6 U. Sternberg and W. Prieß,
J. Magn. Res. **102**, 160 (1993)
- 7 A. Soderquist, C. A. Hughes, W. J. Horton, J. C. Facelli, and D. M. Grant,
J. Am. Chem. Soc. **114**, 2826 (1992)

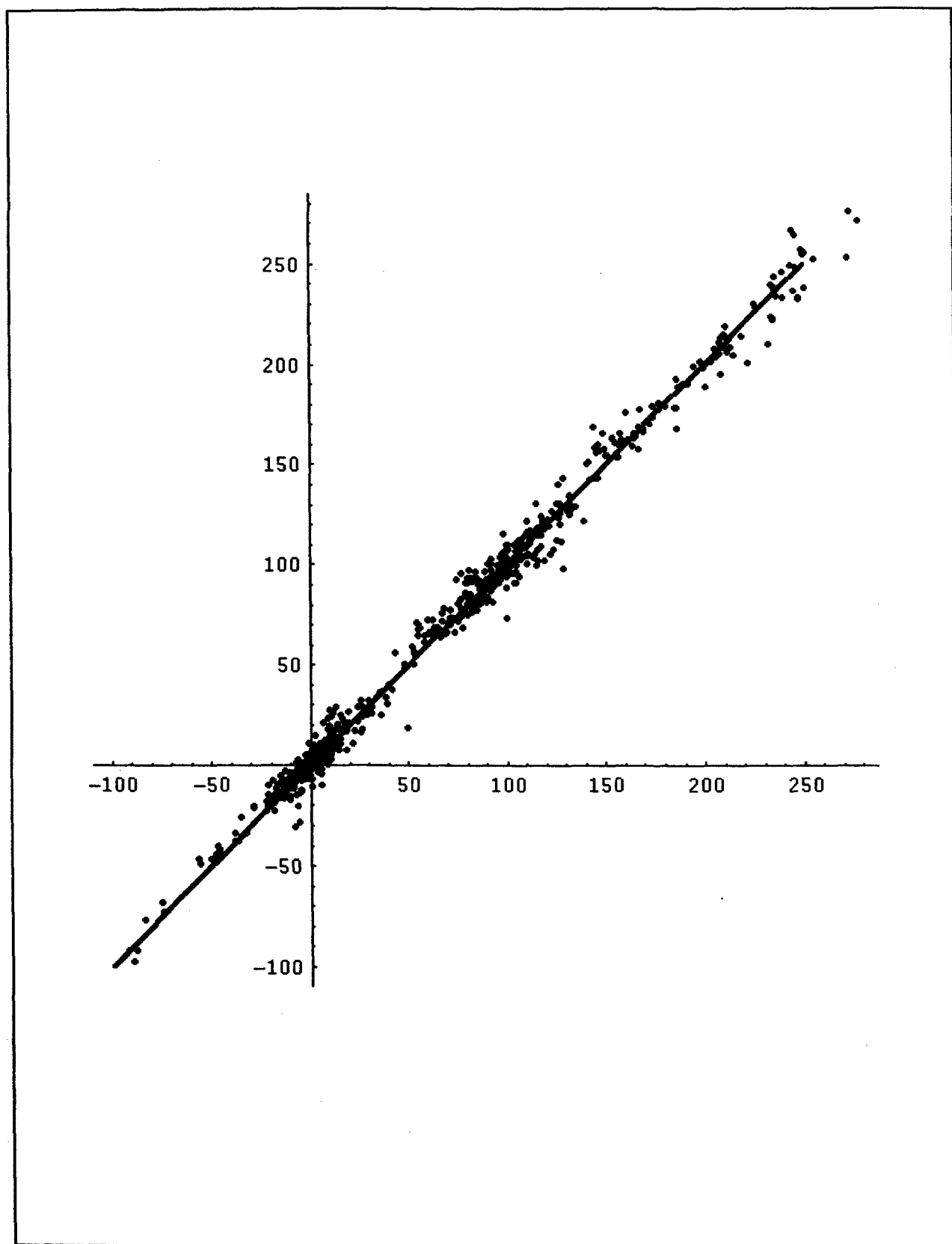


Figure 1: Plot of observed ^{13}C -chemical shift tensors against calculated values

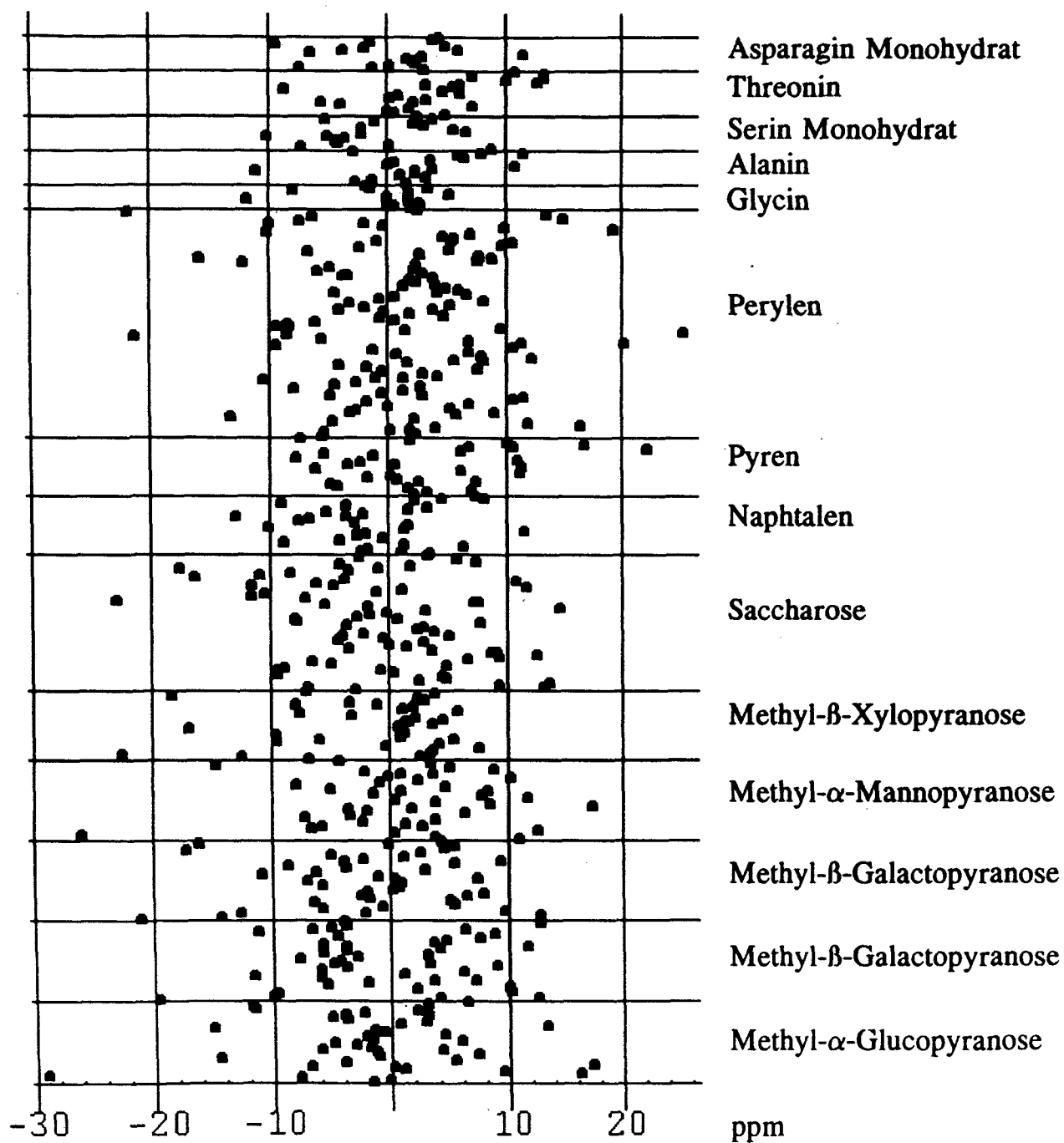


Figure 2: Differences between observed and calculated ^{13}C chemical shift tensor values for several molecules

Elucidation of Metabolic Pathways Employing One- and Two-Dimensional NMR Spectroscopy

George L. Mendz

*School of Biochemistry and Molecular Genetics,
The University of New South Wales, Sydney, NSW 2052, Australia*

Introduction

Multinuclear NMR methods have been employed to study the physiology of *Helicobacter pylori*, a Gram-negative, spiral, vibrioid bacterium that has a pathogenic role in gastrointestinal disease in humans. Previous work established that the microorganism utilizes glucose via the pentose phosphate (1-3) and Entner-Doudoroff (4) pathways, and that fumarate (5) and pyruvate (6) intermediate metabolism is carried out by fermentative pathways.

H. pylori can grow and proliferate in broth containing only aminoacids as basic nutrients. Several aminoacids including L-asparagine, L-aspartate, L-arginine and L-serine are utilized at fast rates in liquid cultures (7), and L-arginine is an essential requirement for growth (8). Multinuclear one- and two-dimensional NMR techniques were used to investigate the pathways of arginine catabolism.

Materials and Methods

H. pylori laboratory adapted strains, and low passage wild type strains were grown on Blood Agar Base No. 2 plates and incubated in an atmosphere of 10% CO₂ in air, 95% humidity at 37 °C (9). Cells were washed three times in isotonic NaCl by centrifuging at 17,000g (6 °C, 3 min), discarding the supernatant, collecting the pellet, and resuspending it in saline. Lysates were prepared by twice freezing in liquid nitrogen and thawing packed cells suspended in 150 mM KCl.

Cell suspensions or lysates were transferred to 5 or 10 mm tubes for metabolic studies employing NMR spectroscopy, and were incubated at 37 °C for up to 24 h after addition of L-arginine. ¹H-NMR free induction decays were collected using a Bruker DMX-500 spectrometer, operating in the pulsed Fourier transform mode with quadrature detection. The instrumental parameters were: operating frequency 500.13 MHz, spectral width 5000 Hz, memory size 16 K, acquisition time 1.638 s, number of transients 144 and relaxation delays with solvent presaturation 1.0 s. Spectral resolution was enhanced by Gaussian multiplication with line broadening of -1.0 Hz and Gaussian broadening factor of 0.19.

One-dimensional natural abundance ¹³C-NMR spectra were acquired with composite pulse decoupling using a Bruker ACP-300 spectrometer. The instrumental parameters were: operating frequency 75.5 MHz, spectral width 16129 Hz, memory size 16 K, acquisition time 1.508 s, number of transients 3000, and pulse angle 66° (9 μs). Exponential filtering of 3 Hz was applied prior to Fourier transformation. ¹³C chemical shifts are quoted relative to L-Arg-α-CH at 55.32 ppm.

One-dimensional ¹⁴N-NMR spectra were acquired using the ACP-300 spectrometer. The instrumental parameters were: operating frequency 21.69 MHz, spectral width 13157.89 Hz, memory size 16 K, relaxation delay 0.626 s, and the number of transients 2944. Spectra were acquired with a standard antiringing program. Exponential filtering of 40 Hz and a left shift of two data points were applied prior to

Fourier transformation.

The time-evolution of substrates and products were followed by acquiring sequential spectra of the reactions. Progress curves were obtained by measuring the integrals of substrate and product resonances at each point in time. Maximal rates were calculated from good fits (correlation coefficients ≥ 0.99) of the data to straight lines for 30-60 min of the incubations. Calibrations of the peaks arising from substrates were performed by extrapolating the resonance intensity data to zero time and assigning to this intensity the appropriate concentration value. The intensity of resonances corresponding to products were calibrated by adding the appropriate metabolite to cell suspensions and constructing standard concentration curves.

Incubations products were separated by centrifuging samples at 17,000g (6 °C, 8 min), collecting the supernatants, and filtering through membranes with a molecular weight cutoff of 1000. The identification of catabolic products was carried out employing two-dimensional NMR methods. Phase-sensitive $\{^1\text{H}-^{13}\text{C}\}$ heteronuclear single quantum coherence (HSQC) experiments were acquired in the DMX-500 spectrometer using a customer-designed programme. The acquisition parameters were: ^1H spectral width 4990.02 Hz, ^{13}C spectral width 5030.31 Hz, recycling

time 1.0 s, and 64 free-induction decays were averaged over 2048 memory locations. Contour maps of 2048 X 1024 data points were obtained from 512 individual experiments by zero filling in the evolution time domain. The plots are phase-sensitive mode with square sine-bell apodization and a shift for sine-bell window of $\pi/2$ along the acquisition and evolution time domains.

Phase-sensitive double quantum-filtered ^1H homonuclear correlated (DQFT-COSY) experiments with pre-saturation of the solvent resonance were acquired in the DMX-500 spectrometer employing a standard programme. The acquisition parameters were: spectral width 4990.02 Hz, 3.5 s recycling time, and 32 free-induction decays were averaged over 4096 memory locations. Contour maps of 4096 X 1024 data points were obtained from 1024 individual experiments. The plots are phase-sensitive mode, with square sine-bell apodization and a shift for sine-bell window of $\pi/3$ along the acquisition time domain, and square sine-bell apodization along the evolution time domain.

Results

Rapid catabolism of arginine was observed in suspensions of bacterial cells in isotonic NaCl or lysates in KCl (Fig. 1).

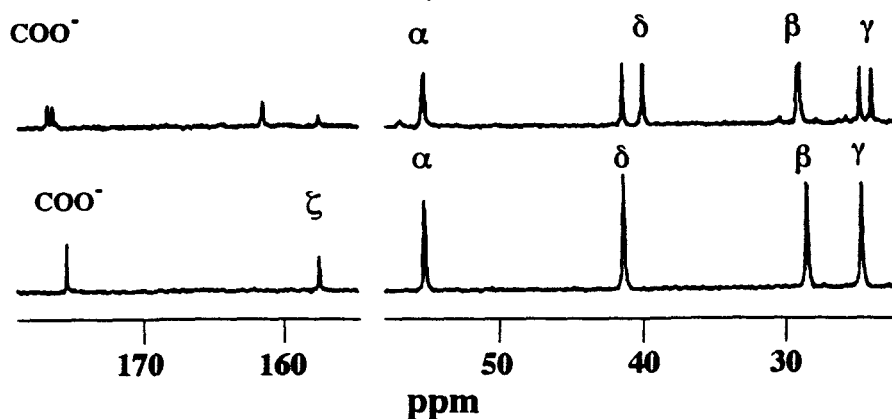


Figure 1. ^{13}C -NMR spectra of a time-course of the conversion of L-arginine by *H. pylori* lysates suspended in KCl. The substrate concentration was 50 mM. The resonances corresponding to the α , β , γ and δ carbons of L-arginine are indicated on the bottom spectrum, and those corresponding to L-ornithine on the top spectrum.

The metabolism of arginine by cells and lysates was followed also in time-courses acquired employing ^1H - or ^{14}N -NMR spectroscopy. Rates of arginine utilization by lysates of strain N6 in the presence of 50 mM substrate were 44.8 ± 2.9 nmole/min/mg protein. The measured rates depended on the strain used.

The six ^{13}C -NMR resonances arising from the carboxylic, guanidino ζ , and aliphatic α , β , γ and δ carbon atoms of L-arginine decreased with time in the sequential spectra of *H. pylori* suspensions during incubations, and five other resonances at 174.97, 55.20, 40.01, 28.40, and 23.74 emerged. The identity of these new resonances was investigated employing two-dimensional NMR techniques. The $\{^1\text{H}-^{13}\text{C}\}$ HSQC map of ultrafiltrates from incubation products showed correlations between the aliphatic carbon resonances at 55.20, 40.01, 28.40, and 23.74 ppm and proton resonances at 4.389, 3.178, 1.900, 1.823, and 1.734 ppm, respectively (Fig. 2).

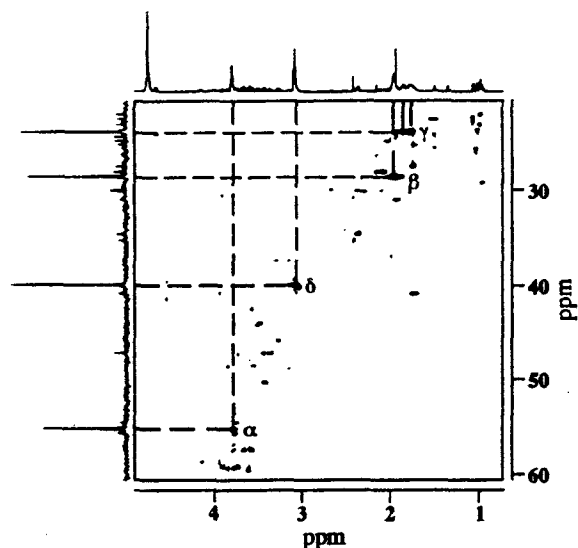


Figure 2. Aliphatic region of the two-dimensional $\{^{13}\text{C}-^1\text{H}\}$ shift-correlated contour map of ultrafiltrates from incubations of L-arginine with *H. pylori* cells suspended in NaCl. The resonances corresponding to the product L-ornithine are indicated on the figure. The correlations between the resonances in the ^{13}C and ^1H spectrum are indicated by dashed lines.

The DQFT-COSY contour map of ultrafiltrates indicated connectivities between the proton resonances at 4.389 and 1.900, 1.823 ppm; 3.178 and 1.734 ppm; and 1.734 and 1.900, 1.823 ppm (Fig. 3). The correlations shown in the heteronuclear correlation map, the connectivities of the homonuclear correlation plots, and the chemical shifts of all the resonances allowed a unique assignment of these peaks to the α (^{13}C : 55.20 ppm, ^1H : 4.389 ppm), β (^{13}C : 28.40 ppm, ^1H : 1.900, 1.823 ppm), γ (^{13}C : 23.74 ppm, ^1H : 1.734 ppm), and δ (^{13}C : 40.01 ppm, ^1H : 3.178 ppm) moieties of ornithine. The peak at 174.97 ppm corresponded to the carboxylic carbon of ornithine.

Time-courses of the metabolism of arginine in suspensions of lysates in KCl observed using ^{14}N -NMR spectroscopy, showed the formation of NH_4^+ as well as ornithine (Fig. 4). The results indicated that L-arginine is converted directly to ornithine and ammonium.

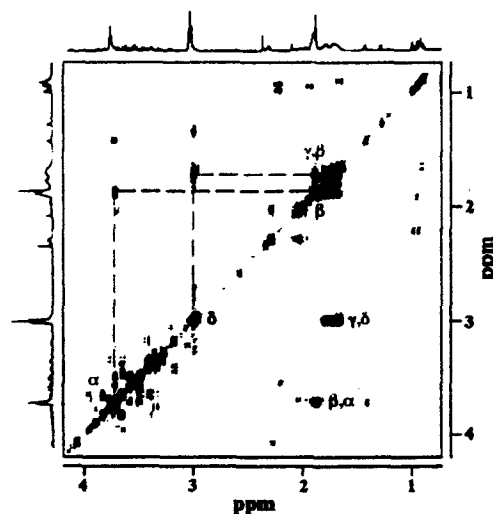


Figure 3. Aliphatic region of the two-dimensional ^1H DQFT-COSY contour map of ultrafiltrates from incubations of L-arginine with *H. pylori* cells suspended in NaCl. Indicated on the figure are the L-ornithine resonances corresponding to the α , β and δ protons, the α,β , β,γ and δ,γ cross-peaks and the connectivities between the different resonances of L-ornithine.

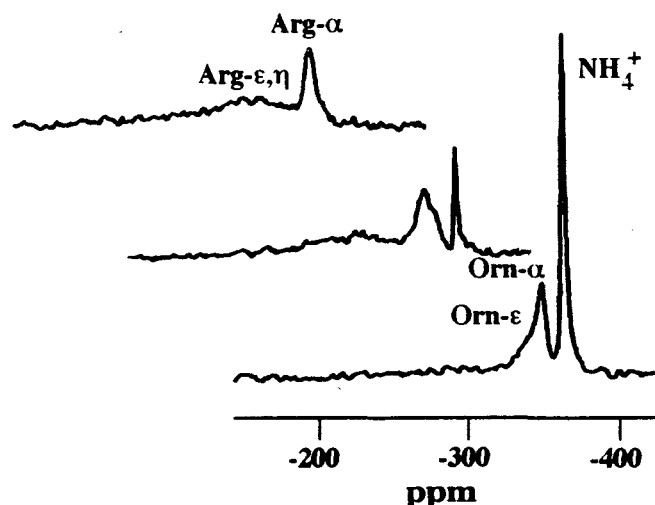


Figure 4. ^{14}N spectra of a time-course of *H. pylori* lysates in KCl incubated with 50 mM L-arginine as the sole substrate at 37 °C. The resonances corresponding to the Arg- α , - ϵ , - η_1 and - η_2 , Orn- α and - ϵ and NH_4^+ are indicated on the figure. Spectra were acquired at 30, 120 and 300 min incubation, from top to bottom respectively.

Discussion

Fast rates of arginine catabolism were measured in lysates and cell suspensions by NMR spectroscopy (Fig. 1), and the products of these reactions were identified as ornithine and ammonium (Figs. 2, 3 and 4), indicating hydrolytic cleavage of the substrate by arginase activity, and hydrolysis of urea by a urease enzyme located outside the cells.

The data suggested that the arginase pathway is the main route of L-arginine catabolism in *H. pylori*. The presence of this enzyme activity opens the possibility that the bacterium may have a complete urea cycle since arginase is the most characteristic enzyme of the cycle.

The results of the study showed that multinuclear NMR spectroscopy methods are a powerful tool to investigate bacterial metabolic pathways.

Acknowledgments. This work was made possible by the support of the National Health and Medical Research Council of Australia, and the Clive and Vera Ramaciotti Foundations.

References

1. Mendz, G. L., and Hazell, S. L. (1991) *FEMS Microbiol. Lett.* **84**, 331-336.
2. Mendz, G. L., and Hazell S. L. (1993) *Arch. Biochem. Biophys.* **300**, 522-525.
3. Mendz, G. L., Hazell S. L., and Burns, B. P. (1993) *J. Gen. Microbiol.* **139**, 3023-3028.
4. Mendz, G. L., and Hazell S. L. (1993) *Arch. Biochem. Biophys.* **312**, 349-356.
5. Mendz, G. L., and Hazell, S. L. (1993) *Biochem. Mol. Biol. Int.* **31**, 325-332.
6. Mendz, G. L., Hazell S. L., and van Gorkom, L. (1994) *Arch. Microbiol.* **162**, 187-192.
7. Mendz, G. L., and Hazell, S. L. (1995) *Int. J. Biochem. Cell Biol.* (in press).
8. Reynold, D. J. and Penn, C. W. (1994) *Microbiology* **140**, 2649-2656.
9. Mendz, G. L., Lim, T. G., and Hazell S. L., (1993) *Arch. Biochem. Biophys.* **305**, 252-260.

2D and 3D ^{15}N NMR Studies of Long [Arg3]-IGF-I

E.R. Le Breton*, J.A. Carver*, G.L. Francis#, G. Shooter#, J.C. Wallace#,
B.N. Gray+ and M.A. Keniry+

*Department of Chemistry, The University of Wollongong, Wollongong, NSW 2522, Australia

#Department of Biochemistry, The University of Adelaide, Adelaide, South Australia 5000,
Australia.

+Research School of Chemistry, The Australian National University, Canberra, ACT 0200,
Australia

I Introduction

Insulin growth factors (IGFs) are a class of single-chain polypeptides that stimulate growth and differentiation in a wide variety of cell types (1). The two forms, IGF-I and -II, are found in plasma and most biological fluids and are responsible for a large proportion of the mitogenic activity in serum used in cell culture. IGFs are naturally found bound to a heterogeneous group of high-molecular-weight binding proteins (IGFBPs) which facilitate in the transport and delivery of IGFs to membrane-bound target cell receptors (2).

IGF-I and IGF-II consist of 70 and 67 amino acids respectively, are highly homologous to insulin and have similar folded structures. The IGFs have four well-defined domains: B, C, A and D beginning from the N-terminus (2). In the A and B domains, 70% of residues in IGF-I and II are identical and 50% of the residues in the IGFs are identical to those in the A- and B-domains of insulin. The C-domain of the IGFs corresponds to the C-domain of proinsulin, but it has no sequence homology with each other or with proinsulin. The D-domain has no equivalent in insulin. The solution structures of IGF-I and IGF-II have recently been determined by 2D (3, 4) and 3D (5,6) NMR spectroscopy. Both proteins adopt similar structures. The main features in IGF-I are three α -helices, one in the B domain and two in the A-domain (3). The C- and D-domains are both poorly defined.

Recombinant fusion protein analogues of IGF-I, in which the N-terminal region of the native form has been modified, provide a more potent class of proteins. This increased potency is proposed to result from the analogues having poor binding affinity to the IGFBPs in serum and other body fluids. Thus, more free protein is available to cellular IGF receptors. The most potent of these variants is Long [Arg3]-IGF-I and Long [Gly3]-IGF-I, where Glu-3 in the

human IGF-I sequence has been replaced by Arg or Gly, and the N-terminus has a 13 amino acid extension consisting of the first 11 amino acids of the methionyl porcine growth hormone followed by the dipeptide Val-Asn (7). It is not clear whether the increased potency of Long-IGF analogues is due to the N-terminal region having a direct effect on IGFBP binding or is a result of the masking effect of residues on the surface of the IGF-I molecule which are involved in the binding reaction (7).

We present here the first stages in our determination of the solution structure of Long [Arg3]-IGF-I by NMR techniques. The overall goal is to provide a rationale as to the structural preferences of this analogue which leads to its increased potency.

II Experimental

Long [Arg3]-IGF-I was labelled with ^{15}N by standard methods. All spectra were recorded at 303K on a Varian VXR-500 NMR spectrometer equipped with an actively shielded z-gradient probe and gradient amplifier units. Standard 2D ^{15}N HSQC, ^{15}N HSQC-TOCSY and ^{15}N HSQC-NOESY spectra were acquired (8). Mixing times of 30ms and 80ms were used for the 2D HSQC-TOCSY and 100ms, 150ms and 200ms for the 2D HSQC-NOESY experiments. 3D ^{15}N TOCSY-HSQC spectra with mixing times of 30ms and 80ms, and 3D ^{15}N NOESY-HSQC spectra with a mixing time of 140ms were acquired. For all the 3D spectra, linear prediction was performed prior to Fourier transformation, with 60 and 38 point extensions in F1 and F3 respectively.

III Results and Discussion

Sequential assignments The sequential assignment method of Wüthrich (9) was used to assign the majority of the ^1H spectrum and thereby to determine secondary structural features of Long [Arg3]-IGF-I. Firstly, types of spin-systems were identified from the 2D HSQC and HSQC-TOCSY or 3D TOCSY-HSQC spectra. Secondly, these spin systems were linked together using sequential d_{NN} , $d_{\text{N}\alpha}$ and $d_{\text{N}\beta}$ connectivities from the 3D ^{15}N NOESY-HSQC spectrum (10).

Secondary structural features The sequential assignment of Ala8 to Asn26 of Long [Arg3]-IGF-I is given in figure 1. The various structural features so far determined for Long [Arg3]-IGF-I can be summarised as follows:

(a) *B-domain* The secondary structural features observed in figure 1 are consistent with those found for the B-domain in earlier work on IGF-I (3, 4). Residues Ala8 to Cys18 constitute helix 1, as indicated by the strong sequential d_{NN} nOes and weak $d_{\text{N}\alpha}$ nOes. The $d_{\text{N}\alpha(i,i-4)}$ nOes between Cys18 and Leu14 and Gln15 and Val11 and $d_{\text{N}\alpha(i,i-3)}$ nOes between Ala13 and Leu10, and Cys18 and Glu15 support such a structure. Residues Gly19 to Gly22 appear to adopt a turn-like structure. The presence of two $d_{\text{N}\alpha(i,i-2)}$ nOes, one between Gly22 and Asp20 and the other between Arg21 and Gly19, coupled with the d_{NN} progression of nOes, would suggest that this region forms a turn similar to the type 1 β -turn found in insulin. Finally, residues Gly22 to Asn26 are poorly defined due to the presence of weak sequential d_{NN} nOes or the absence of such nOes, and the presence of strong sequential $d_{\text{N}\alpha}$ nOes.

(b) *C-domain* The presence of strong sequential $d_{\text{N}\alpha}$ nOes from Thr29 to Ala38 and the absence of a significant number of d_{NN} nOes is consistent with a poorly defined C-domain (3,4). Confirmation of some of these connectivities were made through the use of a 3D HSQC-NOESY-HSQC experiment (11) which provided the identification of d_{NN} connectivities between residues with similar amide proton chemical shifts.

(c) *Bridging region between the A- and C-domains* The sequential nOe pattern observed between Gln40 and Ile43 suggests an extended structure for this region due to the presence of medium-strength sequential d_{NN} nOes and strong sequential $d_{\text{N}\alpha}$ nOes. The latter nOes weaken from Val44 and, although the d_{NN}

nOes between Val44 and Asp45 are poorly resolved, this could suggest the beginning of a helical structure, although the paucity of such connectivities makes this inconclusive.

(d) *N-terminal extension* At this stage, only one sequential connectivity, between Met-9 and Ala-10, has been identified through a weak sequential d_{NN} nOe and a medium-strength sequential $d_{\text{N}\alpha}$ nOe. These nOes would suggest that this region is poorly defined; however, more connectivities are required in the N-terminal extension to draw definite conclusions about its conformation. The identification of the N-terminal residues and the structural preference(s) that this region adopts is one of the desired outcomes of this work. Figure 2 summarises the secondary structural features identified in IGF-I (3,4) and Long [Arg3]-IGF-I.

IV References

1. E.R. Froesch, C. Schmid, J. Schwander and T. Zapf, *Annu. Rev. Physiol.* **47**, 44 (1985).
2. R.E. Humbel, *Eur. J. Biochem.* **190**, 445 (1990).
3. R.M. Cooke, T.S. Harvey and I.D. Campbell, *Biochemistry* **30**, 5482 (1991).
4. A. Sato, S. Nishimura, T. Ohkubo, Y. Kyogoku, S. Koyama, M. Kobayashi, T. Yasuda and Y. Kobayashi, *Int. J. Pept. Prot. Res.* **41**, 433 (1993).
5. H. Terasawa, D. Kohda, H. Hatanaka, K. Nagata, N. Higashihashi, H. Fujiwara, K. Sakano and F. Inagaki, *EMBO J.* **13**, 5590 (1994).
6. A.M. Torres, B.E. Forbes, S.E. Aplin, J.C. Wallace, G.L. Francis and R.S. Norton, *J. Mol. Biol.* **248**, 385 (1995).
7. G.L. Francis, M. Ross, F.J. Ballard, S.J. Milner, C. Senn, K.A. McNeil, J.C. Wallace, R. King and J.R.E. Wells, *J. Mol. Endocrin.* **8**, 312 (1992).
8. T.J. Norwood, J.E. Boyd, N. Soffe and I.D. Campbell, *J. Magn. Res.* **87**, 488 (1990).
9. K. Wüthrich, *NMR of proteins and nucleic acids*, Wiley, New York (1986).
10. D. Marion, P.C. Driscoll, L.E. Kay, P.T. Wingfield, A. Bax, A.M. Gronenborn and G.M. Clore, *Biochemistry* **28**, 6150 (1989).
11. M.D. Carr, B. Birdsall, T.A. Fienkel, C.J. Bauer, J. Jimenez-Barbero, V.I. Polshakov, J.E. McCormick, G.C.K. Roberts and J. Feeney, *Biochemistry* **30**, 6330 (1991).
12. O. Zhang, L.E. Kay, J.P. Olivier and J.D. Forman-Kay, *J. Biomol. NMR* **4**, 845 (1994).

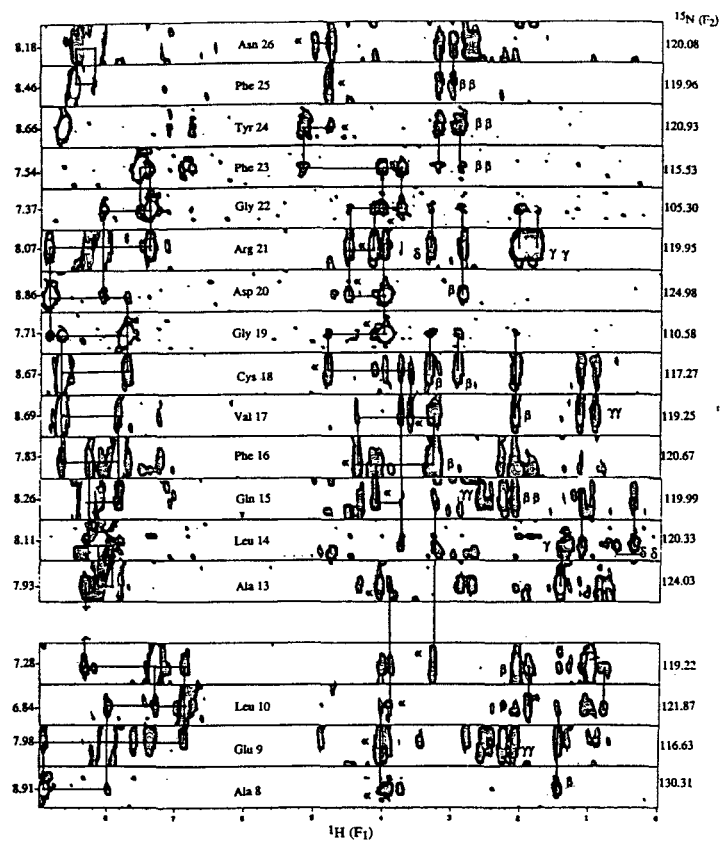


Figure 1: A series of strips from the ^1H - ^1H slices of the 3D NOESY-HSQC spectrum arranged along the ^{15}N dimension to show the d_{NN} and $d_{\text{N}\alpha}$ sequential nOes for the Ala8 to Asn26 region of Long [Arg3]-IGF-I.

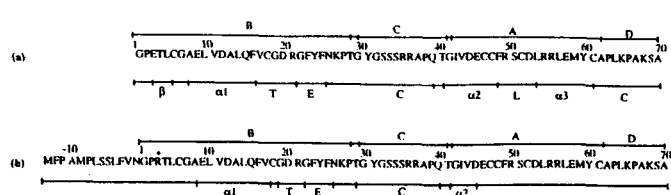


Figure 2: Amino acid sequences and summary of the location of the secondary structural features of (a) IGF-I (4) and (b) Long [Arg3]-IGF-I. Domains are indicated above each sequence. The symbols for secondary structural elements are as follows: α , α -helix; T, β -turn; L, loop; β , β -strand; E, extended; C, coil. The * denotes that Glu3 in IGF-I is replaced by Arg in Long IGF-I.

$^3J(^{113}\text{Cd},^1\text{H})$ Couplings in Cd(S-Cys) and Cd- μ_2 (S-Cys)-Cd Moieties Follow a Karplus-Like Dependence with the $\text{H}^\beta\text{-C}^\beta\text{-S}\gamma\text{-Cd}$ Torsion Angle: Application to Protein Structure

Dean L. Pountney^{†,‡}, Oliver Zerbe[‡], Wolfgang von Philipsborn[‡], J. Barry Egan[†]
and Milan Vasak^{‡,*}

University of Zurich, 8057 Zurich, Switzerland
and University of Adelaide, S.A. 5005, Australia

1. Introduction

The isostructural replacement of native metal ions, in particular zinc, by the NMR active ^{113}Cd nucleus ($I=1/2$) combined with ($^{113}\text{Cd},^1\text{H}$) heteronuclear multiple quantum coherence (HMQC) experiments have frequently been employed in assigning the metal-coordinating ligands in zinc-finger-type DNA binding proteins and metallothioneins (MT)(1-3). However, no geometrical information concerning the metal-binding sites has been obtained from these experiments.

We have used the structurally-characterized ^{113}Cd -substituted proteins *D. gigas* Cd-rubredoxin (Cd-Rd) and rat liver Cd₇-metallothionein (Cd₇-MT) as models to examine the variation of heteronuclear $^3J(^{113}\text{Cd},^1\text{H})$ coupling constants of β -protons of both terminal and bridging cysteine ligands with respect to the $\text{H}^\beta\text{-C}^\beta\text{-S}\gamma\text{-Cd}$ dihedral angle (4-6). The Karplus-type dependence derived enables the geometry of the central metal ion to be predicted in both mononuclear and polynuclear metal-binding domains in ^{113}Cd -substituted metalloproteins based on the corresponding vicinal $^{113}\text{Cd}\text{-}^1\text{H}^{\text{a,b}}$ -cysteine coupling constants. The application of this approach in studying the structural properties of metal centers in the metallothionein-like mammalian neuronal growth inhibitory factor (GIF)(7) and in the coliphage 186 late-gene activating protein, B,(8) are discussed.

2. Theory

In general, heteronuclear couplings involving heavy nuclei depend on orbital angular momentum, electron-nucleus dipole-dipole interaction and Fermi contact terms (9). In the three-bond system considered here, the $\text{H}^\beta\text{-C}^\beta\text{-S}\gamma\text{-Cd}$ dihedral angle, θ , (see Figure 1A) is the principal determinant only in the Fermi contact or through-bond term. The experimental data are described well by a Karplus-like relationship between $^3J(^{113}\text{Cd},^1\text{H})$ coupling constants and θ (see Section 4), indicating that the contributions from the orbital angular momentum and electron-nucleus dipole-dipole interaction terms are negligible. Similar relationships have been established for

vicinal couplings involving lighter nuclei, such as $^1\text{H},^1\text{H}$ (10), $^{15}\text{N},^1\text{H}$ and $^{13}\text{C},^1\text{H}$ (11), however, the current work represents the first demonstration of such a dependence involving a heavy nucleus, i.e. $^{113}\text{Cd},^1\text{H}$.

3. Experimental

The NMR spectra (0.5 ml of 2-4 mM protein) were measured on a Bruker AMX-600 spectrometer. The ($^{113}\text{Cd},^1\text{H}$) coupling constants were determined by comparison of either ($^1\text{H},^1\text{H}$) DQF-COSY or ($^{113}\text{Cd},^1\text{H}$) HMQC spectra run with and without ^{113}Cd -decoupling achieved by broad-band low-power irradiation during acquisition (4-6). As the superposition of scalar couplings from the two coordinated ^{113}Cd nuclei in Cd- μ_2 (S-Cys)-Cd moieties makes the unambiguous measurement of such coupling constants using only ($^{113}\text{Cd},^1\text{H}$) HMQC experiments employing broad-band ^{113}Cd -decoupling impossible, the ($^{113}\text{Cd},^1\text{H}$) coupling constants of bridging cysteine ligands were obtained using in addition selective decoupling of individual ^{113}Cd -nuclei by narrow-band irradiation. All spectra were measured in phase-sensitive mode and, following single zero-filling, the data were apodized using a cosine-bell window function. Defocussing and refocussing delays, Δ , in the HMQC experiments were optimised for 12-50 Hz couplings. Small couplings were extracted from the two-dimensional ($^{113}\text{Cd},^1\text{H}$) HMQC data by taking F2-slices at the positions of the ^{113}Cd resonances and assuming Lorentzian lineshapes.

4. Results and Discussion

Heteronuclear $^3J(^{113}\text{Cd},^1\text{H})$ coupling constants (0-50 Hz) were determined for both bridging and terminal cysteine C^β protons in Cd₇-MT and Cd-Rd (see Figure 1B and Figure 2A). In both cases, the structures of the metal-binding sites have been defined at high-resolution by X-ray crystallography. In the case of MT, a structural model of rat liver Zn₂Cd₅-MT is available at 2.0-Å resolution (12) and comparison with earlier NMR studies on Cd₇-MT (13) show that both metalloforms exhibit identical molecular

* Author to whom correspondence should be addressed. [†] University of Adelaide. [‡] University of Zurich.

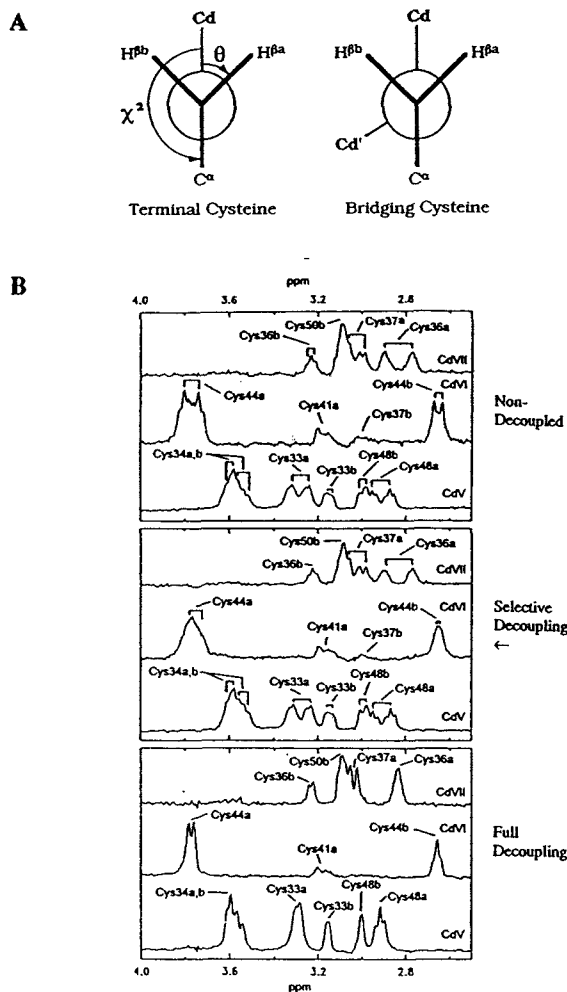


Figure 1. (A) Newman projection of Cd(S-Cys) and Cd- μ_2 (S-Cys) moieties. (B) F2-slices of indicated ^{113}Cd nuclei from representative (^{113}Cd , ^1H) HMQC spectra of Cd7-MT.

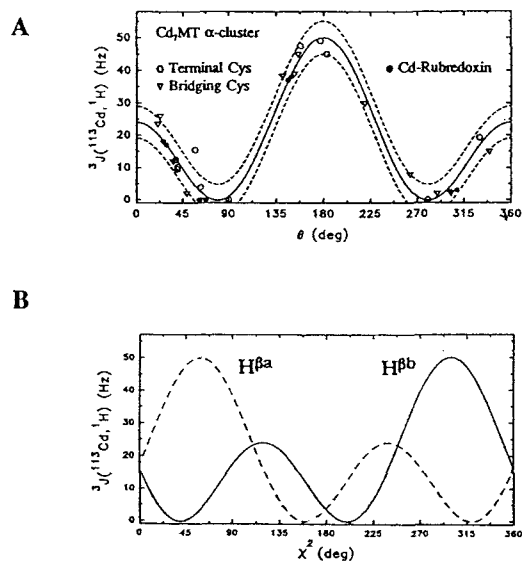


Figure 2. (A) Plot of $^3J(^{113}\text{Cd}, ^1\text{H})$ coupling constant vs. θ . (B) Theoretical variation of $^3J(^{113}\text{Cd}, ^1\text{H}\beta_{a,b})$ coupling constants with χ^2

architectures. This protein contains $[\text{Cd}_4(\text{S-Cys})_{11}]$ and either $[\text{Cd}_3(\text{S-Cys})_9]$ or $[\text{Cd}_1\text{Zn}_2(\text{S-Cys})_9]$ clusters with a total of 12 terminal and 8 bridging cysteine ligands. In this study, $^3J(^{113}\text{Cd}, ^1\text{H})$ coupling constants were extracted only from cysteines in the crystallographically-defined Cd_4 -cluster (α -cluster). The structure of *D. gigas* rubredoxin, which contains a mononuclear $\text{Fe}(\text{S-Cys})_4$ center is known to 1.4-Å resolution (14) and the Cd-derivative has been shown to be isostructural with the native protein (4) Figure 2A illustrates the Karplus-like relationship, $^3J = 36(\cos^2\theta) - 13(\cos\theta) + 1$, obtained when the measured cysteine $\text{H}\beta$ $^3J(^{113}\text{Cd}, ^1\text{H})$ coupling constants are plotted versus the $\text{H}\beta$ - $\text{C}\beta$ - $\text{S}\gamma$ -Cd dihedral angle, θ , derived from the respective crystal structures.

As each possible Cd-S γ -C β -C α dihedral angle, χ^2 (see Figure 1A) in the cadmium center can be defined by a unique pair of $\text{H}\beta^a$ - $\text{C}\beta$ - $\text{S}\gamma$ -Cd and $\text{H}\beta^b$ - $\text{C}\beta$ - $\text{S}\gamma$ -Cd dihedral angles, θ_a and θ_b , (see Figure 2B) the determination of the corresponding pair of $^3J(^{113}\text{Cd}, ^1\text{H}\beta_{a,b})$ coupling constants enables an estimate of χ^2 to be made. Hence, this relationship can readily be applied to define the orientation of the cysteine ligands in ^{113}Cd -substituted metalloproteins such as zinc-finger-like and metallothionein-like proteins, which contain either mononuclear $[\text{Cd}(\text{S-Cys})_x\text{L}_y]$ or polynuclear $[\text{Cd}_x(\text{S-Cys})_y\text{L}_z]$ motifs.

5. Further Studies

The neuronal growth inhibitory factor, GIF (or MT-3), is a 68-amino-acid metallothionein isoform which has a substantially different primary structure compared to other mammalian MTs and which contains both Zn(II) and Cu(I) ions. Current spectroscopic evidence on the Cu,Cd-GIF derivative indicates the presence of adamantane-like Cu- and Cd-cysteinate clusters (7). Further NMR studies will permit a more detailed cluster model to be developed.

The 72-amino-acid coliphage 186 B-protein belongs to a family of late-gene transcription activators occurring in P2-related phage which contain a novel class of zinc-finger-type presumptive DNA-binding domain characterized by a Cys-X₂-Cys-X₂₂-Cys-X₄-Cys motif (8). Preliminary spectroscopic studies on the Cd-B derivative show the presence of a mononuclear $[\text{Cd}(\text{S-Cys})_4]$ center. The development of a structural model of this protein will employ angular constraints derived from $^3J(^{113}\text{Cd}, ^1\text{H})$ coupling constant data.

Acknowledgements

We are grateful to the Swiss National Science Foundation (Grant Nos. 31-32572.91 and 3100-31012.91) and the Australian Research Council (Grant No. AO933141101) for financial support.

References

- [1] P. Schultze, E. Wörgörter, W. Braun, G. Wagner, M. Vasák, J.H.R. Kägi and K. Wüthrich, *J. Mol. Biol.*, **203** (1988) 251.
- [2] L.C. Myers, M.P. Terranova, A.E. Ferentz, G. Wagner and G.L. Verdine, *Science*, **261** (1993)

- 1164.
- [3] G.C. Pérez-Alvarado, C. Miles, J.W. Michelsen, H.A. Louis, D.R. Winge, M.C. Beckerle and M.F. Summers *Structural Biology*, **1** (1994) 388.
- [4] C.J. Hennehan, D.L. Pountney, O. Zerbe and M. Vasák, *Protein Sci.*, **2** (1993) 1756.
- [5] O. Zerbe, D.L. Pountney, W. von Philipsborn and M. Vasák, *J. Am. Chem. Soc.*, **116** (1994) 377;7957.
- [6] D.L. Pountney, O. Zerbe, D. Nanz and M. Vasák, - manuscript in preparation.
- [7] D.L. Pountney, S.M. Fundel, P. Faller, N.E. Birchler, P. Hunziker and M. Vasák, *FEBS Lett.*, **345** (1994) 193.
- [8] J.B. Egan and I.B. Dodd, "P2, P4 and Related Bacteriophages" in *Encyclopaedia of Virology*, Academic Press, NY (1994) 1003.
- [9] R.K. Harris, *Nuclear Magnetic Resonance Spectroscopy. A Physico-Chemical View*, Pitman, London (1983) pp 216.
- [10] M. Karplus, *J. Chem. Phys.*, **30** (1959) 11.
- [11] V.F. Bystrov, *Prog. NMR Spectrosc.*, **10** (1976) 41.
- [12] A.H. Robbins, D.E. McRee, M. Williamson, S.A. Collet, N.H. Xuong, W.F. Furey, B.C. Wang and C.D. Stout, *J. Mol. Biol.*, **221** (1991) 1269.
- [13] W. Braun, M. Vasák, A.H. Robbins, C.D. Stout, G. Wagner, J.H.R. Kägi and K. Wüthrich, *Proc. Natl. Acad. Sci. USA*, **89** (1992) 10124.
- [14] M. Frey, L. Sieker, F. Payan, R. Haser, M. Bruschi, G. Pepe and J. LeGall, *J. Mol. Biol.*, **197** (1987) 525.

FMR STUDIES OF COBALT SUBSTITUTED MAGNETITE PREPARED BY NOVEL MECHANOCHEMICAL METHOD

W. A. Kaczmarek* and S. J. Campbell#

**) Research School of Physical Sciences and Engineering
Australian National University, Canberra, ACT 0200, Australia.*

*#) School of Physics, University College, University of New South Wales,
Australian Defence Force Academy, Canberra, ACT 2600, Australia*

Abstract The magnetic properties of fine particles of Co substituted magnetite of nominal composition $(\text{Co}_x\text{Fe}_{1-x})_3\text{O}_4$, $x=0.037-0.38$, which have been prepared by reactive ball milling followed by annealing have been investigated by ferromagnetic resonance. The investigation also includes X-ray diffraction, dc magnetometry and scanning electron microscopy measurements.

I. Introduction

This study is an extension of our recent investigation of the highly efficient reduction of hematite to magnetite which occurs on milling [1]. The previous results show clearly that complete transformation from hematite to magnetite takes place on water assisted, mechanical activation of $\alpha\text{-Fe}_2\text{O}_3$ powder at room temperature but without oxygen being present in the milling atmosphere. Microstructural analyses based on the X-ray diffraction data indicated average crystal block sizes for the milled products of $\langle D \rangle \approx 30$ nm [2]. Further evidence from Mössbauer spectroscopy [3] and neutron diffraction [4] shows that the vacancy concentration v in the $\text{Fe}_{3-v}\text{O}_4$ increases with milling time, with the vacancies localised primarily in the octahedral ($\text{Fe}^{3+} / \text{Fe}^{2+}$) sites rather than the tetrahedral (Fe^{3+} sites). Such transformation processes offer the possibility for microstructural and stoichiometric modifications in iron oxide fine particles. In particular, preparation of fine Co-doped/substituted Fe_3O_4 or $\gamma\text{-Fe}_2\text{O}_3$ particles is important both for applications purposes, as well as for the study of modifications to the intrinsic ferrimagnetic structure.

Recently we reported on the crystallographic and magnetization measurements [5], here we outline the effects of the cobalt-iron stoichiometry of as milled and annealed cobalt substituted magnetite on their magnetic properties. The FMR technique was used in order to obtain information about the magnetic homogeneity in the prepared ferrite powders.

II. Experimental

The milling conditions have been described previously [1]. A ~13 g mixture of powder $\alpha\text{-Fe}_2\text{O}_3$ (Koch-Light Labs. Ltd.) and powder $\text{Co}(\text{OH})_2$ (Aldrich Inc.), both with analytical purity 99.99% and typical particle size distribution in the range 0.5-50 μm , were introduced into the vial with ~8 ml of water and sealed. $\text{Co}(\text{OH})_2$ is almost insoluble in water (3.2 mg/l at 20° C) thus the water works mainly as a dispersing agent. The milling process was conducted for a maximum of 215 h in a slight overpressure of nitrogen. Annealing of the milled powders was performed in air for 2 hours at 550 K. The compositions of the starting powder mixtures were calculated according to the stoichiometric formula $(\text{Co}_x\text{Fe}_{1-x})_3\text{O}_4$ ($x = 0.38, 0.234, 0.133, 0.071$ and 0.037). In the following discussion, the samples milled for 215 h are denoted B1 - B5 and, after subsequent annealing, C1 - C5 respectively with the numbers denoting the decreasing Co content. Measurements for a commercial magnetite powder (denoted A1), as well as for magnetite prepared by wet milling hematite for 144 h [2] (denoted A2) are included for reference purposes.

The ferromagnetic resonance (FMR) measurements were carried out using a conventional microwave X band reflection cavity spectrometer operating at frequency 9.04 GHz and the first derivatives of absorption were recorded (Varian V4502). All measurements were conducted at room temperature on spherical samples (~1 mm in diameter) prepared from dry powders immersed in liquid wax.

III. Results and discussion

Given that the same milling conditions apply to all powder mixtures, the observed structure evolution is considered to be due to the Co hydroxide interaction with hematite particles during mechanical treatment. From detailed analysis of the XRD patterns [5], it was found that the full transformation occurs only for Co content ≤ 13.3 at.% and for these powders, the final XRD patterns show only peaks characteristic of the spinel type structure. For higher concentrations of $\text{Co}(\text{OH})_2$ in the starting mixture, milling for 215 h produces multiphase material with remanent unreacted starting compounds. SEM micrographs reveal that all final powders have a similar particle size distribution in the range 10-100 nm.

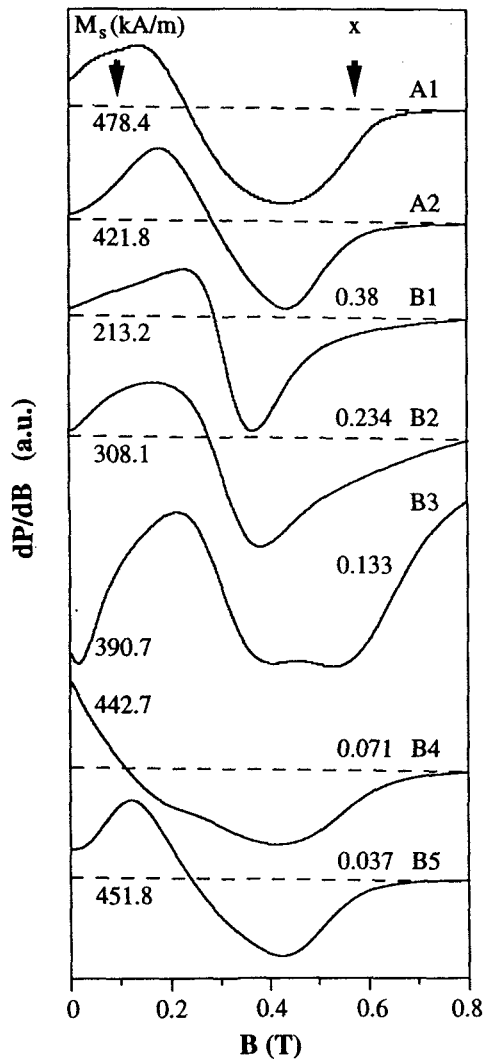


Fig. 1. FMR spectra of reference samples A1 and A2 and the as milled $(\text{Co}_x\text{Fe}_{1-x})_3\text{O}_4$ powders B1 - B5 as described in text. The M_s (1T) values ($1 \text{ kA/m} \approx 12.6 \text{ G}$) are also given.

The room temperature FMR spectra for reference samples A1 and A2 and for the as milled samples B1 - B5 are shown in Fig. 1, with the annealed samples C1 - C5 being shown in Fig. 2. As shown in Fig. 1 the signals (the first derivative of the microwave adsorption, (dP/dB)) for our reference samples A1 and A2 are more or less symmetric. However depending on the Co concentration the asymmetry of the FMR line becomes evident for the as milled samples (cf. B1 - B5 in Fig. 1), as well as for the annealed samples with Co concentration $x \leq 13.3$ at.% (Fig. 2). Line asymmetry is due mainly to resonance on unsaturated samples and is observed clearly in the low magnetic field range $B < 0.2 \text{ T}$ (Figs. 1 and 2). DC magnetization measurements are in good agreement with the FMR results. The "low field" feature around $B \approx 0 \text{ T}$, which is particularly evident in the FMR spectra of the low Co concentration samples B5 ($x = 0.037$) and B4 ($x = 0.071$), is linked with the large magnetisation observed for these samples in low magnetic fields. For example magnetisation values of around 90 % of the saturation magnetisation values as measured at 1 T, $M_s(1\text{T})$, were obtained for fields in the range $\sim 0.2 - 0.3 \text{ T}$. The $M_s(1\text{T})$ values for all samples are given in Figs. 1 and 2.

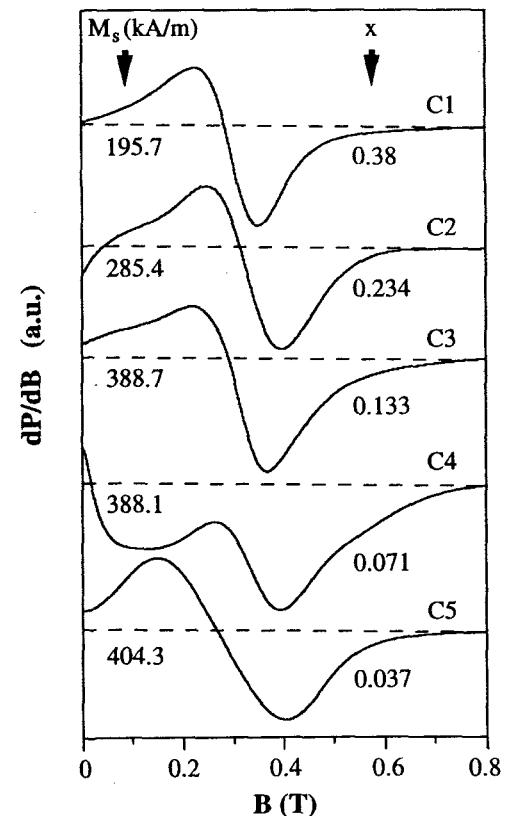


Fig. 2. FMR spectra of annealed $(\text{Co}_x\text{Fe}_{1-x})_3\text{O}_4$ powders.

The observed line widths (ΔB_{pp}) have large values between 0.12 and 0.3 T as is usual for polycrystalline materials in comparison with monocrystals. The damping parameter $\alpha = \Delta B_{pp}/B_{res}$ for all samples is found to be relatively large (0.4 - 1.1), with relaxation times determined from the relation $\tau = 2B_{res}/\omega\Delta B_{pp} = 1/\omega\alpha$ found to be in the range $1 \cdot 10^{-10}$ - $3 \cdot 10^{-10}$ s. No particular dependence of $\tau(x)$ on Co concentration (as might be expected for rapidly relaxing Co^{2+} ions in octahedral positions) is noted in the samples. However, the fastest relaxation time was obtained for the sample containing the lowest Co concentration ($x = 0.037$). In analysing the results, structural effects such as the distribution of particle sizes and crystalline grains have to be taken into consideration. Given that this influence is similar for A2 and all of the samples containing Co (B1 - B5), we conclude that intrinsic properties provide the main contribution to the FMR line broadening and asymmetric spectra.

The resonance field B_{res} observed in our polycrystalline samples does not obey the relation $\omega = \gamma B$ found in single crystals. Usually the dependence of the resonance frequency $\omega = 2\pi\nu$ on the applied field can be represented by a relation of the type $\omega = \gamma(B_{res} - B_{eff})$, where B_{eff} is an internal field which depends on the shape and porosity of the sample. For the spherical samples used in the FMR experiments, $B_{eff} = \mu_0 M_s(1 + 1/3p)$ where p is the porosity [6]. Given the generally similar particle shape and porosity expected for the present range of Co-substituted samples, milled under identical conditions, we conclude that resonance absorption line broadening effects should be similar for all samples. The different resonance field values are therefore considered to be due primarily to the different magnetisation values as noted above.

Acknowledgments

We would like to thank Dr. R. Bramley, The Research School of Chemistry, ANU for use of the ESR spectrometer. We also acknowledge the support of the ANU - UNSW Research Collaborative Scheme.

References

- 1 W. A. Kaczmarek and B. W. Ninham, *IEEE Trans. Magn.* **30**, 732 (1994).
- 2 W. A. Kaczmarek, I. Onyszkiewicz and B. W. Ninham, *IEEE Trans. Magn.* **30**, 4725 (1994).
- 3 S. J. Campbell, W. A. Kaczmarek and G-M. Wang, *NanoStructured Materials* **6**, 735 (1995).
- 4 M. Hofmann, S. J. Campbell and W. A. Kaczmarek, *Proceedings of The European Powder Diffraction Conference*, Chester, UK, July 1995, (submitted)
- 5 W. A. Kaczmarek, *J. Magn.Magn.Mater.* (1995) in press.
- 6 C. J. Kriessman and N. Goldberg in *Magnetism*, vol.III, G. T. Rado and H. Suhl, Eds. New York, Academic, 1963, p.576.

NMR, CD and Molecular Modeling Studies on the Solution Conformation of a Modified Fragment of the First Extra-Cellular Loop of the Angiotensin II AT₁ Receptor.

A. Spisni*, L. Franzoni,* G. Sartor*, C.R. Nakaie[§], R.S.H. Carvalho[§], A.C.M. Paiva[§], R.K. Salinas[#], T.A. Pertinhez[#], S. Schreier[#]

*Istituto di Chimica Biologica, Università di Parma, 43100 Parma, Italy

[§]Escola Paulista de Medicina, 04044-020, São Paulo, Brazil

[#]Instituto de Química, Universidade de São Paulo, CP 26077, 05599-970 São Paulo, Brazil

Introduction

The differential role in hormone binding, played by some amino acids present in the extra-cellular loops of the Angiotensin II AT₁ receptor, is drawing particular attention since studies, carried out by Hjorth *et al.* (1), have shown that, for the rat AT₁, some amino acid residues in various extra-cellular loops are specifically involved in this process. In particular, it has been observed that Tyr⁹², located in the first extra-cellular loop, EL1, close to the transmembrane segment II, is essential for hormone binding. In addition to that, it can be noticed that the residue Y⁹² together with the sequence WPF⁹⁴⁻⁹⁷ and C¹⁰¹, belonging to the same loop, are highly conserved in the Angiotensin II AT₁ receptor expressed in various species (2-4). Though the importance of the conformation assumed by this loop, as well as by the other ones, is well recognized as a concept, the epitopes that are essential for the agonist binding as well as the active conformation of these loops are not yet fully understood.

We are mainly interested in elucidating that active conformation and the role played by the amino acids in the definition of such peculiar molecular conformation. Aim of this study, in particular, is to obtain some information on the importance of the length of the peptide sequence in modulating the conformation of the loop. In this respect the peptide, YRWPF⁹⁴⁻⁹⁷NH₂,

fEL1⁺¹, that is a modification of fragment 92-100, fEL1, of EL1 in the rat AT₁ receptor, has been synthesized. The rationale behind it, is the observation that the same fragment in the human AT₁ differs only for a Tyr/His in position 99 (1, 3). Therefore, exchanging the last amino acid at the peptide carboxyl terminal, L¹⁰⁰, far from Y⁹² and from the other well conserved stretch WPF⁹⁴⁻⁹⁷, with YL, that is the 99-100 fragment in the human AT₁ receptor, we have obtained a non conventional chimeric fragment of EL1 generated by the combination of the YRWPF⁹⁴⁻⁹⁷ fragment of rat AT₁ with the YL⁹⁹⁻¹⁰⁰ fragment of the human AT₁ and characterized by being a one residue extension of fEL1.

As there are evidences that the antibody raised against this peptide is able to recognize the native rat Angiotensin II AT₁ receptor (A.C.M. Paiva, *et al.* unpublished results), suggesting therefore that the peptide fEL1⁺¹ exists in a conformation consistent with the one of fEL1 in the rat AT₁ receptor (5), we decided to study the solution conformational properties of this peptide. 2D ¹H NMR and CD spectroscopy were chosen to describe its structure in solution using as solvent DMSO and H₂O. Combining TOCSY, DQF-COSY, NOESY and ROESY all the peptide's resonances have been assigned. In addition, molecular modeling calculations have been performed using as constraints, interproton distance ranges derived from NOESY in DMSO

and from ROESY in H₂O as well as some backbone dihedral angles derived from the $^3J_{\text{NH}\alpha}$ coupling constants.

Material and Methods

Peptide synthesis. The modified fragment 92-100 of the EL1 of rat Angiotensin II AT₁ receptor, YRWPFGNHYL-NH₂, fEL1⁺, was synthesized by solid phase method and purified using standard procedures.

NMR experiments. NMR measurements were carried out in 90% H₂O/10% D₂O and in DMSO-*d*₆. Peptide's concentration, calculated spectrophotometrically (molar absorption coefficient 7953 M⁻¹ at 280nm), was 3.32 mM and the pH was set to 4.0 for the H₂O experiments. In the case of DMSO-*d*₆ the peptide was simply dissolved at the same final theoretical concentration. 1D and 2D ¹H NMR spectra were recorded on a Bruker AMX 400 spectrometer and the resonance peaks were referred to the TSPSA sodium salt for the experiments in 90% H₂O/10% D₂O or to the residual proton resonance of DMSO in that solvent. Measurements were performed at 298 K. 2D experiments such as DQF-COSY, TOCSY, NOESY, ROESY and TOCSY were recorded using standard methods. The water signal was partially suppressed by preirradiation of the H₂O protons with a selective gated pulse for 2.0 sec during the recycle time. The carrier frequency was set at the water resonance to remove images from imperfect quadrature detection.

Computational methods. Energy minimization as well as the molecular dynamics protocols were performed using the software *Sybyl 6.1* (Tripos St. Louis MO, USA). Tripos force field was used without solvent molecules and introducing two types of experimental constraints: interproton range distances and some ϕ dihedral angles.

The simulated annealing protocol produced a set of structures that were further minimized until an energy change lower

than 0.001 kcal/mole was reached and the lower energy structures were selected. Due to the experimental evidences of *cis-trans* isomerization of the Pro⁴ ω torsion angle, a value of 0° for that angle (*cis* configuration) was introduced as a constraint, and the same simulated annealing protocol followed by energy minimization was repeated.

Results

Assignments of NMR signals. Resonances assignment of the proton signals for fEL1⁺ both in H₂O (pH 4.0) and in DMSO-*d*₆ were accomplished using a combination of phase-sensitive DQF-COSY, TOCSY, ROESY and NOESY. In both solvents the existence of a *cis-trans* isomerization of the Trp³-Pro⁴ peptide bond was observed. In DMSO-*d*₆ the doubling of the spin systems was present only for some residues suggesting, for that solvent, a reduced conformational modification of the peptide structure in the two isomeric states.

Interproton distances. To verify the existence of Overhauser effects, NOESY spectra were recorded in DMSO-*d*₆, while rotating frame experiments, ROESY, were carried out in aqueous solution, due to the relative small size of the peptide and to its associated short correlation time. The connectivities obtained from ROESY and NOESY spectra have been used for molecular modeling calculations.

Dihedral angles. The $^3J_{\text{HN}\alpha}$ coupling constants were measured from DQF-COSY spectra.

Molecular modeling and dynamics. The results indicate the existence of a twisted conformation in DMSO while, as suggested both by ROESY experiments as well as CD spectra (data not shown), a more extended structure exists in H₂O. Figure 1 reports the more stable structure of the *trans* isomers of the peptide in the two solvents.

Conclusions

The results of this work clearly support the hypothesis that it is possible to obtain valuable information on the structure organization of large macromolecules, such as the Angiotensin II AT₁ receptor, by studying fragments of them in solution (5).

Though not yet complete, our data indicate that the fragment $fEL1^{+1}$ is able to assume, in solution, a conformation that ought to be compatible with the one assumed by the $fEL1$ fragment in the native rat Angiotensin II AT₁ receptor. This hypothesis appears to be supported by immunological data and by some preliminary molecular modeling calculations suggesting that the bend formed by the peptide fragment in solution could be consistent with the dimension and organization of the loop in the rat AT₁ receptor (A. Spisni *et al.* data not shown). The existence of a twisted structure in DMSO, resembling EL1 of AT₁ makes this peptide a very good model not only for studying the importance of the peptide length on the loop conformation but also for the study of the spatial organization of the AT₁-Tyr⁹² residue (Tyr¹ in $fEL1^{+1}$) known to be essential for agonist binding (1). Studies are now carried out to refine the peptide's structure and to better define its biological properties.

Finally, more extended studies are under way to understand if the existence of a *cis-trans* isomerization of the Trp³-Pro⁴ peptide bond, that seems to bring about a peculiar molecular flexibility, could play an important role in the molecular mechanism of hormone-receptor recognition.

Acknowledgements

The work was partially supported by CNR, MURST (Italy) and CNPq, FAPESP (Brazil).

We are indebted to Centro Interfacoltà Misura and to Centro di Calcolo Elettronico of the University of Parma for the use of the NMR and computational facilities.

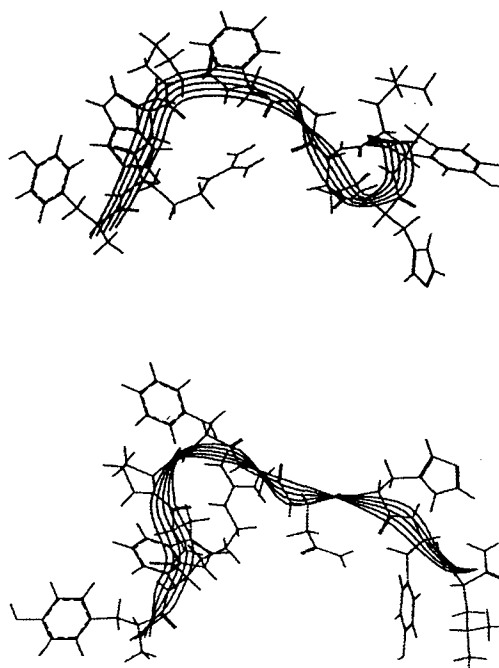


Figure 1. Lower energy structure, obtained from molecular modeling calculations, of the modified fragment $fEL1^{+1}$ of the first extra-cellular loop of AT₁ Angiotensin II receptor, in the *trans* configuration: in DMSO-*d*₆ (Top) and in water (Bottom).

References

- 1) S.A. Hjorth, H.T. Schambye, W.J. Greenlee, and T.W. Schwartz *J. Biol. Chem.* **269**, 30953-959 (1994)
- 2) H. Ji, M. Leung, Y. Zhang, K.J. Catt and K. Sandberg *J. Biol. Chem.* **269**, 16533-536 (1994)
- 3) H.T. Schambye, S.A. Hjorth, D.J. Bergsma, G. Sathe, and T.W. Schwartz *Proc. Natl. Acad. Sci. USA* **91**, 7046-7050 (1994)
- 4) D.J. Bergsma, C. Ellis, P.R. Nuthulaganti, P. Nambi, K. Scaife, C. Kumar and N. Aiyar *Mol. Pharmacol.* **44**, 277-284 (1993)
- 5) H.J. Dyson, K.J. Cross, R.A. Houghten, I.A. Wilson, P.E. Wright and R. A. Lerner *Nature* **318**, 480-483 (1985)

MEASUREMENT AND COMPENSATION OF SUSCEPTIBILITY INDUCED INHOMOGENEITIES IN B_e

F.O. Zelaya, S. Crozier, S. Dodd, R. McKenna and D.M. Doddrell.

Centre for Magnetic Resonance,
University of Queensland, St.Lucia, Queensland 4072,
Australia.

INTRODUCTION

The perturbation imposed on the homogeneity of a constant magnetic field B₀, by the presence of media of different magnetic susceptibilities is well known (1,2,3). This situation is encountered in most NMR Spectroscopy and Imaging applications, either by the existence of different material and component boundaries in the gradient and RF coils and probes (4); or by multiple susceptibility differences within the sample itself (5-9).

In this work we demonstrate a simple strategy that can be used to compensate for susceptibility induced artefacts caused by the presence of metallic conductors and electronic components used in RF probe production.

THEORY

Consider an infinitely long cylinder of copper of radius *a* and diamagnetic susceptibility χ_a, surrounded by a homogeneous medium *e* of magnetic susceptibility χ_e, and immersed in a constant and spatially homogeneous magnetic field B₀ perpendicular to the cylinder axis (in this case, the *z* axis). The effect of the Cu cylinder upon the homogeneity of B₀ in the outer medium (and inside the cylinder), can be determined by solving LaPlace's equation for the correct vector potential and under the correct boundary conditions (1). Outside the cylinder, a distance *r* away from the cylinder axis, we have

$$B_e(r,z) = \chi_a B_0 + \frac{a^2}{r^2} \cdot \frac{(\chi_a - \chi_e)}{(\chi_a + \chi_e)} \cdot \{2z^2/r^2 - 1\} \chi_e B_0 \quad [1]$$

and inside the cylinder,

$$B_a(r,z) = \chi_a B_0 \cdot (2\chi_e / (\chi_a + \chi_e)) \quad [2]$$

Consider the same Cu cylinder, coated with a layer of material of total radius *b* and

paramagnetic susceptibility χ_b. The resulting field outside the concentric cylinders (in the medium *e*) is now given by (2) :

$$B_e = B_0 \left\{ 1 + \chi_e/3 + \frac{(\chi_b - \chi_a)a^2 + (\chi_e - \chi_b)b^2}{(x^2 - z^2)/2(x^2 + z^2)^2} \right\} \quad [3]$$

It can be seen in the above equation that for a fixed value of *a*, χ_a and χ_b, the thickness of the paramagnetic material (*b*) can be chosen so that the third term in equation [3] above vanishes ((χ_b - χ_a)a² + (χ_e - χ_b)b² = 0). In such circumstances,

$$B_e = B_0 (1 + \chi_e/3)$$

thus removing the spatial dependence of the magnetic field. Since χ_e << 1 for most media surrounding an NMR sample (e.g. air), we obtain that B_e ≈ B₀, thus removing the loss of field homogeneity caused in this case by the Cu cylinder, but in principle, any non-ferrous metal object.

To verify the validity of this model, the value of the magnetic field B_e outside a Cu cylinder coated with Rhodium and immersed in silicone oil, was calculated using equation [3] (χ_{Cu} = -5.46 × 10⁻⁶, χ_{Rh} = +111.0 × 10⁻⁶ and χ_{SiO_i} = +7 × 10⁻⁷ (11)). The model predicted an optimum Rh thickness of 67 μm.

NMR MEASUREMENTS

A phantom consisting of a rod of high purity Cu of 25 mm length and 5 mm diameter, was plated electrochemically with different quantities of Rh. The rod was supported inside a teflon cell filled with Si oil. ¹H NMR images were taken from a 2 mm slice across the centre of the rod. The images were acquired with a modified 2DFT spin echo protocol (TE = 12 ms, TR = 800 ms, matrix size 256 × 256, FOV = 7 cm, 8 averages), preceded by two trains of DANTE (12) RF pulses in the

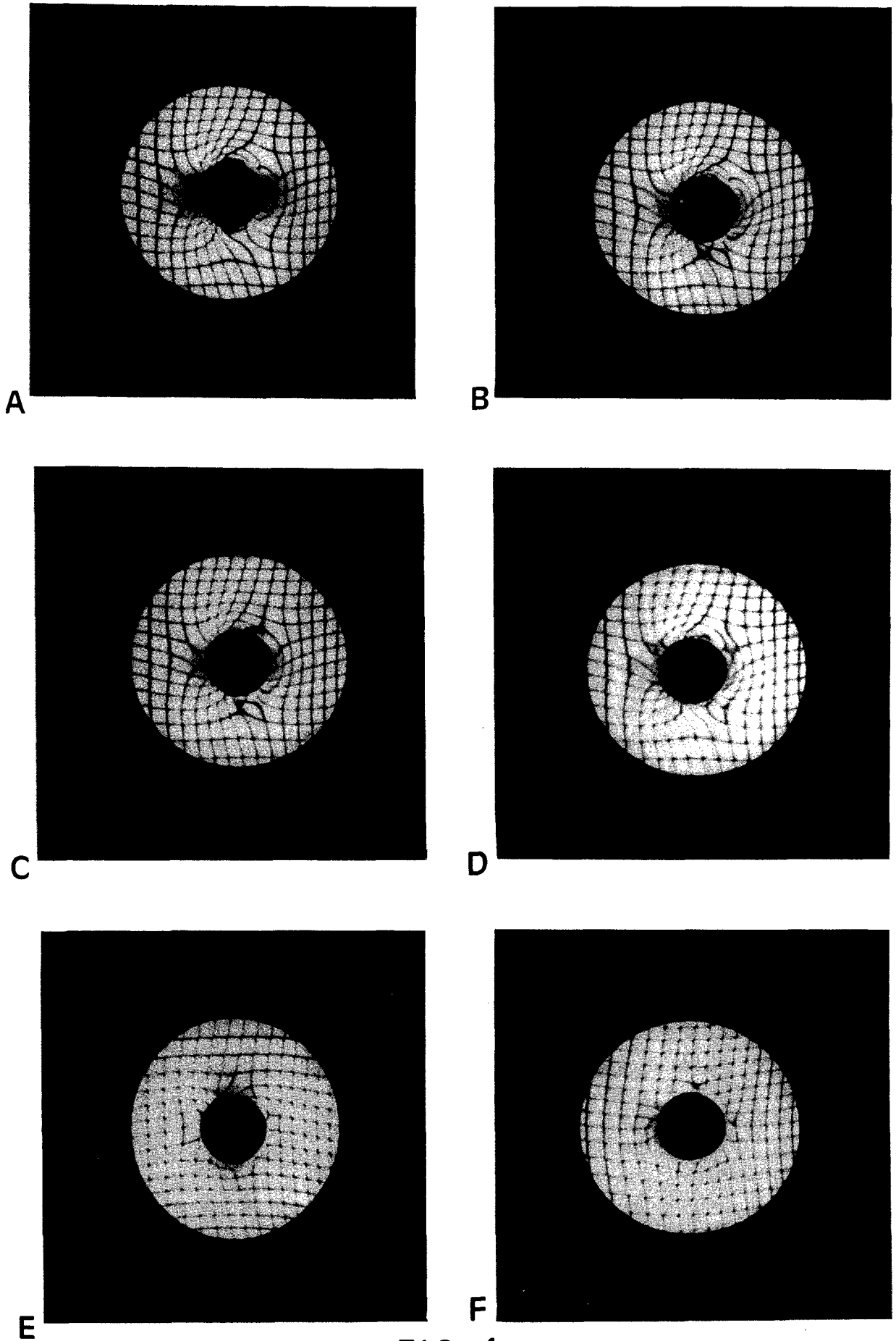


FIG 1

presence of z and x gradients (the tagging gradients(13)).

The DANTE train contained six RF pulses (6.63 μ s each) separated by 25 ms. The tagging gradient strength was chosen at 40 Hz/mm. With this parameter, the sequence produced horizontal and vertical tagging lines of 0.16 mm thickness, and a separation of 1 mm. These experiments were performed using an extensively modified BRUKER 200 MHz console, equipped with purpose built birdcage resonators and shielded gradients. Figures 1A - 1F show the results of the DANTE tagging MRI evaluation as the Rh layer thickness is increased from 0 to 70 μ m.

REFERENCES

1. P.T. Callaghan, *J. Magn. Reson.* **87**, 304 (1990).
2. D.T. Edmonds and M.R. Wormald, *J. Magn. Reson.* **77**, 223 (1988).
3. P.T. Callaghan, "Principles of Nuclear Magnetic Resonance Microscopy", Clarendon Press, Oxford, 1991.
4. J.F. Schenck, Abstracts of the Second Meeting of The Society of Magnetic Resonance, San Francisco, California, August 6-12, 1994, p. 220.
5. F. Schick, T. Nagele, O. Lutz, K. Pfeffer and J. Giehl, *J. Magn. Reson.*, Series B, **103**, 39 (1994).
6. K.M. Ludeke, P. Roschmann and R. Tischler, *Magn. Reson. Imaging*, **3**, 329 (1985).
7. A.J. Lucas, S. Gibbs, E.W.G. Jones, M. Peyron, J. Andrew Derbyshire and L.D. Hall, *J. Magn. Reson.*, Series A, **104**, 273 (1993).
8. P.T. Callaghan, L.C. Forde and C.J. Rofe, *J. Magn. Reson.*, Series B, **104**, 34 (1994).
9. P.W. Kuchel and B.T. Mulliman, *NMR in Biomedicine*, **2**, No.4, 151 (1989).
10. J.D. Jackson, "Classical Electrodynamics", John Wiley and Sons, Inc. (1967)
11. "CRC Handbook of Chemistry and Physics", CRC Press Inc., (1983).
12. G. A. Morris and R. Freeman, *J. Magn. Reson.*, **29**, 433 (1978).
13. T. J. Mosher and M. B. Smith, *J. Magn. Reson.* **93**, 624 (1991).
14. R. Bhagwandien, M.A. Moerland, C.J.G. Bakker, R. Beersma and J.J.W. Lagendijk. *Magn. Reson. Imaging*, **12**, 101 (1994).

High Resolution Solid State ^1H NMR of Organic Nanoparticles by Brownian Motion (UFP-NMR Method)

K.Kimura*, A.Naito, H.Saito and N.Satoh#

Faculty of Science, Himeji Institute of Technology,
Science Garden City, Kamigohri, Hyogo 678-12, Japan

Tokyo Research Laboratories, Kao Corporation
1-3 Bunka 2, Sumida-ku, Tokyo 131, Japan

1. Introduction

It is well established that high resolution solid state NMR is a powerful tool to probe a structural and a chemical information in the research field of polymers, catalyst, biological pigments and various interesting solid state samples in their physical properties. Among various techniques to obtain high resolution solid state proton NMR, the combined rotation and multiple-pulse spectroscopy (CRAMPS) is a widely accepted method up to now. However with this technique, it is still difficult to obtain high resolution NMR spectra for protons in a level of several Hz. In this short report, we introduce a new technique named UFP-NMR (ultrafine particle NMR) method[1] which utilizes a real space random reorientational motion of samples at a level of 10^6 Hz ($5\mu\text{s}$ for correlation time) for rotational diffusion of a 10 nm particle. This rapid and random motion can completely decouples interatomic strong magnetic dipole interaction even if a target proton is surrounded by abundant proton nuclei[2]. According our method, ultimate resolution at a level of 1 Hz can be attained as indicated in the J-coupling of ortho-ring protons of an aromatic compound.

2. Experimental

The preparation technique of nanometer-sized particles engaged in this report is the gas evaporation technique combined with the matrix isolation method[3] especially modified for the organic nano-particles dispersed in CCl_4 liquid as a colloidal state[4]. The average size of particles of terephthalic acid (TPA: Fig.1) was determined by the dynamic laser scattering method and was about 10nm. ^1H NMR measurements were carried out by a conventional liquid state FT NMR spectrometer operated at a frequency of 400 MHz. Colloidal and liquid samples were sealed into a 5-mm

conventional sample tube with 17 Hz spinning rate. All chemical shifts were quoted from an reference sample, tetramethyl-silane. The solid state ^1H NMR was measured by a CRAMPS method with a Chemagnetics CMX-400 spectrometer with a BR-24 pulse-sequence. All measurements were carried out at room temperature.

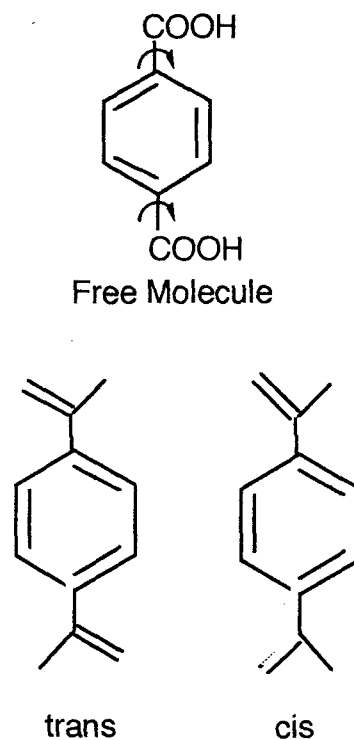


Figure 1. Molecular structures of terephthalic acid in solution (above) and in crystal.

3. Results and Discussion

A various kind of samples were tested and the spectra are shown in Fig.2. A colloidal dispersion of TPA UFP coated with acetone- d_6 (Fig.2a) or with methanol- d_4 (Fig.2b) dispersed in CCl_4 , TPA UFP dispersion with no-coating in CCl_4 (Fig.2.c),

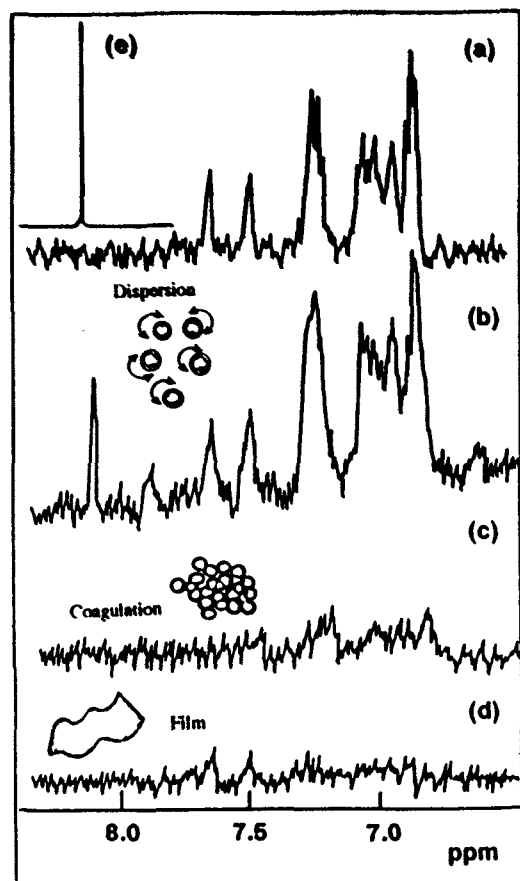


Figure 2. ^1H NMR spectra of aromatic proton region of several TPA preparations taken by a conventional liquid state FT NMR spectrometer. (a) TPA-UFP/ acetone- d_6 / CCl_4 , (b) TPA-UFP/ methanol- d_4 / CCl_4 , (c) TPA-UFP aggregates in CCl_4 , (d) TPA-UFP film (230 nm thickness) in CCl_4 , (e) TPA/acetone- d_6 solution.

TPA film (230 nm in thickness) in CCl_4 (Fig. 2d), molecularly dispersed TPA in methanol- d_4 (Fig. 2e) or supernatant of TPA/ CCl_4 mixture were measured. Carbon tetrachloride was selected as a dispersing medium because of the low solubility for TPA to suppress molecular signals of TPA and yet its stabilizing ability for UFP-state. The dispersion state can be easily checked by naked eye observation. When opalescence is appeared, the size is in the range from $1\ \mu\text{m}$ to $0.1\ \mu\text{m}$. If the size is of the order of nm, then the solution is transparent by the naked eye observation but shows strong scattering upon laser irradiation.

Among listed above, TPA UFP coated with deuterated acetone or methanol only exhibits high resolution NMR signals. In Fig. 2(a), we can observe six peaks from 6.8 to 7.8 ppm region. The full width at half maxima of these six peaks are of the order of 40 Hz. In addition to these peaks, rather sharp peak was appeared in TPA-

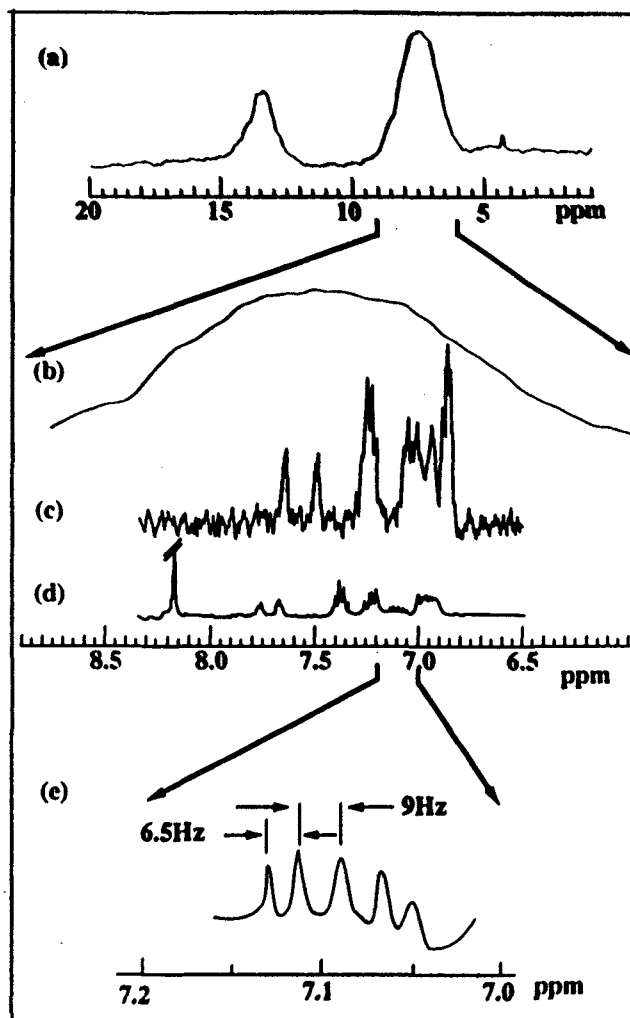


Figure 3. Comparison of CRAMPS spectrum with that by UFP method. (a) CRAMPS spectrum. (b) Expansion of aromatic ring proton region. (c) UFP-NMR spectrum of the same region. (d) NMR spectrum of clustered sample. (e) Expansion of spin-spin coupling structure. The coupling constants are 9 Hz for central two splits with 6.5 Hz on both sides.

UFP/methanol- d_4 / CCl_4 preparation. Comparing with Fig. 2(e), this peak at 8.15 ppm found in Fig. 2(b) is assigned to that from molecularly dissolved TPA in methanol. Other preparations were coagulated to sediment (c and d) or completely dissolved to a molecule (e). As shown in Fig. 1, all four aromatic protons are equivalent in a free molecule due to the free rotation of carboxylic group. Thus we have only one signal in the ring proton region and this is observed in Fig. 2(e). On the other hand in solid, several polymorphs were reported with trans-conformation giving at least 4 unequivalent protons. Moreover, cis- or gauche-conformations may be possible at the surface of UFPs. This

variety in the proton environment is a cause of multiplet structures in the aromatic ring protons.

In Fig.3, comparison of CRAMPS spectrum was made with that by UFP-NMR method. In the topmost figure is shown the CRAMPS spectrum of powdered TPA sample in which the peak at 7.5 ppm is originated from ring protons and that at 13.5 ppm is from carboxylic proton. Figure 3(b) shows an expanded spectrum of ring proton region from 6 to 9 ppm obtained by CRAMPS method. No fine structure is perceived. Figure 3(c) is identical to the one shown in Figure 2(a). There are apparent six peaks at aromatic ring proton region. The size of particles is estimated at about 10 nm. We can get much smaller particles (clusters) by degradation technique and is shown in Fig. 3(d). In this spectrum, there is coexistence of the signals from molecular TPA (8.15 ppm) and from clusters. A fact that a part of UFP dissolves into solvent through the degradation process may be a cause of this molecular signal. We should note that each signal of aromatic ring protons of UFP-TPA shifted toward that of molecular position via those peaks of clusters. Figure 3(e)

shows the most expanded spectrum of spectrum (d) indicating J-coupling of ring protons. The vicinal spin-spin coupling constant 3J for ortho-position from literature is around 6~10 Hz. The observed average value for the signals at 7 ppm from the Carr-Purcell-Meiboom-Gill Method was 8 Hz and from the UFP-NMR method, the splittings are 6.5 and 9 Hz. All these values are compatible each other.

The assignments of six signals and comparison of ^{13}C spectrum with the present spectra are now in progress.

References

1. N. Satoh and K. Kimura, *J. Amer. Chem. Soc.* **112**, 4688 (1990).
2. N. Satoh and K. Kimura, *Chem. Lett.* 2155 (1994).
3. K. Kimura and S. Bandow, *Bull. Chem. Soc. Jpn.* **56**, 3578 (1983).
4. N. Satoh, A. Naito and K. Kimura, *Bull. Chem. Soc. Jpn.* (1995) in press.

^{71}Ga NMR Investigations for Gallium Microparticles in a Pore Glass.

E. Shabanova, K. Schaumburg
University of Copenhagen, Symbion Science Park, CSMI,
Fruebjergvej 3, DK-2100, Copenhagen Ø, Denmark
E.V.Charnaya

St-Petersburg State University, Institute of Physics,
Ulianovskaya ul.1., St.-Petersburg, 198904, Russia

Yu.A.Kumzerov

A.F.Ioffe Physiko-Technical Institute RAN
St.-Petersburg, 194021, Russia

I. Introduction.

Porous media play an important role in many aspects of science and technology [1,2]. One aspect is to study systems of small particles in porous media. The advantage of such materials is the possibility to use processing techniques suitable for bulk specimens while at the same time they reveal the common features of an ensemble of microparticles. Small clusters of atoms of metallic elements have intriguing physical and electronic properties, which differ significantly from those of bulk materials [3]. Gallium is a remarkable metal, noted for its specific properties in comparison with other elements of its group [4-9]. The idea of the present investigation is to combine these attractive features with the added features from microparticles.

We present the first report about NMR studies of melting-freezing phase transition (PT) in the system of metallic microparticles. As an example Ga is inserted into the porous sodiumboronsilicate glass. The pore size is about 40Å [4]. Pores together with narrow interpore connecting channels take up approximately 80% of the sample volume and form a random three-dimensional network in the bulk glass. Liquid gallium was inserted into the pore glass under high pressure up to 9 KBar. The sample is a gray 5×3×3 mm³ parallelepiped of 225 mg.

II. Experimental.

Experiments were performed on a Bruker MSL300 spectrometer in a constant magnetic field of $B_0=7$ Tesla, which correspond to a ^{71}Ga nuclear Larmor frequency $\nu_0=91.6\text{MHz}$. Spectral width was 10^6 Hz. Dead time delay equal to 5 μs and recycle delay equal to 10 ms are used. Spectra were sampled in 2K data points and were obtained accumulating 30000 induction decays. The sample was mounted in a Doty probehead DSI418. A single {x}-pulse was used in experiments. Amplitude of the rf field was 4.5 Gauss.

Investigations were carried out over the melting-freezing PT temperature range for Ga microparticles : 160K - 390K. The temperature was changed with the rate of 0.5 K/min. After each temperature change the sample was kept at a fixed temperature for about 5 min prior to acquisition of spectra.

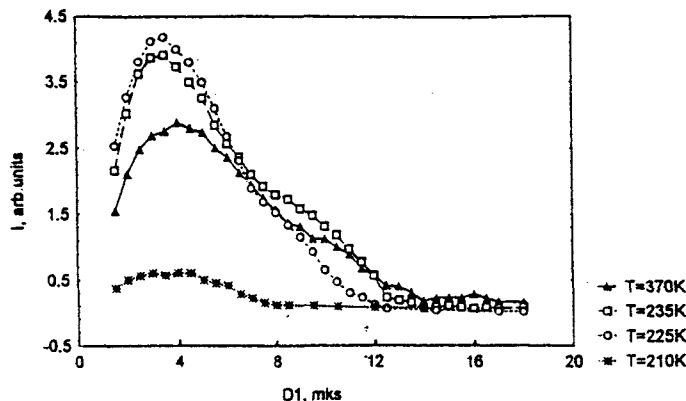
III. Results and discussion.

A typical ^{71}Ga NMR signal in the pore glass over the Ga melting point (303K) represents a single line with the half width of the order of 5KHz. For comparison, the liquid ^{71}Ga NMR signal was also measured in the sample of pure bulk Ga. Taking the bulk Ga as a reference the chemical shift of the liquid Ga signal in the pore glass was found to be shifted 6,5 KHz. It may be noted that for the Ga signals from the liquid fraction of the supercooled phases at 295K the half width of the bulk signal is half that of the Ga in the pore glass and it continuously decreases at higher temperatures as nuclear surroundings become more isotropic. The half width of the liquid Ga signal from the pore glass stays unchanged within the temperature range considered. This phenomena can be caused by restrictions due to the small size of pores, which prevent the isotropic averaging of nuclear interactions. It can be estimated, that the distance between gallium atoms is $\sim 2.5\text{Å}$ [7], therefore any nucleus within a pore of 40Å has maximum 8 nuclei along the axis connecting the nucleus with the pore wall. As a consequence, nuclei must experience a strong inhomogeneity reflecting the nuclear position in the pore. The effect of nuclear motion in the liquid phase can thus be considered as the next order perturbation.

For nuclei with spin $I>1/2$ the presence of the quadrupole interaction requires the $\pi/2$ -pulse shorter than for a spin $1/2$ nucleus with the same gyromagnetic ratio [8]. Using the theory of nutation NMR of half integer quadrupole nuclei it has been shown [10], that the nutation frequencies for a spin $3/2$ determined via the single {x}-pulse nutation experiment can be classified as three 'single' and one 'triple' quantum coherences.

In the particular case of the metal microparticles in the pore glass a very fast relaxation takes place. At 370K ^{71}Ga NMR signal shows a complete recovery at a recycle delay equal to 10ms, which lead to the expectation that nutation should be suppressed by the relaxation processes. Experimental data reflecting the behavior of the liquid ^{71}Ga NMR signal integrated intensity as a function of the single excitation {x}-pulse duration at different temperatures are presented in Fig.1. The data were obtained in a sequence when the temperature has been decreasing. The intensity changes at

Fig.1. Magnetization intensity vs. pulse duration at different temperatures.



different temperatures correspond to the PT features (*vide infra*). Opposite to the general situation of sinusoidal intensity behavior, there are almost no signal left after the pulse duration $D1 = 14 \mu\text{s}$. That situation may arise if quadrupole effects and relaxation is fast enough to influence the nuclear system already during the pulse, so that at $D1 > 14 \mu\text{s}$ there is no magnetization to detect.

At lower temperatures one should expect relaxation to be faster, and consequently the earlier suppression of the signal intensity with $D1$. It is supported experimentally in Fig.1. The characteristic feature of the data is that all intensity maxima occur at the same $\{x\}$ -pulse duration $D1 \approx 4 \mu\text{s}$ for all temperatures. This value has been chosen as the ^{71}Ga " $\pi/2$ "-pulse in the further investigations of the melting-freezing PT.

As a consequence of the fast relaxation in the liquid Ga phase it is obvious to expect the more rapid relaxation for the solid structure. In the case of very rapid relaxation for solid state the nuclear system may show no real signal, but a mixture of different phase magnetizations, which are left in the x - y -plane as a result of simultaneous fast relaxation and excitation $\{x\}$ -pulse. Therefore, as the relaxation time becomes shorter the NMR line intensity becomes smaller and phasing of the signal may also change. Accordingly a distinguishable spectra from the pure solid phase at low temperatures was possible to obtain only after accumulation of minimum 90000 spectra (that is three times more than we used for the liquid signal), but still the signal intensity was very poor. Chemical shift between the signals from solid and liquid fractions may be estimated as about 315KHz.

One of the examples reflects the pronounced difference in the physical properties of a material confined within small pores in comparison with those of bulk material is the temperature reduction of the melting point [1,11-14]. Indeed, a network of the microparticles is more disordered system than the bulk material. Therefore it will lead to the melting PT at lower temperature, which is a function of the pore size. This gives us a possibility to make a conclusions about the pore size distribution based

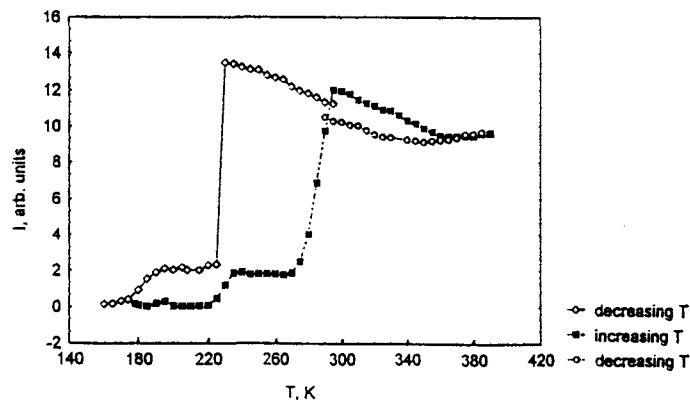
on the melting temperatures of the microparticle network. The true melting temperatures may be precisely measured by increasing the temperature after a complete solidification of the microparticles, which will be ensured by the absence of the liquid fraction NMR signal.

The freezing point should also be shifted to lower temperatures. In Ga the appearance of a metastable supercooled phase prevent a precise observation of a transition temperature.

In the present paper we report the behavior of the liquid ^{71}Ga NMR signal intensity obtained during the heating-cooling cycle within the temperature range of the melting-freezing PT. Results are presented in Fig.2. Fig.2 shows the characteristic temperature dependence of the Ga liquid fraction when the experiments were started from room to lower temperatures. The curve reflects a hysteresis behavior and shows the two phase transition steps under both melting and freezing. Since the melting point is determined by the pore size, we believe, that the high transition step is caused by the Ga within the pores, and the short step reflects the PT of the small Ga amount which belongs to the pore interconnecting channels.

It should be noted that Ga in the pore glass has earlier been subject to the PT acoustic investigations [4]. In the acoustic studies the temperature dependence of the relative sound velocity showed an abrupt increase of velocity value at $\sim 230\text{K}$ in the cooling process and smooth decrease of velocity value in the range of $\sim 250 - 265\text{K}$ in the heating process, where the melting has been interpreted as a smeared PT, and the freezing process - as a first order PT. Similar asymmetry of Ga microparticle temperature behavior during heating and cooling processes were obtained in our NMR investigations for the high PT step, which support the idea of different order PT during melting and freezing processes.

Fig.2. Temperature dependence of the liquid Ga fraction.



IV. Conclusions

In this paper for the first time NMR studies of the system of metallic gallium microparticles is reported. It has been shown that the rapid nuclear relaxation

processes in Ga microparticles takes place along with the effect of the excitation pulse, and consequently influences nuclear nutation.

The interesting features of the temperature dependence of Ga liquid fraction was measured by ^{71}Ga NMR. It reflects the hysteresis behavior and shows the two PT steps under both melting and freezing conditions. The asymmetry of the decreasing and increasing of the Ga liquid fraction during the heating - cooling process reflects the different order phase transitions. It is possible, that different processes of microparticle melting can coexist in the ensemble of metallic microparticles embedded in a porous media.

REFERENCES

1. J.H.Strange, M.Rahman, E.G.Smith, Phys.Rev.Let.71,3589(1993)
2. J.A.Duffy,N.J.wilkinson, H.M.Fretwell, M.A.Alam,J.Phys.:Condens.Matter7,L27(1995)
3. W.P.Halperin, Rev.Mod.Phys.58,533(1986)
4. B.F.Borisov, E.V.Charnaya, Yu.A.Kumzerov et all., Solid State Commun.92,531(1994)
5. X.G.Gong, G.L.Chiarotti, M.Parrinello, E.Tosatti, Europhys.Let.21,469(1993)
6. X.G.Gong, G.L.Chiarotti, M.Parrinello, E.Tosatti, Phys.Rev.B 43,14227(1991)
7. S.Lee, R.Rousseau, C.Wells, Phys.Rev.B 46,12121(1992)
8. A.Diaz, R.Monque, M.Bussolo, Bulletin of Magn.Res.15,113(1993)
9. C.R.Bayense, A.P.Kentgens et all.,J.Phys.Chem.96,775(1992)
- 10.R.Janssen,W.S.Weeman,J.Chem.Soc.,Faraday Trans.1,84,3747(1988)
11. K.A.Jackson, B.Chalmers,J.Appl.Phys.29,1178(1958)
12. J.W.Gibbs, Collected Works (Longmans,Green,New York,1928)
13. W.Thompson,Philos.Mag.42,448(1871)
14. C.L.Jackson, G.B.McKenna, J.Chem.Phys.93,9002(1990)

MRI OBSERVATIONS OF HIPPOCAMPAL LESIONS IN THE THIAMIN DEFICIENT RAT BRAIN UNDER GLUCOSE LOAD

Therese Wholohan⁺, Fernando Zelaya*, Peter Nixon⁺, Stephen Rose*,
Adrian Bower[@] and David Doddrell*.

*Centre for Magnetic Resonance, ⁺Department of Biochemistry
and [@]Department of Anatomical Sciences, University of Queensland,
St. Lucia QLD 4072 AUSTRALIA.

INTRODUCTION

The consequences of thiamin deficiency, often a result of alcoholism in humans, are numerous. Severe thiamin deficiency can result in acute Wernicke's encephalopathy, which is usually recognised in post-mortem examinations by a distinct distribution of periventricular brain lesions (1). This condition can give rise to disorders of peripheral nerves (beri beri), and in some instances decreased consciousness, ataxia, nystagmus and paralysis of extraocular muscles.

In rats, as well as in humans, the symptoms of acute encephalopathy can be precipitated in subjects with sub-clinical thiamin deficiency by the administration of glucose. This is due to the intrinsic role of thiamin in the metabolism of glucose. It has also been shown that glucose administration to undernourished patients in hospitals, can bring about Wernicke's encephalopathy, thus unmasking previously unidentified thiamin deficiency (2,3).

Sometimes, Wernicke's encephalopathy is followed by Korsakoff psychosis, a chronic amnesic syndrome. While non-Korsakoff's amnesic syndromes are always associated with pathology in the hippocampus, in long term Korsakoff's patients the hippocampus appears normal under the light microscope (4).

We have used a rat model of Wernicke's syndrome to investigate the biochemical and anatomical changes that arise after administration of glucose to thiamin deficient animals. These observations have been carried

out *in vivo* and *in situ* by the application of NMR imaging and localised ¹H spectroscopy (5).

METHODS

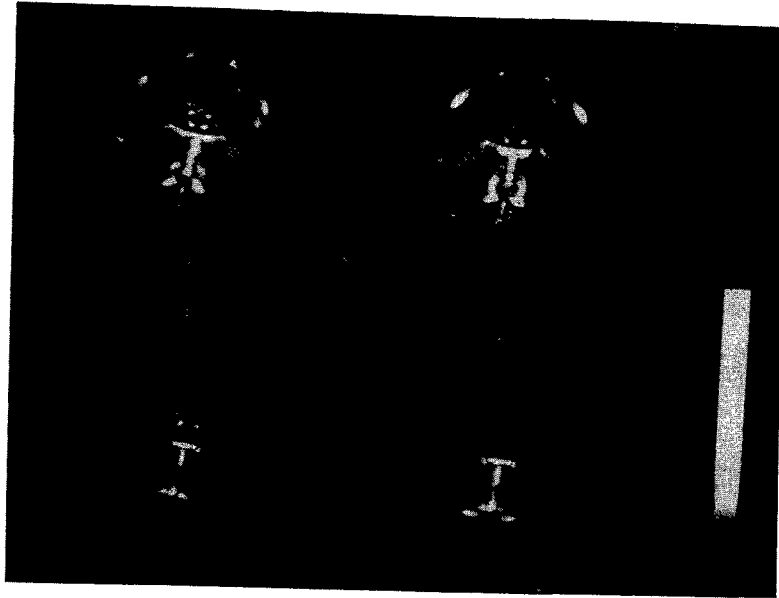
ANIMALS

A total of 8 female Wistar rats, weighting 100 - 150 g, have been examined. The rats were fed a pelleted diet deficient in thiamin but otherwise meeting the AIN-76 standard, supplied by Dyets, Inc., US, for a period of 4 weeks. After such time the rats were also administered daily injections of the thiamin antagonist, pyriethiamin (50 µg / 100g body weight i.p.) for 4 to 8 days. After this time, rats showed neurological signs of thiamin deficiency. These signs were ataxia in moderate deficiency, followed by opisthotonus, loss of righting reflex and convulsions in severely deficient animals.

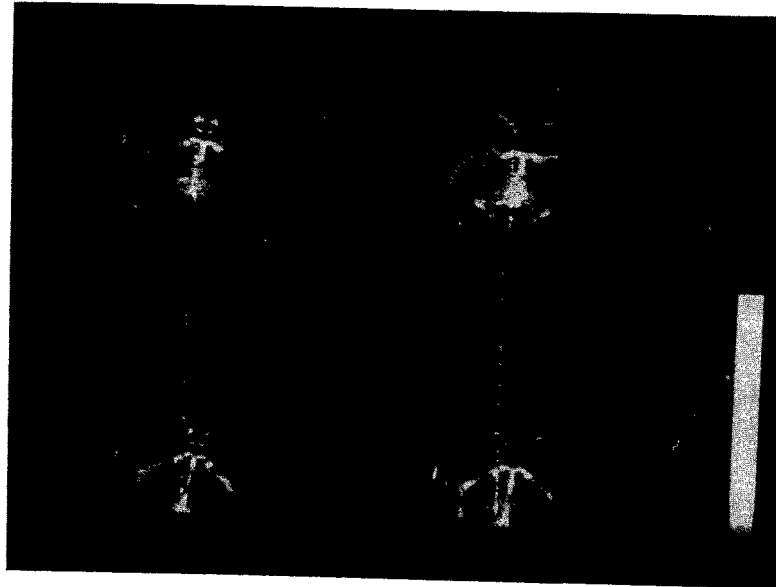
Anaesthesia was maintained with 1.5 % isoflurane in O₂, (0.4 l min⁻¹) throughout the entire MRI examination. Control images were obtained (see NMR protocol below) and thereafter, a dose of glucose (0.5 g per 100 g body weight) was administered to the rats via an i.p. cannula. T₂ weighted NMR images were acquired every thirty minutes for a period of two hours after glucose administration.

MRI PROTOCOL

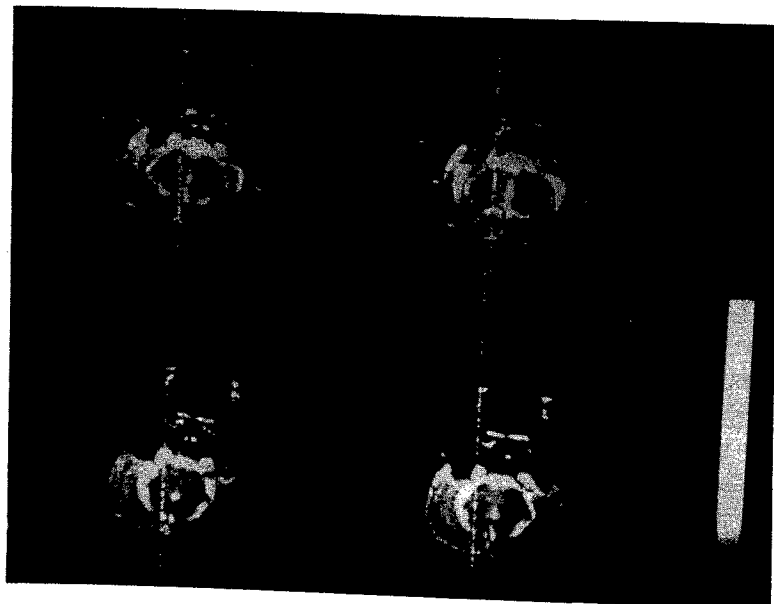
All images were obtained using a BRUKER MSL 200 spectrometer equipped with a horizontal, 40 cm BRUKER magnet. Purpose built shielded gradients were used in this application. The rat was accommodated in an animal handling device which was attached to



1



2



3

a 32 mm diameter birdcage resonator designed for rat brain imaging. This hardware (including the shielded gradient set) were fabricated at the Centre for Magnetic Resonance.

We employed a standard Spin Echo 2DFT sequence with an echo time of 18 ms, and repetition time of 2 s. Four echo images per slice were generated by successive addition of two echoes, hence each echo image corresponds to an averaged T_2 weighting of 27, 63, 99 and 135 ms. Slice thickness was 1 mm in all cases, and a total of 4 averages per scan were employed. Six transverse slices were chosen from a sagittal pilot scan, so as to encompass the region between the middle of the lateral ventricles and the front of the fourth ventricle. This region contained most of the hippocampus as well as the thalamic nuclei and mamillary bodies.

RESULTS AND DISCUSSION

Figures 1- 3 show six contiguous slices through the middle of the brain of a thiamin deficient animal before glucose (left hand side), and 2 hr after glucose administration (right side). They all have a T_2 weighting of 135 ms. Enhanced signal intensity can be seen in the third ventricle (Figs.1&2), lateral ventricles (Fig.1), thalamic nuclei (Fig.2, upper), hippocampus, (Fig.2, lower, Fig. 3, upper), mamillary bodies (Fig.3), and in the space between the brain stem, and the lateral hemispheres (Fig.3). No observations were made more than two hours after glucose administration.

In the case of the hippocampus, the mamillary bodies and the thalamic nuclei, this hyperintensity at relatively long echo times is consistent with oedema. In the ventricles, and in the space between the brain stem and the cerebral hemispheres, the hyperintensity is most probably a consequence of increased fluid mobility, which is consistent with breakdown of the blood brain barrier, which we have previously observed in these areas by means of Gd-DTPA enhanced MRI(6). It is important to note that the observed hyperintensity in the

hippocampus can be enhanced by repeated glucose loading over a period of up to 3 days, and is not observed in control animals or in animals whose thiamin deficiency has been reversed by thiamin administration.

Our rat model demonstrates that some hippocampal damage could be a component of the pathogenesis of Korsakoff's amnesia, as well as of other amnesic syndromes. To our knowledge, this is the first non-invasive observation of lesions in the hippocampus of thiamin deficient animals, *in vivo*.

REFERENCES.

1. C G Harper. *J Neurol. Neurosurg. Psychiatry*, **47**, 426-441 (1979).
2. A T S Watson, J F Walker, G H Tomkin, M M R Finn and J A B Keough. *Irish.J.Med.Sci.* **150**, 301-303 (1981).
3. W E Wallis, E Willoughby and P Baker. *Lancet* *ii*, 400-401 (1978).
4. L R Squire, D G Amaral and G A Press. *J. Neuroscience*, **10**, 3106-3117 (1990).
5. S Rose, P Nixon, F Zelaya, B T Wholohan, C Zimitat, L N Moxon, S Crozier, I M Brereton and D M Doddrell. *NMR in Biomedicine*, **6**, 324-328 (1993).
6. F Zelaya, S E Rose, P F Nixon, B T Wholohan, A J Bower, C Zimitat, J Schoutrop and D M Doddrell. *Magnetic Resonance Imaging*, **13**, 4 (1995).

NMR Structure of Parathyroid Hormone-related Protein (1-34)

J. A. Barden and ¹B. E. Kemp

Department of Anatomy and Histology, The University of Sydney, NSW 2006 and ¹St. Vincent's Institute of Medical Research, 41 Victoria Pde. Fitzroy, Vic. 3065 Australia

I. Introduction

Parathyroid hormone-related protein (PTHrP) is a fetal hormone¹ expressed by a great many human tumors² and originally identified as a tumor product causing PTH-like symptoms of humoral hypercalcemia of malignancy, a major contributor to morbidity and mortality with a quarter of all cancer patients becoming affected³. It binds tightly to both skeletal and renal PTH receptors⁴⁻⁶, and disrupts homeostatic control of serum calcium by restricting excretion through the kidney and by promoting the resorption of bone.

Only the N-terminal domain (1-34) of PTHrP shares any sequence homology with PTH, with 8 of the first 13 residues being identical while many other residues in the sequence 14-34 are somewhat conserved⁷. In particular, many residues in the putative primary receptor binding site (24-31) have conserved hydrophobic or charged side chains⁸. The N-terminal domain also exhibits full PTH-like adenylate cyclase agonist activity⁷. Moreover, the C-terminal residues in this domain form a site responsible for exerting mitogenic effects on chondrocytes and osteoblasts in a cAMP-independent manner¹⁰. In addition, this C-terminal segment of the domain is involved in the regulation of sodium-dependent phosphate transport by the messenger system mediated by protein kinase C¹¹.

Binding and activity studies have been performed using both N-terminal and C-terminal truncated PTH and PTHrP peptides^{7,9}. These have shown that agonist activity depends on the presence of the intact N-terminal residues, whereas binding to the glycoprotein PTH receptors depends more on the presence of the C-terminal residues in the domain. Thus, the signal transduction site is confined to the N-terminus whereas the bulk of the receptor binding site is located within the C-terminal region of 1-34.

NMR studies have been performed using both PTHrP(1-34)¹²⁻¹³ and PTH(1-34)^{8,14-15} in a range of solvents. These investigations have revealed that separate N-terminal and C-terminal

helices are present and with the exception of PTH in the presence of 10% F₃EtOH-d₂, a reverse turn was found in the segment 16-19 making PTH in water and PTHrP generally partially globular. However, when 10% F₃EtOH-d₂ was added to PTH(1-34), the reverse turn at 16-19 became incorporated in the C-terminal helical segment starting at Ser17^{8,15} suggesting that PTH(1-34) overall has a tendency to form more extended structures than PTHrP(1-34). The principal receptor binding site was expected to involve the C-terminal helical residues and thus the Ala26 mutant was made in an attempt to disrupt the binding¹². The structure of the PTHrP[Ala26] mutant was found to continue changing with increasing concentration of amphiphile up to 30% F₃EtOH-d₂ and a second bend was induced around the mutation site making the C-terminal helix more compact than is the case with PTH in water¹³. A reinvestigation of the structure in more dilute amphiphile (10% F₃EtOH-d₂) found the helix remained folded on the opposite side of the reverse turn residues in the center of the molecule but without the mid-helix distortion¹⁴. This finding reinforces the observation that a flexible hinge is present between residues 21/22¹²⁻¹⁴.

A comprehensive understanding of the structure-activity relationship of the PTHrP/PTH pair of hormones requires a detailed knowledge of their structure and mobility. In particular, the design of effective antagonists useful for the control of hypercalcemia of malignancy firstly requires that the structure of the receptor binding domain be determined in detail. We have used two-dimensional NMR spectroscopy to study the structure of the fully active mutant PTHrP[Ala9](1-34)-amide in 10% F₃EtOH-d₂ and to compare the principal structural features of this hormone with the tertiary solution structures of other homologous hormones. Confirmation of the stabilization of the structure in the presence of 10% F₃EtOH-d₂ was obtained along with the determination of the stabilized structure of the receptor binding site. A similar process was carried out with PTHrP[Ala15](1-34)-amide in

which the hydrophobic core of the residues around the turn was disrupted by replacing Ile15 with Ala and the receptor binding site structures compared.

II. Methods

Spectra at both 400MHz and 600MHz were recorded from the PTHrP samples (2.5 mM) at pH 4.1 and 293 K without sample spinning. Complete spin system assignments were made using 2D TOCSY spectra obtained with a MLEV-17 pulse sequence using 2.5 ms π pulses, mixing time of 100 ms and spin-lock field strength of 9 kHz. Residual water was suppressed using continuous coherent irradiation throughout both relaxation (1.8 s) and mixing periods. 2D NOESY experiments with a mixing time build-up of up to 250 ms recorded using the time-proportional-phase-increments method were used for sequence-specific resonance assignments and for estimations of proton-proton distance constraints. An F2 time-domain of 4 K was acquired with 512 separate free induction decays, each of 160 scans. The data were zero-filled to 4 x 1 K and apodized using Gaussian multiplication in F2 and shifted sine-bell in F1 prior to Fourier transformation.

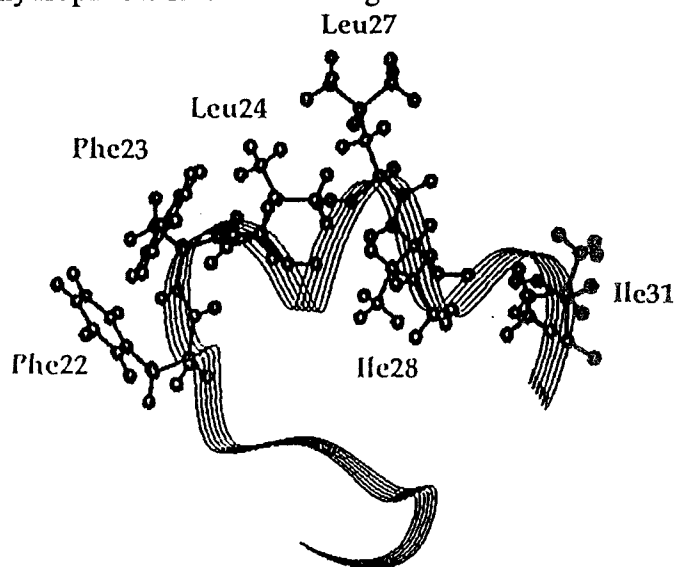
NOE cross-peaks were separated into distance categories of 0.3, 0.35, 0.4 and 0.45 nm using volume integrals and calibrated using the Thr33 α CH/ β CH crosspeak. Corrections for pseudoatoms were applied where stereospecific identification was not obtained. The torsion angles (ϕ) were constrained within the range -90° to -30° for all values of the coupling constant $^3J_{\alpha\text{CHNH}}$ of 5 Hz or less measured either using high-resolution 1D spectra or high-resolution 2D DQF-COSY spectra. 2000 DIANA¹⁶ structures were calculated for each peptide. The best 20 distance geometry structures were refined using a dynamic simulated annealing protocol (X-PLOR 3)¹⁷ to account for non-bonded interactions. In the initial stage of the simulation 500 cycles of energy minimization were applied and standard parameters were used to constrain covalent geometry. Non-bonded interactions were modelled with a repel function which ignored electrostatic interactions. The second stage involved heating the molecule to 1000 K by assigning high kinetic energies to the atoms from a Maxwellian distribution. The dynamic trajectory of the molecule was then followed for 50 ps in steps of 2 fs following which the NOE restraint term was increased linearly over 25 ps in 2 fs steps to place a gradually increased weight on covalent geometry. Stage 4 cooled the peptide from 1000 K to 300 K over 10 ps and equilibration

then commenced at 300 K for 1 ps followed by 2000 cycles of energy minimization.

III. Applications

All NMR distance and angle constraints used in the DIANA protocol were satisfied within 5 pm and 0° . The 20 structures with the lowest penalty values refined using XPLOR 3 all displayed good covalent geometry in each of the peptides. The mean rms deviation from ideal bond lengths for the Ala9 mutant was 0.095 ± 0.005 pm while the rms deviation from ideal bond angles was $0.152^\circ \pm 0.005^\circ$ while values for the Ala15 mutant were 0.0013 ± 0.0001 pm and $0.174 \pm 0.026^\circ$. The mean Lennard-Jones potential of -498 ± 23 kJ.mol⁻¹ showed good non-bonded contacts. Each family of refined and energy minimized structures was superimposed over the C-terminal segment 22-34 encompassing the putative receptor binding site and the root mean square (rms) deviation of backbone atoms measured. Values of 56 ± 7 pm and 85 ± 15 pm were found for the Ala9 and Ala15 mutants respectively. Some conformational averaging occurs at the C-terminal ends.

The principal features observed in the structures are a single helical segment stabilized by interactions with the mid-portion of the domain. A backbone schematic is shown with the hydrophobic sidechains along one face.



IV. Conclusions

The consistency of a hinge around Lys13/Ser14 suggests that it plays a functional role in enabling the residues N-terminal to the helix and essential for signal transduction to be positioned at the appropriate site within the receptor. This structure is conserved in both peptides. The reverse turn (Gln16-Arg19) is not

conserved in PTHrP[Ala15] and yet binding and activity are maintained. Consequently, it is the maintenance of the C-terminal helix from Phe22 to Ala34 which must be responsible for receptor binding, stimulation of sodium-dependent P_i transport and for exerting mitogenic effects on chondrocytes and osteoblasts. PTH(1-34) amide in water shows a less stable helix extending only to Gln29¹³. The figure shows that this region forms an amphipathic helix, a feature present in all the peptide variants. The hydrophobic face comprises the side chains of Phe22, Phe23, Leu24, Leu27, Ile28 and Ile31 with the three Arg side chains 19-21 separating two hydrophobic clusters formed by Ile15/Leu18 on one side and Phe22, Phe23 and Leu24 on the opposite side in the peptides with the reverse turn but in the Ala15 mutant, the C-terminal helix is stabilised by a helical extension through this mid-portion of the molecule. The opposite face of the C-terminal helix contains the three charged side chains of His 25, His26 and Glu 30.

Localization of the bulk of the receptor binding site to this C-terminal helix helps to explain how progressive C-terminal deletions reduce biological activity. Removal of residues Glu30 to Ala34 results in both the osteogenic sarcoma cell cAMP and the chicken kidney adenylate cyclase activities declining by 90%⁷. The fundamental purpose of the structure work is to provide a solid basis for the design of effective PTHrP and PTH antagonists. These must mimic the structure of the amphipathic α -helix forming the bulk of the receptor binding site using either peptide or organic analogs.

V. Acknowledgements

This work was supported by the National Health & Medical Research Council of Australia.

VI. References

- ¹L. Suva, G.A. Winslow, R.E.H. Wettenhall, R.G. Hammonds, J.M. Moseley, H. Diefenbach-Jagger, C.P. Rodda, B.E. Kemp, H. Rodriguez, E. Chen, P.J. Hudson, T. J., Martin, and W.I. Wood, *Science* **237**, 893-896 (1987).
- ²J.M. Moseley, M. Kubota, H.D. Diefenbach-Jagger, R.E.H. Wettenhall, B.E. Kemp, L.J. Suva, C.P. Rodda, P.R. Ebeling, P.J. Hudson, J.D. Zajac, and T.J. Martin *Proc. Natl Acad. Sci. USA* **84**, 5048-5052 (1987).
- ³G.R. Mundy, and T.J. Martin, *Metabolism* **31**, 1247-1277 (1982).
- ⁴N. Horiuchi, M.P. Caulfield, J.E. Fisher, M.E. Goldman, R.L. McKee, J.E. Reagan, J.J. Levy, R.F. Nutt, S.B. Rodan, T.L. Schofield, T.L. Clemens, and M. Rosenblatt, *Science* **238**, 1566-1568 (1988).
- ⁵H. Jüppner, A.B. Abou-Samra, S. Uneno, W.X. Gu, J.T. Potts Jr., and G.V. Segre, *J. Biol. Chem.* **263**, 8557-8560 (1988).
- ⁶R.A. Nissenson, D. Diep, and G.J. Strewler, *J. Biol. Chem.* **263**, 12866-12871 (1988).
- ⁷B.E. Kemp, J.M. Moseley, C.P. Rodda, P.R. Ebeling, R.E.H. Wettenhall, D. Stapleton, H. Diefenbach-Jagger, F. Ure, V.P. Michelangeli, H.A. Simmons, L.G. Raisz, and T.J. Martin, *Science* **238**, 1568-1570 (1987).
- ⁸J.A. Barden, and R.M. Cuthbertson, *Eur. J. Biochem.* **215**, 315-321 (1993).
- ⁹R.L. McKee, M.E. Goldman, M.P. Caulfield, P.A. DeHaven, J.J. Levy, R.F. Nutt, and M. Rosenblatt, *Endocrinology* **122**, 3008-3010 (1988).
- ¹⁰D. Sömjen, I. Binderman, K.D. Schlüter, E. Wingender, H. Mayer, and A.M. Kaye, *Biochem. J.* **272**, 781-785 (1990).
- ¹¹M. Arao, T. Yamaguchi, T. Sugimoto, M. Fukase, and K. Chihara, *Biochem. Biophys. Res. Commun.* **199**, 1216-1222 (1994).
- ¹²F.R. Ray, J.A. Barden, and B.E. Kemp, *Eur. J. Biochem.* **211**, 205-211 (1993).
- ¹³J.A. Barden, and B.E. Kemp, *Biochemistry* **32**, 7126-7132 (1993).
- ¹⁴J.A. Barden, and B.E. Kemp, *Biochim. et Biophys. Acta* **1208**, 256-262 (1994).
- ¹⁵V. Wray, T. Federau, W. Gronwald, H. Mayer, D. Schomburg, W. Tegge, and E. Wingender, *Biochemistry* **33**, 1684-1693 (1994).
- ¹⁶P. Güntert, W. Braun, and K. Wüthrich, *J. Mol. Biol.* **217**, 517-530 (1991).
- ¹⁷M. Nilges, G.M. Clore, and A.M. Gronenborn, *FEBS Lett.* **239**, 129-136 (1988).

Structure of the Pseudosubstrate Domain of Chicken Smooth Muscle Myosin Light Chain Kinase

J. A. Barden and ¹B. E. Kemp

Department of Anatomy and Histology, The University of Sydney, NSW 2006 and ¹St. Vincent's Institute of Medical Research, 41 Victoria Pde. Fitzroy, Vic. 3065 Australia

I. Introduction

Myosin light chain kinase (MLCK) plays an important role in regulating smooth muscle contraction¹. MLCK phosphorylates Ser19 in chicken smooth muscle myosin light chain in a highly tissue specific manner. Exogenous substrates are phosphorylated to only a very small extent². The kinase binds tightly to calmodulin with the chicken gizzard sequence 796-815 known to bind calmodulin stoichiometrically with an estimated dissociation constant of about 1 nM³. This calmodulin binding site partially overlaps the C-terminal segment of the sequence 780-808 which forms the autoregulatory domain of the enzyme⁴. Peptides from the N-terminal portion of the autoregulatory domain such as 774-787 do not inhibit the kinase whereas peptides from within the pseudosubstrate sequence such as 787-807 are potent inhibitors⁴. These data indicate that the autoregulatory and pseudosubstrate regions of MLCK are identical.

The pseudosubstrate sequence contains very similar numbers and spacing of basic residues to that found in the myosin light chain surrounding the site of phosphorylation at Ser19. It was thus proposed that the pseudosubstrate sequence binds to the active site in the catalytic core of MLCK thus maintaining the enzyme in an inactive conformation⁵. When Ca²⁺·calmodulin binds next to the pseudosubstrate sequence, the active site is exposed to the myosin light chain substrate. Calmodulin binding may induce an extension in α -helical structure through this domain of MLCK⁶. Such a change may of itself induce a rotation of the pseudosubstrate away from the active site. However, the binding of calmodulin may cause the pseudosubstrate to rotate away from the active site by using a hinge between the pseudosubstrate and the peptide connecting the pseudosubstrate to the catalytic core.

MLCK(783-804) acts as a substrate antagonist⁵ by inhibiting the calmodulin-dependent activation of chicken gizzard MLCK (IC₅₀ = 46 nM). Inhibition of the 61kDa

constitutively active MLCK(282-779) by synthetic peptides and studies with proteases have demonstrated that the pseudosubstrate encompasses Ser787-Lys802⁷. This finding indicates MLCK autoinhibition is caused by the pseudosubstrate sequence alone. Recently, the twitchin kinase structure was determined and provides strong support for the intrasteric model of protein kinase regulation⁸.

Chicken smooth muscle MLCK(787-807) is a potent inhibitor of the constitutively active MLCK core (K_i = 11.7 nM) while the longer peptide MLCK(774-807) containing both pseudosubstrate and connecting sequences is even more potent (K_i = 0.33 nM)⁹. Thus, the connecting peptide contributes substantially to pseudosubstrate binding. This extended binding of pseudosubstrate and connecting peptides to the catalytic core appears to explain why some mutation experiments appeared inconsistent with the pseudosubstrate model¹⁰.

This work has sought to establish the solution structure of the very potent synthetic MLCK peptide Leu774-Val807 incorporating all of the pseudosubstrate domain together with the connecting peptide Leu774-Leu786. The pseudosubstrate structure is compared with that of the calmodulin binding peptide 796-815 determined in complex with calmodulin¹¹. Knowledge of the structure of the pseudosubstrate is directed towards elucidating the likely mechanism of binding to and release of the pseudosubstrate from the active site.

II. Methods

Spectra at 400MHz were recorded from MLCK(774-807)amide samples (2.0 mM) at pH 4.1 and 293 K without sample spinning. Spin systems were assigned fully using two-dimensional TOCSY spectra obtained with a MLEV-17 pulse sequence using 2.5 ms trim pulses and a mixing time of 100 ms. The spin-lock field strength was 9 kHz. The water resonance was suppressed using continuous coherent irradiation throughout both relaxation

(1.8 s) and mixing periods. Two-dimensional NOESY experiments with a mixing time up to 250 ms recorded using the time-proportional-phase-increments method were used to aid in making sequence-specific resonance assignments as well as for estimations of proton-proton distance constraints. An F2 time-domain of 4 K was acquired with 512 separate free induction decays, each of 160 scans. The data were zero-filled to 4 x 1 K and apodized using Gaussian multiplication in F2 and shifted sine-bell in F1 prior to Fourier transformation.

NOE cross-peaks were separated into the conservative distance categories 0.3, 0.35, 0.4 and 0.45 nm using volume integrals and calibrated using the Thr803 α CH/ β CH crosspeak. Corrections for pseudatoms were applied where stereospecific identification was not obtained. The torsion angles (ϕ) were constrained within the range -90° to -30° for all values of the coupling constant $^3J_{\alpha\text{CHNH}}$ of 5 Hz or less measured either using high-resolution 1-D spectra or high-resolution 2-D DQF-COSY spectra. A total of 2000 distance geometry structures were calculated from random starting structures using the program DIANA¹² on a Silicon Graphics RS4000 workstation while molecular graphics were processed using the program Insight II operating on a Silicon Graphics Indigo 2 workstation.

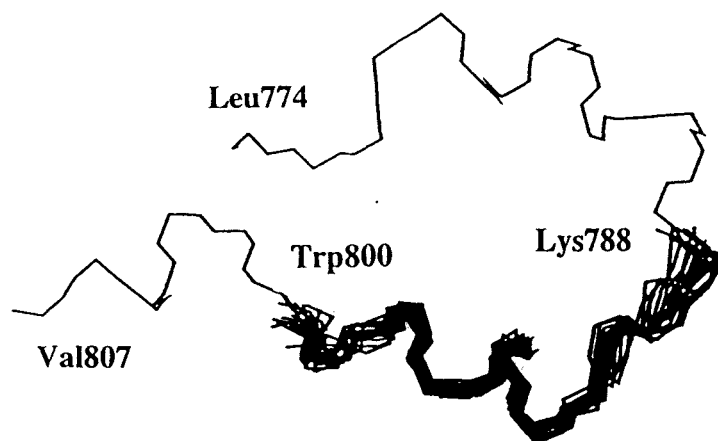
The best 20 distance geometry structures possessing the lowest penalty values were refined using a dynamic simulated annealing protocol (XPLOR 3)¹³. DIANA structures exhibited poor potential energies by not considering non-bonded interactions. In the initial stage of the simulation 500 cycles of energy minimization were applied and standard parameters were used to constrain covalent geometry. Non-bonded interactions were modelled with a repel function which ignored electrostatic interactions. Stage 2 involved heating the molecule to 1000 K by assigning high kinetic energies to the atoms from a Maxwellian distribution. The dynamic trajectory of the molecule was then followed for 50 ps in steps of 2 fs following which the NOE restraint term was increased linearly over 25 ps in 2 fs steps which placed a gradually increased weight on covalent geometry. Stage 4 cooled the peptide from 1000 K to 300 K over 10 ps and equilibration then commenced at 300 K for 1 ps followed by 2000 cycles of energy minimization.

III. Applications

136 distance constraints and 15 angle constraints were used in the DIANA protocol to

generate refined structures from random starting conformations satisfying all the NMR distance constraints within 5 pm and all angle constraints. The 20 structures with the lowest penalty values refined using XPLOR 3 all displayed good covalent geometry. The mean rms deviation from ideal bond lengths was 0.10 ± 0.01 pm while the rms deviation from ideal bond angles was $0.141^\circ \pm 0.021^\circ$. The mean Lennard-Jones potential of -294 ± 84 kJ.mol⁻¹ showed good nonbonded contacts. This family of refined and energy minimized structures were superimposed and the root mean square (rms) deviation of backbone atoms measured throughout all segments of the peptide. Asp777 - Lys785 and Lys788 - Trp800 possessed low rms deviations. Some conformational averaging is present at both N- and C-terminal ends but Lys779-Lys788 and Lys792-Trp800 maintain consistent conformations.

The main features in the structures are the helical segment (Asp777-Lys785), the turn (Leu786-Asp789) and second helical segment (Arg790/Met791-Trp800). 20 structures were superimposed over the backbone atoms in the pseudosubstrate sequence 788-800 is shown in the figure. The mean rms deviation between these structures and the mean structure in the N-terminal region is 54 ± 7 pm while in the C-terminal domain the rms deviation is 69 ± 11 pm indicating the conformational space defined by the molecule is well-defined.



IV. Conclusions

The carboxy-terminal limit of the pseudosubstrate inhibitory region (Lys802)⁷ forms the end of the C-terminal helix. The structure of the C-terminal segment is affected by interactions between residues at the C-terminal end of the pseudosubstrate segment and the N-terminal end

of the connecting peptide. It is unlikely that this interaction occurs in the same sequence within the intact enzyme since the two helical segments would be kept separated by N- and C-terminal connections to the remaining structure. This is consistent with the findings that the residues Ala796-Ser815 form a helix when bound to calmodulin¹¹.

The structure of the equivalent cAPK inhibitor peptide PKI(5-24) has been determined in complex with the cAPK catalytic subunit¹⁴. The N-terminal portion of the inhibitor PKI(5-17) forms an amphipathic α -helix which binds to a hydrophobic groove on the major lobe of catalytic cAPK while the consensus site (18-24) forms an extended structure which binds in a cleft between the two lobes [34]. PKI(5-24) has a similar function to the MLCK pseudosubstrate and so should exhibit a similar tertiary structure. Sequence comparison between the two peptides reveals MLCK(789-808) in the pseudosubstrate peptide is equivalent to PKI(5-24)⁹. Comparing their structures reveals a high degree of similarity. The PKI helix (5-17) is duplicated in the pseudosubstrate peptide and the C-terminal segment PKI(18-24) is similarly extended in the pseudosubstrate (801-807). This close structural equivalence implies that the MLCK pseudosubstrate sequence is likely to interact with the active site in the catalytic core in a similar way to the demonstrated interaction of PKI with cAPK¹⁴. The structure of the pseudosubstrate peptide revealed here agrees with earlier results using peptides overlapping the pseudosubstrate peptide sequence at the C-terminal end forming the calmodulin binding site which has been shown to form a helix in complex with calmodulin after the central helix is disrupted¹⁵. The connecting peptide in the pseudosubstrate sequence MLCK(774-786) appears largely helical and may therefore bind to the catalytic core in a similar fashion to that expected for the C-terminal helical segment, i.e. interacting with a groove on the catalytic core to increase the K_i of MLCK(774-807) about 30-fold compared with the pseudosubstrate sequence MLCK(787-807) alone⁹.

V. Acknowledgements

This work was supported by the National Health & Medical Research Council of Australia.

VI. References

- ¹R.S. Adelstein, and E. Eisenberg, *Annu. Rev. Biochem.* **44**, 921-956(1980).
- ²R.S. Adelstein, and C.B. Klee, (1981) *J. Biol. Chem.* **256**, 7501-7509.
- ³T.J. Lucas, W.H. Burgess, F.G. Prendergast, W. Lau, and D.M. Watterson, *D.M. Biochemistry* **25**, 1458-1464 (1986).
- ⁴N.J. Olson, R.B. Pearson, D.S. Needleman, M.Y. Hurwitz, B.E. Kemp, and A.R. Means, *Proc. Natl Acad. Sci. USA* **87**, 2284-2288 (1990).
- ⁵B.E. Kemp, R.B. Pearson, V. Guerriero, I. Bagchi, and A.R. Means, *J. Biol. Chem.* **262**, 2542-2548 (1987).
- ⁶R.E. Klevit, D.K. Blumenthal, D.E. Wemmer, and E.G. Krebs, *Biochemistry* **24**, 8152-8157 (1985).
- ⁷R.B. Pearson, M. Ito, N.A. Morrice, A.J. Smith, R. Condron, R.E.H. Wettenhall, B.E. Kemp, and D.J. Hartshorne, *Eur. J. Biochem.* **200**, 723-730 (1991).
- ⁸S.-H. Hu, M.W. Parker, J.Y. Lei, M.C.J. Wilce, G.M. Benian, and B.E. Kemp, *Nature* **369**, 581-584 (1994).
- ⁹D.R. Knighton, R.B. Pearson, J.M. Sowadski, A.R. Means, L.F. Ten Eyck, S.S. Taylor, and B.E. Kemp, *Science* **258**, 130-135 (1992).
- ¹⁰K. Yano, Y. Araki, S.J. Hales, M. Tanaka, and M. Ikebe, *Biochemistry* **32**, 12054-12061 (1993).
- ¹¹W.E. Meador, A.R. Means, and F.A. Quioco, *Science* **257**, 1251-1255 (1992).
- ¹²P. Güntert, W. Braun, and K. Wüthrich, *J. Mol. Biol.* **217**, 517-530 (1991).
- ¹³M. Nilges, G.M. Clore, and A.M. Gronenborn, *FEBS Lett.* **239**, 129-136 (1988).
- ¹⁴D.R. Knighton, J. Zheng, L.F. Ten Eyck, V.A. Ashford, N.-H. Xuong, S.S. Taylor, and J.M. Sowadski, *Science* **253**, 414-420 (1991).
- ¹⁵M. Ikura, G.M. Clore, A.M. Gronenborn, G. Zhu, C. Klee, and A. Bax, *Science* **256**, 632-638 (1992).

Developments in STRAFI for the Quantitative Relaxation Analysis
of Solvent Imbibition into Polymers

T. B. Benson and P. J. McDonald
Department of Physics
The University of Surrey
Guildford
Surrey
United Kingdom.

Abstract

In this paper we present recent developments made to the STRAFI experiment, both in terms of pulse sequences used and in the interpretation of relaxation data. These improvements permit us to measure with high spatial resolution materials with short T_2 relaxation times. The applications of the new techniques are illustrated by a study of the imbibition of solvent mixtures into polymethylmethacrylate.

Introduction

The Stray Field Imaging technique (STRAFI) [1], is used to produce high resolution images of solid materials where the T_2 or spin spin relaxation time is relatively short. STRAFI utilises the high fringe field gradient (typically 50 T/m) produced at the edge of a superconducting magnet to spatially isolate the nuclear spins in a thin slice of the sample orthogonal to the gradient. A spin density profile is created by moving the sample through the resonant position in the field gradient and applying a quadrature echo sequence at each point to provide relaxation information. Further dimensions may be imaged by rotating the sample through space.

As polymers find increasing application as engineering materials, their response to various chemical environments becomes important. Many polymers are subject to attack by solvents and the long term usefulness of polymer materials in hostile environments may well be dependent on their resistance to chemical ingress. Ingress may also be used as a probe of the polymer morphology, as the rate of imbibition is highly dependent on the microscopic structure of the polymer. Solvent diffusion in solid polymers may exhibit both Fickian and Case II behaviour, the latter being especially prevalent in polymers below the glass transition temperature and characterised by a short induction period and linear kinetics. The diffusion mechanism is dependent on both the type of polymer, its structure and the solvent used.

Although conventional MRI may be used to provide information on the spatial distribution of solvent within the polymer [2], the diffusion itself is strongly dependent on the relaxation response of the polymer matrix to the chemical imbibition. STRAFI may be used to image the swollen polymer chains, as well as the mobile solvent, which leads to a greater understanding of the diffusion mechanism [3].

Developments in Stray Field Imaging

Due to the strong magnetic field gradient present across the sample during the application of RF pulses, the quadrature echo trains produced using STRAFI are heavily modulated. In the limit of a long T_2 relaxation time, the amplitude of the second echo is greater than that of the first. The modulation means useful spin spin relaxation information is difficult to obtain from the echo trains. Simulations have been developed in order to investigate the origin of the modulation [4] and may be used to extract accurate values of the sample T_2 by accounting for the effect of the gradient on the echo train.

In addition new pulse sequences have been developed in order to enhance the signal to noise ratio and the accuracy of relaxation information obtained in STRAFI experiments. Hitherto, STRAFI experiments have used the quadrature echo sequence to provide relaxation contrast. The sequence has component pulses of equal length, which is important for STRAFI experiments as a variation in pulse length alters the slice excitation width. This means the conventional spin echo sequence $90_x-(\tau-180_y-\tau\text{-echo})_n$ cannot be used. However, by doubling the amplitude of the rephasing pulses, the pulse length of the spin echo sequence may be kept constant. Spin echoes have several advantages over the quadrature echoes. In particular the signal to noise ratio of the first few echoes is improved and the relaxation response of the echo train tends towards normal T_2 decay as the RF pulse length is decreased, causing less errors in the interpretation of data [5]. Unfortunately, the alternating phase variant of the spin echo sequence $90_x-(\tau-180_y-\tau\text{-echo}-\tau-180_y-\tau\text{-echo})_n$ may not be used, due to the creation of an unfavourable slice excitation profile. Figure 1 shows the theoretically calculated amplitudes for the first eight echoes of the three sequences.

T. B. Benson and P. J. McDonald - Developments in STRAFI.

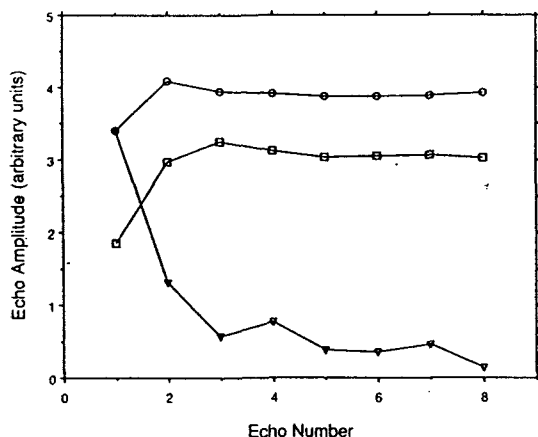


Figure 1. Calculated echo amplitudes for the quadrature echo sequence (squares), the spin echo sequence (circles) and the alternating phase variant of the spin echo sequence (triangles). The signal to noise advantages of the spin echo sequence over the conventional quadrature echo sequence are clearly visible.

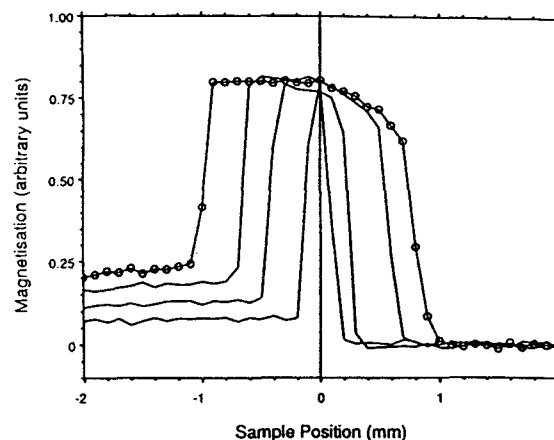


Figure 2. The imbibition of a 1:1 mixture of methanol and acetone observed as a function of time. The profiles are displayed at 6 hour intervals. The rigid polymer can be seen to the left of the picture, the swollen region in the centre. The vertical line marks the surface of the polymer at the start of the experiment.

Studies of Solvent Imbibition into PMMA

Polymethylmethacrylate (PMMA) is transparent, mechanically strong and relatively inert. It has many engineering uses and also has applications in bone repair and dental restoration. Samples of both linear and crosslinked PMMA were exposed to various mixtures of methanol, acetone and water vapour. STRAFI experiments were performed to follow the imbibition of the solvent mixtures as a function of time at high spatial resolution (~50 μm).

The results of one experiment, the imbibition of the vapour produced by a 1:1 mixture by mass of liquid acetone and methanol can be seen in Figure 2. As the solvent penetrates the polymer swells. This can be seen to the right of the zero line. To the left of the zero line, the solvent penetrates via Case II diffusion. By varying the solvent composition and polymer type, different kinetic behaviour is observed, for example, crosslinked PMMA is more resistant to solvent ingress as the relaxation of the polymer chains is inhibited by the molecular structure. In addition, increasing the methanol concentration reduces the rate of ingress, as the methanol diffusion process is much slower than that of the acetone. Strong molecular associations between the different solvent molecules may also contribute to variations in the vapour composition and affect the rate of diffusion.

Summary

Theoretical techniques have been developed in order to obtain relaxation information from STRAFI experiments. In addition, new pulse sequences have been developed to enhance STRAFI data quality. The usefulness of STRAFI in the study of solvent ingress into polymers has been demonstrated. Further experiments will lead to a greater understanding of the structure of polymers, as well as assessing their suitability for engineering and medical applications.

Acknowledgements

T. B. Benson would like to thank the United Kingdom EPSRC for a research studentship and travel grant.

References

- [1] A.A. Samoilenko, D. Yu. Artemov and L. A. Sibel'dina, *JETP Lett.* **47** 348 (1988).
- [2] A.G. Webb and L.D. Hall, *Polymer* **32** 2926 (1991).
- [3] K.L. Perry, P.J. McDonald, E.W. Randall and K. Zick, *Polymer*. **35** 2744 (1994).
- [4] T.B. Benson and P.J. McDonald, *J. Magn. Reson. Series A*. **112** 17 (1995).
- [5] T.B. Benson and P.J. McDonald, *J. Magn. Reson. Series A*. Accepted for publication.

^2H NMR Spectroscopy of D_2O in Silicate Sol-Gel Glasses

S. Wonorahardjo, J. Hook and G. Moran

School of Chemistry, The University of New South Wales, Sydney 2052, Australia

Introduction

NMR spectroscopy of quadrupolar nuclei and particularly deuterium is an important technique to study molecular mobility within solid materials like glasses, polymers and membranes [1].

Transparent silica gels made from alkoxy silanes by sol-gel processing can be used to encapsulate analytical reagents and hence can be used as the basis of solid-state chemical sensors [2]. The porosity of the gels must be controlled so that the reagent molecules are effectively trapped within the gel and yet are accessible for rapid reaction with analyte species absorbed from the surrounding solution. Factors affecting gel porosity include gelling rate and time and the use of additives such as drying control agents [2,3]. ^{29}Si NMR spectroscopy has previously been used to monitor the hydrolysis of alkoxy silanes [4]

In this study, an acid-base indicator is used as a model analytical reagent in order to test the suitability of various gel compositions for optical sensing. Once the optimum reaction conditions are obtained it is also necessary to be able to stop the gelation reaction at the required level of crosslinking. ^2H NMR spectroscopy of deuterated gels is used to characterise the solvent phase within the gels and to test for termination of the gel-forming reactions.

Experimental

The tetramethoxysilane gels were prepared according to the method of Rotmann et al. [3] with some modification. $\text{Si}(\text{OCH}_3)_4$ (1.15ml), water (1.25ml) and methanol (1.25 ml) were mixed and 0.25 mL of 1.0×10^{-3} M NaOH was added as the catalyst along with 0.25 ml methanolic solution (3.8 % w/w) of cetyltrimethyl ammonium bromide (CTAB). The mixture was stirred until a homogeneous

solution was obtained, transferred to sample tubes covered with perforated aluminium foil and left to react at room temperature. The indicator used was phenol red (6.6E^{-6} mol).

Gelation was terminated by addition of H_2O or D_2O 98%. Deuterated samples for NMR were equilibrated for at least 24 hours. ^2H NMR spectra were measured on a Bruker ACP 300 spectrometer at 46 MHz. FIDs were acquired with a pulse width of 4 ms and a spectral width of 10 KHz which gave an acquisition time of 0.102 s. The T_1 data were obtained with the inversion-recovery pulse sequence.

Result and discussion

The ^2H NMR spectra of the tetramethoxysilane (TMOS) gel after 4 and 10 days reaction time are shown in Figure 1. The spectra show single broad peaks with linewidths of 374 and 662 Hz respectively. It is likely that not all Si-OH groups are deuterated under the condition used but the observed resonance will include a contribution from those Si-OD groups which can undergo D^+ exchange with the absorbed D_2O .

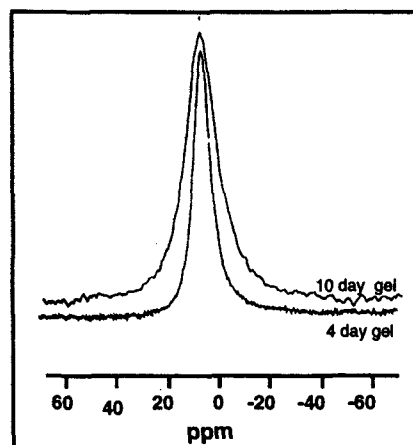


Figure 1. ^2H NMR spectra of TMOS gel after 4 and 10 day reaction times.

The ^2H spin lattice relaxation times were measured as a function of reaction time for two samples of the gel (Table 1). The mobility of the D_2O phase within the gel continues to decrease over the first 10 days as indicated by the decrease in T_1 but there is relatively little change subsequently.

Gelling Time (days)	T_1 values (ms)	
	1A	2A
4	240	252
10	110	118
17	99	101

Table 1. ^2H T_1 values for TMOS gels as a function of reaction time

Since the porosity of the gels is reduced on aging by continued crosslinking of the Si-OH groups the possibility of stopping this process by addition of water was tested. Samples were kept humidified in D_2O vapour or immersed in $\text{D}_2\text{O}(\text{l})$ and the relaxation times were measured over a 14 day period. The results in Table 2 show that the T_1 values remain almost constant or show a slight increase in solvent mobility indicating that the condensation process has been stopped.

Equil Time (day)	T_1 (ms)			
	1A	2A	1B	2B
1	240	252	110	118
7	232	259		
8			118	123
14	249	262		

Table 2. ^2H T_1 values for TMOS gels after equilibration in D_2O liquid (A) and vapour (B)

Typical reactivity data for phenol-red doped gels are given in Table 3 for 4- and 13-day gel samples. The rate of reaction of phenol-red in base solution, monitored at 567 nm is slower in more cross-linked gels indicating reduced rates of diffusion of the aqueous phase within the gels. Phenol-red is not leached from the samples under these conditions. The slower response times and the shorter ^2H T_1 values for the older gels correspond to smaller pore sizes and greater cross-linkage.

Time (min) in NaOH	DA at 567 nm	
	4 days gel	13 days gel
1	0.102	0.088
4	0.162	0.141
12	0.239	0.190

Table 3. Absorbance change for phenol red in 4 days gel (A) and 7 days gel (B) on reaction with NaOH(aq).

Conclusion:

^2H spin-lattice relaxation times can be used to monitor the mobility of the aqueous phase within the silica gels. The results are consistent with UV-visible experiments which show lower reaction times in older gels. T_1 measurements are a useful tool for characterisation of solvent mobility in these gels.

References

1. Kaufmann, E.N., Shenoy, G.K., *Nuclear and Electron Resonance Spectroscopies Applied to Materials Science*, (1981), North Holland, New York.
2. Zuzman, R., Rottman, C., Ottolenghi, M., Avnir, D., *J. Non-Cryst. Solids*, **122**, 107-109, (1990)
3. Rottman, C., Ottolenghi, M., Zusman, R., Lev, O., Smith, M., Gong, G., Kagan, M.L., Avnir, D., *Materials Letters*, **13**, 293-298, (1992).
4. Sugahara, Y., Okada, S., Kuroda, K., Kato, C., *Journal of Non-Crystalline Solids*, **139**, (1992), 25-34.

Bulk and Surface Relaxation in Spheres during NMR Diffusion Measurements: Analytical Expressions using Neuman's Approach

Philip W. Kuchel, Alison J. Lennon and Christopher Durrant

Department of Biochemistry and School of Mathematics, University of Sydney, Sydney, NSW 2006, Australia.

INTRODUCTION

The rate of translational diffusion of a solute inside cells can directly influence its rate of metabolism, or the rate at which it can convey a chemical 'signal' [1]. NMR methods that are suitable for studying molecular diffusion in cells have reached an advanced state of development [2,3].

We present an outline (the details have been submitted for publication elsewhere) of the mathematical solutions, for two different boundary conditions, of the equation that describes the spin-echo NMR signal intensity in the steady-gradient-diffusion experiment [4]; the extension of the theory to the pulsed-gradient experiment [5] has also been achieved. The particular physical system is that of diffusion of nuclear spins inside spheres of fixed radius, where relaxation takes place both in the bulk phase and, at a different rate, on the (inner) surface; that such a system serves as a simple model of a cell should be apparent.

The significance of this work lies in the ability to estimate the *intrinsic* diffusion coefficient of a solute under conditions when its motion is restricted and its measured (*extrinsic*, or apparent) value of D is much less than the intrinsic value. For diffusion of a solute in an isotropic and unbounded medium the distribution of phases of the nuclear magnetisations in a spin-echo experiment is Gaussian (the GPD condition; [6,7]); such is not the case for restricted diffusion, but under many circumstances a Gaussian distribution is a very good approximation [8,9].

THEORY

The NMR Signal

The general expression for the NMR spin-echo signal intensity, R , obtained from a system of spins diffusing in a linearly inhomogeneous magnetic field, when the distribution of spins is gaussian, is [7]:

$$R = e^{-\langle \varphi^2 \rangle / 2} \quad (1)$$

where the mean-square phase change at time 2τ in the spin-echo experiment is given by,

$$\langle \varphi^2 \rangle = \gamma^2 g^2 \left(\int_0^\tau dt \int_0^\tau dt' - 2 \int_0^\tau dt \int_\tau^{2\tau} dt' + \int_\tau^{2\tau} dt \int_\tau^{2\tau} dt' \right) \langle z[t] z[t'] \rangle \quad (2)$$

Thus the derivation of the expression for R requires the evaluation of Eqs (1) and (2), in which $\langle z[t] z[t'] \rangle$ refers

to the ensemble average of the products of the physical displacements of the spins in the direction of the magnetic-field gradient, at time t . It is apparent that the problem is divisible into two parts, viz., the 'time part' involving the integrals enclosed in the round brackets, and the 'spatial part' defined by the term in angle brackets.

Statement of the Problem...the Modified Diffusion Equation

The diffusion is assumed to occur in a sphere with the magnetic field gradient lying in the same fixed direction as the main field B_0 . Thus the system has axial symmetry; so, in a spherical-polar coordinate system (r, θ, ϕ) there is no ϕ -dependence in the formulation of the problem (and its solution). The motion is described in terms of the conditional probability-density operator, or propagator, P [11,12]. Thus the diffusion equation, modified to include bulk relaxation is [7,10]:

$$\frac{\partial^2 P}{\partial r^2} + \frac{2}{r} \frac{\partial P}{\partial r} + \frac{1}{r^2} \frac{\partial^2 P}{\partial \theta^2} + \frac{\cot \theta}{r^2} \frac{\partial P}{\partial \theta} - F P = \frac{1}{D} \frac{\partial P}{\partial t} \quad (3)$$

where, D is the translational diffusion coefficient, the product $F D$ is the bulk relaxivity (or rate constant, with units of s^{-1} , so F itself has units of m^{-2}), and t is time. The general solution is [13,14]:

$$P[r, \mu, t] = \sum_{n=0}^{\infty} \left\{ \sum_{m=0}^{\infty} A_{n,m} (\alpha_{n,m} r)^{-1/2} \times \right. \\ \left. J_{n+1/2}[\alpha_{n,m} r] P_n[\mu] \right\} e^{-(\alpha_{n,m}^2 + F) D t} \quad (4)$$

where $J_{n+1/2}$ and P_n are the spherical Bessel functions and Legendre functions of order $n+1/2$ and n , respectively, and $\mu = \cos \theta$.

The coefficients of Eq. (4) for the three different boundary conditions (A, no surface relaxation; B, infinitely rapid surface relaxation or "absorbing wall" [15]; C, finite surface relaxation) were obtained by the method of Neuman [7] and will be presented elsewhere. The integration function of *Mathematica* [16] prove to be invaluable for the generation of the solutions.

RESULTS AND DISCUSSION

Figure 1 shows the results of two random walk simulations of field gradient spin-echo NMR experiments [17]. In the first it was assumed that there was no surface relaxation, and the parameter values were similar to those encountered in real systems, such as

water in a cell of dimensions similar to that of a human erythrocyte. The Neuman [7] expression describes the data quite closely, but the curve lies systematically above the random walk data; this deviation has been observed by Balinov et al. [8]. It represents a systematic failing of the analytical theory that is based on the GDP approximation and yet the under the present and similar real conditions the error is evidently relatively small. It was apparent from the Monte Carlo simulations, and the analytical theory, that the bulk relaxation effect could be ignored; this is because the signal from the field gradient experiment is normalised to one without the field gradient, and the bulk relaxation properties are not normally affected by magnetic field gradients. On the other hand, the inclusion of a non-zero value for F in the evaluation of the expressions relating to all three boundary conditions, did detrimentally affect the convergence characteristics of the series solutions. Therefore, in all subsequent analysis F was set to zero.

The inclusion of surface relaxation, with a relaxivity value of $M = 4 \times 10^{-4} \text{ m s}^{-1}$, yielded simulated normalised echo-intensities that were greater than those obtained without surface relaxation. The qualitative explanation for this effect is that in the presence of surface relaxation the sub-population of nuclei that retain their high energy nuclear magnetic states are those that do not encounter the inner surface of the sphere, whereas the members of the sub-population that do encounter the surface have a high probability of having their 'signal' quenched; thus the echo-signal arises primarily from those nuclei that have moved in a smaller volume nearer the centre of the sphere. Diffusion in a sphere of smaller radius gives rise to a spin-echo signal that is less attenuated than for a sphere of larger radius simply because the mean displacement of all the spins is smaller.

Furthermore, the general theory developed here for boundary condition C, yielded a curve in Fig. 1 that was not perceptibly different from the Neuman [7] solution for values of M up to $\sim 1 \times 10^{-7} \text{ m s}^{-1}$. This and other more extensive testing indicated convergence of the general theory (boundary condition C) solutions to those given by Neuman's equation [7] for small values of M , thus providing one 'check' on the analysis. Notwithstanding the complexity of the solutions developed in this work, they do constitute a means of rapidly simulating experimental outcomes from field-gradient spin-echo experiments. Incorporation of the expressions into non-linear regression programs for the purpose of estimating intrinsic values of D , from the relevant data, should be feasible.

REFERENCES

1. H. A. Berthon and P. W. Kuchel, *Adv. Mol. Cell Biol.* **11**, 147 (1995).
2. P. T. Callaghan, "Principles of Nuclear Magnetic Resonance Microscopy", Oxford Univ. Press, Oxford, 1991.
3. P. Stilbs, *Prog. NMR Spectrosc.* **19**, 1 (1987).
4. E. L. Hahn, *Phys. Rev.* **80**, 580 (1950).
5. E. O. Stejskal and J. E. Tanner, *J. Chem. Phys.* **42**, 288 (1965).
6. J. S. Murday and R. M. Cotts, *J. Chem. Phys.* **48**, 4938 (1968).
7. C. H. Neuman, *J. Chem. Phys.* **60**, 4508 (1974).
8. B. Balinov, B. Jönsson, P. Linse, and O. Söderman, *J. Magn. Reson. A* **104**, 17 (1993).
9. J. E. M. Snaar and H. Van As, *J. Magn. Reson. A* **102**, 318 (1993).
10. K. R. Brownstein and C. E. Tarr, *Phys. Rev. A* **19**, 2446 (1979).
11. E. O. Stejskal, *J. Chem. Phys.* **43**, 3597 (1965).
12. J. Kärger and W. Heink, *J. Magn. Reson.* **51**, 1 (1983).
13. P. Moon and D. E. Spencer, "Field Theory for Engineers". Van Nostrand, Princeton, 1961.
14. I. N. Sneddon, "Special Functions of Mathematical Physics and Chemistry," Oliver and Boyd, Edinburgh, 1956.
15. J. Kärger, H. Pfeifer, and W. Heink, *Adv. Magn. Reson.* **12**, 1 (1988).
16. S. Wolfram, "Mathematica. A System for Doing Mathematics by Computer". Addison-Wesley, Redwood City, 1991.
17. A. J. Lennon and P. W. Kuchel, *J. Magn. Reson. A* **107**, 229 (1994).

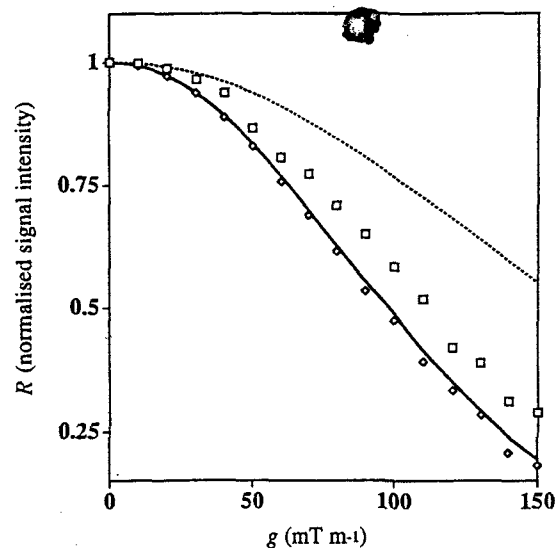


FIG. 1. The normalised NMR signal intensity (R) predicted by random walk (Monte Carlo) simulations of a spin-echo experiment [17], involving a sample with spin diffusion in a sphere with (squares) and without (diamonds) surface relaxation, compared with the corresponding analytical solutions (lines). The parameter values were: $D = 2 \times 10^{-9} \text{ m}^2 \text{ s}^{-1}$; $a = 5 \text{ }\mu\text{m}$; $M = 0$ (diamonds), and (squares) $4 \times 10^{-4} \text{ m s}^{-1}$; $\tau = \Delta = \delta = 40 \text{ ms}$; and for the Monte Carlo simulations the number of individual particle-trajectories recorded = 1,266,000. The solid line was given by the Neuman [7] solution and the dashed line is the corresponding curve given by the 'absorbing wall' boundary condition; this latter case is equivalent to having $M = \text{infinity}$.

Multinuclear (^1H , ^{13}C , ^{15}N , ^{59}Co) NMR studies of dithiocarbacinic acid derivative complexes of cobalt (III) in solution

Uwe Himmelreich^{1,2}, Frank Tschwatschal¹ and Rolf Borsdorf¹

¹ University of Leipzig, Department of Chemistry, Linnestr. 5 - 7, Leipzig, D 04130, Germany

² present address : University of Sydney, Department of Biochemistry, Sydney, NSW 2006, Australia

Introduction

The chelates of the corresponding Schiff bases of hydrazine-S-methyl dithiocarboxylate **1** to **5** exhibit a wide range of stereochemistries in octahedral complexes with transition metal ions like Co^{3+} . These Schiff bases can act as single negatively charged bidentate ligands coordinating to metal ions via the mercapto sulphur and the β -nitrogen atoms or they can act as tridentate ligands coordinating via an additional heteroatom in the substituent R.

Two different arrangements are possible for the bidentate ligands in the CoL_3 chelates, the *facial* (*fac*) and the *meridional* (*mer*) structure (see Figure 1). The particular nuclei in the *fac* arrangement are magnetically equivalent and therefore one set of signals is expected while the nuclei in the *mer* structure are magnetically different and three sets of signals with equal intensities are expected.

Eight different isomers can theoretically be obtained in the chelates according to the E / Z configurations of the C=N bond, found in the parent organic ligands /1/ and in the zinc chelates /2/. These isomers are *fac*-EEE, *fac*-EEZ, *fac*-EZZ, *fac*-ZZZ, *mer*-EEE, *mer*-EEZ, *mer*-EZZ and *mer*-ZZZ, with E and Z indicating the configuration of the ligands. These eight structures can result in 24 sets of signals.

We measured chemical shift differences in the ^1H -, ^{13}C -, ^{15}N - and ^{59}Co -NMR spectra, C-H coupling constants and NOE difference measurements in order to determine the coordination pattern and the configurational composition. An unequivocal assignment of the signals of the different isomers was necessary for the interpretation of these NMR-data.

The proton-proton coupling networks were analysed by H,H-COSY-90 and delayed H,H-COSY-45 techniques. These assignments were established and transferred to the ^{13}C signals by the ^1H -detected HMQC and HMBC spectra. Because of the weak solubility of the chelates and the line broadening caused by the quadrupole nucleus, ^{59}Co , we could not record a high resolution ^{15}N -NMR spectra and only obtained a reasonable ^{15}N -NMR spectrum for **Co 2** in CDCl_3 . The transfer of the assignment to the ^{15}N signals by a long-range H,N correlation (HMBC) as done for the zinc chelates /2/ failed.

Experimental

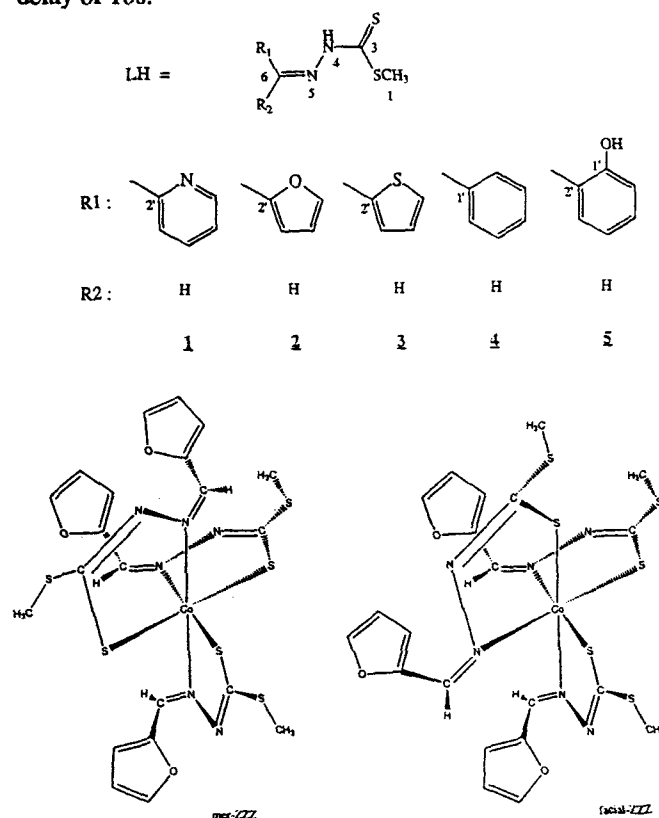
The reaction of the ligands **1** to **5**, in absolute ethanol, with a large excess of cobalt(III)acetate yielded the tris-ligand chelates, CoL_3 .

NMR experiments were carried out on a Varian UNITY 400 spectrometer operating at 399.252 MHz (^1H), 100.577 MHz (^{13}C), 40.534 MHz (^{15}N) and 95.416 MHz (^{59}Co). Saturated CDCl_3 and DMSO-d_6 solutions of the cobalt(III) chelates were used. Chemical shifts were refer-

enced to internal TMS ($\delta=0\text{ppm}$), the solvent signals ($\delta(\text{DMSO})=2.6\text{ppm}$, $\delta(\text{DMSO})=39.5\text{ppm}$ and $\delta(\text{CDCl}_3)=77.0\text{ppm}$) and to external CH_3NO_2 ($\delta=0\text{ppm}$) as well as to external $\text{K}_3[\text{Co}(\text{CN})_6]$ ($\delta=0\text{ppm}$) or $[\text{Co}(\text{NH}_3)_6]\text{Cl}_3$ ($\delta=8160\text{ppm}$) for the ^1H , ^{13}C , ^{15}N and ^{59}Co NMR, respectively.

2D H,H-COSY-90, 2D delayed H,H-COSY-45 ($\tau_2=100\text{ms}$ according to long range H,H couplings around 2Hz) /3/, ^1H detected HMQC (τ_1 delays were adjusted to $^1J(\text{C,H}) = 160\text{Hz}$) /4/, ^1H detected HMBC (τ_1 delays were adjusted to $^1J(\text{C,H}) = 160\text{ Hz}$ and τ_2 delays were set to 70 ms or 140 ms according to $^nJ(\text{C,H})$ long range couplings around 7 Hz and 3 Hz, respectively) /5/ and 2D H,H-NOESY (mixing time was set 150ms) were used to assign the signals of the different isomers of the cobalt chelates.

The samples for NOE experiments were degassed to exclude paramagnetic oxygen in the solutions. The 1D NOE spectra were obtained with a total preirradiation delay of 10s.



(All nitrogen cobalt bonds are coordinative bonds.)

Figure 1: Ligands of the chelates **Co 1** to **Co 5** and structure of **Co 2** in CDCl_3 and DMSO

Results and Discussion

(a) Coordination pattern

From results on the zinc chelates /2/ the most important parameters that indicate a coordination via the sulphur and the β -nitrogen are: (1) no NH-signal in the ^1H NMR spectra; (2) an upfield shift of 13 to 20 ppm for C-3 compared with the parent organic ligands; (3) a downfield shift of 80 to 100 ppm and no direct NH coupling for the N-4 signal (only for **Co 2** in CDCl_3); (4) a coordination shift of 5 to 10 ppm upfield for N-5 (only for **Co 2** in CDCl_3) /6/ and (5) a downfield shift for C-6 of 10 to 20 ppm. These NMR data indicate a N_3S_3 coordination pattern for the complexes **Co 2** to **Co 5**.

The ligand **1** coordinates in the zinc chelate via the nitrogen N-4 and the pyridine nitrogen N-1'. The microanalysis of the complex **Co 1** resulted in a cationic $[\text{CoL}_2]^+$ chelate. The NMR data indicate a coordination via the mercapto sulphur (upfield shift for C-3 of 11 ppm) and N-5 (downfield shift for C-6 of 10 ppm). The additional coordination via N-1' was detected by an enhancement for $^1\text{J}(\text{C-6}, \text{H-6}')$ of 10 Hz (compared with the parent organic ligand) and smaller enhancements for $^1\text{J}(\text{C-5}', \text{H-5}')$ and $^1\text{J}(\text{C-4}', \text{H-4}')$ (approximately +2 Hz) as well as by a diminution of the long range coupling $^2\text{J}(\text{C-5}', \text{H-6}')$ of 3 Hz /2, 7/. As well a relatively large NOE effect was obtained for H-6 (11.9%) during saturation of H-3' which indicates a fixation of the pyridine ring by coordination with the cobalt via N-1'.

The chemical shifts of **Co 2** to **Co 5** in the ^{59}Co NMR spectra were similar while those of **Co 1** differed greatly which is consistent with the different coordination pattern.

(b) Configuration according to the C=N bond

We used the following NMR-data for the determination of the configuration of the ligands according to the C=N bond:

(1) The coupling constant $^1\text{J}(\text{C-6}, \text{H-6})$ is 8 to 12 Hz larger in the Z configuration than for those ligands in the E configuration.

(2) The signal C-6 is shifted 3 to 6 ppm downfield in the E configuration compared with the signals in the Z configuration.

(3) Nuclear Overhauser Effects were measured between H-1 and H-2'/ H-3' (1.5 to 3 % by saturation of H-1). Semiquantitative calculations of the distances between these atoms in the different structures show that this is only possible between protons which belong to the same ligand in a Z configuration (distance between H-1 and H-2'/ H-3' approximately 2 to 2.5 Å).

These parameters agree qualitatively with those obtained for the parent organic ligands and the zinc chelates. In these previously investigated compounds an additional evidence was available through the vicinal coupling $^3\text{J}(\text{N-4}, \text{H-6})$ which differs greatly in the two isomers.

(c) Ligand arrangement

Considering the arrangement of the ligands in the *fac* structures it is obvious that the substituents on C-6 (H-6 in the Z and R in the E configuration) are near the mercapto sulphur of a neighbouring ligand. In the *mer* structures there is one ligand in which substituents are arranged over

the sulphur of another ligand and two ligands in which substituents are arranged over the coordinating nitrogen of a neighbouring ligand. The last two ligands differ in their long range environments.

Because of the large size of the S atom compared with the N the polarisation of the electron cloud of the H-6 protons or the protons in R, respectively, is much larger in this case than in the case of a neighbouring N atom. This larger electrical field effect of the sulphur atom results in a large deshielding effect and we found for the *mer* isomer of **Co 2**, with all ligands in a Z configuration, that one H-6 proton had a large downfield shift and the two H-6 protons were shifted much less compared to the parent organic ligand.

On the other hand NOE effects between signals of different ligands gave additional information. We found for the abovementioned isomer NOE's of 6 to 8 % between the two H-6 protons at 7.10 ppm and 8.71 ppm, which is only possible between one H-6 proton near the S and one near the N of a neighbouring ligand according to semiquantitative calculations of distances in the different isomers.

Summary

It was possible on the basis of these considerations to assign all sets of signals to the corresponding structures. The number of sets of signal found in solution varies from one up to over 10. In the last case only the signals of a relative intensity larger than 5% were identified. The Z configuration is the preferred configuration in the chelates (*mer-ZZZ*, *mer-EZZ*, *fac-ZZZ* and *fac-EZZ*). We found smaller differences in the amount of *mer* and *fac* arrangement in dependence of the solvent.

Comparisons with x-ray structural investigations of the chelates in solid state showed structures that are the same as those found in solution, but the variety of the structures in solution was much higher.

References

- /1/ U.Himmelreich, R.Häßner, P.Thomas, F.Tschwatschal and R.Borsdorf: *Monatsh. f.Chem.* **121**, 923 (1990)
- /2/ U. Himmelreich, F. Tschwatschal, H. Hennig and R. Borsdorf: *Inorg. Chem. Acta* submitted (1995)
- /3/ A.Bax and R.Freeman: *J.Magn.Reson.* **44**, 542 (1981); A.Kumar, R.V.Hosur and K.Chandra-sekhar: *J.Magn. Reson.* **60**, 143 (1984)
- /4/ L. Müller: *J. Am. Chem. Soc.* **101**, 4481 (1979)
- /5/ A. Bax and M.F. Sumner: *J.Am.Chem.Soc.* **108**, 2093 (1986)
- /6/ J. Mason: *Chem. Rev.* **81**, 205 (1981)
- /7/ P. Sandor and L. Radics: *Org. Magn. Reson.* **14**, 98 (1980); H. Seel and H. Güther: *J. Am. Chem.Soc.* **102**, 7051 (1980)

FRACTION OF H₂¹⁷O BOUND TO MACROMOLECULES MEASURED BY TRIPLE QUANTUM NMR

E. Baguet, B. E. Chapman and P. W. Kuchel

Department of Biochemistry, the University of Sydney, N.S.W. 2006, Australia

INTRODUCTION

The water in living cells and solutions of proteins can be considered to be composed of two phases, usually called 'bound' and 'bulk' water, with different dynamic properties (1, 2). Recently, the existence of bound water in biological systems has been observed unambiguously by triple-quantum filtered ¹⁷O NMR (3); this different approach complements the vast literature on 'biological' water studied by ¹H NMR relaxation methods. Water bound to macromolecules is particularly important as it usually stabilises the proteins and is involved in arranging them in solution. Some bound water is in fast chemical exchange with the bulk water; our aim was to determine its fraction relative to the total amount of water. This was done for aqueous solutions of bovine serum albumin and for red blood cells in osmotically-altered sizes.

THEORY

The natural way to describe spins $I > 1/2$ quadrupolar relaxation is to use the irreducible tensor operator formalism (4, §2.1.10). In this basis set, for uncoupled spins in an isotropic medium, the magnetisation components of odd and even rank vary independently. Then, the magnetisation timecourse of a spin 5/2 after a 90° or a 180° pulse can be described by a 3×3 relaxation matrix, called $R^{(1)}$ for transverse relaxation, or $R^{(0)}$ for longitudinal relaxation. The matrices $R^{(0)}$ and $R^{(1)}$, whose components are given in (5), are diagonal only if the nuclear correlation time satisfies the inequality $\omega_0 \tau_c \ll 1$. Elsewhere, in the slow-motion limit, the longitudinal and transverse magnetisations evolve triexponentially. If the spins are in fast chemical exchange between two sites with different relaxation behaviours, then the relaxation matrix will be the weighted sum of the two relaxation matrices of the two sites (6).

Water, in the presence of macromolecules, can be considered to be composed of two populations, bulk water, and water bound to macromolecules, which are in fast chemical exchange. Its relaxation matrix is then:

$$R_{\text{water}}^{(n)} = p_b R_{\text{bound}}^{(n)} + p_f R_{\text{bulk}}^{(n)} \quad \text{with } n = 0 \text{ or } 1.$$

Because water bound to macromolecules is rotationally hindered, its relaxation matrix is non-diagonal; then, the magnetisation of water evolves triexponentially. This multiexponential behaviour can be studied by standard one-quantum pulse-sequences but it is more readily studied with triple-quantum filtered sequences (7). This sequence also permits the observation of exclusively internal water in whole cells.

EXPERIMENTAL

Preparation of the samples. Bovine serum albumin from Sigma-Aldrich Pty., Australia, and urea were diluted in deuterated water and then mixed, to obtain the desired sample. Human erythrocytes were obtained fresh by venipuncture from a healthy donor in our laboratory. Prior to the NMR experiments, cells were centrifugally washed (2×) in three volumes of ice-cold isotonic saline and resuspended in D₂O saline with 10 mM glucose prior to being bubbled with carbon monoxide (CO) for 5 min. They were packed by centrifugation and were then ready for the NMR experiments. The haematocrit (Ht) of the cell suspension was determined in duplicate by capillary centrifugation.

NMR. All ¹⁷O NMR experiments were performed on a Bruker AMX400 spectrometer at 54.25 MHz; 3 ml of the sample was studied in a 10-mm (o.d.) NMR tube; and the probe temperature was set at 298 ± 1 K. The pulse sequences employed for triple-quantum filtered experiments were those described in (5). Single-quantum longitudinal relaxation times were determined by a standard inversion-recovery sequence. A one-pulse sequence permitted the determination of the water magnetisation at thermodynamic equilibrium.

The data analysed in the frequency domain were characterised by their amplitude. Those analysed in the time domain were analysed on a Macintosh PowerPC. The comparison of theoretical simulations with experimental results permitted the determination of the fraction of bound water, its correlation time, and the relaxation time of bulk water.

RESULTS

BSA solutions of different concentrations were analysed. The results are given in Table 1.

Table 1
Water properties as a function of the BSA concentration

[BSA] (g L ⁻¹)	R_{bulk} (s ⁻¹)	p_b (%)	τ_c (ns)	$n_{\text{D}_2\text{O}/\text{BSA}}$
0	174	0		
50	226	0.062	5.7	40
85	247	0.076	7.6	30
150	289	0.096	9.0	21

R_{bulk} , relaxation rate constant of bulk water; p_b , fraction of bound water; τ_c , correlation time of bound water; $n_{\text{D}_2\text{O}/\text{BSA}}$, number of bound D₂O molecules per BSA molecule.

The fraction of bound water and its correlation time increased when the BSA concentration was increased. However, the number of bound water molecules per BSA molecule decreased. At the same time, the relaxation rate constant of bulk water increased significantly.

The effect of urea on water in a BSA solution was analysed in the same way, for a given concentration of BSA. The relaxation rate constant of bulk water and the correlation time of bound water did not change significantly for the different concentrations of urea. The fraction of bound water decreased significantly for urea concentrations higher than 4 M (Fig. 1).

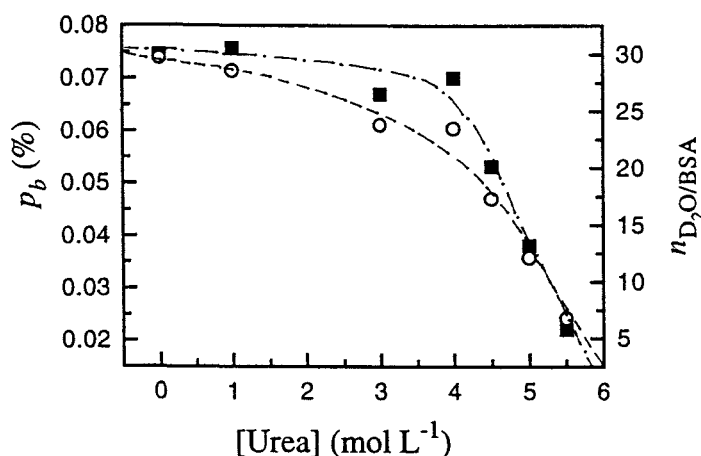


Fig. 1. Bound water as a function of urea concentration. [BSA] = 85 g L⁻¹; solvent, D₂O. Symbols: ■ p_b fraction of bound water; ○ number of D₂O bound per BSA molecule. Parameters: R_{bulk} = 248 s⁻¹, τ_c = 7.6 ns. The lines are empirical fits to the data.

The fraction of intracellular bound water was determined in human erythrocytes of physiological volume for different Ht values. The fraction did not vary significantly and was ~0.25%. In contrast, red blood cells with osmotically-altered sizes showed significant fluctuations of the bound-water fraction (Table 2).

Table 2. Intracellular-water properties of human erythrocytes with osmotically-altered sizes

[NaCl] (mM)	R_{bulk} (s ⁻¹)	p_b (%)	τ_c (ns)
110(a)	367	0.169	6.3
154(b)	407	0.221	6.3
257(c)	445	0.272	5.3

R_{bulk} , p_b , and τ_c have the same significance as in Table 1. Ht = 87%. (b) corresponds to the physiological RBC volume, while (a) and (c) correspond to hypervolume and hypovolume erythrocytes, respectively.

The parameters p_b , R_{bulk} and τ_c , obtained for red blood cells washed in an isotonic saline solution are close to those obtained for a haemoglobin solution of 30% w/w.

CONCLUSIONS

The simultaneous analysis of transverse and longitudinal triple-quantum NMR experiments permits the determination of the fraction of the total water that is bound to macromolecules, and their correlation times, either in protein solutions or in whole cells. The experiments are complementary to those done by ¹H NMR using 'conventional' relaxation analysis.

It has been assumed in the past that there are three types of water in presence of macromolecule: (i) type I, which has similar properties to pure water, (ii) type II, which is weakly bound and does not freeze at 0°C, and (iii) type III, considered as irrotationally bound (1). The value of the fraction of bound water which we have determined is substantially smaller than the fraction of non-freezing water and it seems to correspond to the type III water; however its correlation time is smaller than that of the surrounding macromolecules. The type II water would have a correlation time small enough to be in the extreme narrowing limit but still important to modify the relaxation rate constant of what we have called 'bulk water'. This multi-quantum-filter method does not permit the determination of the fraction of type II water, but it does enable the recording of its evolution via the knowledge of the 'bulk water' relaxation behaviour.

In conclusion, the method employed will be useful for studying the properties of water in biological systems, particularly in cellular systems.

REFERENCES

1. R. Cooke and I. D. Kuntz, *Ann. Rev. Biophys. Bioeng.* 3, 95 (1974).
2. G. Otting, E. Liepinsh and K. Wüthrich, *Science* 254, 974 (1991).
3. C. W. Flesche, M. L. H. Gruwel, A. Deussen and J. Schrader, *Biochim. Biophys. Acta* (1995).
4. R. R. Ernst, G. Bodenhausen and A. Wokaun, *Principles of Nuclear Magnetic Resonance in One and Two Dimensions*, Oxford University Press, London (1991).
5. C.-W. Chung and S. Wimperis, *Mol. Phys.* 76, 47 (1992).
6. T. E. Bull, *J. Magn. Reson.* 8, 344 (1972).
7. G. Jaccard, S. Wimperis and G. Bodenhausen, *J. Chem. Phys.* 85, 6282 (1986).

Urea Exchange across the Erythrocyte Membrane measured using Pulsed Field Gradient NMR Spectroscopy

B. E. Chapman, A. R. Waldeck and P. W. Kuchel

Department Of Biochemistry, The University of Sydney, Sydney, NSW 2006, Australia

The human erythrocyte membrane possesses a very high permeability to urea, which is orders of magnitude greater than permeabilities reported for lipid bilayers. The transport of urea shows characteristics that are associated with facilitated exchange; it is saturable at high urea concentrations and can be inhibited by phloretin and sulphhydryl reagents.

Previous studies carried out to determine the kinetic parameters of urea exchange, using a variety of techniques, have shown that it obeys Michaelis-Menten type kinetics, but have resulted in a wide range of estimates of $K_{1/2}$, the urea concentration required for half saturation, and V_{max} , the maximal velocity (1, and references therein).

Pulsed Field Gradient (PFG) NMR has been used to determine diffusion coefficients in biological systems. Cell suspensions form a heterogeneous two-region system with slow, or restricted, diffusion inside the cell and faster free, or obstructed, diffusion outside the cell. The analysis of diffusion in the presence of fast exchange, in two-site systems has been developed by Kärger (2). The diffusion experiment consists of applying two identical magnetic field gradient pulses of duration δ and separation Δ , and magnitude G , applied during the dephasing and rephasing intervals τ , of a spin echo sequence. The attenuation of the echo signal, for a two region system with fast exchange, is the superposition of two exponentials:

$$R = P_1 \exp(-KD_1\Delta) + P_2 \exp(-KD_2\Delta) \quad (1)$$

where R is the normalised signal intensity, and D_1 , D_2 , P_1 and P_2 are apparent diffusion coefficients and populations and are related to the true parameters by:

$$D_1 = 1/2 \{ D_e + D_i + 1/K(1/\tau_i + 1/\tau_e) - \sqrt{[D_i - D_e + 1/K(1/\tau_i - 1/\tau_e)]^2 + 4/(K^2\tau_i\tau_e)} \}$$

$$D_2 = 1/2 \{ D_e + D_i + 1/K(1/\tau_i + 1/\tau_e) + \sqrt{[D_i - D_e + 1/K(1/\tau_i - 1/\tau_e)]^2 + 4/(K^2\tau_i\tau_e)} \}$$

$$P_1 = 1 - P_2$$

$$P_2 = (P_e D_e + P_i D_i - D_1) / (D_2 - D_1)$$

$$K = \gamma^2 \delta^2 G^2$$

where D_i and D_e are the diffusion coefficients of the solute in the intra- and extra-cellular compartments, respectively, in the absence of exchange. P_i and P_e are the intra- and extra-cellular population fractions and τ_i and τ_e are the mean residence lifetimes in the intra- and extra-cellular compartments. The equation is based on the assumption that differential relaxation in the two compartments can be ignored and the phase dispersion of the nuclei during δ is negligible compared with that occurring during Δ , ($\Delta \gg \delta$).

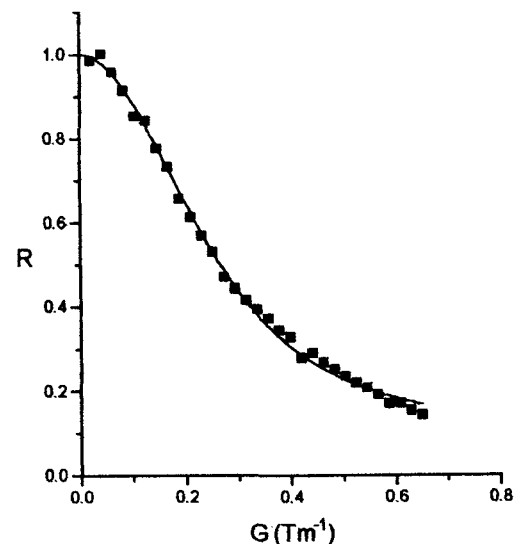


Fig. 1. Non-linear regression of Eqn. 1 onto the data from the erythrocyte sample with 100 mM urea. The parameters D_e and τ_i were floated while all others remained fixed.

Erythrocytes were washed in isotonic saline and the required amount of ^{15}N urea was added.

The PFG longitudinal eddy current delay pulse sequence (3) was used to obtain ^1H spectra. The water peak was suppressed during the relaxation delay and GARP decoupling of ^{15}N was applied during acquisition. Relevant parameters used were $\delta = 3\text{ms}$, $\Delta = 50\text{ms}$ and G was varied from 0 to 0.651 Tm^{-1} . Experiments were performed on a Bruker AMX-400 NMR Spectrometer at 298 K. Fig 1. shows a plot of reduced echo intensity vs gradient magnitude for a cell suspension with 100 mM urea.

The rate constant for urea efflux from the cell, k , is the reciprocal of the lifetime inside the cell. The urea efflux velocity (kC) vs concentration, C , is plotted in Fig. 2. For a saturable system the dependence of velocity, v , on concentration is characterised by two parameters, V_{max} , the maximal transport rate and $K_{1/2}$, the concentration at half saturation as:

$$v = V_{\text{max}}C/(K_{1/2} + C) \quad (2)$$

Non-linear regression of Eqn. 2 onto the data in Fig. 2 yields a V_{max} of $10.1 \pm 0.9\text{ mol/l cell water/s}$ and $K_{1/2}$ of $577 \pm 113\text{ mM}$.

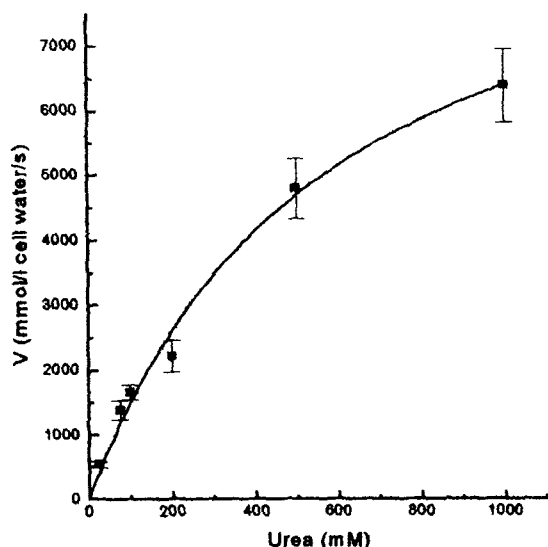


Fig. 2. Plot of urea efflux velocity vs urea concentration for the erythrocyte suspensions.

In the literature V_{max} is usually given as membrane permeability, the moles of urea

transported across a square cm of membrane per second. This is determined from the known water volume and membrane surface area of the erythrocyte and here is $4.1 \times 10^{-7}\text{ mol/cm}^2/\text{s}$. Transport parameters obtained by other workers (1, and references therein), give a range for $K_{1/2}$ of 218 - 968 mM and for V_{max} of $0.8 - 4.1 \times 10^{-7}\text{ mol/cm}^2/\text{s}$. This method appears suitable for measuring rapid transport rates in heterogeneous biological systems.

(1) D. M. Karan and R. J. Macey, *Biochim. Biophys. Acta.*, **1024**, 271 (1990).

(2) J. Kärger, *Ann. Phys.*, **24**, 1 (1969).

(3) S. J. Gibbs and C. S. Johnson, *J. Magn. Reson.*, **93**, 395 (1991).

Solid State NMR Study of a New Combined Type Liquid Crystalline Polymer and Related Materials

Oc Hee Han,[§] Jung-II Jin,[†] Jong-Sung Kim,[†] Yong-Kook Yoon[†] and Sung-Mu Huh[†]

[§]Korea Basic Science Institute, Yeuundong 52, Yooosungoo, Taejeon, 305-333, Korea

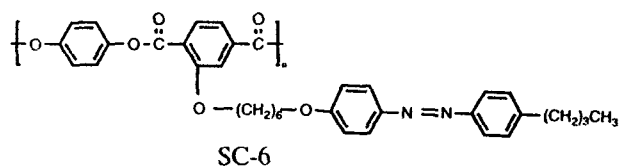
[†]Department of Chemistry and Advanced Materials Chemistry Research Center, Korea University, Anamdong, Seoul, 136-701, Korea

Introduction

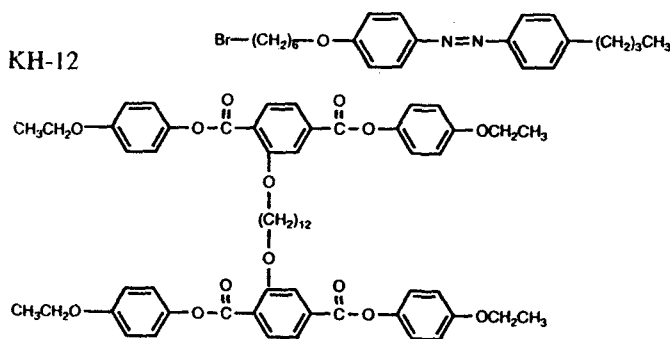
It is well known that substitution either on the hydroquinone or the terephthalic acid moieties of poly(p-phenylene terephthalates) lowers phase transition temperatures such as crystal-nematic and nematic-isotropic transition temperatures (1). The substitution also degrades crystallinities although regularity along the polymer backbone direction is maintained (1, 2). These observation suggest that the substitution alters dynamics and structure of the polymer dramatically.

The polymer of which the molecular formular is shown below, named as PAZO-6 in our group, is one of substituted poly(p-phenylene terephthalates). The terephthalic acid moieties are substituted by azo groups via flexible alkyl chains. Not only p-phenylene terephthalates but also azo groups are mesogens. Thus, PAZO-6 is one of the new combined type liquid crystalline polymers (LCP) (3) which have two or more types of mesogens combined nonlinearly. Ordering of branch mesogen, azo group, in PAZO-6 is an important parameter to observe as well as the substitution effect on the backbone. Photoisomerization of azo group (4) also can affect structure and dynamics of the polymer. As the first step to study dynamics and structure of this polymer systematically, not only the polymer itself but also related small molecules such as monomers and branch groups only were studied by solid state NMR techniques. The molecular formulas of the related small molecules we studied, SC-6, MAZO-6, and KH-12 are shown below. Preliminary ¹³C CP/MAS (cross polarization/ magic angle spinning) spectral results are discussed with respect to ordering of each type mesogen.

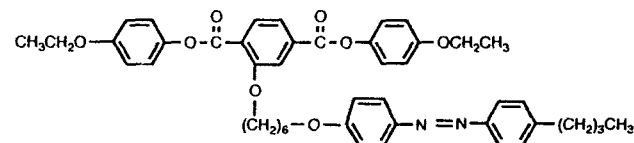
PAZO-6



KH-12



MAZO-6



Experimental Section

Synthetic details for the preparation of SC-6, MAZO-6 and PAZO-6 have been reported in the MS thesis by one of the authors (5). Synthetic procedure of KH-12 will be described in a future publication.

¹³C CP/MAS NMR spectra of the samples were acquired at room temperature and at an MSL 200 instrument with the carbon Larmor frequency of 50.3 MHz. Typical spinning rate was between 3.0 ~ 3.8 KHz with 7 mm outer diameter rotors. The 90° pulse length for both ¹³C and ¹H was 4.5 μs and repetition time was 5 sec. The contact time was 800 μs for SC-6, MAZO-6, and KH-12 and 1ms for PAZO-6. To get the spinning sideband free spectra, four π TOSS (total suppression of spinning sidebands) pulse sequence (6) was utilized.

Results and Discussion

Representative ¹³C CP/TOSS spectra of SC-6, MAZO-6, PAZO-6, and KH-12 are shown in Fig. 1. Spectra of KH-12 and SC-6 have relatively narrow peaks implying crystalline property. MAZO-6 has both narrow peaks and a broad feature underneath. PAZO-6 shows amorphous character with broad and severely overlapped peaks. Although amorphous character of PAZO-6 agrees with observed glass transition temperature, the partial disorder of MAZO-6 was not indicated clearly by the phase transition temperatures obtained by DSC (in Table I).

Table I. Phase transition temperatures obtained by DSC (differential scanning calorimetry)

Sample	T _g (°C)	T _m (°C)	T _i (°C)	LC
SC-6	—	66	86	nematic
MAZO-6	---	101	145	nematic
PAZO-6	~53	188	>300	nematic
KH-12	---	111	120	nematic

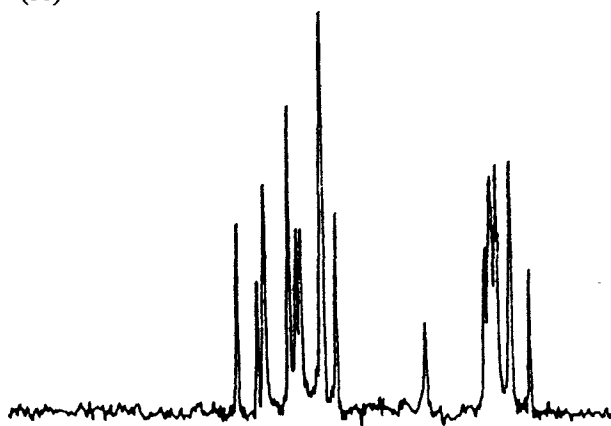
T_g: glass transition temperature

T_m: melting temperature

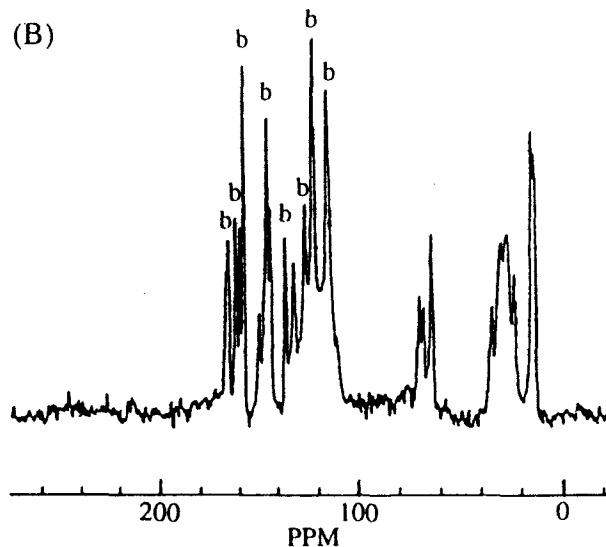
T_i: isotropic transition temperature

Comparison of the spectra of KH-12 and MAZO-6 indicates that aromatic carbons of p-phenylene terephthalate moieties in both samples have the same chemical shifts and linewidths. On the other hand, dramatically different resonances of the azo group aromatic carbons in the spectra of SC-6 and MAZO-6 were observed. Most protonated aromatic carbons of azo group in MAZO-6 lost sharpness of the peaks and appear as a broad component covering from 110 to 130 ppm in the spectra. This observation suggests that azo groups in SC-6 and MAZO-6 are in very different microscopic environments. Azo groups in MAZO-6 are not aligned with themselves as in SC-6 and probably poorly ordered between well ordered p-phenylene terephthalate moieties. Similar disordering tendency of the azo group in PAZO-6 is deduced from the overall aromatic carbon peak positions, considering much broader linewidths, which are not much different from those of MAZO-6. However, backbone chains in PAZO-6 is expected to have relatively regular spacing from close similarity of the spectrum (not shown) of PAZO-6 quenched from the liquid crystalline state and the amorphous PAZO-6 spectrum.

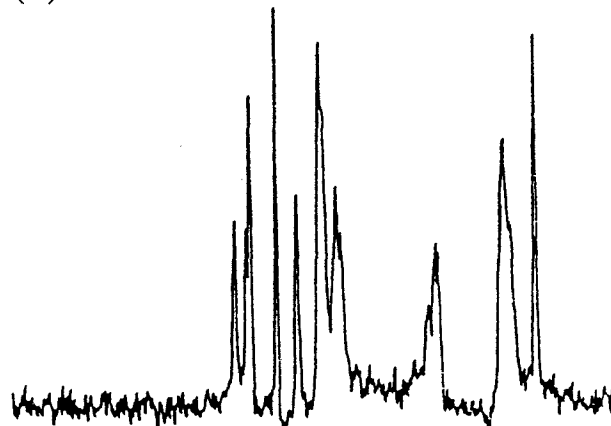
(A)



(B)



(C)



(D)

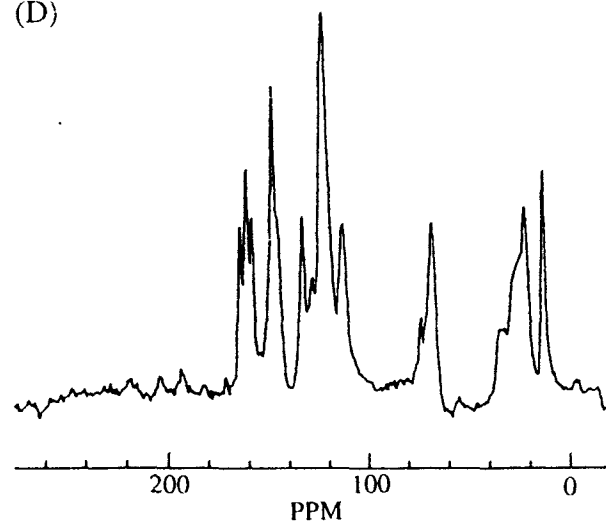


Figure 1: 4.7 T ^{13}C CP/TOSS spectra of (A) SC-6 at 3.8 kHz, (B) MAZO-6 at 3.6 kHz, (C) KH-12 at 3.0 kHz, and (D) PAZO-6 at 3.5 kHz. The marks 'b' in (B) indicate the aromatic peaks which appear at the same positions in the KH-12 spectrum (C).

Acknowledgment

This work was partially supported by the Korean Ministry of Science and Technology. J.-I. Jin would like to acknowledge the support of this work (BSRI-95-3406) by the Korea Ministry of Education through the Basic Science Research Institute of Korea University. The authors also acknowledge Mr. K. S. Hong for technical support in NMR experiments.

References

1. W. R. Krigbaum, H. Hakemi, and R. Kotek, *Macromolecules* **18**, 965 (1985)
2. J.-I. Jin, E.-J. Choi, and B. W. Jo, *Macromolecules* **20**, 934 (1987)
3. B. Beck and H. Ringsdorf, *Makromol. Chem.* **190**, 2511 (1989)
4. A. Natansohn, P. Rochon, M. Pezolet, P. Audet, D. Brown, and S. To, *Macromolecules* **27**, 2580 (1994)
5. J.-S. Kim, MS thesis, Korea University, Seoul, Korea, Dec. 1994
6. W. T. Dixon, *J. Chem. Phys.* **77**, 1800 (1982)

Solid-State MAS ^{207}Pb NMR of Lead Compounds

Michael Logan, ¹ Abdussallam El-Dewik, Russell Howe, ¹ Nagindar Singh, ¹ Leon C. M. van Gorkom, ²

James M. Hook ²

¹ Department of Physical Chemistry, and ² NMR Facility, UNSW, Sydney, 2052, Australia

Introduction

Lead compounds still have numerous applications in our society, in spite of their known toxicity ¹. For example they are used in batteries and petroleum additives, paints and housing materials, catalysts and ceramics, glasses and semi-conductors. Elemental analysis will readily show the presence of lead but precise knowledge of the form it takes should be accessible with solid-state ^{207}Pb NMR, because NMR can probe the local environment of the lead atom(s) ²⁻⁸. The enormous chemical shift range, >15,000 ppm, already established for lead ⁹ suggests that small changes in its environment will lead to easily detected changes in chemical shift provided that the usual line narrowing techniques developed for solids, such as magic angle spinning (MAS), are successful. On the other hand, distortions from regular geometry around the lead atom will induce large changes in chemical shift anisotropy, and make detection more difficult as has been found for ^{199}Hg ¹⁰. The aim of this work has been to investigate parameters and variables required for the successful detection of this nucleus which has very favourable properties (spin 1/2, 21% natural abundance) in the solid state. We have recently shown that ^{207}Pb NMR spectra of solid lead(II) nitrate are significantly and uniformly dependent on temperature ⁷. Here we present results for some simple lead compounds as well as for model systems related to soils such as lead-exchanged zeolites ¹¹.

Experimental

Lead compounds used in this study are all commercially available, except for $\text{PbCl}_6(\text{NH}_4)_2$ ¹². The lead-exchanged zeolites were prepared by heating (75°C) the zeolite in solutions of lead(II) nitrate at pH 5.

Solid-state Pb-207 MAS NMR spectra were acquired on a Bruker MSL 300S NMR spectrometer operating at 62.55 MHz as described previously ⁷ in a 4mm probe at MAS speeds ranging from 0 - 12 kHz. The data were acquired with a Bloch decay experiment without high-power proton decoupling, using a pulse width of 1 - 2 ms and recycle delays according to the T_1 of the species. The isotropic peak was determined by comparing MAS spectra run at different speeds. Spectra were referenced externally to the Pb-207 signal of tetra-*p*-tolyllead,

δ_{Pb} -148.8 ppm with respect to $(\text{CH}_3)_4\text{Pb}$ ⁶. Relaxation times, T_1 , were measured using the inversion-recovery sequence, and the resulting spectra analysed using Bruker software.

Results and Discussion

There are 4 parameters which we have examined to characterise the lead compounds in this study: chemical shift, linewidth at 1/2 height, the span, $\Omega = \delta_{33} - \delta_{11}$ and the T_1 relaxation. The results for some inorganic lead compounds and the Pb-exchanged zeolites are presented in Table 1.

Table 1*

Species	δ_{Pb} ppm	$W_{1/2}$ kHz	Ω ppm	T_1 s
PbSO_4	-3621	0.7	500	11.5
$\text{Pb}(\text{NO}_3)_2$	-3501	0.03	55	8.0
$\text{Pb}(\text{NO}_3)_2(\text{aq})$	-2961	-	-	0.825
PbCO_3	-2636	0.3	700	4.5
	(-2645)			
PbCrO_4	-2297	0.8	500	-
$\text{Pb}(\text{Cl}_6)(\text{NH}_4)_2$	-2066	2.3	-	18.8
$\text{Pb}(\text{O}_2\text{CCH}_3)_2$	-1913	0.1	1600	-
PbCl_2	-1729	1.6	750	10.4
	(-1735)			
$\text{Pb}(\text{SCN})_2$	-1606	0.4	1200	5.7
Pb_3O_4	-1103	0.4	100	-
	(-1119)			
	786	2.0	3000	-
	(1383)			
PbO	1529	0.5	3600	-
PbY	-2860	2.1	-	0.023
PbA	-1850	17	-	-

*Values in parentheses are from ref. 8

The chemical shifts in this selection of pure compounds are diverse, ranging from the sulphate and the nitrate (-3600 ppm), to the oxides (-1100 -1529). They are quite different from those reported for the same compounds in an earlier review ⁹ and are more in agreement with values reported recently ^{5,8}. The discrepancies between our values for the oxides and those of Yoko et. al. ⁸ are probably due to their incorrect assignment of the isotropic resonance. The choice of a reference can be a problem with ^{207}Pb NMR in general, because of

the huge chemical shift range for this nucleus, and care must be exercised in its selection. For example lead nitrate spectra of both solid and solution exhibit a marked temperature dependence ⁷, that could introduce errors and may be the reason for disparities in the literature values for chemical shifts.

Yoko and co-workers ⁸ have recently proposed that the ²⁰⁷Pb chemical shifts in the solid state shows a strong correlation with co-ordination number around the lead atom. Our data in Table 1 are in general agreement with this hypothesis. For example, the acetate ¹³, the chloride ⁸ and the thiocyanate ¹⁴ with co-ordination numbers 8 - 9 are relatively close in chemical shift even though they have quite different ligands.

MAS certainly does assist in the sensitivity of the experiment, but the broadest signals from the oxides for example would require spinning speeds far greater than we have currently available (12kHz). The linewidth and the span, are both indicators of the sensitivity of the species to detection. With high symmetry around the lead atom both are small and make detection straightforward as in spectra of the nitrate. Even those in which the linewidth is less than 1 kHz, for example the acetate, can be detected quite easily as can those in which the span is less than 1000 ppm. Difficulties arise when both the linewidth and the span are large and the sensitivity drops enormously, as in the spectra of PbO₄ unit in Pb₃O₄. The T₁ relaxation times of selected samples were measured to optimise spectral acquisition parameters. and they were found to vary from 5 - 20 seconds.

The chemical shifts found for the lead exchanged zeolites differ by 1000 ppm, which presumably reflect the unique pore structures where the lead atom is most likely to reside. PbY would be expected to have a more symmetrical site than the PbA, from comparison of the linewidths and the chemical shifts. The signal for PbY behaves as hydrated Pb²⁺ bound strongly to a much larger host. The T₁ relaxation time for the PbY signal is 40 times faster compared to that of aqueous lead nitrate solution, but is another two orders of magnitude faster than that of solid lead nitrate. MAS had little effect on the PbY signal as we found for the other compounds in which the Pb atom has octahedral co-ordination.

Conclusions

The ability to detect a ²⁰⁷Pb signal in a particular species and to determine its isotropic chemical shift depends critically on setting the correct instrumental parameters that take into account the linewidths, the large chemical shift anisotropy and the relaxation

times of the signals of lead compounds. It is clear from this and other work ⁴⁻⁸ that ²⁰⁷Pb MAS NMR is an extremely useful technique for probing the co-ordination environment of the lead atom in solid hosts. We are currently investigating the effects of partial or complete dehydration on the ²⁰⁷Pb spectra of lead exchanged zeolites, and will extend this study to lead in environmentally important materials such as clays and humic substances.

References

1. K. A. Winship, Toxicity of Lead: A Review. *Adverse Drug React. Acute Poisoning Rev.* 8, 117 (1989)
2. M. Nizam, M. Allavena, Y. Bouteiller, B. H. Suits and D. H. White, *J. Magn. Reson.* 82, 441 (1989) and references cited therein.
3. A. Nolle, *Z. Naturforsch.* 32A, 964 (1977) and references cited therein.
4. D. J. Burton, R. K. Harris and L. H. Merwin, *J. Magn. Reson.* 39, 159 (1980); R. K. Harris and A. Sebald, *Magn. Reson. Chem.* 25, 1058 (1987); H. D. Burrows, C. F. G. C. Gerald, T. J. T. Pinheiro, R. K. Harris and A. Sebald, *Liq. Cryst.* 3, 853 (1988); R. K. Harris and A. Sebald, *Magn. Reson. Chem.* 27, 81 (1989); A. Sebald and R. K. Harris, *Organomet.* 9, 2096 (1990); B. Wrackmeyer, K. Horchler, A. Sebald and L. H. Merwin *Magn. Reson. Chem.* 28, 465 (1990); E. Klaus and A. Sebald, *Magn. Reson. Chem.* 32, 679 (1994).
5. A. D. Irwin, C. D. Chandler, R. Assink, and M. J. Hampden-Smith, *Inorg. Chem.* 33, 1005 (1994).
6. J. R. Ascenso, R. K. Harris and P. Granger, *J. Organomet. Chem.* 301, C23 (1986)
7. L. van Gorkom, J. M. Hook, M. Logan, J. Hanna, and R. Wasylshen, *Magn. Reson. Chem.* in press.
8. T. Yoko, K. Tadanaga, F. Miyaji and S. Sakka, *J. Non-Cryst. Solids*, 150, 73 (1992).
9. R. K. Harris, J. D. Kennedy and W. McFarlane in "NMR and The Periodic Table", Academic Press, London, 1978, p. 368.
10. M. J. Natan, C. F. Millikan, J. G. Wright and T. V. O'Halloran, *J. Amer. Chem. Soc.* 112, 3254 (1990); R. A. Santos, E. S. Gruff, S. A. Koch and G. S. Harbison, *J. Amer. Chem. Soc.* 113, 469, (1991)
11. J. Liang and B. L. Sheriff, *Geochim. Cosmochim. Acta* 57, 3885 (1994).
12. We thank Prof. Phil Dean of University of Western Ontario, Canada, for this compound.
13. R. G. Bryant, V. P. Chacko and M. C. Etter, *Inorg. Chem.* 23, 3580 (1984)
14. J. A. A. Mokuolu and J. C. Speakman, *J. Chem. Soc. Chem. Commun.* 25 (1966)

MRI/S of the Middle Cerebral Artery Occlusion Model of Stroke in the Mouse

P.D. Hockings*, D.A. Middleton#, S.J. Bailey^o, D.G. Reid# and D.M. Doddrell*

*Centre for Magnetic Resonance, University of Queensland, 4072, Australia.

#Analytical Sciences Department, SmithKline Beecham Pharmaceuticals, The Frythe, Welwyn, Herts. AL6 9AR, UK.

^oDepartment of Neurology, SmithKline Beecham Pharmaceuticals, Harlow, Essex CM19 5AD, UK.

Introduction

The search for compounds to protect the brain from post-ischaemic neurodegeneration has created a significant need for a variety of animal models of acute stroke. Some of the most common are based on temporary or permanent middle cerebral artery occlusion (MCAO). The effects of MCAO have been well characterized by MRI in the rat and the findings shown to correlate well with those gained by histological and enzymatic techniques. Reports of MRI studies of the effects of MCAO in the mouse, however, are much sparser. In addition, spectroscopic examination of the pathophysiology of cerebral ischaemia is being used as a diagnostic tool with the potential to assess neuroprotective compounds in animal models *in vivo*.

Materials and Methods

MRI MR images were acquired using a Bruker Image Directed Spectroscopy RF probe on a Bruker AMX 300 spectrometer interfaced to a 89 mm 7 T vertical magnet, 5 G/cm gradient strengths being obtained by pulsing the room temperature shims. Scout horizontal images from each animal were used to identify anatomical landmarks for positioning 8 contiguous transverse images. The field of view was 1.5 cm and slice thickness 1.0 mm. Diffusion weighted images were acquired using the standard T₂ weighted, 2D FT sequence modified to include a pair of Stejskal-Tanner gradient pulses. Diffusion gradients (5 G/cm) were applied in the slice direction (15 ms gradient pulses and 28 ms

between the leading edges of the diffusion pulses, *b* value 925 radians s/mm²).

MRS Localized VOIs were selected from images to span known areas of ischaemic damage. Localization was provided by SPACE (7 ms TE; 6 s TR; 256 scans) to obtain proton spectra from cubic volumes of 14 mm³. Water suppression was achieved by selective excitation and gradient crushing (SUBMERGE).

Middle Cerebral Artery Occlusions
Unilateral MCAO's were performed on 30-40 g male CD-1 mice. The MCA was occluded distal to the branch point, by bipolar diathermy. All experiments comply with the provisions of the U. K. Animal (Scientific Procedures) Act 1986 and with the SmithKline Beecham Code of Practice for Animal Experimentation.

Results and Discussion

At the 2 hour time point diffusion weighted (DW) images provide the best visualisation of the newly formed lesion (not shown), but between one and three days both DW and spin echo methods are equally effective. Figure 1 shows six contiguous transverse slices, which effectively span the entire lesion, through the brain of one animal at one day post MCAO, from which effective estimates of lesion volume can be made (ca. 18 mm³). The lesions appear in the cortex as uniform regions of hyperintensity relative to surrounding unaffected tissue probably due to cytotoxic oedema. However, the appearance of the lesion at day 6 is strikingly different (not shown). The damaged area is still

distinguishable from surrounding tissue by SE and DW MRI, but appears somewhat shrunken. There is a distinct differentiation between a hypointense core region and a hyperintense peripheral zone. At all time points measurement of lesion volumes is straightforward. After imaging on day six the animals were anaesthetized with a lethal pentobarbitone injection and their brains were excised and stored in phosphate buffered formalin for histology. The sizes of lesions ($N = 7$) measured histologically correlated well with the SE imaging measurements at this time point ($R = 0.81$). MRI would thus be an appropriate tool for following, on a routine basis, the progression of MCAO-induced lesions in mice and their response to neuroprotective compounds.

Observation of a lesion before administration of a compound would allow design of experiments in which each lesion

acted as its own control. To assess whether a correlation existed between lesion volumes measured at early and late time points, and hence, whether each lesion could be used as its own control in studies of the actions of neuroprotective compounds, 16 subjects were examined by multi-slice SE imaging 1 day and 6 days after MCAO. Mean lesion volumes at the two time points, measured by summation of manually determined lesion areas from each image slice, were 18.0 mm^3 ($SD = 8.0 \text{ mm}^3$) and 8.2 mm^3 ($SD = 4.0 \text{ mm}^3$). Linear regression analysis of lesion volumes measured for each animal at the two time points yielded a correlation coefficient of 0.86 ($p < 0.001$).

Magnetic resonance spectroscopy of the lesions showed a characteristic increase in the glutamine signal and signal at 1.3 ppm attributed to lactate and/or macromolecules relative to the naive animals (Fig. 2).

Fig. 1
SE Images 1 day post-ischaemia

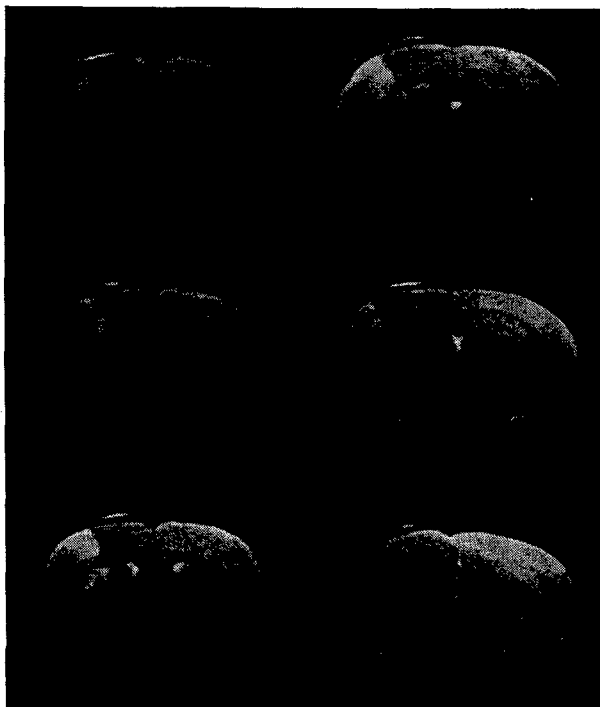
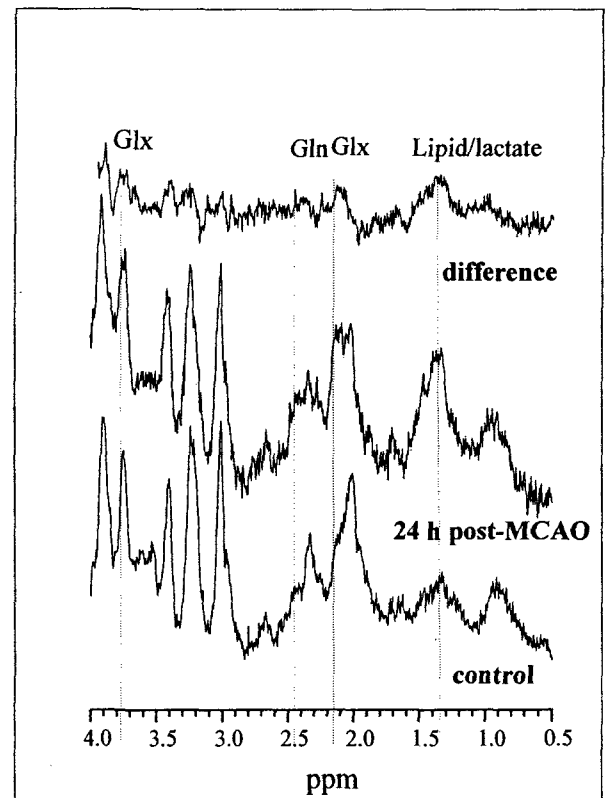


Fig. 2
Localised ^1H NMR spectra from 14 microlitres of mouse brain



MR Assessment of Oxidative Stress Processes in Rat Liver and Kidneys

R.A. Towner¹, J.P. Williams¹, Z.H. Endre², M. Kadkhodae², S. Wilson², I.M. Brereton²,
G. Hanson² and D.M. Doddrell²

¹James Cook University of North Queensland, Townsville, Qld 4811, Australia

²University of Queensland, Brisbane, Qld. 4072, Australia

ABSTRACT

This paper focuses on the development and utilisation of *in vivo* MR techniques to assess oxidative stress processes, such as acute halocarbon-induced hepatotoxicity and ischaemia-reperfusion injury (IRI) in rat kidneys. Non-invasive, image-guided (IG) high resolution ³¹P- and ¹H-NMR spectroscopic techniques were used to monitor localised *in vivo* biochemical tissue-damage markers induced by either halocarbon hepatotoxicity or renal IRI. Many of the biotransformation products formed from the metabolism of halocarbons or IRI are free radical intermediates. The inhibitory effect of free radical scavengers, such as spin traps, on halocarbon-induced hepatic damage is also presented. Some free radical intermediates can be trapped and identified by ESR spin trapping techniques.

INTRODUCTION:

Carbon tetrachloride is the prototype and most widely studied hepatotoxin. The mechanism for injury by CCl₄ involves damage to membranes of the hepatocyte and its intracellular organelles. There is evidence that the responsible metabolites are free radicals that appear to cause peroxidation of the unsaturated lipids of cellular membranes and probably convert other cellular molecules to secondary free radicals that extend the injury, eventually leading to hepatocellular necrosis.

With the use of ESR (electron spin resonance) spectroscopy and the spin trap PBN (α -phenyl-*tert*-butyl nitron) it has been possible to detect four radical species *in vitro* from the metabolism of CCl₄ in rat liver, which included: the trichloromethyl radical ($\cdot\text{CCl}_3$), the carbon dioxide radical anion ($\cdot\text{CO}_2^-$), a carbon-centered lipid derived radical with a methylene group ($\cdot\text{CH}_2\text{R}$), and an oxygen-centered lipid derived radical ($\cdot\text{OR}$) [1,2].

There is increasing evidence that oxygen radicals are involved in IRI in various tissues (eg. heart, brain, and kidney). The most common type of acute renal failure is ischaemic renal cell injury from lack of blood flow to the kidneys. Most of the cell injury is thought to occur during the reperfusion stage when oxygen is re-introduced into the tissue. This large influx of oxygen is thought to result in an increase in the formation of oxygen radicals.

MRI or *in vivo* NMR imaging, which is an appropriate non-invasive observable, can be used to study rat liver free radical metabolism of halocarbons and renal

IRI *in vivo*. With the use of respiratory gating, it is possible to study *in vivo* acute halocarbon-induced hepatotoxic or renal IRI tissue effects in rats by proton NMR imaging.

METHODS:

A. Image-Guided NMR Spectroscopy

Anaesthetised rats were placed in an NMR probe, and their livers localised by imaging. Oxidative stress was induced by exposure to halocarbons (160 μl of CCl₄ in saline/corn oil mixture, 0.5 ml/200 g rat via i.p. injection; or 2% Halothane by inhalation).

NMR measurements were made with either a Spectroscopy Imaging Systems (SIS) 7.0 Tesla/18 cm (JCU) or 4.7 Tesla/40 cm (Varian Application Lab., Fremont CA) bore imaging spectrometer or a Bruker 4.2 Tesla/40 cm bore imaging spectrometer (at the CMR, U. of Q.). Respiratory gating was used to trigger acquisition of the phase-encoding steps in the imaging sequence. Multiple ¹H-NMR image slices were taken in the transverse plane. IG ¹H-NMR spectra were then obtained using the water-suppressed (CHESS) VOSY localisation technique in 40-100 μl volumes. IG ³¹P-NMR spectra were obtained using the ISIS localisation technique in 1 ml volumes.

For renal ischaemia-reperfusion studies, the right renal artery was surgically exposed and fitted with an adjustable mechanical occluder. ly.

B. ESR Spin Trapping

ESR spin trapping studies were done on either a Bruker 200D EPR spectrometer (U. Guelph, Canada) or a Bruker ESP 300E EPR spectrometer (CMR, U.Q.) operating at X-band microwave frequencies. For halocarbon studies, the halocarbon free radical metabolites were detected *in vitro* in rat liver microsomes. For renal ischaemia-reperfusion injury studies, free radicals were detected in a perfused kidney model. The spin trap DMPO was administered at concentrations of 25 mM for the halocarbon studies, and 25 mg/ml (infusion of a total of 50 mg) for the perfused kidney ischaemia-reperfusion injury study.

RESULTS:

I. Halocarbon Toxicity Studies

a. Image-Guided NMR Spectroscopy

For the halocarbon toxicity studies, proton MRI

was used to detect acute localised CCl_4 -induced oedema in the region surrounding the major branch of the hepatic portal vein of the right lobe within a period of 1-2 hours [3,4]. Administration of the free radical spin trap PBN (α -phenyl *N*-*tert*-butyl nitron), 30 min prior to CCl_4 exposure, was found to effectively inhibit the CCl_4 -induced hepatic oedematous response observed in the proton NMR images [4].

Preliminary IG ^{31}P -NMR studies in rat liver (1 ml), exposed to CCl_4 , obtained at 4.7 Tesla, indicated image-associated regional changes in phosphorous metabolism from CCl_4 toxicity [5]. Regional hepatocellular pH was found to decrease from 7.4 to 7.0 in 1-2 hrs in proximity to the hepatic portal vein. In addition, changes such as a decrease in the ATP/Pi ratio and an increase in levels of phosphomonoesters, particularly phosphocholine [6], were detected mainly in the vicinity of the hepatic portal vein [5].

Localised water-suppressed ^1H -NMR spectroscopy can also be implemented to assess *in vivo* levels of lactate and GSH, both biochemical markers of tissue damage, in halocarbon-treated rat livers. Water-suppressed IG ^1H -NMR spectra, in 40-80 μl volumes, obtained from control rat livers at 4.2 Tesla (CMR, U of Q), demonstrated that it is feasible to detect tissue-damage indicators, such as glutathione, lactate and lipid.

b. ESR Spin-Trapping

ESR spectroscopy in conjunction with spin trapping techniques (DMPO) was used to detect and monitor *in vitro* formation of free-radical metabolites from the metabolism of halocarbons.

II. Renal Ischaemia-Reperfusion Injury Studies

a. Image-Guided NMR Spectroscopy

Localised ^1H -NMR spectra (20-40 μl) were obtained from rat renal medulla and cortex (Fig. 6), using coordinates from rat kidney ^1H -NMR images (4.2 Tesla, CMR, U.Q.). Renal osmolytes such as TMAs (eg. betaine and glycerol phosphorylcholine) and inositol were readily detected mainly in the renal medulla, and GSH was readily detected primarily in the renal cortex.

Preliminary ischaemia-reperfusion water-suppressed IG ^1H -NMR studies in rat kidneys, obtained at 4.2 Tesla (CMR), demonstrated that renal medulla lactate levels (1.25-1.33 ppm) increased during 30 min of ischaemia. After reperfusion, lactate decreased to pre-ischaemic levels over 1-2 hours.

b. ESR Spin-Trapping

With the use of ESR spectroscopy and the spin trap DMPO, two spin adducts were observed following IRI. The two spin adducts are identified as the DMPO-OH adduct (characteristic 1:2:2:1 quartet pattern) and the carbon-centered DMPO-CR adduct (six-line pattern).

Reaction of the oxygen-derived $\cdot\text{OH}$ radicals with cellular macromolecules (eg. lipids) can generate $\cdot\text{CR}$ radicals.

CONCLUSIONS:

A number of MR techniques can be used to assess the metabolic and tissue-damaging effects of xenobiotic-induced toxicity or IRI. ESR spin-trapping techniques can be used to monitor and identify damaging xenobiotic biotransformed free radical metabolites (eg. halocarbon metabolites), or oxygen-derived free radical metabolites from IRI. Free radical mediated attack on hepatocellular membranes, after acute halocarbon intoxication, results in an increase in cell permeability to extracellular ions and water, leading to an edematous response that can be detected by *in vivo* ^1H -NMR imaging. NMR imaging and spectroscopy techniques (either ^1H - or ^{31}P -NMR) can be used to localize and quantitate the degree of halocarbon-induced hepatic injury. *In vivo* NMR imaging and spectroscopy can also be used to monitor the effect of free radical scavengers on halocarbon-induced hepatotoxicity. Inhibition of the observed halocarbon-induced 'tissue damage' in rat liver by spin traps supports the hypothesis that free radicals are the major causal factors in acute CCl_4 hepatotoxicity. PBN and other suitable spin traps (DMPO (5,5-dimethylpyrroline-N-oxide)) have the potential to be used as inhibitory agents in biological systems undergoing oxidative stress.

By monitoring biochemical changes as a result of cellular abnormalities developing during toxic renal injury, such as IRI, it is possible to gain a better understanding of the pathogenesis of kidney diseases such as acute renal failure. This NMR technology is presently the only way to study biological and physiological processes in living systems, non-invasively.

REFERENCES:

1. EG Janzen *et al.*, *FRRC* **3**, 357, 1987.
2. EG Janzen *et al.*, *FRRC* **4**, 359, 1988.
3. M Brauer *et al.*, *MRM* **2**, 229, 1989.
4. EG Janzen *et al.*, *FRRC* **2**, 325, 1990.
5. RA Towner *et al.*, *MRI* **10**, 679, 1992.
6. RA Towner *et al.*, *BBA* **993**, 92, 1989.

BIOACTIVE PEPTIDES: SOLUTION STRUCTURE DETERMINATION, BY NMR METHODS, OF CYCLODECAPEPTIDES INHIBITING THE CHOLATE UPTAKE IN HEPATOCYTES

Teodorico Tancredi, Gabriella Saviano, Paola Fucile and Giancarlo Zanotti[§]
 Istituto di Chimica di Molecole di Interesse Biologico del CNR, Via Toiano 6,
 I-80072 Arco Felice, Italy

[§]Centro di Chimica del Farmaco, CNR, University of Roma "La Sapienza, Roma, Italy

Introduction

Cyclic peptides related to cyclolinopeptide A [1], antamanide [2] and somatostatin [3] form a class of natural cyclopeptides acting as competitive inhibitors toward the cholate uptake in hepatocytes. The structure-activity relationships of cyclic peptides related to cyclolinopeptide A have been the object of a systematic study carried out in our laboratories in the last few years [4-9].

In order to study the influence of the -Pro-Phe-Phe- sequence and of the lipophilicity on the activity and conformation of these peptides, we synthesized the symmetric cyclodecapeptides



with Xaa = Ala, Leu, Glu(otBu) or Lys(ϵ ClZ).

In the present work we report the structure of the four peptides as determined by nmr spectroscopy in acetonitrile solution; their cation complexing ability in the same solvent has been also investigated.

Results and Discussion

The in vitro bioassays show for these peptides an activity comparable to that of cyclolinopeptide A. Their CD₅₀ values, i.e. the peptide concentration required to inhibit by 50% the cholate uptake into hepatocytes, are reported in Table I.

The room temperature proton nmr spectra of the four peptides in acetonitrile are similar and indicate the existence in solution of only one conformer.

The analysis of the spectral data allows us to propose common structural features characterizing all peptides.

Table I

peptide	CD ₅₀ [μ M]
c[P-P-F-F-L-I-I-L-V] (CLA)	0.8
c[P-F-F-A-E(OtBu)] ₂	0.6
c[P-F-F-A-K(ϵ Z(Cl))] ₂	1.8
c[P-F-F-A-L] ₂	2.2
c[P-F-F-A-A] ₂	13.0

The essential features of this structure are:

- i) complete symmetry of the two pentameric unities,
- ii) a backbone with an all *trans* conformation of the peptide bonds,
- iii) two antiparallel extended structures, stabilized by interstrand Xaa->Phe hydrogen bonds, closed at both ends by
- iv) two β -turns of type I centred on the -Xaa-Pro-Phe-Phe- moieties.

The proposed structure has two well separated surfaces, a hydrophilic one mainly containing the peptide backbone and a hydrophobic one, above the peptide backbone plane, formed by the protruding side chains of all residues. A similar separation of two different surfaces has been already observed by us in the barium complexed form of cyclolinopeptide A [6].

The ion complexing ability of these peptides has been investigated using sodium and calcium ions. Addition of sodium ions doesn't alter at all the spectra of the peptides. Calcium ions, on the contrary, affect extensively all spectra, and it is possible to monitor the formation of equimolar cation/peptide complexes. At a first glance, the most interesting structural feature that can be derived from nmr data is the reversal of the Xaa-Pro peptide bond conformation: we go in fact

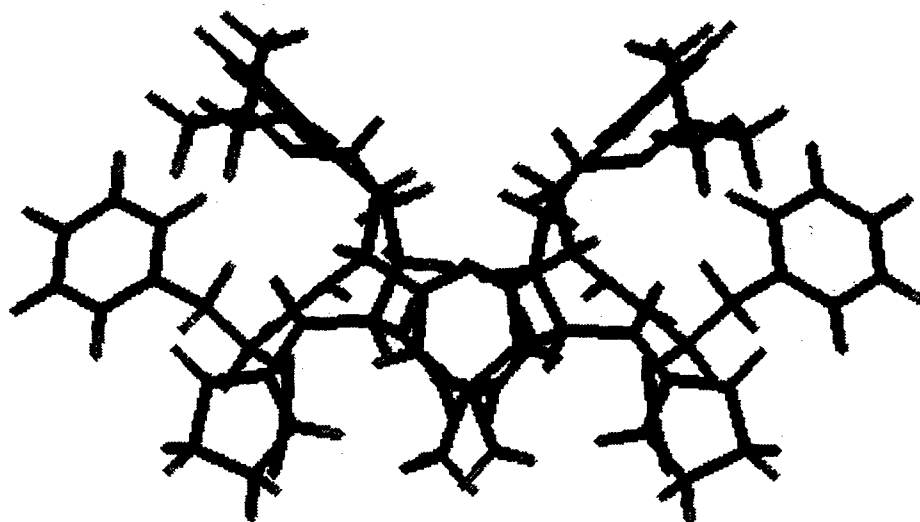


Figure 1 - Molecular model of the calcium complexed cyclo[Pro-Phe-Phe-Ala-Glu(otBu)]₂

from the *trans* conformation of the free peptide to the *cis* one in the calcium complexed peptide.

The preliminary analysis of the whole nmr data seems to indicate that in fact the overall structure of the peptide, in its complexed form, preserves the relevant feature already observed in the structure of its free form: a clear separation of two surfaces, with the hydrophobic one containing all side chains. Figure 1 shows a plausible molecular model of the calcium complexed [Glu(otBu)]-cyclodecapeptide.

The preliminary indications of the present work indicate that the solution structures of all four peptides are very similar. It seems than possible to conclude that the difference in activity depicted by the data of Table I should be attributed to the different bulkiness of the side chain of the fifth residue more than to different conformations of the four peptides.

Acknowledgements: the skillful technical assistance of Mrs. Mariarosaria Mosca is gratefully

acknowledged.

References

- 1) H.P. Kaufmann and A. Tobshirbel *Chem. Ber.* (1959) **92**, 2805.
- 2) T. Wieland in *Peptides of Poisonous Amanita Mushrooms* Springer Verlag, New York, N.Y., 1986.
- 3) S. S. Dzabo and K.H. Usadel *Experientia* (1982) **38**, 254.
- 4) B. Di Blasio, F. Rossi, E. Benedetti, V. Pavone, C. Pedone, P.A. Temussi, G. Zanotti and T. Tancredi *J. Amer. Chem. Soc.* (1989) **111**, 9089.
- 5) M.A. Castiglione Morelli, A. Pastore, P.A. Temussi, G. Zanotti and T. Tancredi *Int. J. Peptide Protein Res.* (1991) **37**, 81.
- 6) T. Tancredi, E. Benedetti, M. Grimaldi, C. Pedone, F. Rossi, M. Saviano, P.A. Temussi and G. Zanotti *Biopolymers* (1991) **31**, 761.
- 7) B. Di Blasio, F. Rossi, E. Benedetti, V. Pavone, M. Saviano, C. Pedone, G. Zanotti and T. Tancredi *J. Amer. Chem. Soc.* (1992) **114**, 8277.
- 8) G. Zanotti, A. Maione, F. Rossi, M. Saviano, C. Pedone and T. Tancredi *Biopolymers* (1993) **33**, 1083.
- 9) G. Zanotti, F. Rossi, M. Saviano, T. Tancredi, G. Saviano, A.

**STUDY OF RELAXATION VIA EPR LINEWIDTH OF Gd³⁺ IN
DILUTED VAN VLECK PARAMAGNETS Tm_xLu_{1-x}PO₄ AND Ho_xY_{1-x}VO₄**

Sushil K. Misra and Serguei I. Andronenko

Physics Department, Concordia University, 1455 de Maisonneuve Boulevard West,
Montreal, Quebec, H3G 1M8, Canada.

EPR linewidth of the Gd³⁺ ion in diluted Van Vleck paramagnets Ho_xY_{1-x}VO₄ (x = 0.0, 0.02, 0.05, 0.1, 0.15, 0.25, 0.3) and Tm_xLu_{1-x}PO₄ (x = 0.0, 0.1, 0.2, 0.4, 0.6, 0.8, 1.0) were measured in the temperature range 77 - 300 K. It was found that the dipole-dipole and exchange interactions significantly influenced the linewidths in Ho_xY_{1-x}VO₄ and Tm_xLu_{1-x}PO₄ for concentrations x > 0.1, and x > 0.6, respectively. In addition, in Ho_xY_{1-x}VO₄ samples with x > 0.3 the linewidth behaviour was predominantly governed by the formation of percolation clusters leading to sharp broadening of the EPR linewidth. On the other hand, in Tm_xLu_{1-x}PO₄ samples with 0.1 < x < 0.8 it was the disorder that dominated the Gd³⁺ EPR linewidth due to the rather large difference in the ionic radii of Tm³⁺ and Lu³⁺ ions, unlike that for the Ho³⁺ and Y³⁺ ions.

The EPR linewidths of the impurity ion Gd³⁺ can be used to estimate the spin-relaxation times of the host paramagnetic ions Ho³⁺ and Tm³⁺ in Ho_xY_{1-x}VO₄ and Tm_xLu_{1-x}PO₄ crystals, respectively. The spin-lattice relaxation times of the host paramagnetic ions in the lattice can be expressed as follows [1]:

$$\tau_{\text{host}} = (3\Delta B g^2 \beta) / (110 h g^2 \langle \Delta v^2 \rangle_{\text{av}}), \quad (1)$$

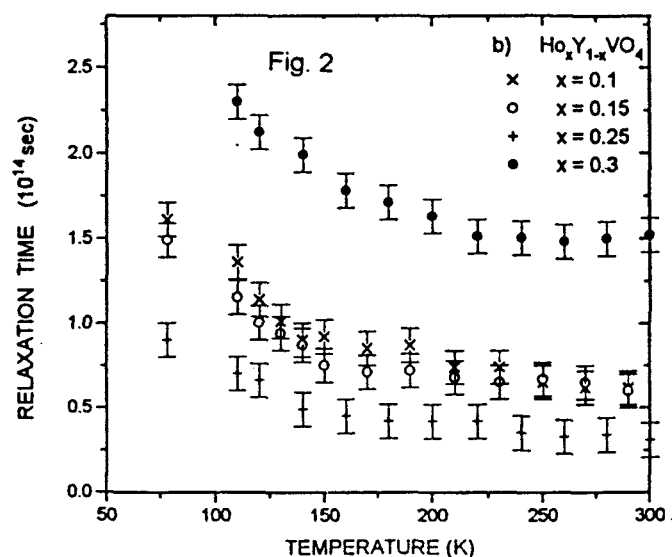
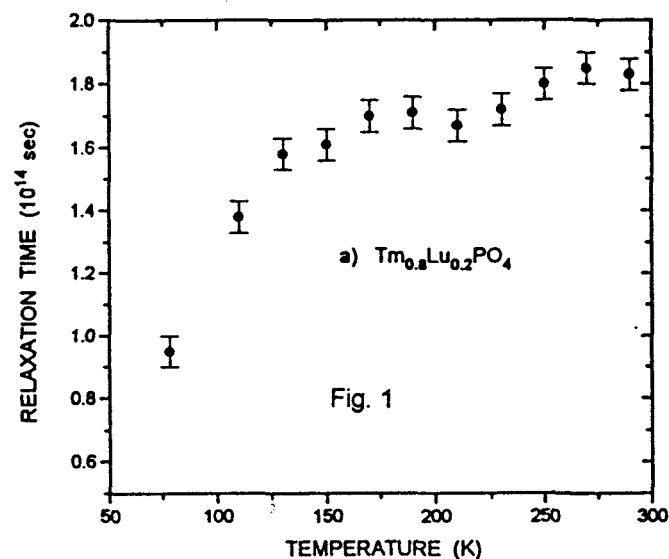
where the second moment is given by

$$\begin{aligned} \langle \Delta v^2 \rangle_{\text{av}} = & S'(S'+1)(1/3h^2) \{ N J_p^2 + N_1 (J_p')^2 \\ & + (g g')^2 \mu_B^4 \mu_0^2 \sum_k (1 - 3\gamma_{jk}^2)^2 r_{jk}^{-6} + \\ & 2 J_p g g' \mu_B^2 \mu_0 \sum_k (1 - 3\gamma_{jk}^2) r_{jk}^{-3} + \\ & 2 J_p' g g' \mu_B^2 \mu_0 \sum_k (1 - 3\gamma_{jk}^2) r_{jk}^{-3} \} \end{aligned} \quad (2)$$

In Eqs. (1) and (2), ΔB is the experimentally observed impurity-ion Gd³⁺ EPR linewidth, J_p is the average host-impurity pair exchange constant of interaction between the Gd³⁺ ion and the nearest host ions, J_p' is the average pair exchange interaction constant of the interaction between the Gd³⁺ ion and the next-nearest ions, g and g' are respectively Lande factors for the impurity and the host paramagnetic ions, μ_0 is the permeability constant, N is the number of the nearest neighbours, N_1 is the number of the next nearest

neighbours, μ_B is the Bohr magneton, γ_{jk} is the direction cosine of \vec{r}_{jk} with the external magnetic field, where \vec{r}_{jk} is the vectorial distance between the j and k ions.

The experimental values of the exchange constant J_p and J_p' for TmPO₄ and HoVO₄ are not available. The results of Mehran et al. [2] were used to this end. As for Tm³⁺ - Gd³⁺ and Ho³⁺ - Gd³⁺ interactions, they were both assumed to be $J_p = 0.05 \text{ cm}^{-1}$ and $J_p' = J_p/20$. The results are exhibited in Figs. 1 and 2.



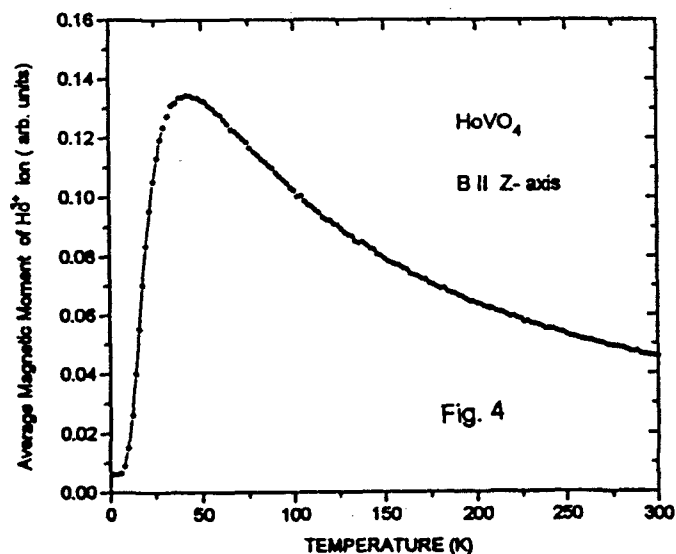
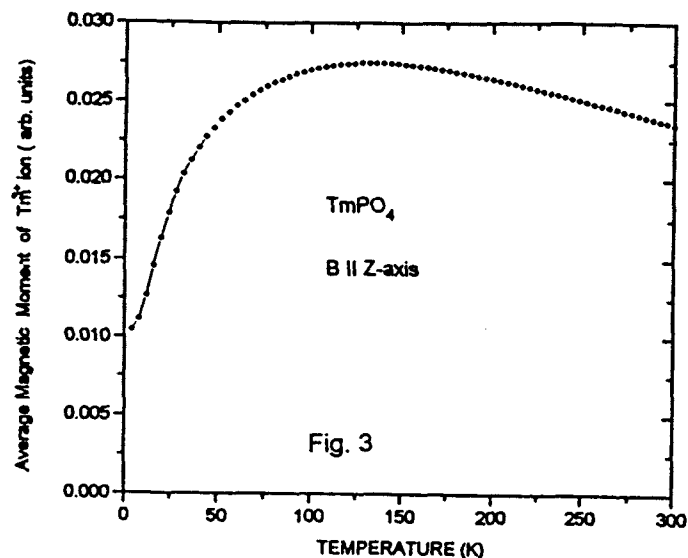
$\text{Ho}_x\text{Y}_{1-x}\text{VO}_4$. It is seen that with increasing values of x the relaxation times of Ho^{3+} in $\text{Ho}_x\text{Y}_{1-x}\text{VO}_4$ decrease with x . In the present calculations the average values of ΔB for the various EPR lines were used at each temperature. That part of ΔB which was not due to dipolar and exchange interactions, i.e. the Gd^{3+} EPR linewidth in the purely diamagnetic compounds ($\Delta B_{pp} = 5$ G), was subtracted off from the observed EPR linewidth, to be substituted in Eq. (1). For the samples with $x = 0.1 - 0.3$ it was found that the calculated relaxation times increased with decreasing temperature, in the range $(0.4 - 2.4) \times 10^{-14}$ sec.

$\text{Tm}_x\text{Lu}_{1-x}\text{PO}_4$. For these crystals there exist a strong influence of disorder on the EPR linewidth as discussed above. Thus, this part of EPR linewidth, i.e. is the average EPR Gd^{3+} linewidth in the almost diamagnetic $\text{Tm}_{0.1}\text{Lu}_{0.9}\text{PO}_4$, was also subtracted off from the observed EPR linewidth in order to estimate τ_{host} . Only in the $\text{Tm}_x\text{Lu}_{1-x}\text{PO}_4$ compound with $x = 0.8$ was there found temperature dependence of the relaxation time of Tm^{3+} ; it became slightly shorter with decreasing temperature. For the samples with smaller concentrations ($x < 0.8$), no temperature dependence of the relaxation times was found.

The temperature dependences of the relaxation times are in accordance with those of the calculated average magnetic moments of the host paramagnetic ions, as exhibited in Figs. 3 and 4.

References

- 1). F. Mehran, K.W.H. Stevens, T.S. Plaskett and W.J. Fitzpatrick, Phys. Rev. B22, 2206 (1980).
- 2). S.K. Misra, U. Orhun, Phys. Rev. B39, 2856 (1989).



GROESY and Related Selective 1D Analogs of Gradient-Enhanced nD Sequences

P. Adell, T. Parella, F. Sánchez-Ferrando, and A. Virgili.

Departament de Química, Universitat Autònoma de Barcelona, E-08193, Bellaterra, Barcelona, Catalonia.

INTRODUCTION

The advantages of the combined use of selective excitation and pulsed field gradients for coherence selection have been recently demonstrated convincingly with the development of the GOESY experiment (1), a selective 1D NOESY sequence employing gradients which yields ultrahigh quality NOE spectra. We now report on the analogous GROESY sequence (Gradient-enhanced ROESY experiment) (2) which also yields artifact-free, high-quality 1D ROESY spectra.

In addition, a slight modification of GROESY, using a stronger spin-lock rf field, yielded a ge-1D TOCSY sequence providing extremely clean 1D TOCSY spectra without the need of a long phase cycle procedure. Alternatively, combination of pairs of sequences yielded doubly-selective 1D equivalents of 3D sequences. Thus, we have developed gradient-based pseudo-3D experiments such as ge-1D COSY-NOESY (CONO), ge-1D TOCSY-NOESY (TONO), and ge-1D TOCSY-ROESY (TORO) (3) which allow the fast, easy and reliable measurement of selective Overhauser enhancements even from protons deeply buried in crowded regions of the conventional 1D spectrum.

GROESY EXPERIMENT.

This experiment starts with a gradient-based selective excitation scheme that offers improved results with respect to conventional shaped pulses because pure in-phase magnetization without phase distortions is obtained in their whole excitation bandwidth. This cluster only rephases the selected magnetization affected by the 180° pulse and avoids any evolution of the J-coupling during this period. Other advantages of all these methods are the absence of out-of-band sidelobes, the refocusing of scalar coupling evolution and the lack of need of difference spectroscopy or phase cycling.

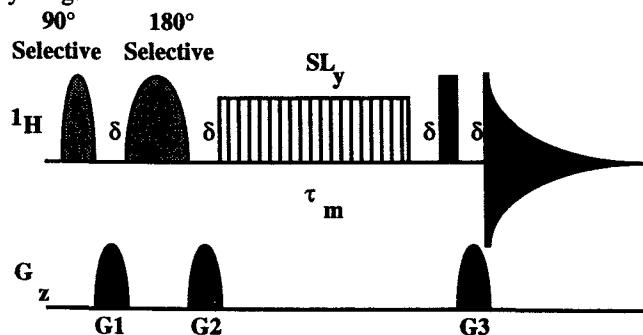


Figure 1: Basic pulse sequence and CP diagram for gradient-based spin-locked 1D experiments. A 1:-1:2 gradient ratio selects N-type data. When SL stands for a z-filtered DIPSI-2 pulse train, a ge-1D TOCSY is performed. On the other hand,

when SL stands for a T-ROESY pulse train, a GROESY experiment is performed. δ stands for the gradient length.

ge-1D COSY-NOESY EXPERIMENT.

The first part of the selective ge-1D COSY-NOESY (ge-1D CONO) experiment (Fig. 2) is a refocused COSY block in which in-phase magnetization of the relayed proton is achieved from the starting one. A selective 90° pulse applied on the relayed target creates z-magnetization that will permit selective cross-relaxation from this proton to other spins close in space. The last 90° pulse turns the z-magnetization into the transverse plane, where it is refocused by the final gradient G4. The length and strength of G1, G2 and G4 gradients are set so that the magnetization defocused by the two first is refocused by the third and fourth ones. In addition, it should be also possible to extend the CONO sequence to further distant spins using a multiple-step transfer relay block in which coherence transfer should be achieved step-by-step in a whole J-coupling network.

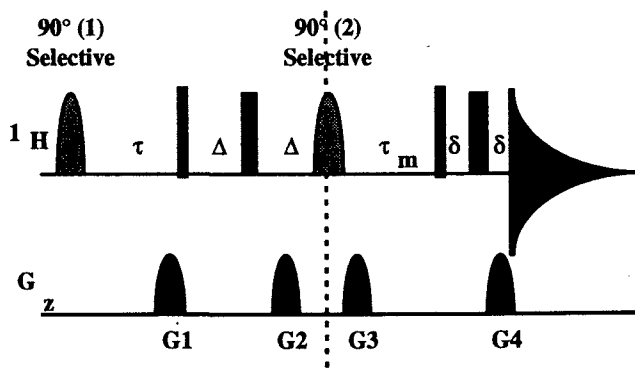


Figure 2: Pulse sequence and CP diagram for the ge-1D CONO experiment. Experimentally, a 1:1:3:2 gradient combination selects N-type data.

ge-1D TOCSY-NOESY EXPERIMENT.

A second alternative is based on the initial J transfer of magnetization by a coherent transfer in the SL state. This ge-1D TOCSY-NOESY (TONO) experiment (Fig. 3), seems to be more suitable than the CONO experiment. The first step is built as in the ge-1D TOCSY experiment. The resulting in-phase magnetization is allowed to evolve during a mixing period by means of the application of a strong SL field which aligns the magnetization along the SL axis. The transferred magnetization also shows in-phase behaviour and, therefore, in order to effect NOE transfers, the magnetization of the selected proton is easily aligned onto the z axis by the

simple application of a selective 90° pulse on the relayed proton.

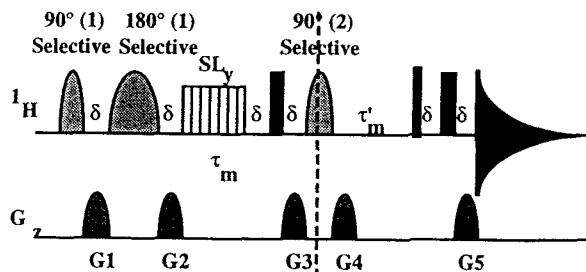


Figure 3: Pulse sequence and CP diagram to perform ge-1D TONO experiment. Experimentally, a 1:-1:-1:6:3 gradient combination selects N-type data.

ge-1D TOCSY-ROESY EXPERIMENT.

In a ge-1D TOCSY-ROESY (TORO) experiment (Fig. 4), the NOE transfer step is replaced by a ROE transfer which is more suitable for medium size molecules. Here, the selected in-phase magnetization obtained by the TOCSY block is allowed to evolve in the x-y plane. In order to select the relayed proton, a selective 180° pulse is used to invert it, leaving all other spins unaffected. Subsequently, the second transfer step is a ROESY block, applied parallel to the TOCSY one, and a final gradient G3 is used in order to refocus all magnetization defocused by the first two gradients, G1 and G2.

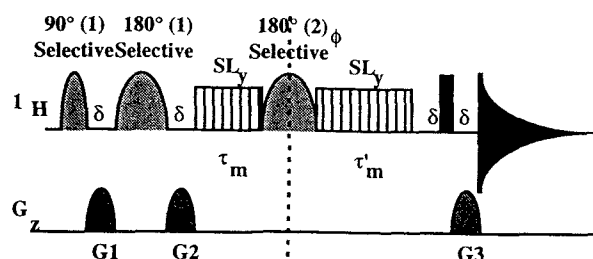


Figure 4: Pulse sequence and CP diagram to perform ge-1D TORO experiment. Experimentally, a 1:-1:2 gradient combination selects N-type data using a basic four-step phase cycle ($\phi=y,-x,-y,x$ and receiver= x,y,x,y).

As in GROESY experiment, a decrease of the sensitivity by a factor of 2 results from gradient selection. But, in comparison to the CONO and TONO experiments, an improvement by a factor of 2 is achieved because of the smaller number of gradients. Fig. 5 shows several spectra obtained on a sample of erythromycin in Chloroform-d.

REFERENCES.

1. J. Stonehouse, P. Adell, J. Keeler, and A.J. Shaka, *J. Am. Chem. Soc.* **116**, 6037 (1994).
2. P. Adell, T. Parella, F. Sánchez-Ferrando, and A. Virgili, *J. Magn. Reson. B* in press (1995).
3. P. Adell, T. Parella, F. Sánchez-Ferrando, and A. Virgili, *J. Magn. Reson. A* **113**, 124 (1995).

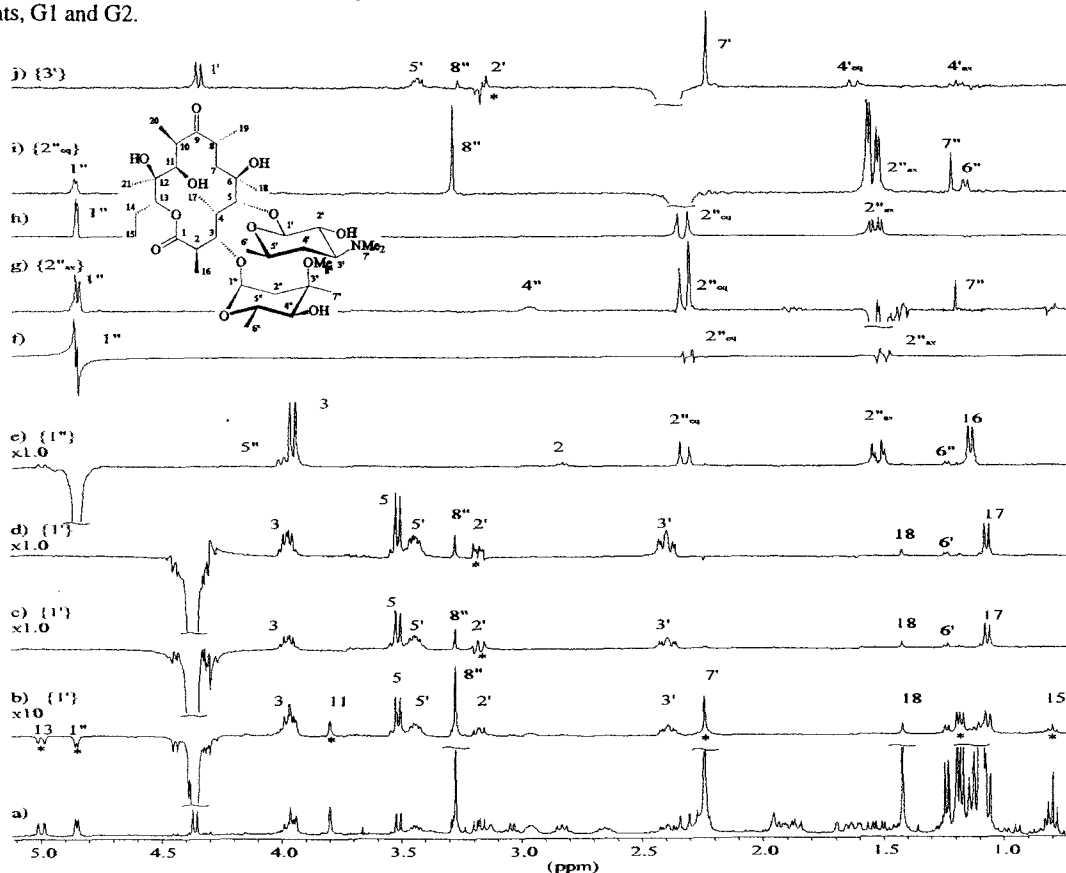


Figure 5: a) Proton spectrum of 1; b) Phase-cycled 1D ROESY spectrum after pulsing H-1' proton, with a mixing time of 450ms. Selective excitation was achieved by a 90° gaussian pulse of 20ms; c) GOESY spectrum acquired with a mixing time of 450ms; d) GROESY spectrum with a mixing time of 450ms; e) as d) but pulsing on the H-1'' proton. b)-e) spectra were acquired with 1024 scans and a recycle time of 1s with no dummy scans. f) Selective ge-1D COSY spectrum after pulsing H-1'' proton ($t=60$ ms); g) Doubly-selective ge-1D CONO spectrum after polarization transfer from H-1'' to H-2'' (G1=6, G2=6, G3=21 and G4=12 G/cm, $t=60$ ms, $t_m=450$ ms); h) Selective ge-1D TOCSY spectrum after pulsing H-1'' proton ($t=90$ ms); i) Doubly-selective ge-1D TONO spectrum after polarization transfer from H-1'' to H-2'' (G1=3, G2=3, G3=3, G4=18 and G5=9 G/cm, $t=90$ ms, $t_m=450$ ms); j) Doubly-selective ge-1D TORO spectrum after polarization transfer from H-1'' to H-3'' (G1=6, G2=6, G3=0, G4=0 and G5=12 G/cm, $t=50$ ms, $t_m=450$ ms). Spectra f) and h) were accumulated with 32 scans. The other spectra (g, h and j) were accumulated with 4096 scans and a relaxation delay of 1s.

NMR of ${}^7\text{Li}$ and EPR of Cr^{3+} in Ferroelectric LiTaO_3 Single Crystals

S. H. Choh, T. H. Yeom[†], and S. W. Ahn

Department of Physics, Korea University, Seoul 136-701, Republic of Korea

I. Introduction

Lithium tantalate and lithium niobate are interesting and useful materials in the fields of opto-electronics and acoustics.[1,2] At room temperature, LiTaO_3 is ferroelectric with the C_3 point group symmetry. The Li^+ and Ta^{5+} ions lie along the c -axis with the 3-fold symmetry. [3]

Magnetic resonance technique is useful to study the local electric field and crystal structure. Studies of ${}^7\text{Li}$ NMR and Cr^{3+} EPR in LiTaO_3 have been reported.[4-7] Recently, we determined the nuclear quadrupole coupling constant (e^2qQ/h) and asymmetry parameter (η) of ${}^7\text{Li}$ in LiTaO_3 single crystal[8] and the temperature dependence of e^2qQ/h and relaxation rate of ${}^7\text{Li}$ were investigated as a function of temperature in the range of 140 ~ 420 K.[9,10] An induced Cr^{3+} center in γ -irradiated LiTaO_3 crystal has been also studied by employing an EPR spectrometer at room temperature.[11]

II. Results and discussion

A single crystal, grown by the Czochralski method, is used for the experiments. The crystallographic principal axes of the specimen were determined by the x-ray Laue method. The resonance spectra of ${}^7\text{Li}$ NMR are found to be independent of the direction of magnetic field on the crystallographic ab -plane, whereas the resonance spectra on the ca -plane are angular dependent. From the above rotation patterns, the asymmetry parameter is determined to be zero. The maximum separation of the resonance fields was observed when the magnetic field

was applied along the crystallographic c -axis. The obtained value of e^2qQ/h for ${}^7\text{Li}$ in LiTaO_3 is larger than that of ${}^7\text{Li}$ in LiNbO_3 [4]. This may be partially explained by the shorter length (r) between Li^+ and O^{2-} ions because the electric field gradient of Li^+ ion is inversely proportional to r^3 . If we consider only the nearest neighbours of Li ion, the Li-O bond length of 2.041 Å in LiTaO_3 is shorter than that of 2.068 Å in LiNbO_3 .

The temperature dependence of e^2qQ/h and the spin-lattice relaxation rate for ${}^7\text{Li}$ nucleus investigated with FT NMR spectrometer, are shown in Figure 1. The obtained e^2qQ/h as a function of temperature could be fitted by a linear equation of the form $e^2qQ/h = 78.3 + 0.030 (T - T_r)$ kHz, where T_r refers to the room temperature. This temperature dependence may be explained as follows. As the temperature increases up to T_c (893 K), Li ions move away from the center towards the oxygen plane, consequently, the distance between lithium and oxygen ions (r) is becoming shorter. Thus, as far as the nearest oxygen ions are concerned, the electric field gradient at the Li nucleus may increase as the temperature increases. The relaxation rate, T_1^{-1} , is also measured to be linearly increasing with increasing temperature. The best linear fit to data may be written by $T_1^{-1} = \alpha + \beta T$, (s^{-1}) where $\alpha = (3.10 \pm 0.09) \times 10^{-2} \text{ s}^{-1}$ and $\beta = (1.19 \pm 0.04) \times 10^{-4} (\text{sK})^{-1}$. This relaxation behavior implies that the spin-lattice relaxation mechanism in this temperature range is mainly caused by the direct process of scattering with a single phonon. Our finding is different from that of powder sample[6] which showed a temperature independent rate possibly due to the paramag-

[†] Present address: Department of Physics, Seonam University, Namwon 590-170.

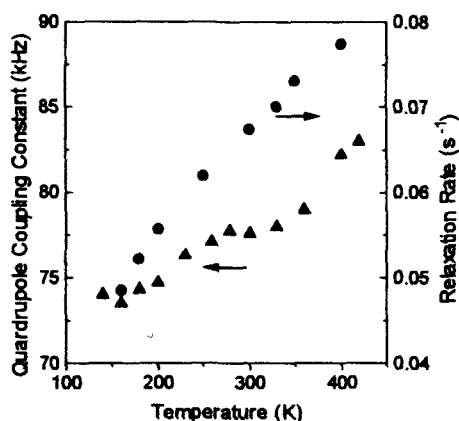


Fig. 1 Temperature dependence of e^2qQ/h and T_1^{-1} for ${}^7\text{Li}$ in LiTaO_3 crystal.

netic impurity contained in the sample. Our result displays more reliable intrinsic behavior of the relaxation rate in LiTaO_3 , because the crystal we employed hardly contained paramagnetic impurity as confirmed by EPR.

An as-grown crystal, transparent but slightly yellow, was prepared for EPR measurements of Cr^{3+} in LiTaO_3 at 300 K, 77 K, and 4 K. Since no EPR signals were detected with this crystal, it was irradiated up to 1.5 Mrad of γ -ray. EPR spectra obtained with this γ -irradiated sample are angular independent on the crystallographic ab-plane. Therefore, the induced Cr^{3+} ion seems to be at Li^+ or Ta^{5+} ion. The parameters of $g = 1.964$ and $D = 0.441 \text{ cm}^{-1}$ for the induced Cr^{3+} center are determined and found to be similar to the reported Cr^{3+} center[7]. However, the signal intensities of the induced Cr^{3+} center rapidly reduced as time passed. The centre was no longer detectable at room temperature 72 hrs after the irradiation. This induced center is very unstable unlike the previously reported stable center[7]. A possible origin of this induced Cr^{3+} center in γ -irradiated LiTaO_3 may be proposed in terms of the mechanism $h\nu + \text{Cr}^{2+} \rightarrow \text{Cr}^{3+} + e^-$, where Cr^{2+} ions were present in the crystal.

III. Summary

${}^7\text{Li}$ NMR in the ferroelectric LiTaO_3 crystal has been investigated. The z-axis of the electric

field gradient tensor is found to be along the crystallographic c-axis with axial symmetry. The obtained e^2qQ/h as a function of temperature could be fitted by a linear equation of the form $e^2qQ/h = 78.3 + 0.030 (T - T_r) \text{ kHz}$ for the temperature range of 140 - 420 K. The relaxation rate of ${}^7\text{Li}$ is determined to be linearly increasing with increasing temperature. This linear dependence may well be accounted for the model of direct process due to a single phonon. EPR parameters of the γ -induced Cr^{3+} center in LiTaO_3 was similar to the previously reported Cr^{3+} center, but the center turned out to be thermally unstable. A possible origin of this induced Cr^{3+} center is the mechanism $h\nu + \text{Cr}^{2+} \rightarrow \text{Cr}^{3+} + e^-$.

Acknowledgement

This work was supported by the KOSEF through the RCDAMP at Pusan National University (1994-97).

References

- [1] P. Gunther, Phys. Rep. **93**, 199 (1982).
- [2] C. M. Verber, N. F. Hortman and A. M. Glass, Appl. Phys. Letters, **30**, 272 (1977).
- [3] S. C. Abrahams and J. L. Bernstein, J. Phys. Chem. Solids, **28**, 1685 (1967).
- [4] G. E. Peterson and P. M. Bridenbaugh, J. Chem. Phys. **48**, 3402 (1968).
- [5] J. S en egas and M. Zriouil, J. Solid State Chem. **58**, 137 (1985).
- [6] D. S. Ellingsen and B. Pedersen, Phys. Stat. Sol. **24**, 191 (1974).
- [7] G. Burns, D. F. O'Kane, and R. S. Title, Phys. Rev. **167**, 314 (1968).
- [8] T. H. Yeom and S. H. Choh, Sae mulli, **31**, 610 (1991).
- [9] T. H. Yeom, S. H. Choh, and K. S. Hong, J. Korean Phys. Soc. **25**, 62 (1992).
- [10] T. H. Yeom, K. T. Han, S. H. Choh, and K. S. Hong, J. Korean Phys. Soc. **28**, 113 (1995).
- [11] S. W. Ahn, J. S. Kim, S. H. Choh, and T. H. Yeom, J. Korean Phys. Soc. **27**, 535 (1994).

Nuclear Magnetic Resonance of ${}^7\text{Li}$ in $\text{Li}_2\text{B}_4\text{O}_7$ and LiB_3O_5 Single Crystals

In Gyoo Kim, Nak Kyun Sung, Sung Ho Choh, and Jung Nam Kim[†]

Department of Physics, Korea University, Seoul 136-701, KOREA

[†]Department of Physics, Pusan National University, Pusan 609-735, KOREA

I. Introduction

The piezoelectric $\text{Li}_2\text{B}_4\text{O}_7$ (lithium diborate) and the nonlinear optical LiB_3O_5 (lithium triborate) single crystals have tetragonal and orthorhombic structure, respectively. The space group of the lithium diborate is $I4_1cd$ (a point group $4mm$, $z=8$, $a=9.48$ and $c=10.29\text{\AA}$) and that of the lithium triborate is $Pna2_1$ (a point group $mm2$, $z=4$, $a=8.45$, $b=7.38$ and $c=5.15\text{\AA}$)[1-3]. Nevertheless of difference in crystal structure, their local atomic arrangements have some similarities, i.e. the lithium atoms have four nearest oxygen atoms (distorted oxygen tetrahedra) the boron atoms have 4-fold (BO_4 radical) and 3-fold coordinations (BO_3 radical) in both crystals.

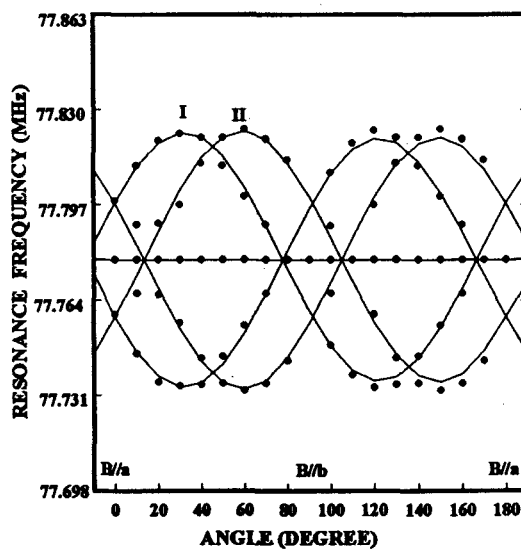
Ivanov et al.[4] reported the heating-cooling cycle effect on ${}^7\text{Li}$ and ${}^{11}\text{B}$ NMR in $\text{Li}_2\text{B}_4\text{O}_7$ single crystal at 80-300 K and Matsuo et al.[5] reported the relaxation study of ${}^7\text{Li}$ NMR in both $\text{Li}_2\text{B}_4\text{O}_7$ single crystal and glass up to 900 K. We measured NMR of ${}^7\text{Li}$ ($I=3/2$, 92.58%) in $\text{Li}_2\text{B}_4\text{O}_7$ and that of ${}^7\text{Li}$ and ${}^{11}\text{B}$ ($I=3/2$, 80.42%) in LiB_3O_5 at room temperature[6]. Here, we discuss the quadrupole coupling constant (qcc), asymmetry parameter (η), and principal axes of the electric field gradient (efg) tensor of ${}^7\text{Li}$ nucleus in both crystals in terms of the angular dependences of ${}^7\text{Li}$ NMR signals.

II. Experiments and Analysis

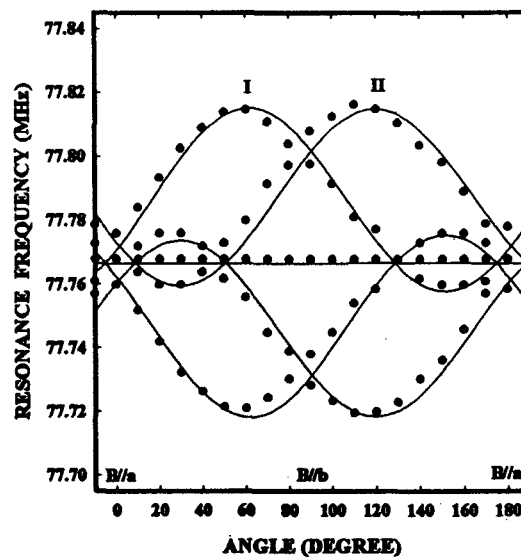
The lithium diborate single crystal was grown by the Czochralski method and the lithium triborate single crystals by the top seed slow cooling (or the flux pulling) method[7]. First, we mounted the samples along their crystallographic axes through the x-ray Laue back scattering method. Then, we measured ${}^7\text{Li}$ -NMR on the crystallographic planes; ab-, bc-, and ca-plane with angular increment of 10° by employing the Bruker MSL200 NMR spectrometer (Seoul Branch, KBSI). The static magnetic field was 4.7 T and all measurements were carried out at room temperature.

Figure 1 shows the rotation patterns of the ${}^7\text{Li}$ NMR signals in both crystals on the ab-plane. There are two sets of data (I and II) symmetric about the central line and they are also symmetric about the crystallographic a- and b-axis. We analyzed the data by means of the

Computer Program EPR (ver. 4.4)[8] and summarized the results in Table 1.



(a)



(b)

Figure 1. Rotation patterns of ${}^7\text{Li}$ NMR signals in $\text{Li}_2\text{B}_4\text{O}_7$ (a) and in LiB_3O_5 (b). Experimental data are marked by dots and calculations using the best fit parameters are shown by solid lines.

Table 1. Quadrupole parameters of ${}^7\text{Li}$ in $\text{Li}_2\text{B}_4\text{O}_7$ and LiB_3O_5 at room temperature.

			$\text{Li}_2\text{B}_4\text{O}_7$	LiB_3O_5
qcc (kHz)			104.5 ± 0.5 $93.5[4]$	288.5 ± 7.4
η			0.65 ± 0.05	0.62 ± 0.05
Principal axes*	I	V_X	(0.78, 0.51, -0.35)	(0.26, 0.91, 0.33)
		V_Y	(-0.35, -0.10, -0.93)	(0.87, -0.07, -0.49)
		V_Z	(-0.51, 0.85, 0.10)	(0.42, -0.42, 0.81)
	II	V_X	(0.49, 0.80, -0.34)	(0.35, -0.28, -0.90)
		V_Y	(-0.07, -0.36, -0.93)	(0.84, 0.52, 0.16)
		V_Z	(0.87, -0.48, 0.12)	(0.42, -0.81, 0.42)
Transform matrix R			-0.04 0.99 -0.01 0.99 0.04 0.02 -0.02 0.00 1.00	0.99 0.04 0.09 0.08 0.04 -0.99 0.04 -1.00 -0.04

* V_j is the j-axis of the efg tensors corresponding to I and II, respectively. The coordinates are direction cosines with respect to the crystallographic axes (a, b, c).

The quadrupole Hamiltonian is as usual[9]

$$H_Q = \frac{e^2qQ}{4I(2I-1)} [3I_Z^2 - I(I+1) + \frac{1}{2}\eta(I_+^2 + I_-^2)]$$

where eq is the largest component of the principal efg tensor and eQ is the electric quadrupole moment. The Zeeman energy is of the order of 10^{-25}J and the quadrupole energy is of the order of 10^{-30}J . Thus the quadrupolar interaction is small enough to be treated as a first order perturbation and the central line is independent of the field direction in both crystals. Furthermore from the selection rule two satellite lines exist for each data set.

The principal axis system of the efg tensor was also determined as summarized in Table 1. Though there are two sets of data in both crystals, the quadrupole coupling constants for the two sets are equal separately, in both crystal. Even though the quadrupole coupling constants for both data set are same, the principal axes are different. If we consider column matrices of the principal axes system for I and II as V_I and V_{II} in each crystal, then there exists a transform matrix R connecting two column matrices, with the matrix equation $V_I = R V_{II}$. The R matrix is also shown in Table 1. Their approximate values reflect the crystallographic symmetry and explains why the data sets I and II are always symmetric about any crystallographic axis.

III. Conclusion

The qcc is 104.5 ± 0.5 kHz and η is 0.65 ± 0.05 for lithium diborate, and 288.5 ± 7.4 kHz and 0.63 ± 0.05 for lithium triborate. The average of four nearest Li-O bonds is 2.06 Å for $\text{Li}_2\text{B}_4\text{O}_7$ and 2.04 for LiB_3O_5 , respec-

tively. Thus, the difference in the qcc is not fully understood, but the similar asymmetry parameter implies that the lithium atoms in both crystals are located at similarly distorted oxygen tetrahedra. The transform matrix R can be obtained by multiplying the mirror reflection matrix and the $\pi/2$ rotation matrix for $\text{Li}_2\text{B}_4\text{O}_7$, and the mirror reflection matrix and the π rotation matrix for LiB_3O_5 as expected from the crystal structure.

Acknowledgment

This work was supported by the KOSEF through the RCDAMP at Pusan National University (1994-97), and in part by BSRI-95-2410.

References

- [1] J. Krogh-Moe, *Acta Cryst.* **15**, 190 (1962).
- [2] M. Natarajan, R. Faggiani, and I.D. Brown, *Cryst. Struct. Comm.* **8**, 367 (1979).
- [3] Z. Shuqing, H. Chaoen, and Z. Hongwu, *J. of Crystal Growth*, **92**, 805 (1990).
- [4] Y.N. Ivanov, Y.V. Burak, and K.S. Aleksandrov, *Sov. Phys. Solid State*, **32**, 1955 (1990).
- [5] T. Matsuo, M. Shibasaki, T. Katsumata, and Y. Onoda, *Jpn. J. Appl. Phys.* **33**, 3913 (1994).
- [6] I.G. Kim, H.W. Shin, S.H. Choh, and J.N. Kim, *Bull. Korean Phys. Soc.* **13**, 176 (1995).
- [7] C. Chen, Y. Wu, A. Jiang, B. Wu, G. You, R. Li, and S. Lim, *J. Opt. Soc. Am.* **B6**, 612 (1989).
- [8] D.G. McGavin, J.A. Weil, *Computer Program EPR*, Department of Chemistry, University of Saskatchewan, SK, Canada, 1989.
- [9] A. Abragam, *The Principles of Nuclear Magnetism* (Oxford University Press, 1961), Chap. 7.

Novel Designs for High Purity, Shielded Z^n Coils

Stuart Crozier, Stephen Dodd and David M. Doddrell

Centre for Magnetic Resonance, University of Queensland, St Lucia, Queensland, 4072, Australia

1. Introduction

In this paper we present a methodology for the design of very pure, higher order longitudinal coils that can be shielded to reduce the eddy current generation upon switching. Further these shielded Z^n coils have low inductance, are very pure, compact and may also be designed for power efficiency. The design methodology is the simulated annealing (SA) of spherical harmonic errors. We have recently shown that the SA technique may be successfully applied to the design of compact, high quality shielded linear field gradients [1]-[3]. Here we present a different approach where the spherical harmonics of the field generated by a coil are used directly in the error function for minimization. By attempting to annul all but one harmonic, pure harmonic coils can be effectively designed. By placing a second coil external and co-cylindrical with the first and combining the total field external to the coil set with the harmonic error function and calculations of inductance a shielded, pure, low inductance coil set results. In this work we detail the results for longitudinal coil designs.

2. Spherical Harmonic Expansion

Longitudinal coils are constructed of a series of interconnected hoops on a cylindrical cross-section, for any geometry of hoops and any number of turns per hoop position we require the generated spherical harmonics. A spherical harmonic deconvolution method for use in characterizing temporal fields following a gradient transition via NMR signals [4] has been adapted to the problem at hand.

Perhaps the most straightforward approach to obtaining a spherical harmonic expansion of a magnetic field is to measure the magnetic field at points on a spherical surface surrounding the coil origin. Spherical harmonics take the form

$$B_{z_{nm}} = r^n (a_{nm} \cos m\phi + b_{nm} \sin m\phi) P_{nm}(\cos\theta)$$

and are solutions of Laplace's equation $\nabla^2 B_z = 0$. $B_{z_{nm}}$ is the spherical harmonic of order n and degree m , a_{nm} and b_{nm} are constants, r is the radial distance from the magnet isocentre and $P_{nm}(\cos\theta)$

are the associated Legendre functions. The spherical harmonic $B_{z_{nm}}$ and the surface spherical harmonic T_{nm} , where

$$T_{nm} = (\cos m\phi + \sin m\phi) P_{nm}(\cos\theta)$$

have the property of being orthogonal when integrated over the surface of a sphere. This information can be used to determine the spherical harmonic coefficients a_{nm} and b_{nm} .

The field due to the coil structure was calculated at 112 positions around the coil centre at 22.5° azimuthal steps and on 7 longitudinal planes, allowing zonal and tesseral harmonics up to degree and order 6 to be calculated. The position of the seven planes was given by the radially scaled roots of the Legendre polynomial $P_7(\cos\theta)$. The field at these 112 points was calculated by Biot-Savart summations in which each hoop was segmented into 100 pieces. The above analysis was then used to deduce the harmonics generated by each coil configuration. The full field and harmonic deconvolution for the coils described here took less than 30 seconds to run on a Sun SPARCstation 10.

3. Simulated Annealing Parameters

SA is a stochastic optimization method [5] based on Boltzmann statistics that has the potential to find the global minimum of a defined error function in response to system re-arrangements. For longitudinal coils designed to generate zonal harmonics an array of hoops is allowed to move randomly and independently along a defined length. The spherical harmonics for each re-arrangement are then calculated. For a shielded coil set a typical error function may be:

$$E = \frac{k_1 \sum B_{nm}(r, \theta, \phi)^2}{B_d(r, \theta, \phi)} + k_2 L_t + k_3 \sum B_s + k_4 I^2$$

where $B_d(r, \theta, \phi)$ is the desired harmonic and the numerator of the first term is the summation of the squares of all other harmonics. L_t is the total inductance of the coil, B_s is the field outside the shield coil, I^2 is a power proportionate term and

$k_1 - k_n$ are the weighting factors. An arbitrary error function can be chosen by adjusting the weighting factors and thus duly influencing the properties of the coil structure. The hoops are then re-arranged by a random amount and the error function re-calculated. If the error function is smaller the re-arrangement is accepted. Positive error excursions are also accepted based on the pseudo-Boltzmann function $\exp(-dE/T)$, where dE is the change in the error function and T is a "temperature" variable. After a set number of re-arrangements T is lowered and the re-arranging continues until no more improvements can be made.

4. Results and Discussion

Coil designs for 5 harmonics (Z^0 to Z^4) were obtained. A maximum of 200 hoops per coil was set with the final positions and turns per position being dictated by the algorithm. In all of the coils shown the error function was an equal weighting of purity, inductance, and shielding. Run times for descent into a frozen state varied from 1 to 2 hours on a Sun SPARCstation 10. The inductance of all of the coils was $< 200 \mu\text{H}$. The primary radius was 50 mm and the secondary 70 mm and the total coil length restricted to 400 mm. The harmonics were calculated on a sphere of radius 32 mm and in all cases undesirable harmonics were less than 0.3% of the major harmonic. As we were able to include the zero order harmonic in our error function, the resultant zero order error is small, reducing the frequency shifts that occurs when using a Z^2 shim (for example) for homogeneity correction.

To test the validity of the design process a shielded Z^0 coil was built and tested. The coil has an inner radius of 50mm and an outer of 70 mm, the total coil length was 280 mm and 0.8 mm diameter enamelled copper wire was used for the prototype construction. The coil set's inductance was measured at 203 μH and its resistance at 3.7 Ω while the predicted values were 185 μH and 3.45 Ω . Figure 1 shows the first 20 contour of the resultant field at 0.01% contour interval normalized to the centre of the coil, where the sensitivity was $5e-5 \text{ T/A}$. At 1 cm outside the shield along the longitudinal axis of the coil, the ratio of the theoretical rms shielded/rms unshielded field was 1.8%, indicating excellent shielding (see Figure 2). The experimental ratio was 2.4%, indicating close correlation with theory. Experimental measurements were made with a 5 mm pick-up coil driven with a 1 kHz

sinusoidal waveform.

5. Conclusion

A new and versatile optimization process based on the simulated annealing of spherical harmonic errors has been presented and its application to longitudinal coils for NMR was shown to produce high quality designs. Further prototypes of the coils are in production for use in image-directed localized spectroscopy and the application of this methodology to the design of tesseral coils is being undertaken.

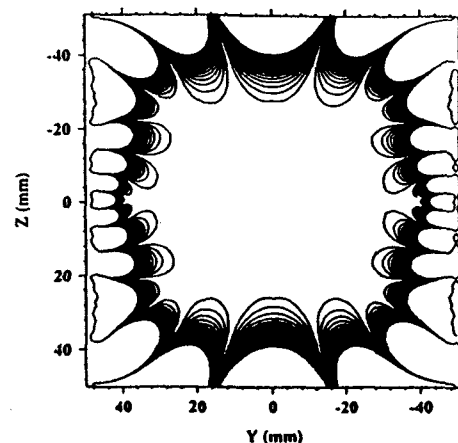


Figure 1. The shielded Z^0 homogeneity. Contours are at 0.01% intervals from central field value.

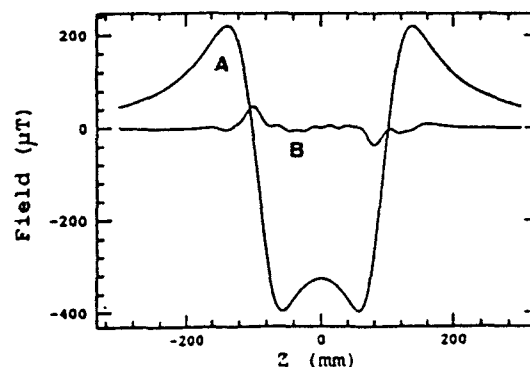


Figure 2. The axial unshielded (A) and shielded (B) fields 1 cm outside the Z^0 assembly.

- [1] Crozier S and Doddrell D M 1993 *J. Magn. Reson.* 103 354-57
- [2] Crozier S, Dodd S and Doddrell D M 1994 *IEEE Trans. Magn.* 30 1242-46
- [3] Crozier S, Forbes L K and Doddrell D M 1994 *J. Magn. Reson.* 10 126-28
- [4] Eccles C D, Crozier S, Westphal M and Doddrell D M 1993 *J. Magn. Reson.* 103 135-41
- [5] Kirkpatrick S, Gelatt C D and Vecchi M P 1983 *Science* 220 673-680

EPR Studies of Fe^{3+} Ion in Mg-doped LiNbO_3 Single Crystal*

T. H. Yeom,† S. H. Choh,‡ and S. H. Lee#

† Department of Physics, Seonam University, Namwon 590-170, Korea

‡ Department of Physics, Korea University, Seoul 136-701, Korea

Department of Physics, ChongJu University, CheongJu 360-764, Korea

I. Introduction

LiNbO_3 is an important material for many applications due to its physical and chemical properties.[1] However, laser-induced refractive index inhomogeneities, which have been labelled "optical damage", degrade the quality of the optical components based on LiNbO_3 . Particularly in the area of integrated optics these undesired effects strongly impede the utilization of LiNbO_3 crystal. It was reported that the addition of magnesium oxide to LiNbO_3 can raise the resistance against optical damage of the crystal by two orders of magnitude.[2] The enhanced photoconductivity was attributed to a greatly reduced trapping cross-section of Fe^{3+} for electrons, and the smaller trapping cross-section may be due to a changed substitutional site for Fe^{3+} . [3] The site of Fe seems to be an important factor for the susceptibility of LiNbO_3 to the laser-induced refractive index inhomogeneities.

At room temperature, the C_3 symmetry is characterized by a displacement of the Li^+ and Nb^{5+} along the c -axis.[4] Due to the displacement of the cations, both ions are surrounded by an octahedron of six oxygen ions (O^{2-}) distorted in a similar way. The stacking order of the octahedral sites along the c -axis is Li, Nb, structural vacancy (V_s), Li, Nb, V_s , and so on.

Transition metal and, to a lesser extent, rare earth dopant ions play an important role in most of the applications of LiNbO_3 . A number of studies have been performed on Fe^{3+} doped LiNbO_3 crystals.[5-11] But, only a few electron paramagnetic resonance (EPR) studies on Fe^{3+} in LiNbO_3 doped with Mg have been reported.

[12,13] According to refs. 12 and 13, two different sets of EPR spectra for Fe^{3+} in $\text{LiNbO}_3:\text{Mg}$ were obtained and their rotation patterns of $aa-$ ($xy-$) plane showed no angular variation. In our study, two sets of rotation pattern of Fe^{3+} ion in $\text{LiNbO}_3:\text{Mg}$ single crystal are obtained. One of them is angular independent, whereas, another set is angular dependent on the xy -plane. The Fe^{3+} center showing angular variation seems to be a new center with low local site symmetry by comparing with previous reports[12,13].

II. Experimental Aspects and Discussion

The crystallographic axes of the specimen were determined by the x-ray Laue method. An X-band Jeol spectrometer was employed to record the EPR spectra at room temperature. The rotation patterns of the resonance fields for Fe^{3+} ion (0.05 mol%) in $\text{LiNbO}_3:\text{Mg}$ (5 mol%) crystal were obtained on the $xy-$ (crystallographic $aa-$), $yz-$, and $zx-$ (crystallographic $ca-$) planes. Two sets of Fe^{3+} EPR spectra are obtained in these three mutually perpendicular planes. One set of them shows axially symmetric resonance fields on the $xy-$ ($aa-$) plane. The other displays asymmetric resonance fields on the xy -plane.

The Fe^{3+} ion has the electron configuration $3d^5$ and is an S-state ion with $S = 5/2$ and a basic level of ${}^6S_{5/2}$. The experimental results of the resonance fields for the set of axially symmetric spectra can be analyzed with the usual spin Hamiltonian with C_3 symmetry.[14]

EPR parameters for the symmetric set in the $aa-$ ($xy-$) and $ca-$ ($zx-$) planes at room temperature are calculated with the least square

fitting of the C_3 spin Hamiltonian. The obtained parameters are $g_{\parallel} = 2.006$, $g_{\perp} = 1.999$, $b_2^0 = 1650$, $b_4^0 = -38$, $b_4^3 = 2001$ and $b_4^{-3} = 1001$ in unit of 10^{-4}cm^{-1} . This center turned out to be the same Fe^{3+} center in LiNbO_3 crystal of refs. 5 and 11 as well as the usual Fe^{3+} center in $\text{LiNbO}_3:\text{Mg}$ of refs. 12 and 13. This usual Fe^{3+} center substitutes for Li^+ or Nb^{5+} which has the C_3 local site symmetry in $\text{LiNbO}_3:\text{Mg}$ single crystal.

The rotation pattern of Fe^{3+} EPR spectra for a new center on the aa -plane shows that the Fe^{3+} ion does not reside at an axially symmetric site. We consider here two possible sites of Fe^{3+} in Mg -doped crystal. The Fe^{3+} ion can have an oxygen vacancy (V_o) in its oxygen octahedron. ($\text{Fe}^{3+} - V_o$ complex center) There is also another possibility that the Fe^{3+} ion may have a Mg ion at the nearest cation site (Li^+ or Nb^{5+} or vacancy site) along the crystallographic c -axis. ($\text{Fe}^{3+} - \text{Mg}$ complex center) If this is the case, the Fe^{3+} ion may have the super-hyperfine interaction with ^{25}Mg nucleus, since ^{25}Mg has the nuclear spin $5/2$. However we have not observed any sign of super-hyperfine spectra of Fe^{3+} ion due to ^{25}Mg nucleus possibly due to its low natural abundance: 10.13 %. Some new Fe^{3+} centers which are different from the usual center in $\text{LiNbO}_3:\text{Mg}$ crystal were obtained by Feng et. al.[12] and Böker et. al.[13]. However their centers also have axial symmetry. Therefore our asymmetric Fe^{3+} center obtained with $\text{LiNbO}_3:\text{Mg}$ crystal turns out to be a new one.

III. Summary

Two sets of Fe^{3+} centers have been obtained in $\text{LiNbO}_3:\text{Mg}$ single crystal. EPR parameters for one with axial symmetry are similar to those previously reported Fe^{3+} center residing at the C_3 local site symmetry. The Fe^{3+} ion resides at axially symmetric Li^+ and/or Nb^{5+} site. However, the other Fe^{3+} center showing angular dependence in the aa - (or xy -) plane, is a new Fe^{3+} center different from previous reports in $\text{LiNbO}_3:\text{Mg}$ crystal. This implies that the new Fe^{3+} center is not at the C_3 local site symmetry. We tentatively propose that it may

be an $\text{Fe}^{3+} - V_o$ complex or $\text{Fe}^{3+} - \text{Mg}$ complex center.

* This work was supported by the KOSEF through the RCDAMP at Pusan National University (1994-97).

References

- [1] A. Räuber, in *Current Topics in Material Science* (Edited by E. Kaldis, North-Holland, Amsterdam, 1987). Vol. 1.
- [2] G.G. Zhong, J. Jin, and Z.K. Wu, Proc. 11th Int'l Quantum Electronics Conf. IEEE Cat. No. 80 CH1561-0, p. 631. (1980).
- [3] R. Gerson, J.F. Kirchhoff, L.E. Halliburton, and D.A. Bryan, J. Appl. Phys. **60**, 3553 (1986).
- [4] S.C. Abrahams, J.M. Reddy, and J.L. Bernstein, J. Phys. Chem. Solids **27**, 997, 1013, 1019 (1966).
- [5] M.D. Glinchuk, G.I. Malovichko, I.P. Bykov and V.G. Grachev, Ferroelectrics **92**, 477 (1989).
- [6] C.R.A. Catlow, A.V. Chadwick, M. Cole and S.M. Tomlinson, Radiation Effects and Defects in Solids **119**, 565 (1991).
- [7] C. Prieto and C. Zaldo, Solid State Commun. **83**, 819 (1992).
- [8] H. Söthe and J.M. Spaeth, J. Phys.: Condens. Matter **4**, 9901 (1992).
- [9] I.W. Park, S.H. Choh, K.J. Song, T.H. Yeom, and C. Rudowicz, J. Korean Phys. Soc. **26**, 168 (1993).
- [10] G.I. Malovichko, V.G. Grachev, O.F. Schirmer and B. Faust, J. Phys.: Condens. Matter **5**, 3971 (1993).
- [11] T.H. Yeom, S.H. Choh, Y.M. Chang and C. Rudowicz, Phys. Stat. Sol. (b), **185**, 409 (1994).
- [12] H. Feng, J. Wen, J. Wang, S. Han, and Y. Xu, J. Phys. Chem. Solids **51**, 397 (1990).
- [13] A. Böker, H. Donnerberg, O.F. Schirmer, and X. Feng, J. Phys.: Condens. Matter **2**, 6865 (1990).
- [14] S. A. Al'tshuler and B. M. Kozyrev, *Electron Paramagnetic Resonance in Compounds of Transition Elements*, (John Wiley & Son, New York, 1974), Chap. 3.

^{15}N NMR Spectroscopy in Phosphazene Compounds

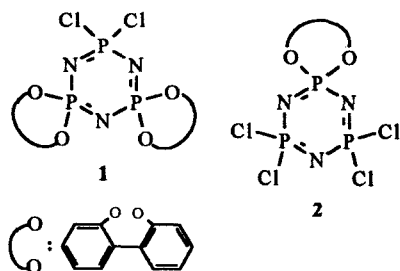
F. López-Ortiz* and E. Peláez-Arango

Universidad de Oviedo
 Instituto Universitario de Química Organometálica Enrique Moles,
 Unidad Asociada al CSIC
 33071 Oviedo, Spain

I. Introduction

^{15}N NMR spectroscopy of phosphorus-nitrogen compounds is an interesting tool that could be used to establish qualitative structure-reactivity relationships. Generally, ^{15}N characterization is readily achieved by indirect detection through proton. For λ^5 -phosphazenes with ^{15}N in natural abundance the method is inefficient because of the small value of $^nJ_{\text{NH}}$, if any. However, in phosphazenes the nitrogen is directly bonded to phosphorus, a highly receptive nucleus showing generally large coupling constants to ^{15}N . Therefore, the indirect detection scheme can be adapted so that the ^{31}P would act as a source of enhancement in the coherence transfer step as well as the probe during the acquisition period. In this way an increase of the signal to noise ratio of $(\gamma_{\text{P}}/\gamma_{\text{N}})^{5/2}$ over the direct nitrogen observation can be obtained.

We have previously applied the HMQC pulse sequence of Bax et al modified to include total proton decoupling to the ^{15}N characterization (J_{PN} , $\Delta^{15/14}\text{N}(^{31}\text{P})$ and $\delta(^{15}\text{N})$) of some phosphazeny derivatives (1).



Here we have extended the study to the cyclotriphosphazenes 1 and 2, two compounds currently used as models for the design of new polymeric materials (2).

II. Results

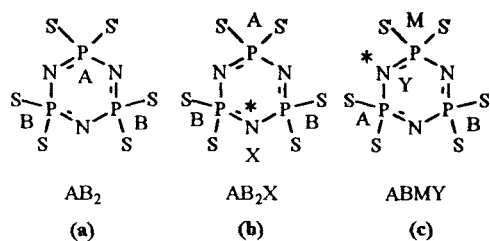
The method involves four steps:

- I) Analysis of the ^{31}P NMR spectrum to obtain $\delta(^{31}\text{P})$ and $^2J_{\text{PP}}$ (see table 1).

Table 1: ^{31}P NMR data of compounds 1 and 2.

Compound	$\delta(^{31}\text{P})$, ppm	$^2J_{\text{PP}}$, Hz
1	P(A), 29.66	79.4
	P(B), 19.96	
2	P(A), 13.15	72.5
	P(B), 24.91	

- II) Running the 1D ^{31}P , ^{15}N HMQC experiment to identify the ^{15}N satellites in the ^{31}P NMR spectrum. In simple cases this allows to extract ^{31}P , ^{15}N coupling constants and ^{15}N isotope induced shifts $^n\Delta^{15/14}\text{N}(^{31}\text{P})$, calculated as the frequency difference between the center of the ^{31}P , ^{15}N doublet and the residual signal corresponding to the parent phosphorus singlet. In cases where signals are overlapped a better resolution is obtained when the pulse sequence includes a refocusing period in order to perform ^{15}N decoupling during the acquisition.
- III) The ^{15}N chemical shifts are obtained from the 2D ^{31}P , ^{15}N HMQC correlation spectra.
- IV) The presence of ^{15}N in natural abundance in compounds 1 and 2 originates three isotopomers a-c as indicated in scheme 1. In all cases, the resulting spin systems are non first order and consequently, the experimental spectral parameters must be refined through simulation.



Scheme 1: $^{14/15}\text{N}$ isotopomers present in compounds 1-2. The ^{15}N isotope is marked with an asterisk.

The results obtained are summarized in table 2. The ^{15}N chemical shifts afforded by the 2D ^{31}P , ^{15}N correlation are straightforward assigned as follows: $\delta_{\text{N(X)}} = -312.0$ ppm; $\delta_{\text{N(Y)}} = -282.8$ ppm for 1 and $\delta_{\text{N(X)}} = -251.9$ ppm; $\delta_{\text{N(Y)}} = -277.8$ ppm for compound 2.

Table 2: ^{15}N NMR data of compounds 1 and 2.

Isotopomer	$^n J_{\text{PN}}$, Hz	$^n \Delta^{15/14}\text{N}(^{31}\text{P})$, ppb
1b	$^1 J_{\text{P(B)N(X)}}$, 12.2	$^1 \Delta_{\text{N(X)P(B)}}$, -19.1
1c	$^1 J_{\text{P(M)N(Y)}}$, -26.6	$^1 \Delta_{\text{N(Y)P(M)}}$, -21.6
1c	$^1 J_{\text{P(A)N(Y)}}$, 2.9	$^1 \Delta_{\text{N(Y)P(A)}}$, -30.8
2b	$^1 J_{\text{P(B)N(X)}}$, -33.4	$^1 \Delta_{\text{N(X)P(B)}}$, -21.6
2c	$^1 J_{\text{P(M)N(Y)}}$, 5.7	$^1 \Delta_{\text{N(Y)P(M)}}$, -18.5
2c	$^1 J_{\text{P(A)N(Y)}}$, -27.0	$^1 \Delta_{\text{N(Y)P(A)}}$, -24.7
2c	$^3 J_{\text{P(B)N(Y)}}$, +1.0	$^3 \Delta_{\text{N(Y)P(B)}}$, +6.2

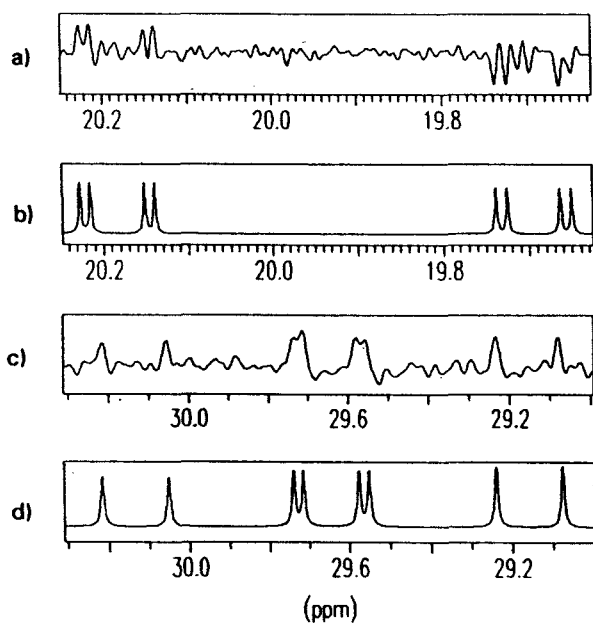


Figure 1: (a), (c) simulated and (b), (d) experimental N(Y) satellites of isotopomer 1c corresponding to P(M) and P(A/B), respectively.

In figure 1 are compared the experimental and simulated subspectra of the ^{15}N satellites corresponding to isotopomer 1c. The magnitude of $^1 J_{\text{P(A)N(Y)}} + ^3 J_{\text{P(B)N(Y)}} = 2.9$ Hz used in the simulation has been derived from the ^{15}N , ^{31}P INEPT spectrum of 1.

For compound 2 the ^{15}N , ^{31}P INEPT spectrum afford $^1 J_{\text{P(A)N(Y)}} + ^3 J_{\text{P(B)N(Y)}} = 26.0$ Hz. According to the literature (3) this value must be considered as the algebraic sum of a negative $^1 J_{\text{PN}}$ and a positive $^3 J_{\text{PN}}$. The magnitude of these coupling constants is derived from the simulated spectra. The best fit for P(A) and P(B) in isotopomer 2c is shown in figure 2.

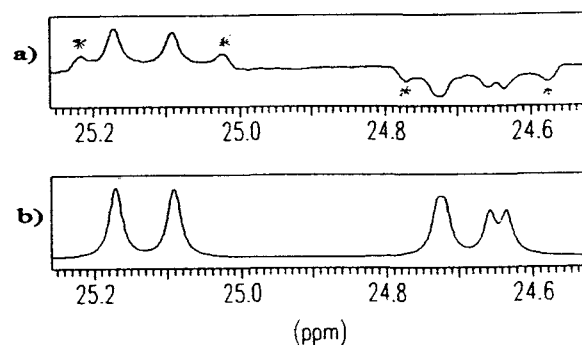


Figure 2: N(Y) satellites of P(A) and P(B) in isotopomer 2c. a) Simulated and b) experimental spectrum. Signals marked with an asterisk correspond to N(Y) coupled to P(M).

In summary ^{31}P , ^{15}N coupling constants, ^{15}N induced isotope shifts and ^{15}N chemical shifts of phosphorus-nitrogen compounds can be easily obtained by a combination of 1D and 2D ^{31}P , ^{15}N HMQC experiments. In complex cases, the data are refined by spectral simulation. In this way a positive $^3 \Delta^{15/14}\text{N}(^{31}\text{P})$ has been identified for the first time in cyclotriphosphazenes.

III. References

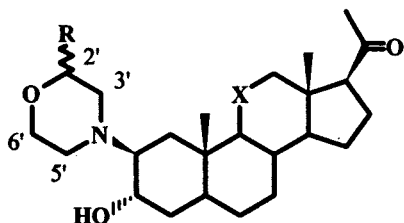
- ¹F. López-Ortiz, E. Peláez-Arango and P. Gómez-Elipé, submitted for publication.
- ²C. W. Allen, *Coord. Chem. Rev.* **130**, 137 (1994).
- ³B. Thomas, G. Grossmann and H. Meyer, *Phosphorus Sulfur* **10**, 375 (1981).

STEREOCHEMISTRY OF SOME ANAESTHETIC STEROIDS BY ^{13}C NMR

L. Fielding, N. Hamilton, R. McGuire, M. Maidment and A. C. Campbell.

AKZO-Nobel Pharma Division, Organon Laboratories Ltd.,
Newhouse, Lanarkshire, Scotland, ML1 5SH.Introduction.

A series of 2 β -amino-3 α -hydroxy-5 α -pregnan-20-ones where the amino group is a 2-alkylmorpholine (**III** to **X**) were synthesised from 2 α ,3 α -epoxy-5 α -pregnan-11,20-dione or 2 α ,3 α -epoxy-5 α -pregnan-20-one and the corresponding 2-alkyl morpholines [1]. Information about the stereochemistry (configuration) of some diastereomeric pairs of 2 β -(2-alkylmorpholinyl)-3 α -hydroxy-5 α -pregnanes was available from the ^{13}C chemical shifts of the C $_3'$ and C $_5'$ morpholine carbons. The compounds could be allocated to one group of *R* configuration at the 2-alkylmorpholine with C $_3'$ and C $_5'$ at around 52 and 51 ppm, and another group of *S* configuration with C $_3'$ and C $_5'$ at around 57 and 45 ppm.



	R		X
I	H		CO
II	H		CH ₂
III	CH ₃	<i>R</i>	CH ₂
IV	CH ₂ CH ₃	<i>R</i>	CH ₂
V	CH ₃	<i>R</i>	CO
VI	CH ₂ CH ₃	<i>R</i>	CO
VII	CH ₂ C ₆ H ₅	<i>R</i>	CO
VIII	CH ₂ CH ₃	<i>S</i>	CH ₂
IX	CH ₂ CH ₃	<i>S</i>	CO
X	CH ₂ C ₆ H ₅	<i>S</i>	CO

Discussion.

The ^{13}C NMR spectra of compounds **III** through **X** are simply that of the morpholine carbon signals superimposed on the spectrum of the steroid. It was noted that the ^{13}C chemical shifts of the 21 steroid carbons were identical (± 0.2 ppm) to those observed in the "parent" 2 β -morpholino-3 α -hydroxy-5 α -pregnan-11,20-dione (**I**) and 2 β -morpholino-3 α -hydroxy-5 α -pregnan-20-one (**II**), i.e. the 2-alkyl substituent has no significant impact on the steroid spectrum. The following patterns were noted from the ^{13}C chemical shifts of carbons in the 2-alkylmorpholine moiety of compounds **III** to **X**. The chemical shift of C $_2'$ was slightly dependent on the nature of the alkyl group (R), but not the stereochemistry of R, and the shift of C $_6'$ was essentially independent of either the nature or position of R. The chemical shifts of C $_3'$ and C $_5'$ were not dependent on the nature of the substituent, but they were strikingly dependent on its configuration. The C $_3'$ and C $_5'$ chemical shifts fell into two clearly defined groups. In one group, (**III**, **IV**, **V**, **VI** and **VII**) the shifts of C $_3'$ and C $_5'$ were in the range 51.9 ± 0.2 and 50.9 ± 0.8 ppm, and in the other group (**VIII**, **IX** and **X**) C $_3'$ and C $_5'$ were in the range 57.2 ± 0.6 and 45.1 ± 0.3 ppm. This grouping of ^{13}C chemical shifts must directly reflect the relative stereochemistry of the substituent R.

Although NMR experiments clearly distinguish pairs of diastereoisomers it is not a trivial problem to determine spectroscopically the absolute stereochemistry of these compounds.

It is known that all of the steroids described here exist in non-polar solvents with ring A in a twist-boat conformation and with an intramolecular hydrogen bond [2,3]. The hydrogen bond might be expected to act as a strong conformational lock and it might effectively prevent rotation of the morpholine moiety about the C₂-N bond. Molecular modelling of **III** revealed only one energetically favourable minimum and a deep and steep sided energy profile for rotation about the C₂-N bond. In the minimum energy conformation the mean plane of the morpholine ring (chair, with equatorial CH₃) is rotated approximately 90° to the mean plane of the steroid and one carbon of the morpholine pair C₃' and C₅' is approximately over the β face of the steroid and the other is approximately on the α side of the steroid. Whichever carbon is on the β face is sterically crowded because of the interactions of its geminal protons with the 1β and 3β protons of ring A. There are no bad contacts on the other side of the morpholine ring.

It is instructive to compare the observed ¹³C chemical shifts of the morpholine carbons, C₃' and C₅' in compounds **III** to **X** with those for "model" (non sterically hindered) N-alkyl-2-alkylmorpholines. In N-butyl-2-methylmorpholine and N-butyl-2-ethylmorpholine, C₃' and C₅' are at 59-61 and 53-54 ppm respectively [4]. We suggest that the steric crowding mentioned earlier is the cause of the difference between observed and model ¹³C chemical shifts, and the difference is also a solution to the absolute stereochemistry problem. The least sterically crowded carbons (C₃' or C₅' in **III** to **X**) will have ¹³C chemical shifts that most closely match those observed in the model compounds. An upfield shift of one of these carbons compared to the model compounds indicates steric crowding. It is now possible to see that the observed shift of C₃' in compounds **III**, **IV**, **V**, **VI** and **VII** are different to the model compounds, (approximately 8 ppm

upfield) but the observed shift of C₅' in that group match well with those observed in the model. In the other group of compounds, **VIII**, **IX** and **X**, the reverse is true. The observed shifts of C₃' match those of the non-hindered model and the shifts of C₅' appear approximately 8 ppm upfield. Hence in compounds **III**, **IV**, **V**, **VI** and **VII**, C₃' is located above the β face of the steroid. Inspection of a molecular model shows that in this configuration the absolute stereochemistry at C₂' is *R*. In the compounds **VIII**, **IX** and **X**, C₅' is above the β face and the absolute stereochemistry at C₂' is *S*.

Conclusion.

This simple NMR procedure is essentially a variation of the well known Mosher's ester methodology where the absolute configuration of a stereogenic centre is determined by coupling to a second chiral molecule to produce a diastereoisomer. In this work some of the pairs of diastereoisomer were unknowns. The method was validated by preparation of **III** from material of known stereochemistry.

The procedure should be applicable to determine the absolute stereochemistry of any 2-alkylmorpholine.

References.

1. European Patent Number 93309663.8
2. L. Fielding and G. Grant, *J. Am. Chem. Soc.*, **113**, 9785-9790 (1991).
3. L. Fielding and G. Grant, *J. Am. Chem. Soc.*, **115**, 1902-1907 (1993).
4. H. Schiefer, J. Berger, D. Scheller and G. Grossmann., *J. prakt. Chem.*, **328**, 797 (1986).

Trimethylammonium Group as a Relay to Control the Lipid Headgroup Dynamics by the Reorientation of Water Dipoles

Wen-guey Wu and Chang-Huain Hsieh

Institute of Life Sciences, National Tsing Hua University, Hsinchu, Taiwan 30043

Abstract : We report herein a reversible headgroup transition of hydrated dimyristoylphosphatidylcholine (DMPC) bilayers at temperature close to homogeneous nucleation temperature of ice formation ($T_H = -40^\circ\text{C}$), using ^2H NMR. The transition is attributed to a concerted change in the dynamic state of interbilayer water and trimethylammonium group in the headgroup region. This is evidenced by an abrupt change in the slope of the temperature dependent profiles of T_{2e} , spin-spin relaxation times measured by the two pulse echo, of the ^2H NMR signals from their respective deuterium-labeled molecular groups near -40°C . The headgroup transition of samples with lower hydration states exhibit lesser change in the dynamic states and have no significant effect on the transition temperature. The T_H values of water molecules in the interbilayer space and in the bulk are thus similar. The apparent activation energy and reorientation rate of the signal from water in the interbilayer space show that a significant population of water reorients with tetrahedral symmetry at subzero temperatures. This results in the rotation of the loosely bound trimethylammonium group. These observations, together with other hydration dependent studies of similar systems at room temperature, indicate that hydration affects the headgroup dynamics by modulating the electrostatic interactions at the trimethylammonium group.

Introduction : There has been a significant progress recently in the understanding of the molecular response of lipid headgroup at different hydration or electric charge in membranes.^{1,2,3,4} The ^2H NMR studies of selectively deuterium-labeled choline group at the liquid crystalline phase of membrane bilayers have revealed that an increase in hydration state or the presence of a positive charge at the membrane surface causes the N^+ end of the phosphocholine dipole to move toward the water layer; progress hydration, however, induces a concerted change in headgroup conformation together with an increase in its rate of motion.² Most models proposed to explain this effect emphasize on the conformational change near the phosphate segment.^{4,5} In the present communication we show that the reorientation of the interfacial water molecules affect the headgroup dynamics by modulating the electrostatic interactions at the trimethylammonium group. This conclusion is arrived at partially due to the fact that the molecular origin of a headgroup transition,⁶ detected close to homogeneous nucleation temperature of ice formation ($T_H = -40^\circ\text{C}$),⁷ for fully hydrated dimyristoylphosphatidylcholine (DMPC) bilayers is now identifiable.

Results and Discussion : Figure 1 shows ^{31}P and ^2H NMR spectra obtained from d_4 -DMPC and d_{13} -DMPC at a hydration state of 8 ± 2 water molecules per lipid. The spectra represent the dynamic states of three different regions, i.e., phosphate, methylene and trimethylammonium moiety of the PC headgroup at the indicated temperatures. All spectra were completely reversible during the heating and cooling mode within the experimental time span of several hours, regardless of the hydration states of the samples. The only irreversible signals were the ^2H NMR signals from $\text{D}_2\text{O}/\text{DMPC}$ samples with excess water (data not shown), suggesting that the bulk water molecules may be undercooled in the temperature range from 0°C to -40°C , the melting, T_M , and homogeneous nucleation, T_H , temperature of ice, respectively.

Two coexisting headgroup structures, one exhibiting only $-\text{CD}_3$ rotation and the other exhibiting both $-\text{CD}_3$ and $-\text{N}(\text{CD}_3)_3$ rotation as evidenced by the quadrupolar splitting of two coexisting NMR signals from $-\text{CD}_3$, are detected at temperatures below T_H .⁸ Since only a single type of NMR signal is obtained from the phosphate and methylene moiety below T_H , the results suggest that the trimethylammonium group is the most sensitive group at the PC headgroup. It further indicates that the mobility of trimethylammonium group in hydrated DMPC bilayers is somehow related to the mobility of interbilayer water molecules because the ^2H NMR signal representing static $-\text{N}(\text{CD}_3)_3$ group, as emphasized by the arrow shown in Fig. 1, disappears at temperatures above T_H .

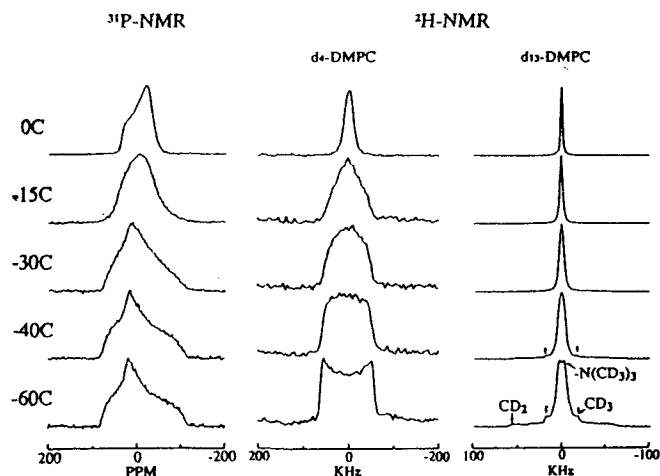


Fig. 1. Representative ^{31}P NMR and ^2H NMR spectra for deuterated DMPC with hydration state of 8 ± 2 water molecules per lipid.

Figure 2 shows the temperature dependent profiles of the apparent spin-spin relaxation time as measured by the two pulse echo (T_{2e}).^{9,10} It should be pointed out that although one single relaxation process can be used to describe the echo intensity decay for the ^2H NMR signals from interbilayer D_2O , at least two relaxation processes are required to account for those from d_{13} -DMPC, which consist of two superimposed components from the $-\text{CD}_2$ and $-\text{N}(\text{CD}_3)_3$ (data not shown). NMR signals of water molecules from the interbilayer space are identifiable because they are isotropic and their spin-lattice relaxation times are two order magnitudes lower than those from the bulk ice.⁶ Upon fitting the echo intensities, the relaxation times of methylene and trimethylammonium group, respectively, fall in the range of 30 -90 μsec and 200 -1500 μsec . The later values are similar to those from the water signals, suggesting that the reorientation rates of the trimethylammonium group are similar to those of the interbilayer water.

In Figure 2, we show that the detected reversible transition at the headgroup region originates from the dynamic change of the interbilayer water molecules near T_H . The detection of an abrupt change in the slope of the temperature dependent profiles of T_{2e} near T_H for lipid at high hydration state, but only a slight change for lipid at low hydration state (Fig. 2A), strongly suggests that the interbilayer water is mainly responsible for the dynamic change of the headgroup in PC bilayers. The activation energy as estimated from the slope of the T_{2e} temperature dependent profile of the water signal in the temperature range of -11 C to -40 C is about 13 Kcal/mol, which is comparable to the value of 13.5 Kcal/mol estimated previously from the dielectric relaxation and tetrahedral reorientation of water molecules of hexagonal ice at the temperature range of

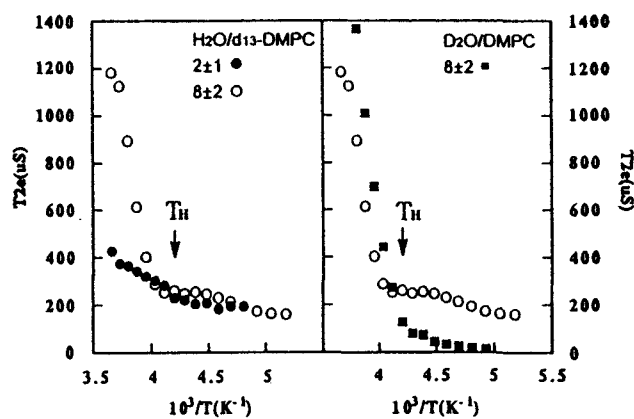


Fig. 2. Temperature dependence of the experimental ^2H NMR spin-spin relaxation times as measured by two pulse echo at magnetic field of 7.05 T.

T_M and T_H .^{11,12} The naturally occurring orientation defects responsible for the tetrahedral reorientation of water molecules in hexagonal ice are expected to be prevalent in the water layers between two membrane surfaces, although the close similarity in the T_H values of interbilayer water and bulk ice is rather surprising. Nevertheless, the reorientation of water dipoles near the membrane surface will change the dielectric constant at the interface and thus modulate the electrostatic interactions in the region. The loosely bound trimethylammonium group in bilayers may act as a relay controlled by the water dynamics.

Finally, we performed a study on the effect of hydration at room temperature. The spectra obtained at hydration state of 2 ± 1 water molecules per DMPC are comparable to those obtained at -40C for fully hydrated lipid bilayers (Fig. 1). At slightly higher water content of 4 ± 2 water per lipid, the most significant change in the spectra occurs at the trimethylammonium group. ^{31}P NMR spectra remained axially asymmetrical under identical condition. At hydration state of 5 to 6 water molecules per lipid, the ^{31}P NMR spectra changed to axially symmetrical pattern.¹³ Therefore, the initial change of the headgroup dynamics occurs at the trimethylammonium group rather than phosphate group, probably because the phosphate segment is also constrained by other hydrogen bonds near the headgroup region. Although this conclusion is drawn mainly from the studies at the gel phase, it is consistent with previous hydration dependent studies of POPC at the liquid crystalline phase. A change of the quadrupolar splittings of specifically deuterium-labeled PC headgroup was detected, while the ^{31}P chemical shift anisotropy remained the same.¹

Acknowledgement: This work was supported by National Science Council, Taiwan.

References:

1. Bechinger, B. & Seelig, J. *Chem. Phys. Lipids*. 1991, 58, 1-5
2. Ulrich, A.S. & Watts, A. *Biophys. J.* 1994, 66, 1441-1449
3. Roux, M., et al., *Biochemistry* 1989, 28, 2313-2321
4. Seelig, J., et al., *Biochemistry* 1987, 26, 7535-7541
5. Scherer, P.G. & Seelig, J. *Biochemistry* 1989, 28, 7720-7728
6. Wu, W., et al., *Biol. Chem.* 1991, 266, 13602-13606
7. Bronshteyn, V.L. & Steponkus, P.L. *Biophys. J.* 1993, 65, 1853-1865
8. Hsieh, C-H. & Wu, W. *Biophys. J.* 1995, in press
9. Pauls, K.P., et al., *Eur. J. Biophys.* 1985, 12, 1-11
10. Griffin, R.G. *Methods in Enzymology* 1981, 72, 108-174
11. Auty, R.P. & Cole, R.H. *J. Chem. Phys.* 1952, 20, 1309-1314
12. Wittebort, R.J., et al., *J. Am. Chem. Soc.* 1988, 110, 5668-5671
13. Griffin, R.G. *J. Am. Chem. Soc.* 1976, 98, 851-853

Bioactive Conformation of Stromelysin Inhibitors Determined by Transferred Nuclear Overhauser Effects

Nina C. Gonnella, Regine Bohacek, Xiaolu Zhang, István Kolossváry, C. Gregory Paris, Richard Melton, Cindy Winter, Shou-Ih Hu, and Vishwas Ganu

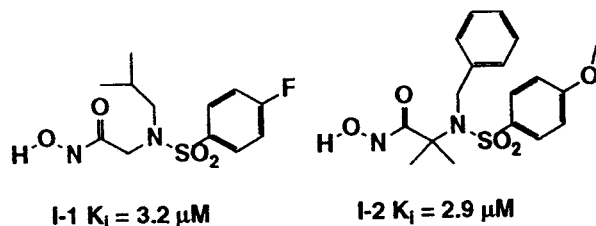
Research Department, Pharmaceutical Division, Ciba-Geigy Corporation, Summit, New Jersey 07901

Introduction:

Stromelysin-1 (SLN), a zinc metalloendopeptidase (MMP-3), is secreted by synoviocytes and articular chondrocytes in response to inflammatory mediators such as interleukin-1 (1). This enzyme is believed to cause the destruction of cartilage proteoglycans associated with osteo- and rheumatoid arthritis (2). Stromelysin has also been implicated in the enhancement of collagenase induced cartilage degradation (3). Currently there are no therapies available to treat cartilage degradation that occur in these arthritic diseases. Because of stromelysin's link to cartilage degradation, it is anticipated that the design of SLN inhibitors could result in the next major class of drugs for the treatment of arthritis.

As part of a rational drug design strategy, it is important to obtain structural knowledge of the enzyme-inhibitor complex. Most NMR methods which allow complete structure elucidation of an enzyme-inhibitor complex require significant amounts of enzyme as well as isotopic labeling of the enzyme or inhibitor (4,5). The transferred nuclear Overhauser effect (TR-NOE) however provides a different approach which focuses on the conformation of the inhibitor in the bound state. This experiment involves the generation of cross relaxation effects between two protons in the bound state which are subsequently transferred to the free state via chemical exchange (6). The technique has an advantage over other NMR methods in that it does not require large amounts of enzyme or expensive isotopic labeling.

Here we report the first enzyme-bound conformations of two hydroxamic acid stromelysin inhibitors, I-1 and I-2, which were obtained using the transferred nuclear Overhauser effect and 2D NMR spectroscopy.



Experimental:

Sample Preparation: Truncated rh-stromelysin (28-kDa) was cloned, expressed and isolated by modification of the procedure of Marcy et al. (7). The mature enzyme was prepared by incubating at 52°C (8). Concentration and exchange with deuterated buffer, containing 10 mM Tris_{d11}, 5 mM CaCl₂, 0.15M NaCl, 0.02% NaN₃, in D₂O with pD

adjusted to 7.6, yielded a final volume of 0.5 ml. Final molar concentrations were 0.025-0.070 mM.

The enzyme-inhibitor complex was prepared by dissolving 1 mg of inhibitor in 1 ml of D₂O. The solution was adjusted to pD 7.6 and dried on a SpeedVac system (Savant). The dried inhibitors were dissolved in 100 μl buffer and added to the concentrated enzyme solution. Final pD was 7.6 ± 0.1 .

NMR: The high resolution 1D and 2D ¹H-NMR experiments were performed at 500.13 MHz on a Bruker AMX FT-NMR spectrometer. All spectra were recorded at 30°C. NMR data were acquired in the pure phase absorption mode with time proportional phase incrementation (9,10). Proton resonance assignments were obtained from two-dimensional proton-proton chemical shift correlation (COSY) (11), nuclear Overhauser enhancement (NOESY) (12,13) and rotating frame Overhauser enhancement (ROESY) (14) spectroscopy. All NOE assignments were made using the NOESY experiment. Data processing was carried out on a Silicon Graphics 4D/35TG computer using the FELIX program (BIOSYM Technologies, Inc., San Diego, CA).

Molecular Modeling: A set of low energy conformations were generated by Monte Carlo/ Energy Minimization (MC/EM) techniques (15,16) using the MM2 force field (17). A program was written to identify all conformations that satisfied the NOE derived distance constraints.

Results and Discussion:

The TR-NOE experiment allows the determination of conformations of loosely bound enzyme inhibitors ($K_i \approx 10^{-3} - 10^{-6}$ M) (6). Hence two stromelysin inhibitors were chosen for study based on their structural interest and because of their weak binding characteristics. One dimensional spectra for the enzyme ligand complex showed a single set of broadened resonances and a slight change in the chemical shifts. This indicates a fast binding equilibrium between enzyme and inhibitor. Another very sensitive indication of ligand binding with the enzyme is a dramatic decrease in the spin lattice relaxation times on going from the free to the bound state. This finding was not unexpected in these experiments since slower diffusional motions will affect the spin relaxation (18)

Two dimensional NOE spectra were collected for each inhibitor in the presence of stromelysin. All NOE cross peaks were integrated and the corresponding interproton distances were calculated. Thirteen distance constraints were obtained for I-1 and eleven for I-2. The enzyme-bound conformations of each inhibitor were obtained by identifying all low energy conformers that satisfy the NOE distance constraints. The NOE derived

structures for the enzyme bound inhibitor are shown in figure 1.

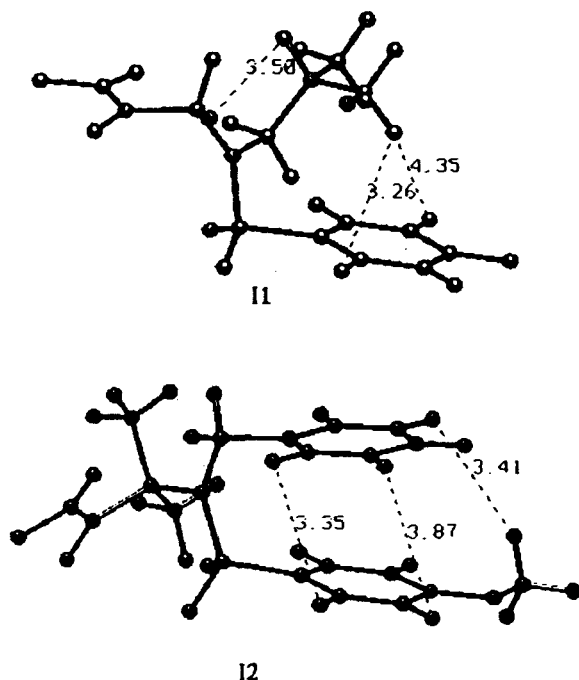


Figure 1. The bioactive conformations of I-1 and I-2 bound to stromelysin. Key distance constraints defining the conformations are displayed.

Since the mirror images or conformational enantiomers of these bound conformers will also satisfy the NOE constraints, the correct conformational enantiomers were identified based on comparison of these conformers with the conformation of a similar chiral inhibitor bound to stromelysin (Gonnella, N., *CIBA Geigy Corp.* unpublished data).

Experiments were carried out to determine the degree to which stromelysin bound conformers of I-1 and I-2 could be accommodated in the thermolysin binding pocket. The results showed that only the mirror image of I-1 docked reasonably well in thermolysin's active site. These results suggest that the shape and orientation of the S1' and S2' binding pockets (19) must be quite different for stromelysin relative to thermolysin in order to allow stromelysin to accommodate the enzyme-bound conformations of I-1 and I-2. This study shows that caution must be exercised when using an enzyme with similar binding characteristics for conformationally restricted drug design.

To exploit the utility of these structures as templates in the drug design process, the conformation of I-2 and a similar chiral inhibitor (unpublished data) were transformed into a 3D query for use in searching a MACCS-3D version of the Ciba Pharmaceuticals proprietary database (20). When this query was used to perform a conformationally-flexible search of the Ciba database, 23 compounds were identified for which stromelysin binding data existed. Of the 23 compounds identified, 5 exhibited SLN binding > 200 nM, 4 exhibited binding in the range

100 to 200 nM, and 14 exhibited binding < 100 nM. The high success rate of the 3D database search in identifying tight binding SLN inhibitors served to validate the concept as well as the query itself.

In conclusion, the first enzyme bound conformations of two hydroxamic acid stromelysin inhibitors have been determined using the transferred NOE technique. Comparisons of stromelysin inhibitors docked in thermolysin show that the S2' binding pocket possesses a significantly different shape in stromelysin as well as a different orientation of the S1' pocket relative to S2'. These studies have provided a conformationally restricted template for the design and structural modification of stromelysin inhibitors.

References:

1. G. Murphy, R.M. Hembry and J.J.Reynolds, *Collagen Relat. Res.* **6**, 351 (1986).
2. C. Flannery, M.W. Lark and J.D. Sandt *J. Biol. Chem.* **267**, 1008 (1992).
3. G. Murphy, M.I. Cockett, P.E. Stephens, B.J. Smith, and A.J.P. Docherty *Biochem. J.* **248**, 265 (1987).
4. G. Otting and K. Wuthrich, *Quarterly Rev. of Biophys.* **23**, 39 (1990).
5. A.M. Gronenborn and G.M. Clore *Anal. Chem.* **62**, 2 (1990).
6. G.M. Clore and A.M. Gronenborn *J. Mag. Reson.* **48**, 402 (1982).
7. A.I. Marcy, L.L. Eiberger, R. Harrison, H.K. Chan, N.I. Hutchinson, W.K. Hagmann, P.M. Cameron, D.A. Boulton and J.D. Hermes *Biochemistry* **30**, 6476 (1991).
8. P.A. Koklitis, G. Murphy, C. Sutton and S. Angal *Biochem. J.* **276**, 217 (1991).
9. A.G. Redfield and S.D. Kuntz *J. Magn. Reson.* **19**, 250 (1975).
10. D. Marion, and K. Wuthrich *Biochem. Biophys. Res. Commun.* **113**, 967 (1983).
11. W.P. Aue, E. Bartholdi and R.R. Ernst *J. Chem. Phys.* **64**, 2229 (1976).
12. J. Jeener, B.H. Meier, P. Bachmann and R.R. Ernst *J. Chem. Phys.* **71**, 4546 (1979).
13. S. Macura and R.R. Ernst *Mol. Phys.* **41**, 95 (1980).
14. A. Bax and D.G. Davis *J. Magn. Reson.* **63**, 207 (1985).
15. G. Chang, W.C. Guida and W.C. Still, *J. Am. Chem. Soc.* **111**, 4379 (1989).
16. F. Mohamadi, N.G.J. Richards, W.C. Guida, R. Liskamp, M. Lipton, C. Caufield, G. Chang. T. Hendrickson and W.C. Still, *J. Comp. Chem.*, **11**, 440 (1990). MacroModel 3.5 and BATCHMIN 3.5 were obtained from W.C. Still, Columbia U., NYC, 10027.
17. N.L. Allinger, *J. Am. Chem. Soc.* **99**, 8127 (1977).
18. T. Kushnir and G. Navon, *J. Mag. Reson.* **46**, 23 (1982).
19. I. Schechter, and A. Berger, *Biochem. Biophys. Res. Commun.* **27**, 157 (1967).
20. T.E. Mook, D.R. Henry, A.G. Ozkabak and M. Alamgir *J. Chem. Inf. Comput. Sci.* **34**, 184 (1994). MACCS-3D is available from MDL Info. Systems, Inc., 14600 Catalina Street, San Leandro, CA 94577.

Development of a solenoidal nanoliter-volume RF coil for NMR

A.G. Webb, D.L. Olson, T.L. Peck, J.V. Sweedler and R.L. Magin,

Magnetic Resonance Engineering Laboratory and School of Chemical Sciences,
University of Illinois at Urbana-Champaign, IL 61801.

Nuclear magnetic resonance (NMR) along with Fourier-transform infrared spectroscopy (FT-IR) and mass spectrometry (MS) are the three major spectroscopic methods used for the characterization of molecular structure and environment. NMR is particularly sophisticated since it allows full three-dimensional structure to be determined. Its major drawback, however, is its limited sensitivity. FT-IR commonly has limits of detection (LOD) in the 10^{-12} - 10^{-15} mole range, MS has achieved LODs of 10^{-18} moles, but NMR has LODs of 5×10^{-9} moles. Until recently, the only approach to increasing this sensitivity has been to move to higher static magnetic field strengths with the associated large cost increases. Even with this methodology, a large number of studies are precluded solely on the basis of limited mass available. One recent approach from commercial (Varian, Bruker) and academic institutions (1) has been to use high-temperature superconductor probes to increase the LOD by reducing the coil resistance, and therefore noise. Results have shown that sensitivity can be increased by up to one order of magnitude. We have taken an alternative approach of increasing the signal from mass limited samples by designing solenoidal microcoils. These coils have diameters 50-400 μm , and typical length 1 mm, giving sample volumes in the 5-50 nL range. It has been shown that as the coil dimensions become smaller, the B_1 per unit current (and hence signal intensity) becomes larger (2). This partially offsets the decrease in sample volume when working in this size regime. We have previously shown that capillary electrophoresis separations can be monitored on-line using such microcoils (3,4).

For small samples, whether for NMR spectroscopy or imaging, experiments usually use high static magnetic fields and small highly sensitive RF coils. The sensitivity of a coil is defined as the magnitude of B_1 produced by unit current flowing through the windings of the coil. Of the common RF coil geometries, the solenoid has the highest sensitivity. The on-axis sensitivity in the center of a multiturn solenoid is given by:

$$(B_1/i) = \frac{\mu_0 n}{d_{\text{coil}} \sqrt{1 + [h/d_{\text{coil}}]^2}} \quad [1]$$

where h is the coil height, d_{coil} is the coil diameter, and μ_0 is the permeability of free space. Sensitivity therefore varies inversely with coil diameter for coils where the height to diameter ratio is constant. Therefore, if the sample volume is reduced by a factor of eight, the SNR for a matched coil is reduced by a factor of four. Peck et al. (5) have explicitly shown the dependence of the SNR per unit volume on the microcoil diameter.

One of the challenges in microspectroscopy is to reduce the effects of magnetic susceptibility which broadens the lineshape and makes proton scalar coupling unobservable. The major effect arises from the proximity of the copper wire to the sample. Therefore we use a thick walled capillary to minimize these effects, albeit at the expense of the filling factor. Immersing the RF coil in a susceptibility matched fluid - Fluorinert (FC-43) further reduces this effect. The volume magnetic susceptibility of FC-43, measured with a Gouy balance, is within 2% of the value of copper. With this improvement we now routinely obtain linewidths of less than 1 Hz.

5 nL volume solenoidal microcoils are wound using 50 μm diameter copper wire (99.99% purity, coated with 3 μm polyurethane) around a capillary of o.d. 389 μm (with the 16 μm polyimide coating intact), i.d. 76.5 μm . Cyanoacrylate adhesive is used to hold the coil in place instead of epoxy as previously. The coil is wound past the number of desired turns, then glue is applied at points 17 turns apart. Excess turns are removed from each end. The polyurethane coating is removed using sulphuric acid. Susceptibility matched FC-43 surrounds the coil and the capillary tube. The capacitors used are 2.2 pF (fixed matching) and 1-30 pF variable.

A typical spectrum of 70% ethanol is shown in Figure 1, with a linewidth of 0.6 Hz. The coil used is 1 mm in length, 389 μm o.d. with a capillary i.d. of 77 μm .

The major aim is to improve the filling-factor from its current value of approximately 5% in order to increase our sensitivity. The use of zero-susceptibility wire will be the next step.

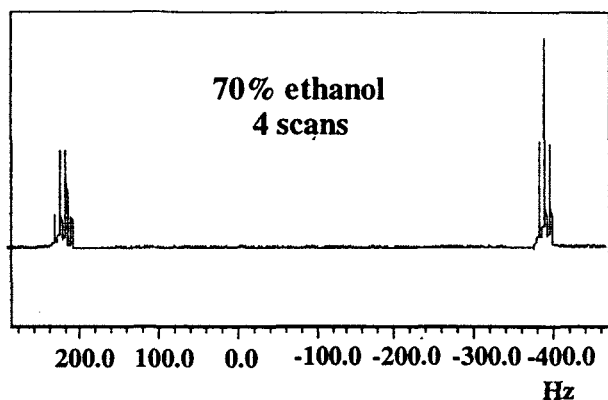


Figure 1.

High resolution spectra of nanomole quantities of biochemicals have also been achieved. Figure 2 shows a microcoil spectrum of *Aplysia californica* a-bag cell peptide 1-7, acquired from 3.0 μg (3.3 nmol) of sample. 256 signal averages are taken for a total data acquisition time of 12 mins.

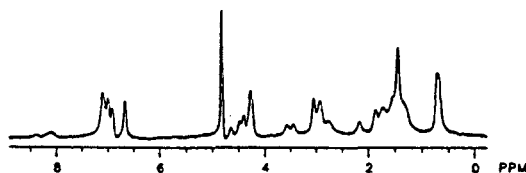


Figure 2

In order to compare the sensitivity of the microcoils to that of commercially available probes for mass limited samples, we used two solutions: arginine hydrochloride and sucrose, both in D_2O . Data for the microcoil and 5 mm spinning tube within a commercial 10 mm probe are compared on the same machine, a GN-300 WB spectrometer. We define the sensitivity enhancement to be the increase in signal-to-noise per mole of sample for the microcoil with respect to the commercial probe. The value obtained in both cases was 130 ± 5 . This corresponds to a time saving of over 10,000. The limits of detection (defined as a S/N of 3) were determined to be 34 ng (162 pmol) in 1 minute.

These nanoliter probes can also be used for on-line NMR detected microbore liquid chromatography. In this case we construct a 50 nL detector cell by wrapping a 355 μm diameter solenoid around a capillary with i.d. 250 μm . The length is 1 mm as previously. Figure 3 shows a two dimensional chromatogram of 67 mM alanine, 33 mM arginine,

35 mM lysine, 17 mM leucine-arginine and 11 mM oxytocin. Each NMR spectrum is 64 signal averages with a 60 ms interpulse delay.

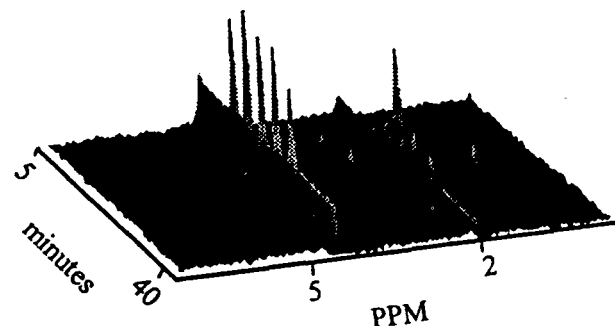


Figure 3

In conclusion, a high resolution detection cell has been developed for analysis of nanogram quantities of sample, with provides high resolution NMR data comparable to conventional systems. The improvements in sensitivity are roughly two orders of magnitude.

References.

1. R.D.Black, T.A.Early, P.B.Roemer, O.M. Mueller, A.Mogro-Campero, L.G.Turner and G.A.Johnson, *Science* 259, 793 (1993)
2. D.I.Hoult and R.E.Richards, *J.Magn.Reson.*, 24, 71 (1976).
3. N.Wu, T.L.Peck, A.G.Webb, R.L.Magin and J.V.Sweedler, *J.A.C.S.* 116, 7929 (1994).
4. N.Wu, T.L.Peck, A.G.Webb, R.L.Magin and J.V.Sweedler, *Anal.Chem.*, 64, 3864 (1994).
5. T.L.Peck, R.L.Magin and P.C.Lauterbur, *J.Magn.Reson.*, in press.

Acknowledgements.

The financial support of a David and Lucille Packard Fellowship, and a National Science Foundation National Young Investigator Award (JVS) are appreciated. Microseparations were carried out at the Biomedical Magnetic Resonance Laboratory at the University of Illinois which is supported by the National Institutes of Health Research Resource grant 1P1PR05964-01, and the Servants United Foundation.

Fluorine-based MRI agents for in-vivo temperature mapping

A.G. Webb

Magnetic Resonance Engineering Laboratory,
Beckman Institute for Advanced Science and Technology,
University of Illinois at Urbana-Champaign. IL 61801. USA

A number of proton MRI techniques have been developed to map temperature: the relevant parameters being the chemical shift of the water peak (1), the proton T_1 relaxation time (2), and the diffusion coefficient of the water protons in tissue (3). Liposome encapsulated cobalt complexes have also been shown to be effective *in-vivo* (4). The main advantages of the MRI techniques are their non-invasive character, and the high spatial and temporal resolution attainable. Using such MRI methods, the field of mapping temperature *in-vivo* has shown a recent rapid expansion. The proton based methods of mapping temperature are particularly suited to studies of muscle and other relatively stationary organs. The reticuloendothelial system (RES) in particular presents problems due to motion artifacts and local changes in magnetic susceptibility due to respiration.

Our new approach utilizes the magnetic resonance properties of solid/liquid phase transitions. Signal intensity is present when a compound is in the liquid phase and absent when it becomes solid. The key problem thus far has been the lack of a single fluorocarbon compound which combines high NMR signal intensity with a phase-transition temperature in a range relevant to, for example, hyperthermia studies. We have developed a mixture of compounds that has these desirable properties. Using sonochemical encapsulation, a fluorocarbon-hydrocarbon mixture, designed to melt at a specific temperature range, can be prepared and targeted to the RES.

Ultrasound irradiation at the interface of an aqueous protein solution and a non-polar liquid has been shown to produce proteinaceous microspheres at high concentrations with narrow size distributions (5). The protein forms a thin shell surrounding the encapsulated non-polar liquid. Microencapsulation was carried out using high-intensity ultrasound irradiation of a 1:2 (v/v) mixture of perfluorocarbon/hydrocarbon with 5% (w/v) aqueous BSA solution. The BSA solution was layered over the mixture at an initial temperature of 23°C and pH 7.0. With a titanium acoustic horn positioned at the organic-aqueous interface, the mixture was irradiated for 3 minutes at an acoustic power of approximately 150 W/cm². The microspheres remained as a suspension in the native protein solution. In order to separate the microspheres from the non-reacted protein, a centrifuge filter with a molecular weight cut-off of 100 kD was used. Centrifugation was done at 5000 G for 5 minutes, the microspheres were then resuspended in buffer. This

process was repeated five times. Particle size distribution was determined with an Elzone particle counter and confirmed by light microscopy. Analysis showed that the purified microspheres have a Gaussian-like size distribution with mean diameter $2.5 \pm 1 \mu\text{m}$.

The first mixture used contained 2-trifluoromethyl benzamide (m.p. 161-2°C) and methyl laurate (m.p. 4.3°C), combined in a molar ratio of 5.2:1. In-vitro imaging experiments have been carried out. 1 ml of the encapsulated mixture was heated to 44°C and allowed to cool in the magnet. Fluorine spectra were acquired every 10 seconds and correlated with temperature measurements from a fiber optic probe inserted into the sample. Figure 1(a) shows the decrease in signal intensity in going from the liquid to the solid phase, corresponding to a 20-fold decrease in signal intensity over a 7 degree temperature range.

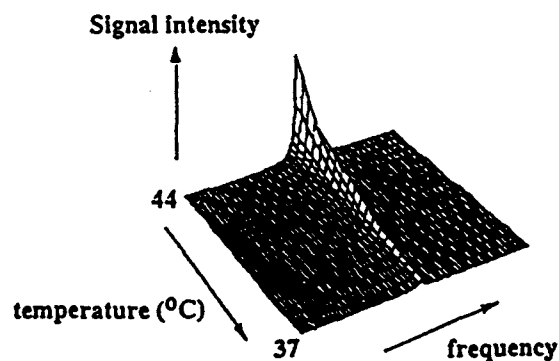


Figure 1(a)

A second mixture used consisted of poly(chlorotrifluoroethylene) (2 g, m.p. 58-60°C) and n-C₉F₂₀ (0.15 ml, b.p. 125-6°C) which were combined to give a mixture that melted in the range 45-50°C. Once encapsulated in the microspheres this fluorocarbon mixture was injected into the rat via the tail vein at a dose of 1ml/ 100g. After 30 minutes the rat was sacrificed and the liver excised. The liver was then heated with a 15 mm. diameter ceramic-filled surface contact microwave diathermy applicator (2.45 GHz, power rating 15W, Elmed Corporation). The change in the fluorine NMR signal intensity was monitored upon heating and subsequent cooling. As the core of the microsphere melts, the fluorine linewidth narrows and a substantial increase in signal-to-noise was observed. Figure 1(b) shows the fluorine signal intensity plotted as

a function of temperature, showing a reversible phase-transition upon heating and subsequent cooling.

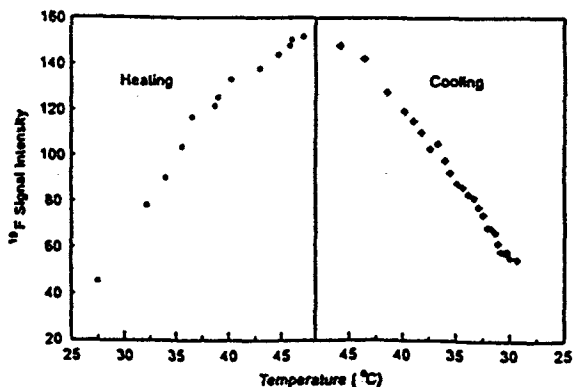


Figure 1(b)

Perfluorooctylbromide (PFOB) has been used as a blood-substitute, and as an imaging agent in MRI, ultrasound and CT. Here, we use the temperature dependent chemical shift of the CF_3 and terminal CF_2-Br groups to measure temperature. Figure 2 (a) shows the temperature dependence of the difference between the two chemical shifts.

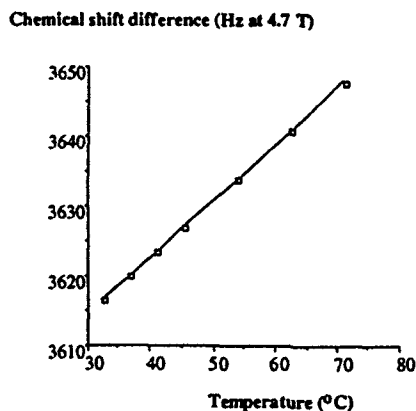


Figure 2(a)

The problem with temperature mapping techniques based on chemical shift changes is that an apparent thermal change can be induced by a change in the local magnetic susceptibility due to, for example, inhalation. A 10 Hz shift would correspond to an apparent 5°C change using the proton resonance frequency at 4.7 Tesla. However, by using the difference in chemical shifts of the two fluorine nuclei, the effects of susceptibility changes are cancelled out. In order to demonstrate this, a sample of PFOB was held at constant temperature, and the shim currents varied as a function of time to simulate changes in magnetic susceptibility. Figure 2(b) shows the built-in

compensation of measuring the difference in chemical shift rather than the absolute value.

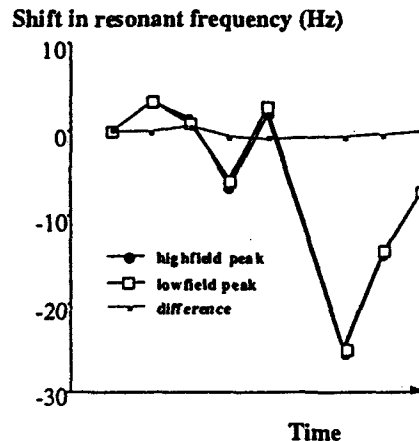


Figure 2(b)

Preliminary results have been obtained using focussed ultrasound heating of the liver. The PFOB is encapsulated as described previously and injected into the rat via the tail vein. After 5 minutes of CW ultrasound exposure the chemical shift of the PFOB indicated that the temperature rise within the liver was 2.0 ± 0.4 degrees Celsius. This was seen to return to normal upon cessation of heating. The acoustic power was independently determined in a water bath using a calibrated hydrophone. Theoretical results based on the acoustic power and beam shape using the monopole source solution for estimating tissue temperature gave a rise of 2.1 degrees Celsius based on steady state conditions.

This work was supported by the Whitaker Foundation. Magnetic resonance imaging experiments were carried out at the Biomedical Magnetic Resonance Laboratory at the University of Illinois which is supported by the NIH Research Resource grant 1P1PR05964-01, and the Servants United Foundation. The assistance of Professor Ken Suslick, Mike Wong, Nadine Smith and Ken Kolbeck is gratefully acknowledged.

1. De Poorter J., De Wagter C, De Deene Y., Thomsen C., Stahlberg F., and Achten E., *Magn.Reson.Med.*, 33, 74-81 (1995).
2. Parker D.L., *IEEE. Trans.Biomed.Eng.*, 31, 161-7 (1984).
3. Lebihan D., Delannoy J., and Levin R.L. *Radiology*, 171, 853-7 (1989).
4. Niesman M.R., Khoobehi B., Magin R.L. and Webb A.G., *J. Liposome Research*, 4(2), 741-68 (1994).
5. Suslick K.S. and Grinstaff M.W., *J.A.C.S.*, 112, 7807 (1990).

Use of ^{15}N NMR Peak Heights to measure Rate and Equilibrium Constants for Reactions of Platinum(II) Amine Complexes

Trevor G. Appleton and Kevin J. Barnham

Chemistry Department, The University of Queensland, Brisbane, Qld. 4072 Australia

1. Introduction

When N-donor ligands are highly enriched in ^{15}N (>98%), ^{15}N NMR spectroscopy is very useful for characterization of complexes in solution, and for qualitative monitoring of reactions of these complexes. This is because (1-4):

- (i) ^{15}N NMR lines are typically sharp, so that a separate line is usually resolved for each chemically distinct ^{15}N atom, with minimal problems from overlap.
- (ii) For a particular ligand and metal ion, δ_{N} depends primarily on the ligand *trans* to nitrogen, and especially on its donor atom.
- (iii) When the metal nucleus M couples with ^{15}N (e.g., M = ^{195}Pt , ^{103}Rh), $J_{\text{M-N}}$ also depends on the nature of the *trans* ligand, but in a different way to δ_{N} .

The pH dependence of δ_{N} or $J_{\text{M-N}}$ may be used to determine acid dissociation constants for water molecules also bound to the metal ion (5,6). For such applications, there is no need to measure peak intensities. However, if ^{15}N NMR is to be used to measure concentrations of species in solution, to obtain kinetic parameters or to measure equilibrium constants, it is necessary to use conditions under which ^{15}N peak intensities may be related to concentrations, as is commonplace with ^1H NMR.

2. Results

Because ^{15}N NMR lines are usually very sharp (width approx. 1 Hz), peak heights are usually more readily measured accurately than peak areas. It is then necessary to ensure that digital resolution is sufficient to allow peak heights to be measured reproducibly. For 20.2 MHz ^{15}N NMR spectra measured on a Bruker AC-200F spectrometer equipped with a 5 mm quadrupole probe

($^1\text{H}/^{13}\text{C}/^{15}\text{N}/^{19}\text{F}$), a spectrum width of 2000 Hz, with 64K data points (i.e., 16 points/Hz) gave reproducible results. Ratios of peak heights were always used in calculations, which minimized the effects of variations in instrument tuning.

Relaxation of ^{15}N nuclei is frequently very slow, and very dependent on the environment about nitrogen. In the compounds studied here, containing $^{15}\text{NH}_3$ or ^{15}N -substituted ethylenediamine(en), $\text{H}_2^{15}\text{NCH}_2\text{CH}_2^{15}\text{NH}_2$, bound to an inert metal ion, exchange of ^1H with solvent ^1H is slow on the NMR time scale, except in strongly alkaline solutions. Spectra are run in $^1\text{H}_2\text{O}$ (without lock) rather than in $^2\text{H}_2\text{O}$, because, in the deuterated solvent, slow replacement of ^1H bound to ^{15}N by ^2H might occur.

When ^{15}N is directly bound by protons, the magnitude of the nuclear Overhauser effect in a ^1H -decoupled ^{15}N NMR spectrum is probably always close to the maximum:

$$\text{nOe enhancement} = 1 + \gamma_{\text{H}}/2\gamma_{\text{N}} = -4.$$

The long acquisition times which result from the acquisition parameters used to ensure high digital resolution allow sufficient time for complete relaxation of the ^{15}N nuclei between pulses, counteracting the effects of any small differences in relaxation efficiency.

For ^{15}N nuclei directly bound to protons, much greater signal enhancement is possible with the use of the DEPT pulse sequence (7,8). This sequence is very useful in enhancing signal intensity in qualitative applications of ^{15}N NMR (3,8). For quantitative applications it may be used only under appropriate conditions. Because the number of protons directly bound to ^{15}N is used in determining the optimum proton pulse angle θ in the DEPT pulse sequence, DEPT cannot be used to measure concentrations of species with different

Table I: Ratios of rate constants for reactions of platinum(II) aqua complexes with guanosine.

B	C	k_B/k_C
$cis\text{-[Pt(NH}_3)_2(\text{H}_2\text{O})_2]^{2+}$	$cis\text{-[Pt(NH}_3)_2\text{Cl}(\text{H}_2\text{O})]^+$	5.1
$[\text{Pt}(\text{en})(\text{H}_2\text{O})_2]^{2+}$	$[\text{Pt}(\text{en})\text{Cl}(\text{H}_2\text{O})]^+$	4.4
$[\text{Pt}(\text{en})(\text{H}_2\text{O})_2]^{2+}$	$cis\text{-[Pt(NH}_3)_2(\text{H}_2\text{O})_2]^{2+}$	4.7
$[\text{Pt}(\text{tmen})(\text{H}_2\text{O})_2]^{2+}$	$[\text{Pt}(\text{tmen})\text{Cl}(\text{H}_2\text{O})]^+$	2.7
$[\text{Pt}(\text{en})(\text{H}_2\text{O})_2]^{2+}$	$[\text{Pt}(\text{tmen})(\text{H}_2\text{O})_2]^{2+}$	12.9
$trans\text{-[Pt(NH}_3)_2\text{Cl}(\text{H}_2\text{O})]^+$	$trans\text{-[Pt(NH}_3)_2(\text{H}_2\text{O})_2]^{2+}$	9.3
$cis\text{-[Pt(NH}_3)_2(\text{H}_2\text{O})_2]^{2+}$	$trans\text{-[Pt(NH}_3)_2(\text{H}_2\text{O})_2]^{2+}$	15.9

numbers of protons bound to ^{15}N . For example, it cannot be used to measure concentrations for coordinated $^{15}\text{NH}_3$ and free NH_4^+ ion in the same solution. Because the delay τ in the DEPT sequence depends on the value of $J(^{15}\text{N}-^1\text{H})$, DEPT cannot be used for quantitative applications when the value of this coupling constant varies. It depends on the nature of the ligand *trans* to ammine, for example, having the value 70 Hz when ammine is *trans* to another ammine and 50 Hz when ammine is *trans* to chloride. For *cis*-diammineplatinum(II) complexes, *cis*- $[\text{Pt}(^{15}\text{NH}_3)_2\text{XY}]$, $J(^{15}\text{N}-^1\text{H})$ varies, and DEPT spectra cannot be used reliable to determine concentrations from ^{15}N NMR peaks heights. For *trans*-analogues, $J(^{15}\text{N}-^1\text{H})$ is almost constant, and DEPT spectra can be used for such applications.

An example of the use of this technique is the study of reactions of the nucleoside guanosine with a variety of platinum(II) aqua complexes. In these reactions, guanosine displaces H_2O to bind to the metal through one of the nitrogen atoms (N_7). These reactions are too fast to obtain kinetic parameters directly from NMR measurements, but ratios of peak heights may easily be used to determine ratios of rate constants.

Consider the situation where a limited quantity of A is added to a solution containing a mixture of reagents B and C. Then the competing reactions occur, with rate constants k_B and k_C respectively:



If both of these reactions are second order, and proceed until all of A is consumed, it may be

shown (9) that

$$\ln(b_f/b_o) = (k_B/k_C)\ln(c_f/c_o)$$

where b_o and c_o are the initial concentrations of B and C and b_f , c_f are their final concentrations. The ratios of concentrations may be obtained from ratios of peak heights. Some results for reactions where A is guanosine are given in Table I, including for comparisons some complexes of N,N,N',N'-tetramethylethylenediamine (tmen) where ratios of ^{13}C peak heights from the methyl signals were used. These results will be discussed in detail elsewhere, but are affected by the trans effect order Cl , amine $\gg \text{H}_2\text{O}$, and by the steric hindrance order $\text{tmen} \gg cis\text{-}(\text{NH}_3)_2 > \text{en}$.

3. References

- ¹T. G. Appleton, J. R. Hall, and S. F. Ralph, *Inorg. Chem.* **24**, 4685 (1985).
- ²T. G. Appleton, J. R. Hall, and S. F. Ralph, *Inorg. Chem.* **27**, 4435 (1988).
- ³T. G. Appleton, D. R. Bedgood, and J. R. Hall, *Inorg. Chem.* **33**, 3834 (1994).
- ⁴R. E. Norman, J. D. Ranford, and P. J. Sadler, *Inorg. Chem.* **31**, 877 (1992).
- ⁵T. G. Appleton, J. R. Hall, S. F. Ralph, and C. S. M. Thompson **28**, 1989 (1989).
- ⁶S. J. Berners-Price, U. Frey, J. D. Ranford, and P. J. Sadler, *J. Am. Chem. Soc.* **115**, 8649 (1993).
- ⁷D. M. Doddrell, D. T. Pegg, and M. R. Bendall, *J. Magn. Reson.* **48**, 323 (1982).
- ⁸S. J. Berners-Price and P. W. Kuchel, *J. Inorg. Biochem.* **38**, 305 (1990).
- ⁹G. Pannetier and P. Souchay, "Chemical Kinetics", pp. 182-4, Elsevier, London 1967.

Chemical Shift Selective Flow Imaging: Applications in Membrane Filtration of Oil-water Emulsions

S. YAO, J. M. POPE* AND A. G. FANE#

School of Physics, #UNESCO Centre for Membrane Science and Technology,
The University of New South Wales, Sydney, NSW 2052, Australia

INTRODUCTION

Crossflow membrane filtration, employing a flow configuration in which the feedstock is fed parallel to the filtering membrane surface and perpendicular to the filtrate flow, is increasingly used for the separation and/or concentration of particulate suspensions, micro- and macro-solutes, bacteria and emulsion droplets. During the filtration process a higher concentration of retained particles, molecules or droplets (in comparison with that in the bulk of the feedstock) builds up at the membrane surface. This phenomenon is called *particle or concentration polarisation*. It has a very important influence on the economy of the filtration process because in general it limits or restricts the flow of permeate and results in an interaction between retained components and the membrane, which can give rise to membrane fouling. However, in many instances the factors influencing the distribution and fluidity of the concentration polarisation layers are still not yet clear due to lack of convincing non-invasive experimental results.

In a previous publication (1), chemical shift selective NMR imaging has been successfully used to obtain 2-D cross sectional images of the oil concentration polarisation layers in a multihollow fibre membrane module. In this paper, a chemical shift selective NMR flow imaging sequence using stimulated echos for data acquisition is presented. The sequence is used to investigate the fluidity of concentration polarisation layers formed from the oil droplets during crossflow membrane filtration of a 5 % (vol./vol.) emulsion made from a soluble cutting oil, using a tubular membrane module.

MATERIALS AND METHODS

The chemical shift selective flow imaging sequence, a phase sensitive flow imaging sequence (2,3) employing stimulated echos for signal acquisition (in order to facilitate measurement of slow flow rates) is shown in Fig. 1. The tubular membrane module used to study flow of the oil polarisation layers is shown schematically in Fig. 2. The length of the module was 40 cm, with an effective length for the membrane of 35 cm. The tubular membrane was an 'Acuriel' (polypropylene) membrane manufactured by Enca, with an average pore

size of 0.2-0.4 μm , inner diameter 5.2 mm and a wall thickness of approximately 1.65 mm. The glass tube forming the outer wall of the module had an outer diameter of 12 mm and a wall thickness of approximately 1 mm. The oil-water emulsion was fed into the lumen of the module at one end and removed from the other end, while the permeate was collected from the shell region between the membrane and the outer glass tube. The module had previously been used extensively to filter similar emulsions to those employed in the present study thus ensuring that it was always operating under 'well fouled' conditions. The oil-water emulsions were prepared from a soluble cutting oil (Caltex Trusol DD) containing a metallic petroleum sulphonate surfactant as emulsifying agent. This was mixed (5 % or 20 % vol./vol.) with distilled water doped with 0.6 mM CuSO_4 and shaken or stirred by hand to provide adequate mixing and dispersion of the oil. The average size of the oil droplets in the 5 % vol./vol. emulsion was $r=0.15\mu\text{m}$, obtained from light scattering measurement at a temperature of 25 °C.

RESULTS

The pulse sequence was first applied to a flow phantom comprising two standard 5 mm NMR tubes respectively containing stationary distilled water doped with 0.6 mM CuSO_4 and a stationary 20 % (vol./vol.) oil-water emulsion, together with a 2.5 mm i.d. glass tube through which was flowed a similar oil-water emulsion. When the emulsion was flowed through the tube, the 2-D velocity maps from the oil and water selective flow images gave peak velocities of 1.50 mm/s and 1.35 mm/s respectively. These compare with a value of 1.4 mm/s obtained from the gravimetrically measured volume flow rate on the assumption of laminar flow.

The pulse sequence was then applied to the tubular membrane filtration process, to investigate the fluidity of the oil polarisation layer. Fig. 3 presents (a) a conventional oil selective image after the filtration had reached steady state conditions showing the formation of the oil concentration polarisation layer at the inner surface of the membrane under operating conditions of trans-membrane pressure difference, 70 kPa and crossflow Reynolds number 500, and (b) the velocity map (stack plot) exhibiting a stationary oil layer after correcting for a constant offset due to eddy current effects. The experiments were then repeated with different crossflow Reynolds numbers over a range from 100 to 1000 (as the crossflow increases the thickness of the oil layer decreases and finally, when the Reynolds

*: Present Address: School of Physics, Queensland University of Technology, GPO Box 2434, Brisbane Qld 4001, Australia.

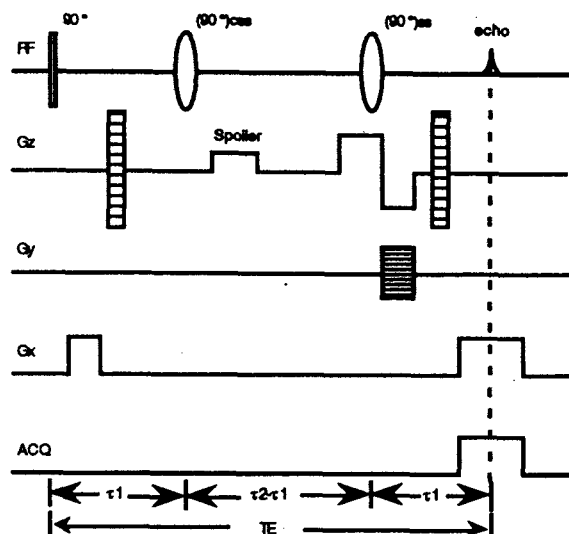


Fig. 1 Schematic diagram of the pulse sequence used for chemical shift selective flow imaging.

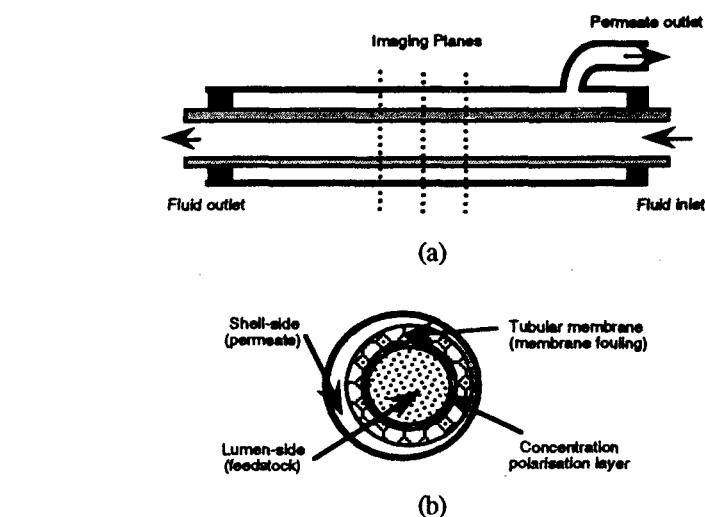
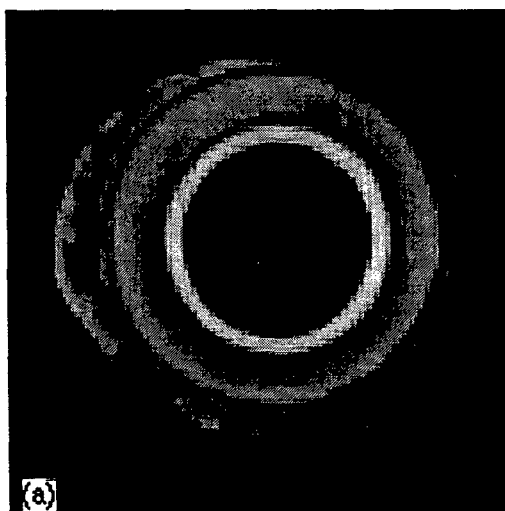


Fig. 2 Schematic diagram of the tubular membrane module used in this study. (a) A longitudinal section and (b) a cross section.

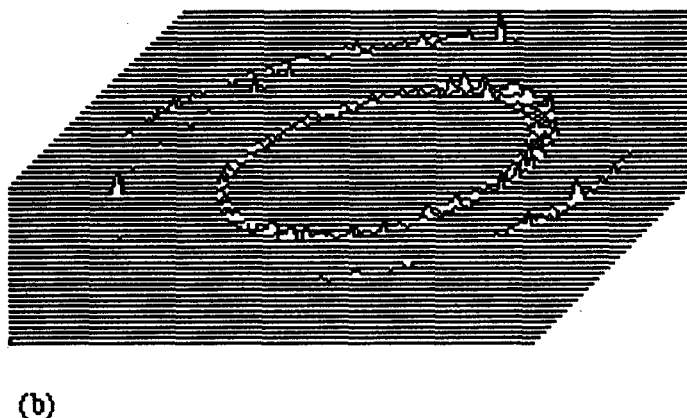


Fig. 3 (a) Cross-sectional oil selective image and (b) stack plot of the velocity distribution map from the tubular membrane filtration module.

number exceeds approximately 1000, the concentration polarisation layer becomes too thin to be measured). Similar results were obtained in all cases, setting an upper limit for the flow rate of the oil polarisation layers of $\leq 7.5 \mu\text{m/s}$ under these operating conditions.

CONCLUSIONS

1. By using the pulse sequence presented here, the velocity distributions or flow profiles of chemically distinct nuclear species may be monitored separately, which allows for optimisation of the dynamic range in the velocity dimension in each case.
2. By applying the sequence to the membrane filtration of oil water emulsions, an experimental investigation of the fluidity of the concentration polarisation layers can be carried out non-invasively.

3. The results suggest that, within experimental error of $\pm 7.5 \mu\text{m/sec}$, the oil droplets in the polarisation layer remained stationary over the range of operating conditions accessible to our measurements. This conclusion has implications both for a better understanding of the mechanisms of concentration polarisation and fouling, and for improved design of membrane filtration modules.

REFERENCES

1. S. Yao, M. Costello, A.G. Fane and J.M. Pope, *J. Membrane Sci.* **99**, 207 (1995)
2. P.T. Callaghan and Y. Xia, *J. Magn. Reson.* **91**, 326 (1991)
3. P.R. Moran, *Magn. Reson. Imag.* **1**, 197 (1982)

HIGH RESOLUTION PROTON MAGNETIC RESONANCE IMAGING IN EXPERIMENTAL ACUTE RENAL FAILURE

IA Leditschke^a, G Cowin^a, S Crozier^b, ZH Endre^a.

*Department of Medicine^a and Centre for Magnetic Resonance^b,
University of Queensland, Brisbane, Australia 4029.*

INTRODUCTION

High resolution proton magnetic resonance imaging allows the monitoring of anatomical changes and biochemical events in intact cells and tissues, and can be correlated with traditional indices of structure or function.

MR microscopy has been applied to the isolated perfused rat kidney (IPRK), allowing anatomical resolution not possible in vivo (increased magnetic field strength and elimination of respiratory artifact).

Previously the inversion-recovery gradient-echo FLASH sequence was found to be the most suitable for optimal anatomical resolution and image contrast (1, 2).

We have used the Rapid Acquisition with Relaxation Enhancement (RARE) sequence to image the IPRK, since this eliminates the susceptibility artifact inherent in the gradient-echo FLASH sequence.

METHODS

Right kidneys from 150g male Sprague Dawley rats were perfused with Krebs Henseleit Buffer with 6.5% albumin gassed continuously with 95%O₂/5%CO₂. Perfusion pressure and flow were continuously monitored.

The preparation stabilisation time of 30 minutes was used to position the kidney in a 20 mm NMR tube in the Bruker AMX 300 magnet. During perfusion the kidneys were immersed in a constant volume of outflowing perfusate using a special holder. Urine was collected by gravity flow via a ureteric catheter which allowed renal function to be measured if required.

Acquisitions of 20-40 minutes using standard RARE and inversion-recovery RARE sequences were obtained at 7.2 T, with 16 averages and a slice thickness of 0.7-1.5 mm. The in-plane resolution was 80 μ m.

After the acquisition of baseline images, ischaemia was induced and further images obtained both during ischaemia and after reperfusion.

RESULTS

Excellent cortico-medullary contrast was demonstrated using the above imaging sequences (Figure 1).



Figure 1.
¹H NMR micro-image of perfused rat kidney using the standard RARE sequence. Slice thickness was 1.5 mm, with 16 averages and a 35 minute acquisition.

The most visually acceptable images were those with bright cortex and some residual medullary intensity. These could be obtained using the inversion-recovery RARE sequence, where cortical versus medullary brightness could be modified using the gradient set-up parameters (Figure 2).

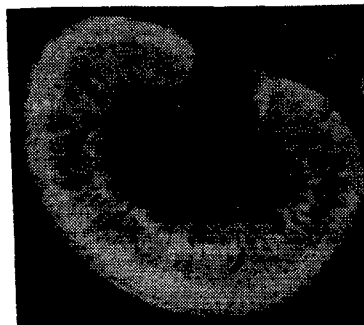
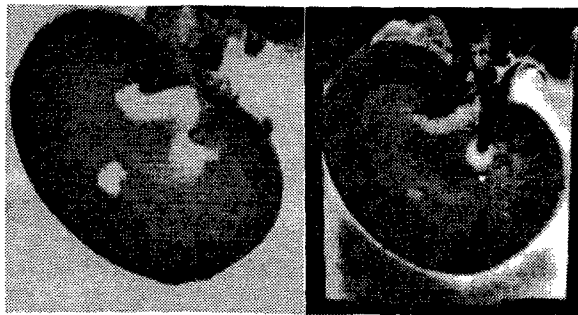


Figure 2.
¹H NMR micro-image of perfused rat kidney using the inversion-recovery RARE sequence, with a 30 minute acquisition. Parameters $t_0=1.8s$, G phase null.

The additional benefit of the inversion recovery pulse was that image brightness became heavily flow dependent. The images obtained in this way highlight the much higher

flows known to be present in renal cortex versus medulla.

Using standard RARE, post ischaemia images demonstrated a decrease in cortical intensity, disappearance of the medullary rays, and loss of the low flow medullary region between the vascular bundles (Figure 3).



(a) (b)
Figure 3. Standard RARE micro-images of perfused rat kidney (a) during ischaemia and (b) after reperfusion.

CONCLUSIONS

We conclude that these sequences are very useful for studying renal injury in intact kidney under controlled conditions.

The RARE and inversion-recovery RARE sequences may be more useful than FLASH, since susceptibility differences will not interfere with image quality.

Further work to elucidate the physiological, anatomical and biochemical events underlying the changes observed with ischaemia is in progress.

REFERENCES

1. ZH Endre, WE Hull, K-P Fichtner, W Kriz, U Werner, S Pomer, E Ritz. *Magnetic Resonance Imaging*. Submitted.
2. ZH Endre, K Solez. *Transplantation Reviews*. In Press.

T_2 Effects in PFG NMR Analysis of Ligand Binding to Macromolecules

A. J. Lennon, B. E. Chapman and P. W. Kuchel

Department of Biochemistry, University of Sydney, Sydney NSW, 2006, Australia.

Introduction

The dissociation constant, K_d , of a complex consisting of a ligand and a macromolecule can be estimated using pulsed field gradient (PFG) NMR measurements of the extrinsic diffusion coefficient, D , of the ligand. We have used this, so-called, two-site binding model to estimate the K_d of complexes of 2,3-bisphosphoglycerate (DPG) with the carbonmonoxy-, oxy- and deoxy-states of haemoglobin (Hb) in solution using ^{31}P PFG NMR measurements of the D of DPG [1]. The effects of transverse (T_2) relaxation on this initial analysis were not considered. Subsequent measurements of the T_2 relaxation time constants of the ^{31}P DPG resonances, in the presence of Hb, have however, suggested that T_2 relaxation needed to be incorporated in the analysis because the relaxation rates of the ^{31}P nuclei of the free and bound forms of DPG were significantly different thus resulting in a different fraction of the bound and free forms of DPG being observed in the NMR spin-echo signal.

DPG is the most abundant phosphorylated metabolite in many mammalian erythrocytes. In humans it occurs in approximately equimolar concentration (5 mM) with Hb [2]. The allosteric binding of DPG to Hb results in a dramatic decrease in the oxygen affinity of the Hb molecule and thus facilitates the delivery of oxygen to the tissues by erythrocytes. This effect, in humans, results from the ~100 times higher affinity of the deoxygenated form (deoxyHb) over the oxygenated form of the Hb molecule (HbO_2) for DPG [2].

We present here a refined analysis of the data which was obtained from PFG experiments involving DPG in Hb solutions and reported by Lennon *et al.* [1]. In the present analysis the effect of the different transverse relaxation rates of the bound and free forms of DPG was considered.

Theory

Molecular motion can be routinely measured using the PFG NMR method [3]. In solutions containing a ligand and a macromolecule (to which the ligand binds), the D of the ligand, measured by a PFG experiment, can be expressed as the sum of the values of D of the free and bound forms, weighted by the number fraction of the two forms:

$$D = D_b P_b + D_f (1 - P_b), \quad (1)$$

where D_b and D_f are the values of D of the bound and free form of the ligand, respectively, and P_b is the fraction of the total ligand population which is bound to the

macromolecule. An expression for P_b can be written in terms of K_d and the total ligand and macromolecule concentrations. Equation 1 represents a simple two-site binding model and was used to estimate the value of K_d of the HbCO, HbO₂ and deoxyHb complexes with DPG from a series of measurements of D of DPG (the ligand), obtained using different ligand concentrations, in the presence of a known concentration of Hb (the macromolecule) [1].

When the transverse relaxation rates of the nuclei in the bound and free forms of the ligand are sufficiently different and, when one or both of these rates are sufficiently rapid that the entire ligand population is not visible in the spectra of the PFG experiment, then the relative visibilities of the nuclei in the bound and free ligand need to be incorporated into Eq. 1 using,

$$D = \frac{D_b R_b P_b}{R_b P_b + R_f (1 - P_b)} + \frac{D_f R_f (1 - P_b)}{R_b P_b + R_f (1 - P_b)}, \quad (2)$$

where R_b and R_f are given by,

$$R_b = \exp\left[\frac{-2\tau}{T_{2b}}\right], \text{ and } R_f = \exp\left[\frac{-2\tau}{T_{2f}}\right], \quad (3)$$

where T_{2b} and T_{2f} are the T_2 values of the bound and free forms of the ligand, respectively, and τ is the SE delay, or transverse relaxation delay, used in the PFG NMR experiments.

Experimental

Haemoglobin solutions were prepared as described by Lennon *et al.* [1]. The D of DPG was measured in solutions containing HbCO, HbO₂ and deoxyHb for DPG concentrations ranging from 2.5 mM to ~80 mM using the PFG longitudinal eddy current delay (LED) pulse sequence [4]. The T_2 values of the 2P and 3P resonances of DPG (^{31}P nuclei attached to C2 and C3 of DPG, respectively) were also measured in these solutions as a function of DPG concentration (Fig. 1). The values of T_{2b} and T_{2f} for the ^{31}P DPG resonances were estimated from the asymptotic values of T_2 that were measured in the Hb solutions in which the DPG concentration was low and high, respectively (Table 1). The values of K_d of the HbCO, HbO₂ and deoxyHb complexes with DPG were then estimated using the simple two-site binding model (Eq. 1), and the two-site binding model that incorporated the effects of T_2 relaxation (Eqns 2 and 3). The results of these analyses are shown (Fig. 2) for HbO₂ and deoxyHb. The resulting estimates of K_d were

comparable to previously reported values obtained by more conventional means [5-7].

Conclusions

The effects of transverse relaxation need to be incorporated in the two-site binding model (by using Eqns 2 and 3) if the (T_2) relaxation rates of the nuclei in the bound and free forms of the ligand are sufficiently different, and the entire ligand population is not visible in the spin- or stimulated-echo spectra of the PFG experiment.

Estimates of the T_2 values of the free and bound forms (i.e., T_{2b} and T_{2f}) can be obtained from graphs of the T_2 values of the ligand resonance(s) which are measured as a function of ligand concentration (e.g., Fig. 1).

References

1. Lennon, A. J., Scott, N. R., Chapman, B. E. and Kuchel, P. W. (1994) *Biophys. J.*, **67**, 2096-2109.
2. Benesch, R. and Benesch, R. E. (1969) *Nature*, **221**, 618-622.
3. Stejskal, E. O. and Tanner, J. E. (1965) *J. Chem. Phys.*, **42**, 288-292.
4. Gibbs, S. J. and Johnson, C. S. (1991) *J. Magn. Reson.*, **93**, 395-402.
5. Berger, H., Jänig, G., Gerber, G., Ruckpaul, K. and Rapoport, S. M. (1973) *Eur. J. Biochem.*, **38**, 553-562.
6. Hamasaki, N. and Rose, Z. B. (1974) *J. Biol. Chem.*, **249**, 7896-7901.
7. Labotka, R. J. and Schwab, C. M. (1990) *Anal. Biochem.*, **191**, 376-383.

Table 1. Values for T_{2b} and T_{2f} averaged over the two ^{31}P resonances of DPG, and estimated from the values of T_2 that were measured in Hb solutions in which the DPG concentration was low and high, respectively (e.g., Fig. 1). The values of R_b and R_f were calculated using Eq. 3; the value of τ used for the PFGLED experiments was 15 ms.

Hb Ligand-State	T_{2b} (ms)	R_b	T_{2f} (ms)	R_f
HbCO	100±20	0.74±0.05	460±20	0.937±0.003
HbO ₂	100±20	0.74±0.05	485±20	0.940±0.003
DeoxyHb	120±20	0.80±0.03	530±20	0.945±0.003

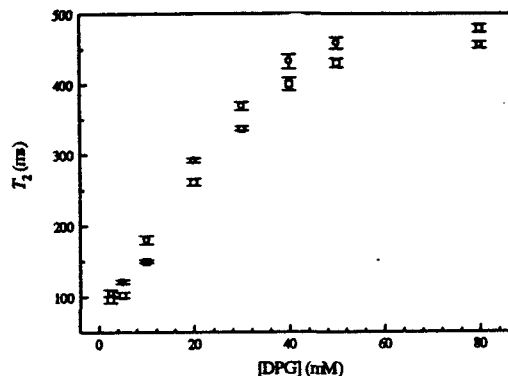


Figure 1. The T_2 of the 2P (O) and 3P (□) resonances of DPG in HbCO solutions ($[\text{Hb}] = 4.93 \pm 0.10$; $\text{pH} = 6.86 \pm 0.04$) as a function of DPG concentration at 25 °C.

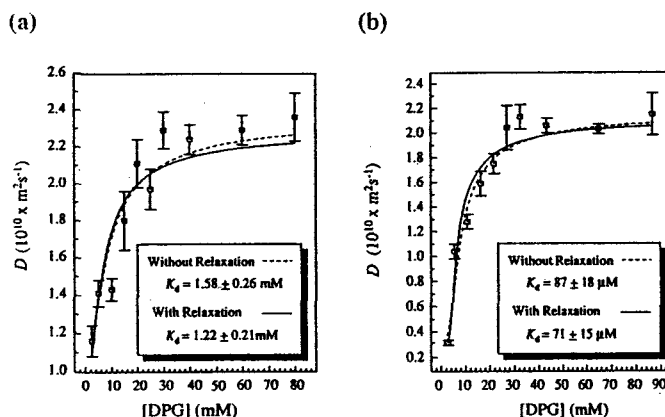


Figure 2. The D of DPG in HbO₂ (a) and deoxyHb (b) solutions as a function of DPG concentration. Each value of D was derived from a PFGLED experiment ($\tau = 15$ ms; $\delta = 12$ ms; $\Delta = 35$ ms) conducted at 25 °C. The Hb concentrations (mM) were 3.75 ± 0.09 and 4.0 ± 0.2 in (a) and (b), respectively. The mean pH was 6.90 ± 0.10 and 6.98 ± 0.15 for the HbO₂ and deoxyHb solutions, respectively. The dashed and solid curves resulted from nonlinear least-squares regression of Eq. 1 (simple two-site binding model) and Eq. 2 (two-site binding model including relaxation), respectively, onto the diffusion data. The resulting estimates of K_d are noted on the graphs.

Mercury-Polymer Interactions Characterised by ^{199}Hg -NMR

N. Onyewuenyi, J. Hook and G. Moran.
School of Chemistry, University of New South Wales, Sydney, NSW 2052, Australia

Mercury compounds such as mercury(II) nitrate play important roles in ecotoxicology [1]. A more detailed understanding of the molecular speciation and interactions of mercury within a system would be highly fruitful in providing information on transport and permeability in polymeric materials and cellular membranes.

Previous studies on aqueous mercury(II) nitrate [2] failed to show any dependence of the relaxation time, T_1 , on temperature. However, Kruger et al [2] reported temperature-dependence of the chemical shift. In this report, we show that there is a dependence of δ_{Hg} and T_1 on temperature (K) for $\text{Hg}(\text{NO}_3)_2$ solution and compare this behaviour with that of Hg(II) bound to a polymeric ionomer membrane, the perfluorosulfonate Nafion - Nafion- $\text{SO}_3\text{Hg}(\text{II})$ (Nafion- $\text{SO}_3\text{-Hg}^{2+}$).

$\text{Hg}(\text{NO}_3)_2$ was obtained from Adrich. Nafion membrane (m/eq. 0.91) was obtained from Du Pont. ^{199}Hg NMR measurements were made on a Bruker ACP 300 spectrometer, using a 10 mm broad band probe tuned to 53.72 MHz. No attempt was made to degas the Hg(II)-Nafion samples. About 1000 scans were accumulated to obtain a satisfactory signal-to-noise ratio for the aqueous solution of $\text{Hg}(\text{NO}_3)_2$ and the immobilised $\text{Hg}(\text{NO}_3)_2$ in the polymeric media.

The chemical shifts (δ) were measured as a function of pH, temperature and polymeric material. The chemical shift of each system was referenced to the external standard diphenyl mercury (-745ppm) in 1M CH_2Cl_2 and measured at 300 K [3] and were reproducible to ± 3 ppm.

The ^{199}Hg -NMR spectra of $\text{Hg}(\text{NO}_3)_2$ in solution and in Nafion membrane {Hg(II)-Nafion} at 300 K are shown in Figure 1. The sharp signal of ^{199}Hg of $\text{Hg}(\text{NO}_3)_2$ solution is broadened from 3 to 279 Hz in Hg(II)-polymer medium and spin-lattice relaxation time is changed from 14 s in solution to 179 ms in the Hg^{2+} -exchanged Nafion membrane

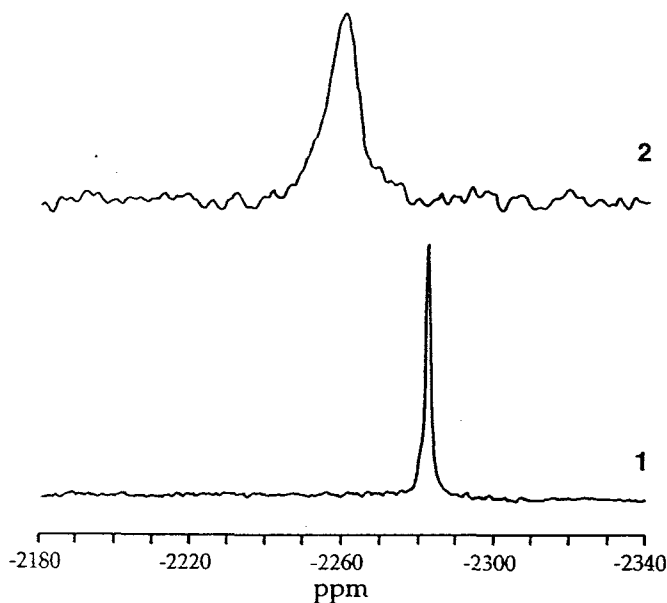


Figure 1:

^{199}Hg NMR spectra of $\text{Hg}(\text{NO}_3)_2$ in (1) aqueous solution and (2) Hg(II)-Nafion membrane at 300 K

The large ^{199}Hg line width of saturated Hg(II)-Nafion membrane as well as the shift in line position relative to that seen for aqueous $\text{Hg}(\text{NO}_3)_2$ are strong indicators that there is a significant interaction between Hg(II) ions and the polymer. The effect of temperature on the ^{199}Hg resonance of $\text{Hg}(\text{NO}_3)_2$ in Nafion polymer was studied in the temperature range 260-310 K. It was observed that line width increased with temperature.

When the spin-lattice relaxation time (T_1) was measured for ^{199}Hg in $\text{Hg}(\text{NO}_3)_2$ solution and Hg(II)-Nafion membrane as a function of temperature (cf Fig. 2), the observed temperature dependence indicates that the major operative spin-lattice mechanism is that due to the spin-rotation interaction (T_1 decreases with increasing temperature). Furthermore, the field dependence experiment of T_1 (^{199}Hg) at both 300 and 500 MHz field strengths gave almost identical relaxation times for both the $\text{Hg}(\text{NO}_3)_2$ solution and Hg(II)-Nafion membrane. This indicates that relaxation is dominated by the spin-rotation mechanism and that there was little or no contribution from chemical shift anisotropy (CSA).

It is noteworthy that T_1 of $\text{Hg}(\text{NO}_3)_2$ solution varied with concentration at 300 K

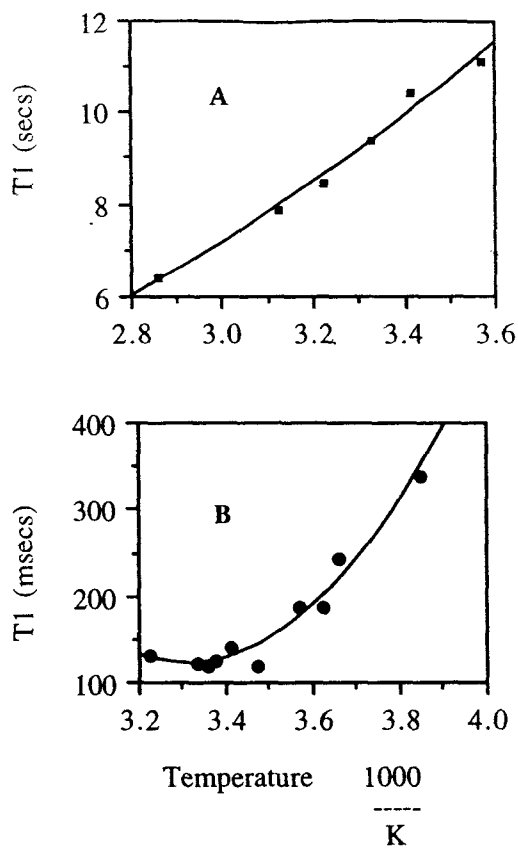


Figure 2:

Plots of T_1 (^{199}Hg) vs $1/T$ for Hg^{2+} in (A) 0.1 M $\text{Hg}(\text{NO}_3)_2$ solution and (B) Nafion membrane

It is clear from this work that ^{199}Hg NMR is a valuable tool for investigating mercury-polymer interaction that can be characterised by distinct changes in chemical shift, line width and relaxation.

Further investigations of the interaction of Hg^{2+} ions with polymeric materials such as sulfonated polystyrene and water-soluble poly(vinyl alcohol) are being undertaken in our laboratory and will be reported shortly.

References

- [1] Delnomdedieu, M.; Boudou, A.; Georgescauld, D. and E.J. Dufourc, *Chem. Biol. Interactions*, **81**, 243 (1992).
- [2] Kruger, H.; Lutz, O.; Nolle, A. and Schwench, *Z.Physik A* **273**, 325-330 (1975).
- [3] Kidd, R.G. and Goodfellow, R.J. In *NMR and the Periodic Table*; Harris, R.K; Mann, B.E, Eds.; Academic Press; London, 1978; Chapter 8

Spin Echo Measurements with Pulsed NMRON

W.D. Hutchison, N. Yazidjoglou and D.H. Chaplin

Department of Physics, University College, The University of New South Wales
Australian Defence Force Academy, Canberra, ACT 2600 Australia

I. Introduction

In nuclear magnetic resonance on oriented nuclei (NMRON), magnetic resonance of thermally oriented radioactive nuclei is detected via measurement of the variation in the anisotropic distribution of emitted radiation (normally γ -ray) occurring when a resonant radio-frequency (rf) field perturbs the nuclear Zeeman populations. Historically NMRON first developed (1) as an addition to the integral nuclear orientation technique with NMR greatly increasing the accuracy of measurements. To date, the technique has been predominately used to measure nuclear parameters (and associated hyperfine fields) of unstable nuclei in ferro-magnetic metal hosts. Indeed, with the experimentally demanding need for very low (milli-Kelvin) temperatures, NMRON has remained largely a specialist technique. However, radiative detection requires far less nuclei than conventional NMR (where nuclear precession is detected with an rf coil) and this advantage in sensitivity makes NMRON a powerful tool in some areas of condensed matter physics, particularly the study of very dilute alloys and/or essentially isolated impurity sites, and in the measurement of low dimensional magnetism.

The bulk of NMRON to be found in the literature has used the continuous wave technique. Pulsed NMRON pioneered in Canberra almost two decades ago (2) has not been as widely used. This is almost certainly because of the experimental complexity and the seemingly contradictory requirement of high power rf and milli-Kelvin temperatures. Nevertheless, pulsed NMRON does have a unique role. Not only have pulsed techniques enabled the location of some resonances in difficult systems (for example, with unfavourable spin lattice relaxation (SLR) (3)), but they enable studies of density matrix dynamics associated with the rank 2 (and 4) radiative detection (recent Canberra work including the oscillatory free induction decay (4) and the two pulse stimulated echo (5)), and relaxation studies of dilute impurity nuclear spins at milli-Kelvin temperatures (e.g. the UBC work on the insulating antiferromagnetic $^{54}\text{Mn-MnCl}_2 \cdot 4\text{H}_2\text{O}$ (6)).

For spin-spin relaxation (T_2) measurements in ferromagnetic metal hosts with pulsed NMRON, as with conventional NMR, the Hahn type spin echo may be used. In the NMRON case, a third 'read' pulse is required to rotate the spin echo coherence to the z-axis detection direction (2). (See (7) for a full summary of all pulsed NMRON techniques.) The early work (2,8) found that NMRON spin echoes in Fe hosts were extremely small (despite the most favourable rf enhancement) due largely to limitations on rf power compared with inhomogeneous magnetic broadening and skin effect attenuation/dephasing. Therefore T_2

measurements were frustrated by this lack of signal as well as the undetermined contribution of a perturbative electric quadrupole interaction (EQI) (at the impurity site in nominally cubic Fe hosts). The development of another transient NMRON technique, modulated adiabatic passage on oriented nuclei or MAPON (9), has since enabled precise measurement of the EQI. Now in this work, NMRON spin echo results clearly isolating the EQI contribution are shown and an unambiguous T_2 measurement is made. Four pulse 'stimulated' echo NMRON (10) has also been used to estimate the SLR rate for $^{60}\text{CoFe}$ at milliKelvin temperatures.

II. Experimental Details

For this work a $^{60}\text{CoFe}$ sample was prepared by thermal diffusion. The ^{60}Co activity was loaded onto the electropolished surface of an iron single crystal (cut along the (110) plane), from aqueous solution, dried, and then heated under an atmosphere of flowing hydrogen to 830°C for 5 minutes. After removal from the furnace the crystal surface was lightly etched to remove any undiffused activity. The remaining specimen activity was $24 \mu\text{Ci}$.

The $^{60}\text{CoFe}$ specimen was soldered to the copper cold finger of a dilution refrigerator with the applied field and the γ -detection direction along the surface (100) (easy axis) direction as previously identified by Laue back diffraction.

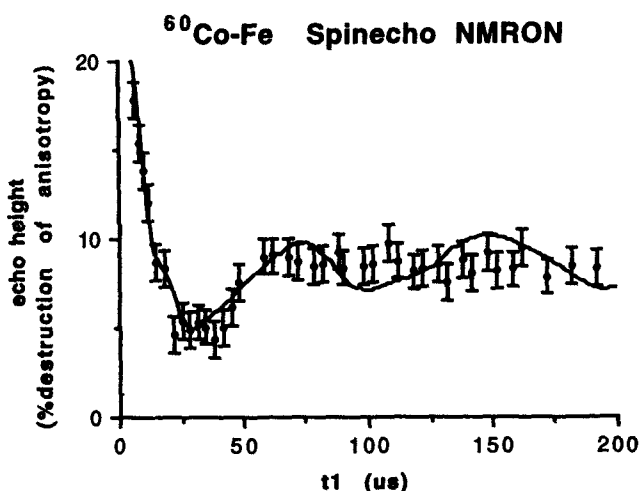


Figure 1 Spin echo amplitude for $^{60}\text{CoFe}$ with t_1 separation out to $200 \mu\text{s}$. Applied field was 0.3T , rf $1000 \text{V}_{\text{pp}}$ and all pulse widths $0.4 \mu\text{s}$. The solid line is a theoretical damped quadrupolar modulation for $^{60}\text{CoFe}$ (see text).

A pair of loops of copper wire generated the rf field perpendicular to the applied field and parallel to the specimen surface. Temperatures of ~ 8 mK were achieved during the measurements. A gated broad-band power amplifier was used to produce rf pulses of ~ 1000 V_{pp} (measured into 50 Ω load). For the results shown in this paper, with an applied field of 0.3 T, the rf frequency was 164.8 MHz. A HP Ge detector was used for the γ -ray counting, with the sum of the 1.17 and 1.33 MeV lines being presented.

III. Results and Discussion

Three pulse NMRON measurements on $^{60}\text{CoFe}$ are shown in Fig. 1 for the separation of the first and second pulses (t_1) out to 200 μs . In Fig. 1 the echo amplitude, which is the difference between 'on echo' (pulse separation $t_2 = t_1$) and 'off echo' ($t_2 = t_1 - 1.5 \mu\text{s}$), shows the first $\sim 3/4$ of a period of rapidly damped modulation before reaching a plateau at $t_1 = \sim 60 \mu\text{s}$. This result is the most convincing yet example for NMRON on ferromagnetic metals of EQI induced spin echo modulation as documented by Abe et. al. (11). The rapid damping of the echo modulation of Fig. 1 reflects the large spread of EQI's relative to the mode value of the distribution for $^{60}\text{CoFe}$. The solid line in Fig. 1 is a theoretical curve for a damped quadrupolar modulation obtained by averaging the formula of (11) (up to $2P/h$ term only) over a typical $^{60}\text{CoFe}$ EQI distribution as measured by MAPON (12), (EQI mode value $P/h = \frac{3eQV_{zz}}{4I(2I-1)\hbar} = +4.5(10)$ kHz and FWHM $\Delta P/h = 7.5(5)$ kHz). There is reasonable agreement between this curve and the experimental data (ignoring the small persistent artefactual oscillation in the theoretical curve resulting through the limited number of points available for the EQI integration). Since EQI distributions can vary significantly between individual nominally identical specimens even better agreement would result for spin echo and MAPON measurements done on the same specimen. The addition of higher frequency terms in the modulation formulation may also improve the fit. Further three pulse

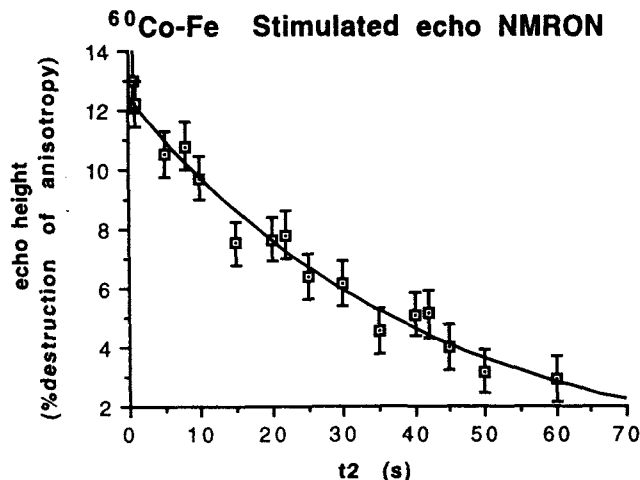


Figure 2 Stimulated echo amplitude for $^{60}\text{CoFe}$ with t_2 separation from 1 to 75 s. Applied field 0.3T, rf 1000 V_{pp}, all pulse widths 4 μs and $t_1 = 5 \mu\text{s}$.

spin echo measurements were made out to $t_1 = 200$ ms (not shown) with a resulting measurement of the relaxation constant $T_2 = 17(4)$ ms at ~ 8 mK.

Four pulse stimulated echo NMRON is presented in Fig. 2. Here the first pulse interval is $t_1 = 5 \mu\text{s}$, while t_2 varies from 1 to 70 s. ('On echo' $t_3 = t_1$ and 'off echo' $t_3 = t_1 - 1.5 \mu\text{s}$.) The data has been fitted with a single exponential curve to yield $T_1 = 40.3(7)$ s. This result is somewhat shorter than ~ 100 s expected for $^{60}\text{CoFe}$ at these temperatures as measured with non-resonant techniques (13) or by two pulse stimulated echo (5). Further work is therefore required to establish whether the SLR measured here relates to a particular starting population or may be specimen dependent.

IV. Acknowledgement

This work was supported by a grant from the Australian Research Council.

V. References

- ¹E. Matthias and R.J. Holliday, *Phys.Rev.Lett.*, **17**, 897 (1966).
- ²H.R. Foster, P. Cooke, D.H. Chaplin, P. Lynam and G.V.H. Wilson, *Phys.Rev.Lett.*, **38**, 1546 (1977).
- ³K.D. Bures, W.D. Brewer and G.V.H. Wilson, *Hyperfine Interact.*, **8**, 59 (1980).
- ⁴W.D. Hutchison, N. Yazidjoglou, D.J. Isbister, D.H. Chaplin and L.N. Shakhmuratova, *Hyperfine Interact.*, **80**, 1173 (1993).
- ⁵L.N. Shakhmuratova, W.D. Hutchison, D.J. Isbister and D.H. Chaplin, "Nutational Two-Pulse Stimulated Echo in Angular Distribution of γ -Radiation from Oriented Nuclei", to be published.
- ⁶M. Le Gros, A. Kotlicki and B.G. Turrell, *Hyperfine Interact.*, **77**, 131 (1993).
- ⁷D.H. Chaplin and G.V.H. Wilson, in "Low Temperature Nuclear Orientation", Ch.14, N.J. Stone and H. Postma (Eds.), Elsevier Science Publishers BV (1986).
- ⁸H.R. Foster, P. Cooke, D.H. Chaplin, P. Lynam, D.E. Swan and G.V.H. Wilson, *Hyperfine Interact.*, **4**, 357 (1978).
- ⁹P.T. Callaghan, P.J. Back and D.H. Chaplin, *Phys.Rev. B*, **37**, 4900 (1988).
- ¹⁰H.R. Foster, P. Cooke, D.H. Chaplin, P. Lynam, D.E. Swan and G.V.H. Wilson, *J. de Physique*, **39**, C6-1182 (1978).
- ¹¹H. Abe, H. Yasuoka and A. Hirai, *J.Phys.Soc. Japan*, **21**, 77 (1966).
- ¹²P.J. Back, Ph.D. thesis, The University of New South Wales (1988).
- ¹³E. Klein, in "Low Temperature Nuclear Orientation" Ch. 12, N.J. Stone and H. Postma (Eds.), Elsevier Science Publishers BV (1986).

OSCILLATORY FREE INDUCTION DECAY IN NMRON: THE EXTENSION OF THE THEOREM ON COHERENT TRANSIENTS FOR HIGHER RANK STATISTICAL TENSORS

D.H.Chaplin, L.N. Shakhmuratova, W.D. Hutchison and D.J. Isbister*
Department of Physics, University College, The University of New South Wales, ADFA,
Canberra ACT 2600, Australia

* Kazan State Pedagogical University, Kazan 420021, Russia

I. Introduction

The extension of the oscillatory free induction decay (OFID)[1,2] to the angular distribution of gamma radiation from thermally oriented nuclei has been extensively theoretically investigated and experimentally observed for the system $^{60}\text{CoFe}$. Preliminary calculations restricted to statistical tensors of rank $\lambda = 2$ and encouraging experimental data were first presented in [3,4]. In this paper the results of detailed comparisons of extended calculations to rank 4 with new experimental data are provided thereby establishing a new phenomenon in pulsed NMRON.

Pulsed NMRON and the associated coherent transient formation detected via gamma radiation are characterised by a substantial dependence on the geometry of experiment (GE). For multilevel spin systems, the dynamics of the higher rank statistical tensors (ST's) are displayed, in contrast to [1,2] where the dynamics of only the first rank ST's were investigated. In addition, for pulsed NMRON experiments on metals the skin-effect for metallic specimens containing the radioactive, gamma-emitting probe nuclei plays an important role in signal form and amplitude. For pulsed NMRON, population sensitive axial GE is utilised with an auxiliary read pulse transforming the transverse coherence (OFID) of the spin system onto the quantization axis; this results in two-pulse OFID signal formation as opposed to the conventional single pulse OFID.

2. Theoretical Results

The theoretical analysis of the ST's dynamics for rank $\lambda = 1, 2, 3, 4$ for two-pulse excitation, under severe inhomogeneous broadening, has been carried out by use of concatenation of perturbation factors (PF's)[5] to obtain the final PF G_{11}^{ω} for axial GE. An analytical study of the final PF under infinite inhomogeneous broadening ($R = \omega_1 / \Delta \rightarrow 0$, where ω_1 is the rf amplitude in angular frequency units and Δ is the HWHM of the inhomogeneously broadened line) by use of Laplace transforms demonstrates that the OFID duration is λ times the active pulse duration, which is supported by computing for finite values of R .

The onset of oscillations in the OFID signal also depends on the ST's rank λ starting when the active pulse area is $\omega_1 \Delta t_1 \geq 2\pi / \lambda$. For meaningful comparison with experiment the situation when the second pulse is not pure rotating but also participating in the OFID signal formation, the so called "soft" pulse case, is examined. It is demonstrated that under this condition the OFID duration is defined by λ times the sum of the two active pulses' duration (the second one of which is still necessary to examine the spin dynamics in the transverse plane using a longitudinal detector). The influence of the skin-effect on the duration and its very severe damping of the OFID in NMRON is investigated, the relevant dimensionless parameter being $W = d/\sigma$ [6]. Interesting effects of OFID signal "leakage" to longer durations with skin-effect are analysed in comparison with no skin effect; for example, assuming a pure rotating $\pi/2$ second pulse, the OFID signal duration for the second rank ST's is twice as long as the first pulse duration, whereas without skin effect it is, for pathological geometrical reasons, only of single pulse duration. Similar effects of "leakage" for higher rank ST's have been investigated.

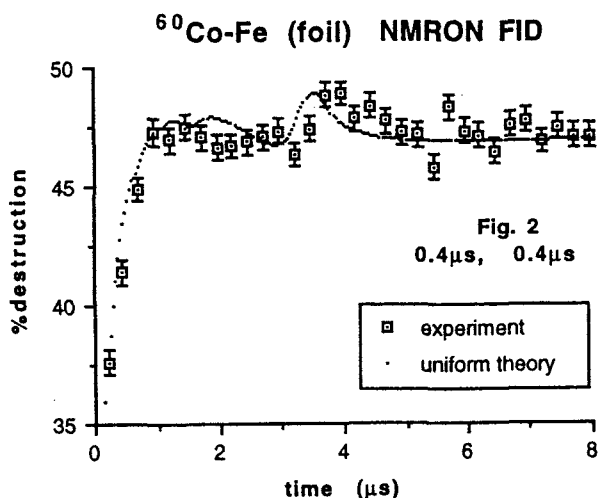
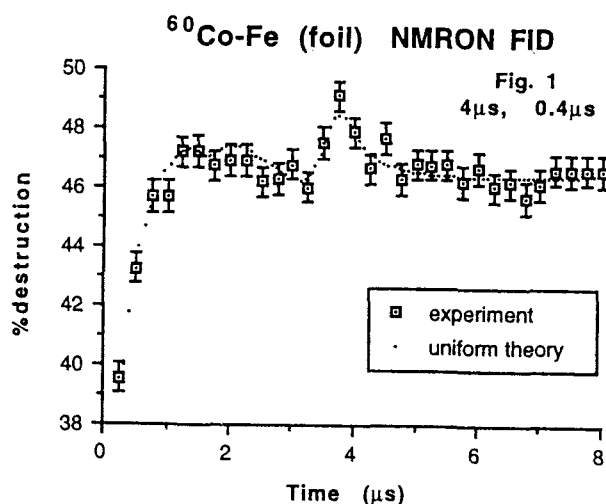
3. Experimental Results

Experimentally the OFID has been investigated for a variety of different pulse areas by varying the inter-pulse separation on a $0.5\mu\text{m}$ polycrystalline $^{60}\text{CoFe}$ sample, uniformly diffused with the ^{60}Co activity. The experiments were performed at -7mK in a field of 0.25T with constant RF amplitude of $1000\text{V pp}(50\Omega)$. Figure 1 and Figure 2 are for complementary unequal pulse widths of $4\mu\text{s}$ and $0.4\mu\text{s}$, and $0.4\mu\text{s}$ and $4\mu\text{s}$, respectively. Figure 3 shows the result for two very short pulses, each of $0.3\mu\text{s}$, falling below in pulse area the threshold for the onset of oscillations if there was no skin effect. Figure 4 shows the result for two long pulses each of $1.6\mu\text{s}$ where the oscillations are clearly present. Similar strong oscillations were observed for equal pulses of $1.2\mu\text{s}$ (not shown).

4. Discussion

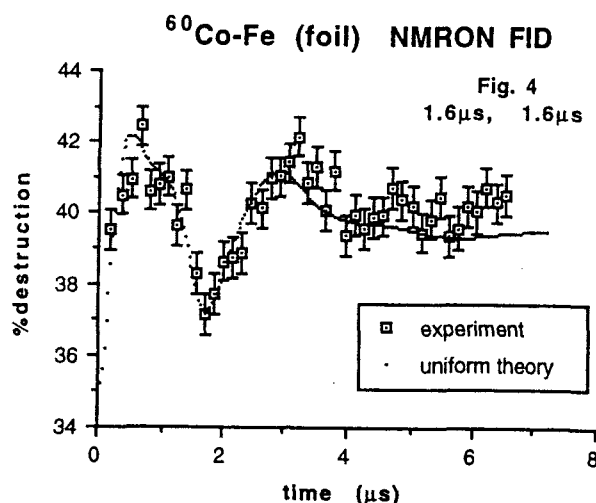
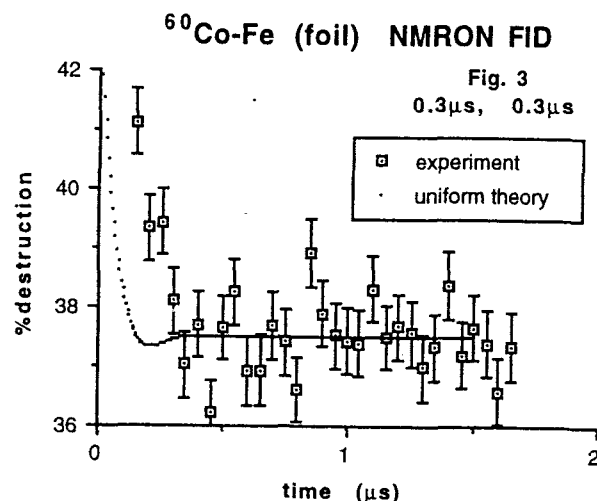
The theoretical fits are obtained for R and W values determined by independent single pulse nutational

experiments(not shown). For the shortest pulses in Figure 3 the relatively poor fit is due to pulse distortion. In Figure 1 the localised structure at a pulse separation equal to the first pulse width was at first conjectured[4] to be due to the fourth rank PF but additional computing demonstrates it is present for the second rank PF and is a very sensitive parameter to pulse width. It is likely to reflect the Larmor dephased spins during the first pulse application being partially refocussed by the inter-pulse interval and second pulse. In figure 2 the dephasing is more important in the inter-pulse interval than in the first short pulse, but this contributes as well, with the second pulse partially refocussing. The fact that the oscillations are virtually washed out(Fig 1) by the skin effect for unequal pulses one of which is clearly long enough to produce oscillations(for no skin effect), but present for two equal pulses of shorter length(Fig 4) suggests that the negative influence of the skin effect of the first pulse is largely compensated by a positive influence of the skin effect during the equal area second pulse.



5. Acknowledgements

This work was supported by a grant from the Australian Research Council. LNS acknowledges the support of DITARD and University College, UNSW, ADFA. The authors wish to acknowledge the assistance with the experiments by Dr N. Yazidjoglou.



6. References

1. A. Schenzle, N.C. Wong and R.G. Brewer, *Phys.Rev. A* 21, 887(1980); *ibid*, A 22, 635 (1980).
2. M. Kunitomo, T. Endo, S. Nakanishi and T. Hashi, *Phys. Lett.* 80A, 84(1980); *Phys. Rev. A* 25, 2235(1982). T. Endo, S. Nakanishi, T. Muramoto and T. Hashi, *Opt.Comm.* 37, 369 (1981).
3. L.N. Shakhmuratova, D.J. Isbister and D.H. Chaplin, *Hyp Int.* 80, 1167(1993).
4. W.D. Hutchison, N. Yazidjoglou, D.J. Isbister, D.H. Chaplin and L.N. Shakhmuratova, *Hyp.Int.* 80, 1173(1993).
5. L.N. Shakhmuratova, *Hyp.Int.* 23, 103(1985).
6. D.J. Isbister and D.H. Chaplin, *Z. Naturforsch* 45a, 43(1990).

**^7Li and ^{19}F NMR Study of LiCF_3SO_3 containing polymer electrolytes:
the effect of plasticizers**

M.C. Garcia, M.E. Smith and J.H. Strange

Department of Physics, University of Kent, Canterbury, Kent CT2 7NR, U.K.

M. Forsyth*, D.R. MacFarlane and S. Ng

Department of Materials Engineering* and Department of Chemistry,
Monash University, Wellington Rd., Clayton 3168, Australia

Introduction

Polymer electrolytes are ionically conducting solid phases formed by the dissolution of salts in ion-coordinating macromolecules. Such materials are considered as replacements for conventional low molecular weight liquid based electrolytes for practical electrochemical devices such as power sources, variable transmission windows and displays. A handicap of these materials is that the room temperature conductivity is still too low for the applications envisioned. Therefore an understanding of the mechanism for ionic transport in polymer electrolytes would help to increase the conductivity.

Recently, the addition of a second, low molecular weight solvent (plasticizer) has been used to improve the conductivity in many systems. The mechanism by which this component enhances the conductivity is still not clear. Certainly its effect in most cases is not limited to the traditional decrease in T_g , the temperature below which the polymer changes from the rubbery to the glassy state.

NMR represents a powerful tool for studying this transport mechanism since the relaxation rates of the ionic nuclei are closely related to molecular motion. Furthermore the fact that both ionic conducting species (Li^+ and CF_3SO_3^- in our case) contain nuclei with a magnetic moment permit the separate study of the ion-mobilities.

Experimental

1. Sample Preparation

The polymer investigated was a random copolymer of ethylene oxide and propylene oxide (3:1 mol ratio) of molecular weight 5000g/mol (referred to as 3PEG5000) and bearing three terminal OH groups per molecule.

Samples were prepared by adding the LiCF_3SO_3 (1 molal) and the desired concentration of plasticizer (dimethylformamide, DMF, and propylene carbonate, PC) to the dried, liquid polymer. To the resultant polymer solution was added a

stoichiometric amount of hexamethylene diisocyanate and a small amount of Thorcat 535 catalyst for the crosslinking.

Samples were cast into 10 mm glass tubes and were subsequently removed after crosslinking was complete.

2. NMR-Measurements

^7Li relaxation measurements were performed at 29.876 MHz on an upgraded Bruker CXP equipped with a superconducting magnet operating at 1.75T.

^{19}F relaxation measurements were carried out on a laboratory-built NMR spectrometer operating at 13.65 MHz equipped with a 0.34T permanent magnet.

Standard pulse sequences were used for relaxation measurements with T_1 determined by inversion recovery. Data were collected over the temperature range 140 to 345K.

Results and Discussion

In figure 1 the relaxation time T_1 for the different plasticizer concentrations has been plotted against the reduced temperature.

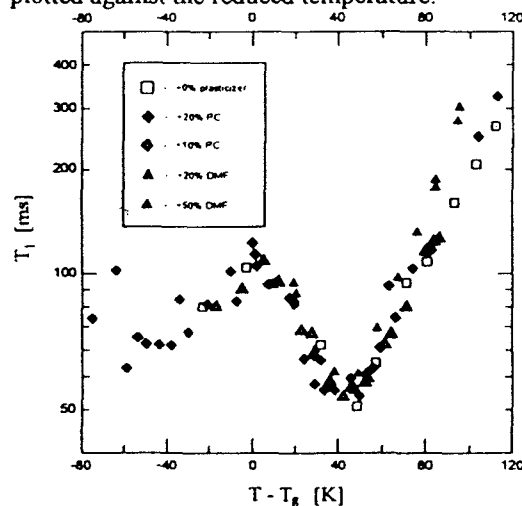


Figure 1. ^{19}F spin lattice relaxation time for different plasticizer concentrations as a function of the reduced temperature.

We can see, that for both plasticizers (DMF and PC), the increase in anion mobility by adding plasticizer corresponds rigorously to the decrease in T_g .

For a temperature below T_g all the samples show a decrease in T_g hinting at a second minimum. This effect can be explained as another relaxation mechanism taking over after the polymer chain motion freezes below T_g . A comparison of these results to a study of the pure salt carried out by Williams [1] indicates, that the first minimum is due to a homonuclear, intramolecular F-F dipolar interaction, whereas the second minimum corresponds to a lower Larmor frequency and must therefore be due to a heteronuclear interaction. This latter minimum is due to the F-H dipolar interaction modulated by the CF_3 rotation around the C-S-bond. However for higher temperatures, where the first minimum occurs, T_2 and PFG measurements have shown [2, 3], that the triflate ion or aggregate is undergoing substantial translational motion, which is responsible for the relaxation of the ^{19}F nuclei.

In the case of the Li relaxation time T_1 a plot against reduced temperature allows us to see, that the effect of either plasticizers, PC and DMF, on the cation mobility is not just related to the decrease in T_g (see figure 2).

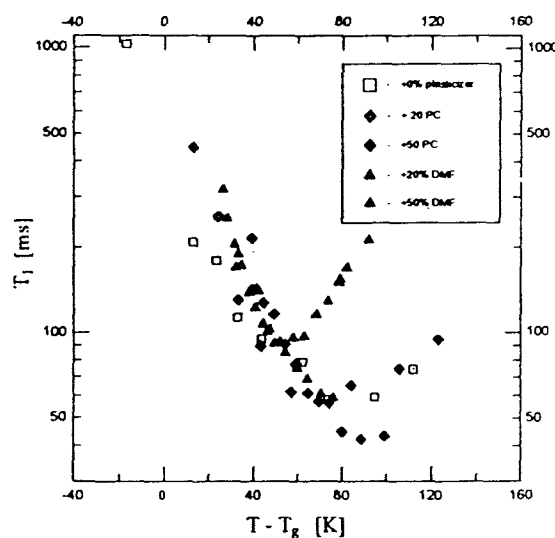


Figure 2. 7Li spin lattice relaxation time for different plasticizer concentrations as a function of the reduced temperature.

The DMF plasticizer causes the T_1 minimum to shift to lower temperatures, which means that the increase in mobility upon plasticizer addition is bigger for the cation than for the polymer. This is due to the fact, that the DMF solvates the Li ion and enables it to move faster. This also gives rise to an increase in the distance between the interacting nuclei, which leads to less effective relaxation. Therefore T_1 at the minimum becomes longer for the most plasticized sample.

Although PC like DMF causes a decrease in T_g , its effect on the microscopic cation mobility measured by NMR is opposite. PC, as a solvent of high dielectric constant, screens the Coulomb cation-anion interactions reducing in this way the number of ion pairs. Therefore the liberated cations are then more able to coordinate to the polymer oxygen atoms. This will explain the shorter relaxation time at the minimum upon PC addition. A greater cation-polymer interaction will restrict also the motions of both the polymer in the vicinity of the co-ordination site and the cation. That this restriction of mobility of the Li ions and also the polymer segments does not play a large role in the overall effect of plasticizer on T_g is a reflection of the fact that the T_g of the plasticized system is a result of the combined motional properties of all the components.

Conclusion

The incorporation of dimethylformamide (DMF) and propylene carbonate (PC) plasticizers results in a shift of the T_1 minima for both nuclei to lower temperatures indicating an increasing mobility consistent with a decreasing T_g and higher conductivity. Both plasticizers enhance the anion mobility indirectly by increasing the segmental motion, whereas the effect on the cation varies with plasticizer and it is not merely determined by the change in T_g .

References

- [1] Williams M A K, (1994) *PhD thesis*, Open University, U.K.
- [2] Forsyth M, MacFarlane D R, Meakin P, Smith M E and Bastow T J 4th International Conference on Polymer Electrolytes, *Electrochim. Acta* in press
- [3] Ali F, Forsyth M, Garcia M C, Smith M E and Strange J H, *Solid state NMR* in press

Paramagnetic Ion Relaxation in Rare-earth Doped Phosphate Glasses via ^{31}P NMR

I.P. Goudemond, J.M. Keartland, M.J.R. Hoch,
Department of Physics, University of the Witwatersrand, Johannesburg, South Africa
 H.B. Senin and G.A. Saunders
School of Physics, University of Bath, U.K.

Phosphate glasses doped with high concentrations of rare earth ions are important in laser technology. In the present work we have used ^{31}P NMR to investigate the stable metaphosphate systems $(\text{R}_2\text{O}_3)_x(\text{La}_2\text{O}_3)_{25-x}(\text{P}_2\text{O}_5)$ with $\text{R} \equiv \text{Nd}^{3+}$ and Gd^{3+} for $x = 0.01, 0.06$ and 0.25 . Measurements of the ^{31}P relaxation times, T_1 , and linewidths have been made over the temperature range 3K - 300K. The NMR lines are inhomogeneously broadened by the paramagnetic ions with the degree of broadening, and the nuclear T_1 , depending on the correlation time of the ions. A model has been developed to interpret the results incorporating ideas which have previously been applied to dilute systems. Spin-lattice relaxation processes are found to dominate in determining the correlation time of the rare-earth ions. For Nd^{3+} , where crystal field effects are important, direct, Raman and Orbach processes are found while for Gd^{3+} only direct and two phonon processes occur. Measurements carried out on a sample doped with 1% Nd^{3+} are discussed here.

Experimental Details.

Samples were prepared from the melt at Bath University. Measurements were made using a coherent pulsed NMR spectrometer operating at 8.5MHz and 19.25MHz. Low temperatures were achieved by means of a Janis ^4He cryostat.

Theory.

Existing theory^{1,2} of nuclear relaxation due to fixed paramagnetic impurities for dilute systems, has been extended to obtain expressions for nuclear spin-lattice relaxation rates for the highly paramagnetic systems investigated, in the limit of fast electronic relaxation. Where nuclear spin diffusion is operative the nuclear relaxation rates for the diffusion limited (DL) and rapid diffusion (RD) cases are given by

$$\frac{1}{T_1} = \left[\frac{8\pi}{15} \gamma_I^2 \gamma_S^2 \hbar^2 S(S+1) n_s D^3 \frac{\tau_e}{1 + \omega_I^2 \tau_e^2} \right]^{\frac{1}{4}},$$

and

$$\frac{1}{T_1} = \frac{8\pi}{15} \gamma_I^4 \gamma_S^2 \hbar^2 S^{-\frac{1}{2}} (S+1) n_s \left[\frac{\Delta \omega_I k_B T}{3 a_0 B} \right]^{\frac{3}{4}} \frac{\tau_e}{1 + \omega_I^2 \tau_e^2}$$

respectively. n_s is the number of magnetic impurities per unit volume and τ_e the electron relaxation time. In the absence of nuclear spin diffusion^{3,4} (ND) the rate is given by

$$\frac{1}{T_1} = \frac{9}{10} (\gamma_I \gamma_S \hbar)^2 S(S+1) n_s^2 \frac{\tau_e}{1 + \omega_I^2 \tau_e^2}.$$

The temperature dependence of the electronic relaxation rate is given by⁵

$$\frac{1}{\tau_e} = \frac{1}{C_D \Delta^2} T^4 + \frac{1}{C_R \Delta^2} T^7 + \frac{\Delta^3}{C_O} \frac{1}{\exp\left[\frac{\Delta}{k_B T}\right] - 1},$$

where the three terms represent the direct, Raman and Orbach processes respectively. Δ is the crystal field splitting of the rare earth ion energy levels.

Results and discussion.

Nuclear relaxation data have been fitted with an equation of the form

$$\frac{M(\tau)}{M(\infty)} = 1 - 2v \left[f \exp\left[-\frac{\tau}{T_1}\right] + (1-f) \exp\left[-\frac{\tau}{\beta T_1}\right]^{\frac{1}{2}} \right]$$

where v is a scaling factor and f is the fraction of the sample volume in which nuclear spin diffusion operates. β (~ 1) is the ratio of the nuclear relaxation rates with and without spin diffusion. Further discussion of this fitting procedure is given in a companion paper⁶. T_1^{-1} data versus T^{-1} at 4.9kG and 11kG are shown in figure 1. The curves shown represent fits of the nuclear relaxation expressions to the 11kG data. In fitting the different expressions the only constraint placed on the electronic relaxation parameters C_D , C_R and C_O is that they must be the same for all cases. The peak in the relaxation data represents the point at which $\omega_I \tau_e = 1$. On the high temperature side of the peak the nuclear rate is field dependent, showing that the RD expression must apply.

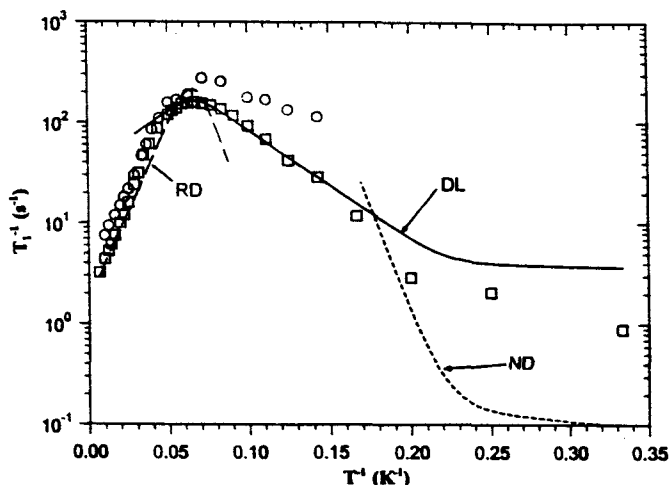


Figure 1. T_1^{-1} vs T^{-1} for 1%Nd doped phosphate glass at B=4.9kG (circles) and 11kG (squares). The curves are described in the text.

Through the peak and down to $T \approx 7K$ the data are best described by the DL expression. From 20K to 50K there is a crossover region where the data are probably described by a combination of DL and RD. Below 7K the data cannot be fitted with any single expression, but appear to be described by a combination of DL and ND. ND is expected to be dominant at low temperatures where the local electronic fields are large and the volumes surrounding impurities, in which spin diffusion does not operate, represent a large fraction of the total sample volume. From the fits:

$$C_D = 1.3 \times 10^{-5} \text{ sK}^{-1}, \quad C_R = 3.2(3) \times 10^1 \text{ sK}^5,$$

$$C_O = 1.1(2) \times 10^{-5} \text{ sK}, \quad \Delta = 97(5) \text{ K}.$$

Figure 2 shows a plot of the electronic relaxation rates versus T^{-1} generated using these parameters. The curves represent the direct, Raman and Orbach processes. The Raman process is more efficient than

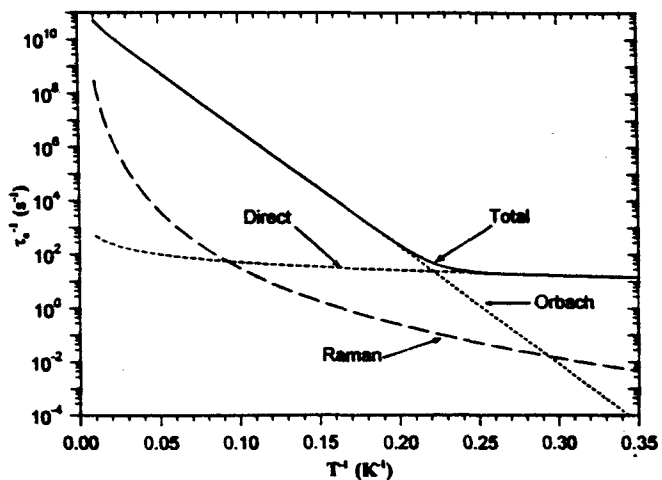


Figure 2. Electronic relaxation rates for 1%Nd³⁺ in phosphate glass at 11 kG.

the direct process above 10K, but above 5K the Orbach process dominates. The total electronic rate increases from $\approx 10^2 \text{ s}^{-1}$ at 3K to $\approx 10^{11} \text{ s}^{-1}$ at 100K.

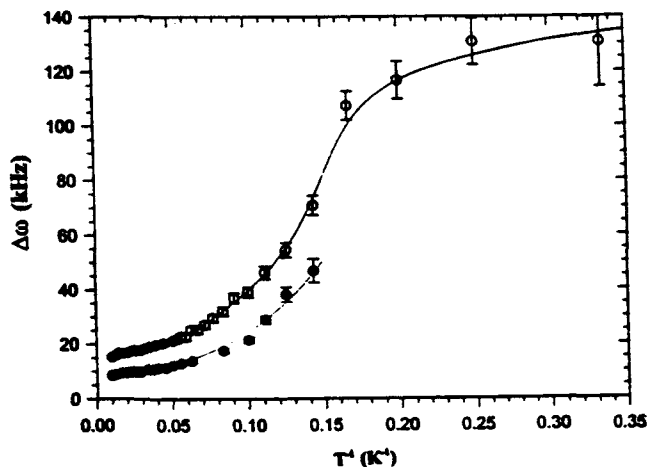


Figure 3. Nuclear linewidths vs T^{-1} at 4.9kG (solid) and 11kG (open). The curves are a guide to the eye.

A plot of the nuclear resonance linewidth versus inverse temperature for external fields of 4.9kG and 11kG is shown in figure 3. The field dependence of the linewidth is consistent with fast relaxation of the electrons. There is a rapid change in linewidth at $T \approx 15K$. It is estimated that the onset of motional narrowing should occur when $\tau_e \approx 10^7 \text{ s}^{-1}$. From figure 2 it can be seen that this occurs at $T \approx 13K$, corresponding roughly with the rapid change observed in the linewidth data.

Conclusion.

The ³¹P NMR for the doped glasses has produced results for the nuclear relaxation times and linewidths which are consistent with relaxation due to paramagnetic impurities and with line broadening due to changes in electron-nuclear coupling. The temperature dependence of the electronic spin-lattice relaxation rate is consistent with a model based on direct, Raman and Orbach relaxation processes. The method allows indirect measurement of very high electronic relaxation rates.

References.

1. Bloembergen N., Physica 15, 386 (1949)
2. Rorschach H. E. Jr, Physica 30, 38 (1964)
3. Blumberg W.E., Phys.Rev. 119, 79 (1960)
4. Tse D & Hartmann S, Phys.Rev.Lett. 21, 511 (1968)
5. Orbach R., Proc.Roy.Soc. (London) A264, 488 (1961)
6. Goudemond et al., Accompanying paper in these proceedings.

Non-exponential Nuclear Magnetization Recovery in Magnetic Glasses

I.P. Goudemond, J.M. Keartland, M.J.R. Hoch,
Department of Physics, University of the Witwatersrand, Johannesburg, South Africa

Introduction.

Stretched exponential relaxation behaviour has commonly been found in glasses and is a characteristic of such systems. We have observed such effects for ^{31}P NMR in phosphate glasses doped with rare-earth ions. The non-exponential behaviour is markedly temperature dependent.

Relaxation Expressions.

Non exponential relaxation in glassy materials is often described in terms of the stretched exponential, or Kohlrausch curve¹:

$$\frac{M(\infty) - M(\tau)}{M(\infty)} = \exp \left[- \left(\frac{\tau}{T_1} \right)^\alpha \right] \quad [1]$$

It has been suggested that non-exponential relaxation in solids may be the result of a distribution of relaxation times within samples¹. Narayanan et al² have described the characterization of non-exponential relaxation in solids, with reference to relaxation due to paramagnetic impurities, in terms of the Kohlrausch curve, where α is typically 0.5 or 1, but can have intermediate values. If nuclear spin diffusion establishes a nuclear spin temperature throughout the sample then the nuclei relax exponentially following³

$$\frac{M(\infty) - M(\tau)}{M(\infty)} = \exp \left[- \frac{\tau}{T_1} \right]. \quad [2]$$

If spin diffusion does not operate then the nuclei relax according to⁴

$$\frac{M(\infty) - M(\tau)}{M(\infty)} = \exp \left[- \left(\frac{\tau}{\beta T_1} \right)^{\frac{1}{2}} \right], \quad [3]$$

where the factor β has been introduced because the relaxation times are not necessarily equal in the two cases. In solids doped with paramagnetic ions, nuclei close the ions experience frequency

shifts, dependent on their separation from the ion. The local field set up by a dopant ion is given by

$$B_{100} = \frac{\mu_0}{r^3} \quad (\tau_e \gg T_2), \quad [4]$$

or

$$B_{100} = \frac{\mu_0^2}{r^3} \frac{B}{k_B T} \quad (\tau_e \ll T_2), \quad [4b]$$

where τ_e is the spin-lattice relaxation time of the electron and T_2 is the nuclear spin-spin relaxation time. Adjacent nuclei can communicate via spin diffusion if resonance frequencies are sufficiently close together, differing by less than the natural linewidth. This condition is satisfied when

$$a_0 \frac{d}{dx} [\gamma_I B_{100}]_{r=b_0} = \Delta \omega_I, \quad [5]$$

where a_0 is the internuclear spacing. b_0 describes a sphere, the diffusion barrier, inside which spin diffusion is inoperative. Its magnitude (for $\tau_e \ll T_2$) is given by

$$b_0 = \left[\frac{3 a_0 \gamma_I \mu_0^2 B}{k_B T \Delta \omega} \right]^{\frac{1}{4}}. \quad [6]$$

At any given temperature, the sample is made up of regions in which spin diffusion operates, and regions in which it does not. If the fraction of the sample in which diffusion does operate is f , then the nuclear magnetization recovery may be described by an expression of the form

$$\frac{M(\tau)}{M(\infty)} = 1 - 2\nu \left[f \exp \left[\frac{-\tau}{T_1} \right] + (1-f) \exp \left[\frac{-\tau}{\beta T_1} \right] \right] \quad [7]$$

where ν is a scaling factor.

The value of β is difficult to calculate precisely, and may be temperature dependent. Where experimental data do not allow easy separation of the relaxation rates for the diffusive and non-diffusive cases, it is convenient to set $\beta \sim 1$. This is discussed below.

The relaxation rate for a single nucleus situated at a distance r from an ion is given by⁵

$$W(r) = \frac{3(\gamma_I \gamma_S \hbar s \sin\theta \cos\theta)^2 S(S+1)}{r^6} \frac{\tau_0}{1 + \omega_I^2 \tau_0^2} \quad [8]$$

Owing to the rapid falloff of $W(r)$ with distance, the average relaxation rate over the sample region in which diffusion operates is determined by nuclei close to the diffusion barrier radius. Since experimental apparatus typically has limited bandwidth, nuclei very close to ions are excluded from observations due to large frequency shifts. Following arguments similar to those introduced with the diffusion barrier radius, a cutoff radius ρ can be defined such that nuclei within a sphere of radius ρ and centered at an ion site will be excluded from observations. If, for example, the cutoff criterion is that adjacent nuclei have resonance frequencies differing by five natural linewidths, then it can be shown that $\rho \approx 0.7b_0$.

In calculating the average relaxation rate for the nuclei inside the diffusion barrier spheres, we follow the approach of Tse and Hartmann⁴. The greatest contribution to the average will, for geometrical reasons, come from nuclei close to the diffusion barrier. This means that the average nuclear relaxation rates for the observable nuclei inside and outside of the diffusion barrier spheres will not be greatly different, and, for practical purposes, in fitting the relaxation expression given in equation 7 to measured recovery curves, β may be set to be 1.

Figure 1 shows a typical nuclear magnetization recovery curve obtained from the metaphosphate glass $(\text{Nd}_2\text{O}_3)_{.01}(\text{La}_2\text{O}_3)_{.24}(\text{P}_2\text{O}_5)_{.75}$.

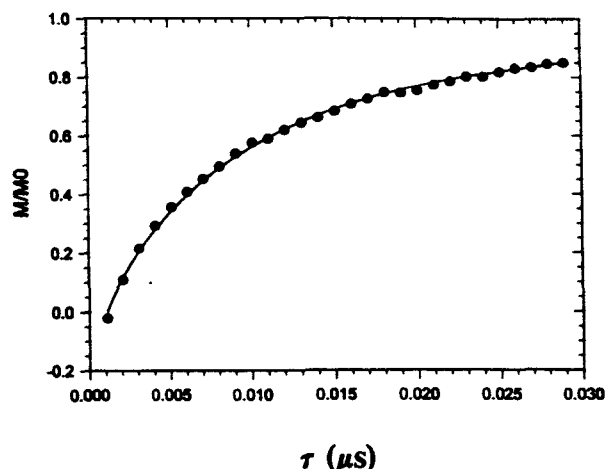


Figure 1. Plot of $M(\tau) / M(\infty)$ vs τ for 1% Nd^{3+} doped phosphate glass.

These data cannot be fitted with either equation 2 or 3. The curve represents a fit to the data of expression 7, with $\beta=1$ for convenience. From the fit we obtain $T_1 = 8.5(1) \times 10^{-3}$ s and $f = 0.35(1)$.

Conclusion.

We have examined non-exponential relaxation in systems with high concentrations of paramagnetic ions. A two component model based on accepted expressions for relaxation due to fixed paramagnetic centres has successfully been used to fit experimental data for a rare earth doped phosphate glass.

References.

1. W. Schnauss, F. Fujara, K. Hartmann and H. Sillescu, 25th Congress Ampere extended abstracts, 80 (Springer-Verlag, Stuttgart 1990) Eds. M. Mehring, J.U. von Schutz and H.C. Wolf.
2. A. Narayanan, J.S Hartman and A.D. Bain, J. Mag. Res. A112, 58 (1995).
3. W.E. Blumberg, Phys.Rev. 119(1), 79 (1960).
4. D. Tse and S.R. Hartmann, Phys.Rev. Lett. 21(8), 511 (1968).

Conformational Mapping of a Fusion Peptide by Electrospray MS/MS, Isotope-Enhanced FTIR Spectroscopy and ESR Spin-Labeling

A. J. Waring,¹ K. Faull², C. C. Curtain,³ and L. M. Gordon¹

¹ Departments of Pediatrics, Drew University/King Medical Center-UCLA, Los Angeles, CA 90059, USA. ² Center for Molecular and Medical Sciences Mass Spectrometry, UCLA, Los Angeles, CA 90024, USA. ³ Monash University, Clayton, Victoria 3052, Australia.

There is a growing body of evidence that the N-terminal amino acid sequences of viral envelope proteins play critical roles in the fusion and cytopathic processes underlying infection of target cells. With influenza virus, respiratory syncytia virus (RSV) and the Human Immunodeficiency Virus Type-1 (HIV-1), the putative fusion site on the viral envelope protein is a highly-conserved hydrophobic amino acid sequence at the N-terminus. Gallaher (1987) and Gonzalez-Scarano *et al.* (1987) each noted extensive homologies for these viral sequences, and suggested that they may function in membrane fusion. Experimental support for this hypothesis with HIV-1 comes from site-directed mutagenesis studies showing that substitution of hydrophobic amino acids with polar residues in the N-terminal peptide lowered infectivity and multi-cell syncytia formation (Felser *et al.*, 1989; Freed *et al.*, 1990; Freed *et al.*, 1992). Also in support of a fusogenic role for these N-terminal sequences are studies of synthetic peptides having the same sequence as that of the native protein. A 23-residue peptide (AVGIGALFLGFLGAAG-STMGARS-CONH₂) of the N-terminal sequence of the HIV-1 glycoprotein 41,000 (gp41) has been shown to induce vesicle-vesicle lipid intermixing of model liposomes (Rafalski *et al.*, 1990; Nieva *et al.*, 1994) and red blood cell ghost membranes (Moblely *et al.*, 1995), as did a 16-residue

peptide having a homologous sequence (Martin *et al.*, 1993). Furthermore, the same 23-residue synthetic viral peptide promoted the mixing of aqueous lipid vesicle contents, suggesting a functional role in cellular infection (Nieva *et al.*, 1994).

Because of the hydrophobicity and pleomorphic nature of viral fusion peptides, conventional analyses such as X-ray crystallography and two-dimensional proton magnetic resonance spectroscopy have not yielded residue-specific, structural models. Fortunately, alternative experimental approaches are now available to obtain detailed conformational maps for these peptides in membrane-mimic environments. Initial studies were performed here to examine deuterium exchange of the hydrogens of fusion peptides using electrospray mass spectrometry (ESI-MS/MS). Since amino acid residues of protein domains that participate in 'defended' elements of secondary structure (i.e., helix, beta sheet) exchange protons more slowly than residues in disordered (i.e., random structures), a preliminary segment-specific conformation map was determined. Further residue-specific information on fusion peptide conformation was obtained using Fourier transform infrared (FTIR) spectroscopy of isotopically-enhanced peptides and Electron Spin Resonance (ESR) spectroscopy of spin-labeled peptides.

The residue-specific backbone conforma-

tion of the N-terminal fusion peptide of HIV-1 gp41 (FP; amino acid residues 519-541) was characterized by the above-mentioned biophysical techniques. For FP fragments in structure-promoting solvents, the time-dependent deuterium exchange was monitored by MS/MS electrospray spectrometry. In hexafluoroisopropanol:water:formic acid (7:3:0.01; v:v:v), the half-times for deuterium exchange for the FP fragments encompassing residues 519-541 were short compared to that for FP fragments encompassing residues 519-536. FTIR measurements of FP labeled with ^{13}C -carbonyl at residues 523-533 indicate that these 'defended' residues assume an α -helical conformation in structure-promoting solvents, including hexafluoroisopropanol:water:formic acid and methanol:water:formic acid. ESR spectroscopy of a spin-labeled fusion peptide (FP*; FP nitroxide labeled at the N-terminal Ala-519) in methanol shows a polarity typical of a covalently-attached nitroxide group participating in the helical conformation of the FP parent. These complementary measurements indicate that the HIV-1 fusion peptide, between residues Ala-519 and Thr-536, possesses definitive α -helical structure when suspended in membrane-mimic solvents.

References

- Felser, J., Klimkait, T. and Silver, J. (1989) *Virology* 170, 566-570.
- Freed, E.O., Myers, D.J. and Risser, R. (1990) *Proc. Natl. Acad. Sci. U.S.A.* 87, 4650-4654.
- Freed, E.O., Delwart, E.L., Buchschacher Jr., G.L. and Panganiban, A.T. (1992) *Proc. Natl. Acad. Sci. U.S.A.* 89, 70-74.
- Gallaher, W.R. (1987) *Cell* 50, 327-328.
- Gonzalez-Scarano, F., Waxham, M.N., Ross, A.M. and Hoxie J.A. (1987) *AIDS Res. Human Retroviruses* 3, 245-252.
- Martin, I., Defrise-Quertan, F., Decroly, E., Vandenbranden, M., Brasseur, R., and Ruyschaert, J.-M. (1993) *Biochim. Biophys. Acta* 1145, 124-133.
- Mobley, P.W., Lee, H.-F., Curtain, C. C., Kirkpatrick, A., Waring, A.J. and Gordon, L.M. (1995) *Biochim. Biophys. Acta* 1271, 304-314.
- Nieva, J.L., Nir, S., Muga, A., Goñi, F.M. and Wilschut, J. (1994) *Biochemistry* 33, 3201-3209.
- Rafalski, M., Lear, J.D., DeGrado, W.F. (1990) *Biochemistry* 29, 7917-7922.

³¹P-NMR Visibility of ATP and Phosphocreatine *In Vivo*

John P. Williams and John P. Headrick

*Division of Biochemistry and Human Physiology, Department of Molecular Sciences,
James Cook University of North Queensland, Townsville, Queensland 4811, AUSTRALIA*

ABSTRACT:

³¹P-spectra of left ventricular myocardium, left cerebral cortex, and right thigh skeletal muscle in intact rat yielded phosphocreatine (PCr) to ATP ratios (PCr/ATP) 45-90% higher than chemically determined values. In myocardial and cerebral tissue NMR determined and total tissue [PCr] values were in good agreement whereas NMR determined [ATP] was 24% and 40% lower than chemically determined total tissue [ATP] values, respectively. Alternatively, in skeletal muscle the NMR determined [PCr] was significantly higher than the chemically determined value. The data indicate that: i) an NMR "invisible" pool of ATP exists in *in situ* myocardial and cerebral tissues, ii) freeze-clamping and extraction of skeletal muscle may permit significant ATP and PCr breakdown, and iii) the traditional method of equating total tissue [ATP] with NMR determined [ATP] may be invalid in *in situ* organs such as heart and brain. In these tissues total tissue [PCr] may be a better index.

INTRODUCTION:

An important assumption in essentially all *in vivo* NMR studies is that tissue ATP and PCr are 100% NMR visible.

Perhaps the most common technique for quantitating metabolites is normalisation of one or more NMR intensities (eg. ATP, PCr) to total tissue freeze-clamped values. Predominantly, the β -NTP peak integral is normalised to total tissue [ATP].

In this study we use an external standard, applicable to use with NMR surface coils, to quantitate intracellular metabolites *in vivo* with as few assumptions as possible. We apply this method to quantitate free intracellular phosphate metabolites in *in situ* brain, myocardium and skeletal muscle, and critically examine assumptions regarding NMR visibility of phosphate metabolites *in vivo*.

METHODS

Mature male Sprague Dawley rats (420±20 g) were anaesthetised with an injection of 60 mg/kg sodium pentobarbitone I.P.. Following instrumentation and surgical preparation, animals were placed in a purpose-built plexiglass holder and the coil positioned over the organ of interest.

³¹P-NMR spectra were acquired at 121.461 MHz employing a 10000 Hz sweep width with 9984 data points, and a pulse width of 53 μ sec. The coil used was a purpose-built, 6 mm diameter double-tuned

surface coil with a flexible-arm described elsewhere⁴.

For quantitation of spectral intensities an external standard (12.5 mM phenylphosphonic acid and 120 mM KCl in deuterated water within a thin walled latex balloon) was used. A 4.5±0.2% difference between signal intensities above and below the coil was observed and corrected for in all calculations.

³¹P control spectra of 512 signal averaged FID's using an interpulse delay (d1) of 1.0 sec were acquired from each tissue. A fully-relaxed spectrum (d1= 21 sec) of 512 signal averaged FID's was then acquired, followed by another control spectrum to ensure no deterioration of metabolic state.

³¹P NMR spectral intensities represent total nucleotide concentrations observed. Assuming proportionate visibility of each of the nucleotide components, ATP will contribute ≥93%^{3,5} to the total area of each of the three phosphate resonances in myocardial spectra. This ratio is used to calculate final ATP concentrations from NMR spectral data in all three tissues.

Three methods were used to compare PCr and ATP cytosolic concentrations from fully-relaxed ³¹P spectral intensities. Each method differs in the reference metabolite used to calculate cytosolic concentrations.

Method 1:

$$\text{Cytosolic [PCr]} = (\text{PCr/PPA})_{\text{NMR}} \times [\text{PPA}]$$

$$\text{Cytosolic [ATP]} = (\text{ATP/PPA})_{\text{NMR}} \times [\text{PPA}]$$

Method 2:

$$\text{Cytosolic [PCr]} = [\text{PCr}]_{\text{total tissue}}$$

$$\text{Cytosolic [ATP]} = (\text{ATP/PCr})_{\text{NMR}} \times [\text{PCr}]_{\text{total tissue}}$$

Method 3:

$$\text{Cytosolic [ATP]} = [\text{ATP}]_{\text{total tissue}}$$

$$\text{Cytosolic [PCr]} = (\text{PCr/ATP})_{\text{NMR}} \times [\text{ATP}]_{\text{total tissue}}$$

Statistical comparisons of methods was carried out using a two-tailed unpaired t-test.

RESULTS

Figure 1 gives PCr/ATP ratios for each tissue calculated using fully relaxed ³¹P-NMR data and chemically determined total tissue values. In all three tissues NMR determined [PCr]/[ATP] ratios were significantly higher than chemically determined ratios.

In brain and heart, Method 1 concentrations are lower than those calculated from Method 3, which is the most commonly employed methodology. The [PCr] and [ATP]'s calculated using Method 1 do not differ significantly from values calculated using

Method 2. Note that chemically determined [PCr] is slightly lower than [PCr] calculated using Method 1, whereas [ATP] calculated using Method 1 are 60% and 76% respectively of chemically determined [ATP].

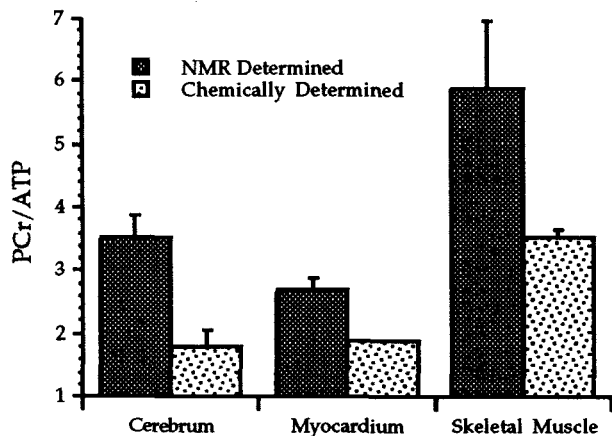


FIGURE 1.

Skeletal muscle data differs substantially from heart and brain. The [PCr] determined using Method 1 is almost twice the chemically determined value, which, in turn, is not significantly different from the concentration calculated using Method 3. The [ATP] calculated using Method 1 is significantly higher than the concentration calculated using Method 2, and the chemically determined [ATP] is slightly lower than the [ATP] calculated using Method 1.

DISCUSSION

The β -NTP peak in ^{31}P spectra is often assumed to be 100% ATP, whereas studies in myocardial tissue have shown that ATP is responsible for 93% of this peak^{3,5}, leading to underestimation of [ATP] (and therefore overestimation of [PCr] and inorganic phosphate when using [ATP] as an internal standard).

The PCr/ATP ratios are significantly higher when calculated from NMR versus chemically derived data. This can only be due to: i) underestimation of total tissue [PCr] by chemical analysis, and/or ii) less than 100% NMR visibility of ATP. Since NMR determined [PCr] is in close agreement with chemically determined [PCr] in heart (93%) and brain (95%), we are led to conclude that ATP is ~76% NMR visible in the *in situ* myocardium, and ~60% NMR visible in the *in situ* brain.

The NMR visibility of ATP has been the subject of several studies in the past. Bak and Ingwall¹ found no significant differences between NMR determined β -NTP and HPLC determined [ATP] in isolated perfused hearts. Most importantly, this study was conducted on Langendorff perfused rat

heart, which has been shown to be at a lower energy state than the *in situ* heart⁴.

Skeletal muscle has a high creatine kinase activity compared to brain and heart which may explain the discrepancies between NMR and chemically determined [PCr]'s, as well as the slightly lower chemically determined [ATP] compared to NMR determined [ATP]. Note that chemically determined [ATP] is slightly lower than NMR determined [ATP], possibly indicating that ATP is also hydrolysed in the time it takes the muscle core to cool to liquid N_2 temperatures during freeze-clamping.

The data discussed above demonstrate that NMR visibility of ATP in *in situ* organs is significantly less than 100%, and differs between tissues. What is the experimental relevance of this observation? Assuming that NMR visibility of ATP does not change during experiments, relative changes in NMR determined metabolites remain accurate. However, if the degree of NMR visibility is variable, as postulated for P_i by Garlick *et al.*,² then changes observed will not accurately describe changes in the *in vivo* environment. Since NMR visibility of ATP in isolated perfused hearts appears to be 100%¹, it is likely that NMR visibility of ATP may change during physiological or pathophysiological perturbations. Under these conditions, not only are absolute values incorrect, but relative changes in metabolite levels would be erroneous.

CONCLUSION

Our data reveals an apparent weakness in current analytical methodologies. We show that there is much better agreement between chemically and NMR determined [PCr] than [ATP] in *in situ* organs. We would advocate the use of total tissue [PCr] as a standard in NMR studies of the *in situ* myocardium and cerebral cortex, but not in skeletal muscle where there is apparently poor agreement between all metabolites when determined using NMR versus freeze-clamp data.

ACKNOWLEDGMENTS

This research was supported in part by grants from the National Heart Foundation of Australia (#G93B3769) and the Australian Research Council.

REFERENCES

- 1 Bak and Ingwall (1992), *AJP*, **262**, E943-E947
- 2 Garlick and Townsend (1992), *AJP*, **263**, H497-H502
- 3 Geisbuhler *et al.* (1984), *Circ Res*, **54**, 536-546
- 4 Headrick *et al.* (1994), *AJP*, **267**, H1074-H1084
- 5 Swain *et al.* (1982), *AJP*, **242**, H818-H826

Advantages of Long-Range-INEPT Measurements for Structure Determination of Catechin Esters

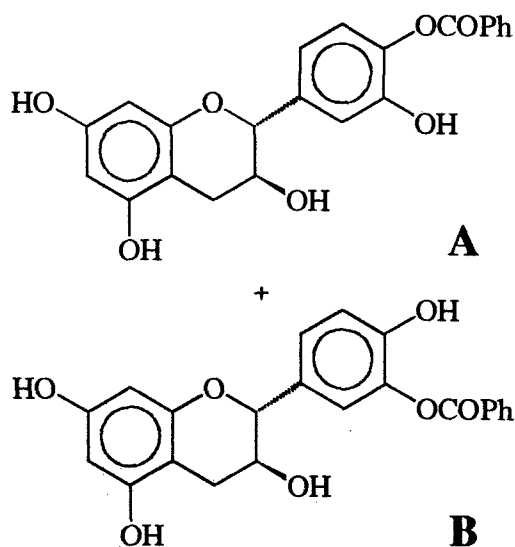
A. De Groot, R. Dommissie, G. Lemière, J. Lepoivre
Department of Organic Chemistry, University of Antwerp (RUCA),
Groenenborgerlaan 171, 2020 Antwerp, BELGIUM

R. Marek

Department of Organic Chemistry, Fac. of Science, Masaryk University,
Kotlarska 2, 611 37 Brno, CZECH REPUBLIC

This work was motivated by the observation of the antiviral activity of procyanidin B₃, which is increased in the presence of gallic acid esters of the aliphatic hydroxyl groups. Therefore we started to prepare esters of catechin with benzoic and gallic acid. Different NMR techniques were used for the determination of the esterification positions.

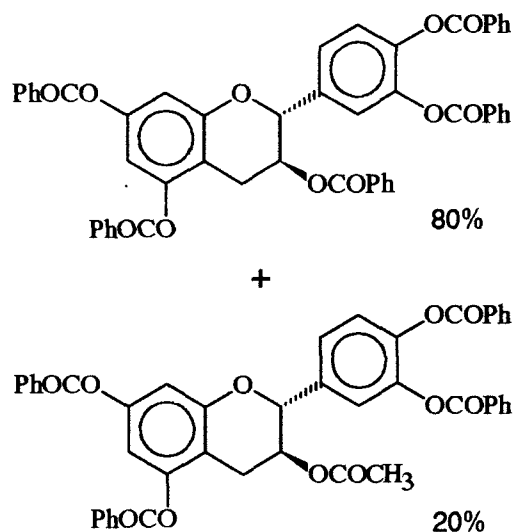
Esterification of catechin with one equivalent of benzoic acid in the presence of



N,N'-dicyclohexylcarbodiimide (DCC) and a catalytic amount of 4-*N,N*-dimethylaminopyridine (DMAP) in DMF gave a few monoesters and *N*-benzoyl-*N,N'*-dicyclohexylurea as a byproduct.

The two major products could be isolated from the mixture, however only together. NMR measurements enabled us to identify them as the 3' and 4' benzoic monoesters of catechin.

When a large excess of benzoic acid (15:1) was added to catechin and DCC in pyridine, two products were formed together with some *N*-acylurea. They could be identified as the 3,6,8,3',4'-pentabenzoyl ester and the 3-acetyl-6,8,3',4'-tetrabenzoyl ester of catechin.



The latter product, which was 5 times less abundant than the former one, can be regarded as a tetra-ester, due to incomplete esterification, which was further

esterified in the workup stage when acetic acid was added. (The acetic acid of the workup was replaced by water in the second reaction of 1.) We proved that it was not formed due to acid exchange by exposing the pentaester to some acetic acid for a day in the workup conditions. No changes to the pentaester were observed.

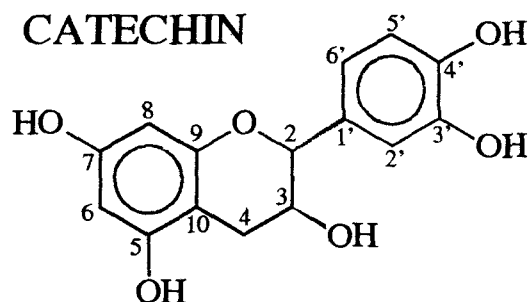
Attempts to make some triacetyl gallic acid esters of catechin, only resulted in the formation of pentaacetic ester of catechin. It seems that the acetyl protection group on the gallic acid is more eager to move to the catechin than the gallic acid itself can react.

Therefore we changed to *t*-butyldimethylsilyl- as protecting group for the hydroxyl groups on the gallic acid, which can be easily removed without harm to the esterified catechin. First results indicate that esterification of tri-TBDMS-gallic acid with catechin seems to be analog to the benzoic acid.

NMR Study

The structures were determined by ^1H - and ^{13}C -NMR spectroscopy. For assignment of most of the signals, COSY and HETCOR pulse sequences were used. However for the determination of the position at which esterification occurred these techniques were not sufficient. For this we used the LONG-RANGE INEPT (INAPT) pulse sequence. The power of this technique is its ability of revealing correlations between hydrogens and carbons at low coupling constant levels (about 1 Hz) even with heteroatoms in the coupling path. That is where the normal long range HETCOR and its analogues seem to suffer from a strong decrease of sensitivity. In our case these

techniques never showed the wanted correlation in an acceptable time. Instead using INAPT came out quite clear for



example for the 4'-benzoyl ester (1A) where the irradiation of the A5'-H doublet gives a correlation with the carboxyl carbon of the ortho (4') benzoyl group. Moreover, using this 1D sequence gives the possibility to optimize the long range coupling constants in a much shorter time than necessary in 2D experiments.

Although there are other and more recent sequences known in literature which can do these assignments in a better and more sensitive way (like 1D HMBC), they require some additional hardware which not all of the NMR users possess. We proved that the INAPT sequence can solve the proposed problems nicely in such cases, waiting for upgrade. INAPT was and will still be of great help for us to identify the synthesized products.

Acknowledgement

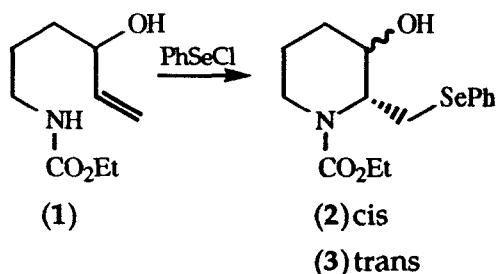
This work was supported by 'Geconcerteerde Onderzoeksactie 92/94-09 UIA', project leader A. Vlietinck.

Unusually Stable Hydrates of *N*-Substituted 3-Hydroxy-2-(phenylselenenyl)methylpiperidine Derivatives.

Where is the Water? - An NMR Study.

M. A. Cooper, S. M. Pyke* & A. D. Ward
Department of Chemistry, University of Adelaide, S.A. 5005, Australia.

As part of ongoing studies of selenium induced cyclization reactions, treatment of the carbamate (1) with phenylselenenyl chloride gave a mixture of cyclized products (2) & (3) [m/z 343] in a 3:1 ratio of *trans*:*cis* isomers in moderate yield.



Upon extended reaction times formation of (2) & (3) was accompanied by the appearance of a more polar

crystalline solid. The 300 MHz proton NMR spectrum revealed a 3:1 mixture of two diastereomers, which upon recrystallization gave a product of high diastereomeric purity (4). The 300 MHz proton NMR spectrum of pure (4) is shown with signal assignments in Figure 1; two new signals which do not appear in the mixture (2/3) are indicated. Signals were assigned by use of a COSY spectrum and by comparison with other derivatives.

Mass spectral analysis of this product revealed a molecular ion at m/z 361, which corresponds to the addition of water. The carbon NMR spectrum of (4) was similar to that of (2) with corresponding resonances within 4 ppm of each other. In addition, a C/H COSY experiment revealed no correlation between the two protons indicated in Figure 1 with any carbon atom. This, along with further chemical derivatization, suggested that the water was not covalently bound to the carbon skeleton

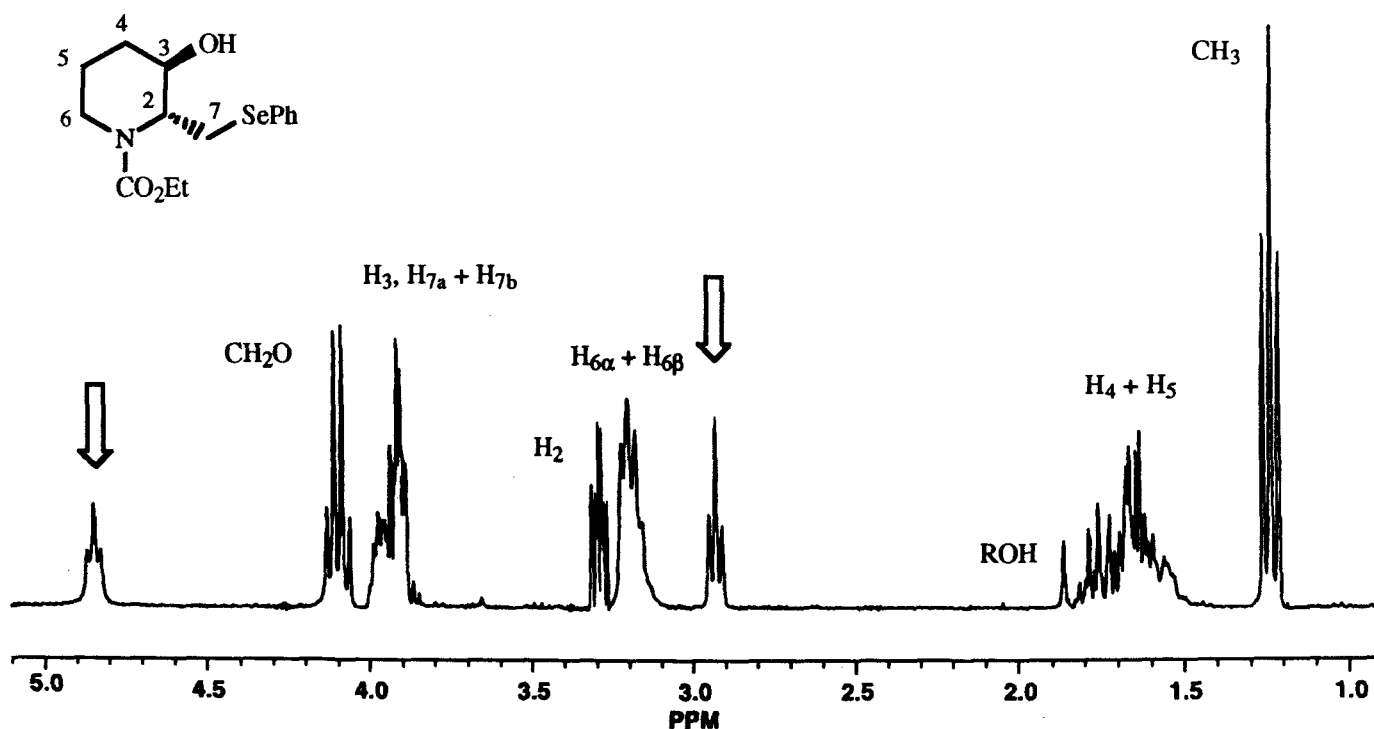


Figure 1: ¹H NMR Spectrum of (4) (CDCl₃)

of the hydroxy piperidine and that (4) was in fact a stable hydrate of (2). The two protons indicated in Figure 1 were therefore labelled as OH_a (downfield signal) and OH_b (upfield signal)

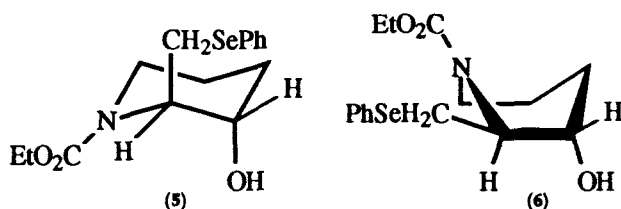
The stereochemistry of (2) was established as *trans* by coupling constant ($J_{2,3} = 9.6$ Hz) and NOE enhancements. Since the stereochemistry of (2) is unlikely to be changed in the transformation to (4), the stereochemistry of (4) is therefore also *trans*.

Having assigned all the resonances, it was apparent that the signal for H_2 was complicated by through space spin-spin coupling. The signal for H_2 was simplified by decoupling of the OH_b signal. Examination of this spectrum revealed the AB portion of an ABX spectrum (H_{7a} & H_{7b}) and the X portion of an ABX spectrum (H_2), so analysis was carried out by the use of the effective Larmor frequency method, followed by spectral simulation (PANIC). The results of this analysis are listed in Table 1.

Table 1: Coupling Constants from OH_b Decoupled Spectrum

$J_{2,3}$	3.1 Hz
$J_{2,7a}$	4.5 Hz
$J_{2,7b}$	6.0 Hz
$J_{7a,7b}$	11.7 Hz

As $J_{2,3}$ was found to be 3.1 Hz, substituents at positions 2 & 3 must clearly both be axial in a chair conformation (5), or the ring is in a boat conformation (6).



From the COSY spectrum, it was found that OH_a is coupled to H_2 , and OH_b is coupled to one of the protons next to selenium (H_7). In addition, decoupling of OH_a reduced OH_b to a doublet. It appears therefore that each end of the included water molecule (OH_a & OH_b) must be in close proximity to H_2 and either H_{7a} or H_{7b} respectively. This information in conjunction with $J_{2,3}$ of 3.1 Hz implies that the conformation of the ring must be a *trans*-diaxially substituted chair (Figure 2).

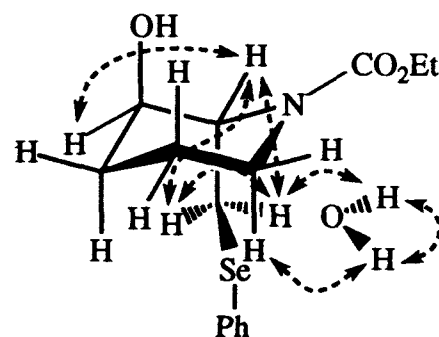


Figure 2: Conformation and Principal Coupling Interactions of (4)

It is proposed that the included water is held firmly in place by dipole-dipole interactions from the ring nitrogen (δ^+ due to the carbamate) and selenium (Figure 3).

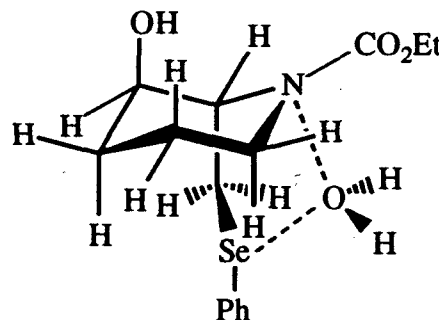


Figure 3: Position of Included Water

Exchange of the water by D_2O is slow; methanol- d_4 appears to promote H/D exchange more rapidly. The conformation of the ring is still a *trans*-diaxially substituted chair in methanol- d_4 as demonstrated by $J_{2,3} = 1.9$ Hz (Table 2).

Table 2: Coupling Constants from CD_3OD NMR Spectrum of (4)

$J_{2,3}$	1.9 Hz
$J_{2,7a}$	4.8 Hz
$J_{2,7b}$	9.4 Hz
$J_{7a,7b}$	11.3 Hz

Additional spectra of the stable hydrate (4) will be recorded at higher field in order to completely resolve all the resonances (particularly H_3). Attempts to prepare crystals suitable for X-ray crystallographic analysis have not been successful to date. Preparation and NMR studies of a D_2O inclusion complex will be commenced shortly.

Receipt of an Australian Postgraduate Award (M. A. Cooper) is gratefully acknowledged.

The Application of Nuclear Magnetic Resonance Spectroscopy to the Analysis of Archaeological Materials

L.T. Byrne¹, E.L. Ghisalberti¹ and I.M. Godfrey²

¹Department of Chemistry, The University of Western Australia, Nedlands Western Australia 6907.

²Department of Materials Conservation, Western Australian Maritime Museum, Fremantle, Western Australia, 6160.

The application of Nuclear Magnetic Resonance Spectroscopy to the study of archaeological materials can provide a wide range of extremely valuable information of interest to both the archaeologist and the conservation scientist. In addition to details of chemical composition, analysis of spectra arising from archaeological samples can provide information concerning their provenance, the extent of their degradation as well as early technological practices.

We have examined a variety of archaeological samples from both marine and terrestrial sources. Examples from ¹³C and ³¹P studies of solid ivory artefacts, ¹H and ¹³C analyses of pitches and tars from marine archaeological sites and ¹³C CP/MAS studies of ancient timber samples are presented to illustrate the utility of NMR spectroscopy in the analysis of archaeological materials.

¹H and ¹³C Spectra of Pitch/Tar Samples

Pitch/Tar samples from five Western Australian shipwreck sites have been examined(1). ¹H and ¹³C spectra of samples from the *Vergulde Draeck* (1653-1656), the *Eglinton* (1848-1852) were compared with spectra of modern Stockholm tar. We were also able to examine a sample of tar from the *Mary Rose* (1509-1545) which had previously been studied(2). The similarity of the spectra indicate a common source (retorted pine resin from *Pinus sylvestris*) and also provides evidence that pitch production practices were similar over many

centuries. The stability of the samples is also demonstrated.

¹³C and ³¹P Studies of Ivory Samples from the Vergulde Draeck (1653-56)

Similar ¹³C CP/MAS spectra were obtained from both the inner and outer sections of modern ivory. In contrast, the outer sample of ivory from the *Vergulde Draeck* (GT 993 - outer) showed a small residual collagen signal whilst the inner sample (GT 993 - inner) showed no discernible signal (see Figure 1).

³¹P CP/MAS and single pulse MAS spectra for each of the above samples were compared. All four spectra of modern ivory are similar, but differ from the spectra of both of the GT 993 samples.. Slight differences in sideband intensity between CP/MAS and single pulse MAS spectra for both of the GT 993 samples indicate the likelihood of structurally different phosphates in these samples.

Ancient Timber Samples

Two contrasting ¹³C CP/MAS spectra of samples of ancient timber were compared. The spectrum of Beenup I (2-3 million years old) showed the cellulose and hemicellulose had been degraded in preference to lignin - the usual case when wood is buried(3). In the sample from Botany Bay (~9000 years old) the lignin had been preferentially depleted indicating photochemical degradation of lignin prior to burial.

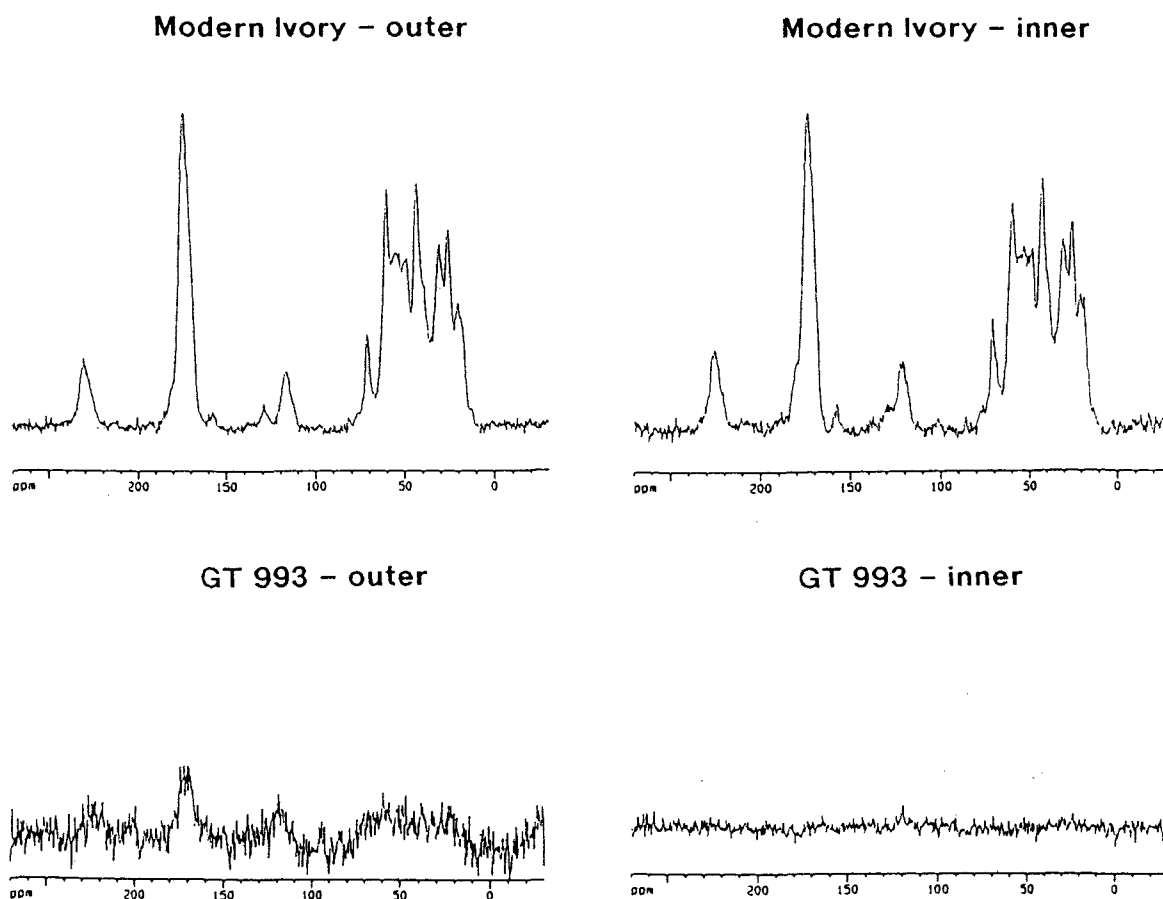


Figure 1. ^{13}C CP/MAS spectra of the inner and outer sections of modern ivory and ivory from the *Vergulde Draeck* (GT 993)

¹E.L. Ghisalberti and I. Godfrey, *Bull. Aust. Inst. Maritime Arch.*, **14**, 1-8(1990).

²N. Robinson, R.P. Evershed, W. J. Higgs, K. Jerman and G. Eglinton, *Analyst*, **112**, 637-644(1987).

³ M.A. Wilson, I.M. Godfrey, J.V. Hanna, R.A. Quezada and K.S. Finnie, *Org. Geochem*, **20**, 599-610 (1993) and references therein.

The Mixed Alkali Effect in Li/Na Disilicate Glasses

F.A.Ali^{a,b}, A.V.Chadwick^a, G.N.Greaves^c, M.C.Jermy^b and M.E.Smith^b

a: Chemical Laboratory, University of Kent at Canterbury, Kent, CT2 7NH, U.K.

b: Physics Laboratory, University of Kent at Canterbury, Kent, CT2 7NR, U.K.

c: DRAL, Daresbury Laboratory, Warrington, Cheshire, WA4 4AD, U.K.

Introduction:

Nuclear Magnetic Resonance NMR is a valuable tool in studying both glass structure (MAS-NMR) and dynamic ionic motion by relaxation measurements.

The pronounced change in properties resulting from the addition of a second alkali oxide to a glass keeping the total alkali constant is known as the mixed alkali effect (MAE).

Mechanism by NMR:

The mechanism of ionic transport in glass is still unclear in spite of the extensive amount of work that has been done theoretically and experimentally. The two most popular techniques that are applied to study such behaviour are a:- the spin-lattice relaxation as monitored by NMR in which the rate of decay of the nuclear magnetization is affected by ion motion and, b:- the electrical conductivity where the movement of ions in response to an external ac electric field can be observed.

The BPP model for the description of relaxation is based on the assumption that there is a single exponential correlation function. However for glasses this model is inadequate due to the following failures: The $\log T_1$ vs $1/T$ plot is asymmetrical about the T_1 minimum. The values for activation energies from both sides of the minimum are different¹ and the low temperature side T_1 is not proportional to ω^2 . Alternatively the data can be fitted very well if the exponential correlation is replaced by the stretched exponential function which is based on the presence of a distribution of correlation times known as the Kohlrausch-Williams-Watts (KWW) function

$$\Phi(t) = \exp \left[- \left(t / \tau^* \right)^\beta \right] \quad \beta < 1$$

Relating the data from both NMR and conductivity σ based on this model will give the equation

$$E_{NMR} = \beta E_\sigma$$

Experimental Procedure:

$1-x\text{Li}_2\text{O} \cdot x\text{Na}_2\text{O} \cdot 2\text{SiO}_2$ glasses were prepared from the appropriate amounts of alkali carbonates and SiO_2 in a Pt/Au (95/5) crucible via the normal conventional melt quench method. The samples were remelted at least twice to ensure the homogeneous glassy state. Two sets of identical composition were prepared, one for ^7Li , ^{23}Na MAS-NMR and relaxation while the other is doped with 0.1 mole% MnO for ^{29}Si MAS-NMR to reduce the T_1 of ^{29}Si . All samples were examined by XRD, and SEM to ensure they were amorphous and homogenous. The conductivity measurements were made using a Wayne-Kerr bridge at a frequency of 1592 Hz up to 400°C. Readings were recorded every 10°C several times for each composition. Spin-lattice relaxation T_1 for ^7Li were determined on a Bruker CXP spectrometer operating at 29.86 MHz using saturation recovery over the same temperature range as for conductivity. MAS-NMR spectra were accumulated on a Bruker MSL 400 equipped with a 9.4 T magnet operating at 79.4 MHz (^{29}Si), 105.2 MHz (^{23}Na) and 155.5 MHz (^7Li).

Results:

MAS-NMR: For all the compositions the main Q unit in both systems was Q^3 at ~ 90.0 ppm as expected for disilicate glasses and only small changes were found in the disproportionation equilibrium constant k . ^7Li MAS-NMR show that as the lithium content increases the line width increases. Disproportionation is quantified by $k = [Q^2][Q^4]/[Q^3]^2$

Table 1: Q- distribution and ^7Li line width

Na/ Na+Li	%Si Q2	%Si Q3	%Si Q4	K	^7Li Hz Li/Na FWHM
0.23	21	63	16	.085	680
0.36	17	69	15	.054	610
0.54	19	68	13	.053	480
0.70	20	68	12	.052	350
0.84	15	76	9	.023	250

Errors in chemical shifts ± 0.5 ppm, and ± 50 Hz in ^7Li line widths.

Dynamics: The conductivity data shows linear behaviour (Fig.1) and the lowest value at a given temperature was at the intermediate composition $x=0.5$. ^7Li T_1 measurements shows that the minimum moves to higher temperatures with decreasing lithium concentration (Fig.2). The activation energies from both data were determined applying the Arrhenius formula and E_{σ} is higher than E_{nmr} (Table 2). This data is analysed and discussed in much more detail elsewhere².

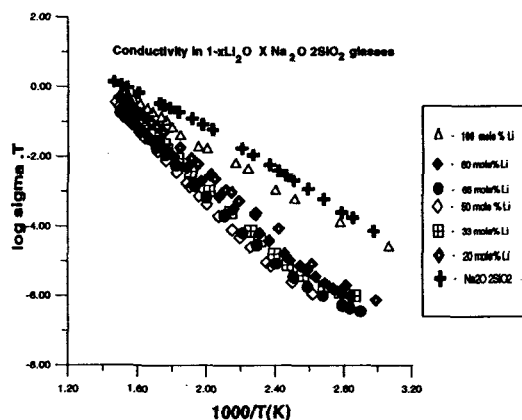


Fig.1 Conductivities of Li/Na disilicate glasses

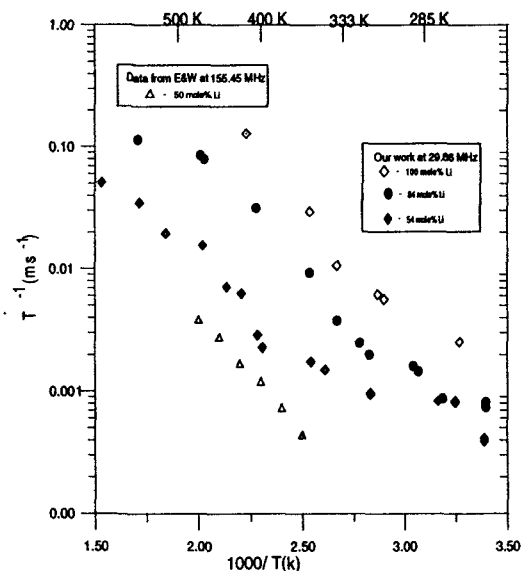


Fig.2 T_1 of Li/Na disilicate glasses

Conclusion:

The MAS-NMR results show that with substituting one alkali by another the network former (silicate) changes only slightly. From the line width it is clear that there is no clustering occurring and as the lithium content increases the dipole coupling increases. The T_1 data shows as the lithium content decreases the minimum moves to higher temperatures and the activation energies E_{nmr} which indicate the microscopic energies increases monotonically with decreasing lithium and no marked MAE is seen. While from the conductivity activation energies E_{σ} there is a marked MAE at the intermediate composition $x=0.5$. The E_{σ} was found to be higher than E_{nmr} .

Table 2: Activation energies determined from conductivity E_{σ} and ^7Li NMR T_1 E_{nmr}

x	E_{σ}	E_{NMR}
0.23	0.78	0.38
0.36	0.88	0.34
0.54	0.97	0.39
0.70	0.87	nd
0.84	0.82	0.45

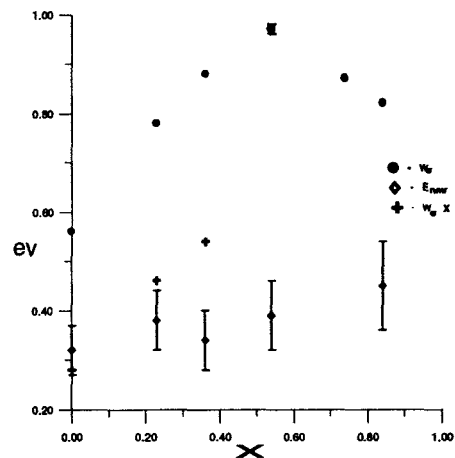


Fig.3 Activation energies from ^7Li relaxation NMR and conductivity

References:

- 1- Detlef Brinkmann, Progress in NMR spectroscopy 1992, vol.24, pp.527.
- 2- F.Ali, A.V.Chadwick, M.C.Jermy and M.E.Smith Solid State NMR(in press)1995.

Acknowledgements: F.Ali thanks KISR-Kuwait for providing a scholarship to study at Kent.

Solid State Satellite Transition MAS NMR Spectroscopy of Quadrupole Nuclei.

T.J. Bastow^a, C.Jaeger^b, G. Kunath-Fandrei^b and M.E. Smith^{a,c,*}.

a. CSIRO Division of Materials Science and Technology, Private Bag 33, Clayton, Victoria 3169, Australia.

b. Friedrich-Schiller Universität Jena, PATF, D-07743 Jena, Germany.

c. Physics Laboratory, University of Kent, Canterbury, Kent, CT2 7NR, U.K.

Abstract.

The application of satellite transition ^{27}Al MAS NMR spectroscopy to an amorphous transitional alumina is presented. Simulation of the sideband envelope allows the quadrupole interactions to be deduced for the AlO_4 , AlO_5 and AlO_6 sites and subsequent simulation of the centreband provides accurate quantification of the aluminium distribution.

Introduction.

One of the first nuclei to be extensively studied by solid state MAS NMR was ^{27}Al as a result of its high natural sensitivity and the technological importance of many aluminium-containing materials. The ability of NMR to distinguish AlO_4 and AlO_6 , even in amorphous materials has proved to be very informative for characterisation. It has become clear in recent years that AlO_5 units are to be widely found in amorphous materials. Provided fast MAS at high fields is applied the three resonances can clearly be distinguished. However in amorphous materials asymmetric, often strongly overlapping resonances are observed. The asymmetry results from the distribution of second-order quadrupole effects (1). It has become a challenge for ^{27}Al NMR from solids to provide more accurate quantification of such centrebands.

A range of techniques are available for the study of quadrupole nuclei. Even MAS can be carried out as a function of applied magnetic field (our work routinely uses up to 14.1 T). There are other more involved methods such as double angle rotation which applied to a partially calcined alumina hydrate revealed $\alpha\text{-Al}_2\text{O}_3$, gibbsite and an amorphous transitional alumina, although there was still strong overlap which made accurate quantitative analysis difficult (2).

Satellite transition NMR spectroscopy involves examination of the sidebands of the non-central transitions. For $I=5/2$ nuclei the inner ($\pm 3/2$, $\pm 1/2$) satellite transitions have much reduced second-order quadrupole broadening giving improved resolution of the overlapping sites. The other advantage is that simulation of the sideband envelope can be used to deduce the quadrupole parameters which is particularly useful for small quadrupole interactions when no second-order structure is apparent in the centreband. Such an

approach has been applied to $\text{Al}_2(\text{MoO}_4)_3$ where only two almost Gaussian resonances are apparent in the centreband. Simulation of the sidebands requires four resonances, in agreement with the crystal structure, and two sites differ in their isotropic chemical shift by only 0.8 ppm (3).

For aluminas rather than identifying intermediate phases in terms of their crystallography, which can be somewhat ambiguous for amorphous samples, the distribution in terms of AlO_x species could be a much more versatile characterisation approach.

Experimental Details.

An amorphous partially dehydrated alumina was formed by calcining gibbsite to give an X-ray amorphous product with an H_2O content of 1.2 mol%.

^{27}Al MAS NMR spectra were recorded on a Bruker ASX 500 spectrometer at 130.32 MHz, using $< 15^\circ$ pulses and MAS at *ca* 14 kHz. An initial probe deadtime of only 8 μs was necessary.

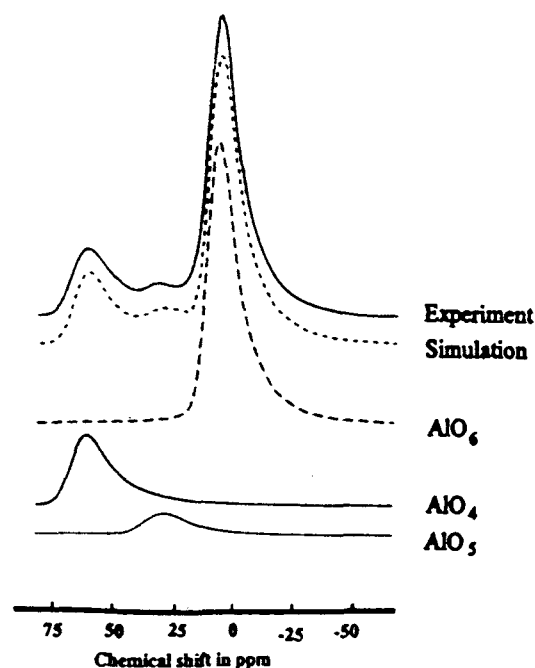


Figure 1. ^{27}Al MAS centreband of a partially dehydrated alumina.

Results and Discussion.

The MAS centreband clearly shows three resonances at 65, 35 and 10 ppm (Fig. 1) which are confirmed as being from individual resonances by recording MAS spectra at 14.1 T. The strong overlap is clear, as is the asymmetric lineshape of AlO_6 . The centreband is collected on a 400 kHz sweep with a 15s recycle delay that produces a fully relaxed spectrum.

The procedure is to then record the satellite transitions at various offset frequencies. Several corrections are necessary to obtain the true sideband intensities; including the bandwidth of the probe and baseline roll caused by the initial deadtime. Once these corrections have been performed the sidebands can be simulated (Fig. 2).

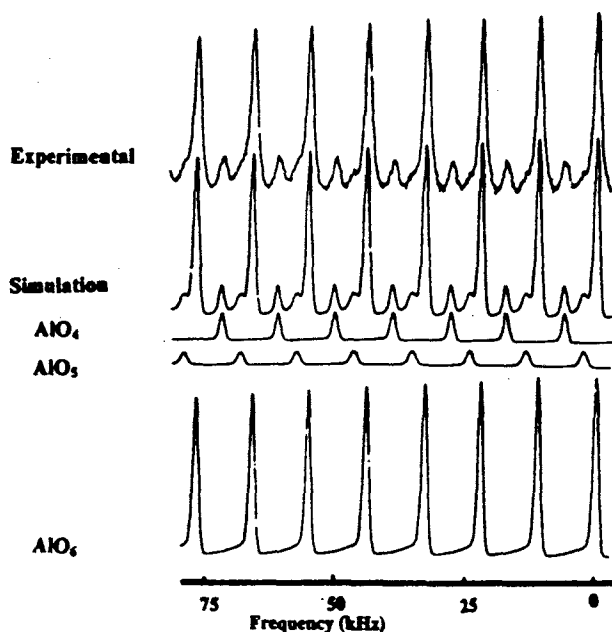


Figure 2. Expansion of some sidebands and their simulation clearly showing AlO_4 , AlO_5 and AlO_6 sites.

The increased symmetry of the three resonances is apparent so that they can be simulated by Gaussians. The increased resolution is also clear with the AlO_4 peak separated to the baseline and distinct AlO_5 and AlO_6 resonances are apparent. The satellite spectra are collected at 1s recycle delay and with a 2 MHz sweep since the relative intensities of the different sites are not important here, but the signal to noise is. From the simulations the intensity distribution of the sidebands from each site can be deduced. These sideband intensities are then simulated by a function that depends on the mean C_Q , the width of the distribution of C_Q and the mean asymmetry parameter of the quadrupole interaction. A large range of parameters is examined to ensure that the true best fit is found. The sideband envelop is in fact very much more sensitive than the

centreband, emphasising that fitting the centreband alone can be somewhat ambiguous. Much greater detail of how the spectra were obtained and the extraction and evaluation of the NMR interaction parameters can be found elsewhere (4).

The fit parameters from the sidebands are then taken to produce a simulation of the centreband, with the only parameter that is now allowed to vary being the relative intensity of the three resonances. The integrated intensities are then in the ratio of 22.5%:7.5%:70% (AlO_4 : AlO_5 : AlO_6), with an accuracy of around 2%. Several additional points about this quantification are necessary. There has long been a question about very distorted sites being lost from ^{27}Al NMR spectra. Under the conditions of this study C_Q 's a factor of 6 larger than the mean value here are known to be detected rigorously quantitatively (5), so that effectively all of the aluminium is seen in these spectra. Secondly account has to be taken of the amount of magnetisation that appears in the centreband, but here this is calculated to > 97%, so that again no additional correction is necessary.

The aluminium distribution identifies the phase as being χ - Al_2O_3 like, rather than ρ - Al_2O_3 which is the other possibility. Distinguishing these would be very difficult from conventional X-ray diffraction.

Conclusion.

Satellite transition MAS NMR spectroscopy has been used to produce accurate quantification of the aluminium distribution of the centreband between AlO_4 , AlO_5 and AlO_6 sites in an amorphous alumina. The methodology used here is generally applicable to amorphous aluminium-containing materials.

Acknowledgements.

The British Council and DAAD are thanked for funding the collaboration between Kent and Germany. MES thanks the EPSRC for funding the high field NMR work through GR/K43667.

References.

1. C. Jäger, *NMR Basic Principles and Progress*, **31**, 134 (1994).
2. T.J. Bastow, J.S. Hall, M.E. Smith and S. Steuernagel, *Mater. Lett.*, **18**, 197 (1994).
3. G. Kunath-Fandrei, T.J. Bastow, C. Jäger and M.E. Smith, *Chem. Phys. Lett.*, **234**, 431 (1995).
4. G. Kunath-Fandrei, T.J. Bastow, J.S. Hall, C. Jäger and M.E. Smith, *J. Phys. Chem.* (accepted for publication).
5. L.B. Alemany, D. Massiot, B.L. Sherriff, M.E. Smith and F. Taulelle, *Chem. Phys. Lett.* **177**, 301 (1991).

Nuclear Magnetic Resonance of X in XMnCl_3 (X=Na, Cs) Single Crystals*Ae Ran Lim[†], Sung Ho Choh[#] and Se Young Jeong^{**}[†]Department of Physics, Jeonju University, Chonju 560-759, South Korea[#]Department of Physics, Korea University, Seoul 136-701, South Korea^{**}Department of Physics, Pusan National University, Pusan 609-735, South Korea

I. Introduction

The NaMnCl_3 and CsMnCl_3 single crystals belong to the space groups $R\bar{3}$ and $R\bar{3}m$, respectively.[1,2] Experimental investigations such as x-ray diffraction,[3,4] antiferromagnetic resonance,[5] nuclear magnetic resonance[6,7] and optical properties[8] have been made for these crystals. These crystals have excellent optical quality and have found increasing application in recent years as electro-optic deflectors and other devices for controlling laser beams.[9]

Our present work reports the X NMR in XMnCl_3 (X=Na, Cs) single crystals grown by the Czochralski method. The quadrupole coupling constant, the asymmetry parameter and the directions of the principal axes of the electric field gradient (EFG) tensor of ^{23}Na (I=3/2) and ^{133}Cs (I=7/2) are determined at room temperature.

II. Crystal Structure

NaMnCl_3 is a hexagonal structure with the lattice parameters $a=6.591$ Å and $c=18.627$ Å at room temperature.[1] The primitive cell of NaMnCl_3 contains two Na^+ ions. The Na^+ and Mn^{2+} ions are surrounded by six Cl^- ions located at the corners of slightly distorted octahedra. The crystal structure of CsMnCl_3 is hexagonal with the lattice parameters $a=7.291$ Å and $c=27.440$ Å at room temperature.[2] There are two kinds of sites for the Cs^+ ions which occupy two physically inequivalent positions. At room temperature, Cs(I) and Cs(II) in CsMnCl_3 have 3 and 6 atoms, respectively, per unit cell.

III. Experimental Results

X NMR signals in the XMnCl_3 (X=Na, Cs) single crystals were measured using a Bruker MSL 200 FT NMR spectrometer. The static magnetic field strength was 4.7 T. The

orientation of the specimen was determined by the x-ray Laue method.

The three line structure is a result of the quadrupole interaction of the ^{23}Na (I=3/2) nucleus. Only one set of the NMR spectra of ^{23}Na is obtained even though there are two sodium nuclei per unit cell. This means that two sites are crystallographically and magnetically equivalent. The central transition is stronger than the satellite lines, and the separations between adjacent lines are almost equal. The rotation pattern of Na, measured in the crystallographic ac-plane, is shown in fig. 1.

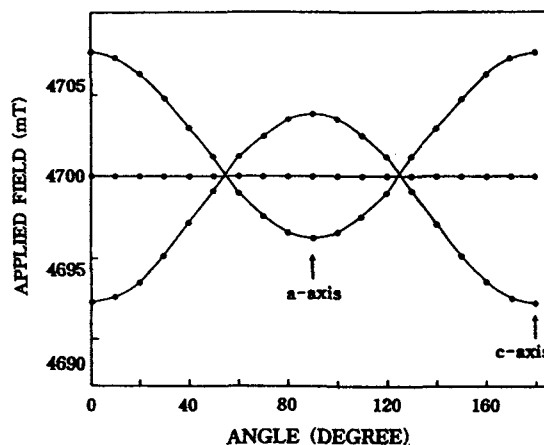


Fig. 1. Rotation pattern of ^{23}Na NMR measured in the ac-plane at room temperature.

The maximum separation resulting from the quadrupole interaction was observed when the magnetic field was applied along the c-axis of the crystal. The satellite lines show the angular dependence of $3\cos^2\theta - 1$, where the polar angle θ is the direction of the magnetic field with respect to the c-axis, whereas the central lines are angular independent. However, the rotation pattern in the aa-plane is angular independent.

The seven line structure is a result of the

quadrupole interaction of the $^{133}\text{Cs}(I=7/2)$ nucleus. However, two different groups of Cs resonances were recorded. The signals of these two groups, one weaker and the other stronger, represent the transition of ^{133}Cs NMR lines due to Cs(I) and Cs(II), respectively. The spectra showing an approximate intensity ratio of 1 to 2 are associated with two physically inequivalent positions of cesium atoms in the unit cell. The rotation pattern of Cs(I), measured in the crystallographic *ac*-plane, is shown in fig. 2. The rotation pattern of Cs(II) was similar to that of Cs(I), as shown in fig. 2 in the *ac*-plane. There was no angular dependence of Cs(II) in the *aa*-plane, similar to Cs(I).

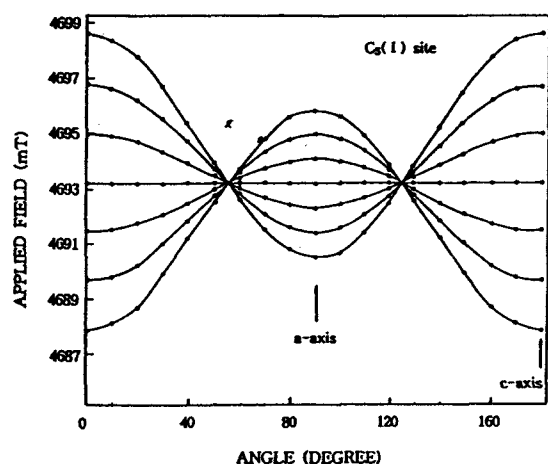


Fig. 2. Rotation pattern of Cs(I) NMR measured in the *ac*-plane at room temperature.

From these results, the EFG tensor of Na is axially symmetric ($\eta=0$), and the EFG tensors of Cs(I) and Cs(II) are both axially symmetric. The principal Z axis is parallel to the crystallographic *c*-axis for XMnCl_3 single crystals. The orientations of the principal axes of the EFG tensor coincide for the Cs(I) and Cs(II) sites. The quadrupole parameters are determined by the least squares fit using the experimental data of fig. 1 and 2, respectively. The quadrupole coupling constant is 155 ± 2 kHz for ^{23}Na at room temperature. Also, two different Cs resonance groups recorded with different magnitudes of the quadrupole splitting were analysed. The quadrupole coupling constants obtained for Cs(I) and Cs(II) are 153 ± 14 kHz and 212 ± 14 kHz, respectively.

IV. Discussion and Conclusion

The *c*-axes of the NaMnCl_3 and CsMnCl_3 crystals have threefold symmetry. Therefore, the asymmetry parameters of the Na and Cs nucleus, $\eta = 0$, are consistent with the crystal structure. The maximum separation of the resonance line due to the quadrupole interaction was observed when the magnetic field was applied along the *c*-axis of the crystal. This direction is determined to be the Z axis of the EFG tensor. Cs(I) and Cs(II) in the unit cell have 3 and 6 atoms, respectively. The Cs NMR intensity ratio of approximately 1 to 2 enabled us to designate Cs(I) and Cs(II) in the unit cell. From the NMR results, Cs(I) and Cs(II) sites are clearly distinguished. The quadrupole coupling constant of ^{23}Na nucleus in the NaMnCl_3 crystal was similar to that of the ^{133}Cs nucleus in the CsMnCl_3 crystal. This result is consistent with the similar crystal structures; the space groups $R\bar{3}$ and $R\bar{3}m$, respectively.

*This work was supported by KOSEF through the RCDAMP at Pusan National University (1994-97) and in part by the Basic Science Research Institute Program, Ministry of Education, 1995, Project No. BSRI-95-2410.

References

- [1] M. Melamud, J. Makovsky and H. Shaked, Phys. Rev. B3, 3873 (1971).
- [2] M. Kestigian and W. J. Croft, Mat. Res. Bull. 4, 877 (1969).
- [3] J. Goodyear and D. J. Kennedy, Acta Crystallogr. B29, 744 (1973).
- [4] C. J. J. Van Loon and G. C. Verschoor, Acta Cryst. B29, 1224 (1973).
- [5] A. V. Andrienko and L. A. Prozorova, Sov. Phys.-JETP 51, 1213 (1980).
- [6] A. R. Lim, S. H. Choh and S. Y. Jeong, J. Phys. : Condens. Matter 6, 10141 (1994).
- [7] A. R. Lim, T. H. Yeom, S. H. Choh and S. Y. Jeong, J. Phys. : Condens. Matter in press (1995).
- [8] U. Kambli and H. U. Gudel, J. Phys. C : Solid State Phys. 17, 4041 (1984).
- [9] S. V. Mel'nikova, A. T. Anistratov and B. V. Beznosikov, Sov. Phys. Solid State 19, 1266 (1977).

¹H Nuclear Magnetic Resonance of Liquid Crystalline Polymer BlendsJin-Hae Chang^{*} and Kwan-Soo Hong[#]^{*}Department of Polymer Science & Engineering, Kum-Oh University of Technology, Kumi 730-701, Korea[#]Seoul Branch, Korea Basics Science Institute, Seoul 136-701, Korea

I. Introduction

The blends of main chain thermotropic liquid crystalline polymers (TLCPs) with commercial thermoplastics have been studied systematically in many laboratories. Studies on blends of LCPs with other polymers focus on the characterization of rheology, phase behavior, morphology, and mechanical properties [1,2]. Some of the polymers [3] blended with LCPs are: polycarbonate, polystyrene, polyethersulfone, poly(ethylene terephthalate), poly(butylene terephthalate), and polyamides.

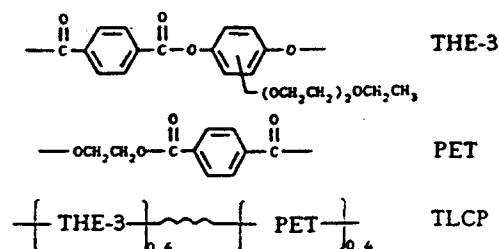
A common observation is that wholly aromatic liquid crystalline polymers are immiscible with other polymers. Recently, the blends of a side-group LCP with thermoplastic resins were studied by some authors [4]. Heitz et al. [5] described that the side-group LCP in blends not only improved solubility and reduced transition temperatures, but also changed the morphology of their blends. This result implies that the existence of the flexible side group in the LCP plays an important role in reinforcing the thermoplastic matrix.

In this work, we have measured the linewidth and spin-lattice relaxation time (T_1) according to the amount of LCP in polyblends. In addition to knowledge about the molecular orientation, information concerning the molecular motion is expected to give insight into the nature of liquid crystalline copolyester blends.

II. Experimental

For simplicity, the blends will be described as 0% LCP/PBT, 3% LCP/PBT, 5% LCP/PBT et al. Where LCP and PBT represent the polymer components used to prepare the blend, the numbers denote the amount of LCP in the blend

in weight percent. For example, 0% LCP/PBT represents pure PBT while 10% LCP/PBT indicates that the blend contains 10 weight percent LCP. The chemical structure of the THE-3, PET and TLCP are as follows:



The relaxation time of ¹H in the LCP/PBT was investigated using a Bruker MSL 200 FT NMR spectrometer. The ¹H NMR spectra was measured with a static magnetic field of 4.7 T.

III. Results and Discussion

Temperature dependencies of the full width at half maximum according to the amount of LCP and PBT are shown in Fig. 1 as a function of the inverse of temperature. The linewidth

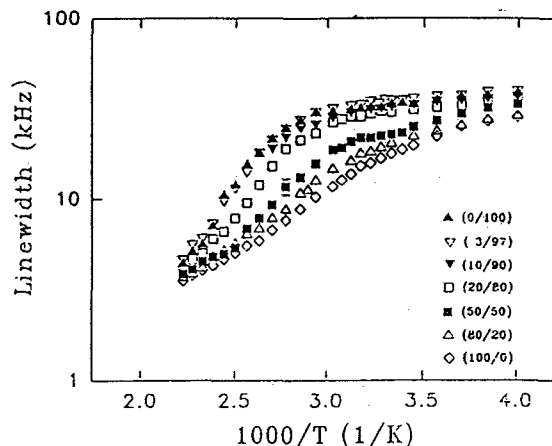


Fig. 1. Linewidth of LCP/PBT as a function of temperature.

gradually decreases with increasing temperature. The tendencies of the change with respect to the temperature are similar with each other, but the linewidth is varied with temperatures more drastically as lowering the LCP percent. Near the temperature which varied most drastically, the intramolecular dipolar interaction became the average by motion. Also, the decrease of the linewidth with increasing temperature is due to the motional narrowing effect.[6]

The nuclear magnetization $M_z(t)$ for 3% LCP/PBT sample was determined from the height of the free induction decay-tails following the inversion recovery sequence (180° - t - 90°) pulse. [7] The T_1 values were determined from $\log[(M_0 - M_z)/2M_0]$ vs. time plot, where M_0 is the nuclear magnetization of ^1H in thermal equilibrium. Temperature dependence of $1/T_1$ is shown in Fig. 2. The inverse T_1 relaxation rates

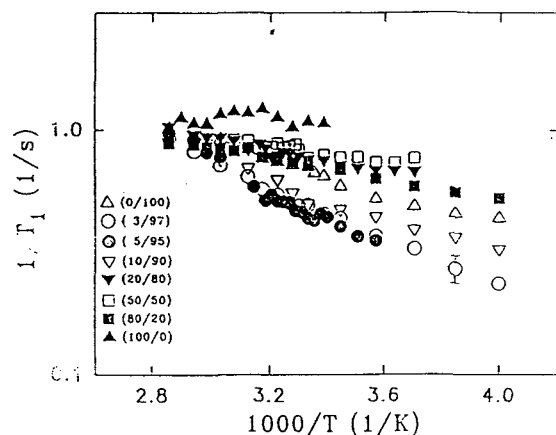


Fig. 2. Temperature dependence of T_1 for LCP/PBT as a function of temperature.

increases as the temperature increases. From this result, we know that the dominant mechanism of the relaxation is related to the changes in motion on blending. The behavior of $1/T_1$ is nearly linear with $1/T$, which indicates that the relaxation is mostly determined by a single mode of the thermal fluctuation with correlation frequencies lower than of 200.13 MHz.[8] This T_1 behavior can be analyzed with the equation given by [9]

$$1/T_1 \propto \exp(-E_a/kT) \quad (1)$$

where E_a is activation energy for the modulation, k Boltzmann constant. The

activation energy vs. LCP ratio is obtained by eq. (1). The activation energy decrease with the increase in the LCP concentration in the blends.

IV. Conclusions

We have been investigating by linewidth and T_1 of ^1H according to the LCP concentration in the wide temperature range. The decrease of the linewidth with increasing temperature is due to the motional narrowing effect. The dominant mechanism of the relaxation is related to the changes in motion on blending. The activation energy is decreased as the LCP ratio increases. Activation energies were estimated to be 8.3 kJ mol^{-1} for the pure LCP. The value of pure LCP are larger than that of 50 and 80 % LCP/PBT.

Reference

- [1] K. Friedrich, M. Hess, and R. Kosfeld, *Makromol. Chem., Macromol. Symp.*, **16**, 251 (1988).
- [2] M. Ameno and K. Nakagawa, *Polymer*, **28**, 263 (1987).
- [3] C. U. Ko and G. L. Wilkes, *J. Appl. Polym. Sci.*, **37**, 3063 (1989).
- [4] G. Sigaud, M. F. Achard, F. Hardouin, and H. Gasparous, *Mol. Cryst. Liq. Cryst.*, **155**, 443 (1988).
- [5] T. Heitz, P. Rohrbach, and H. Hocker, *Makromol. Chem.*, **190**, 3295 (1989).
- [6] A. Abragam, *The Principles of Nuclear Magnetism*, p451 (1961).
- [7] E. Fukushima, S. B. W. Roeder, *Experimental Pulse NMR*, p169 (1981).
- [8] N. Bloembergen, E. M. Purcell, and R. V. Pound, *Phys. Rev.* **73**, 679 (1948).
- [9] B. C. Gerstein, C. R. Dybowski, *Transient Techniques in NMR of Solids*, p84 (1985).

In-Vivo and In-Vitro Analysis of CNS Cancers by ^1H -NMR Spectroscopy

S. Dodd \diamond , B.P. Shehan*, O. Hennessy \diamond and D.J. Craik*

\diamond Department of Radiology, University of Melbourne, Parkville 3052, Australia

*Monash University, Victorian College of Pharmacy, 381 Royal Pde, Parkville 3052, Australia

Many types of neoplastic disease can effect the central nervous system, including primary cancers of the CNS such as gliomas and meningiomas as well as secondary metastatic growths from primaries in any of a number of sites. Neoplastic growth of all types may display biochemistry different to their host tissue and alter the biochemistry of the tissue and fluid immediately surrounding the neoplasm. The use of NMR spectroscopy to detect these biochemical changes may well be of value in diagnostic medicine, particularly if those changes can be detected in-vivo by a method which is quick, safe and non-invasive. In-vitro analysis of specimens collected from cancer patients is also useful research, as this strategy is more likely to identify diagnostic markers of cancer due to the vastly superior resolution with in-vitro spectroscopy compared to in-vivo spectroscopy.

Our research goals were tested by analysing human cerebrospinal fluid (CSF) collected from patients with cancers in their CNS as well as control subjects and by analysing male Wistar rats post cell passage of the glioblastoma multiforme C6 cell line. Resected rat brain specimens were also analysed ex-vivo. Analysis by ^1H -NMR spectroscopy was conducted using a wide bore spectrometer operating at 300MHz.

Cerebrospinal Fluid:

The cerebrospinal fluid is a clear fluid which bathes the brain and spinal cord and freely exchanges with the extracellular fluid of the CNS. Perturbations in the biochemical balance in the CNS can sometimes be detected in specimens of CSF. Specimens can be collected by puncturing the arachnoid membrane with a 22G 150mm needle passed usually between the third and fourth lumbar vertebrae of a patients spine. The fluid drips freely from the end of the needle. One hundred and eighty-four specimens of human CSF were collected for research purposes from patients at the Austin Hospital, some of these specimens coming from patients afflicted with CNS cancers. None of the specimens were collected from healthy controls so a control group of normal

specimens was assembled by selecting twenty-five specimens from patients afflicted with medical conditions unlikely to effect the composition of their CSF. Specimens were lyophilised and reconstituted in deuterium oxide. Quantification of metabolites was achieved in the control and experimental specimens by comparing integral of metabolite peaks to the integral of TSP, which had been added as an exogenous reference. Comparing NMR spectra from the control group and the cancer patients revealed raised levels of lactate, alanine, valine, β -hydroxybutyrate and lowered glucose. The raised lactate and lowered glucose in the cancer patients is most likely explained by anaerobic glycolysis in the neoplastic cells, the raised alanine and valine as a product of increased cell proliferation and death, and the raised β -hydroxybutyrate possibly as a mechanism for compensating against the increased glucose consumption. There also appeared to be a correlation between the severity of the biochemical imbalance and the extent to which the cancer had advanced.

Glioblastoma multiforme in Wistar rats:

Research was conducted using forty Wistar rats. Glioblastoma multiforme cells, washed and suspended in 0.9% saline solution, were passaged in 10 μL boluses into the left forebrains of twenty-two rats. Seventeen other rats underwent sham operations and one rat died perioperatively. In-vivo ^1H NMR spectroscopy was performed regularly on the rats' brains over a period of up to three weeks post surgery using a surface coil positioned against the rats' craniums. The spectra obtained were not of a high enough quality to recognise distinct characteristic diagnostic markers in the spectra of the rats with GBM. However when analysing the differences between spectra

from the control and experimental groups some trends could be noted. Integrals between 1.13ppm and 1.53ppm, the region of the lactate and alanine methyl peaks, were significantly greater ($p < 0.05$) for the rats with GBM than for the control group. In-vitro ^1H NMR spectroscopy was conducted on ex-vivo specimens simultaneously collected from the left and right hemispheres of rats from both the control and experimental groups. Spectra from the control group were all similar and normal appearing. Spectra from the rats with GBM showed considerable variation. Raised lactate, probably from anaerobic glycolysis, and reduced N-acetylaspartate, from neuronal depletion, were common in many left forebrain spectra.

Conclusion:

The research demonstrated that ^1H NMR

spectroscopy could be used to demonstrate the presence of CNS cancers. Results from the study of patients and rats showed considerable variability though some clear trends did emerge. Lactate peaks, characteristic of anaerobic glycolysis, were high with CNS cancer when compared to controls in both groups and peaks characteristic of cell death were present in both groups; lowered N-acetylaspartate in the rats and raised alanine and valine in the CSF.

Results specific and definitive enough to be used to confidently make diagnostic decisions based on NMR spectra did not emerge, although the results do not negate but rather reinforce the position that NMR spectroscopy may have a more significant role in diagnostic medicine in the future.

Spectral Editing in ^{13}C CP/MAS Experiment at High Magnetic Field

Jian Zhi Hu, Xiaoling Wu, Nianhua Yang, Liyun Li, Chaohui Ye
Laboratory of Magnetic Resonance and Atomic and Molecular Physics, Wuhan Institute
of Physics, The Chinese Academy of Sciences, Wuhan 430071, P. R. China

R. J. Pugmire and David. M. Grant

Departments of Chemistry and Chemical and Fuels Engineering,
University of Utah, Salt lake City, Utah 84112

Kuangzong Qin

Petroleum University at Beijing, P.O. Box 902, Beijing 100083, P. R. China

In a system with quite a few chemically distinct nuclei, the standard ^{13}C CP/MAS spectrum is usually very crowded, and spectral assignment may be very difficult. A spectral editing technique, such as the DEPT experiment in liquid state ^{13}C NMR, is highly desirable to simplify complex spectrum and to make unambiguous spectral assignment. Great efforts have been made in the past in order to design a general spectral editing pulse sequence in solid state, among them, a technique recently reported by Wu et al [1] can be used as a routine, complete spectral editing in ^{13}C CP/MAS experiment. This elegant technique uses a proper combination of polarization, polarization-inversion and depolarization periods in ^{13}C CP/MAS experiment to generate subspectra for each kind of carbon according to its attached proton multiplicity. The advantages of Wu et al's technique are in the following. First, it is simple in implementation. Second, a reliable spectral assignment in ^{13}C CP/MAS spectrum can be generally obtained. Besides, the subspectra generated are semi-quantitative. All of these features make it an attractive tool for the analysis of compounds with complex molecular structure such as

coal.

There are five basic experiments in the original spectral editing technique [1], i.e., the LCP, SCP, SCPPI, SCPD and LCPD experiments. Among them the SCPPI and SCPD experiments are rather time consuming. Compared with the standard ^{13}C CP/MAS experiment, only about 1/5 of the sensitivity is obtained by SCPPI and about 1/10 of the sensitivity by SCPD. Sensitivity enhancement is highly desirable. Performing spectral editing at high magnetic field is one of the relevant ways to achieve this goal. It is shown that the elegant spectral editing technique can be extended to high magnetic field by simply incorporating the sideband suppression pulse sequence, i.e., the TOSS pulse sequence [2], into the basic spectral editing pulse sequences. The advantages and disadvantages at high magnetic field will be addressed in detail elsewhere [3].

The elegant spectral editing technique of Wu et al would be more useful if the following two problems are properly solved.

1. The nonprotonated and methyl carbons in the LCPD experiment were separated in the original paper by simply setting a boundary

chemical shift value, i.e., 35 ppm, where the resonances with chemical shift value of larger than 35 ppm are assigned to nonprotonated carbons, while those with chemical shift value less than 35 ppm are assigned to methyl carbons. Although such a boundary chemical shift value is valid for most organic solids, however it is not true for a system containing methoxy group since a chemical shift value of larger than 50 ppm is generally obtained for the methoxy carbon. The situation becomes even worse when resonances for nonprotonated and methyl carbons are overlapped, where no clear separation can be made by any suggested boundary chemical shift value.

2. In the original paper, the (CH + CH₂) only spectrum is produced in the following way. First, a standard ¹³C CP/MAS short contact time (SCP) spectrum is acquired. The residual polarizations for both the nonprotonated and methyl carbons in SCP spectrum are then subtracted out by a compensated experiment, i.e. the short contact time polarization and depolarization (SCPD) experiment. Unfortunately, elimination of the residual signal for the nonprotonated and methyl carbons in SCP spectrum is incomplete because the relative ratio of the signal intensity for the methyl carbons to the nonprotonated carbons in SCP (24.8/8.4) is different from that in SCPD (10.4/7.2) [1].

It is shown in this work that the large difference of ¹³C spin-lattice relaxation time between the nonprotonated carbons and the methyl carbons generally encountered in solids can be used as an additional criterion in distinguishing the nonprotonated carbons from the methyl carbons in ¹³C CP/MAS spectral editing process. This

is helpful for a system with complex molecular structure, especially when a spectral overlapping for the nonprotonated and methyl carbons is encountered. As long as the resonances for the nonprotonated carbons and the methyl carbons are clearly separated, the SCPD TOSS spectrum at high field, or alternatively the SCPD spectrum at low field, which has the lowest sensitivity, can be simply omitted. In this way, the problem associated with the different relative ratios of the nonprotonated carbons to the methyl carbons in the SCPD TOSS (SCPD) and the SCP TOSS (SCP) spectra is avoided. A complete spectral editing in ¹³C CP/MAS experiment can thus be achieved with proper combinations of the SCP TOSS, SCP PIT OSS, LCPD TOSS spectra and a partially relaxed LCPD TOSS spectrum at a recovery time suitably chosen.

References:

- [1] X. Wu, S. Burns and K. W. Zilm, *J. Magn. Reson. A*, 111 (1994) 29.
- [2] W. T. Dixon, *J. Chem. Phys.* 77 (1982) 1800.
- [3] J. Z. Hu, X. Wu, N. Yang, L. Li, C. Ye and K. Qing, *Solid State NMR*, in press.

PFG-INADEQUATE for Detection of Two and Three Bond ^{13}C - ^{13}C Couplings

Hiroyuki Koshino and Jun Uzawa

The Institute of Physical and Chemical Research (RIKEN)
Wako, Saitama 351-01, Japan

The 2D-INADEQUATE (Incredible Natural Abundance Double QUAntum Transfer Experiment) experiment (1,2) is useful and powerful technique for structural determination and assignments of carbon signals of a molecule because the carbon-carbon connectivities of a molecule are easily established by the analysis of the network of one-bond AX and AB spin systems. However, there are some limitations to use the INADEQUATE widely, because of the low natural abundance of the ^{13}C nuclei. To improve the S/N ratio, polarization-transfer from more-sensitive protons have been employed in the INEPT-INADEQUATE (3) and DEPT-INADEQUATE experiments (4). To overcome the low sensitivity of ^{13}C nuclei, proton detected INSPID (5) and INEPT-INADEQUATE experiment (6,7) have been reported. Recently pulsed field gradient (PFG) have been successfully used to coherence selection in several multi-dimensional NMR spectroscopy (8). We also recently showed that PFG-INADEQUATE (9) using PFG to select double quantum coherence (10) improved the S/N ratio by drastic suppression of unwanted t_1 noise and artifact signals without any noise suppression such as symmetryzation procedure (11). Here we present the application of PFG-INADEQUATE experiment for detection of two and three bond carbon-carbon connectivities and measurement of the coupling constants ($^2J_{\text{CC}}$ and $^3J_{\text{CC}}$).

The pulse sequence of PFG-INADEQUATE for indirect coupling is the same pulse sequence using for direct couplig(Fig. 1). If phase sensitive mode is necessary to enhance the resolution, the pulse sequence can be modified by addition of one more 180° pulse at the end of evolution time, and measurement of P- and N-type spectra using inversion of one gradient in each separate scan (12). To detect indirect carbon-carbon correlations, the delay time $\tau = (2n+1)/4J_{\text{CC}}(n = 0, 1, 2, \dots)$, usually $1/4J$ (1), in the preparation pulse sequence is simply optimized for average of indirect coupling constant values. If there is little or no information about indirect carbon-carbon coupling constants for a target molecule, two or more experiments using different delay time will avoid missing of some signals with coupling constant value of $nJ_{\text{CC}} = n/2\tau$ ($n=1, 2, \dots$). PFG-INADEQUATE spectrum of nicotine at natural abundance as a model sample is shown in Fig. 2 with delay time optimal for $nJ_{\text{CC}} = 2.5\text{Hz}$ ($\tau = 100\text{msec}$). All possible two and three bond correlations are observed except four correlations which have 0Hz coupling constant. All coupling constants could measure from each slice data of three experiments ($\tau = 5.0, 31.25$ and 100 msec) and are summarized below.

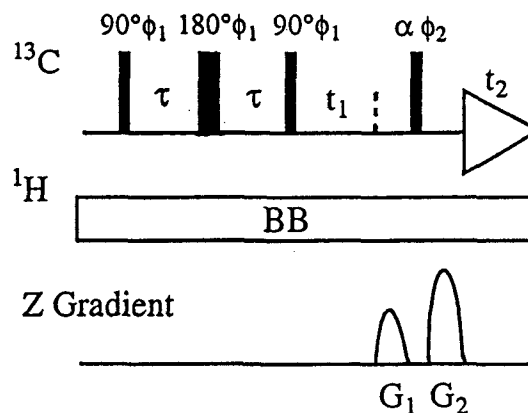


Fig. 1. Pulse sequence of the PFG-INADEQUATE. For N-type spectrum, gradients ratio of $G_1 : G_2 = 1 : 2$ and read pulse of $\alpha = 120^\circ$ were used. For P-type spectrum, gradients ratio of $G_1 : G_2 = -1 : 2$ and read pulse of $\alpha = 60^\circ$ were used (20). For the gradients, a sine shape was used. Phase cycling was same that of conventional one as follows: $\phi_1 = x, y, -x, -y, -x, y, x, y$; $\phi_2 = 4x, 4y, 4(-x), 4(-y)$; $\text{rec} = 2(x, -x), 2(-y, y), 2(-x, x), 2(y, -y)$.

One-bond: $^1J(\text{C}2, \text{C}3) = 56.6\text{Hz}$, $^1J(\text{C}3, \text{C}4) = 55.7\text{Hz}$, $^1J(\text{C}4, \text{C}5) = 54.2\text{Hz}$, $^1J(\text{C}5, \text{C}6) = 55.2\text{Hz}$, $^1J(\text{C}3, \text{C}2') = 49.1\text{Hz}$, $^1J(\text{C}2', \text{C}3') = 35.2\text{Hz}$, $^1J(\text{C}3', \text{C}4') = 31.7\text{Hz}$, $^1J(\text{C}4', \text{C}5') = 34.2\text{Hz}$, Two-bond: $^2J(\text{C}2, \text{C}4) < 0.5\text{Hz}$, $^2J(\text{C}2, \text{C}6) = 6.4\text{Hz}$, $^2J(\text{C}2, \text{C}2') = 3.9\text{Hz}$, $^2J(\text{C}3, \text{C}5) = 2.5\text{Hz}$, $^2J(\text{C}3, \text{C}3') < 0.5\text{Hz}$, $^2J(\text{C}4, \text{C}6) = 2.5\text{Hz}$, $^2J(\text{C}4, \text{C}2') = 1.2\text{Hz}$, $^2J(\text{C}2', \text{C}4') = 0\text{Hz}$, $^2J(\text{C}2', \text{C}5') = 3.2\text{Hz}$, $^2J(\text{C}2', \text{C}6') = 0\text{Hz}$, $^2J(\text{C}3', \text{C}5') = \text{ca } 0.5\text{Hz}$, $^2J(\text{C}5', \text{C}6') = 0\text{Hz}$, Three-bond: $^3J(\text{C}2, \text{C}5) = 12.2\text{Hz}$, $^3J(\text{C}2, \text{C}3') = 1.2\text{Hz}$, $^3J(\text{C}3, \text{C}6) = 12.2\text{Hz}$, $^3J(\text{C}3, \text{C}4') = 2.9\text{Hz}$, $^3J(\text{C}3, \text{C}5') = 4.4\text{Hz}$, $^3J(\text{C}3, \text{C}6') = 0\text{Hz}$, $^3J(\text{C}4, \text{C}3') = 1.0\text{Hz}$, $^3J(\text{C}5, \text{C}2') = 2.7\text{Hz}$, $^3J(\text{C}3', \text{C}6') = 3.4\text{Hz}$, $^3J(\text{C}4', \text{C}6') = 4.4\text{Hz}$, Four-bond: $^3J(\text{C}6, \text{C}2') < 0.5\text{Hz}$.

The INADEQUATE data of indirect carbon-carbon correlations usually supports the data of direct correlations of INADEQUATE and other 2D NMR data, because one bond carbon-carbon network is cut off by heteroatoms in many molecules and carbon-carbon three bond correlation corresponds with proton-carbon four bond correlation. In some case, e.g. a molecule have a symmetrical part, or chemical shift difference of each coupled carbons with AB quartet pattern is very small, detection of direct carbon-

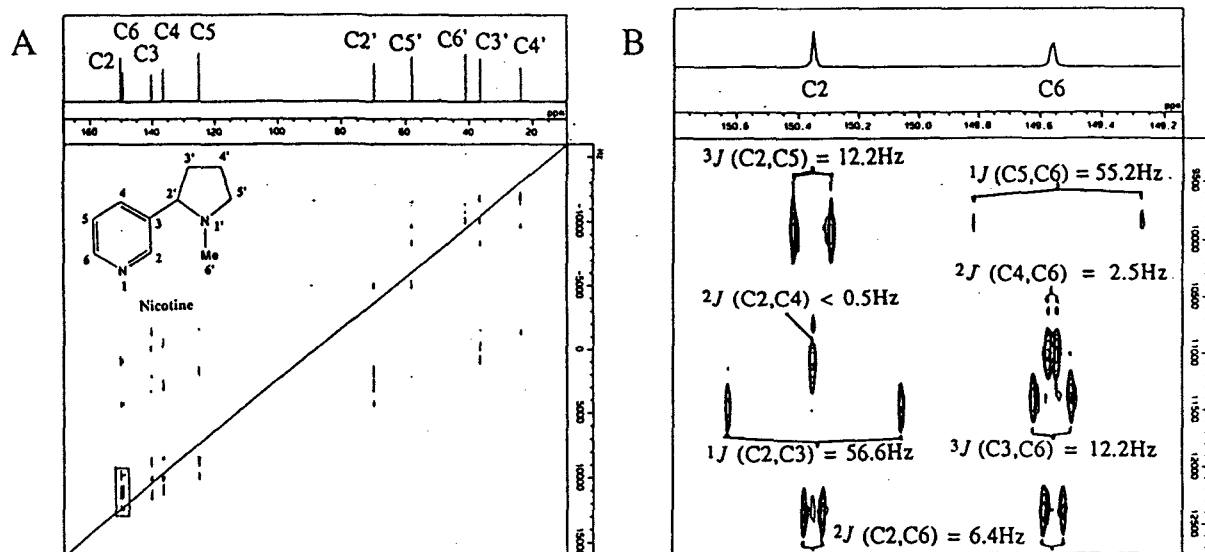


Fig.2. PFG-INADEQUATE spectra of nicotine(394mg in CD_3OD) at 100MHz. A 16K(F2) x 128(F1) data matrix with 48 scans / t_1 increment and spectral width of 16KHz in ω_2 and 32KHz in ω_1 was zero-filled once in both ω_1 and ω_2 . $\tau = 100$ msec. G_1 and G_2 are 5.76 and 11.52 G/cm with 1msec duration. A) Full spectrum. (B) Expanded region of the box in (A).

carbon connection may be impossible or quite difficult (13). Geminal coupling constants $^2J_{CC}$ provide some useful structural information e.g. presence of carbonyl group (14) or presence of four membered ring(15), and vicinal coupling constants $^3J_{CC}$ have dependence on the dihedral angle similar to proton-proton and proton-carbon vicinal coupling constants(16, 17). However there have been not so much application of carbon-carbon indirect coupling constant values for structural analysis before now, by reason that specific labelling by ^{13}C isotope is sometimes necessary, and there are little techniques easily available for target molecules at natural abundance (18, 19).

For the purpose of indirect coupling detection the INADEQUATE spectrum must be free from t_1 noise and artifact signals. If some t_1 noise are present in a spectrum, correlation peaks may be overlapped on t_1 noise because indirect carbon-carbon coupling constants are usually small. Direct carbon-carbon coupling constants are larger than the width of t_1 noise, therefore remaining t_1 noise is not severe problem for analysis of one-bond connectivities. The PFG-INADEQUATE technique is suitable to detect indirect carbon-carbon couplings by reason of t_1 noise free.

References

- 1A. Bax, R. Freeman, and T. A. Frenkiel, *J. Am. Chem. Soc.* **103**, 2102 (1981).
- 2A. Bax, "Two-Dimensional Nuclear Magnetic Resonance in Liquids" p.155, Delft Univ. Press, Delft, The Netherlands, 1982.
- 3O. W. Spørensen, R. Freeman, T. Frenkiel, T. H. Mareci, and R. Schuck, *J. Magn. Reson.* **46**, 180 (1982).
- 4S. W. Sparks and P. D. Ellis, *J. Magn. Reson.* **62**, 1 (1985).
- 5P. J. Keller and K. E. Vogele, *J. Magn. Reson.* **68**, 389 (1986).
- 6J. Weigelt and G. Otting, *J. Magn. Reson. A*, **113**, 128 (1995).
- 7B. Reif, M. Köck, and C. Griesinger, "Book of Abstracts, 36th Experimental NMR Conference, Boston, March 26-30, 1995", p.104.
- 8R. E. Hurd, *J. Magn. Reson.* **87**, 422 (1990).
- 9J. Uzawa and H. Koshino, "Book of Abstracts, 36th Experimental NMR Conference, Boston, March 26-30, 1995", p.115.
- 10I. M. Brereton, S. Crozier, J. Field, and D. M. Doddrell, *J. Magn. Reson.* **93**, 54 (1991).
- 11J. Lambert and J. Buddrus, *J. Magn. Reson. A*, **101**, 307 (1993).
- 12J. Balbach and H. Kessler, *J. Magn. Reson. B*, **105**, 83 (1994).
- 13A. Bax and R. Freeman, *J. Magn. Reson.* **41**, 507 (1980).
- 14F. J. Weigert and J. D. Roberts, *J. Am. Chem. Soc.* **94**, 6021 (1972).
- 15M. Stöcker and M. Klessinger, *Org. Magn. Reson.* **12**, 107 (1979).
- 16P. E. Hansen, *Annu. Rep. NMR Spectrosc.* **11A**, 65 (1981).
- 17H. O. Kalinowski, S. Berger, and S. Braun, "Carbon-13 NMR Spectroscopy", p. 549, John Wiley & Sons Ltd., 1988.
- 18A. Bax, R. Freeman, and S. P. Kempell, *J. Am. Chem. Soc.* **102**, 4849 (1980).
- 19A. Bax, R. Freeman, and S. P. Kempell, *J. Magn. Reson.* **41**, 349 (1980).
- 20T. H. Mareci and R. Freeman, *J. Magn. Reson.* **48**, 158 (1980).

^1H -NMR Spectroscopic Studies on the Interaction between Local Anesthetic Dibucaine and a Na^+ -Channel Inactivation Gate Peptide

Yoshihiro Kuroda, Masahiro Ogawa, Nobutaka Fujii, and Terumichi Nakagawa

Faculty of Pharmaceutical Sciences, Kyoto University, Kyoto, 606-01, Japan

Introduction

Recently, it has been shown that a cluster of hydrophobic amino acids, Ile-1488, Phe-1489, and Met-1490 within the intracellular linker between domains III and IV of the rat brain type IIA Na^+ -channel protein α -subunit serves as an essential component of the inactivation particle for occluding the intracellular mouth of the activated Na^+ -channel [1]. Since local anesthetics are known to enhance the inactivated state of the Na^+ -channel, the interaction between local anesthetic dibucaine and a model peptide which includes the hydrophobic amino acids, Ac-GGQDIFM-TEEQK-OH (MP-1), and the one in which Phe has been substituted by Gln (MP-2) has been studied by ^1H -NMR spectroscopy. Presently, we focussed our attention on the expected π -stacking interaction between the quinoline ring of dibucaine and the benzene ring of Phe in MP-1, because this π -stacking interaction can be considered to play an essentially important role for stabilizing the inactivated state of the Na^+ -channel which may results in local anesthesia.

Experimental

Dibucaine hydrochloride and bovine brain L- α -phosphatidylserine (PS) were obtained from Sigma. Peptides, MP-1 (Ac-GGQDIFMTEEQK-OH) and MP-2 (Ac-GGQDIQMTEEQK-OH) were synthesized by the solid phase method using Fmoc chemistry; their N-termini were acetylated and their C-termini were free carboxylic acids. ^1H -NMR spectra were observed on a Bruker AM-600 (600 MHz) spectrometer with a digital resolution of 0.18 Hz/point. The chemical shifts were referenced to TSP (3-trimethylsilyl-propionic acid- d_4 sodium salt).

Results and Discussion

Figure 1 shows the changes in chemical shifts of the quinoline ring proton resonances of dibucaine which were caused as a result of interaction with MP-1 or MP-2 in sonicated unilamellar PS liposomes. It is worth noting that all the quinoline ring proton resonances shifted to low frequency as a result of interaction with both MP-1 and MP-2; however, more remarkable is that MP-1 caused

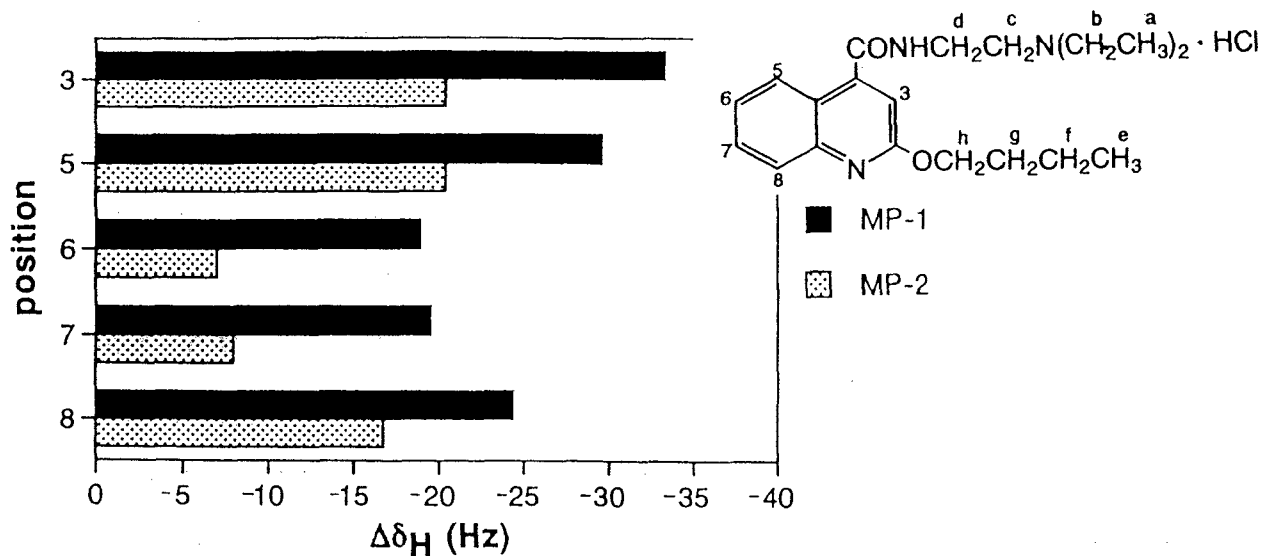


Fig. 1 Changes in ^1H Chemical Shifts (in Units of Hz at 600 MHz) of Dibucaine (3 mM) as a Result of the Interaction with MP-1 (3 mM) or MP-2 (3 mM) in Unilamellar PS Liposomes (15 mM) at pH 7.4.

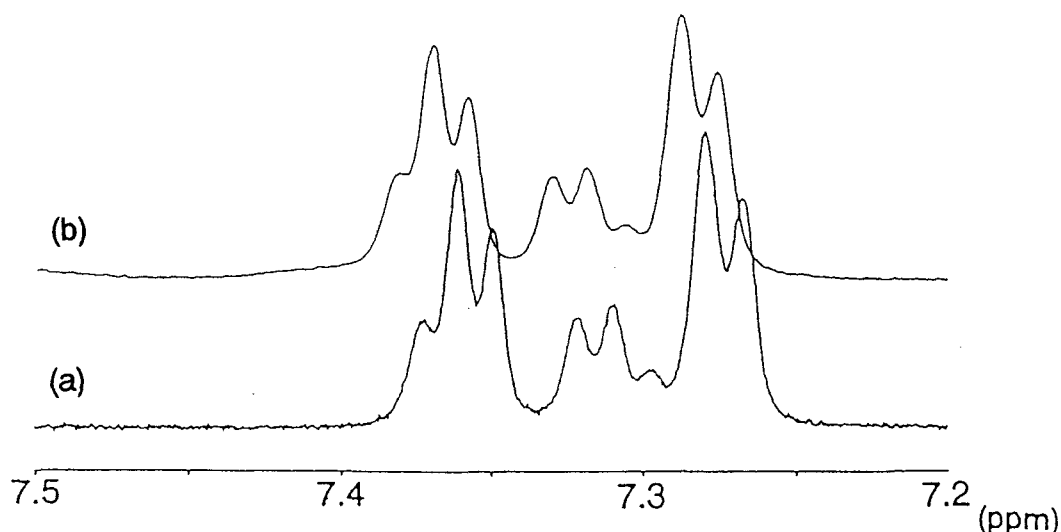


Fig. 2 (a) ^1H -NMR Spectrum of the Phenyl Group Protons of MP-1 in the PS Liposomes (15 mM) at pH 7.4; (b) ^1H -NMR Spectrum of the Phenyl Group Protons of MP-1 (3 mM)-Dibucaine (3 mM) Solution in the PS Liposomes at pH 7.4.

larger low frequency shift to those resonances than did MP-2. The reasoning for the low frequency shift on addition of MP-2 is not clear at present; this should be explained together with the changes in chemical shift of those resonances as a result of interaction with PS liposomes. However, undoubtedly, the larger low frequency shift caused by MP-1 than by MP-2 should be ascribed to the π -stacking interaction between the quinoline ring of dibucaine which locates at a polar head group moiety of lipids [2] and the phenyl group of Phe in MP-1 coming close to the surface of the lipids.

Figure 2a and b shows ^1H -NMR spectra of the phenyl group protons of Phe, in the absence and presence of dibucaine in the PS liposomes, respectively. The spin-coupled peaks at around 7.36, 7.32, and 7.27 ppm are due to meta-, para-, and ortho-protons, respectively. We notice that in contrast to the low frequency shift of the quinoline ring proton resonances of dibucaine, the phenyl group resonances of MP-1 shifted to high frequency. According to the theory for the aromatic ring-current effect, this result indicates that the two aromatic rings are so arranged that the phenyl group protons of Phe locate at the side of the quinoline ring of dibucaine and the quinoline ring-protons on the plane of the phenyl group of Phe. Although we cannot imagine an interaction model which satisfies these situations for the whole ring-protons within one relative arrangement of the two aromatic rings, an edge-on or T-shaped geometry for the two π -stacking aromatic rings seems to be a reasonable one [3]. Taking Hunter et al's rule 6 into account [3], the quinoline ring can be considered to be " π -deficient atom" and the phenyl group to be " π -rich atom". This finding agrees well with *a priori* expectable one when we consider the differences in the substituents on the aromatic rings. In conclusion, the

presently obtained data can afford firm evidence to our proposals for the molecular mechanisms of local anesthesia that the drug residing at a polar head group region of the so-called boundary lipids locating in the vicinity of the Na^+ -channel pore, binds with the clustered hydrophobic amino acids of the linker between domains III and IV, especially with the phenylalanine residue and results in stabilization of the inactivated state which causes local anesthesia.

References

- ¹J. W. West, D. E. Patton, T. Scheuer, Y. Wang, A. L. Goldin, and W. A. Catterall, Proc. Natl. Acad. Sci. USA 89, 10910 (1992).
- ²Y. Kuroda, M. Ogawa, H. Nasu, M. Terashima, Y. Fujiwara, and T. Nakagawa, The 36th ENC, Boston, Massachusetts, 1995, P-230.
- ³C. A. Hunter and J. K. M. Sanders, J. Am. Chem. Soc. 112, 5525 (1990).

Cerebral Metabolic Compartmentation as Revealed by ^{13}C NMR, ^{13}C - ^{13}C and ^{13}C - ^{15}N Isotopomer Analyses

Aviva Lapidot

Department of Organic Chemistry, The Weizmann Institute of Science, Rehovot 76100, Israel

Introduction

In acute hyperammonia, increased efflux of glutamate to glutamine by glutamine synthetase activity, combined with ammonia-mediated inhibition of glutaminase, may result in depletion of the neurotransmitter pool of glutamate, leading to a coma, often observed in hepatic encephalopathy. Since glutamine synthetase is associated with the anaplerotic pathway in astrocytes, it was of interest to investigate whether the activity of the other key anabolic enzyme pyruvate carboxylase is induced in order to replenish the neurotransmitter pool.

We have recently described (1) a quantitative approach by ^{13}C isotopomer analysis for measuring glucose flux mediated by pyruvate dehydrogenase and pyruvate carboxylase activity in the brain following $[\text{U-}^{13}\text{C}]$ glucose administration to young rabbits. In this study we apply ^{13}C - ^{13}C and ^{13}C - ^{15}N coupling parameters for studying any derangement of cerebral metabolic compartmentation caused by hyperammonemia.

Animals and Experimental Procedures

Young rabbits received either $[\text{U-}^{13}\text{C}]$ glucose (99% enriched) or non-labeled glucose as a primed dose-constant infusion for 60 minutes (~ 1.0 mg / Kg body wt / min). Hyperammonemia was induced by either i.v. infusion of NH_4Cl or $^{15}\text{NH}_4\text{Cl}$. Methionine sulfoximine was given i.p. as an inhibitor of glutamine synthetase. Rabbits treated with $^{15}\text{NH}_4\text{Cl}$ were infused with non-labeled glucose. Neutralized brain extracts were analyzed by ^{13}C NMR.

Results and Discussion

1. ^{13}C NMR studies of $[\text{U-}^{13}\text{C}]$ glucose metabolites: ^{13}C - ^{13}C spin coupling analysis.

The results presented in this study indicate the feasibility of quantitating cerebral compartmentation and determining trafficking between the compartments.

The isotopomers 1,2,3- ^{13}C and 2,3- $^{13}\text{C}_2$ of glutamate or glutamine arise only when D- $[\text{U-}^{13}\text{C}]$ glucose is metabolized via the anaplerotic pathway, where pyruvate carboxylase and glutamine synthetase reside.

Our results show that the populations of these isotopomers are significantly higher in glutamine than in glutamate in the brains of control animals and even much higher in the brains of animals infused with NH_4^+ and D- $[\text{U-}^{13}\text{C}]$ glucose (Fig. 1). This marked difference in isotopomer population of glutamate and glutamine is the result of different isotopomer populations of oxaloacetate associated with different tricarboxylic acid cycles in the neurons and glia.

The labeling pattern and ^{13}C isotopomer population of glutamine indicate that this amino acid is preferentially synthesized in the compartment where glucose is metabolized to pyruvate, followed by carboxylation to oxaloacetate by pyruvate carboxylase. In contrast, the labeling patterns and ^{13}C isotopomer population of glutamate and GABA carbons indicate that these amino acids are preferentially synthesized in the compartment where glucose is metabolized to acetyl-CoA by pyruvate dehydrogenase for entry into the tricarboxylic acid cycle. The relative fluxes via pyruvate carboxylase and pyruvate dehydrogenase activities are reflected by the ratio of the isotopomer populations of glutamate and glutamine C-3/C-4 or C-2/C-4. The ratio of these isotopomer populations is 2.8-fold higher in glutamine than in glutamate in hyperammonemic rabbits. Thus, the contribution of pyruvate carboxylase activity to glutamine synthesis increased to 60% in hyperammonemic rabbits, while its contribution to glutamate synthesis increased to 23% in hyperammonemic rabbits.

These results are related to metabolic trafficking between astrocytes and neurons, the flux of glutamate and GABA from neurons to astrocytes, and the flux of glutamine and tricarboxylic acid cycle intermediates from astrocytes to neurons. Although the pool of glutamate localized in the neurons is significantly higher (80% of the brain glutamate) than its precursor, the brain glutamine, which is located within the astrocyte, consists of about 40% of glutamate molecules obtained from their precursor glutamine in control animals and

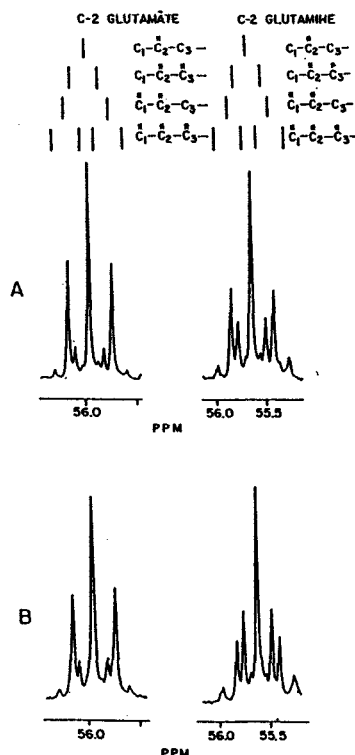


Fig. 1. Schematic presentation of isotopomer populations of glutamate and glutamine C-2 coupled to either one ^{13}C , $[1,2-^{13}\text{C}_2]$ or $[2,3-^{13}\text{C}_2]$ - doublet resonance, or two adjacent ^{13}C , $[1,2,3-^{13}\text{C}_3]$ (quartet). The corresponding observed superposition spectra reveal different populations of doublets and quartet resonances in glutamate in comparison to glutamine in control (A), and hyperammonemic (B) rabbits with a significantly higher population of the isotopomer $[2,3-^{13}\text{C}_2]$.

Table: Natural abundance ^{13}C NMR detected by ^{13}C - ^{15}N spin coupling pattern and ^{15}N -induced upfield isotopic shifts in the carbons of glutamate, glutamine and alanine in neutralized brain extracts at 125.76 MHz (at 23°C).

Observed carbon	$J_{\text{C-N}}$ (Hz)	Isotope effect (ppm)
Gln	C-2 $^1J_{(\text{C}_2-\text{N}_2)} = 5.4$	0.022
	C-4 $^2J_{(\text{C}_4-\text{N}_5)} = 7.3$	0.003
	C-5 $^1J_{(\text{C}_5-\text{N}_5)} = 16.2$	0.016
Glu	C-2 $^1J_{(\text{C}_2-\text{N}_2)} = 5.6$	0.019
Ala	C-2 $^1J_{(\text{C}_2-\text{N}_2)} = 5.6$	0.023

in hyperammonemic rabbits.

As a result of inhibiting glutamate synthesis by MSO, alanine concentration and its ^{13}C enrichment increased. Thus, pyruvate obtained from cerebral glycolysis is an important substrate for ammonia removal.

II. Natural abundance ^{13}C NMR of ^{15}N labeled brain metabolites; ^{13}C - ^{15}N spin couplings and ^{15}N isotope effects on ^{13}C chemical shifts.

It is worth noting that when $^{15}\text{NH}_4^+$ was infused into rabbits under similar conditions described in the study for non-labeled ammonium chloride, we were able to measure ^{13}C - ^{15}N spin-spin couplings by natural abundance ^{13}C NMR. The ^{15}N enrichments of $[^{15}\text{N}]$ glutamate, $[2-^{15}\text{N}]$ -glutamine, $[5-^{15}\text{N}]$ glutamine and $[^{15}\text{N}]$ -alanine, as well as their concentrations under hyperammonemic conditions were determined. The ^{15}N enrichments of glutamine at positions 2 and 5 were ~40% and 54%, respectively, while the glutamate ^{15}N enrichment was only ~12% under hyperammonemic conditions. These results indicate once again that glutamate and glutamine syntheses occur in different compartments, and are in agreement with the suggested metabolic compartmentation of glutamate and glutamine in the study of ^{13}C - ^{13}C spin coupling. The level of ^{15}N enrichment of glutamate, about 40% of that of $[2-^{15}\text{N}]$ glutamine, may be comparable to results obtained in the study based on ^{13}C isotopomer analysis, showing that about 40% of glutamate molecules are derived from their precursor glutamine. ^{15}N -alanine, which could be analyzed by ^{13}C - ^{15}N spin-spin coupling, reflects high ^{15}N enrichment, 30-54%, which supports the high ^{13}C enrichment and concentration of alanine, using $[U-^{13}\text{C}]$ glucose and non-labeled NH_4Cl .

The $^1J_{\text{CN}}$ and long range $^2J_{\text{CN}}$ of C-4 glutamine on the amide ^{15}N , as well as the ^{15}N isotope effects on ^{13}C chemical shifts are presented in the table.

References

1. A. Lapidot and A. Gopher (1994) J. Biol. Chem. 269, 27198-27208.
2. A. Lapidot and A. Gopher (1992a,b) 11th Annual Meeting of the Society of Magnetic Resource in Medicine, p. 79; 2110, 1992, Berlin, Germany.

Biodynamics and NMR

R. Lenk

Pavillon des Isotopes, Université de Genève
CH - 1211 Genève 4, Switzerland

Living systems are characterized by a great number of possible molecular configurations, high entropy and significant Brownian (random) motion. Because of the absence of symmetry and regularity of these systems, the molecular motion yields the most important information on their state (1, 2).

The fast Brownian dynamics contributes to internal energy and entropy of the system, while the slow cooperative movements of polymer chains play a rôle in the transmission of signals in Physiology.

Biodynamics attempts to investigate the physical state of living beings by the measurements of random movements. It is based on the time-dependent Statistical Thermodynamics.

Entropy: In the living systems one has three categories of entropy. a) Dynamic entropy. b) Configurational entropy. c) Alignment entropy. Entropies in the living systems can be determined by NMR spectroscopy and spin relaxation method (1).

Physiological phase transitions: In some cases, the physiological and the morphological transformations give rise to changes in the state of the living system. A number of these phase transitions is known in Tumour Biology and Plant Physiology.

Over the last 20 years, NMR has been used extensively for the investigations of the relaxation times and diffusion coefficients *in-vitro* in healthy and tumoural tissues. In his pioneer work Damadian (3) reported that in some tumour tissues the NMR relaxation times are *longer* than the corresponding normal tissues.

This observation has been

confirmed by other authors. It acquired the name the *systematic effect*. In this context one can define the following ratio: $R = T_1(\text{tumour})/T_1(\text{normal}) > 1$.

The slower relaxation times and increased molecular diffusion, as seen in cancer tissues, are related to the assumption that a cancerous tissue has a *lower degree of organization* than a normal tissue. Consequently, entropy must increase during the formation of tumours (4). The *systematic effect* has also been confirmed in tissues of the tumour bearing animals (5).

A number of the physiological phase transitions are known in Plant Physiology. The complex transition during the maturation of the bean seed (*Phaseolus vulgaris* L.) toward the 20th day of development is characterized by a significant maximum of the spin-lattice relaxation time (6). The bean seed maturation is accompanied by an important metabolic and structural transformation.

Another example of a phase transition in Plant Physiology is the mechanism of *flowering*. The physiological transition between the early *vegetative state* (production of leaves) and the final *floral state* (production of flowers) can be detected by biochemical methods, by ultrastructural studies and by NMR (7).

The observation of the gradual biological evolution, leads to the definition of the *time-arrow*. This can be also observed by NMR. For example in Animal Biology, Hazlewood et al. (8) reported the variation of the relaxation times as a function of age.

In spite of the extensive applications of NMR in Plant

Biology, little attention was directed to the studies of seeds *in vivo*. Recently we introduced a new procedure, the "NMR Phytotron" to measure the time-dependent evolution of the molecular dynamics in germinating seeds of oat (*Avena sativa* L. cv. Garry) (9) and barley (*Hordeum vulgare*, var. Himalaya) (10). The maturation of seeds is accompanied by a significant increase of the spin-lattice relaxation time. In the case of the "killed" seeds, the increase of the spin-lattice relaxation time is less significant.

Some plant seeds (mustard, sunflower, soybean, peanut) contain oil, which can exist in a liquid-like form. Following the model, presented by Huang (11), the oil in a plant seed is organized in so called "oil bodies". This is a very well organized molecular aggregate of spherical shape, with 0.2 - 2.5 μm in diameter.

In order to contribute to this domain, we studied the mustard seeds and oil, extracted from these seeds by NMR spectra and spin relaxation (12). The comparison of the NMR spectra of the intact seeds and the liquid oil samples shows the similarity of these spectra, in spite of the difference of their spectral line widths. This means that the NMR spectrum of the intact mustard seeds is entirely determined by the protons of the mobile oil components. Further, there is a small difference between the molecular dynamics in the rigid seed and in the extracted oil, as the spin-lattice relaxation in the former is: 92 ± 2 msec and in the latter, 103 ± 3 msec. The

molecular dynamics is little modified by the rigid structure of the seed, as the oil bodies either inside the cell or in isolated preparations, maintain a hydrophilic protecting surface. Consequently, they are remarkably stable and do not aggregate or coalescent.

References

- ¹R. Lenk, Progr. nucl. Med. 8, 55 (1984).
- ²R. Lenk, *Biophysical Application of NMR*. Verlag Dr Kovac, Hamburg, 1993.
- ³R. Damadian, Science 171, 1151 (1971).
- ⁴A. Szent-György, *Bioenergetics*. Acad. Press, New York, 1957.
- ⁵P.T. Beall, D. Medina and C.F. Hazlewood, NMR, Basic Principl. Progr. 19, 39 (1981).
- ⁶A. Grange, A. Dupanloup, P. Descouts and G. Béné, C.R. Acad. Sci. (Paris) B291, 307 (1980).
- ⁷R. Lenk, M. Bonzon and H. Greppin, Z. Pflanzenphysiologie 101, 107 (1981).
- ⁸C.F. Hazlewood, B.L. Nichols, and D.C. Chang, John Hopkins Med. J. 128, 117 (1971).
- ⁹R. Lenk, R. Degli Agosti and H. Greppin, Biologia Plantarum (Prague) 33, 501 (1991).
- ¹⁰R. Degli Agosti, R. Lenk and H. Greppin, Archs Sci. (Genève) 45, 61 (1992).
- ¹¹A.H.C. Huang, Annu. Rev. Plant Physiol. 43, 117 (1992).
- ¹²R. Lenk and R. Degli Agosti, in: Abstracts of the XXVIIth Congress AMPERE, Kazan, August 1994, p. 816.

Cellulose-Cellulase Interaction

M.-L. Mattinen, M. Kontteli, J. Kerovuo, M. Linder*, A. Annila, G. Lindeberg**, J. Ståhlberg***, and T. Drakenberg

VTT, Chemical Technology, P.O.Box 1401, FIN-02044 VTT, Finland

*VTT, Biotechnology and Food Research, P.O. Box 1500, FIN-02044 VTT, Finland

**Department of Medical and Physiological Chemistry, University of Uppsala, Sweden

***Department of Molecular Biology, University of Uppsala, Sweden

The hydrolytic degradation of cellulose is a complex process involving a number of cellulolytic enzymes which together are capable of solubilizing the inert and crystalline substrate. The cellulase system of *Trichoderma reesei* is the most studied and best understood of all cellulolytic systems. Cellohydrolytic enzymes have a domain (CBD¹) specialised for binding to crystalline cellulose. In order to understand the cellulose-cellulase interaction phenomenon we have studied the binding of the engineered CBDs (Y5A, P16R, N29A, Q34A, Y31A, and Y32A) to cellulose by biochemical adsorption measurements, circular dichroism (CD), and nuclear magnetic resonance (NMR) spectroscopy.

Adsorption studies show that all engineered peptides bind to crystalline cellulose except Y5A and Y32A. Y31A binds only weakly (Fig. 1.). One-binding site Langmuir adsorption isotherms were fitted on the data points.

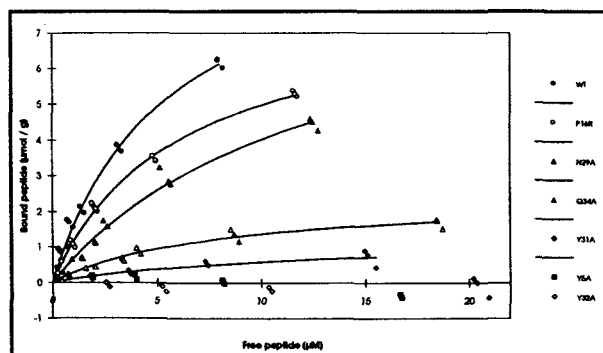


Fig. 1. Adsorption isotherms of the wild-type (WT) and engineered peptides (Y5A, P16R, N29A, Q34A, Y31A, and Y32A).

Using CD spectra it is possible to estimate changes in peptides secondary structure due to

mutation. Because the most dramatic changes in adsorption properties occurred when Y5, Y31, and Y32 were changed to alanine, the CD spectra were measured only for these peptides. The CD spectra of the engineered peptides are similar to the spectrum of the wild type (Fig. 2.).

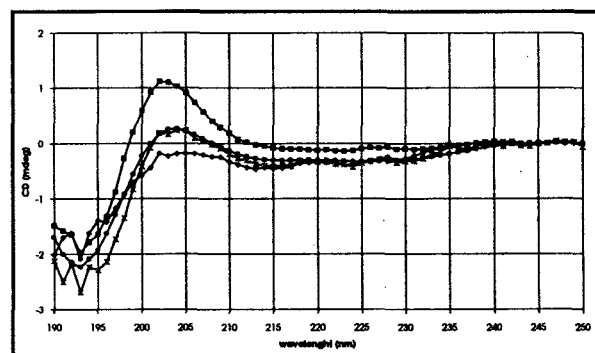


Fig. 2. The CD spectra of Y5A (x), Y31A (◊), Y32A (■), and wild-type (●).

Using NMR studies based on evaluation of chemical shifts, backbone dihedral angles and inter proton distances it could be ascertained, that the secondary structure of all the engineered peptides were preserved and there were mainly local structural changes in the vicinity of the changed residue². However, three dimensional structure determination³ was necessary to get detailed information of the structural changes of Y5A, Y31A, and Y32A. Especially on their flat surface, which presumably binds to cellulose. The three dimensional structures of the peptides show (Fig. 3.), that the antiparallel β -sheet structure is almost unchanged in cases of Y31A and Y32A, but the structure of Y5A is in some extent destroyed. Turns and loops of the engineered peptides are similar to the wild type.

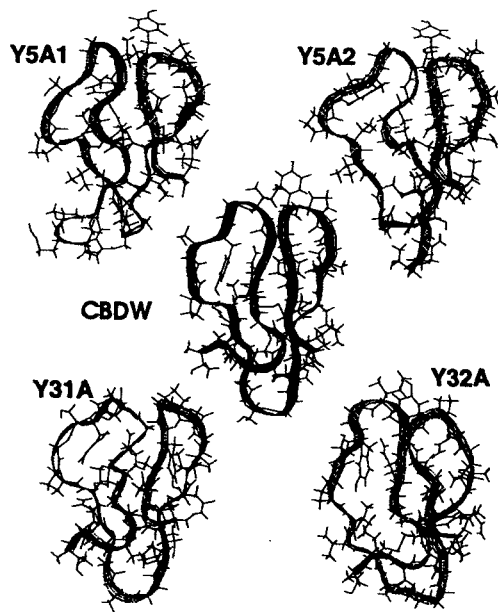


Fig. 3. Three dimensional structures of Y5A (two conformations), Y31A, Y32A, and wild-type (CBDW). Peptides are looked on the top down to flat surface. The ribbon, which is drawn on the molecules shows the folding.

Changes in the engineered peptides flat, hydrophilic surface can be best seen in figure 4, where each peptide is placed on the top of the wild-type.

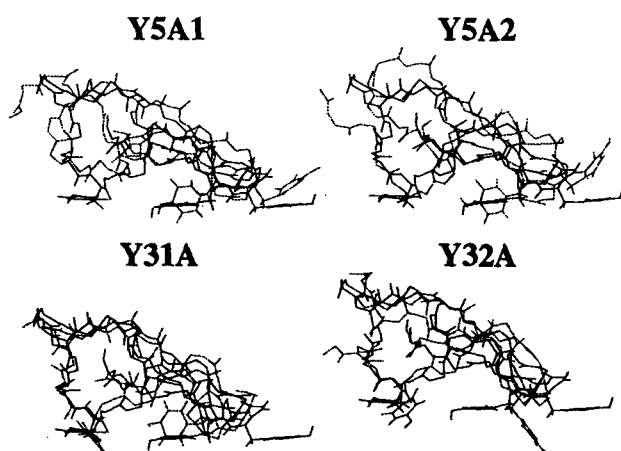
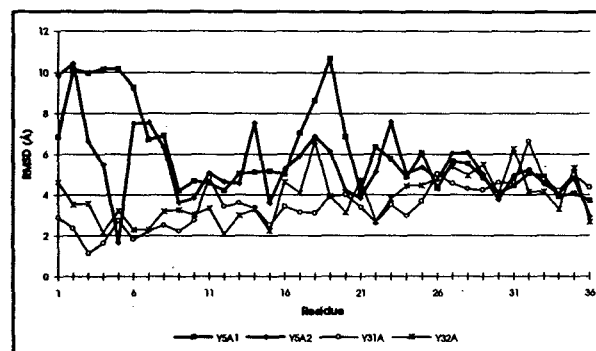


Fig. 4. Y5A, Y31A, and Y32A on the side of the molecule. Only backbone atoms and tyrosines on the flat surface are shown.

In the case of Y5A and Y32A the flat surface of the molecules has changed. This explains, why the peptides can not bind to cellulose. Y31A

binds to cellulose in some extent and as can be seen, the changes in the flat surface are smaller compared to Y5A and Y32A.

RMS deviations were calculated to all atoms per residue and to backbone atoms after superimposing the backbone of the engineered peptides with wild-type. The results are shown in figure 5. The large RMSD values in the N-terminus and region G15-C25 of Y5A are likely due to mobility of the peptide.



Peptide	Y5A1	Y5A2	Y31A	Y32A
RMSD (Å)	4.2	3.9	1.5	2.3

Fig. 5. The upper picture shows RMS deviations to all atoms per residue and lower table to backbone atoms.

Based on these experiments it could be concluded that aromatic residues (Y5, Y31, and Y32) on the flat, hydrophilic surface of CBD are functionally important and Y5 is also structurally indispensable.

1. Kraulis, P., Clore, M., Nilges, M., Jones, A., Pettersson, G., Knowles, J., and Gronenborn, A., *Biochemistry* 28 (1989) 7241-7257.
2. Linder, M., Mattinen, M.-L., Kontteli, M., Lindeberg, G., Ståhlberg, J., Drakenberg, T., Reinikainen, T., Pettersson, G., and Annala, A. *Identification of Functionally Important Amino Acids in the Cellulose-Binding Domain of Trichoderma reesei Cellobiohydrolase I*, accepted for publication in *Protein Science*, June 1995.
3. Mattinen, M.-L., Kontteli, M., Kerovu, J., Linder, M., Annala, Lindeberg, G., Ståhlberg, J., and Drakenberg, T. *The Three Dimensional Structures of Mutated Cellulose-Binding Domains of Cellobiohydrolase I from Trichoderma reesei*, in preparation.

The 2,3-Bisphosphoglycerate Shunt of Human Erythrocytes: Multinuclear NMR and Computer Simulation

P.L. Mulquiney, W.A. Bubb, and P.W. Kuchel

Department of Biochemistry, University of Sydney, Sydney, NSW 2006, Australia

Introduction

A peculiar feature of glycolysis in most mammalian erythrocytes is the possession of an alternative pathway for carbon flux from 1,3-bisphosphoglycerate (1,3BPG). This pathway, known as the 2,3-bisphosphoglycerate (BPG) shunt, bypasses phosphoglycerate kinase (PGK) by converting 1,3BPG to BPG. The bypassing of PGK ensures the metabolism of glucose to lactate without net production of ATP. Thus the shunt is said to be 'stoichiometry breaking'. That is, if any portion of the glycolytic carbon flux passes through the shunt, the glucose:ATP ratio will be less than 2.

Here we present the results of a multinuclear NMR investigation of metabolite flux through the BPG shunt. This investigation involved incubating human erythrocytes with [U-¹³C] glucose and monitoring the timecourse by sequential acquisition of ¹³C and ³¹P spectra as pioneered by Oxley et al. [1]. This method enabled the observation of ¹³C-labelled glucose, and products of its metabolism, labelled lactate, labelled BPG, and total BPG.

The primary motivation of this study was the quantitative measurement of the carbon flux into BPG as a percentage of the rate of glucose consumption. Although this has been measured previously (e.g. [1-5]), the currently discussed method is the only one which has allowed direct measurement of carbon flux into the shunt. Additionally, by constructing a simple model of the BPG shunt which included pH effects on enzyme activities, it was possible to simulate both the total BPG and labelled BPG timecourses, and thus evaluate the kinetic parameters for the enzymes of the shunt.

Experimental

Freshly prepared saline-washed and carbonmonxygenated erythrocyte suspensions (final haematocrit ~0.75; prepared as described elsewhere [6]) were incubated with 10 mM [U-¹³C] glucose, and 10 mM hypophosphorous acid (pH adjusted to 7.4 with 10 M HCl) at 37 °C. The timecourse was monitored with NMR by sequentially acquiring ¹³C and ³¹P spectra.

In order to obtain the maximum signal-to-noise ratio in the time available, spectra were obtained from 'rapidly pulsed' samples [1]. Calibration of spectral resonance intensity to concentration for metabolites which exchanged across the cell membrane (glucose, lactate, and P_i) required two calibration factors due to differences in T₁ values between the intra- and extracellular environments. The intra/extra-cellular ratios of the charged metabolites (monovalent anions) were assumed to be equal to the distribution of the added hypophosphite ion [7], while it was assumed that glucose concentration was equal in both compartments.

Results

Results from the erythrocyte incubations are shown in Fig. 1 and Table 1.

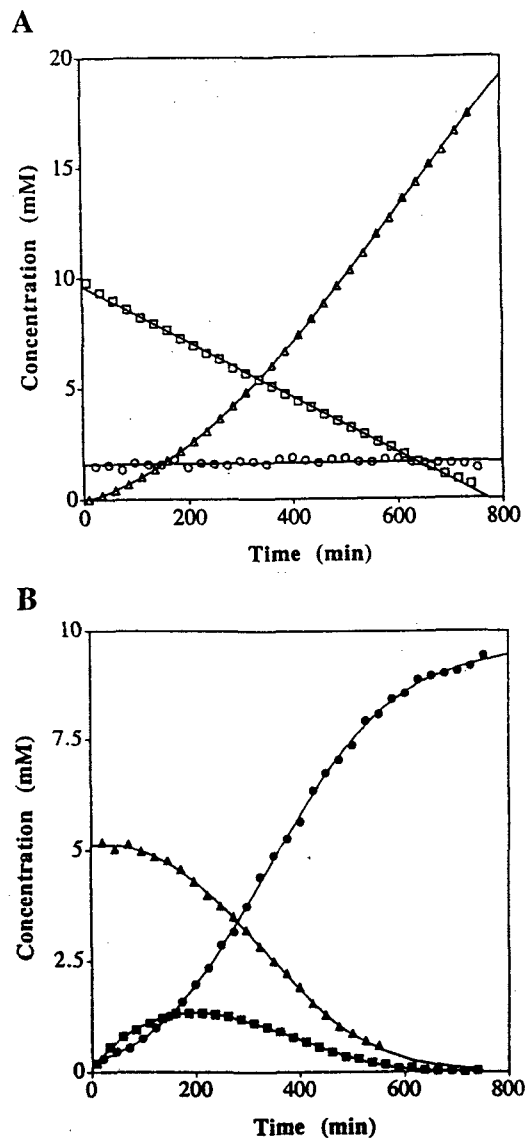


Fig. 1 A and B Metabolite concentrations during an incubation of human erythrocytes with [U-¹³C] glucose at 37 °C as determined by the sequential acquisition of ¹³C and ³¹P NMR spectra. (□) [U-¹³C] glucose, (Δ) [U-¹³C] lactate, (○) ATP, (▲) total BPG, (■) [U-¹³C] BPG, (●) P_i. Concentrations were expressed in mM with respect to total sample volume except for total BPG and [U-¹³C] BPG, P_i, and ATP concentrations which were expressed as mmol (L RBC)⁻¹.

A preliminary model of the BPG shunt was developed in an attempt to simulate the labelled BPG and total BPG timecourses. Equations (1) and (2) are the rate equations used to model 2,3-bisphosphoglycerate synthase (DPGS) and 2,3-bisphosphoglycerate phosphatase (BPGP), respectively.

$$\frac{d[1,3\text{BPG}]}{dt} = \frac{V_{m1} [1,3\text{BPG}]}{[1,3\text{BPG}] + K_{m1} \left(1 + \frac{[\text{BPG}]}{K_i}\right)} \quad (1)$$

$$\frac{d[\text{BPG}]}{dt} = \frac{V_{m2} [\text{BPG}]}{[\text{BPG}] + K_{m2}} \quad (2)$$

The pH dependencies of [1,3BPG], V_{m1} , and K_i were modelled using equations which best modelled the known pH dependence of these parameters [2,4,8]. These equations have no mechanistic basis and are empirical. By monitoring the chemical shift of P_i it was determined that the pH_i decreased linearly at a rate of -0.03 pH units h^{-1} , from an initial value of ~ 7.2 . Thus a zero order rate constant was used to model the change in pH during the timecourse.

Table 1 Metabolic fluxes^a from erythrocyte samples incubated with 10 mM [$U\text{-}^{13}\text{C}$] glucose.

Compound	Metabolic Fluxes (mmol (LRBC) ⁻¹ h ⁻¹)
[$U\text{-}^{13}\text{C}$] glucose uptake	0.96 ± 0.02
[$U\text{-}^{13}\text{C}$] BPG production ^b	0.79 ± 0.01

^a Values reported are mean ($n=2$) ± maximum deviation.

^b Initial rate at pH_i 7.23 ± 0.02. Values were obtained by visual fitting of a computer simulated timecourse to the data.

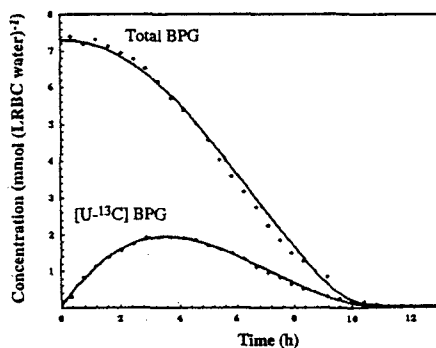


Fig. 2. A computer simulation of the total BPG and [$U\text{-}^{13}\text{C}$] BPG timecourses resulting from the incubation of human erythrocytes with [$U\text{-}^{13}\text{C}$] glucose. Parameters of the model were adjusted until a 'good' match with both timecourses was obtained. The parameter values used in this simulation are found in Table 2.

A 'good' fit between the data and simulations could only be obtained if the pH dependence was exaggerated (Fig. 5). A comparison of the kinetic parameters obtained by fitting the simulations to the timecourse data with literature values is shown in Table 2.

Table 2 A comparison of the kinetic parameters used in the simulation of Fig.2 with literature values at two pH_i values.

Parameter	pH_i 7.2		pH_i 6.9	
	Simulation Value	Literature Value	Simulation Value	Literature Value
1,3BPG	0.7 μM	0.7 μM [4]	0.006 μM	0.08 μM [4]
V_{m1} ^a	863	343 [8]	772	304 [8]
K_{m1}	3.1 μM	3.1 μM [8]	3.1 μM	3.1 μM [8]
K_{i1}	21 μM	21 μM [8]	13 μM	13 μM [8]
V_{m2} ^a	1.2	0.69 [2]	1.2	0.69 [2]
K_{m2}	0.1 mM	0.38 mM [2]	0.1 mM	0.29 mM [2]

^a mmol (L RBC cell water)⁻¹ h⁻¹

Conclusions

The percentage of glycolytic flux which passes through the BPG shunt was measured to be $\sim 41\%$. This gives a glucose:ATP stoichiometry of 1:1.6.

The maximal velocity of the BPGP reaction was found to be ~ 1.7 times that measured in the absence of glucose [2,3]. It is not known what causes this activation.

The pH dependencies of 1,3 BPG concentration and BPGS were not sufficient to model the BPG timecourses. It is possible that the accumulation of lactate, which is known to decrease the NAD/NADH ratio in the cells [9], causes a shift in the mass action ratio of the glyceraldehyde 3-phosphate dehydrogenase step of glycolysis. This would lower the concentration of 1,3BPG, and hence lower the activity of BPGS, during the timecourse. Additionally, the pH dependence of BPGS may be more exaggerated *in vivo* than that measured *in vitro* on purified enzymes, as previously suggested in [2].

References

- S.T. Oxley, R. Porteous, K.M. Brindle, J. Boyd, and I.D. Campbell, *Biochim. Biophys. Acta* **805**, 19 (1984).
- I. Rapoport, H. Berger, R. Elsner, and S.M. Rapoport, *Eur. J. Biochem.* **73**, 421 (1977).
- K. Quadflieg, and K. Brand, *Eur. J. Biochem.* **82**, 523 (1978).
- G. Mømsen, and B. Vestergaard-Bogind, *Arch. Biochem. Biophys.* **10**, 67 (1978).
- M.C. Schrader, C.J. Eskey, V. Simplaceanu, and C. Ho, *Biochim. Biophys. Acta* **1182**, 162 (1993).
- H.A. Berthon, W.A. Bubb, and P.W. Kuchel, *Biochem. J.* **296**, 379 (1993).
- K. Kirk, P.W. Kuchel, and R.J. Labotka, *Biophys. J.* **54**, 241 (1988).
- Z.B. Rose, *Arch. Biochem. Biophys.* **158**, 903 (1973).
- W.M. Tilton, C. Seaman, D. Carriero, and S. Piomelli, *J. Lab. Clin. Med.* **118**, 146 (1991).

Secondary Solution Structure of Calf Thymus Histone H1 Globular Region

Claudio Nicolini, Giuseppe Nicastro and Cesira de Chiara

Institute of Biophysics, University of Genova, Genova, Italy

In this work we describe our preliminary studies on the secondary structure of calf thymus histone H1 globular region by 2D homonuclear ^1H -NMR correlation spectroscopy. The protein is reported to be predominantly helical and the dispersion of the protein's ^1H -NMR signals is poor.

Since NMR studies exhibited several difficulties in the data interpretation because of a significant high number of resonance overlaps, the NMR supersecondary structure presented in a separate full length paper¹ is intended as a description of the fold rather than a high-resolution structure.

The future direction in our studies is to express human Histone H1 by using DNA-recombinant techniques with ^{15}N and ^{13}C labelling in order to overcome the low signal dispersion. Such expression is actually in progress.

It's well known that the lysine-rich chromosomal protein, histone H1, in solution under physiological conditions of pH and ionic strength, consists of three structural domains: two random coil N-terminal and C-terminal regions and a central highly structured and conserved, trypsin resistant, globular region². This globular region or "core", extending from residue 35 to 120^{2,3}, with a molecular weight of about 9 kDa, was suggested that it seals the DNA on the nucleosome surface^{4,5}. We were able to extract specific sequential assignments of 82 residues out of 85 making extensive use of our expert system for automatic peak assignment, PEPTO⁶. The secondary structure determination is based on 231 interproton distance restraints derived from NMR measurements. The secondary structure emerging mostly from interproton NOEs, metric matrix distance geometry, simulated annealing and partly from structural homology with other DNA binding proteins, is supported by several complementary approaches including statistical methods, slow exchange 2D NMR experiments and Circular Dichroism (CD) measurements¹. Our NMR studies show the histone H1 to be made of four helices located at positions 48-56, 60-75, 82-91 and 110-118, while the N-terminal

segment 35-47 and the region 93-109 are mostly in extended conformation. Such a secondary structure is also compatible with secondary structure prediction based on amphipathic criteria.

The results of the present study on calf thymus H1 secondary structure are compared to the NMR secondary structure of the chicken histone H1 globular domain (cGH1)⁷ and to the crystal structure of chicken histone H5 globular domain (cGH5)⁸.

Recently, full assignment and tertiary structure of chicken GH1 have been obtained by ^1H -homonuclear and ^1H - ^{15}N heteronuclear two-dimensional NMR⁷ studies and the tertiary structure of chicken erythrocyte GH5, previously determined by NMR spectroscopy⁹, has been solved by X-ray crystallography to a resolution of 2.5 Å⁷.

The linker histones H1 and H5 are components of chromatin; they are homologous and H5 may be regarded as an extreme variant of H1. H5 has several lysine to arginine substitutions relative to H1. The calf thymus GH1 (ctGH1) 85-residue domain has a partial sequence identity with chicken globular H1 (cGH1) and H5 (cGH5) histones, as shown in Fig. 1.

Fig. 1:



The secondary structure elements of chicken GH1, three helices (S5-A16, S24-A34, N42-

K56) followed by a β -hairpin (L59-L73), are folded in a manner very similar to the corresponding parts of chicken GH5^{7,10} The asymmetric unit in the GH5 crystal⁷ consists of two molecules. Each molecule consists of a three-helix bundle (helices I-III) with a β -hairpin at the C-terminus. Subtle differences have been detected between the two structures. The most important differences are located in the loop between the second and the third helices, a region that could be responsible for the different affinity for DNA^{6,7}.

The secondary structure of calf thymus GH1, derived from a restricted number of constraints (231), consists of four helices (A48-R55, L60-E75, K82-K91, K110-K118). The comparison of secondary structure elements between cGH5 crystal structure, cGH1 NMR solution structure, with our structure are represented in Fig. 1. While exists a partial correspondence of the first three helices of calf thymus GH1 with the other two structures, NMR data available show no evidence of any β -hairpin (L59-L73 in cGH1 and L81-L95 in cGH5) Besides in the globular region of calf thymus H1 appears a fourth helix (K110-K118) in a region not present in globular chicken histones.

Reference.

1. Nicolini, C., Nicastro, G., de Chiara, C., Supersecondary solution structure of calf thymus Histone H1 globular region. in press on *Quart. Magn. Res. Biol. Med.*-Vol. 2, n. 2/95.
2. Hartman, P., G. Chapman, T. Moss, and E. M. Bradbury.: Studies on the role and mode of operation of the Very-Lysine-Rich Histone H1 in Eucaryotic Chromatin. *Eur. J. Bioch.* 1977; 77: 45-51.
3. Nicolini, C., Catasti, P., Nizzari, M., Carrara, E.A. Histone H1 solution structure and the sealing of mammalian nucleosome. in *Protein structure and engineering*. NATO ASI Series. Plenum Press. Ed. Jardetzky, 1989, 221-242.
4. Allan, J., Hartman, P.G., Crane-Robinson, C. and Aviles, F.X.: The structure of histone H1 and its location in chromatin. *Nature* 1980; 288: 675-679.
5. Nicolini, C., P. Catasti, L. Szilágyi, and P. Yau. DNA internal motions within nucleosomes during the cell cycle and as a function of ionic strength. *Biochemistry*. 1993, 32: 6465-6469.
6. Catasti, P., E. Carrara, and C. Nicolini.: PEPTO: an expert system for automatic peak assignment of two dimensional nuclear magnetic resonance spectra of proteins. *J. of Comp. Chem.* 1990; 11: 805-818.
7. Cerf, C., Lippens, G., Ramakrishnan, V., Muyldermans, S., Segers, A., Wyns, L., Wodak, S.J. and Hallenga K.: Homo- and Heteronuclear Two-Dimensional NMR Studies of the Globular Domain of Histone H1: Full Assignment, Tertiary Structure, and Comparison with the Globular Domain of Histone H5. *Biochemistry*. 1994; 33: 11079-11086.
8. Ramakrishnan, V., Finch, J.T., Graziano, V., Lee, P.L. and Sweet, R.M.: Crystal structure of globular domain of histone H5 and its implication for nucleosome binding *Nature* 1993; 362: 219-223.
9. Clore, G.M., Gronenborn, A.M., Nilges, M., Sukumaran, D.K. and Zarbock, J.: The polypeptide fold of the globular domain of Histone H5 in solution. A study using nuclear magnetic resonance, distance geometry and restrained molecular dynamics. *EMBO J.* 1987, 6. 1833-1842.
10. Clore, G.M., Gronenborn, A.M., Nilges, M., Sukumaran, D.K. and Zarbock, J.: The polypeptide fold of the globular domain of Histone H5 in solution. A study using nuclear magnetic resonance, distance geometry and restrained molecular dynamics. *EMBO J.* 1987, 6. 1833-1842.

Studies on Human Calcitonin Fibrillation by Proton Nuclear Magnetic Resonance Spectroscopy: Characterization of the Lyophilized Fibril

Kenji Kanaori and Atsuko Y. Nosaka*

International Research Laboratories, Ciba-Geigy Japan Ltd., P.O. BOX 1, Takarazuka
665 Japan

I. Introduction

Calcitonin (CT), a polypeptide hormone, plays a central role in calcium-phosphorus metabolism (1), and is employed as a drug for various diseases, notably osteoporosis. Human CT (hCT) easily associates and precipitates as insoluble fibrils upon storing in an aqueous solution (2). In this study, the mechanisms of hCT fibrillation and characterization of the fibrils were investigated by ^1H NMR.

II. Results and Discussion

NMR spectra in the fibrillation process of hCT (80 mg/ml) shows a gradual signal broadening of the peptide peaks, followed by a rapid broadening and subsequent disappearance of the peaks 1 h after the dissolution of the peptide. Time-course of the two-dimensional (2D) spectra demonstrated that the molecular association of hCT is initiated by the intermolecular hydrophobic interaction in the N-terminal (Cys¹-Cys⁷) and central (Met⁸-Pro²³) regions, and that the C-terminal (Gln²⁴-Pro³²) region becomes subsequently involved in the fibrillation process (3).

Electron microscopy measurements showed that the fibril consists of helical rods, in which the peptide molecules interact with each other (2,4). Powder of the hCT fibril (fhCT) was obtained by lyophilization of the aqueous solution of hCT (80 mg/ml) after storage at room temperature for 3 h. One-dimensional (1D) NMR spectra were measured at various concentrations (1-80 mg/ml) of fhCT in D₂O. As stated above, NMR signals of fhCT were considered to be too broad to observe. However, as shown in Figure 1, 6 min after the dissolution of fhCT in D₂O, it afforded broad signals, whose chemical shifts were identical to those of hCT. The line widths became broader with increasing the concentration. At higher concentra-

tions (> 40 mg/ml) the peptide precipitated, and the solution promptly became gel.

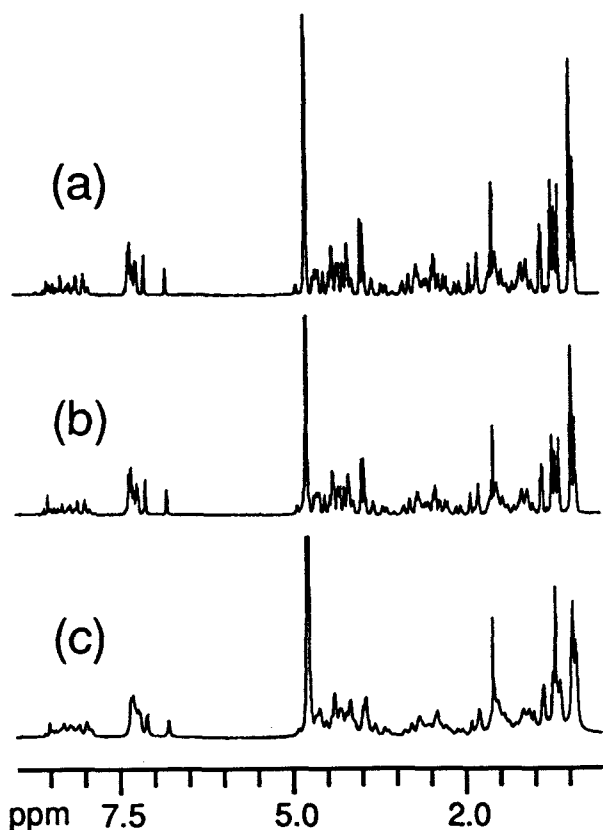


Figure 1: ^1H NMR spectra of hCT (10 mg/ml) (a), fhCT (10 mg/ml) (b), and fhCT (40 mg/ml) (c), all in D₂O at 300 K, pH 2.9.

1D and 2D HOHAHA (mixing time 40 ms) spectra of the peptide in the fhCT solution (40 mg/ml) showed a signal broadening within 1 h, while the signal broadening in the hCT solution at the same concentration of 40 mg/ml did not occur even 24 h after the dissolution. However, the signal broadening feature observed in the fhCT

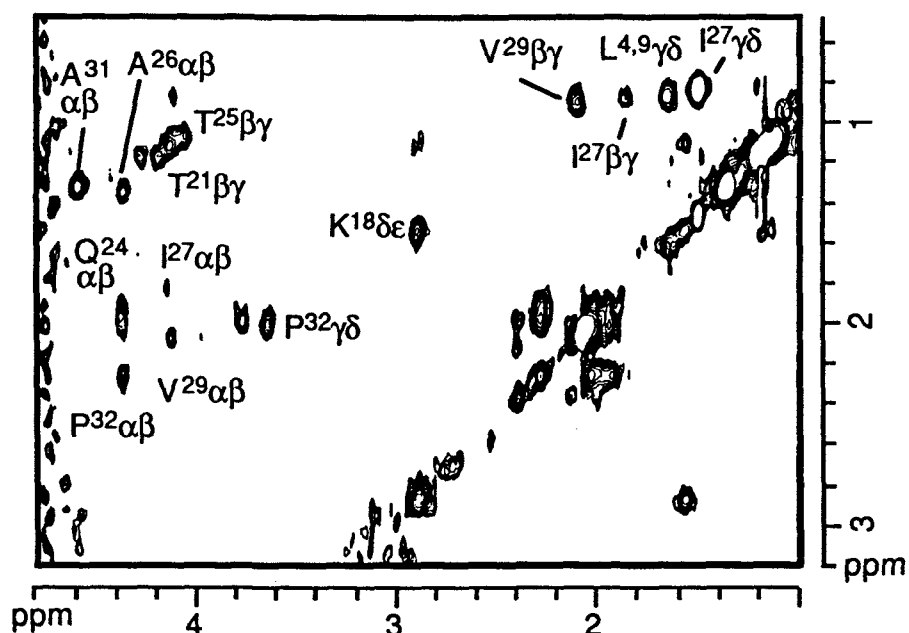


Figure 2: 2D HOHAHA spectrum (mixing time 40 ms) of fhCT (40 mg/ml) after the dissolving the peptide in D₂O for 27-32 min, at 300 K, pH 2.9. Cross peaks are labeled with their amino acid residue name (single letter code) and sequence numbers.

solution appeared to be similar to that of the hCT solution, indicating that the peaks in the N-terminal and central regions disappeared faster than those in the C-terminal region (Figure 2).

These results suggest that a part of the fibrils dissociate to monomer molecules by lyophilization, thereby providing observable NMR signals of the peptide. The small amount of the tightly associated fibril molecules in the fhCT solution would act as a core, forcing the dissociated monomer molecules to reassociate very rapidly in the same way as that of the hCT fibrillation process.

When a small amount of fhCT (10% wt) was added to the hCT solution (total concentration 20 mg/ml), the peaks became broader within several hours, comparable to the 100% fhCT solution at the same concentration (20 mg/ml). This fact also serves to suggest that fhCT promotes the association of the peptide molecules.

In general, urea is known as a denaturant for proteins, and also as a reagent to prevent the association of some peptides by forming hydrogen bonds with the peptide molecules. FhCT was dissolved in a freshly prepared 6 M urea solution. The signals were sharp and identical to that of hCT in the urea solution, and the spectra showed no significant change over several days, indicating that the fibrillation does not occur in the urea solution. Thus, the association of hCT molecules is

prevented by urea, and the fibril core is considered to dissociate to the monomer in the highly concentrated urea solution. This finding suggests that the fibril structure is stabilized by inter or intramolecular hydrogen bonds after the molecular association initiated by the intermolecular hydrophobic interaction (3).

III. Acknowledgment

We thank Drs. R. Andreatta, B. Kamber and B. Riniker in Ciba-Geigy Basel for providing the sample of hCT and supporting this work.

IV. References

- ¹L. A. Austin, and H. Heath *N. Engl. J. Med.* **304**, 296-297 (1981).
- ²T. Arvinte, A. Cudd, and A. F. Drake, *J. Biol. Chem.* **268**, 6415-6422 (1993).
- ³K. Kanaori, and A. Y. Nosaka, *Biochemistry* in press.
- ⁴P. Sieber, B. Riniker, M. Brugger, B. Kamber, and W. Rittel *Helv. Chim. Acta* **53**, 2135-2150 (1970).

The effect of the fourth order zero-field splitting on EPR for $S = 5/2$ ions at the three-fold symmetry

Il-Woo PARK[†] and Sung Ho CHO[†]

[†] Seoul Branch, Korea Basic Science Institute, Korea University, Seoul 136-701, KOREA

[‡] Department of Physics, Korea University, Seoul 136-701, KOREA

I. INTRODUCTION

To investigate the three-fold symmetry effects on EPR, we adopted $\text{Cr}^{3+}(S=3/2)$ and $\text{Fe}^{3+}(S=5/2)$ paramagnetic ions unintentionally contained in an $\alpha\text{-LiIO}_3$ crystal during the crystal growth. The space group of $\alpha\text{-LiIO}_3$ is $P6_3$ with $z=2$. Li^+ ions in the crystal have two sites with chemically equivalent but physically inequivalent 3-fold symmetry.¹⁻²⁾ As previously reported two ^7Li cannot be distinguished by NMR because their spin Hamiltonians(SH) are identical.³⁾ It has been suggested that both impurities in the crystal are located at the site of three-fold symmetry, probably Li^+ .³⁻⁸⁾ Therefore, Fe^{3+} and Cr^{3+} centers in the crystal can be a good example for studying the three-fold symmetry effects on EPR.

II. RESULTS AND ANALYSIS

The SH for a $S=3/2$ center with the three-fold symmetry is described as⁹⁾

$$H_{3/2} = \mu_B(\mathbf{B} \cdot \mathbf{g} \cdot \mathbf{S}) + b_2^0 O_2^0 / 3 \quad (1)$$

where all symbols are conventional ones. For a $S=5/2$ center with the same symmetry the fourth order zero-field splitting(ZFS) terms should be added⁹⁾

$$H_{5/2} = H_{3/2} + (b_4^0 O_4^0 + b_4^3 O_4^3 + b_4^{-3} O_4^{-3}) / 60 \quad (2)$$

where O_4^3 and O_4^{-3} are operators as following.¹⁰⁾

$$O_4^3 \sim \sin^3 \theta \cos \theta \cos 3 \phi \quad (3)$$

$$O_4^{-3} \sim \sin^3 \theta \cos \theta \sin 3 \phi \quad (4)$$

However, the O_4^{-3} operator does not influence in the zx -plane of ZFS because $O_4^{-3}|_{\phi=0} = 0$ in the conventional spherical coordinates.

EPR measurements were carefully made in the crystallographic ca -plane at room temperature with a Bruker ESP300 Q-band($\nu \approx 33.9$ GHz) spectrometer. Among the observed EPR signals, those of Cr^{3+} were easily identified as previously reported.⁸⁾ The z -axes of the principal second order ZFS tensor for Cr^{3+} and Fe^{3+} centers were

found to be the c -axis. EPR signals of $\text{Cr}^{3+}(S=3/2)$ in this crystal were observed as one set no matter where the magnetic field was applied. Even though Cr^{3+} ions may occupy two Li^+ sites in $\alpha\text{-LiIO}_3$, they can not be distinguished with EPR because the ZFS terms for the $S=3/2$ ion must be limited up to the second order. Figure 1 shows the anisotropic resonances of Cr^{3+} in the ca -plane.

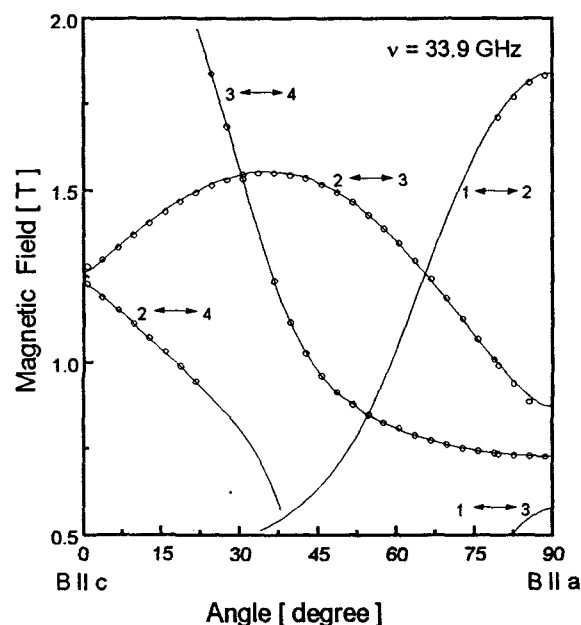


Figure 1. Circles are resonance fields of Cr^{3+} and lines are fitted curves. Here $n \leftrightarrow k$ means the transition between the n th and k th levels, and 1 is the highest one.

When the paramagnetic ion with the high spin($S \geq 2$) substitutes for the 3-fold symmetry site, its SH must include the fourth order term of ZFS as given by eq. (2). EPR signals of Fe^{3+} ions at two Li^+ sites in an $\alpha\text{-LiIO}_3$ crystal were splitted into a pair. However, the splitted signals were superimposed, when the magnetic field was applied parallel to the c - or a -axis(see Figure 2). This is

applied parallel to the c- or a-axis (see Figure 2). This is explained as follows: If we choose the principal x-axis of the second ZFS as the a-axis for one Fe^{3+} center, that of the other Fe^{3+} one becomes $a+\pi/3$ axis. So when the applied magnetic field is parallel to the c- ($\theta=0$) or a- ($\theta=\pi/2$) axis, the b_4^3 terms of two Fe^{3+} centers are simultaneously zero because $O_4^3|_{\theta=0 \text{ or } \pi/2} = 0$. But when the magnetic field is applied off the c- and a-axis, the values of b_4^3 for both Fe^{3+} centers are equal in magnitude but opposite signs because $O_4^3|_{\theta=\theta, \phi=\phi+\pi/3} = -O_4^3|_{\theta=\theta, \phi=\phi}$ in eq. (3). The field difference of two splitted resonance fields is determined by the magnitude of b_4^3 as shown in Figure 3. Considering the typical peak-to-peak linewidth of the first derivative curve is about 3 mT, one may claim that the calculations are in good agreement with the experimental data.

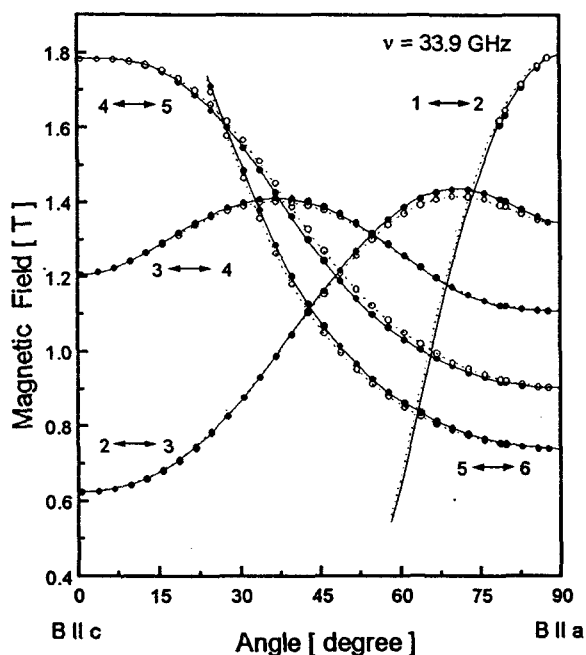


Figure 2. Closed and open circles are measurements for two Fe^{3+} centers, whereas solid and dotted lines are calculated ones, respectively.

III. SUMMARY

The splittings for Fe^{3+} EPR signals are explained by means of the ions at two magnetically different sites and the nonzero b_4^3 term, which determines the magnitude of the splitting. EPR splittings of Fe^{3+} at the trigonal symmetry in other crystals were also observed⁽¹¹⁾ and could be explained by the similar analogy as our proposal.

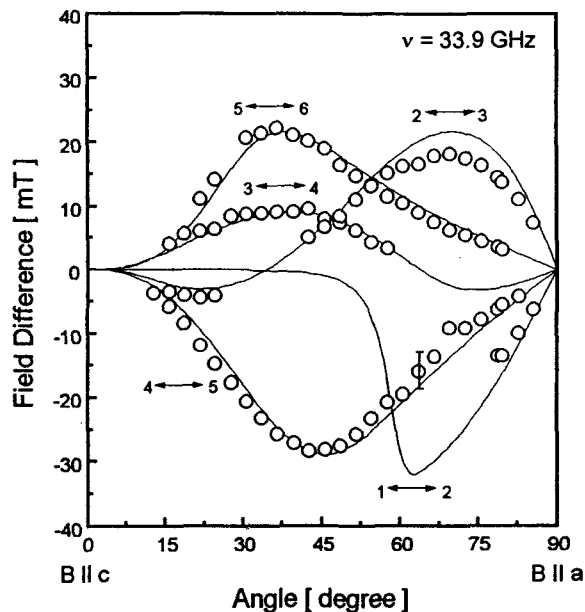


Figure 3. Circles are the field difference of the splitted signals in Figure 2, and the lines are calculations.

ACKNOWLEDGMENT

This work was supported by the government (serial no. : KBSI-PE00088 and PN00019 for IWP, and BSRI-95-2410 for SHC).

REFERENCES

1. A. Rosenzweig and B. Morosin, *Acta. Cryst.* **20**, 758 (1966).
2. J. L. de Boer, F. van Bolhuis, R. Olthof-Hazekamp and A. Vos, *Acta. Cryst.* **21**, 841 (1966).
3. S. H. Choh, D. Y. Jeong, I. -W. Park, Q. Meng and J. H. Ro, *Proc. of 5th Beijing Conf. and Exhib. on Instrum. Analysis* (Beijing, China, 1993), E46.
4. W. Karthe and R. Kühmstedt, *phys. stat. sol. (b)* **63**, K5 (1974).
5. V. O. Martirosyan, M. L. Meilman, I. N. Marov, V. V. Zhukov and K. T. Sevinyan, *phys. stat. sol. (b)* **72**, 441 (1975).
6. A. Bräuer, D. M. Daraselia and T. A. Abramovskaya, *phys. stat. sol. (b)* **72**, K131 (1975).
7. W. Karthe, *phys. stat. sol. (b)* **81**, 323 (1977).
8. I. -W. Park, J. S. Kim, S. H. Choh, J. S. Chae and J. H. Ro, *Sae mulli* **34**, 748 (1994).
9. C. Rudowicz, *Mag. Res. Rev.* **13**, 1 (1987).
10. C. Rudowicz, *J. Phys. C : Solid State Phys.* **20**, 6033 (1987).
11. G. I. Malovichiko, V. G. Grachev, O. F. Shirmer and B. Faust, *J. Phys. : Condens. Matter* **5**, 3971 (1993).

Comparing a Neural Network Based Image Enhancement Technique with Keyhole Magnetic Resonance Imaging

Y. Hui and M. R. Smith

Dept. of Electrical and Computer Engineering
University of Calgary, Calgary, Alberta, Canada T2N 1N4
Email: smith@enel.ucalgary.ca

Abstract—The keyhole imaging technique attempts to provide magnetic resonance imaging (MRI) with the ability to obtain dynamic contrast-enhanced images by improving temporal resolution. However, the trade-off between the spatial and temporal resolutions causes such problems as edge blurring of any wide contrast-enhanced objects and severe intensity distortion of any narrow objects. This paper presents a new neural network based method to overcome the disadvantages of the keyhole technique. A complex domain feedforward neural network is trained on full reference MRI data and then used to do data extrapolation on a sequence of reduced-sized data sets. Simulation experiments show that the proposed method not only can improve the temporal resolution four to ten fold compared with conventional MRI, but also can enhance the edge information and reduce the severe intensity distortion appearing in the keyhole images. The approach can be applied to NMR spectroscopic data to enhance spectral resolution.

I. INTRODUCTION

In dynamic magnetic resonance imaging (MRI), such as the study of the contrast agent uptake, conventional MRI technique is too slow to follow the uptake of the contrast agent with the required time resolution. To solve this problem, a k -space data substitution technique has recently been introduced [1], [2]. This keyhole method collects only one full data set before contrast agent injection and a series of dynamic reduced-sized data sets with only low frequency components during dynamic imaging to reduce the scan time. To overcome the resolution loss associated with the short data set, high-frequency data of the reference data set, instead of zeros, are substituted into the reduced-sized data sets prior to the reconstruction. Although the time resolution of keyhole is improved over the Fourier technique, spatial and contrast resolutions will be decreased since data substitution does not add dynamic high frequency information. This affects the diagnostic value of such dynamic MR images [3].

We will present an image enhancement method to obtain the high time, spatial and contrast resolutions of the dynamic MR images. This method utilizes a complex domain neural network (NN) based data extrapolation algorithm [4], [5] to adaptively recover the high frequency information. This provides better dynamic high frequency information than the simple substitution method.

This work was supported by the University of Calgary and the Natural Sciences and Engineering Research Council (NSERC) of Canada.

II. COMPLEX DOMAIN NN BASED IMAGE ENHANCEMENT METHOD

We model the available data in the finite MRI data set as the output of a complex-valued feedforward network using P^{th} order R -step-ahead prediction

$$\hat{s}[k+R] = H(s[k], s[k-1], \dots, s[k-P+1]);$$

$$P-1 \leq k \leq K-1-R \quad (1)$$

where $H(\cdot)$ denotes an appropriate model, i.e. a complex NN here, $s[k-1] \dots s[k-P+1]$ are the known data, and $\hat{s}[k+R]$ is the estimated data.

The backpropagation (BP) algorithm used to train the complex-valued network is derived in the complex domain. The weight changes during the learning phase can be expressed as

$$\Delta w_{n+1}[i, j] = -\mu \nabla_{w_n[i, j]} E_n \quad (2)$$

with

$$\nabla_{w_{[i, j]}} E_n = -(f'(y_{nR}[i])\delta_{nR}[i] + f'(y_{nI}[i])\delta_{nI}[i])x_n^*[j] \quad (3)$$

where μ is the learning rate, $x_n[j]$ is the output of the j th neuron, $*$ denotes complex conjugate, R and I represent real and imaginary components, $f(\cdot)$ is the activation function, and $\delta_n[i]$ is the local gradient. Details of the derivation can be found in [5], [6].

The signal acquisition scheme in our method is similar to that used in the keyhole. First, a full reference data set is collected before the injection of the contrast agent, then a series of reduced-sized phase-encoding data sets are acquired with required time resolution. Before using the data extrapolation algorithm, a 1D inverse discrete Fourier transform (DFT) is applied to each data set in the untruncated frequency-encoding direction. The complex domain NN is then trained on the full reference data. After training, the available data from each corresponding reduced data set are fed into this network to restore its missing high frequency components. Finally, an inverse DFT is applied to the extrapolated dynamic data set in the phase-encoding direction to reconstruct dynamic images with the enhanced contrast resolution.

III. RESULTS AND DISCUSSION

Figure 1 shows the zoomed section of a 2D simulation dynamic image sequence with a small contrast enhanced "lesion". The first row shows the high resolution images with 128 encodings. The second row shows the differences

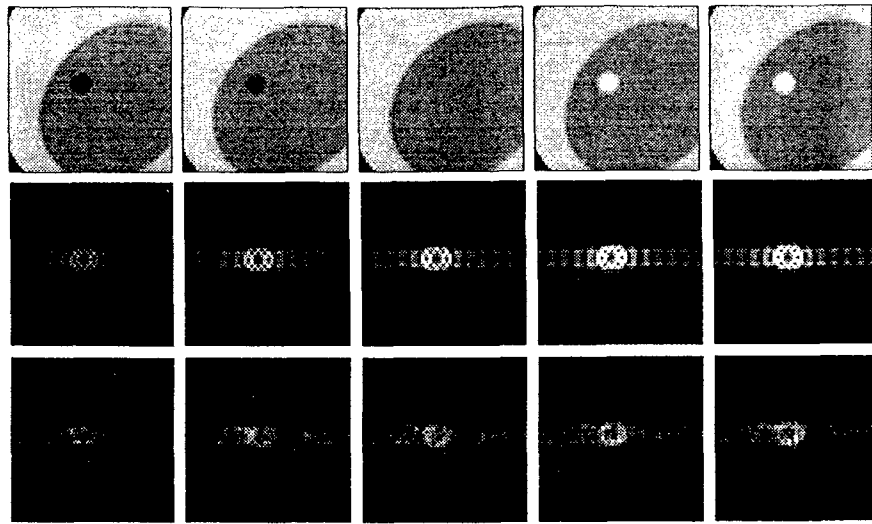


Fig. 1. Zoomed partial dynamic images reconstructed using Fourier method on 128 phase encodings (top). Difference images between the high resolution images (128 phase encodings) and Keyhole images with 32 encodings (middle) and complex-valued NN based method images with 32 encodings (bottom). (Different images have the same scale.)

between the keyhole images and high resolution images. Note the apparent leaking of the contrast agent around and outside of the "lesion". The intensity distortion and artifacts are not as evident in the difference images between the complex NN approach images and the high resolution images (the third row in Fig. 1).

To make a quantitative evaluation of the success of our new method, we use a 1D simulation dynamic image sequence corresponding to a contrast agent uptake through a very narrow area and calculated the average pixel intensity of the contrast enhanced object. It can be seen from figure 2 that the differences of the average pixel intensity of the contrast enhanced object between the keyhole images and high resolution images are evident when less than 32 phase encodings, i.e. 1/4 data, are used. By contrast, there is little intensity difference between images using our complex NN based method and the original high resolution images. The success of the NN based approach is still evident when the temporal resolution is increased by another factor of two, i.e. only 16 phase-encodings.

IV. CONCLUSION

Compared with the keyhole technique under the same time resolution, our approach can significantly enhance the spatial and contrast resolutions by reducing edge blurring and severe intensity distortion. The proposed method may improve the time resolution four to eight fold without losing much spatial and contrast resolution compared with the conventional Fourier technique. It may prove applicable to other dynamic applications, such as functional study of the brain or NMR spectral analysis. Future work will focus on applying the method to the medical MRI data.

REFERENCES

- [1] R. A. Jones *et al.*, *Magn. Reson Med.*, **29**, 830 (1993).
- [2] J. J. van Vaals *et al.*, *J. of MRI*, **3**, 671 (1993).
- [3] T. A. Spraggins, *Magn. Reson Med.*, **31**, 320 (1994).

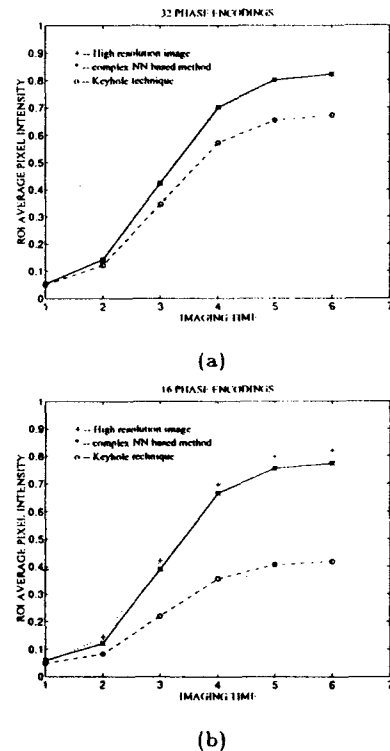


Fig. 2. Average pixel intensity changes in the region of interest (ROI) versus imaging time with different methods and phase encoding numbers. (a) 32 and (b) 16 phase encodings respectively. 256 encodings was used in the high resolution images.

- [4] Y. Hui and M. R. Smith, *Proc. of IEEE CCSP conf.*, 513 (1995).
- [5] M. R. Smith and Y. Hui, *submitted to IEEE Trans. on CAS II*, (1995).
- [6] N. Benvenuto and F. Piazza, *IEEE Trans. Signal Processing*, **40**, 967 (1992).

Solution Structure Studies of the Low-Density Lipoprotein Receptor Ligand-Binding Domain

Norelle L. Daly, Martin J. Scanlon¹, Julianne T. Djordjevic, Paulus A. Kroon and Ross Smith.

Department of Biochemistry and
¹Centre for Drug Design and Development
University of Queensland, Queensland 4072, Australia

The low-density lipoprotein (LDL) receptor plays a central part in mammalian cholesterol metabolism by clearing apolipoprotein E- and apo B-100-containing lipoproteins from plasma. The receptor is a mosaic protein comprised of five discrete functional domains, including a ligand-binding domain containing seven copies of a cysteine-rich repeat (1). Several other receptors also contain multiple copies of this repeat, including the LDL receptor related protein/ α 2-macroglobulin receptor (2), and a renal glycoprotein gp 330 (3). Single copies of the repeat are found in proteins from very diverse sources.

The residues conserved in these repeats include a cluster of C-terminal acidic residues and the six cysteine residues (1). Within the repeats of the LDL receptor the C-terminal acidic residues have been postulated to interact with lysine and arginine residues present in the ligands apo B-100 and apo E (1, 4). It has been proposed that the repeats also bear calcium binding sites, as the association of the LDL receptor with its ligands requires the presence of this ion (5).

Although not essential for ligand association, the amino-terminal repeat (LB1) was initially chosen for characterization because of the availability of an antibody, IgGC7, that could be used to determine whether the isolated repeat folded to the *in vivo* conformation. This antibody, which was raised against the intact receptor, binds to folded LB1 in the presence of Ca²⁺, but does not recognize the unfolded polypeptide. Recombinant LB1 (rLB1) and the second repeat (rLB2) have been separately expressed in *Escherichia coli* as GST-fusion proteins, cleaved using thrombin, and purified using affinity chromatography and reverse-phase HPLC. On oxidation both peptides folded to yield single peaks on isocratic reverse-phase

HPLC, and the refolded rLB1 binds to the IgGC7 antibody in the presence of calcium. The structures of the repeats have been determined using 500 MHz ¹H two-dimensional NMR spectroscopy.

The amino-terminal repeat, rLB1 has a well-defined structure consisting of a β -hairpin followed by a series of reverse turns (6). This motif appears to be unique in the structures lodged in the Protein Data Bank. The three-dimensional structure of this repeat is unaffected by millimolar concentrations of calcium ions.

In contrast, rLB2 has a very flexible structure in water, which is manifested in a very low dispersion of the amide resonances (Fig. 1). However, the conformation of rLB2 is markedly more ordered in the presence of a 4-fold molar

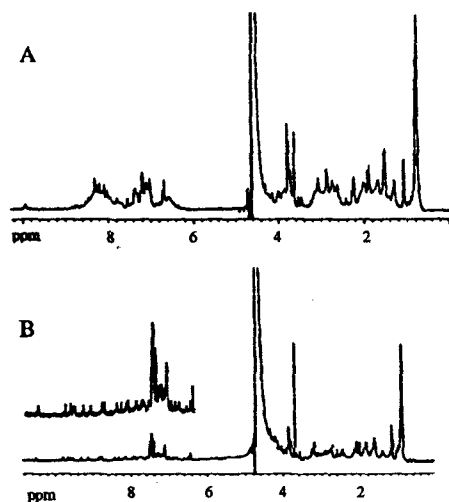


Figure 1: ¹H spectrum of 1 mM rLB2, recorded at pH 5.5 on a Bruker AMX 500 spectrometer, in the absence (A) and presence (B) of 4 mM calcium chloride.

excess of calcium chloride; the proton resonance dispersion and the number of NOESY crosspeaks is greatly enhanced.

The three-dimensional structure of rLB2, obtained from the NMR data by molecular geometry and restrained molecular dynamics methods, parallels that of rLB1, with an amino terminal hairpin structure followed by a succession of turns. However, there are clear differences in the backbone topology and structural flexibility (Fig. 2). As for rLB1, the acidic residues are clustered on one face of the module.

These results provide the first experimental support for the hypothesis that each of the repeats in the ligand-binding domain has a similar global fold, but also highlight significant differences in structure and internal dynamics.

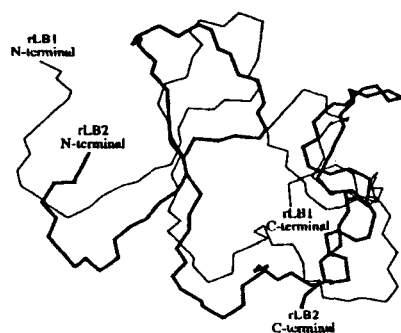


Figure 2: Superposition over residues 10-35 of the backbone atoms (N, C $^{\alpha}$, C $^{\prime}$) of one of the rLB1 (thin line) and rLB2 (thick line) NMR-derived structures (residues 5-41 of both peptides are displayed).

References

- ¹T. Yamamoto, C.G. Davis, M.S. Brown, W.J. Schneider, M.L. Casey, J.L. Goldstein, and D. W. Russell, *Cell* **39**, 27-38 (1984).
- ²J. Herz, U. Hamann, S. Rogne, O. Myklebost, H. Gausepohl and K.K. Stanley, *EMBO J.* **7**, 4119-4127 (1988).
- ³R. Raychowdhury, J.L. Niles, R.T. McCluskey and J.A. Smith, *J.A. Science* **244**, 1163-1165 (1989).
- ⁴J.L. Goldstein M.S. Brown, R.G.W. Anderson, D.W. Russell and W.J. Schneider, *Ann. Rev. Cell. Biol.* **1**, 1-39 (1985).
- ⁵I.R. van Driel, J.L. Goldstein, T.C. Südhof and M.S. Brown, *J. Biol. Chem.* **262**, 17443-17449. (1987).
- ⁶N.L. Daly, M.J. Scanlon, J.T. Djordjevic, P.A. Kroon and R. Smith, *Proc. Natl. Acad. Sci. U.S.A.* **92**, 6334-6338 (1995).

Pulsed NQR in antimony metal at high pressures: changes in the electric field gradient and the electronic structure

G.J. Hill, J.M. Keartland and M.J.R. Hoch

Department of Physics and Condensed Matter Physics Research Unit, University of the Witwatersrand, P.O. Wits, 2050, Johannesburg, South Africa

We report on the first pulsed NQR measurements in antimony metal at high pressures. The quadrupolar resonance frequency (ν_Q) and nuclear spin-relaxation rates have been measured for both the ^{121}Sb and ^{123}Sb isotopes as a function of pressure in the range 0-1.4 GPa. These quantities provide information on the variation of the electric field gradient (efg) and the electronic structure with pressure. The electric field gradient decreases with pressure, a significant contribution to this change appears to be due to changes in the ionic potentials. A comparison of the relaxation rates for the two isotopes indicates that, over the pressure range investigated, the variation in the quadrupolar relaxation rates is negligible, and that the density of states at the Fermi level increases with pressure.

EXPERIMENTAL DETAILS

High purity antimony was crushed to 25 μm , annealed and placed in a container that allowed the pressure fluid to permeate the sample. NQR measurements were made using a standard variable frequency coherent, pulsed, spectrometer operating in the range 18-22 MHz. High pressures at ambient temperature were achieved using a piston-cylinder arrangement (1), with isopentane as the pressure transmitting medium. Pressures were measured using a manganin resistance gauge.

RESULTS AND DISCUSSION

The quadrupolar resonance frequency (ν_Q) for the $^{3/2} \leftrightarrow ^{5/2}$ transition in ^{121}Sb was measured using an echo profile technique to an accuracy of better than 0.1%. ν_Q changes linearly, and the slope of the best line fit is $-17.8 \text{ kHz} \cdot \text{GPa}^{-1}$ in the pressure range 0-1.4 GPa, in agreement with previous CW measurements (2) made in the range 0-0.4 GPa. Small deviations from a linear dependence are observed at the highest pressures. The efg derived from these results is compared with a calculation of the variation of the efg due to changes in the ionic potentials, determined from

measurements of pressure changes in the crystal structure parameters (3), in Fig. 1. As reported previously for arsenic metal (4), a significant contribution to changes in the efg is due to changes in the ionic potentials, although 85% of the efg is due to the carriers.

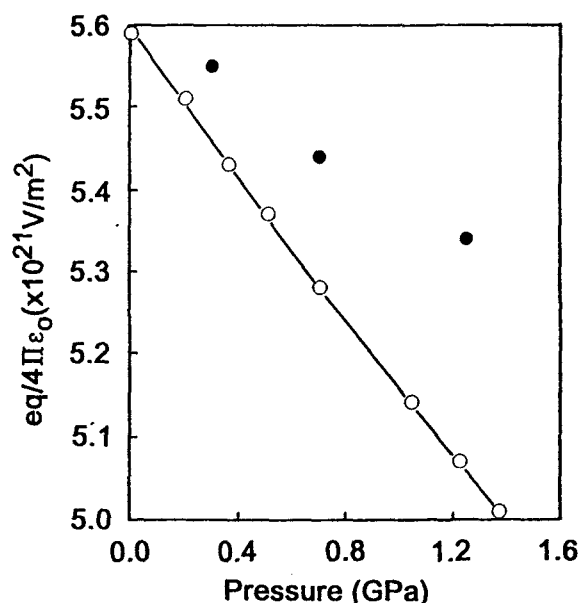


Fig. 1. Pressure variation of the efg derived from our measurement of ν_Q (○) compared with data derived from measurements of the crystal field parameters (●).

The relaxation rate for the $3/2 \leftrightarrow 5/2$ transition in ^{121}Sb was measured using standard spin echo techniques. We have considered only magnetic relaxation, and extracted the relaxation parameter W_m where the relaxation is described by

$$1 - \frac{M(t)}{M(\infty)} = \frac{2\nu}{7} \times [3\exp(-6W_m t) + 4\exp(-20W_m t)]. \quad [1]$$

ν is dependent on experimental setting of the pulses.

W_m increases from 75 s^{-1} to 117 s^{-1} over the range 0-1.4 GPa. Previous measurements in arsenic (4) showed a decrease from 205 s^{-1} to 153 s^{-1} over the same range. Proceeding as we did in our analysis of the arsenic data, we assumed that the probability density of the carriers at the nucleus, averaged over the Fermi surface, remains approximately constant with pressure giving

$$W_m \propto \rho^2(E_F). \quad [2]$$

$\rho(E_F)$ is the density of states at the Fermi level. From this we extract the ratio of the density of states with pressure to that at ambient pressure. Using the relationship

$$\frac{\rho(P)}{\rho(0)} = \frac{v_0(P)}{v_0(0)} \frac{m^*(P)}{m^*(0)} \left[\frac{n(P)}{n(0)} \right]^{-1/3} \quad [3]$$

we extract values for an effective mass parameter, using the pressure variation of the atomic volume (v_0) derived from measurements of the crystal structure (3), and the pressure variation of the carrier concentration (n) (5). The results are shown in Fig. 2, and are in general agreement with changes in the Fermi surface calculated using a pseudopotential method (6). The two isotopes in antimony are approximately equally abundant, and comparison of the relaxation rates shows that quadrupolar relaxation rates (due to a two-phonon Raman process) change negligibly over the pressure range investigated.

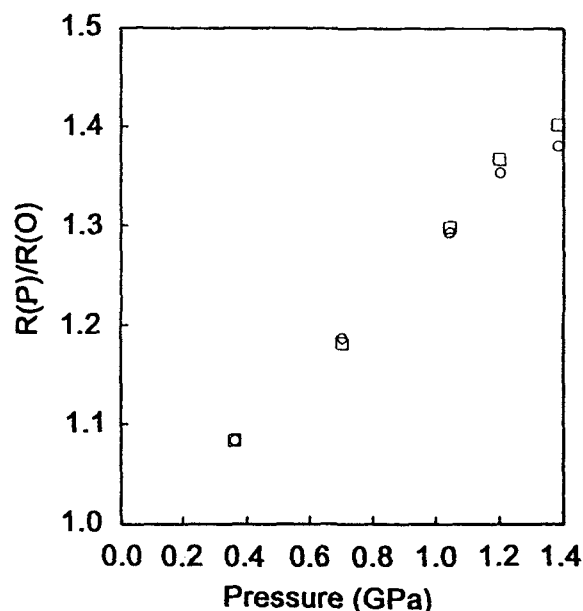


Fig. 2. Pressure variation of the density of states at the Fermi surface (\square) and the average effective mass (\circ).

CONCLUSION

Using NQR methods, information has been obtained on changes in the electronic structure of semimetallic antimony with pressure at ambient temperature. Our results confirm that antimony exhibits an increase in metallic character with pressure up to 1.4 GPa.

REFERENCES

- ¹J.M. Kearthland and M.J.R. Hoch, *Phys. Rev. B*, **46**, 4527 (1992).
- ²W.J. O'Sullivan and J.E. Schirber, *J. Chem. Phys.*, **41**, 2212 (1964).
- ³D. Schiferl, D.T. Cromer and J.C. Jamieson, *Acta Cryst. B*, **37**, 807 (1981).
- ⁴G.J. Hill, J.M. Kearthland and M.J.R. Hoch, *Proceedings of 27th Congress Ampere*, 784 (1994).
- ⁵N.B. Brandt, N. Ya. Minina and Yu. A. Pospelov, *Soviet Phys. JETP*, **28**, 869 (1969).
- ⁶Yu. A. Pospelov, *Phys. Stat. Sol. (b)*, **99**, 173 (1980).

A Water Proton Spin-lattice Relaxation Study Of The Adsorption Of Paramagnetic Ions In Aqueous Colloidal Silica Suspensions

P. Roose, J. Van Craen, G. Andriessens, H. Eisendrath

MARE, Department of Physics, Vrije Universiteit Brussel, Pleinlaan 2, 1050 Brussels, Belgium

Introduction

From the early days of NMR it was observed that water proton relaxation is strongly enhanced in solutions of paramagnetic metal ions. In aqueous solutions this relaxation enhancement is described in terms of magnetic electron-nucleus interactions between hydrated water protons and the paramagnetic ion (known as the modified Solomon-Bloembergen-Morgan (SBM) theory (1)). Major alterations of the water relaxation occur when paramagnetic ions are bound to a macromolecule. In this work water relaxation as well as ion-adsorption was studied in aqueous colloidal silica (SiO_2) suspensions after addition of paramagnetic Mn^{2+} and Fe^{3+} ions. Colloidal suspensions of spherical silica particles are stabilized against aggregation by repulsive Coulombic interactions between the charged particles. The net charge of the particles depends on pH and is negative above pH 2 (PZC). The water proton spin-lattice relaxation time T_1 was measured over a broad magnetic field range (referred to as Nuclear Magnetic Relaxation Dispersion) using the field-cycling technique.

Materials and Methods

Sample preparation and characterization: An aqueous colloidal silica sample was prepared according to the method of Stöber et al. (2). The particle diameter, as obtained from diffusion coefficient measurements using dynamic light scattering, is 11.6 ± 0.5 nm. Microliter amounts of MnCl_2 and FeCl_3 stock solutions were added to the silica sample (typ. 20 μl in 500 μl sample volume). The Mn^{2+} and Fe^{3+} concentrations in the stock solutions were determined by atomic absorption. HCl and NaOH solutions were used to alter the pH of the sample.

Relaxation measurements: The NMRD curves were measured on a home-built automatic 7.5 MHz Field-Cycling relaxometer. The magnetic field ranges from 0.24 mT to 1.2 T

corresponding to proton Larmor frequencies of 0.01 - 50 MHz. Sample temperature was kept at 4°C.

Results

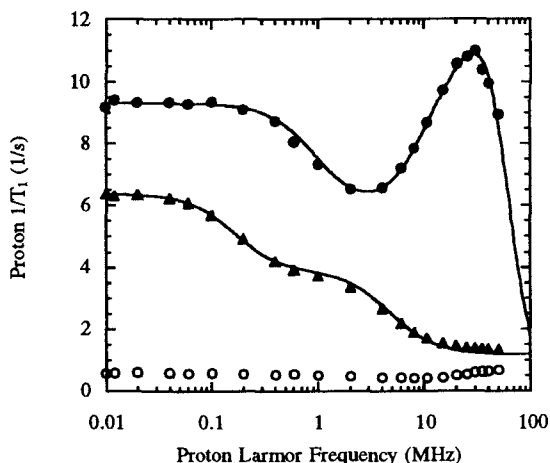


Fig. 1 Paramagnetic contribution to the water proton NMRD curve of 100 μM $\text{Mn}(\text{II})$ adsorbed on silica (filled circles); 100 μM $\text{Mn}(\text{II})$ aquo-ion (filled triangles); 100 μM $\text{Fe}(\text{III})$ adsorbed on silica (open circles). The full lines result from a least-squares comparison of the SBM theory to the data.

The proton NMRD curves of diamagnetic aqueous colloidal silica sols show an inflection very similar to observations in protein solutions (3). In Fig. 1, the paramagnetic contribution to the solvent proton NMRD curve of Mn^{2+} adsorbed on colloidal silica (filled circles) is compared to the aquo-ion (filled triangles). The difference in NMRD profile results essentially from the increase of the reorientational correlation time of the hydrated ion when it is adsorbed on the silica particle. The overall correlation time is then determined by the shorter electron spin relaxation time which itself is field-dependent, hence the relaxation peak at high magnetic fields (4). In both cases the SBM model applies very well to the data. The full lines result from a least-squares comparison of the

theory to the data. Correlations between some of the SBM model parameters lead to ambiguities.

Prior physico-chemical knowledge is helpful to reduce the number of parameters to an independent set. So, using 6 water molecules hydrated to the aquo-ion, one finds an ion-proton spin-spin separation of 2.74 Å. Various adsorption models of hydrolyzable metal ions at the oxide-water interface are available from potentiometric titration studies (5). Evidence exists that adsorbed ions retain their primary hydration shell i.e. 6 water molecules. The SBM fits yield then an estimated value for the ion-proton spin-spin separation of 2.66 Å, very close to the value found for the aquo-ion. The paramagnetic NMRD contribution of adsorbed Fe^{3+} (lower curve of Fig. 1) is about 20 times lower than for Mn^{2+} .

In Fig. 2 the NMRD profiles clearly reflect the pH dependence of the Mn^{2+} adsorption. At pH 2.4 no Mn^{2+} is adsorbed as shown by the typical NMRD profile of free Mn^{2+} (triangles) while at pH 7.5 the paramagnetic peak (filled circles) indicates that Mn^{2+} has been adsorbed. Actually the NMRD curve consists of the sum of a free aquo-ion and an adsorbed ion contribution. One notes from Fig. 1 that for adsorbed ions the relaxation rate remains constant between 0.01 and 0.2 MHz while for aquo-ions a relaxation rate difference is observed. We can take advantage of this fact to estimate the free ion concentration by comparing this relaxation rate difference in the suspension with the corresponding difference of the standard free Mn^{2+} solution (Fig. 1). The full line represents the reconstruction of the free ion NMRD contribution and the open circles correspond to the NMRD contribution of the adsorbed ions, obtained after subtraction of the free ion part of the total NMRD curve. The full line through these datapoints is the best fit of the SBM model using the estimated bound ion concentration. At pH 7.5 the adsorption density $\Gamma_{\text{Mn}^{2+}}$ is 0.07 ions/nm². $\Gamma_{\text{Mn}^{2+}}$ increases rapidly in the pH interval 7-8. In our experiments maximum coverage (saturation) of the silica could not be achieved.

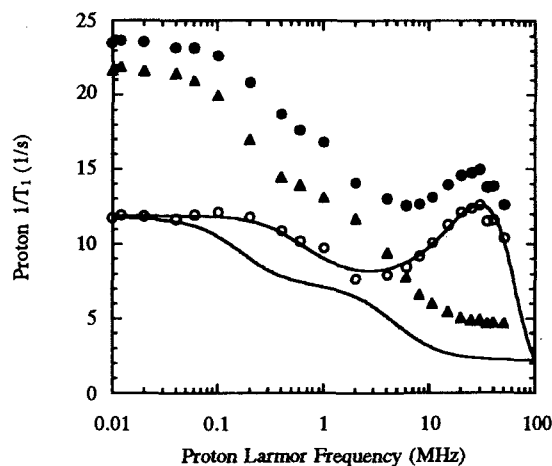


Fig. 2 Proton NMRD curves in $\text{Mn}(\text{II})/\text{silica}$ sols at different pH (4°C). The total $\text{Mn}(\text{II})$ concentration is 317 μM . See text for further explanations.

Conclusions

In this paper it is demonstrated that NMRD yields useful information about the adsorption mechanisms of hydrolyzable paramagnetic ions at oxide-water interfaces. Furthermore the relaxation properties of ion-hydrated water molecules can be investigated for a large variety of ions since most of them adsorb on silica. Moreover the geometry of the ion complex is altered slightly preserving similarities with the aquo-ion.

References

1. J. Kowalewski, L. Nordenskiöld, N. Benetis and P. O. Westlund, *Prog. NMR Spectr.* 17, 141 (1985).
2. W. Stöber, A. Fink and E. Bohn, *J. Colloid Interface Sci.* 26, 62 (1968).
3. P. Roose, J. Van Craen, R. Finsky and H. Eisendrath, *J. Magn. Reson. A*, in press (1995).
4. S. H. Koenig and R. D. Brown III, *Magn. Res. Med.* 1, 478 (1984).
5. R. O. James and T. W. Healy, *J. Colloid Interface Sci.* 40, 65 (1972).

Quick spinning sideband suppression in MAS-NMR experiments

T.J. Bonagamba, H. Panepucci, E.A. Vidoto, and E.L.G. Vidoto
 Instituto de Física de São Carlos, Universidade de São Paulo
 Caixa Postal 369, CEP 13560-970 - São Carlos, São Paulo, Brazil

Introduction

Sidebands in magic-angle-spinning NMR experiments are a common problem for high field spectrometers or low spinning frequency systems. Although these sidebands may be used to gain information after they have been identified, it is necessary to eliminate them to simplify the interpretation of the spectra. We have recently succeeded in suppressing spinning sidebands by continuously varying the speed during the signal acquisition (1).

Method

This method, that we called *variable* low speed sideband suppression (VIABLE), relies on the speed dependence of the sideband positions. It consists in averaging the FIDs acquired while the rotor speed is being continuously swept between a minimum and a maximum value. After a large number of acquisitions, normally used to increase sensitivity, the isotropic spectrum adds continuously while the sidebands do not, because their positions change. The signal average process will then produce a spectrum where the intensity of the sidebands is divided by the number of scans.

The apparatus, that can be easily adapted to any MAS NMR spectrometer, is schematically shown in figure 1. It is basically composed of a stepping motor actuated needle valve that controls the gas flow in the high pressure line, driving the sample rotor. A typical needle valve with several turns can be used for this purpose. The control of the stepping motor can be accomplished either by a dedicated hardwired pulse generator circuit or, as in our case, by the use of a microcomputer (2).

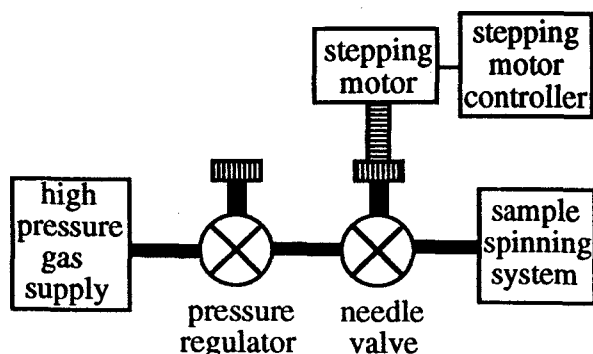


Figure 1: The spinning speed controller.

Results

The apparatus was tested using our Tecmag Libra System in conjunction with a Doty MAS double resonance probe operating at 2 Tesla.

To illustrate the method, we present the ^{13}C MAS NMR spectra of a variety of samples acquired using cross-polarization and high power proton decoupling. Among the samples studied were: hexamethylbenzene, tyrosine, and humic acid.

Hexamethylbenzene has two sets of carbon nuclei with different isotropic chemical shifts, six located in the methyl group and six aromatic carbons. The aromatic carbons show a large chemical shift anisotropy and that gives rise to spinning sidebands at low rotor speeds, whereas carbons located in the methyl groups have little anisotropy and do not produce spinning sidebands. Figure 2a shows the spectrum where the sidebands were eliminated by spinning with a high rotor speed (2500 Hz). Figures 2b through 2d show the spectra obtained at various fixed speeds between 500 Hz and 1500 Hz which exhibit the expected spinning sidebands. Figures 2e and 2f, correspond to the spectra obtained with the variable low speed magic angle spinning technique using the speed controller apparatus.

Figures 3 and 4 show in a similar way the results obtained with more complex spectra. Notice that the sideband-free spectrum in figure 3d has almost the same signal to noise ratio as those in 3b and 3c and was acquired in a much shorter time. In particular, figure 4 illustrate the case of wide isotropic lines that would make difficult the use of some computational methods for the extraction of the isotropic spectrum.

Conclusions

It is clear from the above results, that the simple apparatus described here, can be employed to reduce drastically the intensity of the spinning sidebands in solid NMR MAS spectra, even when the available probes are unable to reach the high speeds necessary to remove them.

The method allows a quick acquisition of the isotropic chemical shift spectra and works well even when the highest available spinning speeds can not clearly resolve the spinning sidebands.

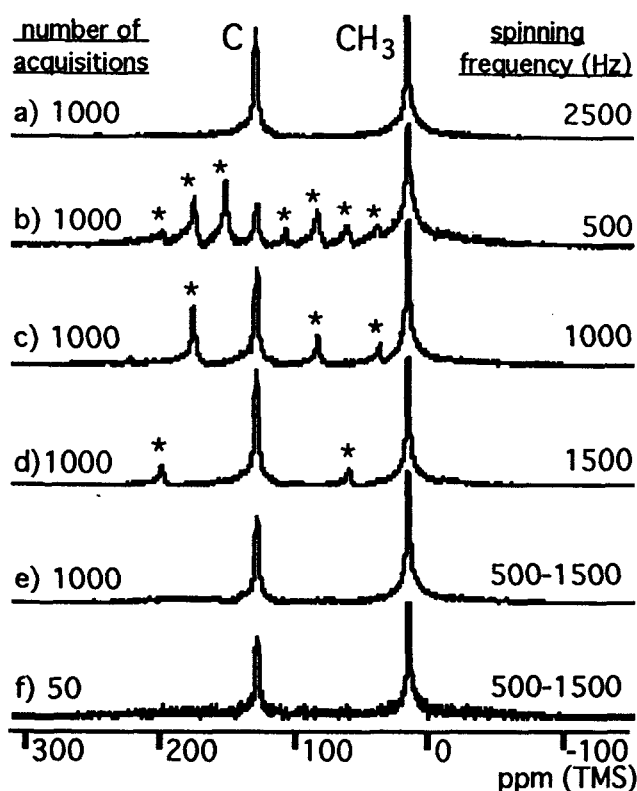


Figure 2: Hexamethylbenzene ^{13}C spectra. (* spinning sidebands).

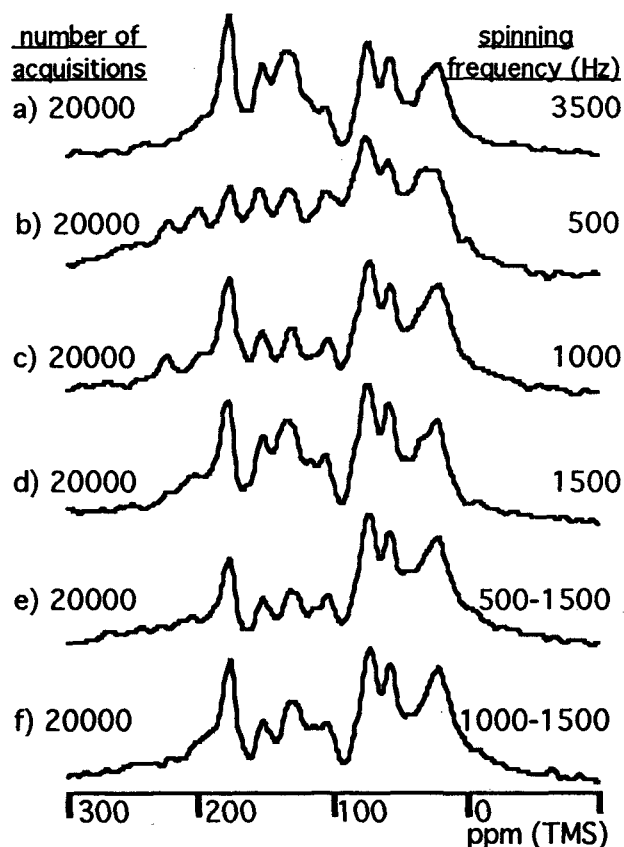


Figure 4: Humic acid ^{13}C spectra.

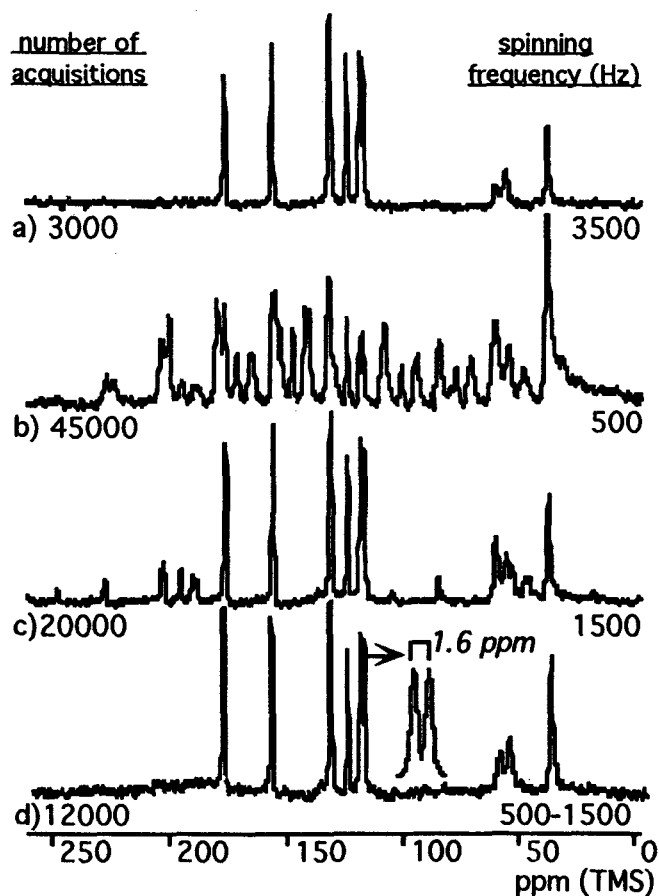


Figure 3: Tyrosine ^{13}C spectra.

Since the method does not involve calculations on the individual signals the signal to noise ratio and the sideband resolution of the individual signals are not direct limitations to its applicability. Furthermore, since spinning sideband suppression and signal to noise ratio improvement occur simultaneously as a result of the signal averaging procedure, the necessary time to obtain the sideband free spectrum is equivalent to that required to obtain a single spectrum with sidebands, at a given with similar signal to noise ratio.

Acknowledgments

We thank J.G. da Silva and O.A. Canevarollo for their technical support. This research was supported by FAPESP, FINEP, CNPq and CAPES (Brazilian Agencies).

References

1. T.J. Bonagamba and H. Panepucci, *J. Magn. Reson. Series A*, 103, 103 (1993).
2. T.J. Bonagamba, H. Panepucci, and E.A. Vidoto, *Review of Scientific Instruments* (to be published).

In vivo ^{31}P NMR and histological investigation of muscle recovery after induced injury

T.J. Bonagamba, T.F. Salvini†, H. Panepucci, E.L.G. Vidoto,
A. Tannús, A.C.M. Zeri, C.C. Morini†
Instituto de Física de São Carlos, Universidade de São Paulo
Caixa Postal 369, CEP 13560-970 - São Carlos - São Paulo - Brazil
† Universidade Federal de São Carlos - Brazil

Introduction

Muscle damage is a common phenomena accompanying exercise both in humans and animals. Signals of acute muscle damage occur in mouse hind legs during first days after running and are usually repaired within two weeks.

The present series of experiments was devised to demonstrate the use of in vivo ^{31}P NMR to allow non invasive and repeatable investigation of the skeletal muscle healing process by following the changes in metabolic activity that take place during muscle repair.

Materials and methods

Eighteen male mice were used at ten weeks of age. The animals were housed in groups in standard plastic cages in an animal room with controlled environmental conditions (12 hours dark/light cycle; temperature 22.5°C). Mice were fed with standard food and they had access to food and water *ad libitum*. They were randomly divided in six groups of three animals each. One group was the sedentary control and the others were submitted to exercise and available 0.5, 3, 5, 8 and 15 days after running.

The animals were exercised on a motor-driven rodent treadmill with running slots of lucite plastic for simultaneous training of 14 animals, but no electroshock facility. All animals were exercised only once on a motor-driven treadmill at 14m/min for two 3 hours periods with 30 minutes rest in between. During the rest in the cages the animals had free access to food and water. Exercise was well tolerated by animals as they kept running spontaneously during these periods.

One animal of each group was analyzed by *in vivo* ^{31}P NMR spectroscopy. The ^{31}P spectra were obtained in a 2.0 Tesla 30 cm bore Oxford magnet using a TECMAG LIBRA spectrometer. Care was taken to avoid saturation using a repetition time of 3s. The mice were kept anesthetized (Thiophental, 5 mg/kg) for about 1 hour which allowed an average of a thousand acquisitions for each spectra.

The probe was designed to accommodate the mouse over a metallic bed which served also as

a Faraday cage. The right hind limb leg extended out of this cage through a hole to fit almost exactly into tapered solenoidal coil which was also shielded. The integrated intensities were evaluated for each spectrum by fitting each line with a lorentzian function. The integrated intensity of the inorganic phosphate line was calculated as a percent of the total integrated spectrum intensity.

The extent of muscle alterations was independently established by histological examination by optical microscopy performed for each animal immediately after the NMR scans.

Results

The ^{31}P NMR spectra shown in figure 1 exhibited a maximum departure from those of the control animals after 3 days and recovered the control values only after 15 days.

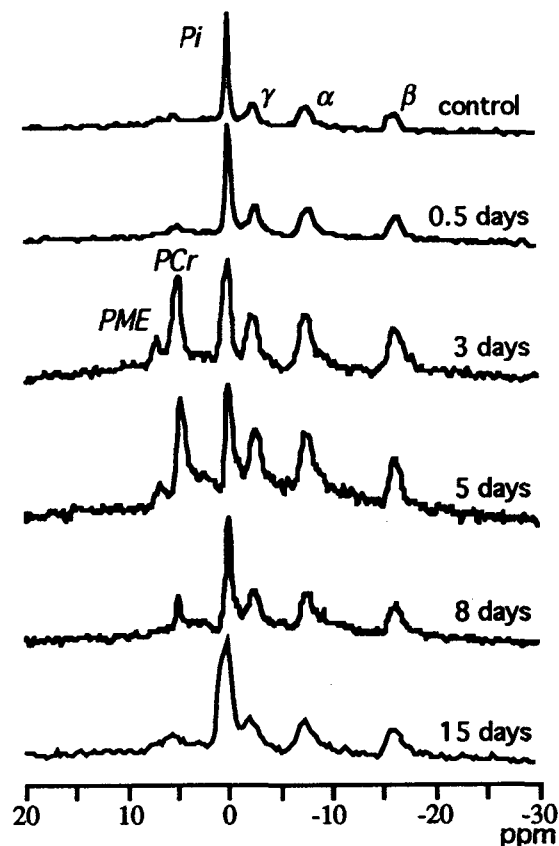


Figure 1: ^{31}P NMR spectra.

A similar behavior was observed through the histological examination for the percentual number of damaged fibers in the injured muscle, table I.

Table I: Incidence of acute muscle damage on the right soleus muscle fibers.

Animals	Groups	Total fibers number	Total damaged fibers number	% damaged fibers $X \pm SD$
1	sedentary	600	0	
2		646	2	0.2 ± 0.2
3		643	2	
4	0.5 day	634	34	
5		589	53	6 ± 2
6		575	27	
10	5 days	676	43	
11		564	64	10 ± 3
12		642	77	
13	8 days	710	38	
14		778	29	4 ± 1
15		803	24	
16	15 days	636	15	
17		562	23	3 ± 1
18		640	14	

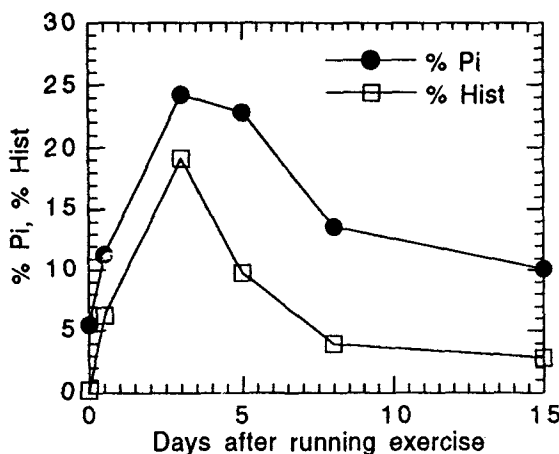


Figure 2: Correlation between the percent of the total integrated spectrum intensity of the Pi line (% Pi) and the percent of muscle damaged fibers (% Hist).

Conclusions

Examination of the spectra in figure 1 shows alterations on the relative concentrations of the metabolites detectable by ^{31}P NMR: ATP, ADP, inorganic phosphate (Pi), phosphocreatine (PCr) and phosphomonoester (PME). The main feature that appear from figure 1 is the initial increase in Pi reaching a maximum around the 3rd day before returning to control level suggest an healing process peaking between 3rd and 5th day.

It is particularly interesting to analyze the correlation between the Pi percentual integrated line and the number of damaged muscle fibers that appear in the histological examination. This is done in figure 2 which shows the evolution of these two values over the 15 days period. Analisis of these data show that a strong correlation ($r=0.9$) exists which indicate that *in vivo* ^{31}P NMR is a potent method for evaluating the metabolic changes produced on the mouse hind limb muscle by acute muscle injury and muscle regeneration after running exercise.

Acknowledgments

We thank J.G. da Silva and O.A. Canevarollo for their technical support. This research was supported by FAPESP, FINEP, CNPq and CAPES (Brazilian Agencies).

References

1. D.I. Hoult, S.J.W. Busby, D.G. Gadian, G.K. Radda, R.E. Richards, and P.J. Seeley, *Nature*, 252, 285 (1974).
2. K. McCully, F. G. Shellock, W.J. Bank, and J.D. Posner, *Med. Sci. Sports Exerc.*, 65, 197 (1992).
3. A. Salminen, and V. Vihko, *Muscle and Nerve*, 6, 596(1983).
4. A. Wernig, T.F. Salvini, and A. Irintchev, *J. Neurocytol.*, 20, 903(1991).
5. A. Irintchev, T.F. Salvini, A. Faissner, and A. Wernig, *J. Neurocytol.*, 22, 955(1993).
6. R.B. Armstrong, *Med Sci. Sports Exer.*, 16, 520(1984).
7. S. Kuno, M. Akisada, and F. Mitsumori, *Eur. J. Appl. Physiol.*, 65, 197(1992).

Demagnetization fields in NMR experiments which employ magnetic field gradients.

G. J. Bowden, T. Heseltine,
School of Physics, University of New South Wales,
NSW 2052, Australia.

M. J. Prandolini
Department of Physics, University College,
Australian Defence Force Academy, ACT 2600, Australia.

The demagnetization term associated with the finite size of the sample is typically $\approx 6 \times 10^{-9} \times H_o$. Despite its small size, effects due to demagnetizing fields, have been observed in NMR experiments which incorporate pulsed magnetic field gradients [1, 2, 3]. More recently, Warren and co-workers have observed intermolecular cross peaks in 2D COSY NMR spectra which employ MQ selective field gradients [2, 3, 4]. The existence of these cross peaks, and their amplitudes, has been ascribed to the generation of multiple spin echoes induced by demagnetizing field effects [2, 5]. In this note we determine the magnitude of the pitch $p (= 2\pi/\gamma Gt)$, generated by the magnetic field gradients needed to eliminate non-linearities in the demagnetization field imposed by the size and shape of the sample.

The local magnetic field H_L experience at the nucleus can be written as

$$H_L = H_o + H_{dip} + M(1/3 - D) \quad (1)$$

where (i) H_{dip} is summed over the Lorentz sphere, and (ii) the demagnetization factor D and the magnetization is M shape and direction dependent, except for samples with an ellipsoidal shape. The dipolar interaction can be summed (or integrated) using

$$H_{dip}(\mathbf{r}_i) = \frac{1}{4\pi} \sum_j \frac{-\mu_j}{r_{i,j}^3} + \frac{3(\mu_j \cdot \mathbf{r}_{i,j})\mathbf{r}_{i,j}}{r_{i,j}^5}. \quad (2)$$

Our task is now to solve a modified Bloch equation

$$\frac{\partial M(\mathbf{r}, t)}{\partial t} = \gamma \mu_o M(\mathbf{r}, t) \times H_L + \text{Relax. terms} \quad (3)$$

Due to the non-local nature of H_{dip} , Eq. (3) is very difficult to solve completely. Nevertheless, under our experimental conditions two important approximations

can be made, (i) when $H_o \gg H_{dip}$, we retain only those terms which conserve I_z , and (ii) the effect of the sample shape on the demagnetization distribution can be suppressed by applying a strong uniform external gradient G_z [6].

Further progress can be made by investigating the Fourier transform of $H_{dip}(\mathbf{r})$. Following [6], the transform of $H_{dip}(\mathbf{r})$ is

$$H_{dip}(\mathbf{q}) = \frac{1}{2} D_z(\mathbf{q})(3M_z(\mathbf{q}) - M(\mathbf{q})), \quad (4)$$

where

$$D_z(\mathbf{q}) = \frac{1}{4\pi} \int e^{i\mathbf{q} \cdot \mathbf{r}} \frac{3 \cos^2 \theta_r - 1}{r^3} d\mathbf{r}. \quad (5)$$

$D_z(\mathbf{q})$ converges to a function dependent on the orientation of $\hat{\mathbf{q}}$, under the following assumptions, (i) the sample size is infinite, and (ii) $q_z (= \gamma G_z t) \gg 1/R$. Thus, given that the magnetic spiral is tight enough ($q \gg 1/R$) then the dipolar field $H_{dip}(\mathbf{r})$ is proportional to the magnetization $M(\mathbf{r})$. For example, if $M(\mathbf{r})$ is twisted into a simple spiral about the z -axis, the field $H_{dip}(\mathbf{r})$ will follow suit.

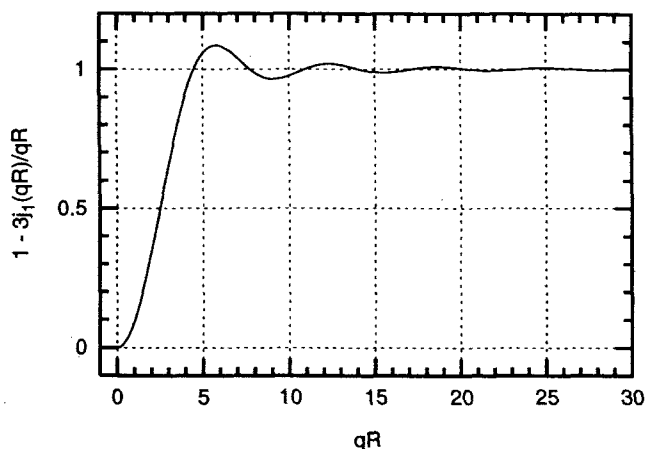
For an infinite lattice it was shown by [7] that

$$D_{inf}^{\alpha\beta}(\mathbf{q}) = -\frac{1}{3} \left(\frac{3q^\alpha q^\beta}{q^2} - \delta_{\alpha\beta} \right) \quad (6)$$

where α and β represent ($x, y, \text{ or } z$). In addition, for a finite spherical lattice of radius R , $D^{\alpha\beta}(\mathbf{q})$ becomes

$$D^{\alpha\beta}(\mathbf{q}) = D_{inf}^{\alpha\beta}(\mathbf{q}) \left[1 - \frac{3j_1(qR)}{qR} \right]. \quad (7)$$

Near $\mathbf{q} = 0$, $D^{\alpha\beta}(\mathbf{q})$ varies rapidly for small changes in \mathbf{q} . From a physical point of view, these oscillations are due to rapidly changing surface poles on the sample, as $\mathbf{q} \rightarrow 0$. Fig. 1 illustrates the dependence of the

Figure 1: A plot of $(1 - 3j_1(qR)/qR)$ vs qR .

term in square brackets in Eq. (7) with qR . Clearly, it should be noted that $D^{\alpha\beta}(\mathbf{q})$, for $qR > 10$, becomes well defined and position independent.

For a finite spherical sample, with spiral directed along the z -axis, Eq. (5) can be broken up into a cosine and sine transforms

$$D_c^{zz}(\mathbf{q}, \mathbf{r}_i) = \sum_{j \neq i} \frac{3 \cos^2 \theta_{i,j} - 1}{4\pi r_{i,j}^3} \cos \mathbf{q} \cdot \mathbf{r}_{i,j}, \quad (8)$$

$$D_s^{zz}(\mathbf{q}, \mathbf{r}_i) = \sum_{j \neq i} \frac{3 \cos^2 \theta_{i,j} - 1}{4\pi r_{i,j}^3} \sin \mathbf{q} \cdot \mathbf{r}_{i,j}. \quad (9)$$

For Eq. (5) to hold, the cosine transform should be constant and independent of \mathbf{r}_i , while the sine transform should be zero. Using a simple lattice of cubic spins, we have calculated the required FT, as a function of distance along the z -axis. The results are summarised in Fig. 2. It will be observed that even for $qR = 20$, there is a sizeable variation in both transforms. Thus we conclude that Eq. (5) holds good when $qR > 20$, therefore as a rule of thumb, the criterion for using Eq. (5) on spherical samples, should be set to

$$q > 20/R \Leftrightarrow \text{with pitch } p < 2\pi \times R/20. \quad (10)$$

Furthermore it can be shown, even in samples characterised by say two magnetic spirals, the local field H_{dip} is still well defined, provided $q_1, q_2 > 20/R$ and $q_1 \neq q_2$. However, if weak magnetic spirals are used with say $p \sim R$, the local field H_{dip} is not well defined, and it is quite plausible that surface demagnetization fields will generate weak intermolecular cross peaks ($\Delta\omega_1 + \Delta\omega_2$), in field gradient, multiple quantum selective 2D NMR experiments on separated samples.

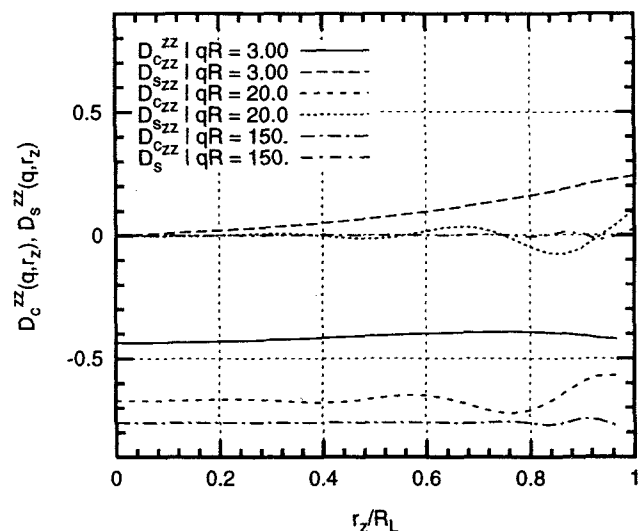


Figure 2: Eqs. (8) and (9) were calculated, using a simple cubic lattice for summation, as a function of distance along the z axis. Three conditions were observed, $qR = 3$, $qR = 20$ and $qR = 150$.

In summary, provided magnetic spirals with say $p < 2\pi \times R/20$ are used, the local dipolar field H_{dip} within the sample should reflect the local magnetization $M(\mathbf{r})$ within a spherical sample, at least for those spins which are not close to the surface of the sample.

References

- [1] R. Bowtell, *J. Magn. Reson.* **100**, 1 (1992).
- [2] Q. He, W. Richter, S. Vathyam, and W. S. Warren, *J. Chem. Phys.* **98**, 6779 (1993).
- [3] W. S. Warren, W. Richter, A. H. Andreotti, and B. T. F. II, *Science* **262**, 2005 (1993).
- [4] W. Richter, S. Lee, W. S. Warren, and Q. He, *Science* **267**, 654 (1995).
- [5] G. J. Bowden, T. Heseltine, and M. J. Prandolini, *Chem. Phys. Lett.* **233**, 639 (1995).
- [6] G. Deville, M. Bernier, and J. M. Delrieux, *Phys. Rev. B* **19**, 5666 (1979).
- [7] M. H. Cohen and F. Keffer, *Phys. Rev.* **99**, 1128 (1955).

NMR Structural Studies of Amphipathic Helices

G.K. Pierens[†], G.W. Buchko, G. Wang, W.D. Treleaven, A. Rozek and R.J. Cushley

Institute of Molecular Biology and Biochemistry, Simon Fraser University,
Burnaby, BC, V5A 1S6, CANADA.

[†]Faculty of Science and Technology, Griffith University, Nathan Campus, Kessels Road,
Brisbane, QLD, 4111, AUSTRALIA.

Introduction. By definition, an amphipathic helix is an α -helix with well demarcated polar and nonpolar faces. A prominent feature of the serum apolipoproteins are repeating amino acid motifs of 11 or 22 residues which, based upon predictions from the primary sequence, may adopt amphipathic helical structures when associated with lipid [1]. Apolipoprotein binding to the surface of lipoproteins purportedly occurs because of the presence of these amphipathic motifs; the hydrophobic face interdigitates into the phospholipid hydrophobic region and the hydrophilic face extends into the aqueous medium. ApoE(267-289), PLVEDMQRQWAGLV-EKVQAAVGT, is a segment of a region of apoE (263-286) that has been shown to bind strongly to dimyristoylphosphatidylcholine [2]. ApoAII(18-30)+, VTDYGKDLMEKV-KEWLNS, is a segment of the purported lipid-binding domain of apoAII (10-30) [3] with five additional residues at the C-terminus. In the present study, we focus on the structures adopted by these two synthetic peptides using deuterated sodium dodecyl sulfate (SDS-*d*₂₅) to model the lipoprotein environment [4]. Standard 2D ¹H NMR experiments were performed on both peptides in the presence of SDS and the helical content estimated from the H^α secondary shifts. Using distance restraints obtained from NOESY experiments, average structures for both peptides in the presence of SDS were obtained with distance geometry and simulated annealing calculations.

Experimental. ¹H NMR Spectroscopy. Samples (3-5 mM) for ¹H NMR spectroscopy were prepared in 90% H₂O/10% H₂O or 99.8% D₂O by dissolving the peptides in 400 μ L of SDS-*d*₂₅ solution. A peptide:SDS ratio of 1:90 (apoE(267-289)) and 1:40 (apoAII(18-30)+) were used to ensure

uniform peptide/SDS complex formation [4]. The pH was adjusted to 6.0 for apoE(267-289) and 5.0 for apoAII(18-30)+ with the addition of 0.1M NaOH (pH meter reading uncorrected for the deuterium isotope effect).

Standard phase sensitive (TPPI) 2D DQF-COSY, TOCSY and NOESY spectra were recorded at 37°C on a Bruker AMX spectrometer operating at a proton resonance frequency of 600.13 MHz. Water was suppressed by WATERGATE (3-9-19 sequence) in the TOCSY and NOESY experiments and by presaturation during the recycling delay (1.5 s) in the DQF-COSY experiments. NOESY data were acquired with mixing times of 75, 150 and 225 ms and TOCSY data were acquired with a 75 ms mixing time. Prior to Fourier transformation, the data were zero-filled to generate a 2K x 1K matrix and apodized by a cosine function in F2 and a sine function in F1. Chemical shifts were referenced to external 4,4-dimethyl-4-silapentane-1-sulfonate (DSS, 0.00 ppm).

Structure calculations. Structures were calculated from the NOE distance data (FELIX, v2.10) using the distance geometry program (DGII) of InsightII (Biosym Technologies Inc., San Diego) as described by Rozek *et al.* [4]. A total of 294 and 309 restraints were used to calculate the final ensemble of structures shown in Figure 2 for apoE(267-289) and apoAII(18-30)+, respectively.

Results and Discussion. All the proton resonances for apoE(267-289) and apoAII(18-30)+ in SDS were assigned to one unique species using TOCSY spectra to identify spin systems, NOESY spectra to obtain interresidue connectivities and to distinguish between degenerate spin systems,

and DQF-COSY spectra to confirm side chain resonance assignments [5]. An estimation of the secondary structure was obtained by subtracting the measured H^α chemical shifts for the peptides in SDS complexes from the corresponding random coil values [5]. With respect to random coil chemical shift values, H^α resonances move upfield in an α -helical conformation and downfield in a β -sheet conformation [5]. As illustrated in Figure 1, most of the H^α secondary shifts move upfield which suggests that both peptides adopt a helical conformation in the presence of SDS. This helical nature is corroborated by the preliminary structures calculated for both

molecules which are illustrated in Figure 2. The backbone atoms (N - C^α - C=O) have been superimposed on the average structure of residues 272-287 (apoE(267-289)) and 20-33 (apoAII(18-30)+). The backbone (N, C^α , C=O) RMSDs for the ensembles shown are $0.39 \pm 0.11 \text{ \AA}$ for apoE(267-289) and $0.39 \pm 0.16 \text{ \AA}$ for apoAII(18-30)+ between residues 272-287 and 20-33, respectively. Some dynamic fraying is observed at the ends of both peptides. With regards to apoE(267-289), note that the helix at the N-terminal is not as well defined as the helix through residues 272-287, perhaps because the N-terminal region of this peptide does not bind as well to the SDS micelle.

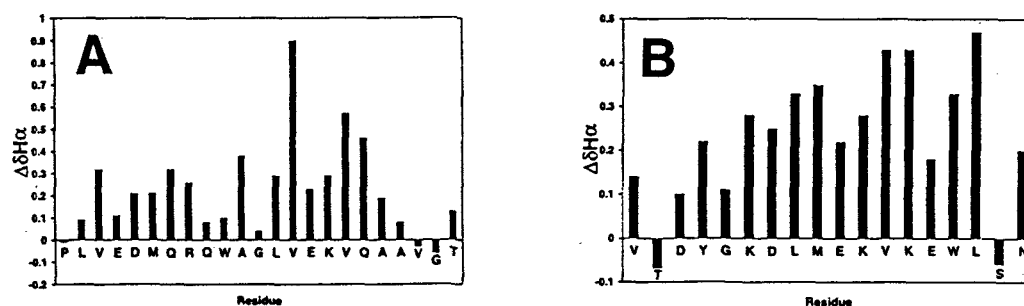


FIGURE 1: Plot of the H^α secondary shifts for the backbone H^α protons ($\Delta\delta H^\alpha = \text{random coil } \delta \text{ value} - \text{observed } \delta H^\alpha$) of apoE(267-289) (A) and apoAII(18-30)+ (B).

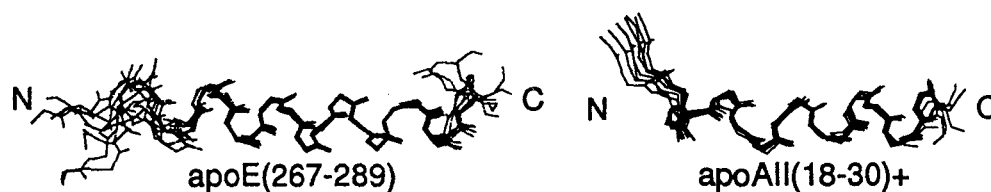


FIGURE 2: Conformational ensembles of 8 out of 10 calculated structures for apoE(267-289) and apoAII(18-30)+.

Conclusions. ApoE(267-289) and apoAII(18-30)+ associate with SDS micelles and adopt helical conformations. Conformational features of the calculated structures for apoE(267-289) and apoAII(18-30)+, relative to the biological activities associated with apoE and apoAII, will be discussed upon further refinement of the structures.

References.

1. Segrest, J.P., Jones, M.K., de Loof, H., Brouillette, C.G., Venkatachalapathi, Y.V., & Anantharamaiah, G.M. (1992) *J. Lipid Res.* 33:141-166.
2. Sparrow, J.T. Sparrow, D.A., Fernando, G., Culwell, A.R., Kovar, M. & Gotto, A.M., Jr., (1992) *Biochemistry* 31: 1065-1068.
3. Segrest, J.P. & Feldmann, R.J. (1977) *Biopolymers*, 16:2053-2065.
4. Rozek, A., Buchko, G.W. & Cushley, R.J. (1995) *Biochemistry* 34:7401-7408.
5. Wüthrich, K. (1986) *NMR of Proteins and Nucleic Acids*, Wiley, New York.

Relaxation Changes in Persimmon Fruit Stored at Low Temperature and Modified Atmosphere

C. J. Clark and J. S. MacFall

HortResearch, Ruakura Research Centre, Private Bag 3123, Hamilton, New Zealand, and,
Department of Radiology, Duke University Medical Centre, Durham, North Carolina 27710, USA.

1 Introduction

Persimmon (*Diospyros kaki* L.) is a subtropical fruit which is affected by the physiological disorder, chilling injury, when subjected to low or non-freezing temperatures to extend its post-harvest storage life [1]. External symptoms commensurate with injury development are frequently absent. Use of MRI to monitor individual fruit during storage has subsequently established that changes in image contrast indicative of fruit degradation are consistent with visual observations describing the development and extent of internal injury in this crop [2].

Besides qualitative morphological descriptions, ^1H MRI is capable of providing quantitative information through analysis of relaxation times in calculated images [3]. These parameters reflect temporal changes in the biochemical environment of the water in plant tissues. This investigation describes changes in the relaxation properties (T_1 , T_2) of component tissues in persimmon which were monitored during a modified atmosphere (MA) storage experiment under temperature conditions leading to development of chilling injury.

2 Experimental

At commercial harvest, fruit (cv. Fuyu) were divided into two treatments ($n=4$): either hermetically sealed in individual polyethylene bags (Modified Atmosphere (MA) treatment), or sealed in perforated bags (Control), which allowed gas exchange but drastically reduced water loss. Samples were stored under conditions likely to induce chilling injury (7°C for 4 weeks), followed by 3 days at ambient temperatures to simulate shelf life. MA storage ameliorates the effects of chilling injury and extends storage life, but does not prevent injury development in persimmon.

Each week fruit were withdrawn from coolstorage in a predetermined sequence for imaging in a 2 T superconducting magnet. Fruit (stem end up), plus capillary tubes containing aqueous CuSO_4 internal standards, were placed in a 10 cm quadrature coil for data collection about axial and coronal equatorial planes. Twenty-eight single-slice, spin-echo images (2 mm slice thickness, 2 acquisitions, 256^2 array, 0.33 to 0.35 mm resolution) were acquired on each fruit using a Hahn spin-echo pulse sequence. Six images ($T_E = 10$ ms) were sequentially acquired through each slice plane with T_R values ranging from 100 to 3200 ms for calculation of T_1 values. A further eight images ($T_R = 3200$ ms) were acquired in each plane ($T_E = 20$ to 160 ms in 20 ms increments) for calculation of T_2 using a CPMG pulse sequence. Total imaging time was 3.5 hours per fruit.

Relaxation values were calculated after MacFall et al. [3], fitting for pseudo-density, flip angle (T_1) and the respective relaxation parameter, T_1 or T_2 . Measurements on selected areas of interest from within 'calculated' images included flesh, locule, and vascular tissues (in coronal images) and from combined flesh and vascular tissue in basal, median and distal regions of axial image slices.

3 Results

T_1 and T_2 times associated with each tissue type and both image planes were significantly ($P<0.05$) shorter in MA-treated fruit, apart from vasculature where no T_2 treatment differences were noted. Measurements of T_1 and T_2 from flesh in the coronal plane, for example, were 1114 vs 1264 ms, and 85.3 vs 94.3 ms, respectively (Fig. 1). T_1 values in MA fruit were generally shorter at various times throughout storage, although there were exceptions, most notably 3 weeks from harvest, after fruit had been stored for 2 weeks. The sharp increase, and decline a week later, was

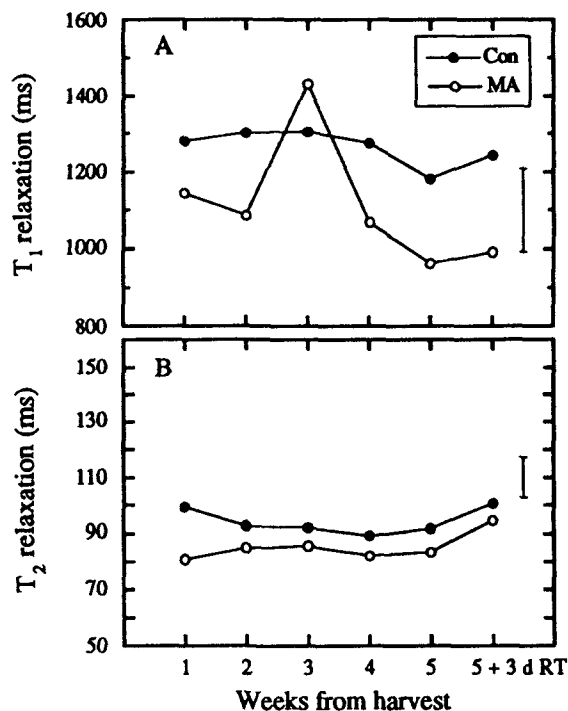


Figure 1. Temporal variation in A), T_1 and B), T_2 measurements in flesh (coronal image slice) of fruit from control and MA treatments stored at 7°C . Error bars represent a 95% confidence interval for a LSD for between-treatment comparisons at any individual imaging date.

evident in all tissues, in both image planes, and in all MA-treated fruit (Fig. 1a). T_2 times were consistently shorter in MA-treated fruit although statistically, treatment means were almost always within experimental error at separate times during coolstorage (Fig. 1b). Unlike T_1 , no sharp rise in T_2 values was observed 3 weeks after harvest.

Within a treatment, no consistent differences between the relaxation times of individual tissues were established that were applicable to each treatment and all imaging dates. Broad trends were evident. In the MA treatment, for example, mean relaxation measurements in flesh (1130 ms) and locules (1102 ms) were similar (Fig. 2a). T_1 times were lower ($P < 0.05$) in vascular tissue (1036 ms) though, especially at the beginning and end of the study (Fig 2a). By contrast, T_2 measurements clearly distinguished individual tissue types, relative values in flesh, locule and vascular tissue being 101.4, 115.9 and 70.6 ms (Fig. 2b). This ranking applied during the first half of the study, but not latterly as T_2 times in the locules gradually declined (Fig. 2b).

In axial sections, there were no gradients in T_1 flesh measurements between the top and bottom of MA-treated fruit. Corresponding T_2 values showed little temporal variation but were consistently longer ($P < 0.05$) in the middle of the fruit (96.6 ms) than at either extremity (88.2 ms).

4 Conclusions

A modified atmosphere (2.4 vs 21.0 % O_2) profoundly altered the relaxation characteristics of the fruit, and from

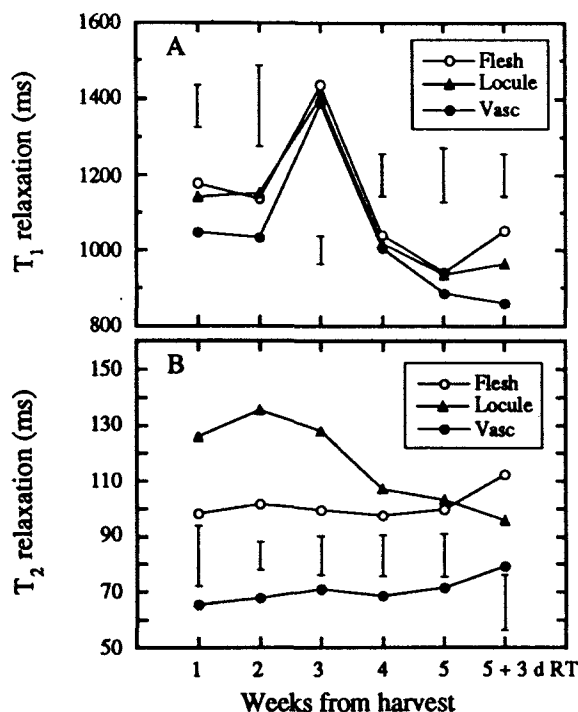


Figure 2. Temporal variation in A), T_1 , and B), T_2 times in flesh, vasculature and locules of MA-treated fruit (coronal plane) stored at 7 °C. Error bars represent a 95% confidence interval for a LSD for between-tissue comparisons at their respective imaging dates.

early after treatments had been imposed. Potential mechanisms consistent with an overall reduction in relaxation times in MA fruit are: increase in the concentration of a paramagnetic species; or increase in soluble macromolecular or carbohydrate composition. Both promote faster relaxation and lead to shorter relaxation times [4 - 6]. Mn and Fe are the major trace metal species accumulated by persimmon. However, there is currently no evidence to suggest that ionic or complexed forms of these elements are influenced by hypoxic conditions in this fruit, as may be the case in soybean [6]. The lower rate of respiration in the MA fruit likely results in reduced metabolism and consequently decreased loss of sugars, carbohydrates and organic acids [7]. Whether this is a valid hypothesis here remains to be confirmed. Note, relaxation times would have been expected to increase in MA-treated fruit if the effect was simply related to removal of a paramagnetic species such as O_2 .

Chilling injury developed in all fruit apart from one in the control (determined by visual examination of the interior of the fruit at the end of the experiment). There was so much between-fruit variability though, that temporal trends in relaxation properties in single fruit failed to differentiate affected and non-affected fruit in the same treatment. This highlights a potential difficulty when using MRI. While we had 4 replicates, individual fruit reacted very differently to the imposed treatments bringing into question the reliability of trends from other NMR studies based on analysis of single samples. Possible solutions include careful sample selection to ensure a more uniform population to choose replicates from, or use of faster pulse-sequence experiments that permit analysis of a greater number of samples in an equivalent or shorter time.

The dramatic and synchronous behaviour affecting T_1 relaxation in all MA fruit (but not controls) 3 weeks after harvest (Fig. 1a), emphasises the inadequacy of our knowledge concerning physiological processes occurring during MA storage. Future studies using a range of O_2/CO_2 atmospheres should help to unravel these events.

References

- 1 E.A. MacRae *NZ J. Exp. Ag.*, 15, 333, 1987.
- 2 C.J. Clark and S.K. Forbes *NZ J. Crop Hort. Sci.*, 22, 209, 1994.
- 3 J.R. MacFall, F.W. Wehrli, R.K. Greger and G.A. Johnson *Magn. Reson. Imaging*, 5, 209, 1987.
- 4 P.G. Morris *In: Nuclear Magnetic Resonance Imaging in Medicine and Biology*, Clarendon Press, 284, 1986.
- 5 S.I. Cho, R.L. Strohshine, I.C. Baianu and G.W. Krutz *Trans. ASAE*, 36, 1217, 1993.
- 6 J.S. MacFall, P.E. Pfeffer, D.B. Rolin, J.R. MacFall and G.A. Johnson *Plant Physiol.*, 100, 1691, 1992.
- 7 C.Y. Wang *In: Food Preservation by Modified Atmospheres*, M. Calderon and R. Barkai-Golan, eds., CRC Press, 197, 1990.

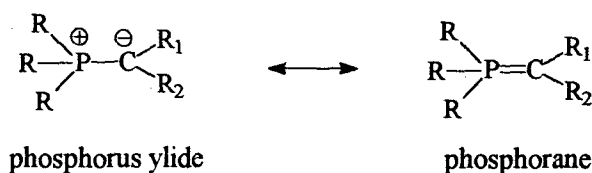
ENDOR Spectra of an X-irradiated Single Crystal of the $R_3P=CH-C(O)CH_3$ Wittig Reagent

T. Berclaz, M. Geoffroy*, G. Rao and Z. Tancic

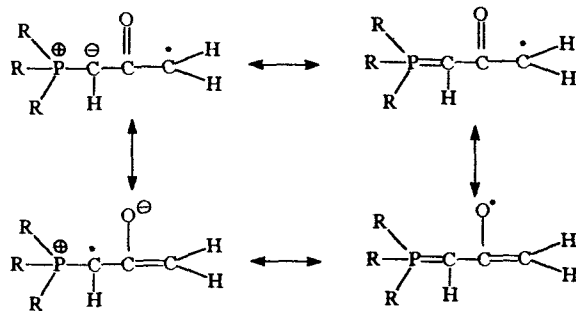
Department of Physical Chemistry, 30 Quai E. Ansermet
1211, Geneva (Switzerland)

1. Introduction

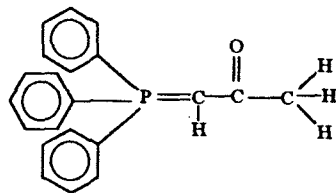
Wittig reagents are hybrid of two canonical forms:



When a radical center is produced on a carbon atom in α -position to a $P=C-C(O)$ group several mesomeric forms are therefore possible¹.

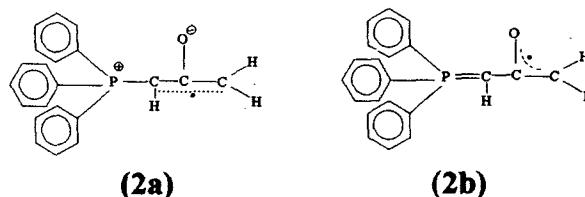


The objective of the present study is to determine, from a single crystal ENDOR study, the real delocalisation of the unpaired electron on a radical derived from the *l*-triphenyl phosphoranylidene-2-propanone (1):



This radical (2), produced by a homolytic scission of a C-H bond of the methyl group, can be written either as an allylic radical

bearing a phosphonium group on a terminal carbon atom (2a) or as a radical delocalized in a π -orbital constructed on the OCC fragment (2b).



2. Experimental

Triphenylphosphoranylidene propanone is a commercial compound (Aldrich). Single crystals were obtained by slow evaporation from a solution in CH_2Cl_2 . These crystals are monoclinic. The ENDOR reference frame was defined as follows: OX, OY, OZ were aligned along c , $-a^*$ and $-b$ respectively

A large single crystal was exposed for 3 hours at room temperature to the radiation of a Philips X-ray tube (30 kV, 30 mA).

The ENDOR spectrometer is a home made cw system². The spectra were recorded at 200 K, the crystal was rotated around the three reference axes in steps of 10° .

The analysis of the spectra was performed by using second order perturbation³ as well as an optimization program which compares the positions of the calculated and experimental lines.

3. Results

The EPR spectrum obtained with an X-irradiated single crystal of (1) is very complex: it exhibits coupling constants with several spin $1/2$ nuclei and, except in the XY plane, it results

from the presence of two magnetically non-equivalent crystallographic sites (two different orientations of the same radical species). Nevertheless, the spectrum obtained with the deuterated species $(C_6D_5)_3PC(H)C(O)CH_3$ is identical to the spectrum obtained with (1), we can therefore rule out the contribution of a radical centered on a phenyl ring (e.g. cyclohexadienyl species) and the most likely trapped radical is indeed the radical (2). It is however impossible to follow the angular variation of the EPR spectrum and to identify, among the various splittings, the coupling which could be due to hyperfine interaction with ^{31}P . An example of ENDOR spectrum obtained at 200 K is shown in Fig. 1.

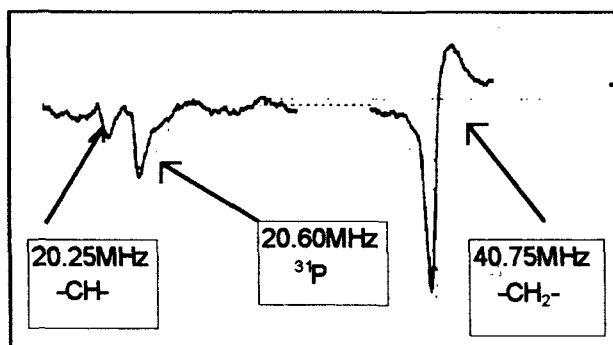


Fig. 1. ENDOR spectrum obtained when the magnetic field lies in the XY plane, 45° from the Y-axis

From these signals, and from their angular dependence in the three perpendicular reference planes it is easy to recognize the lines due to the ^{31}P nucleus. We could thus determine the hyperfine couplings with two protons and one phosphorus atom.

These couplings were compared with the splittings observed on the EPR spectrum and it was possible to simulate some EPR spectra by assuming the presence of an additional spin 1/2 splitting whose signal was not immediately observed by ENDOR. Subsequent measurements showed that additional 1H ENDOR lines were indeed detectable, with difficulty, in the corresponding region of the spectrum.

4. Discussion

The angular variation of the ENDOR lines led to a ^{31}P hyperfine tensor $^{31}P-T$ whose eigenvalues were equal to 29 MHz, 30 MHz

and 33 MHz. One 1H tensor ($^1H-T_1$) was fairly anisotropic (eigenvalues: 46 MHz, 56 MHz and 80 MHz) while the second one ($^1H-T_2$) had smaller eigenvalues: 7 MHz, 11 MHz and 16 MHz. Finally, the third 1H hyperfine tensor, $^1H-T_3$ obtained with a poorer precision since its ENDOR lines were not observed for all the orientations, had eigenvalues approximately equal to 24 MHz, 55 MHz and 83 MHz.

Decomposition of $^{31}P-T$ into isotropic ($A_{iso} = 30.6$ MHz) and anisotropic ($\tau_1 = -1.6$ MHz, $\tau_2 = -0.6$ MHz, $\tau_3 = +2.2$ MHz) coupling constants show, after comparison with the phosphorus atomic coupling constants⁴ ($A^*_{iso} = 13306$ MHz, $2B_o = 734$ MHz) that the delocalisation of the unpaired electron on the phosphorus is very low ($\rho_s = 0.003$, $\rho_p = 0.003$). The hyperfine couplings $^1H-T_1$ and $^1H-T_3$ are rather similar and if we assume that these eigenvalues are all negative the corresponding A_{iso} constants are respectively equal to -60 MHz and -54 MHz. These values are consistent with two protons bound to a hybridized sp^2 carbon atom which contains 80% of the spin in its $2p_z$ orbital. The eigenvectors measured for T_1 and T_3 indicate that the angle between the two C-H bonds is equal to *c.a.* 140° . The last proton tensor $^1H-T_2$ is characterized by a small isotropic coupling constant ($A_{iso} = 11$ MHz) which, on the hypothesis of an α -proton, implies a spin density of *c.a.* 0.16 on the carbon atom. These experimental results show that the most plausible structure for the trapped species 2 is 2a, which in contrast with the non-substituted allyl radical, is largely localized on the terminal carbon. No spin delocalization onto the phosphorus atom is observed; the small ^{31}P coupling is probably due to spin polarization only.

References.

- ¹ M. Geoffroy, G. Rao, Z. Tancic and G. Bernardinelli. *J. Am. Chem. Soc.* **112**, 2826 (1990).
- ² M. Geoffroy and M.V.V.S. Reddy. *Radiat. Phys. Chem.* **26**, 377 (1986).
- ³ M. Iwasaki. *J. Magn. Reson.* **16**, 417 (1974).
- ⁴ J.R. Morton and K. F. Preston. *J. Magn. Reson.* **30**, 577 (1978).

Use of the Pseudocontact Shift as a Structural Constraint for Macromolecules in Solution

Miriam Gochin¹ and Heinrich Roder²,

¹University of the Pacific School of Dentistry, San Francisco, CA and ²Fox Chase Cancer Center, Philadelphia, PA

The presence of paramagnetic metal ions such as low spin iron(III) and high spin cobalt (II) causes (among other effects) paramagnetic shifting of the resonance lines in a strongly bound complex. For atoms at least 5 or 6 bonds from the metal coordination site, the contact contribution to the paramagnetic shift falls to zero, leaving the pseudocontact, or isotropic dipolar term, which is readily calculated:

$$\delta_{pc}(ppm) = \left\{ \left(2\chi_z - (\chi_{xx} + \chi_{yy}) \right) (3\cos^2\theta - 1) + 3(\chi_{xx} - \chi_{yy}) \sin^2\theta \cos 2\phi \right\} / 6r^3 \quad [1]$$

(r, θ, ϕ) are the polar coordinates of the measured nucleus in the principal axis system of the electronic susceptibility tensor, χ . In this poster, we discuss the characteristics of the pseudocontact shift, and its effectiveness as a quantitative structural tool. Systems studied include cytochrome c (Fe^{3+}/Fe^{2+}) and a complex of a DNA oligomer with chromomycin and a divalent metal (diamagnetic Zn^{2+} or paramagnetic Co^{2+}). Pseudocontact shifts are derived experimentally in these systems as the difference between the chemical shift observed in the paramagnetic and diamagnetic forms of the metal complexes, assuming no structural difference between these two forms^a.

From equation [1], some important properties of the pseudocontact shift as a structural constraint become immediately clear. To calculate the value of the shift from a given molecular geometry, it is necessary to know the two principal components of the magnetic susceptibility tensor $\chi_{//} = \chi_{zz} - (\chi_{xx} + \chi_{yy})/2$ and $\chi_{\perp} = (\chi_{xx} - \chi_{yy})$, which define its magnitude, plus three Euler angles, α, β, γ which define the orientation of the tensor in the molecular reference frame. These parameters can be derived experimentally if the coordinates and shifts of at least five nuclear positions are known. Some information on the structure must therefore be derived from other structural methods.

The unpaired electron(s) must generate an asymmetric dipolar field in order for $\chi_{//}$ and/or χ_{\perp} to be non-zero. Rapid electronic relaxation is also required in

order to minimize the contribution of paramagnetic linebroadening to the NMR spectrum (3). Typically, $T_{2e} \leq 10^{-11}s$ is required.

The pseudocontact shift demonstrates some excellent features, namely that it provides long range structural constraints, due to the $1/r^3$ dependence of the shift, it provides model-free constraints, ie. no data manipulation prior to molecular modelling, and it can be measured on any spin-1/2 nucleus, since it is independent of nuclear gyromagnetic ratio, γ_N . This is particularly important both in terms of the potential for analysing heteronuclear spectra that are less crowded than proton multidimensional NOE spectra, and because the contribution of paramagnetic relaxation depends on γ_N^2 , and is thus significantly reduced for heteronuclei.

Equation [1] is a degenerate function in (r, θ, ϕ) so that coordinates cannot be directly calculated from the shift. Instead the shifts have been incorporated into the molecular simulation program X-PLOR (A. Brunger, Yale University) as an experimental energy:

$$E_{pc} = \sum_i f_i \left[\min \left(\left| \delta_{pc,obs,i} - \delta_{pc,i} \right| - 0.02, 0 \right) \right]^2 \quad [2]$$

In this form, the experimental error allowed for in measuring the pseudocontact shift is ± 0.02 ppm. The energy is a sum over all nuclei i for which an experimental shift $\delta_{pc,obs,i}$ is available. $\delta_{pc,i}$ is calculated from equation [1]. f_i is the force constant for the flat-well potential. Energy gradients in the x, y and z directions are calculated from the derivatives of equation [2].

The normal empirical energies in X-PLOR dictate feasible locations for the nuclei, and the pseudocontact shifts have been used to fix the nuclear positions quite precisely. The structural change caused by a mutation of leucine to valine at position 94 of cytochrome c was deduced using the pseudocontact shifts (1). Nuclei in the region of mutation were defined to a precision within 0.2\AA . Final structures conformed to low energy requirements and showed excellent agreement with observed pseudocontact shifts. The precision is clearly a function of the gradient of the susceptibility tensor and is higher for atoms on a steeper part of this gradient. The requirements for an overall bonding network between the nuclei, and the corresponding interdependency of coordinates provides for a best possible scenario in which the precision d_l can be estimated from the steepest gradient of the shift tensor:

^a It is known that this assumption breaks down for certain residues involved in the redox function of cytochrome c (1,2). These residues are not included in our analysis. Nor are nuclei within 6 bonds of the metal, which could be experiencing contact contributions to their paramagnetic shift.

$$d(\delta_{pc}) = \left\{ \left| \frac{d(\delta_{pc})}{dr} \right| + \frac{1}{r} \left| \frac{d(\delta_{pc})}{d\theta} \right| + \frac{1}{r \sin \theta} \left| \frac{d(\delta_{pc})}{d\phi} \right| \right\} \cdot dl$$

.....[3]

In this way, 80% of cytochrome c was defined within 0.3Å.

For the cobalt complex of DNA ($d(\text{TTGGCCAA})_2$) with two molecules of the anti-cancer drug chromomycin (a complex with C_2 symmetry), the structural definition is even better, because the three unpaired electrons in the high spin cobalt lead to a susceptibility tensor with magnitude 5 or 6 times that of heme iron. From the assignment of several protons in the complex (Table I), a preliminary estimate of the susceptibility tensor was obtained: $\chi_{//} = 6035 \text{ ppm} \cdot \text{Å}^{-3}$, $\chi_{\perp} = 441 \text{ ppm} \cdot \text{Å}^{-3}$, $\alpha = -103^\circ$, $\beta = 90^\circ$, $\gamma = -7^\circ$. From this

Table I: Calculation of pseudocontact shifts for several assigned protons in $d(\text{TTGGCCAA})_2 \cdot \text{chr}_2 \cdot \text{Co}^{2+}$		
Group	Obs. shift ^a	Calc. shift ^b
PT2	-0.40	-0.41
PG3	0.27	0.27
PG4	1.02	1.05
PC5	4.41	4.60
PC6 ^c	-9.46	-9.46
PA7	-5.85	-5.95
PA8	0.10	0.12
Me C sugar chr ^c	-5.22	-5.22
H5 C sugar chr ^c	2.92	2.92
H1* chr	-16.49	-23.15
H1'-OMe chr	-9.11	-7.26
H3' chr	-7.41	-7.25
H4' chr	-5.88	-5.94
H5' chr	-4.50	-3.00
H7-Me chr	24.39	19.69

^a Observed paramagnetic shift; ^b Calculated pseudocontact shift using susceptibility tensor given in text; ^c Protons used for defining the susceptibility tensor

tensor, it appears that 85% of the molecule would be defined within 0.3Å precision, assuming an accuracy of shift measurement of only ± 0.1 ppm. Many of the shifts are likely to be determined to greater than 0.1ppm accuracy.

For the assigned group of protons in Table I, the results show that the contact shift is fully attenuated after 6 bonds (Figure 1), with the possible exception of the chromomycin OMe group which is 7 bonds away, but does not demonstrate good agreement to the calculated shift. Due to its close proximity to the metal, however, a small displacement of this methyl group can remove the discrepancy, a possibility that will be tested in molecular simulations.

Work is continuing towards full assignment of the DNA complex, and determination of the improvement in definition of the DNA structure using pseudocontact shifts as opposed to or in conjunction with NOE's.

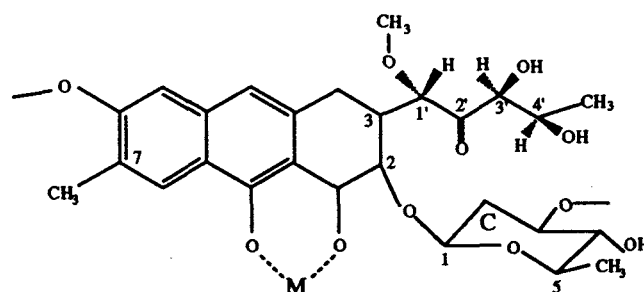


Figure 1: Chromomycin chromophore and C sugar, illustrating positions of protons in Table I.

References

1. M. Gochin and H. Roder. Protein Science, 4, 296(1995)
2. Y. Feng, H. Roder and SW. Englander, Biochemistry, 29, 3494 (1990)
3. I. Bertini and C. Luchinat, "NMR Spectra of Paramagnetic Molecules in Biological Systems", Benjamin/Cummings, 1986

Nuclear Spin-Lattice Relaxations Caused by Paramagnetic Impurities in Layered Silicates : Effect of Magic Angle Spinning

Shigenobu HAYASHI

National Institute of Materials and Chemical Research,
1-1 Higashi, Tsukuba, Ibaraki 305, Japan

1 INTRODUCTION

Spin-lattice relaxations caused by paramagnetic impurities take place through dipolar interaction with electron spins directly and through spin diffusion. The former mechanism is not affected by magic angle spinning (MAS), while the latter is effectively suppressed. Therefore, MAS is useful to distinguish the two mechanisms.

In the present paper, with the aid of the spinning effects, we have studied spin-lattice relaxation mechanisms in kaolinite $\text{Al}_2\text{Si}_2\text{O}_5(\text{OH})_4$ with natural origins. We have measured ^1H , ^{29}Si and ^{27}Al spin-lattice relaxations at room temperature without and with MAS, and have discussed the relaxation mechanism quantitatively.

2 EXPERIMENTAL

Six kaolinite samples with natural origins were used, of which we present mainly the relaxation data of Kanpaku kaolinite.

NMR measurements were carried out at room temperature, using a Bruker MSL400 spectrometer with a static magnetic field strength of 9.4 T. Larmor frequencies of ^1H , ^{29}Si and ^{27}Al were 400.136, 79.496 and 104.263 MHz, respectively. ^1H T_1 was measured by the inversion recovery method. Torchia's sequence was used for ^{29}Si T_1 measurements. ^{27}Al T_1 was measured by the saturation recovery method, in which the first pulse was replaced by a saturating comb sequence for nonselective saturation.

3 RESULTS AND DISCUSSION

3.1 ^1H relaxation

Figure 1 shows ^1H relaxation curves. Since the dipole-dipole interaction between ^1H spins is very large in kaolinite, spin diffusion plays a dominant role and the relaxation is limited by the spin diffusion rate. MAS can affect the relaxation behavior, since the relaxation is diffusion-limited. Indeed, the curve in the figure depends on the spinning rate. Under spinning conditions, the recovery rate becomes slower with increase in the spinning rate. However, the change is very small, since the spinning rate is not large enough to suppress the spin diffusion.

The relaxation curves shown in Fig. 1 have a marked non-exponentiality, and they do not approach an

exponential decay. We consider that the relaxation time has a large distribution. We have attempted to apply several distribution functions in the simulation of the curve. The best fit is obtained when the population p is assumed to have a form $p \propto T_1$. In the diffusion-limited case, $1/T_1$ is proportional to the concentration of paramagnetic impurities, N_p . Accordingly, the population function has a form $p \propto 1/N_p$. N_p is assumed to distribute from the lowest value N_{p1} to the highest value N_{p2} with the middle point N_{pm} ; that is, $N_{pm} = (N_{p1} + N_{p2})/2$. Calculated recovery curves are shown in Fig. 1 by solid lines.

3.2 ^{29}Si relaxation

Figure 2 shows ^{29}Si magnetization recovery curves. We found that the relaxation rate depends on the spinning rate, which demonstrates that spin diffusion plays a role in relaxation at the static and slow spinning regions. When the signal intensity is plotted in log scale against a square root of time, the curve becomes linear, suggesting that ^{29}Si spins relax through dipole-dipole interaction with electron spins directly, and that contribution of spin diffusion between ^{29}Si spins is negligible. However, the spinning rate dependence confirms the contribution of spin diffusion.

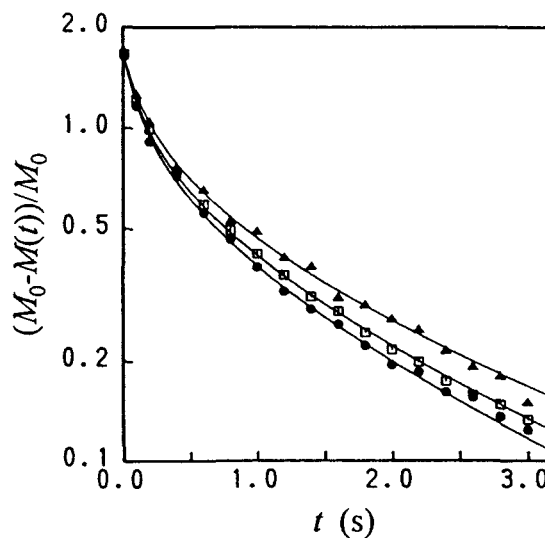


Fig. 1. ^1H magnetization recovery curves. The spinning rates were 0 (\blacktriangle), 8.00 (\bullet), and 12.00 kHz (\square). Solid lines show calculated values.

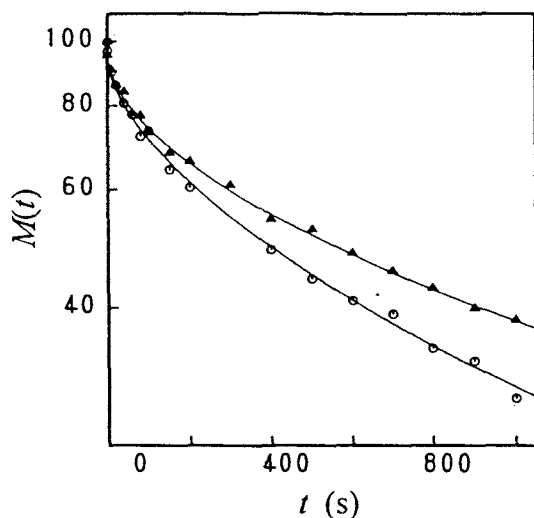


Fig. 2. ^{29}Si magnetization recovery curves. The spinning rates were 0 (\circ) and 1.00 kHz (\blacktriangle). Solid lines show calculated values.

Distribution of N_p inferred from the ^1H relaxation is considered to cause accidental $\exp\{-t/T_{1\text{pa}}\}$ behavior. Solid lines in Fig. 2 show calculated values considering the inhomogeneous distribution of paramagnetic impurities. The increase in the apparent T_1 stops at a spinning rate of about 2 kHz. At spinning rates higher than 2 kHz, the relaxation mechanism is the direct dipolar coupling with electron spins.

The above results teach us that it is dangerous to identify the relaxation mechanism only from the apparent $\exp\{-t/T_{1\text{pa}}\}$ behavior. The use of MAS can unambiguously distinguish the mechanisms.

3.3 ^{27}Al relaxation

Figure 3 shows ^{27}Al recovery curves. The curve shows non-exponential behavior especially for static samples. MAS reduces the non-exponentiality. Detailed inspection of the curves reveals the following facts: (1) MAS reduces the non-exponentiality at a spinning rate up to 2.5 kHz. (2) The curve does not change in the range of 2.5 to 4.0 kHz. (3) The spinning higher than 4.0 kHz slightly enhances the relaxation. (4) The above MAS effects are observed irrespectively of concentration of paramagnetic impurities.

Spin diffusion contributes to the relaxation for a static sample. MAS of 2.5 kHz is considered to suppress the spin diffusion between ^{27}Al spins almost completely. Thus, the relaxation curves between 2.5 and 4.0 kHz are convolution of two mechanisms; direct relaxation and phonon-coupled relaxation. Since ^{27}Al spin is quadrupolar, it can relax through the coupling with acoustical lattice vibrations. Contribution of the direct relaxation is so small that the

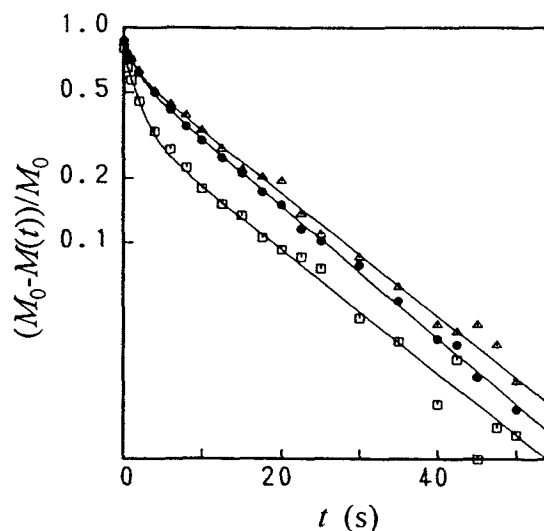


Fig. 3. ^{27}Al magnetization recovery curves. The spinning rates were 0 (\square), 4.00 (\triangle) and 10.00 kHz (\bullet). Solid lines show calculated values.

phonon-coupled relaxation is the dominant mechanism. The phonon-coupled relaxation depends largely on the sample. Structural disorder caused by paramagnetic impurities might enhance this relaxation. Fast spinning gives the sample large stress, and the resulting strain is considered to enhance the relaxation.

4 CONCLUSIONS

With the aid of the magic angle spinning, we have studied spin-lattice relaxation mechanisms in kaolinite with natural origins, and have concluded as follows:

(1) Spin diffusion plays a dominant role in ^1H relaxation. MAS causes only a slight change in the relaxation behavior, since the dipolar coupling between ^1H spins is strong.

(2) ^{29}Si spins relax directly through the dipole-dipole interaction with electron spins under spinning conditions higher than 2 kHz. Spin diffusion effect has been clearly observed in the ^{29}Si relaxation of relatively pure samples under static and slow spinning conditions.

(3) ^{27}Al spins relax through three mechanisms; phonon-coupled quadrupole interaction, spin diffusion and dipole-dipole interaction with electron spins. The first mechanism is dominant, while the last is negligibly small. Spin diffusion between ^{27}Al spins is suppressed completely at a spinning rate of 2.5 kHz.

(4) We have analyzed the relaxation behavior theoretically and discussed quantitatively. Concentration of paramagnetic impurities, electron spin-lattice relaxation time, spin diffusion rates can be estimated.

A COMPARISON OF FREQUENCY AND TIME DOMAIN FITTING OF ^1H MRS METABOLIC DATA

A. Freise*, E. Spencer*, I. Marshall† and J. Higinbotham*

*Department of Applied Chemical and Physical Sciences,
Napier University, 10 Colinton Road, Edinburgh EH10 5DT, Scotland

†Department of Medical Physics and Medical Engineering,
The University of Edinburgh, Western General Hospital,
Crewe Road, Edinburgh, EH4 2XU, Scotland

INTRODUCTION

MRS data from a Siemens 1.5 T SP63 imager has been analysed in the frequency domain using a linear combination of Lorentzian and Gaussian line shapes to fit the metabolites from human brains. Only the three metabolites, NAA, choline and creatine can normally be detected with the current ^1H MRS equipment. The same patient data has been analysed using a standard time domain method, HLSVD [1]. The FID MRS data is provided both with and without water suppression. The water reference data was used to provide a phase correction for the effects of eddy currents [2]. Both the time and frequency domain techniques were checked by applying them to synthetic data with known noise levels.

METHOD

For the frequency domain analysis, a model function of several Lorentzians of arbitrary phase and line width was fitted to the water region of the water-suppressed data. The fitting was performed using the Levenberg-Marquardt non-linear least-squares method implemented in a C programme [3]. After using the model function to remove the residual water resonance from the spectrum, the metabolite resonances were then fitted with a linear combination of Lorentzian

and Gaussian line shapes [4]. For the time domain analysis, the water suppressed region and the metabolite region were fitted simultaneously to a sum of damped sinusoids using the HLSVD method [1]. The position of each resonance was determined by taking the position of the water resonance as 4.7 ppm, with respect to TMS.

RESULTS

For the typical normal brain tissue patient data shown in the frequency domain, three Lorentzians with variable phase were used to fit the residual water peak. The fit was rather poor giving a χ^2 of 12.6. The fit of the metabolite region after the subtraction of the residual water gave a χ^2 of 2.8 and the fit is shown in Fig. 1 after dividing by a factor of 3. The results are given in Table 1. For this fit the fitted line shape is 96% Gaussian. Hence, in this case the amplitudes, A_k of the corresponding sinusoids of the time domain analysis are given by:

$$A_k = a_k \Delta t / (\sqrt{\pi \ln 2} T_2^*) \quad (1)$$

where $\Delta t = 0.25$ ms is the sampling time and a_k is the amplitude of the k^{th} peak in the frequency domain.

Table 1 - Parameters obtained for the fit of the patient data in the Frequency Domain

Metabolite	δ (ppm)	a	A	T_2^* (s)
Choline	3.24	3.96	0.0081	0.081
Creatine	3.06	4.52	0.0112	0.070
NAA	2.05	8.44	0.0285	0.050

The time domain fitting procedure was checked by fitting to a model spectrum with the residual water signal composed of three damped sinusoids and damped sinusoids corresponding to the choline, creatine and NAA resonances at 3.2, 3.0 and 2.0 ppm respectively. A good fit was obtained for low noise levels but when the standard deviation of the noise in the time domain exceeds the amplitude of a damped sinusoid, that component may be omitted from the calculated spectrum. For the same patient data the HLSVD fit is shown in Fig. 2. For the metabolite region from 1.6 to 3.5 ppm $\chi^2 = 6.1$. The corresponding parameters are shown in Table 2.

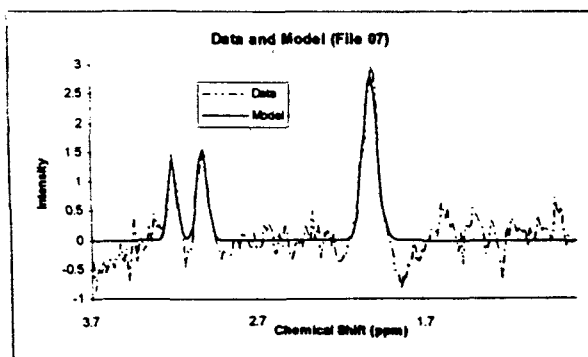


FIG. 1 - Patient metabolite data fitted in the frequency domain

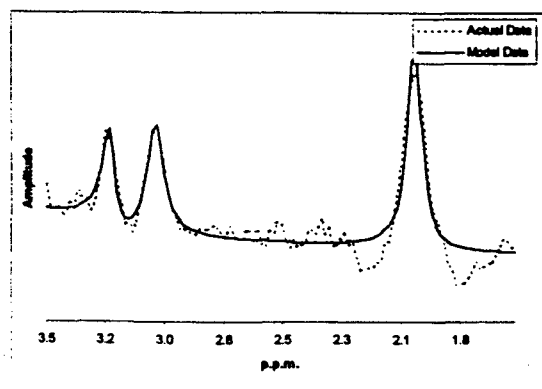


FIG. 2 - Patient metabolite data fitted in the time domain

Table 2 - Parameters obtained from the fit of the patient data in the time domain

Component	δ (ppm)	A	T_2^* (s)	Phase (Deg)
Choline	3.22	0.0136	0.093	-27
Creatine	3.05	0.0214	0.067	2
NAA	2.04	0.0335	0.077	-3

CONCLUSION

Both methods gave similar results for the patient data but the frequency domain method gave a lower value of χ^2 for the metabolite region. This may be due to imposing constraints in the frequency domain fitting of the metabolite region, e.g. zero phase, which cannot be done in the time domain fitting due to the simultaneous fitting of the water region. On the other hand, the time domain method yielded a better fit of the water region.

REFERENCES

1. W.W.F. Pijnappel, A Van Den Boogaart, R. De Beer, and D. Van Ormondt, *J.Magn,Reson.* **97**, 122 (1992).
2. R.J. Ordidge and I.D. Cresshull, *J. Magn. Reson.* **69**, 151 (1986).
3. W.H. Press, , S.A. Teukolsky, W.T. Vetterling, and B.P. Flannery, *Numerical Recipes in C: The Art of Scientific Programming* (Cambridge University Press :Cambridge) (1992), p.683.
4. M.M. Maltempo, *J.Magn.Reson.* **68**, 102 (1986)

Electronic and Molecular Structure of Room-Temperature Stable Triplet Carbene as Studied by ESR Spectroscopy and X-Ray Crystal Analysis of the Diazo Precursor

K. Furukawa,¹ T. Takui,² K. Itoh,³ I. Miyahara,² K. Hirotsu,² T. Watanabe,⁴ K. Hirai,⁴ and H. Tomioka⁴

¹Advanced Science and Technology Center for Cooperative Research, Kyushu University, 6-1 Kasugakoen, Kasuga, Fukuoka 816, Japan; ²Department of Chemistry and ³Department of Material Science, Faculty of Science, Osaka City University, 3-3-138 Sugimoto, Sumiyoshi-ku, Osaka 558, Japan; ⁴Chemistry Department for Materials, Faculty of Engineering, Mie University, Uehama, Tsu, Mie 514, Japan

High-spin carbene is suitable as models for building blocks of high-spin molecular clusters and organic superpara- and ferro-magnets whose molecular designs are based on through-bond approach (topologically controlled π -spin polarization). A weakness of carbene, however, is that in general it is a highly reactive intermediate. Thus, the quest for stable organic high-spin systems with robust π -spin polarization has been an important issue for studying supramolecular functionalities of super high-spin molecules and their molecular assemblages. Among the diverse topics of organic molecular magnetism, syntheses and detection of room-temperature stable triplet carbene as a prototype of stable high-spin systems have been the focus of current topics in high spin chemistry.¹⁻³⁾

In this paper, we report ESR detection of the first triplet carbene, 2,2',4,4',6,6'-hexabromodiphenylcarbene **1** which is stable in solids at room temperature: **1** is stable even in fluid solution.^{1d)} The fine-structure constants of **1** were determined by the fine-structure spectra from random orientation. From the fine-structure spectra observed in the neat crystal of the diazo precursor of **1**, it has been shown that **1** survives at room temperature in the neat crystal upon exposure to air. The X-ray crystal analysis of the diazo precursor of **1** made clear the reason of this stability.

The preparation of the diazo precursor of **1** will be described elsewhere.^{1d)} The diazo precursor was fairly soluble in 2-MTHF. A solution of the diazo precursor was degassed by freeze-pump thaw cycles and sealed off on a vacuum line. 2-MTHF was purified according to usual methods. The solution yielded a dark red glass at 2.3K in the sample site of a cryostat. Upon irradiating the glassy sample with light of 405 nm wave length, several new peaks appeared in the ESR spectrum shown in Figure 1a over a wide range of 0.05–0.75T, indicating the generation of **1**. This ESR spectrum is typical for randomly oriented triplet molecules with the fine-structure constant $D \sim 0.4 \text{ cm}^{-1}$, except for the signal observed at 0.34T. The signal at 0.34T originates from by-products during the sample preparation and/or photochemical decomposition of the diazo precursor. The values of D and E were calculated exactly from the observed resonance fields denoted by H_X , H_Y , and H_Z in Figure 1a and are summarized in Figure 1.

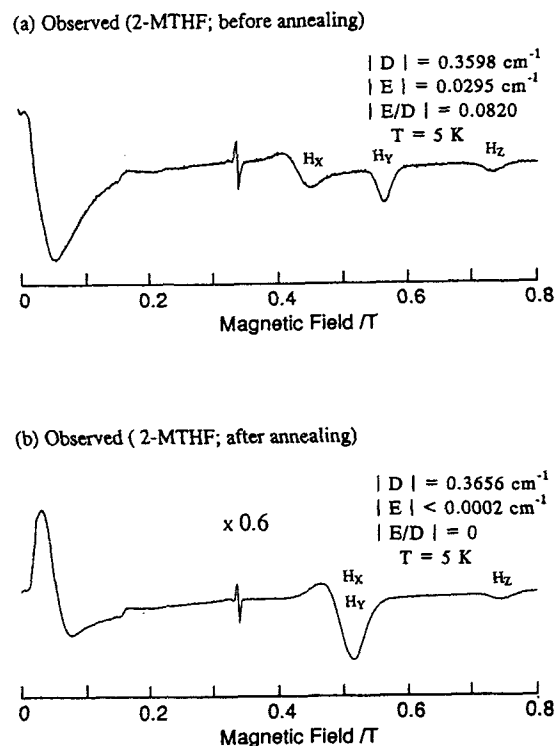


Figure 1 X-band ESR spectra observed at 5K in a 2-MTHF glass from the triplet state of **1**. (a) before annealing (b) after annealing.

When the 2-MTHF glass was warmed to 150K for 10 seconds, there was a striking shift in the positions of the H_X and H_Y lines, which moved closer together (Figure 1b), resulting in nearly zero E value. Re-cooling the sample did not reverse this change. Since the E/D depends on the magnitude of the central C-C-C angle, it indicates that, on warming, the carbene relaxes to a structure with an expand C-C-C angle presumably to gain relief from steric

compression.^{1,2)} These observations are in accord with the UV/vis studies^{1d)} showing that **1** is kinetically stable and undergoes substantial geometrical changes upon annealing.

The molecular and crystal structure of the diazo precursor of **1** was determined by the X-ray diffraction and details will be described elsewhere.³⁾ The crystal of the diazo precursor is monoclinic with cell dimensions, $a=9.933\text{\AA}$, $b=13.261\text{\AA}$, $c=12.743\text{\AA}$, $\beta=91.88^\circ$, $Z=4$ and the space group $P2_1/n$. The two 2,4,6-bromo-substituted phenyl rings make bent perpendicular conformation with 139° of the bond angle at the diazo-methane as shown in Figure 2.

Figure 3 shows the ESR spectra observed from a single crystal [(a) at 2.5K, (b) 300K], indicating that the signals occurred at 2.5K in the neat crystal of the diazo precursor still survived up to room temperature without loss of intensity, considering the effect of Boltzmann factor. The signals have survived at room temperature in a nitrogen gas atmosphere for half a year. These facts indicate the remarkable chemical stability of **1** in comparison with the other diphenylcarbene derivatives. The stabilization of triplet diphenylcarbene derivative **1** regarded as highly reactive intermediates can be accomplished by steric protection, i.e., by the substitution of 2-, 4-, and 6-position of the two phenyl rings, causing the bent perpendicular molecular conformation.

Acknowledgments

This work was partially supported by Grand-in-Aid for Scientific Research on Priority Area (Grant Nos. 02205102 and 04242103), Grand-in-Aid for General Scientific Research (Grant Nos. 02453014 and 03640429), Grand-in-Aid for Scientific Research on Priority Areas "Molecular Magnetism" (Area No. 228/04242103, 0424104, and 04242105) from the Ministry of Education, Science and Culture, Japan, and NEDO project "Organic Magnets" from the Ministry of International Trade and Industry, Japan.

References

- (a) B. C. Gilbert, D. Griller, and A. S. Nazran, *J. Org. Chem.*, **50**, 4738 (1985) and references therein.
(b) H. Tomioka, H. Okada, T. Watanabe, and K. Hirai, *Angew. Chem. Int. Ed. Engl.*, **33**, 873 (1994) and references therein.
(c) K. Furukawa, Y. Teki, T. Takui, K. Itoh, T. Watanabe, K. Hirai, and H. Tomioka, *Mol. Cryst. Liq. Cryst.*, in press.
(d) H. Tomioka, T. Watanabe, K. Hirai, K. Furukawa, T. Takui, and K. Itoh, *J. Am. Chem. Soc.*, **117**, 6376 (1995)
- (a) E. Wasserman, V. J. Kuck, W. A. Yager, R. S. Hutton, F. D. Greene, V. P. Abegg, and N. M. Weinshenker, *J. Am. Chem. Soc.*, **93**, 6335 (1971).
(b) H. Tukada, T. Sugawara, S. Murata, and H. Iwamura, *Tetrahedron Lett.*, **27**, 235 (1986).
- T. Takui, K. Furukawa, K. Itoh, I. Miyahara, K. Hirotsu, T. Watanabe, K. Hirai, and H. Tomioka, *Mol. Cryst. Liq. Cryst.*, to be published.

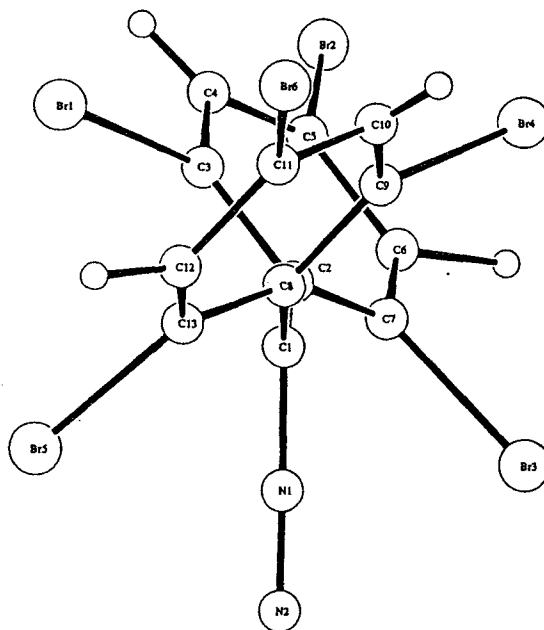


Figure 2 Molecular structure of the diazo precursor of **1**.

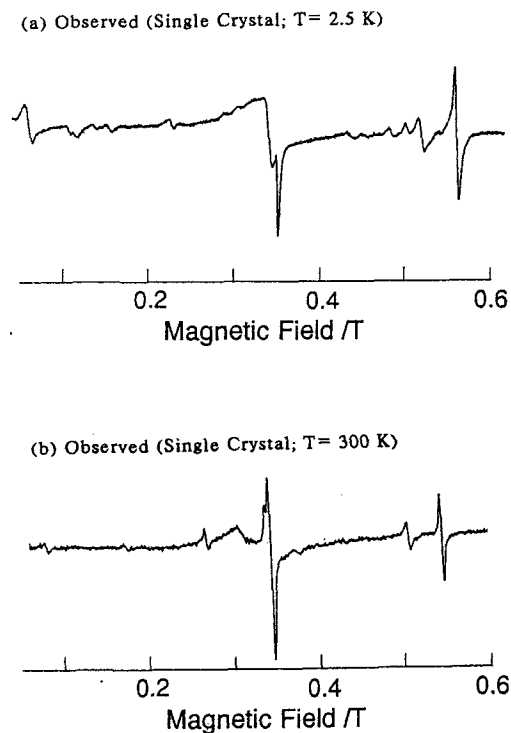


Figure 3 X-band ESR spectra from the triplet state of **1** in the neat crystal of the diazo precursor. (a) $T=2.5\text{K}$ (b) $T=300\text{K}$.

Water Structure and Dynamics in Membranes Studied with Two-dimensional Magic-Angle-Spinning-NMR

Frank Volke¹, André Pampel¹, Richard Scott² and Andreas Bick²

University of Leipzig, Physics, Biomembranes, Linnestr.5, D-04103Leipzig, Germany (1)
and Molecular Simulations Inc., Cambridge, U.K. (2)

It is important to get with non-crystallographic means the 3D structure of biological and model-membranes and biological active molecules interacting with the membrane, like proteins, peptides and as presented in this work, nonionic surfactants which are used for membrane-protein crystallization. The proton-NMR of multilamellar phospholipid-water dispersions (modelmembranes) shows broad featureless lineshapes /1/ with no resolution of all the individual segments of the lipids.

Using MAS /2/ (BRUKER, MSL 500, 4 to 10kHz spinning) several segments of the lipid matrix as well as of the membrane guest molecules are resolved. For some systems like C₁₂EO₄ (dodecyltetra-ethylenoxidether), which forms lamellar model membrane structures, and other surfactants even the J-coupling of adjacent proton pairs can be resolved, giving additional means for structure evaluation /3/.

Having this high-resolved 1D spectra well known 2D-NMR-techniques like NOESY and COSY can be applied to extract structural information from cross-peak data. For a multilamellar phospholipid-water dispersion (POPC, Dipalmitoyl-phosphatidylcholine) there are negative cross peaks of the water resonance with several segments of the polar lipid headgroup, the glycerol backbone and some segments of the fatty acid chains. The negative sign is in accordance with water correlation times as obtained from deuterium NMR of D₂O and PFG (pulsed field gradient)-NMR /4,5/. If the nonionic surfactant C₁₂EO₄ is added (2 mol POPC/ mol surfactant) water cross peaks have only positive signs. Some cross peaks of surfactant segments with the lipid matrix are observed, too. Together with results from ¹³C-MAS NMR using the same systems, it could be shown, the surfactant dehydrates the lipid and that part of the polar chain of the surfactant is placed within the hydrophobic region of the membrane. This is evident by 1) T₁ relaxation time measurements (¹³C, natural abundance), 2) study of the isotropic chemical shift of the carbonyl group as a function of water content with and without the surfactant.

Using an equimolar mixture of chain perdeuterated and headgroup-perdeuterated lipids we could show, that cross-peaks of lipids themselves are also of intermolecular origin. Spin diffusion seems not to play an important role. Such processes may be decoupled by fast segmental reorientations, especially between the chains and the head groups proton reservoir.

There is a lot of structural information in the intra-and intermolecular cross peaks of the matrix as well as of the guest molecules and the matrix including water. Therefore we used the NOE distance constraints (0.25 to 0.4 nm) to get a 3D image of the membrane including water. Software from Molecular Simulation Inc. was used including Quanta, Charm, Cerius2.

This approach opens a new field of studying membrane proteins in natural membrane surrounding. Such investigation may yield structures which than can be compared with structures determined in solution or micelles.

Studies on small polypeptides interacting with membranes are in progress in our laboratory.

(Part of this material was published in Biophysical Journal 68(1995) 1960).

References

- /1/ Bloom, M. et al., J. Chem.Phys. 66(1977)3012
- /2/ Forbes, J. et al., J.Am.Chem.Soc. 110(1988)1059
- /3/ Volke,F., Pampel,A., Biophys.J. 68(1995) 214 and 1960
- /4/ Volke, F.et al., Chem.Phys.Lipids 70(1994) 121
- /5/ Otting,G.et al., Science 245(1991) 974

Calendar of Forthcoming Conferences in Magnetic Resonance

March 1-3, 1996

1996 Structural Biology Symposium, Galvez Hotel, Galveston, Texas

For information contact:

Dr. David G. Gorenstein
Jacqueline Luxon
University of Texas Medical Branch
Sealy Center for Structural Biology
301 University Boulevard, Route 1157
Galveston, TX 77555-1157
Phone: 409-747-6800
Fax: 409-747-6850
Internet: jacky@nmr.utmb.edu

March 17-22, 1996

37th Experimental Nuclear Magnetic Resonance Conference, The Asilomar Conference Center, Pacific Grove, California (USA)

For information contact:

ENC
1201 Don Diego Avenue
Santa Fe, NM 87505
Phone: 505-989-4573
Fax: 505-989-1073

July 22-25, 1996

NMR Symposium at the 38th Rocky Mountain Conference on Analytical Chemistry, Hyatt Regency in downtown Denver, Colorado (USA)

The program will consist of invited lectures and contributed papers for oral and poster presentations on NMR research in areas such as solid-state NMR, spin dynamics, new techniques, macromolecules, solid-state chemistry, calculations/simulations, environmental science and geochemistry.

Each year, a half-day session of the NMR Symposium is dedicated to the memory of Professor

Robert Vaughan. The 1996 Vaughan Memorial lecturer will be Professor Gary Maciel, Department of Chemistry, Colorado State University.

The NMR Symposium is organized by Joel Garbow - chair, James Yesinowski - co-chair, Lucio Frydman, Bernie Gerstein, Clare Grey, Jeffrey Reimer, Hans Thomann and Robert Wind.

For information contact:

Joel R. Garbow
Monsanto Corporate Research
Monsanto Company
700 Chesterfield Parkway North
S. Louis, MO 63198
Phone: 314-537-6004
Fax: 314-537-6806
Internet: jrgarb@snc.monsant.com

August 18-23, 1996

17th International Conference on Magnetic Resonance in Biological Systems, Keystone, Colorado (USA)

For information contact:

Conference Office
1201 Don Diego Avenue
Santa Fe, NM 87505
Phone: 505-989-4573
Fax: 505-989-1073

February 5-7, 1996

Conference on NMR - A Tool for Biology, Paris, France

For information contact:

Simon Mergui (Varian)
e-mail, sm14@calvanet.calvacom.fr
Muriel Delepierre (Institut Pasteur)
e-mail, muriel@pasteur.fr

The editor would be pleased to receive notices of future meetings in the field of magnetic resonance so that they could be recorded in this column.

Instructions for Authors

Because of the ever increasing difficulty of keeping up with the literature there is a growing need for critical, balanced reviews covering well-defined areas of magnetic resonance. To be useful these must be written at a level that can be comprehended by workers in related fields, although it is not the intention thereby to restrict the depth of the review. In order to reduce the amount of time authors must spend in writing we will encourage short, concise reviews, the main object of which is to inform non-experts about recent developments in interesting aspects of magnetic resonance.

The editor and members of the editorial board invite reviews from authorities on subjects of current interest. Unsolicited reviews may also be accepted, but prospective authors are requested to contact the editor prior to writing in order to avoid duplication of effort. Reviews will be subject to critical scrutiny by experts in the field and must be submitted in English. Manuscripts should be sent to the editor, Dr. David G. Gorenstein, Department of Human Biological Chemistry & Genetics, The University of Texas Medical Branch, Galveston, Texas 77555 USA. (409) 747 6800. Fax No. (409) 747 6850.

MANUSCRIPTS must be submitted in triplicate (one copy should be the original), on approximately 22×28 cm paper, type-written on one side of the paper, and double spaced throughout. If the manuscript cannot be submitted on computer tapes, floppy disks, or electronically (see below), please type with a carbon ribbon using either courier 10 or 12, gothic 12, or prestige elite type face with 10 or 12 pitch. All pages are to be numbered consecutively, including references, tables, and captions to figures, which are to be placed at the end of the review.

ARRANGEMENT: Considerable thought should be given to a logical ordering of the subject matter and the review should be divided into appropriate major sections, and subsections, using Roman numerals, capital letters, and Arabic numerals respectively. A table of contents should be included.

TABLES: These are to be numbered consecutively in the text with Arabic numerals. Their place of insertion should be mentioned in the text, but

they are to be placed in order at the end of the paper, each typed on a separate sheet. Each table should be supplied with a title. Footnotes to tables should be placed consecutively, using lower case letters as superscripts.

FIGURES are also to be numbered consecutively using Arabic numerals and the place of insertion mentioned in the manuscript. The figures are to be grouped in order at the end of the text and should be clearly marked along the edge or on the back with figure number and authors' names. Each figure should bear a caption, and these should be arranged in order and placed at the end of the text. Figures should be carefully prepared in black ink to draftsman's standards with proper care to lettering (typewritten or freehand lettering is not acceptable). Graphs should include numerical scales and units on both axes, and all figures and lettering should be large enough to be legible after reduction by 50-60%. Figures should be generally placed on sheets of the same size as the typescript and larger originals may be handled by supplying high-contrast photographic reductions. One set of original figures must be supplied; reproduction cannot be made from photocopies. Two additional copies of each figure are required. Complex molecular formula should be supplied as ink drawings.

REFERENCES to the literature should be cited in order of appearance in the text by numbers on the line, in parentheses. The reference list is to be placed on separate sheets in numerical order at the end of the paper. References to journals should follow the order: author's (or authors') initials, name, name of journal, volume number, page, and year of publication. The abbreviation of the journal follows that used in the Chemical Abstracts Service Source Index. References to books should include in order: author's (or authors') initials, name, title of book, volume, edition if other than the first, publisher, address, date of publication, and pages.

FOOTNOTES should be used sparingly and only in those cases in which the insertion of the information in the text would break the train of thought. Their position in the text should be marked with a superscript Arabic numeral and the footnotes should be typed at the bottom of the relevant page in the text, separated from the latter by a line.

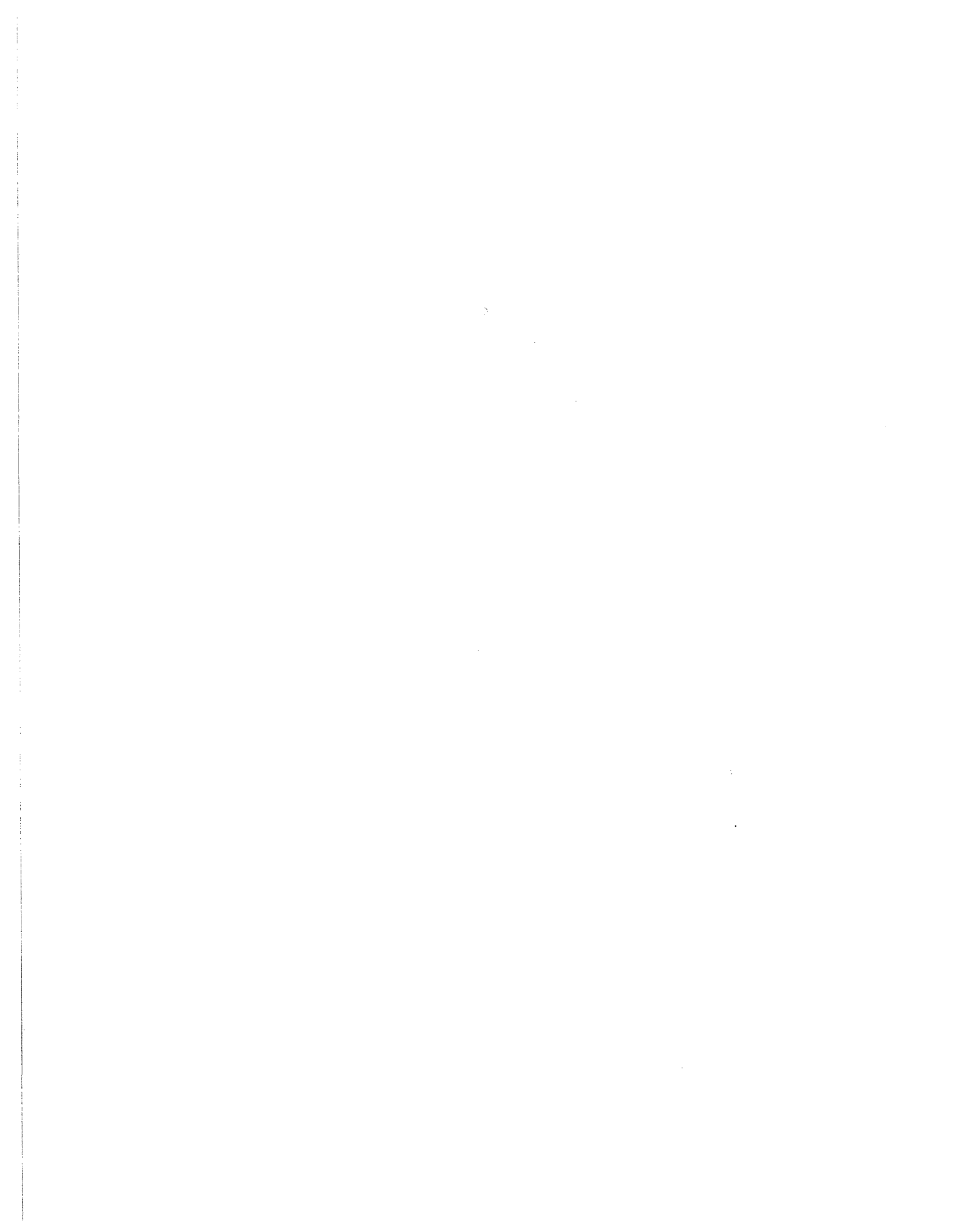
SYMBOLS AND ABBREVIATIONS:

Mathematical symbols should be typewritten wherever possible. Greek letters should be identified in pencil in the margin. In reviews containing a number of mathematical equations and symbols, the author is urged to supply a list of these on a separate sheet for the assistance of the printer; this will not appear in print. Standard abbreviations will follow the American Chemical Society's HANDBOOK FOR AUTHORS names and symbols for units.

PERMISSIONS: It is the responsibility of the author to obtain all permissions concerned with the reproduction of figures, tables, etc, from copyrighted publications. Written permission must be obtained from the publisher (not the author or editor) of the journal or book. The publication from which the figure or table is taken must be referred to in the reference list and due acknowledgement made, e.g. reprinted by permission from ref. (00).

REPRINTS: Thirty reprints of a review will be supplied free to its senior author and additional reprints may be purchased in lots of 100.

INSTRUCTIONS FOR SUBMITTING MANUSCRIPTS ON FLOPPY DISKS OR ELECTRONICALLY: If you have used a word processor to type your manuscript, please forward your manuscript after review and revision, in a computer readable form. Floppy disks or tapes readable on IBM, DEC, SUN, Silicon Graphics, or MacIntosh computers are acceptable. For direct submission over the phone lines use 300 - 9600 baud ASCII transmission. Submission via e-mail (address david@nmr.utmb.edu) is also recommended. Additional details will be provided for the appropriate hand-shake requirements. Please supply us with the code for interpreting superscripts, greeks, etc. on your word processor.



**INTERNATIONAL SOCIETY OF MAGNETIC RESONANCE
(ISMAR)**

MEMBERSHIP APPLICATION AND CALL FOR DUES

Name and Address (Telephone & Fax numbers, e-mail) of ISMAR Member

If this is a new membership application, please check box

If you wish to be registered as a member of the Division of Biology and Medicine,
in addition to ISMAR itself at no extra charge, please check box.

MEMBERSHIP DUES (Yearly)

Regular Member \$25.00
Bona Fide Student \$10.00

1994 \$ _____
1995 \$ _____
1996 \$ _____
1997 \$ _____

SUBSCRIPTION TO "BULLETIN OF MAGNETIC RESONANCE" (Yearly)

ISMAR Members \$30.00
Non-Members \$90.00
Libraries \$90.00

Volume 16 (1994) \$ _____
Volume 17 (1995) \$ _____
Volume 18 (1996) \$ _____

TOTAL \$ _____

**Send this completed form with your
check in US\$ made payable to**

(or)

**Provide your
Mastercard or Visa Account**

International Society of Magnetic Resonance

Prof. Regitze R. Vold, Treasurer
Chemistry & Biochemistry
University of California, San Diego
9500 Gilman Drive
La Jolla, CA 92093-0359 USA

(619) 534-0200; FAX (619) 534-6174
e-mail: rrvold@ucsd.edu

_____ Mastercard _____ Visa

Account # _____

Expires on _____
(month/year)

Signature _____

(Do not wire funds. They will no longer be accepted)